Bhupendra Prakash Sharma
G. Srinivasa Rao
Sumit Gupta
Pallav Gupta
Anamika Prasad   *Editors*

Advances in Engineering Materials

Select Proceedings of FLAME 2020

Springer

Lecture Notes in Mechanical Engineering

Bhupendra Prakash Sharma · G. Srinivasa Rao ·
Sumit Gupta · Pallav Gupta · Anamika Prasad
Editors

Advances in Engineering Materials

Select Proceedings of FLAME 2020

🌐 Springer

Editors
Bhupendra Prakash Sharma
Department of Mechanical Engineering
Amity School of Engineering
and Technology
Noida, Uttar Pradesh, India

Sumit Gupta
Department of Mechanical Engineering
Amity School of Engineering
and Technology
Noida, Uttar Pradesh, India

Anamika Prasad
Department of Mechanical Engineering
South Dakota State University
Brookings, SD, USA

G. Srinivasa Rao
Department of Mechanical Engineering
Amity School of Engineering
and Technology
Noida, Uttar Pradesh, India

Pallav Gupta
Department of Mechanical Engineering
Amity School of Engineering
and Technology
Noida, Uttar Pradesh, India

Preface

This book gets together the pool of cutting-edge research articles on different aspects of engineering materials from the Second International Conference on Future Learning Aspects for Mechanical Engineering (FLAME 2020), which was organized by the Department of Mechanical Engineering, Amity School of Engineering and Technology, Amity University, Uttar Pradesh, Noida, India, from August 5 to 7, 2020. The key role of this conference was to lay a platform that brings academicians, industrialists, scientists, and researchers across the globe together to share their innovative ideas and vision in the areas of thermal, design, industrial, production, materials, and interdisciplinary areas of mechanical engineering. FLAME 2020 played a vital role to set up a bridge between academics and industries. The conference hosted almost 600 participants to interchange scientific ideas. During the 3 days of the conference, researchers from academica and industry offered the most recent cutting-edge findings and went through several technical brainstorm sessions and panel discussions, where they exchanged ideas on practical socioeconomic topics and on the theme "How to Frame the Industry Academia collaboration for "ATMANIRBHAR BHARAT." This conference also provided an opportunity to establish a network for joint collaboration between academicians and industries. Major emphasis was on the recent developments and innovations in various fields of mechanical engineering through plenary and keynote lectures. The book gives an overview of recent developments in the field of engineering materials and covers theoretical and experimental processing and development of noble or composite materials, chemical and mechanical characterizations, and microstructural studies. The book is primarily intended for researchers and professionals working in the field of engineering materials. Experts working in the field of materials will be able to evaluate and differentiate all materials or material combinations currently in use whether they are metals, ceramics, polymers, semiconductors, or composites. The success story of this event from begining to outcome in the form of book can not be completed without acknowledgements. Therefore, we would like to acknowledge all the participants who have contributed to this volume. We also deeply express our gratitude for the generous support provided by Amity University, Noida. We also thank the publishers and every staff of the department and institute who have directly or indirectly assisted to accomplish this goal. Finally, we would also like to express gratitude to the respected

Founder President, Amity University, Uttar Pradesh, Dr. Ashok K. Chauhan, for providing all kinds of support and blessings.

In spite of sincere care, there might be typos and always a space for improvement. We would appreciate any suggestions from the reader for further improvements in this book.

Noida, India	Dr. Bhupendra Prakash Sharma
Brookings, USA	Dr. Anamika Prasad
Noida, India	Dr. Pallav Gupta
Noida, India	Dr. Sumit Gupta
Noida, India	Dr. G. Srinivasa Rao
2020	

About This Book

This book comprises select proceedings of the International Conference on Future Learning Aspects of Mechanical Engineering (FLAME 2020). The book gives an overview of recent developments in the field of engineering materials and covers theoretical and experimental processing and development of noble or composite materials, chemical and mechanical characterizations, and microstructural studies. The book is primarily intended for researchers and professionals working in the field of engineering materials. The researchers, working in the area of material science and engineering will be able to evaluate and differentiate all materials or material combinations currently in use such as smart materials, bio-materials, non-metals, metals, ceramics, polymers, semiconductors, or composites. Also, this book will help the working professionals to comprehend the structure of a material for determining its characteristics and how it subsequently works in technological applications. Materials characterization techniques, which emphasize practical applications and real-world case studies, introduce the principles of commonly used, sophisticated surface, and structural characterization methods for quality assurance, contamination control, and process improvement are the key content of this volume. This volume of the book:

- Explores science procedures for characterizing materials using contemporary techniques
- Analyzes the performance of materials under circumstances of use
- Focuses on interrelationships and interdependence between processing, structure, characteristic, and performance
- Details of the advanced tools engaged in an interdisciplinary approach to understanding the broad variety of interrelationships with processes, mechanisms, and materials
- Covers electron, X-ray photoelectron, and UV spectroscopy; scanning electron, atomic power, transmission electron, and laser confocal scanning fluorescent microscopy; and gel electrophoresis chromatography
- Presents the basics of vacuum as well as the principles of X-ray diffraction.

The writers omit long and often intimidating derivations and formulations to explain suitable uses and associated technical specifications for characterization methods. Rather, they highlight helpful fundamental concepts and applications of contemporary techniques used to characterize engineering materials, helping readers to understand micro- and nanoscale characteristics.

Contents

About the Editors

Dr. Bhupendra Prakash Sharma Associate Professor, Department of Mechanical Engineering, Amity School of Engineering and Technology Noida, Amity University Uttar Pradesh. He has completed his Ph.D. from Motilal Nehru National Institute of Technology Allahabad, Prayagraj, Uttar Pradesh India in 2013 and passed Master of Engineering in Automated Manufacturing Systems from Birla Institute of Technology Mesra, Ranchi in 2007. He has more than twelve years of teaching and research experience at private and government institutes and universities. He has contributed more than 50 papers at the national/international levels with two best paper awards and filed four patents as well. His current areas of interest include manufacturing systems, analysis and processing of composite materials, recyclability, circular economy and knowledge management.

Dr. G. Srinivasa Rao is working as an Assistant Professor III in the Department of Mechanical Engineering, Amity School of Engineering and Technology Noida, Amity University Uttar Pradesh. He has completed his Ph.D. from Jawaharlal Nehru Technological University, Kakinada, Andhra Pradesh India in 2016 and passed Master of Technology in Production Engineering from Acharya Nagarjuna University in 2006. He has more than thirteen years of teaching and research experience at private colleges and universities. He has published more than 20 papers in international conferences and journals. His current areas of interest include the welding of aluminium alloys, corrosion and composite materials.

Dr. Sumit Gupta is an Assistant Professor in the Department of Mechanical Engineering, Amity School of Engineering and Technology (ASET), Noida. He is graduated in Mechanical Engineering from University of Rajasthan in 2008 and earned Master's and Doctorate degree from Malaviya National Institute of Technology Jaipur in 2010 and 2016 respectively. He has 10 years of teaching, research and Industry experience. He has published more than 30 research papers in various national and international journals & conferences and delivered invited lectures at various forums. He is Reviewer of various national and International Journals. His areas of research are sustainable manufacturing, lean manufacturing, Industry 4.0, sustainable product design, sustainable supply chain management and sustainable composite materials. He is a member of various International & National professional Societies.

Dr. Pallav Gupta completed his M.Tech. and Ph.D. from Indian Institute of Technology (Banaras Hindu University), Varanasi (INDIA) in year 2011 and 2015 respectively. Since then he is working as an Assistant Professor in Department of Mechanical Engineering, Amity School of Engineering and Technology, Amity University Uttar Pradesh, Noida (INDIA). He has published more than 75 research papers in reputed journals and conferences. He has also published 06 chapters in books published by Springer. His area of research includes Material Processing; Composite Materials; Metal Matrix Nanocomposites; Coatings/Nanocoatings; Wear; Deformation and Corrosion.

Dr. Anamika Prasad is working as an Assistant Professor with Department of Mechanical Engineering at South Dakota State University, USA. Before this position, she worked Visiting Asst. Prof, Institute of Technology, University of Washington Tacoma. She, also, worked as an Assistant Professor in the department of applied mechanics, Indian Institute of Technology Delhi, Applied Mechanics. She completed her Ph.D. from Massachusetts Institute of Technology in 2007. Her research areas are Materials Science, Biomaterials, Biomedical devices, Solid Mechanics, Mechanical

Testing. She got Gandhian Young Technological Innovation -Technical Edge Appreciation award in 2015. She received Indian patent for A Novel Device for Measuring Pressure Pulses based on Applanation Tonometry.

Challenges and Opportunities in Synthesis of Hybrid Cu-Al$_2$O$_3$-C and Cu-ZrO$_2$-C Composites Through Stir Casting Route

Prateek Mittal, Shailesh Singh Sengar, Sorabh, Mani Kant Paswan, Jimmy Mehta, Dinesh Chawla, and Pallav Gupta

Abstract Composites have been used by mankind from ages in producing different tools and equipment. Metal matrix composites became popular due to their better mechanical and thermo-physical properties as compared to pure metals and alloys. The aim of the present study is to highlight the key challenges in the synthesis of copper matrix-based hybrid Cu-Al2O3-C and Cu-ZrO2-C composites through stir casting route. The reinforcement varied in composition from 1 wt to 4 wt%. Stir casting as a process for synthesis of metal matrix composites (MMCs) has gained popularity due to its cost effectiveness and simplicity. Stir casting involves the mixing of reinforcement with the molten metal matrix through stirring in a furnace and then pouring it in a die for solidification. This liquid metal process requires careful execution and control over the parameters in order to produce the high quality MMCs. Stir

P. Mittal (✉) · S. S. Sengar · Sorabh · J. Mehta · D. Chawla
Department of Mechanical Engineering, Manav Rachna International Institute of Research and Studies, Faridabad, India
e-mail: prateekmittal.fet@mriu.edu.in

S. S. Sengar
e-mail: shaileshsengar@yahoo.com

Sorabh
e-mail: sorabh012@gmail.com

J. Mehta
e-mail: jimmy.fet@mriu.edu.in

D. Chawla
e-mail: dineshchawla.fet@mriu.edu.in

P. Mittal · P. Gupta
Department of Mechanical Engineering, A.S.E.T., Amity University Uttar Pradesh, Noida, India
e-mail: pgupta7@amity.edu

M. K. Paswan
Department of Mechanical Engineering, National Institute of Technology Jamshedpur, Jamshedpur, India
e-mail: mkpaswan.me@nitjsr.ac.in

casting process has some limitations associated with it such as nonuniform dispersion, agglomeration of reinforcement particles, formation of oxides and intermediate phases, porosity and cracks. This paper brings to the fore these limitations and suggests the ways to improve the process so that desired properties can be obtained in the composite. This work also generates the opportunities for the development of new and innovative alternatives to overcome the challenges associated with stir casting in synthesis of MMCs.

Keywords Stir casting · Copper matrix composites · Hybrid MMCs · Composite materials · Metal matrix composites

1 Introduction

Metal matrix composites (MMCs) have gained a definite edge over pure metals and alloys because of their better mechanical and thermo-physical properties like high strength-to-weight ratio, low coefficient of thermal expansion and good fatigue resistance [1, 2]. The low weight advantage makes them suitable for the structural applications in aerospace industry. Good thermal conductivity with low coefficient of thermal expansion makes the MMCs deployable in various thermal management applications. Stir casting is the technique wherein reinforcement is added to the molten metal while stirring the mix with a stirrer to create a vortex so that the particles are sucked into the metal matrix and distribute uniformly inside it. Once the mix is stirred for the required time, the molten mixture is poured in a mould to obtain the required composite specimen [2]. Stir casting has been rigorously used in the mass production of MMCs due to its cost advantage over other popular methods [2]. Addition of a ceramic reinforcement in the copper (Cu) metal matrix reduces the coefficient of thermal expansion which enables these materials to effectively work as heat sink or thermal reservoir [3]. MMCs having ceramics as reinforcements tend to become very hard due to hard nature of ceramic particles which is why, in recent times, softer reinforcements are also added to strike a balance between the mechanical and other properties of the so formed composite [4]. The MMCs having two or more reinforcement within the metal matrix are called hybrid composites. The ceramic particles when added as reinforcement tend to enhance the tribological behaviour of the composites, but the thermal properties are somehow compromised, moreover the mixing ability of copper with the ceramic particles is very poor [5, 6]. Due to improper mixing of ceramic particles, the properties of the composites tend to be nonuniform [7]. Even after the existing limitations, stir casting is used as a popular method of producing metal matrix composites due to its cost effectiveness and simplicity [8]. The mechanical and wear properties of the composite materials depend to a great extent on the nature of the reinforcement, quantity of the reinforcement, production process and matrix material [9–15]. There are several challenges associated with stir casting process such as intermediate phase formation, crack development, oxidation and agglomeration of reinforcement phase. [16–21].

Challenges such as agglomeration and sedimentation are common in stir casting due to poor wetting capability of metal matrix with ceramic particles and larger contact angles. The uniform distribution of particles can be attained at higher stirring speeds as suggested by research works reported in the past [22, 23]. In this work, alumina and zirconia were chosen as reinforcement for development of materials suitable for heat sink and dental implants, respectively.

2　Methods and Materials

Method used for the fabrication of the composites in this work is stir casting. Stir casting method was chosen as it is economical and simple as compared to other methods like powder metallurgy, liquid infiltration and chemical vapour deposition. The composition of the composites consisted of copper as the base material. In the first system of composites, Al_2O_3 and graphite were used as reinforcements. In the second system, ZrO_2 and graphite were used as reinforcements. The reinforcements varied in composition from 1 wt to 4 wt%. Firstly, the copper ingots with 99% purity level were taken in the crucible and put to melt in the furnace. The reinforcement particles were preheated to 200 °C to remove any moisture content before adding them to the molten copper. Once the copper was melted, then the stirring was started using a mild steel stirrer with four blades. The stirring speed was kept at 300 rpm. After the staring of stirring process, the reinforcement particles were added, and the stirring was continued for about 90 min to create a strong vortex to suck the ceramic particles inside the matrix so that homogenous distribution of reinforcement is obtained in the composite. After stirring the melt, the mixture was poured in a mould of cylindrical shape to obtain the required composite specimen. For preparation of samples, the cast specimens were ground and rubbed with emery paper followed by polishing and etching using a mixture of HCl and water. Table 1 shows the composition of prepared samples.

Table 1 Composition of prepared samples

System of samples	Matrix wt%	Reinforcement wt%
System-1 (4 samples)	Cu (98–92 wt%)	Al_2O_3 (1–4 wt%), Graphite (1–4 wt%)
System-2 (4 samples)	Cu (98–92 wt%)	ZrO_2 (1–4 wt%), Graphite (1–4 wt%)
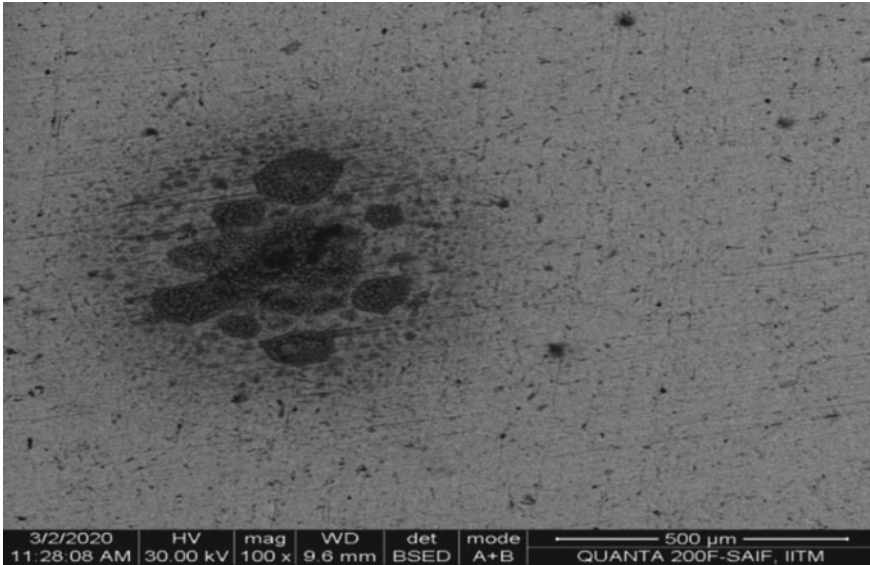
Fig. 1 Agglomeration of reinforcement phase in the metal matrix (Cu-ZrO$_2$-C)

3 Challenges

3.1 *Agglomeration of Reinforcement Phase*

Due to poor mixing between copper matrix and the reinforcement (ceramic particles and graphite), the dispersion of the reinforcement is not uniform, and this promotes the occurrence of agglomeration or formation of clusters of reinforcement phase. Figure 1 shows the image of Cu-ZrO$_2$-C composite wherein agglomeration of ceramic particles is evident with traces of graphite. This agglomeration not only disturbs the homogeneity of the composite but also affects the mechanical and thermo-physical properties [24–27]. This defect in the MMCs prepared by stir casting process can be reduced by the preheating the moulds, dies and reinforcements. Also, addition of some suitable wetting agent like magnesium may yield the desired results.

3.2 *Porosity*

Porosity is another defect which arises in the stir casting process especially with manual pouring. Porosity deteriorates the quality of the metal matrix composites. The small holes according inside the structure of the composites are indicative of the porosity. Porosity leads to weakening of the composites and reduces its endurance

Fig. 2 Porous Cu-ZrO$_2$-C composite formed by stir casting

limit. Figure 2 shows fractured composites indicating the porosity present inside the material. The primary reason for this porosity is intermittent pouring and entrapment of environmental gases. When the material is poured in the mould or die and the pouring is discontinued even for a short span, then porosity may occur due to differential solidification of the poured material. This defect can be avoided by using shielding gas like argon or carbon dioxide and automatic pouring or automation of the complete stir casting process.

3.3 Oxidation

Molten metal has high tendency to get oxidized. In the fabrication of MMCs through stir casting, the chances of the melt being oxidized are high during pouring as reported by Jamwal et al. [2]. This oxidation of the molten mix can be avoided by using an inert environment by any shielding gas like argon or carbon dioxide. The oxide phase is undesirable and can be detected in patterns obtained after X-ray diffraction (XRD) of the composite samples. Jamwal et al. [2] reported the presence of oxide phase in the hybrid copper composite samples containing SiC and graphite as the reinforcement phase in the peaks of the XRD pattern. Figure 4 shows the SEM micrograph of the defect-free specimens produced through stir casting route in the presence of argon gas as shielding agent.
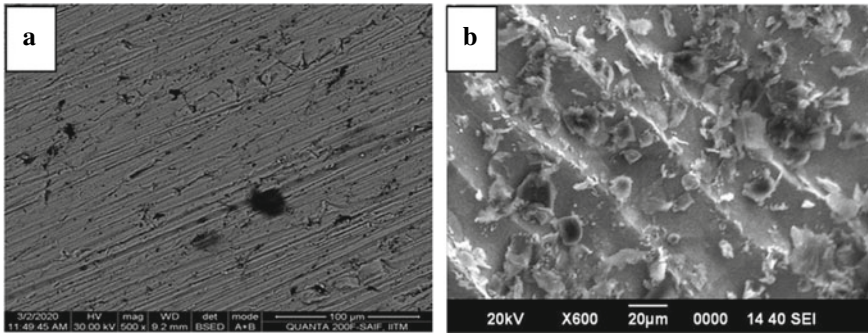
Fig. 3 SEM micrographs of **a** Cu-ZrO$_2$-C & **b** Cu-Al$_2$O$_3$-C composites fabricated through stir casting

3.4 Cracks

Cracks occur in the fabrication of MMCs through stir casting due to variable heat transfer rate during cooling and solidification. This could take place as a result of large difference between mould temperatures and melt temperatures. Also, the improper dispersion of the reinforcement phase in the metal matrix is another reason for crack formation. It has been observed that due to high temperature interaction between reinforcement and matrix material sometimes a new unwanted phase is formed and deters the formation of a strong interfacial bond between reinforcement and matrix. These aforementioned possible reasons of the cracks occurring in the MMCs may be addressed by stirring for longer periods, thereby creating a strong vortex to suck the reinforcements inside the molten matrix. Also, preheating the moulds and reinforcement is one of the ways to avoid cracks. Figure 3 shows a SEM micrograph showing crack in Cu-Al$_2$O$_3$-C hybrid MMC.

4 Opportunities

The limitations of the stir casting process create new opportunities in the development of novel techniques and processes to enhance the quality of composites produced through stir casting. The processes may be modified, or a combination of two or more processes may be used in order to obtain the right quality of hybrid metal matrix composites. The opportunities lie in the following areas:

- Simple shielding environments during fabrication of MMCs to avoid oxidation;
- Stirrer geometries, speeds and materials for different MMCs;
- Pouring techniques to avoid differential solidification;
- Development of new materials which may be added as wetting agents so as to increase the interfacial bonding between metal matrix and reinforcement particles;

Fig. 4 SEM image of crack in Cu-Al$_2$O$_3$-C hybrid MMC

- Quantification of effect of various process parameters on the uniform dispersion of reinforcement particles within the metal matrix.

5 Results and Discussion

After careful examination of the micrographs and other images of composite samples with varied compositions of reinforcement, it has been found that agglomeration of ceramic particles occurs at lower stirring speeds and tends to reduce with the increase in speed. Figure 2 indicates the agglomeration of reinforcement in Cu-ZrO$_2$-C composite samples. The cracks and porosity in the samples may occur due to entrapment of atmospheric gases or differential solidification or impurities being mixed due to forced vortex created at the time of stirring. Figure 3a, b indicate the porosity and cracks in the composite samples of Cu-ZrO$_2$-C and Cu-Al$_2$O$_3$-C specimens, respectively. The use of shielding gas was found to eliminate the formation of oxides and intermediate phases as indicated in the SEM micrographs in Fig. 4.

6 Conclusions

Based on the study of the hybrid copper composites fabricated through stir casting, the following conclusions can be drawn regarding the challenges that may affect the quality of the composites and the opportunities that lie underneath:

- Although stir casting is an economically superior method as compared to other popular methods of fabricating MMCs, it poses some challenges pertaining to the quality of the composites.
- Density difference, wettability factors and stirring parameters affect the distribution of ceramic particles in the metal matrix and interfacial bonding. This can be improved by preheating the reinforcement and using some suitable wetting agent.
- Use of shielding gas like argon reduces the formation of oxides, gas entrapment and impurities in the MMC which contributes to the improvement in properties of the formed composites.
- Cracks and porosity can be eliminated by preheating the mould, continuous pouring and eliminating differential solidification.
- Development of more suitable and precise alternatives apart from the ones mentioned in this paper to address the challenges in stir casting paves the way towards new opportunities in this area for future researchers.

References

1. Miracle, D. B. (2005). Metal matrix composites–from science to technological significance. *Composites Science Technology, 65*(15–16), 2526–2540.
2. Jamwal, A., et al. (2019). Microstructure, wear and corrosion characteristics of Cu matrix reinforced SiC–graphite hybrid composites. *Journal of Composite Materials, 53*(18), 2545–2553.
3. Schubert, T., et al. (2008). Interfacial design of Cu-based composites prepared by powder metallurgy for heat sink applications. *Materials Science and Engineering A, 475*(1–2), 39–44.
4. Ramesh, C. S., et al. (2009). Development and performance analysis of novel cast copper–SiC–Gr hybrid composites. *Materials and Design, 30*(6), 1957–1965.
5. Zhan, Y., & Zhang, G. (2003). The effect of interfacial modifying on the mechanical and wear properties of SiCp/Cu composites. *Materials Letters, 57*(29), 4583–4591.
6. Ibrahim, I. A., et al. (1991). Particulate reinforced metal matrix composites—a review. *Journal of materials science, 26*(5), 1137–1156.
7. Tang, Y., Yang, X., Wang, R., & Li, M. (2014). Enhancement of the mechanical properties of graphene–copper composites with graphene–nickel hybrids. *Materials Science and Engineering A, 599*, 247–254.
8. Valibeygloo, N., Khosroshahi, R. A., & Mousavian, R. T. (2013). Microstructural and mechanical properties of Al-4.5 wt% Cu reinforced with alumina nanoparticles by stir casting method. *International Journal of Minerals, Metallurgy and Materials, 20*(10), 978–985.
9. Zhan, Y., & Zhang, G. (2004). Friction and wear behavior of copper matrix composites reinforced with SiC and graphite particles. *Tribology Letters, 17*(1), 91–98.
10. Zhan, Y., & Zhang, G. (2006). The role of graphite particles in the high-temperature wear of copper hybrid composites against steel. *Materials and Design, 27*(1), 79–84.
11. Gupta, P., et al. (2018). Dependence of wear behavior on sintering mechanism for iron-alumina metal matrix nanocomposites. *Materials Chemistry and Physics, 220,* 441–448.
12. Liu, Q., et al. (2019). Wear behavior of copper-graphite composites processed by field-assisted hot pressing. *Journal of Composites Science, 3*(1), 29.
13. Bandil, K., et al. (2019). Microstructural, mechanical and corrosion behaviour of Al–Si alloy reinforced with SiC metal matrix composite. *Journal Composites Materials, 53*(28–30), 4215–4223.

14. Alip, K., et al. (2019). Microstructural and mechano-tribologicalbehavior of Al reinforced SiC-TiC hybrid metal matrix composite. *Materials Today Proceedings.*
15. Nayim, S. M. T. I., et al. (2019). Effect of CNT and TiC hybrid reinforcement on the micro-mechano-tribo behaviour of aluminium matrix composites. *Materials Today Proceedings.*
16. Sohag, M. A. Z., et al. (2019). Effect of ceramic reinforcement on the microstructural, mechanical and tribological behavior of Al-Cu alloy metal matrix composite. *Materials Today Proceedings.*
17. Gupta, P., et al. (2016). Effect of height to diameter (*h*/*d*) ratio on the deformation behaviour of Fe–Al_2O_3 metal matrix nanocomposites. *Bulletin Materials Science, 39*(05), 1245–1258.
18. Kumar U. J. P., Gupta, P., & Jha, A. K., et al. (2017). Closed die deformation behavior of cylindrical iron–alumina metal matrix composites during cold sinter forging. *Journal of the Institution of Engineers (India): Series D, 98*(01), 155–155.
19. Gupta, P., et al. (2013). Structural and mechanical behaviour of 5% Al_2O_3-reinforced Fe metal matrix composites (MMCs) produced by powder metallurgy (P/M) route. *Bulletin Materials Science*, *36*(05), 859–868.
20. Jamwal, A., et al. (2020). Towards sustainable copper matrix composites: Manufacturing routes with structural, mechanical, electrical and corrosion behaviour. *Journal Composites Materials*, 0021998319900655.
21. Mittal, P., et al. (2017). Solving VRP in an Indian Transportation Firm through Clark and Wright Algorithm: A Case Study. *International Journal of Emerging Technologies in Engineering Research (IJETER)*, 5.
22. Yigezu, B. S., et al. (2013). The key attributes of synthesizing ceramic particulate reinforced Al-based matrix composites through stir casting process: A review. *Materials and Manufacturing Processes, 28*(9), 969–979.
23. Ambhai, K. G. (2007). *Study on machinability of Al-SiC particulate metal matrix composite.* IIT Roorkee: Ph.D theses; Metalergical Engineering Department.
24. Jamwal, A., et al. (2020). Microstructural, tribological and compression behaviour of copper matrix reinforced with Graphite-SiC hybrid composites. *Materials Chemistry and Physics,* 123090.
25. Ahamad, N., et al. (2020). Phase, microstructure and tensile strength of Al–Al2O3–C hybrid metal matrix composites. *Journal Mechanical Engineering Science,* 0954406220909846.
26. Ahamad, N., et al. (2020). Structural and mechanical characterization of stir cast Al–Al2O3–TiO2 hybrid metal matrix composites. *Journal Composites Materials*, 0021998320906207.
27. Barekar, N., et al. (2009). Processing of aluminum-graphite particulate metal matrix composites by advanced shear technology. *Journal of Materials Engineering and Performance, 18*(9), 1230–1240.

Mechanical Characterization of a Fly Ash and Glass Fibers Reinforced Hybrid Epoxy Composite

Sandeep Kumar and Monika Singh

Abstract Epoxy has versatile industrial applications due to its brilliant characteristics, but on the other hand due to the delamination, brittleness, low toughness of epoxy limited its usage. These constraints of epoxy can get over by inclusion with the help of reinforcement before their industrial and aerospace application. In recent days, glass fiber reinforced composites are in demand as structural materials as well as aerospace parts due to low density. Authors have presented the last ten years review articles on different glass fiber composites. The interest of the present study is the focus on the mechanical properties of epoxy hybrid composite, made up of glass fibers, and reinforced with fly ash. Experimental data has been shown by picking various ratios of glass fiber (E-300, MAT form) with epoxy resins and with different composition of fly ash reinforced that fly ash significantly increases hardness as well as compressive strength in epoxy composite.

Keywords Epoxy · Glass fibers (GFRP- glass fibers reinforced polymer) · E-300 MAT form · Fly ash

1 Introduction

Composite materials are constituted of two phases: one is that continuously holds the second phase, i.e., reinforcement. Both phases are not soluble in each other but club together at the macroscopic level [1]. Matrix of epoxy resins are mostly used in fiber-reinforced composites due to their unique balance of chemical and mechanical properties versatile nature in material processing [2]. Due to specific strength, glass fibers reinforced material is most widely applicable in complex structural assemblies [3].

Epoxy resins are one of the best members of plastic group [4]. Epoxy composites have numerous applications in structural industry as well as automobiles and aircraft.

S. Kumar · M. Singh (✉)
Department of Mechanical Engineering, MIT Moradabad, Moradabad 244001, India
e-mail: m_singh@me.iitr.ac.in

S. Kumar
e-mail: sandeep.sun.varshney@gmail.com

Epoxy resins, depends on the microstructure, can be liquids as well as solids with low and high viscosities [5]. Epoxy resins have excellent electrical properties, high toughness, and good adhesion to many meals with high resistance to moisture. These qualities of epoxy resins are the main reason for their wide applications in composite materials [6]. High pressure and high temperature are required to impregnate the fibers with highly viscous resins, although fibers with low viscosity resins do not require high pressure and temperature to impregnate [7].

Nowadays, hybrid epoxy-based composites are getting attraction of researchers because of brilliant mechanical, chemical qualities as well as these are good as environmental concerns and as well as their wide structural applications [8]. The use of natural fibers is increasing day by day as government regulations are also focusing on environmental issues. The center of the study is the mechanical properties of hybrid fiber consisting of glass fibers and fly ash as a filler material [9].

Glass fiber reinforced polymer, i.e., GFRP, has high corrosion resistance, high strength, and low value of modular elasticity. While, glass and other synthetic fibers have high stiffness and specific strength but due to the high cost of producing its use is still limited [10]. Glass fibers have wide application in mechanical joints due to their special physical and mechanical properties [11]. In recent era, natural fibers such as jute, vegetable waste, and cotton are using at the place of glass and carbon fibers [12]. Glass fiber provides the basic structures to the composite material, and fly ash enhances the mechanical and physical properties of the composite [13]. Nowadays, the use of glass fibers is very common in the production of composite [14]. However, the addition of fly ash as filler material gives more environmental friendliness to this hybrid composite. From different researches, it has been shown that the fly ash as the particulate filler can make the composite more compact as well as more compressive because of filling more voids in composite and glass fiber as fiber reinforcement gives directional properties to the composite [7].

The aim of this work is to fabricate a hybrid reinforced composite and testing out its mechanical and physical properties. All the mechanical tests and fabrication of composite have been done in the laboratory of material science in mechanical engineering at MIT Moradabad.

2 Material Used and Fabrication of Hybrid Composite Specimen

Fabricated reinforced composite constituent's fiberglass (matt form) as reinforced and fly ash as filler material. An industrial purposed epoxy resin named "ARALDITE LY556" is used to create acoustic bonding between fly ash and glass fibers. Epoxies are typically cured with stoichiometric or near-stoichiometric quantities of curative to achieve maximum physical properties. To solidify the epoxy resins and matt structure of glass fiber curing agent, "HY951" was used which is manufactured by Araldite. Curing is a process of hardening and toughening of polymers by cross-linking of

Fig. 1 Fiber glass matt form
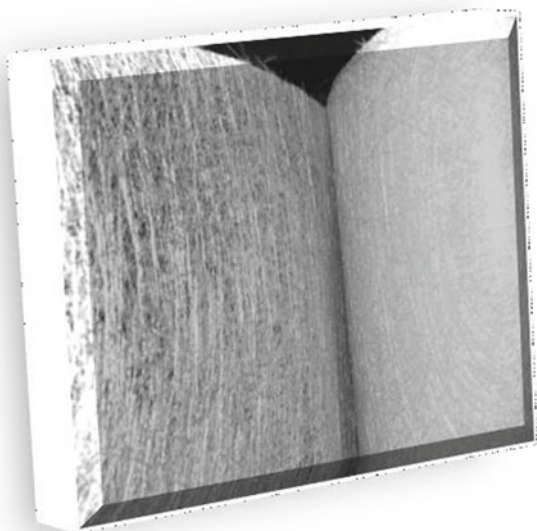
chemical chains and creating an acoustic bond between them. It is very important to select the proper content of hardener to cure the matrix. Quality of curing is based on the position on which hardener is spread out, time for which specimens leave for curing, and the ratio in which hardener is taking. Uniform distribution of resins and temperature and pressure inside are very important parameters to be maintained [15]. In the present study, epoxy resins and hardener are taken in the ratio of 10:1 (Fig. 1).

Matt form glass fibers reinforced polymers consist of glass fibers that haphazardly arranged with the help of binders. The hand layup method is being used for processing, where material sheets are placed and spread with resins. The material easily conforms to various shapes when wetted out due to dissolved binder in resin. After curing of resins, the hardened product is taken out from the mold (Fig. 2).

Chopped strand matt allows a fiber glass with uniform material properties in all direction. Glass fibers are weak in shear loading, and due to its long aspect ratio, fiberglass are also weak in compression, and it buckles easily [14].

GFRP laminates were made by hand layup technique. Curing was performed at a temperature of about 25 °C for about 48 h.

Fly ash is a coal combustion product also called as pulverized fuel ash. It is mainly comprised of the finer particles of fuel that are driven out with the flue gases from coal-fired boilers.

Fly ash contains an amount of SiO_2, Al_2O_3, and CaO as the main compounds depending upon the makeup of the coal being burned [12]. In coal power plants at the boiler outer periphery, some rest part of waste is collected which contained fly ash and bottom ashes [15]. The demand for materials such as fly ash is arising due

Fig. 2 Cross section of fly ash particles at 750 × magnification, microscopic image of MIT laboratory
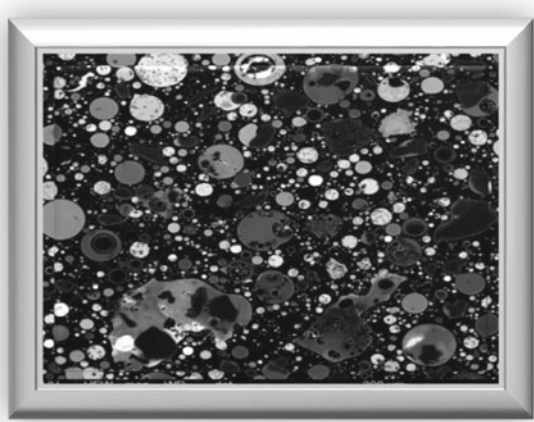
to its lightweight for the development of structures like surfaces of ships. With an increase in the content of fly ash, there is a notable deduction in density, and it makes the composite suitable for applications related to a specific weight. It also increases the modulus and strength of composites.

However, the addition of more fly ash reduces the strength of composite due to the bunching of filler material.

In Britain, fly ash taken from coal has different constituents such as silica (59.5%), alumina (20.3%), FeO/Fe2O3 (6.5%), remaining FeO, MgO, and uncombusted coal, etc. Resistance to tensile and bending flexural stresses of the fly ash/epoxy composite is enhanced by increasing fly ash content, although the mechanical strength (tensile, flexural, and impact strength) continuously decreases with an increase in fly ash volume percentage.

The fiber glass (mat form) was oriented along the mold surface. Then, a specific amount of epoxy is poured into the container, and the ratio of 1/10 hardener is mixed with epoxy. After the proper mix-up of epoxy resins and hardener, the mixer is spread out over the surface of glass fiber. For uniform distribution, rolling is done over the matt. Rolling is done in a proper way to eliminate the chances of voids and trapping of air bubbles. Now, the matt was left for a few minutes to allow the exothermic chemical reactions. The mold was covered with the peel ply film and then mounted over the mold bottom. Around 20 kilograms weights were kept over the mold for curing. After 24 h of curing, the laminate was ejected from the mold using the ejector pins. Now, composite was inspected manually for any voids and extra edges. After this curing step, fly ash is mixed with the epoxy indifferent proportion by weight. Then, the mixture is left to settle down and gain its texture. After this, the mixture and fiber glass are processed by the hand layout process to manufacture the hybrid epoxy composite. Once the mold is ready for the layout process, the fiber glass sheet is oriented over the mold, later the specified amount of the epoxy resin is applied over the glass fiber surface. Then, this layer of epoxy mixture with fly ash is thoroughly applied over rasin using a hand roller (Fig. 3).

Fig. 3 Prepared composites

Then another layer of fiberglass sheet is applied over the layout, and then again, the epoxy and fly ash mixture is rolled over. This process is repeated until the width requirements are met. After this process, the pile is stacked up with a load of 33 kilograms and then left for solidification or setting. After allowing this setting process a prominent amount of time, the cast is removed from the mold. Small pieces are cut off from the casting and then further processed to make them appropriate for the selected test. First the pieces are cut off, and filed to remove the rough surface and provide the consistent surface properties. Some of the specimens (as shown in Fig. 4) are filed and then machined to give them a specific shape required for the mechanical test.

3 Mechanical Test

The newly developed hybrid composites are characterized by different mechanical tests to mark its strengths and weaknesses. As the literature studies tell, there is a visible effect on mechanical properties like strength, resistance to corrosion, and hardness of composite with the different concentration of fly ash [12].

In this experiment, we are going to on the synthesis and study of the deformation behavior of epoxy resin microsphere-based syntactic foams with natural glass fiber. Then, we will examine various mechanical properties of the hybrid composite made up of glass fibers with epoxy resins.
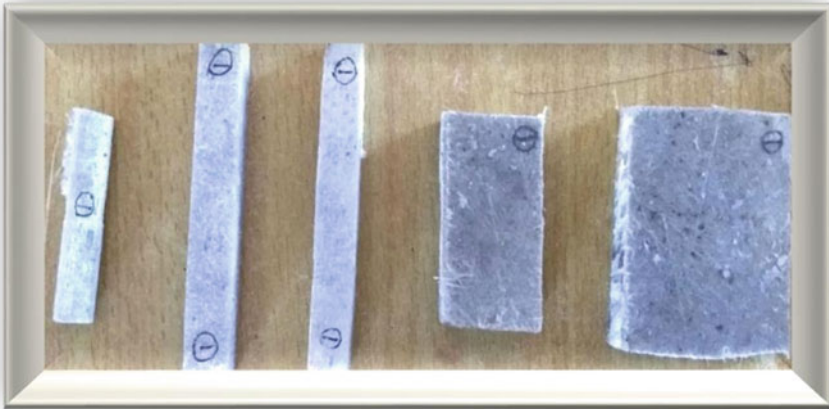
Fig. 4 Prepared specimens

Mechanical properties like hardness, compressive strength, and impact strength are examined by experimental setups available in the laboratory. Different specimen according to fly ash concentration was investigated in all these testing apparatuses.

3.1 Rockwell Hardness Test

Hardness is the ability of a material to resist the indentation, abrasion, and scratching on the surface. The hardness of different fly ash concentrations samples is investigated by the Rockwell hardness test. Rockwell hardness tester having 10–100 kg load-carrying capacity and 1.58 mm ball indenter diameter used to examine hardness results.

3.2 Compressive Test

Compressive strength is the ability of a material to bear the external loading. One can say that it is a load-carrying capacity under compression. In compression test, material undergoes with the external pushing forces from opposite sides. The compressed sample expands in the lateral direction of the applied force by reducing longitudinal dimensions. A universal testing machine was used to examine the compression experiment results. Used machines can also be used to investigate the yield strength, deflection, and modulus.

3.3 *Impact Test*

Impact test is applied to determine the ability of energy absorbed by material under plastic deformation. Impact test gives result according to the specimen geometry as these tests do not give separate material characteristics [11, 12].

An ASTM standard method, i.e., Izod impact testing machine, is used to investigate impact strength under certain loadings and specific height. Sudden fall of arm hit a notched workpiece, and break it. Due to this sudden loading, energy absorbed by the workpiece can be calculated from the height of hitting arm swings. V-typed notched impact test machine was used with an application of 33 kg impact weight.

4   Result and Discussion

As discussed, mechanical testing has been done on the different fly ash concentration specimen. Different trends have been drawn with the results. Table 1 shows the different hardness results with different specimen used (Fig. 5).

Table 1 shows that with increasing fly ash content, hardness strength increases slightly. Table 2 shows the results of compressive test on different specimen (Fig. 6).

Serial number	Fly ash content by weight %	Hardness strength (HRV)
1	0	117
2	5	122
3	10	125
4	15	126
5	20	131

Table 1 Relationship between hardness number and % of fly ash present in composite

Fig. 5 Rockwell hardness test
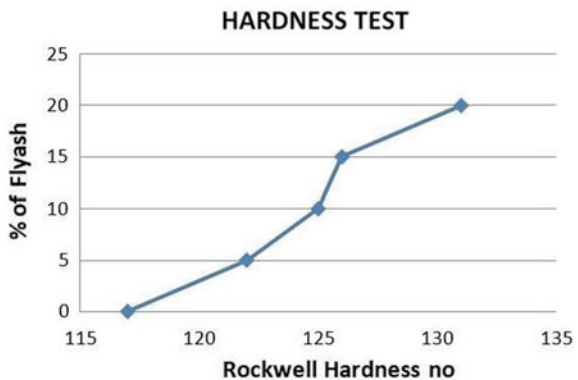
Table 2 Relationship between compressive strength and percentage of fly ash in the composite

S/N	Fly ash content by weight %	Compressive force (Kgf)
1	0	5520
2	5	3200
3	10	5520
4	15	6248
5	20	7520

Fig. 6 Compression test
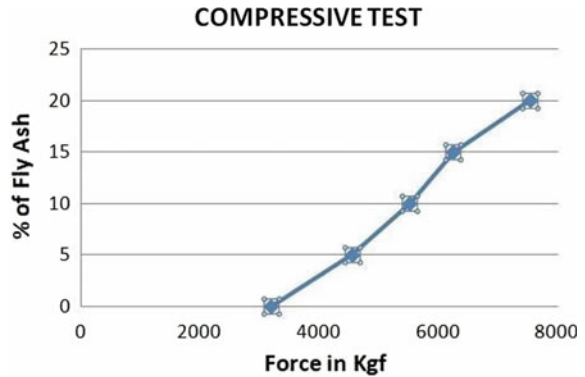
As shown in Table 2, compressive strength of workpiece without fly ash content is good, and it slightly reduced when a little %, i.e., 5%, fly ash is used, but with the increase of fly ash content above 10%, it starts increasing in a great sense. Table 3 shows the results produced by Izod Impact testing machine (Fig. 7).

From Table 3, it is clear that composite losses its impact strength as fly ash content increases. Therefore, higher fly ash content is not desirable; however, compressive strength and hardness give desirable results. Observed decrease in impact energy may be due to the lack of bonding between the fly ash and epoxy resins in the matrix. As some prior study says epoxy systems deliver the higher impact resistance, and they do not exhibit the brittle fracture same as metals.

Table 3 Relationship between impact energy and the percentage of fly ash in the composite

Serial number	Fly ash content by weight %	Impact energy(J)
1	0	10
2	5	8
3	10	6
4	15	5
5	20	4

Fig. 7 Impact test
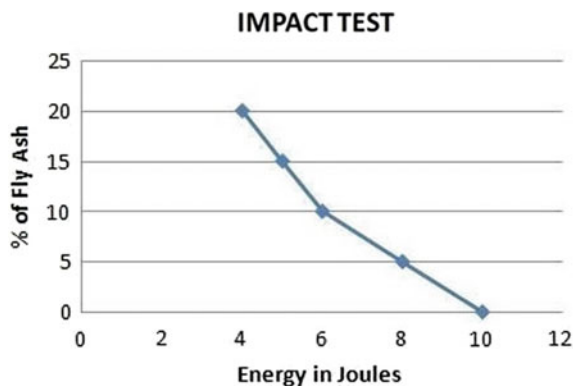
5 Conclusion and Future Scope in This Study

With the intelligent observations of different mechanical testing on a specimen, it is clear that fly ash is a key component that can drastically change the mechanical and physical properties of a glass fiber composite.

An increase in fly ash content provides better compressive strength and hardness of composite material. Although the result of impact testing says that fly ash content in the composite affects impact strength in a negative way.

Further testing for different mechanical and electrical properties with varying epoxy resins can be done for better results in the future.

References

1. Wang, C. J. H. (2012). Effect of fly ash cenospheres on the microstructure and properties of silica-based composites. *Ceramics International*, 4395–4400.
2. Cooke, K. O., & Khan, T. I. (2018). Effect of thermal processing on the tribology of nanocrystalline Ni/TiO 2 coatings. *Emergent Materials, 1*(3–4), 165–173.
3. Paulo, J., & Davim, P. R. (2004). Experimental study of drilling glass fiber reinforced plastics (GFRP) manufactured by hand lay-up. Composites Science and Technology, 289–297.
4. Mandal, S., Das, V. V., Debata, M., Panigrahi, A., Sengupta, P., Rajendran, A., et al. (2019). Study of pore morphology, microstructure, and cell adhesion behaviour in porous Ti-6Al-4 V scaffolds. *Emergent Materials, 2*(4), 453–462.
5. Jina, S. P. (2020). Preparation of epoxy-glass composite with graphene and fly ash filler. Materials today: Procedings. Elsevier.
6. Kishore, S. M. (2002). Effect of filler–fiber interactions on compressive strength of fly ash and short-fiber epoxy composites. *Journal of Applied Polymer Science*, 836–841.
7. Nguyen, L. T., et al. (2018). Simultaneous effects of silanized coal fly ash and nano/micro glass fiber on fracture toughness and mechanical properties of carbon fiber-reinforced vinyl ester resin composites. *Polymer Engineering and Science*.
8. Şimşek, M., Aldemir, S. D., & Gümüşderelioğlu, M. (2019). Anticellular PEO coatings on titanium surfaces by sequential electrospinning and crosslinking processes. *Emergent Materials, 2*(2), 169–179.

9. Czarnecki, J. L. (1980). Shear flow rheological properties, fiber damage, and mastication characteristics of aramid-, glass-, and cellulose-fiber-reinforced polystyrene melts. Journal of Applied Polymer Science, 1217-1244.
10. Vasconcelos, P. V., et al. (2005). Impact fracture study of epoxy-based composites with aluminium particles and milled fibres. *Journal of Materials Processing Technology*, 277–283.
11. Pradeep, Sambyal, G. R. (2015). Advanced anti corrosive properties of poly (aniline-co-o-toluidine)/flyash composite coatings. Surface and Coatings Technology, 129–140.
12. Singla, M., & Chawla, V. (2010). Mechanical properties of epoxy resin–fly ash composite. Journal of Minerals & Materials Characterization and Engineering. 9(3), 199–210.
13. Massingill, J. L. (2000). Epoxy resins. *Applied Polymer Science 21 Century*, 393–424.
14. Davim, J. P., et al. (2004). Experimental study of drilling glass fiber reinforced plastics (GFRP) manufactured by hand lay-up. *Composites Science and Technology*, 289–297.
15. Saafi, H. A. (2000). Flexural behavior of concrete beams reinforced with glass fiber-reinforced polymer (GFRP) bars. *Aci Structural Journal*, S97–S72.

Correlation Assessment of Weld Bead Geometry and Temperature Circulation by Online Measurement in Nd: YAG Laser Welding

Rajesh V. Patil and **Y. P. Reddy**

Abstract   Laser beam welding is popular in microsystems technology by its specific parameters. Mostly, it is categorized by momentary nature and really short period of the method. The laser beam is concentrated on the materials to be welded, and therefore, the process is usually autogenous, does not require any additional filler material. Due to, laser welding could be a fast-growing application area for industrial lasers. Many authors conducted experiments on measurement of penetration depth using large thickness of sheet by varying process parameters and developed thermal model referring to temperature distribution within work piece. The present work selected less than 1 mm stainless steel sheet and trials taken by varying combination of power, speed, and sheet thickness to predict weld bead geometry and validated by image processing technique. Furthermore, the experimental setup is developed to measure online bottom surface temperature of work piece during welding by temperature data logger. Finally, found that the net measured temperature by data logger has shown sensitive indicator of penetration depth and measured value of depth of penetration by experimentation, optimization, and image processing technique satisfactorily.

Keywords   Online temperature measurement · Depth of penetration · Image processing · Nd: YAG laser welding · Temperature data logger

1   Introduction

Stainless steel sheet is extensively demanded in the welded assembly of biopharmaceutical, medical, and aerospace manufacturing industry by its distinctive features of smooth surface, nonmagnetic, and corrosion resistance. To classify the optimum process parameters for attaining quality welds, it is essential to explore the thermal environment by fusion and heat-affected zones in numerous industries. Linked to the methods of MIG-MAG and TIG, laser beam welding process revealed that the

R. V. Patil (✉) · Y. P. Reddy
Sinhgad College of Engineering, Savtribai Phule Pune University, Pune, Maharashtra, India
e-mail: patilraje@gmail.com

extremely thin layer can be sufficient for filling the gap between two parts, and layer should not be thicker than requirement, but all are totally depending upon excellence of weld bead geometry such as penetration depth, bead width, and length. It can achieve better quality of weld using precise selection of the process parameters such as welding speed, beam incident angle, laser incident angle, beam diameter, laser energy, beam power, laser power, laser focal position, and peak power. Many authors contributed their work on correlation of weld bead geometry and process parameters, and its effects, modeling of laser welding process, online temperature monitoring, and imperfections identification by image processing are as follows. Kim et al. [1] found, when focal position moves from the surface; the bead width becomes narrower. However, the bead quality improves therefore the severity of spatter is reduced and the positive angle shows an improved weld quality than the negative angle when their porosities are compared. Liao et al. [2] presented, at the identical incident approach of laser beam, the typical lengths of weld spot, depth of penetration, bead length, and width rise as the laser energy rises. Balasubramanian et al. [3] found the beam power and welding velocity are key limits influencing the penetration depth and bead width but gas flow rate is not having significant influence. Khan et al. [4] found the welding power and speed are utmost important aspects disturbing the weld bead geometry moreover shearing force of weld excluding on the weld zone width. The fiber diameter has slight effect on bead geometry and shearing force. Lankalapalli et al. [5] found the depth of penetration rises with welding power and reductions with welding speed and also difference of width by power and speed is unimportant related to dissimilarity in depth. Jose et al. [6] observed the component circulation in weld region is similar for all laser beam place. Xiu et al. [7] found with growing velocity, the weld width reduces because of heat input cuts and by growing power, the weld width slight rises, and by growing power density, the inside weld width also rises. Anawa et al. [8] found that with growing velocity, the weld evaporation of metal reductions with growing power, the weld width minor rises, and by growing power density, the inside weld width also rises. Kim et al. [9] proposed the grouping heat source model of conical and inverted conical to put on the temperature arena of pulsed Nd: YAG laser welding of A304 stainless steel in diverse conditions. The extreme error of bead width and penetration depth is found around 0.132 mm. Chukkan et al. [10] pretend the pulsed Nd: YAG laser beam welding shape, temperature arena, and welding stress by three grouping heat source models. The intended weld pool shapes of three grouping heat source models look like the experimentally found weld pool shapes with an extreme error around 0.082 mm, 0.13 mm and 0.02 mm. Shi et al. [11] found the grouping heat source model of ellipsoid, inverted conical and conical to pretend the heat source of laser lap welding of stainless steel car frame. The error of bead width and penetration depth is fewer than 0.092 mm. Haodong et al. [12] proposed dual deep convolutional neural networks on the improved image groups via feature-extraction created transfer learning techniques to organize defects over a multi-model ensemble framework, targeting at lesser incorrect detection rate. Li et al. [13] proposed to practice the deep learning network to classify welding defects. Created on the examination of X-ray defect image features, the convolutional neural network model and numeral of layers are calculated. Dong et al. [14] built SVM

multi-classifier model aimed at slag, crack, gas hole, incomplete penetration and fusion and found defect structures for individually class created on the defect record.

2 Experimental Examination of Penetration Depth

The application of experimental techniques will lead to enhanced process yield, lessen changeability, and nearer conformance to minimal of goal necessities, decrease the event time and total costs. Previous investigation of bead on plate welding analysis discovered the influencing process parameters are welding speed, laser power, laser energy, gas rate, beam angle, sheet thickness, fiber diameter and distance. According to survey, the parameters like power, speed, and sheet thickness are major influencing parameters on weld bead geometry are found. The Nd: YAG TruLaser Station 5004 laser welding system used for experiment and depth of penetration; bead width are the dependent output variables. In proposed work, SS 304L is an austenitic stainless steel used because of offering the optimum combination of corrosion resistance, strength, ductility, welded without the resulting issue of carbon precipitation of chromium and also utilized in severe corrosive environments. The 304L austenitic stainless steel sheet is cut into rectangular specimens with the assistance of electric discharge machining. The dimension of plate engaged for welding experiment are 300 mm × 70 mm by thickness of 1–0.6-mm sheet. The specimen is on stand of Nd: YAG laser welding machine with the assistance of supporting magnets on either side of steel sheet and held the specimen firmly butt welding of specimen. The commercial argon as the shielding gas used to avoid the specimen after corrosion and heat degeneracy. Finally, laser weld beads made twelve times within the longitudinal direction along the middle line of specimen by varying combination of welding speed starting from 2 to 10 mm/s, power from 400 to 1500 w, and sheet thickness from 0.6 to 1 mm (Tables 1, 2 and 3).

Experiments planned by the Taguchi scheme via L12 orthogonal array collected of 3 columns and 12 rows. This design of experiments nominated built on four welding parameters based on sheet thickness, power, speed, and energy with three levels each.

Table 1 Chemical configuration and mechanical properties of SS304L

C	Mn	Ni	Mo	Cr	Si	V	N
0.030	2.00	8–12	–	18–20	0.75	0.07	0.1
Proof stress		170 Mpa	Tensile strength		485 MPa	Elongation	40%

Table 2 Process parameters of SS304L

Sheet (mm)	Power (w)	Speed (mm/s)	Pulse D. (ms)	Freq. (hz)	Focal D. (mm)	Energy (J)	Focus (mm)
0.2–1.0	400–1500	2–10	3.50	15–20	150	1.21–3.46	0.60

Table 3 Process variables and levels

Variables	Sheet	Power	Welding speed	Energy
-1	0.2	400	2	1.21
0	0.6	950	6	2.96
1	1	1500	10	3.46

Following optimization techniques calculated the depth DOP and bead width. The response function of weld dimensions can be expressed as Y is the function of the welding power, speed, and sheet thickness Y = f (ST P, WS,), where Y represents response. The second-order polynomial equation applied to denote response surface for the features is given by

$$Y = b_0 \sum_{i=1}^{4} b_i x_i + \sum_{i=1}^{4} b_{ii} x_i 2 + \sum_{i=1}^{4} b_{ij} x_i j_j \tag{1}$$

The said second-order response model can be stated as

$$Y_0 = b_0 + b_1 ST + b_2 P + b_3 WS + b_{11} ST^2 + b_{22} P^2 + b_{33} SW^2 + b_{12} ST \times P + b_{13} ST \times WS + b_{23} SW \times P \tag{2}$$

where b_0 is constant of the regression equivalence, factors b_1, b_2, b_3 are linear terms, the factors b_{11}, b_{22}, b_{33} are quadratic terms, and the factors b_{12}, b_{13}, b_{23} are interaction terms. The value of the coefficients of the polynomial equation for the penetration depth and bead width calculated using statistical analysis software SPSS14.0. After determining the coefficients, the mathematical models are used to develop and are given in Eqs. (3) and (4). All the data are used to generate the regression equations for the estimate of depth of penetration and bead width.

$$BL = 1.21 + 0 * ST - 0.00105 * P - 0.09342 * WS + 0.63230 * ST^2 + 4.8 \times 10^{-7} * P^2 + 0.01205 * WS^2 + 0.000259 * ST * P - 0.10381 * ST * P - 2 \times 10^{-5} * P * WS \tag{3}$$

$$DP = -0.74073 - 0 * ST - 0.00106 * P - 0.0686 * WS - 1.2770 * ST^2 + 5.62 \times 10^{-7} * P^2 0.0114 * WS^2 - 5.5 \times 10^{-5} * ST * P - 0.1 * ST * WS + 1.8 \times 10^{-5} * P * WS \tag{4}$$

The welded samples are successively polished and then lapping polishing process performed by disk polishing. Finally, electrolytic etchings aimed at measurement of penetration depth and bead width with the help of an image analyzer. The presented work taken 12 samples to weld with combination of parameters and identified their

Fig. 1 Measurement of penetration depth and bead length by image analyzer

satisfactorily weld bead and penetration depth. The process parameters like power 950 W, welding speed 10 mm/s, energy 3.46 J, and sheet thickness 1 mm are used for trials, the obtained value of depth of penetration is 0.9483 mm, and bead length is 1.2625 as shown in Fig. 1.
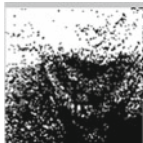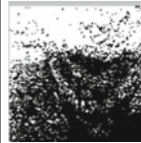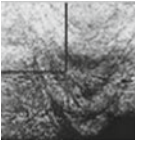
2.1 Welding Image Processing and Feature Extraction

The goals of proposed technique are to verify the validity of approach and to measure the depth of penetration and bead width of weld sheet by image processing and feature extraction technique. The author used 12 number of sample called original images for the proposed technique as given in Table 4. Initially, for the digitization, identified principle characteristics of every images, like minor contrast among related weld areas. Then, through preprocessing stage, remove the noise enfolding in the film and advances its visibility. In the preprocessing, first select area near to seams in images as region of interest (ROI) for processing. Subsequently, ROI selection used contrast improvement to advance intensity contrast in the input image and highlighted the weld areas, while exit the insignificant related areas intact. This enables weld detection stage to better locate and represent each weld in the image. At last, the segmentation determines at the end of final quality of weld image and display measured values

Table 4 Design matrix with process variables

Sam.	1	2	C	4	5	6	7	8	9	10	11	12
ST	1	1	1	1	0.6	0.6	0.6	0.6	0.2	0.2	0.2	0.2
P	0.4	1.5	0.95	0.95	0.4	1.5	0.4	1.5	0.4	1.5	0.95	0.95
WS	6	6	2	10	2	2	10	10	6	6	2	10

Table 5 Measured DOP and BW by threshold and segmented weld images

Original weld image	Thresholding at 0.6	Optimal segmented image (Ostu)	Measurement of DOP and BW

of penetration depth and weld bead. The obtained value of depth of penetration is 0.9967 mm and bead length is 1.367 mm mention in Table 4 and 5.

3 Development of Online Temperature Measurement Data Logger

Laser welding process involves heat flow through welding to achieve desired joint. Depending upon heating and cooling cycle involved, differing kinds of microstructure found in bead geometry and heat-affected region and this primes to varying mechanical properties of diverse zones of a weldment. Apart from the outcome of heat flow in welding, there are additional phenomenon involved such as residual stresses, distortion, chemical and physical changes to attain a weldment of wanted specification to achieve acceptably in provision is to grasp the results of heat through welding. This may be attained by expressing the temperature circulation through welding; therefore, to work out the cooling rate in numerous orders with relative to weld axis, author developed temperature data logger for measurement of online bottom surface temperature. Basically, temperature data logger unit is reliable and accurate data collection device under though environmental conditions as shown in Fig. 2. Eight K-type of thermocouples are mounted on plate at different locations, by interfacing sensor mounting on fixture through coding done by Visual basic. The key
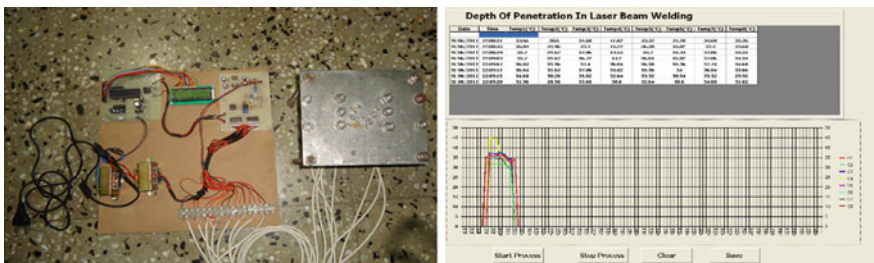
Fig. 2 Measurement of online temperature distribution during welding

criteria regarding mounting is to cover whole area, i.e., length and height of specimen for measurement of online bottom surface temperature. Nd: YAG laser welding is accustomed to make the welds using parameters such as laser power 950 W, welding speed 2 mm/s, energy 3.46 J and sheet thickness of 1 mm. Eight K-type contacts of thermocouple have accustomed to measure the online temperature on underside surface of work piece from different location as shown in Fig. 3. When the welding together with process starts, online measurement of temperature constantly shows the temperature until the welding process stops and at last, it measured the temperature at each sensor with different time on screen as mention in Fig. 2
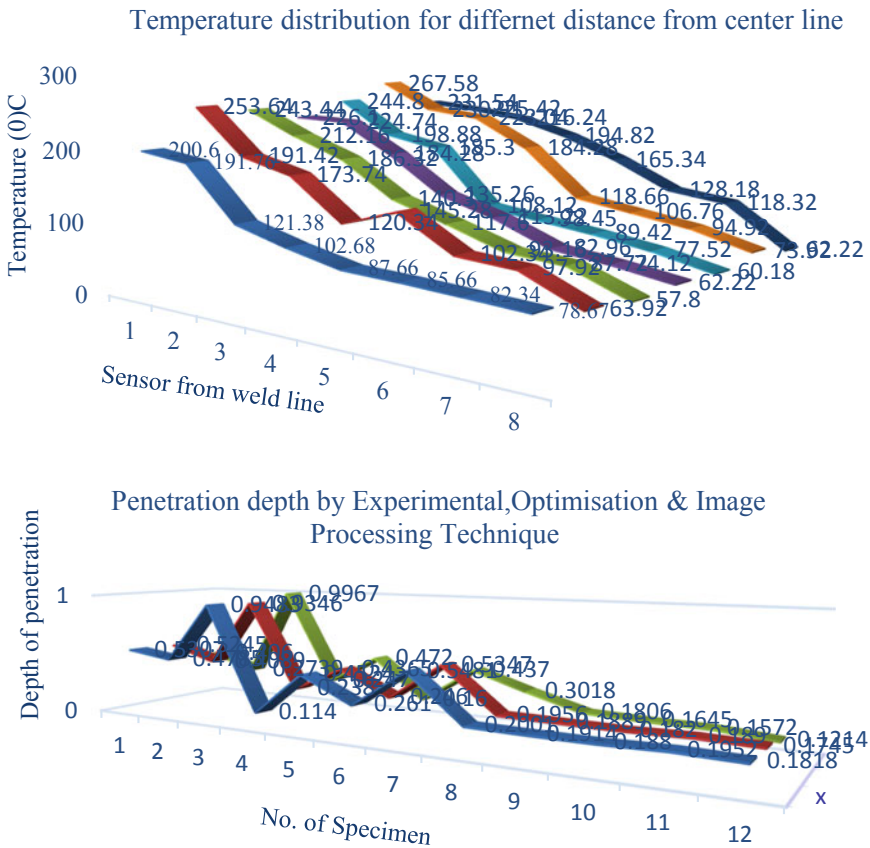
Fig. 3 Online temperature distribution at different times 1. t = 1 s; 2. t = 5 s; 3. t = 9 s; 4. t = 13 s; 5. t = 17 s; 6. t = 21 s; 7. t = 22 s and measurement of penetration depth by experimentation, optimization, and image processing technique

4 Result Discussion

Figure 3 represents the experimental transient temperature distribution history at different sensor locations with different time. It is observed the cooling amount of a material declining with relevance to distance from center weld line as temperature distribution is decreasing. The regions close to weld line feel the highest temperature and severe thermal cycle, by this means producing in homogeneous plastic distortion and residual stress observed. With higher thickness sheet, the thermal conductivity of material also rises the cooling rate. Finally, found the satisfactorily depth of penetration by proposed experimentation and image processing techniques.

5 Conclusion

From the proposed examination, resulting conclusions can be made:

- Numerous authors proposed numerical models to study temperature profiles in the 304L stainless steel sheet and found temperature distribution is the complex indicator for weld pool shapes. The error percentage of calculated and experimentally measured weld pool shapes is around 15–20%, whereas the proposed temperature data logger revealed temperature is the sensitive indicator of penetration depth and error percentage is controlled up to 3–5%.
- Proposed novel data logger revealed temperature profile reductions sharply nearby weld line and therefore reductions slightly within the area secluded from weld line.
- Thermal conductivity of material also rises the cooling rate with higher sheet thickness and even though rise welding velocity rises the cooling rate too.
- Cooling rate of material falling with relevance to distance from center weld line as temperature circulated is falling because the grain growth rates strongly rest on temperature scattered.

References

1. Kim, J. K., & Lim, H. S. (2008) Bead on plate weld ability of AI 5052 alloy using a disk laser. *Journal of Achievements in Materials and Manufacturing Engineering, 28*(2).
2. Liao, Y. C., & Yu, M. H. (2007) Effect of laser beam energy and incident angle on the pulse laser welding of SS thin sheet. *Journal of Materials Processing Technology, 190*, 102–108.
3. Balasubramanian, K. R., & Buvanashekaran, G. (2010). Modeling of laser welding of stainless steel sheet butt joint using neural networks. *Journal of Manufacturing Science &Techology, 99*, 1–5.
4. Khan, M., & Romoli, L. (2010). Exp.design approach to process para. optimization for laser welding of martensitic SS in a constrained. *Optics & Laser Techology, 43*,158–172.

5. Lankalapalli, K. N., & Tu, J. F. (1996). A model for estimating penetration depth of laser welding processes. *Journal of Applied Physics, 29*, 1831–1841.
6. Jose, R. B, de Wagner, R., & das Ivan, M. D. M. (2007). Pulsed Nd: YAG laser welding of AISI 304 AISI 420 stainless steels. *Optics & Lasers in Engineering, 45*, 960–966.
7. Liu, X. B., Yu, G., Pang, M., Fan, J. W., & Wang, H. H. (2007). Dissimilar autogenous full penetration welding of superalloy K418 and 42CrMo steel by a high-power CW Nd: YAG laser. *Applied Surface Science, 253,* 7281–7289.
8. Anawa, E. M., & Olabi, A. G. (2008). Dissimilar laser-welded components. *Optics & Laser Techology, 40*(9), 379–388.
9. Kim, K., Lee, J., & Cho, H. (2010). Analysis of pulsed Nd: YAG laser welding of AISI 304 steel. *Journal of Mechanical Science & Technology, 24*(11), 2253–2259.
10. Chukkan, J. R., & Vasudevan, M. (2015). Simulation of laser butt welding of AISI SS sheet by heat sources & expe. validation. *Journal of Materials Proceedings Technology, 219*, 48–59.
11. Shi, C. (2011). Heat source model for partial penetration lap laser welding of stainless-steel railway vehicles. *Transactions of China Welding Institution, 32*(5), 85–88.
12. Zhang, H., Chen, Z., & Zhang, C. (2019). Weld defect detection based on deep learning method. *IEEE International Conferences on Automatic Science and Engineering*, 1574–1579.
13. Yaping, L., & Weixi, G. (2019). Research on X-ray welding image defect detection based on CNN. *IOP Conference Series: Journal of Physics: Conference Series, 1237*, 1–7.
14. Dong, S., Sun, X., & Xie, S. (2019). Automatic defect identification technology of digital image of pipeline weld. *Natural Gas Industry B, 6,* 399–403.

Experimental and Numerical Investigation of Flat Plate Solar Water Heater

R. B. Chadge, Neeraj Sunheriya, Chetan Mahatme, and Jayant P. Giri

Abstract As the world is developing, energy consumption is also increasing very rapidly. Conventional energy sources are able to fulfill todays energy demand, but they have their own disadvantages. Main conventional sources for energy production are the fossil fuels till now. But these fuels are available in limited quantity as well as the environmental issues make the world think for the renewable energy sources. The weaknesses of conventional sources can be eliminated by renewable energy sources. Among the available renewable energy sources, solar is one of the most promising areas nowadays, in which solar-operated water heating system is most widely used in thermal applications. Solar water heater is not only eco-friendly, but also it requires less maintenance and operational cost. This paper aims to modify the simple solar water heater with V-trough reflectors and compare the experimental results with ANSYS software. The results obtained through the experimentation are quite good to promote the inclusion of V-trough reflector with SSWH. The efficiencies are 79.5%, 91%, and 84% while using V-trough reflector at an inclination of 65, 70, and 75 degrees with absorber plate compared to the 78% efficiency of SSWH during typical days of experimentation.

Keywords Solar water heater (SWH) · V-trough reflector · Numerical analysis

R. B. Chadge (✉) · N. Sunheriya · C. Mahatme · J. P. Giri
Yeshwantrao Chavan College of Engineering, Wanadongri, Hingna Road, Nagpur 441110, India
e-mail: rbchadge@rediffmail.com

N. Sunheriya
e-mail: neeraj.sunheriya@gmail.com

C. Mahatme
e-mail: chetanmahatme@gmail.com

J. P. Giri
e-mail: jayantpgiri@gmail.com

1 Introduction

Solar water heater is a system used to convert the incident solar radiation into thermal energy with the help of flat plate or evacuated tube collector. This thermal energy application-based appliances can be used for domestic and industrial purpose. The rapid growth rate of solar water heater proves that it has great potential worldwide. India, China, and Europe are among the major market share for solar water heater.

Overall, the cost of solar water heater is expensive and less efficient. So, there is a need to investigate and develop high efficient solar water heater (SWH).

1.1 Abbreviation and Acronyms

SHW—Simple water heater, V-SHW—V-trough solar water heater, FPC—Flat plate collector, AP—Absorber plate, DTI—Digital temperature indicator.

1.2 Equations

The efficiency of flat plat collector is generally based on the input radiation and heat utilized [5]. Various equations to analyze the performance are illustrated below:

$$\text{Energy input (Qi)} = \int I \times A \, dt \tag{1}$$

$$\text{Energy Output (Eo)} = m \, c_p(\Delta T) \tag{2}$$

$$\text{Overall Efficiency } (\eta) = (Eo/Qi) * 100\% \tag{3}$$

where

I = Input radiation (W/m^2)
A = Input area (m^2)
m = Water mass flow rate (kg/s)
c_p = Specific heat of water @ constant pressure (J/kg.K)
ΔT = Temperature differential of incoming and outgoing water in Fahrenheit.

2 Literature Review

SWH is used for domestic as well as industrial purposes. SWH is integrated with V-trough reflector installed in Jaipur, India [1]. He investigated the performance at different tilt angle and shadow pattern on the glass cover. The results stated that increase in tilt angle from 15 to 25°, average thermal efficiency of SWH increased from 27 to 30%. It is also observed that shadow (dust deposition) reduced the thermal efficiency of SWH from 30 to 20% at constant tilt angle of 25°.

Today, various types of SWH such as evacuated tube collector (ETC), flat plate collector solar water heater (FPSWH), and solar water heater with concentrating collector and integrated solar collector are easily available in the market. The performance of these solar water heaters can be improved by integrating with V-trough reflector. Chong investigated the stationary V-trough solar water heater experimentally as well as numerically. In this experiment, they optimize the V- trough angle 60 degrees from horizontal surface of the absorber plate to surface of the mirror. They found increment in the efficiency of solar water heater with V-trough setup [2] (Fig. 1).

Tang & Liu, 2011 proposed a mathematical model for estimating the incident radiation on V-trough concentrator [3]. This model based on image principle of planar mirrors, monthly horizontal radiation, and solar geometry. It predicted the performance of a V-troughs reflector with any structural and installation parameters.

A V-trough collector with considering shading, multi and space reflections [4]. The optical analysis optimizes the trough geometries for maximum real acceptance. The thermal performance of the V-trough collector aligned with east–west and tilted to any base angle was also studied [5, 6].
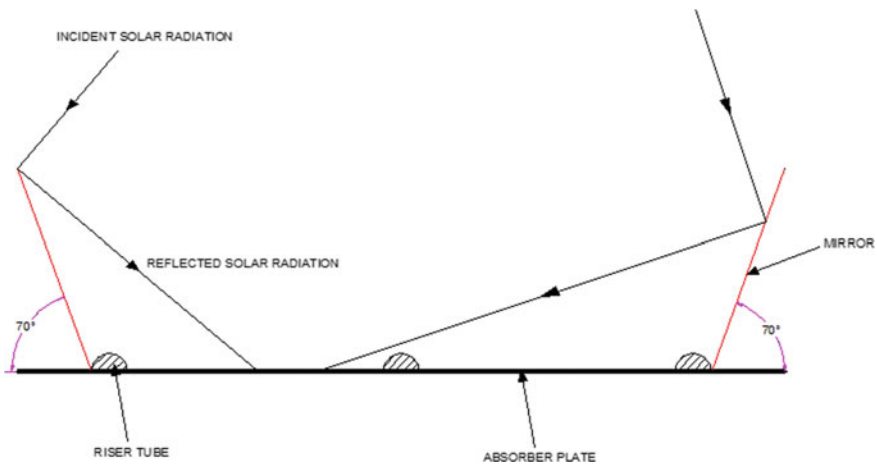
Fig. 1 Geometry of V-trough mirror setup

By doing geometric calculation and using CATIA software, we calculate the angle between mirror and horizontal absorber plate. The angle between mirror and horizontal absorber plate is 70° which reflect maximum sun ray on absorber plate. All calculated dimensions are in mm.

3 Experimental Plan

- Fabrication of V-trough SWH
- Experimentation of fabricated and simple solar water heater at different parameters
- Comparison between both the solar water heaters.

3.1 Experimental Setup

Flat plate SWH: Components of SWH used

1. Absorber plate
2. Connecting tubes
3. Transparent top cover
4. Collector box

The flat plate SWH works on principle of thermosiphon effect. It stated that due to incidence of solar radiation on flat plate collector, the fluid flowing through the riser tube gets heated and due to that the density of the fluid decreases and fluid starts to flow upside; thus phenomenon goes on till the temperature inside the tank, i.e., hot water and cold water temperature get equalize. Table 1 shows the details of the experimental setup:

V-Trough collector.

V-trough reflectors are simple mirror used to concentrate the solar radiation on to the collector, so the absorber plate can absorb the maximum amount of transmitted and diffused solar radiation (Fig. 2).

Components of V-Trough collector

1. The main component of the V-trough setup is a mirror which is used to concentrate the solar radiation on the absorber plate which is placed at 70 ° inclined with absorber plate.
2. Absorber plate.
3. Tubes fixed to the absorber plate through which the liquid to be heated flow.
4. The transparent cover.
5. The collector box.

Table 1 Experimental setup details

Sr. no.	Components	Dimensions	Use
1.	Collector box	2083 mm X 1036 mm X 100 mm Material−aluminum	To provide support and insulation
2.	Header pipe	Diameter = 25.5 mm, Thickness = 2 mm, Material-copper	To put liquid in and out from the collector
3.	Riser pipe	Diameter = 12.5 mm, Thickness = 1 mm No. of tubes = 9, Material-copper	To heat the liquid and allow to flow upward
4.	Absorber plate	Thickness = 0.5 mm, Material-copper	To absorb the solar Radiation
5.	Tank	100 L per day (LPD)	To store water and provide hot water
6.	Glass	Toughened glass. Thickness = 5 mm	To concentrate heat and prevent heat losses
7.	Collector insulation	Rock wool pads	To provide bottom insulation
8.	Piping system	Multilayer composite pipe Diameter = 19.05 mm Thermal conductivity- 0.43 w/m.k	Higher thermal conductivity pipe used to carry hot water from Collector to tank
9.	Pressure gauge	Range 0–4.2 kg/cm2, Least count–0.02 kg/cm2	To measure the pressure of the flowing fluid
10.	Flow sensor	Range 0.5–30 L/hours, Working pressure range = 1.7 MPa	To measure the fluid flow rate of water
11.	DTI	Range 0–199 0C. 6 channels Thermocouple−k type	To measure the temperature

V-reflector are inserted inside the another flat plate water heater, and another frame is required to put the glazing on the top of the collector. Hence, the aluminum frame of the same dimension (2083 mm*1036 mm *100 mm) is used. This aluminum frame is mounted on top of the flat plate water heater and tightened by means of nut and bolt, and V-trough reflector is inserted inside the flat plate solar water heater (Fig. 3).

Collector Configuration for Modeling and Analysis

The riser tube of diameter of 12.5 and 1940 mm long with the thickness of 1 mm. The distance from pipe to pipe is 101.6 mm and consists of header pipe at both inlet and outlet of 25.5 mm diameter and 1030 mm long with the thickness of 2 mm. The overall dimensions of the collector are 2083 mm*1036 mm*100 mm, and the effective glazing area is 2 m^2.

Fig. 2 Simple solar water
heater and solar water heater
with V-trough reflector

Fig. 3 V-trough reflector
solar water heater
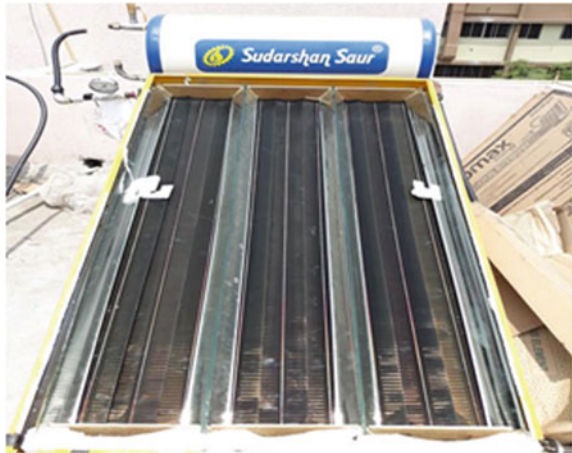
3.2 Modeling

The simple plate collector is modeled in solid works software. The modeling is done
on the basis of actual dimension of flat plate solar water heater as discussed. Complete
geometry is taken as domain of working fluid. Riser tubes are inclined at 21 ° from
the horizontal plane to capture actual flow conditions due to gravitational force. The
modeling is shown in Fig. 4. All nine numbers of riser tubes attached with two header

Fig. 4 Modeling of solar
water heater in solid works
2016
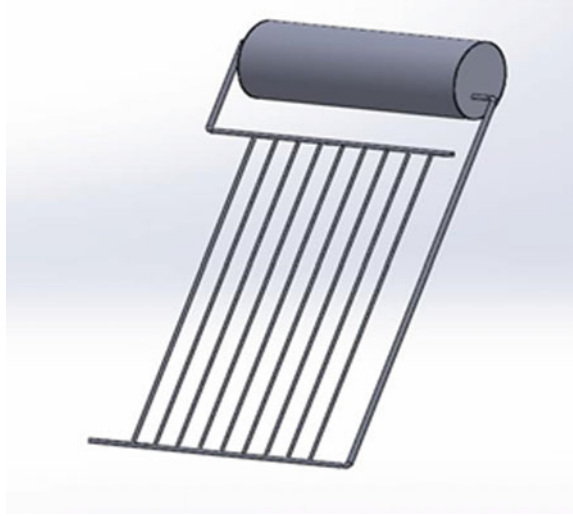
pipes. The lower header pipe is attached at lower point of the insulated tank, and similarly, upper header pipe is attached at the upper point of the insulated tank. The modeling is than exported in IGES file format.

3.3 Analysis

The design model is numerically analyzed by computational Fluid dynamics (CFD) techniques. ANSYS FLUENT software version 16.0 is used for solving the governing equations. Modeling file with IGES file format is imported in the ANSYS FLUENT, and boundary conditions are set at different positions for natural convection. Fixed wall and heat flux boundary conditions are assigned at riser tubes, absorber plate, and header pipes. Fixed insulated wall condition is applied to the tank (Fig. 5).

Grid-independence test and grid refinement are also done for the simulation optimization. Total no of nodes and elements used during the grid refinement process are given in Table 2. It is observed that during grid refinement process, no: of nodes and elements are continually increased from 33678 and 113840 to 40152 and 142958, also the % change in temperature is observed from 5.03 to 3.98% which is quite small; hence, no further refinement was done.

Fig. 5 Meshing of model in
ANSYS 16.0
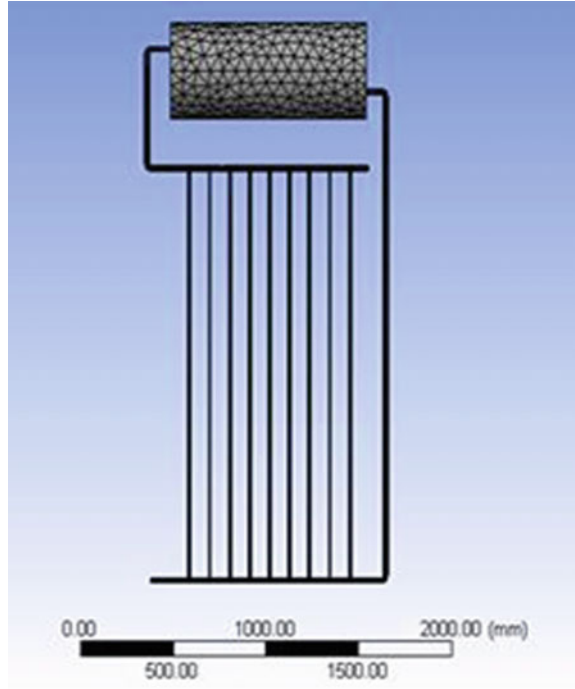
Table 2 Grid independence

Sr. no.	No. of nodes	No. of elements	% Change in temperature
1.	33678	113840	5.03%
2.	35467	134568	4.07%
3.	40152	142958	1.98

4 Results and Discussion

4.1 Results

It is observed that by using V-trough reflector in the simple solar water heater, the temperature of output water increased by a significant amount. The maximum efficiency obtained while using the simple solar water is obtained as 78%. The efficiencies are also calculated while using V-trough collector at different inclinations viz 65, 70, and 75 degrees, and maximum efficiencies obtained are 79.5%, 91%, and 84%, respectively. So, the overall efficiency is also improved. Figure 6 shows the maximum temperature of the glazing of the SSWM and MSWH during a day. Both the glazing temperatures are quite similar throughout the day.
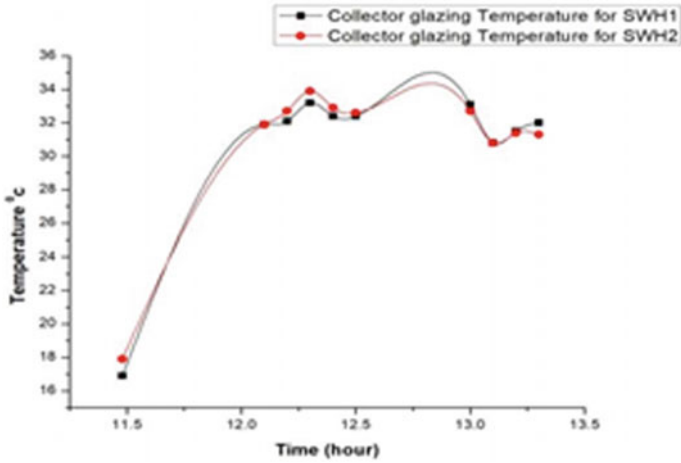
Fig. 6 Time versus collector glazing temperature for SWH 1 and SWH2
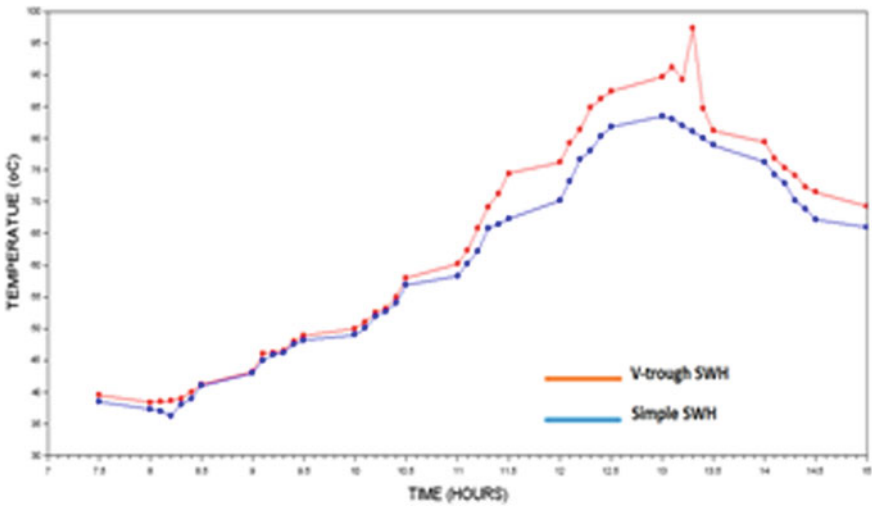
Fig. 7 Comparison of output hot water of V-trough SWH and Simple SWH

Figure 7 shows the comparison of output hot water of V-trough SWH and simple SWH. At each point of time throughout the day, V-trough collector performs significantly better compared to the simple water heater. This is only due to more heat flux is reflected toward the absorber plate and riser tubes. More concentration results much rise in temperature of flowing water in riser tubes.

4.2 Discussion

The efficiency of simple solar water heater can be improved by attaching the concentrated device like V-trough reflector, booster mirror, etc. The concentration ratio is a main factor which have to be maintained for optimal efficiencies. V-trough mirror should be inclined at 70° with the absorber plate to obtain maximum efficiency.

5 Conclusion

As per the working plan, firstly both the simple flat plate collectors are tested around the same inlet conditions at normal temperature pressure (NTP). The inlet cold and outlet hot water temperature are measured using the digital temperature indicator. It is found that both flat plate solar water heaters give nearly the same outlet temperature, which shows that the efficiency of both solar water is nearly same.

Then, arrangement with V-trough reflectors on the simple SWH was fabricated and readings taken regarding that arrangement. Readings were taken for 2–3 days on both the simple and V-trough solar water heater. The comparison of both V-trough collectors with simple solar collector, it was found that the temperature of hot water of V-trough model is more as compared to the simple solar collector, so simultaneously, the efficiency of V-trough collector was improved under the same input or atmospheric conditions.

References

1. Pandya, H., & Kumar, A. (2017). Experimental study of V-Through solar water heater for tilt angle and glass transmissivity. *Energy Procedia*, *109*(November 2016), 377–384. https://doi.org/10.1016/j.egypro.2017.03.034.
2. Chong, K. K., Chay, K. G., & Chin, K. H. (2012). Study of a solar water heater using stationary V-trough collector. *Renewable Energy, 39*(1), 207–215. https://doi.org/10.1016/j.renene.2011.08.002.
3. Tang, R., & Liu, X. (2011). Optical performance and design optimization of V-trough concentrators for photovoltaic applications. *Solar Energy, 85*(9), 2154–2166. https://doi.org/10.1016/j.solener.2011.06.001.
4. Abdou, A. A. M., & Mahmoud, R. A. (1991). Design of stationary finite length V-Trough solar collector. *International Journal of Solar Energy, 10*(1–2), 63–81. https://doi.org/10.1080/01425919108941452.
5. Klevinskis, A., & Bučinskas, V. (2012). Analysis of a flat-plate solar collector/plokščiojo saulės kolektoriaus tyrimas. *Mokslas - Lietuvos Ateitis, 3*(6), 39–43. https://doi.org/10.3846/mla.2011.108.
6. Sangani, C. S., & Solanki, C. S. Ã. (2007). Experimental evaluation of V-trough (2 suns) PV concentrator system using commercial PV modules. *91*, 453–459. https://doi.org/10.1016/j.solmat.2006.10.012.

Experimental Study of Thermal Contact Conductance of Tool-Sample Interface After Heat Treatment

Mohammad Asif and **Mohd Atif Ahad**

Abstract Heat transfer across the metallic interface plays a vital role in metal forming processes for the better design of tools, dies, and other components. Thermal contact conductance (TCC) is the parameter which relates the interfacial heat transfer and interface temperature. Heat treatment is the process commonly employed to improve the thermo-mechanical properties of a material. Thus, the effect of heat treatment on the tool-sample contacts is the main objective of this work. Here, experiments are performed to investigate the thermal properties at the tool steel–mild steel contacts with and without heat treatments. Experiments have been performed on a simple experimental setup which is based on axial heat flow method. The experiments have been conducted under atmospheric environment and varying loading and heat flux conditions so as to study the contact heat transfer for a range of contact pressure and interface temperatures. Steady-state methodology is employed for estimating thermal contact conductance at the joint of two specimens. Heat treatment of tool steel and mild steel specimens has been carried out using normalizing process. Eventually, the combined effect of hardness and thermal conductivity of the tool steel and mild steel on thermal contact conductance has been presented with varying contact pressure and temperature conditions. Moreover, results of TCC have been presented in normalized form to study the combined effect of different parameters and comparing with the pertinent literatures.

Keywords Thermal contact conductance · Heat treatment · Micro-Hardness · Thermal conductivity

---

M. Asif (✉) · M. A. Ahad
Mechanical Engineering Department, Z. H. College of Engineering & Technology, Aligarh Muslim University, Aligarh, India
e-mail: masif@zhcet.ac.in

M. A. Ahad
e-mail: mohdatifahad@gmail.com

1 Introduction

Accurate determination of interface temperature is very essential for the better performance of a thermal system. Thermal contact conductance is the parameter which relates the interfacial heat transfer and interface temperature. In metal cutting process, when the tool comes in contact with the sample, high temperatures are generated in the cutting zones due to large plastic deformations of the sample material. Due to high temperature in the tool rake face, tool wears which leads to deformation of tool and hence tool life is affected [1]. Therefore, the determination of maximum temperature in the tool during metal cutting is very essential which is associated with the thermal conductivity of tool material along with the thermal contact conductance at the interface of tool and sample metal. Other application includes metal forming where tool comes in contact with sample while sample makes contact with die. In the process of tool design, several thermo-physical properties are found to be relevant such as wear resistance, strength, ductility, toughness, and thermal conductivity. Thermal conductivity has significant contribution in thermal fatigue and was found an important parameter for tool life [2]. Ateia [3] studied the effect of heat treatment on thermal conductivity and mechanical properties of grey cast iron using three types of heat treatment, viz. annealing, normalizing, and quenching followed by tempering. Zhang and Gao [4] examined the effect of heat treatment on thermal conductivity of 6063 aluminium alloy. Wilzer et al. [5] investigated the thermal conductivity of tool steel at room temperature using different types of quenching and tempering heat treatment process. Further, Wilzer et al. [6] found that the variation of thermal conductivity with heat treatment was also affected by the degree of alloying. Cingi et al. [7] investigated the influence of heat treatment with the thermal conductivity of aluminium alloys by varying heat treatment temperatures. A considerable increase in thermal conductivity was noted due to heat treatment. Hafenstein et al. [8] studied the effect of heat treatment on thermal conductivity of two different hot work tool steels in the temperature range of 20–500 °C.

Moreover, thermo-mechanical properties of the material, viz. thermal conductivity, strength, and microhardness present a combined effect on thermal contact conductance. Further, it has been observed that an imperfect contact between die and piece resulted in poor heat removal rate, which will lead the undesired mechanical properties of the components. The better contact between piece and die would also be vital for lesser holding times [2]. Therefore, many researchers have presented theoretical models and performed experimental investigations on TCC for tool-sample contacts. In addition, the effect of various parameters on TCC has been examined. For instance, Sridhar and Yovanovich [9] investigated the effect of heat treatment for the TCC of tool steel for a temperature range of 73–121 °C. The authors found that the deformation of untreated tool steel samples was elastoplastic, while samples after heat treatment underwent fully elastic deformation. Abdul Hay et al. [10] estimated the thermal contact resistance for blank-tool contacts for a pressure range of 5–30 MPa. Jam and Fard [11] estimated the TCC at the tool-chip interface using an inverse methodology based on the comparison of finite element analysis results

and experimental results from literatures. Courban et al. [12] analysed the thermal contact of tool-chip during cutting of steel. The experiments had been performed on steel bars with different cutting speeds and feed rates. Norouzifard and Hamedi [13] determined TCC in the tool-chip contact area in the machining operation by inverse thermal solution and infrared thermography. Further, the effect of cutting parameters such as cutting speed and feed rate had been studied. Tariq and Asif [14] performed an experimental study on TCC for nominally flat metallic contacts of stainless steel, brass, and copper specimens under vacuum environment. The contact pressure was varied in the range of 0.6–15 MPa while interfacial temperature range was 30–100 °C. In another important work, Asif and Tariq [15] performed a dimensional analysis to establish a general correlation and various specific correlations for thermal contact conductance for a wide scope of parameters under vacuum environment.

From the literatures, it is evident that the estimation of thermal contact conductance at the tool-sample or die-sample interface is very much essential for the better design of tools and dies. Heat treatment is one of the processes, which is generally used to improve the thermo-mechanical properties of the tool materials. It is the process which changes the microstructure of the material; so causing thermal as well as mechanical properties to be changed by the heat treatment of a material. Further, it may be noted from the literature that very few studies are carried out to investigate the effect of heat treatments of the contacting materials on thermal contact conductance. Hence, work has been done to examine the influence of heat treatment on the thermal contact conductance of tool-sample interface. Tool steel (Grade H13) has been selected as the study material because of its wide range of applications in making tools and dies. Further, mild steel is selected as the sample material which is a common material to be worked upon in making various components. Consequently, axial heat flow experiments have been performed to find out the thermal conductivity of the specimens' materials. Eventually, experiments have been performed on tool-sample pair (TS-MS) with and without heat treatment under varying contact pressures and interface temperatures to study the effect of various parameters on thermal contact conductance.

2   Experimentation

A simple experimental facility has been established based on an axial heat flow method to determine the thermal contact conductance under atmospheric conditions.

2.1   *Experimental Setup*

The two specimens have been placed in contact with the non-contacting ends heated from the top-side and cooled from the bottom side to attain downward heat flow.

Heating system consists of a heating block of copper in which nichrome wire resistance heating element of 150 W is wrapped in coil form. Heating system is connected to a precise and stable PID controller to vary input heat flux so as to perform the experiments at different temperature conditions. Cooling system consists of a cooling block of copper in which chilled water is circulated from a highly precise and stable PID controlled chiller. The insulation blocks (Isomag® 175) of magnesium silicate are kept at the zenith of heating block and at the underneath of cooling block to maintain one-dimensional heat transfer and to minimize radial heat losses. All the interfaces except the specimens' interface are applied with a very conductive silicon thermal grease to reduce the interfacial thermal resistance and to enhance the heat transfer. The loading has been varied by fitting a hydraulic jack below the cooling block and connected with a calibrated digital load cell. The temperatures are recorded at different axial locations in both the specimens using K-type thermocouples of 0.1 mm wire diameter, with 2.5 mm sheath diameter. The thermocouples are mounted in both the specimens up to the centreline. The temperature data has been logged by using a National Instrument NI cDAQ-9178 data acquisition chassis with a NI-9213 module for thermocouple interfacing. A block diagram and a pictorial view of the complete experimental system are shown in Fig. 1. The specimen pairs constitute nominally flat contacts joining together and the required loading has been applied by using hydraulic jack and measured by load cell. Further, heating and cooling system have been started to attain the downward heat flow across. The temperatures at different axial locations of specimens are recorded up to the attainment of steady state. Consequently, the loading has been changed to next stage and
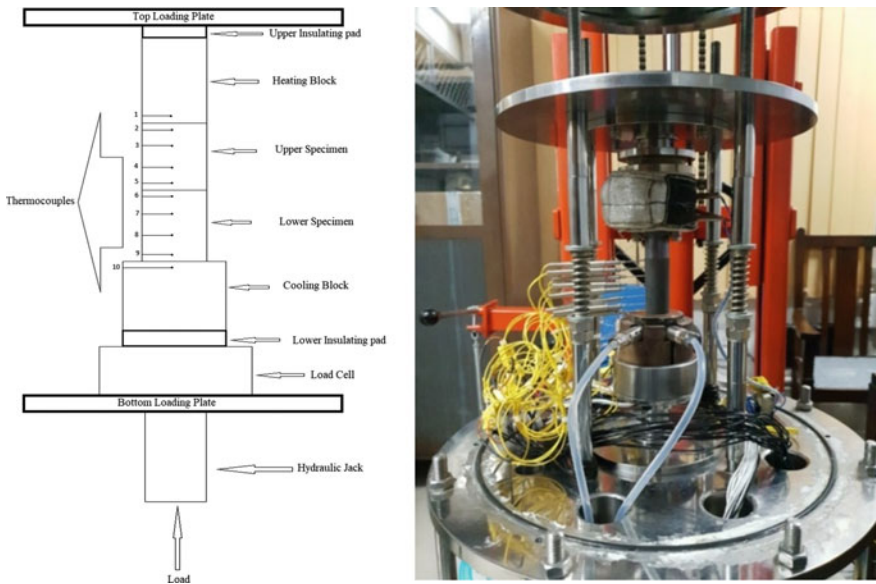
Fig. 1 Block diagram and a pictorial view of the experimental setup

again the temperature data have been recorded in the same way up to the steady state. The similar practise has been repeated for all set of experiments.

2.2 Specimen Preparation and Heat Treatment

The specimens are cylindrical blocks of diameter 25 and length 30 mm. The upper specimen is made of tool steel (TS) of Grade H13, while the lower specimen is made of mild steel. Four fine holes of 12.5 mm deep and 2 mm in diameter have been created at different axial locations with the help of EDM process for inserting the thermocouples. Thereafter, the specimens of tool steel and mild steel have been undergone normalizing process to investigate the influence of heat treatment on the thermal contact conductance of the tool-sample interface. In order to do normalizing heat treatment, the specimens of tool steel and mild steel have been heated in an electric furnace above 900 °C for 2 h and then cooled in still air. The specimen surfaces are fine polished with emery papers. The measurement of RMS roughness 'R_q' and mean arithmetic average slope 'm' of the asperities of all the test surfaces has been done by using Stylus-based profilometer (Mitutoyo: SJ410). The microhardness of the specimens' surfaces has been measured with the help of an Optical Vickers hardness testing machine (VM 50).

3 Data Analysis

3.1 Estimation of Thermal Conductivity

Thermal conductivity of the treated and untreated material of both the specimens, i.e. tool steel and mild steel has been estimated by using a standard method, comparative cut bar technique for axial heat flow thermal conductivity test ASTM E1225 [20]. Stainless steel (304) has been used as a standard material with known thermal conductivity. From the experiments, the thermal conductivity of untreated tool steel and mild steel has been estimated as 26.6 and 44.15 W/m-K, respectively. Further, the thermal conductivity of treated tool steel and mild steel has been measured as 22.69 and 44.66 W/m-K, respectively. Moreover, the variation of thermal conductivity with temperature in the present range (30–130 °C) is found to be negligible for all the samples.

3.2 Estimation of TCC

Transient temperature data has been recorded in both the specimens in contact at different axial locations up to the steady state. The steady-state methodology has been referred to be a simple, easy, and well-validated approach for the estimation of thermal contact conductance at the interface of two bodies. In this approach, heat flux at the interface and axial temperature data in both the specimens at steady state is utilized and TCC has been calculated by using the following equation:

$$\text{Thermal contact conductance,} \quad TCC = \frac{q_{av}}{\Delta T};$$

where q_{av} is the average heat flux: $q_{av} = \frac{(q_1 + q_2)}{2}$. q_{av} has been estimated by using temperature gradient and thermal conductivity of the specimens employing Fourier's law of heat conduction. Further, 'ΔT' is the interfacial temperature drop of specimen pair, estimated by the linear extrapolation of temperature distribution in both the specimens.

3.3 Normalization

Thermal contact conductance is influenced by many factors as discussed earlier. Therefore, to examine the combined effect of different parameters on thermal contact conductance (TCC), a normalization procedure which is commonly used in the literatures [16–18] is adopted.

Thermal contact conductance is normalized as: $h^* = \frac{h\sigma}{mk}$; where 'σ' is the effective root mean square roughness, 'm' refers to the effective average asperity slope, and 'k' is harmonic mean of thermal conductivities of both specimens.

While the contact pressure is normalized as: $P_p = \frac{P}{H}$; **for plastic models** and $P_e = \frac{P\sqrt{2}}{E'm}$ **for elastic models**; where 'P' is the apparent contact pressure calculated on the basis of apparent contact area, 'H' is the microhardness (Vickers) of the softer material of the specimen pair and E' is reduced modulus of elasticity of the specimens' material.

Normalized results have been compared with the selected existing plastic and elastic-based theoretical models, which are as follows:

Plastic Models: $h^* = 1.25(P_p)^{0.95}$: Yovanovich model [16];

$h^* = 1.13(P_p)^{0.94}$: Mikic model [17]; $h^* = 0.9(P_p)^{0.95}$: Asif and Tariq Corrl. [15].

Elastic Models: $h^* = 0.79(P_p)^{0.98}$: BGT elastic model [18];

$h^* = 1.55(P_p)^{0.94}$: Mikic elastic model [17]; $h^* = 1.87(P_p)^{0.98}$: GW model [19].

4 Results and Discussion

4.1 Effect of Contact Pressure

Experiments have been performed on treated and untreated TS-MS specimen pairs with four contact pressures ranging from 1–10 MPa while keeping input heat flux as constant so as to keep average interface temperature as almost constant (~50 °C). Figure 2 shows the variation of temperature drop at the interface with contact pressure. From the figure, it has been observed that interfacial temperature drop reduces with the contact pressure for treated and untreated specimen pairs. However, the range of temperature drop at the interface is 11–22 °C for treated samples while it is 7–10 °C for untreated specimen pairs. The effect of this interfacial temperature drop may also been seen in the variation of TCC with contact pressure in Fig. 3. From Fig. 3, it is observed that TCC increases with contact pressure for treated and untreated specimens. This is due to the deformation of micro-asperities with pressure in the contact region, thereby causing enhanced contact area leading to increase in TCC. Further, it has been found that TCC values of TS-MS contact for untreated samples are higher than that of treated samples. Indeed, thermo-mechanical properties such as thermal conductivity and hardness of the materials are found to change with heat treatment, as reported in the literatures [2–8]. Here, it has been found that microhardness of TS becomes about 2.4 times with normalizing, while mild steel has 0.8 times hardness after normalizing. On the other hand, the thermal conductivity of untreated tool steel is about 1.2 times that of treated ones. Therefore, Fig. 3 shows the combined effect of hardness and thermal conductivity of tool steel primarily after treatment on TCC.

Fig. 2 Interfacial temp drop with pressure
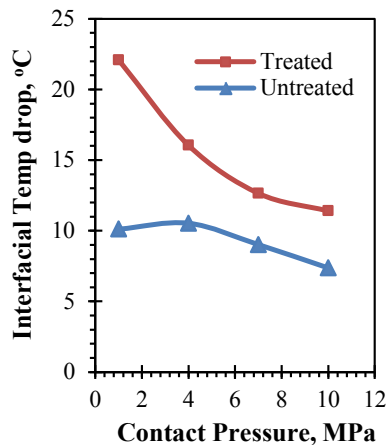
Fig. 3 Variation of TCC
with pressure
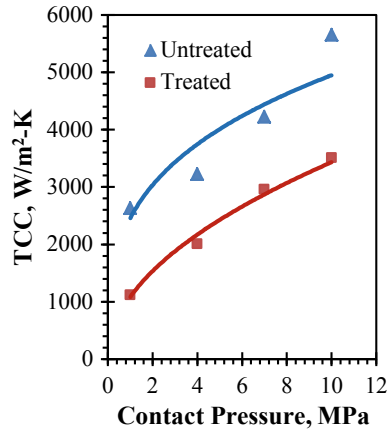
4.2 Effect of Temperature

The experiments have been performed varying the mean interface temperatures by
changing the heat input to the specimen pair while keeping contact pressure as
constant (= 10 MPa). The mean interface temperature has been varied in the range
of 50–110 °C due to the experimental limitations. It has been observed that the inter-
facial temperature drop increases with average interface temperature for treated and
untreated contacts (Fig. 4). Further, it is noted that the rate of change of temper-
ature drop is slightly higher for treated specimen pairs. On the other hand, TCC
also increases with average interface temperature for treated and untreated contacts.
However, the variation of TCC with average interface temperature is '5% for treated
specimen pairs while variation is ~22% for untreated specimen pairs for the present

Fig. 4 Interfacial temp. drop
with Average Interface
temperature
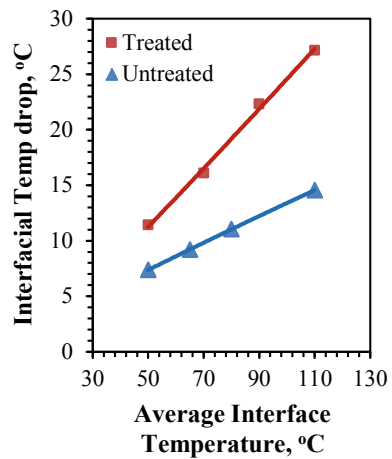
Fig. 5 Variation of TCC
with Average Interface
temperature
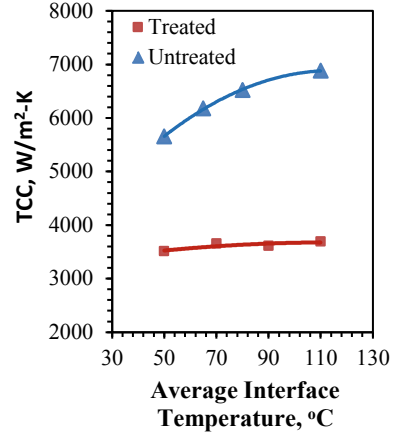
range of temperatures (Fig. 5). Actually, TCC is the combined effect of temperature drop and heat flux at the interface. Moreover, it is observed that the change of heat flux is higher for untreated specimen pairs due to higher conductivity and lower hardness values. Therefore, the percentage change of TCC is higher for untreated specimen pairs. Further, it is experimentally observed that variation of thermal conductivity with temperature in the present range is negligible, as reported in the relevant literature [14].

4.3 Normalized Results and Comparison with Existing Literature

Similar experimental setup and methodology have been used in the various literatures for instance in [9] and [14, 15] but for different materials and working conditions. Therefore, normalized results of the present study have been compared with the existing literatures. The results of TCC for untreated specimen pairs have been compared with existing theoretical models based on plastic deformation and an experimental correlation (Fig. 6); while Fig. 7 shows the comparison with some well-known elastic models. From Fig. 6, it has been observed that experimental results are not matching with the plastic-based models except at lowest load. Further, Fig. 7 presents the considerable agreement of the experimental results with the elastic-based theoretical models except for lowest load. Hence, from the results, it may be concluded that the deformation is more likely to be elastic rather than plastic for untreated TS-MS contacts in the present range of loads. Similar results have been reported for tool steel contacts [9]. Further, the normalized results of TCC for treated specimen pairs have been compared with the elastic models in Fig. 8. It may be noted that the experimental results for treated specimen pairs show well agreement with BGT elastic model in the present range of loads. Hence, the deformation for

Fig. 6 Comparison of
Normalized TCC with
Plastic models for untreated
specimen pairs
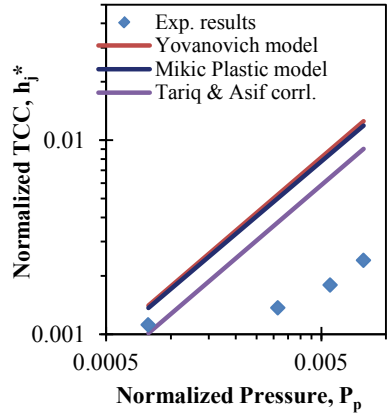
Fig. 7 Comparison of
Normalized TCC with
Elastic models for untreated
specimen pairs
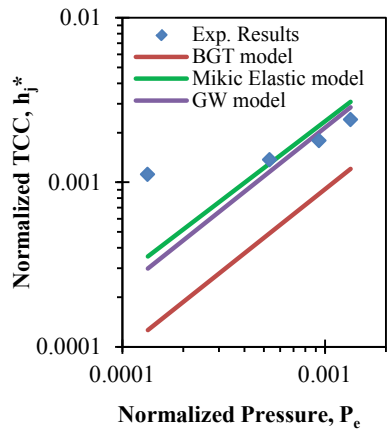
Fig. 8 Comparison of
Normalized TCC with
Elastic models for treated
specimen pairs
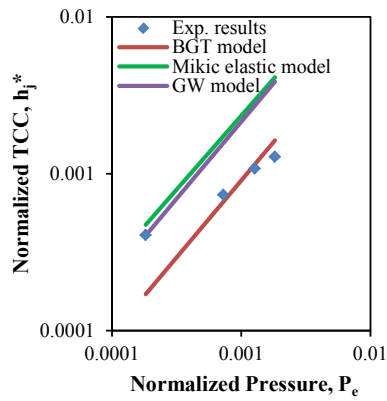
the treated specimen contact seems to be more elastic than untreated ones. Similar findings have also been reported in [9].

It may be due to the increase of mechanical properties of the tool steel with the heat treatment. It may be noted that effect of temperature is not included in the normalization of TCC because it has been resulted earlier that TCC is a weak function of temperature for the present range of temperatures (50–110 °C). On the other hand, TCC has found to be a strong function of contact pressure but depending upon the type of deformation for a particular metal pairs.

5   Conclusions and Scopes of Future Work

The study of thermal contact conductance (TCC) has been performed on tool steel (H-13) and mild steel contacts with and without heat treatment. The following significant conclusions have been drawn from the results:

- Overall, the TCC for treated and untreated specimen pairs has been found to increase with the rise of contact pressure for the present range (1-10 MPa).
- TCC values of TS-MS contact for untreated samples are found to be higher (1.2-2.4 times) than those of treated samples.
- TCC is found to increase with average interface temperature for treated and untreated specimen contacts. However, the variation of TCC is more for untreated specimen pairs than treated ones for the present range of temperatures (50–110 °C).
- The normalized form of experimental results presents well agreement with the elastic models for treated and untreated specimen pairs. However, deformations of treated pairs are more elastic than untreated ones for the present range of parameters.
- The present study would be beneficial for the design of tools, dies and other machine components which are extensively used in machining and metal forming processes.

Scope of Future works

The future work should be focussed towards the study of TCC for other metal pairs like stainless steel, high speed steel, aluminium, etc. Further, the study on TCC should be carried out for many other heat treatment processes like annealing, quenching, tempering, etc.

References

1. Abukhshim, N. A., Mativenga, P. T., & Sheikh, M. A. (2005). Investigation of heat partition on high speed turning of high strength alloy steel. *Journal of Machine Tools and Manufacture, 45,* 1687–1695.
2. Valls, I., Casas, R., Rodriguez, N., & Paar, U. (2010). Benefits from using high thermal conductivity tool steels in the hot forming of steels. In: Italiana 11, 23–28.
3. Ateia, A. A. (2010). Effect of heat treatments on thermal conductivity and mechanical properties of brake rotor material. *Iraqi Journal of Mechanical and Material Engineering, 10*(1), 88–96.
4. Zhang, J., & Gao, A. (2011). Effect of heat treatment on thermal conductivity of 6063 aluminum alloy. In: 2nd International Conferences Mechanical Automation Control Engineering MACE-2011 Proceedings.
5. Wilzer, J., Weber, S., Escher, C., & Theisen, W. (2012). On the relationship of heat treatment, microstructure, mechanical properties, and thermal conductivity of tool steels. In: Proceedings of the 9th International Tooling Conference. Leoben.
6. Wilzer, J., Ludtke, F., Weber, S., & Theisen, W. (2013). The influence of heat treatment and resulting microstructures on the thermophysical properties of martensitic steels. *Journal Materials Science, 48,* 8483–8492.
7. Cingi, C., Rauta, V., Suikkanen, E., & Orkas, J. (2012). Effect of heat treatment on thermal conductivity of aluminum die casting alloys. *Advance Materials Research*, 538–541.
8. Hafenstein, S., Werner, E., Wilzer, J., Theisen, W., & Weber, S. (2015). Influence of temperature and tempering conditions on thermal conductivity of hot work tool steels for hot stamping applications. *Steel Research International, 86*(12), 1628–1635.
9. Sridhar, M. R., & Yovanovich, M. M. (1996). Thermal contact conductance of tool steel and comparison with model. *International Journal of Heat and Mass Transfer, 39*(4), 831–839.
10. Abdul Hay, B., Bourouga, B., & Dessain, C. (2010). Thermal contact resistance estimation at the blank/tool interface: experimental approach to simulate the blank cooling during the hot stamping process. *International Journal of Material Forming, 3,* 147–163.
11. Jam, J. E., & Fard, V. N. (2011). A novel method to determine tool-chip thermal contact conductance in machining. *International Journal of Engineering Science and Technology, 3,* 8491–8501.
12. Courbon, C., Mabrouki, T., & Rech, J. (2013). On the existence of thermal contact resistance at the tool-chip interface in dry cutting of AISI 1045: formation mechanisms and influence on the cutting process. *Applied Thermal Engineering, 50*(1), 1311–1325.
13. Norouzifard, V., & Hamedi, M. (2014). Experimental determination of the tool-chip thermal contact conductance in machining process. *International Journal of Machine Tools and Manufacture, 84,* 45–57.
14. Tariq, A., & Asif, M. (2015). Experimental investigation of thermal contact conductance for nominally flat metallic contact. *Heat and Mass Transfer, 52,* 291–307.
15. Asif, M., & Tariq, A. (2016). Correlations of thermal contact conductance for nominally flat metallic contact in vacuum. *Experimental Heat Transfer, 29,* 1–29.
16. Yovanovich, M. M. (1981). New contact and gap correlations for conforming rough surfaces. In: AIAA 16th Thermophysics Conference, California.
17. Mikic, B. B. (1974). Thermal contact conductance; theoretical considerations. *International Journal of Heat and Mass Transfer, 17,* 205–214.

18. Bush, A. W., Gibson, R. D., & Thomas, T. R. (1975). The elastic contact of a rough surface. *Wear, 35,* 87–111.
19. Greenwood, J. A., Williamson, J. B. P. (1966). Contact of nominally flat surfaces international proceeding royal society, pp. 300–319, A295.
20. ASTM E1225-13 Standard test method for thermal conductivity of solids using the guarded-comparative-longitudinal heat flow technique.

Artificial Neural Network Analysis for Carbon Nanotubes-Based Nanofluid Flow Over Exponentially Stretching Sheet

Srishti Singh and Rajnish Kumar

Abstract The concern of our present investigation is to develop and validate multi-layer feed-forward neural network model to forecast local Nusselt number and skin friction number for convective heat transfer of electrical magneto hydrodynamics (EMHD) flow of water-based nanofluid over an exponentially stretching sheet involving single-walled carbon nanotubes with an impact of thermal radiation. The artificial neural network model developed is a function of various pertinent parameters. The volume fraction of nanoparticle has been varied gradually from 0.0 to 0.20. The weights and bias of the constructed neuromorphic model have been adjusted by Levenberg–Marquardt learning algorithm using datasets obtained from solving the governing equations by implementing finite difference scheme. The bvp4c function of MATLAB has been utilized for this purpose. Statistical accuracy analysis validated that the consequences obtained from the postulated backpropagation neural network model are in remarkable agreement with the numerical results.

Keywords EMHD · Nanofluid · Feed-forward backpropagation · Nusselt number · Skin friction number · Carbon nanotubes

1 Introduction

Carbon nanotubes (CNTs) are widely studied nanomaterial as it has excellent physical, electrical, optical, and thermal properties. Numerous studies have been performed by the researchers that give insight to the fundamental attributes of carbon nanotubes. Many researchers have applied different models of neural network to forecast physical properties of such nanofluids. Artificial neural network (ANN) model

S. Singh (✉)
Department of Electrical & Electronics Engineering, Birla Institute of Technology, Mesra, Ranchi, India
e-mail: srishti.singh1996@gmail.com

R. Kumar
Department of Mathematics, Birla Institute of Technology, Mesra, Ranchi, India
e-mail: rajnish.kumar@bitmesra.ac.in

is an effective and applicable method for forecasting the relation between dependent and independent parameters while mathematical formulation is unavailable or existed relationship has low precision. Afrand et al. [1] developed ANN model to predict viscosity for multi-walled carbon nanotubes/water nanofluid. Alnaqi et al. [2] composed ANN model to analyze the impact of functionalized multi-walled carbon nanotubes on thermal performance factor of water under various Reynolds number. Rabbi et al. [3] designed ANN model to predict entropy generation and MHD flow for copper/water nanomaterial in square cavity with heat sinker. Ahmadi et al. [4] examined three algorithms to predict dynamic viscosity of silver/water nanofluid among which artificial neural network-multilayer perceptron manifested desirable outcomes. Toghraie et al. [5] carried out an experiment to investigate dynamic viscosity of silver/ethylene glycol nanofluid. They also proposed ANN model to forecast the dynamic viscosity by utilizing the experimental data. Akhgar et al. [6] formulated ANN model to predict thermal conductivity of hybrid nanofluid. Reddy and Das [7] constructed ANN model for prediction of influential factors for MHD flow of nanofluid over a permeable stretching cylinder.

Machine learning techniques have the ability to solve complex engineering problems with precision in minimal computational time. The prime target of our current communication is to design an ANN model for prediction of two physical quantities, namely Nusselt number and skin friction number for single-walled carbon nanotubes. The geometrical model of exponentially stretching sheet under influence of electrical magnetohydrodynamics and thermal radiation subjected to convective boundary condition has been taken into consideration. The structured neuromorphic model exhibits appropriate outcomes.

2   Mathematical Model

We have considered two-dimensional steady electrical magnetohydrodynamic convective boundary layer flow of water-based nanofluid over an exponentially stretching sheet in presence of carbon nanotubes. Cartesian coordinates are chosen in such a way that x-axis is along the stretching sheet and y-axis is normal to it. Two equal and opposite forces are applied along the x-axis so that the sheet is stretched with velocity $U_W = U_O \exp\left(\frac{x}{l}\right) at y = 0$. We have taken into consideration magnetic field $B(x) = B_o \exp\left(\frac{x}{2l}\right)$ parallel to y-axis and electric field $E(x) = E_0 \exp\left(\frac{x}{2l}\right)$ applied normal to the flow of nanofluid. The temperature at the sheet is expressed as $T_w = T_\infty + T_0 e^{\frac{x}{2l}}$ where T_0 denotes reference temperature and ambient temperature is denoted as T_∞. Magnetic and electric field obeys Ohm's law defining $J = \sigma(E + V \times B)$ where J is Joule current, σ is the electrical conductivity, and V is the fluid velocity. In addition to it, thermal radiation is taken into consideration at thermal boundary layer while induced magnetic field and slip at the boundary conditions are neglected. Using the above-mentioned description of model, the governing equations can be expressed as:

$$\frac{\partial u}{\partial x} + \frac{\partial v}{\partial y} = 0 \tag{1}$$

$$u\frac{\partial u}{\partial x} + v\frac{\partial u}{\partial y} = v_{nf}\frac{\partial^2 u}{\partial y^2} - \frac{\sigma B^2}{\rho_{nf}}u + \frac{\sigma E B}{\rho_{nf}} \tag{2}$$

$$u\frac{\partial T}{\partial x} + v\frac{\partial T}{\partial y} = \alpha_{nf}\frac{\partial^2 T}{\partial y^2} - \frac{1}{(\rho C_p)_{nf}}\frac{\partial q_r}{\partial y} \tag{3}$$

In the above equations, *u and v* are the components of velocity along the x-axis and y-axis, respectively, v_{nf} represents kinematic viscosity, μ_{nf} represents dynamic viscosity of nanofluid, ρ_{nf} represents effective density of nanofluid, α_{nf} represents thermal diffusivity of nanofluid, k_{nf} represents thermal conductivity of nanofluid, c_p represents heat capacity at constant pressure, $(\rho Cp)_{nf}$ represents effective heat capacity, and T represents nanofluid temperature.

$$\left.\begin{array}{l} \mu_{nf} = \frac{\mu_f}{(1-\emptyset)^{2.5}}\alpha_{nf} = \frac{k_{nf}}{(\rho c_p)_{nf}} \\ (\rho Cp)_{nf} = (\rho Cp)_f(1-\emptyset) + (\rho Cp)_{CNT}\emptyset \\ \rho_{nf} = (1-\phi)\rho_f + \phi\rho_{CNT} \end{array}\right\} \tag{4}$$

As per Xue model, thermal conductivity can be defined as:

$$k_{nf} = k_f \frac{1-\emptyset + 2\emptyset\frac{k_{CNT}}{k_{CNT}-k_f}In\frac{k_{CNT}+k_f}{2k_f}}{1-\emptyset + 2\emptyset\frac{k_f}{k_{CNT}-k_f}In\frac{k_{CNT}+k_f}{2k_f}} \tag{5}$$

According to Rosseland's approximation, radiative heat flux q_r which is applied to Eq. (3) has the form

$$q_{r=} - \frac{4\sigma^*}{3k^*}\frac{\partial T^4}{\partial y} \tag{6}$$

where k^* and σ^* represent the mean absorption coefficient and the Stefan–Boltzmann constant, respectively. We assume that the difference in temperature inside the flow is adequately very small such that T^4 can be expressed as a linear function of temperature. Thus, expanding T^4 using Taylor series about T_∞ and discarding higher-order terms, we obtain

$$T^4 \cong 4T_\infty^3 - 3T_\infty^4 \tag{7}$$

Using Eqs. (6) and (7), Eq. (3) can be rewritten as:

$$u\frac{\partial T}{\partial x} + v\frac{\partial T}{\partial y} = \alpha_{nf}\frac{\partial^2 T}{\partial y^2} + \frac{16\sigma^* T_\infty^3}{3k^*(\rho c_p)_{nf}}\frac{\partial^2 T}{\partial y^2} \tag{8}$$

The boundary conditions for velocity and temperature are expressed as:

$$\left. \begin{array}{ll} u = U_w, \; v = 0, \quad -k_{nf}\frac{dT}{dy} = h_f(T_f - T) \; at \quad y = 0 \\ u \to 0, \;\; T \to T_\infty \qquad\qquad\qquad\qquad at \quad y \to \infty \end{array} \right\} \tag{9}$$

Hereby, self-similarity transformations are introduced which are expressed as:

$$\left. \begin{array}{ll} \eta = \sqrt{\frac{u_0}{2\upsilon l}} e^{\frac{x}{2l}} y, \qquad u = u_0 e^{\frac{x}{l}} f'(\eta), \\ v = -\sqrt{\frac{\upsilon u_0}{2l}} e^{\frac{x}{2l}} \{f(\eta) + \eta f'(\eta)\}, \qquad \theta(\eta) = \frac{T - T_\infty}{T_w - T_\infty} \end{array} \right\} \tag{10}$$

By employing the transformation, governing Eqs. (1–3) are reduced to:

$$f''' - (1 - \emptyset)^{2.5}\left[(1 - \emptyset + \frac{\rho_{CNT}}{\rho_f}\emptyset)(2f'^2 - ff'') + M(f' - E_1) \right] = 0 \tag{11}$$

$$\theta'' + \frac{1}{\left(\frac{k_{nf}}{k_f} + \frac{4}{3}Nr\right)} Pr\left\{ 1 - \emptyset + \emptyset\frac{(\rho Cp)_{CNT}}{(\rho Cp)_f} \right\}\{f\theta' - f'\theta\} = 0 \tag{12}$$

The boundary conditions (9–10) are expressed as:

$$\left. \begin{array}{l} f = 0, \quad f' = 1, \; \theta' = -ABi(1 - \theta) \; at \; \eta = 0 \\ f' \to 0, \; \theta \to 0 \; at \eta \to \infty \end{array} \right\} \tag{13}$$

In the above transformed equations, M symbolizes magnetic field factor, E_1 represents electric field factor, Pr denotes Prandtl number, Nr indicates radiation factor, Bi stands for Biot number, and prime denotes differentiation with respect to η. The involved physical parameters are expressed as:

$$M = \frac{\sigma 2l B_0^2}{\rho_f U_0}, \; E_1 = \frac{E_0}{U_w B_0}, \; Pr = \frac{\upsilon_f}{\alpha_f}, \; Nr = \frac{4\sigma^* T_\infty^3}{kk^*}, \; Bi = \frac{h_f y}{k_f \eta}, \; A = \frac{k_f}{k_{nf}}$$

The physical quantities of practical interest in the present study are skin friction factor C_f and local Nusselt number Nu_X which are defined as:

$$\left. \begin{array}{ll} C_f = \frac{\tau_w}{\rho_f U_w^2} & where \; \tau_w = \mu_{nf}\left(\frac{\partial u}{\partial y}\right)_{y=0} \\ Nu = \frac{xq_w}{k_f(T_w - T_\infty)} & where \; q_w = -\left(\left(k_{nf} + \frac{16\sigma^* T_\infty^3}{3k^*}\right)\frac{\partial T}{\partial y}\right)_{y=0} \end{array} \right\} \tag{14}$$

In the above-mentioned expression, τ_w is the surface shear stress along x-axis and q_w is the heat flux. The local Reynolds number is given as $Re_x = \frac{U_w l}{\upsilon_f}$. The physical quantities are expressed in non-dimensional form as follows:

$$\frac{Re_x^{1/2}}{\sqrt{2}} C_f = f''(0) \frac{1}{(1-\emptyset)^{2.5}} \tag{15}$$

$$\frac{Nu_x \sqrt{2}}{Re_x^{1/2}} = -\left(\frac{k_{nf}}{k_f} + \frac{4}{3} \text{Nr}\right) \frac{x}{l} \theta'(0) \tag{16}$$

3 Neuromorphic Model

Artificial neural network (ANN) is a data handling paradigm inspired by human nervous systems which incorporates the brain preparing the data. A ton of interconnected neurons working in congruity with one another is the primary establishing portions of this framework toward the goals of solving unique issues. Predominantly, neural systems are the scientific techniques developed for performing various tasks. It is a subset of computational intelligence which has emerged as one of the superlative techniques in the field of extrapolation. It has the capability to capture any nonlinear relationship between the input variables and output variables. Figure 1 depicts the schematic diagram for multilayer perceptron network.

The postulated ANN model in the present study embodies an input layer, hidden layer, and an output layer. In this network, two activation functions, namely 'tan-sigmoid' and 'purelin,' are used after hidden layer and output layer, respectively. The input layer is a function of five independent parameters, namely magnetic parameter, electric parameter, volume fraction, radiation parameter, and Biot number. Each neuron in the input layer is interconnected with neurons in the hidden layer with weights and bias. The number of neurons in the hidden layer is chosen empirically and behaves as summing nodes. The flow of signal in feed-forward network is unidirectional in nature. The generated signals are transmitted from input layer to the output layer which comprises one neuron for prediction of skin friction number and Nusselt number alternatively. The expression for MLP has been presented below:

$$Y_i = f\left(\sum_{i=1}^{n} w_{ij} x_{ij} + b_j\right) \tag{17}$$

Figure 2 demonstrates the steps applied to design the proposed ANN model. The network utilizes Levenberg–Marquardt backpropagation training algorithm, one of the widely used supervised learning algorithm, to minimize the chosen error function. In this optimization process, the output unit is compared with its target value to determine the error. The training is accomplished by adjusting the weights and bias and the process is terminated when global minima for the chosen error function is achieved. The expression for updating ANN parameter in LM training algorithm is stated underneath
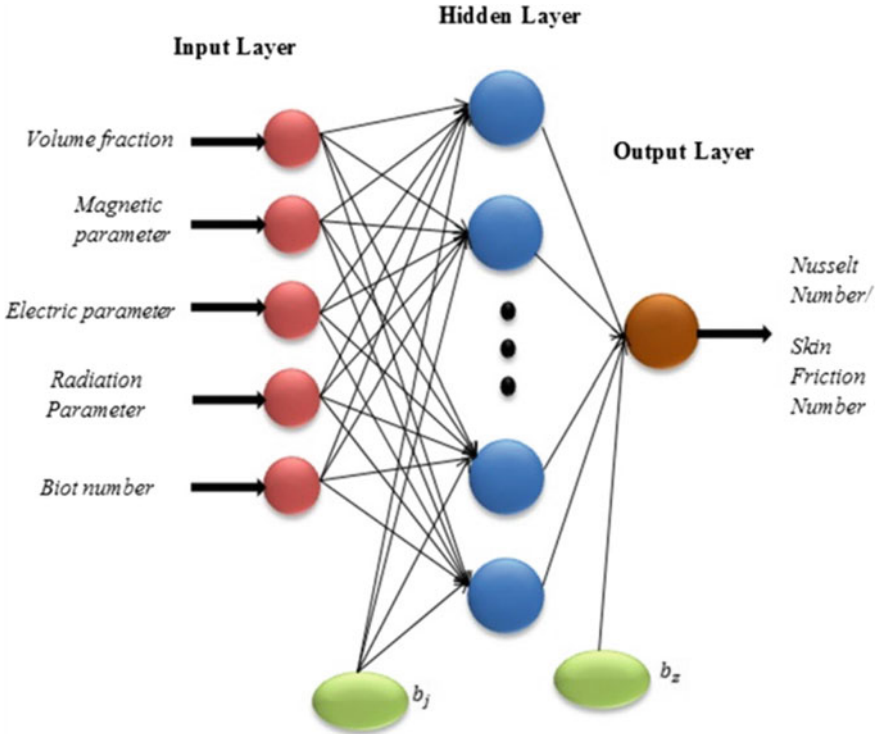
Fig. 1 Schematic diagram of MLP network model

$$w_{s+1} = w_s - \left(J_s^T J_s + \lambda I\right)^{-1} J_s^T e_s \qquad (18)$$

In the above two expressions, w_{ij} denotes weights between ith and jth neuron, x_{ij} denotes input from ith to jth neuron, b_j denotes bias weight, J denotes Jacobian matrix, and λ denotes rate of learning.

3.1 Performance Indices

The performance of suggested multilayer backpropagation model has been determined by computing the mean square error (MSE) and coefficient of correlation (R). These performance metrics have been extensively used in numerous studies and provide an effective means of determining the robustness of neuromorphic model for prediction of skin friction and Nusselt number. The performance indices are described below:
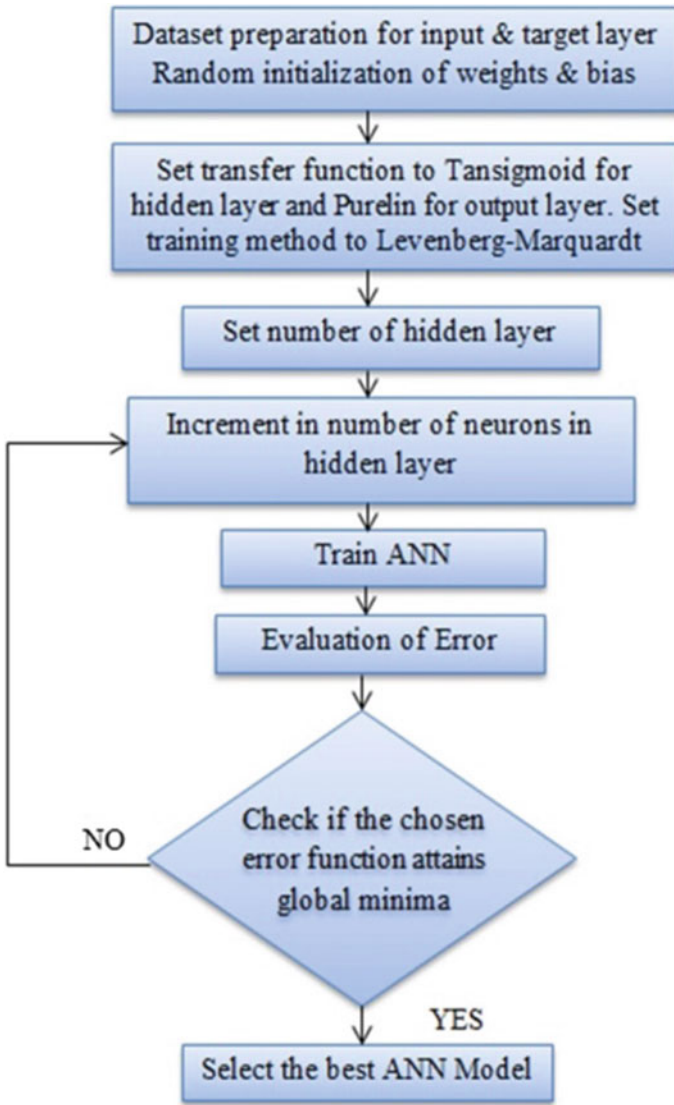
Fig. 2 The applied algorithm to create optimized ANN

$$MSE = \frac{1}{n} \sum_{i=1}^{n} e_i^2 \ where \ e : (target - predicted) \tag{19}$$

$$R = \frac{\sum XY}{\sqrt{\sum X^2 \sum Y^2}} \ where \ X_{target} = (x - \bar{x}) Y_{predicted} = (y - \bar{y}) \tag{20}$$

4 Result and Discussions

The governing Eqs. (1)–(3) are transfigured into a set of nonlinear coupled ordinary differential Eqs. (11)–(12) with suitable self-similarity transformations. These transformed equations are solved using $bvp4c$ function of MATLAB. Nusselt and skin friction number are numerically obtained for five pertinent parameters which are then set as target dataset for multilayer perceptron network. The input parameters for the ANN model which are function of distinct independent variables consists of numerous numeric samples for each physical quantity. Subsequently, the prepared dataset is divided into different subsets of training, testing, and validation in the ratio of 70 : 15 : 15. MATLAB Neural Network Toolbox with batch training mode has been implemented which utilizes backpropagation training algorithm for the purpose of prediction. Figure 3 illustrates the ANN design created in MATLAB environment for the considered problem. The thermophysical properties of nanoparticle and base fluid have been represented in Table 1.

The values of mean square error (MSE) and coefficient of correlation (R) for different architecture of neural network are presented in Table 2. In our current study, construction of MLP considers single hidden layer because it is propounded that any nonlinear relation can efficiently be established by a configuration comprising single hidden layer. To achieve optimum ANN configuration, neurons in the hidden layer are chosen empirically. It is demonstrated that neurons in hidden layer are incremented by one initiating with four. From Table 2, it can be inferred that ANN architecture that comprises of nine neurons in its hidden layer is ideal for accomplishing the task of prediction of skin friction and Nusselt number because this configuration manifests
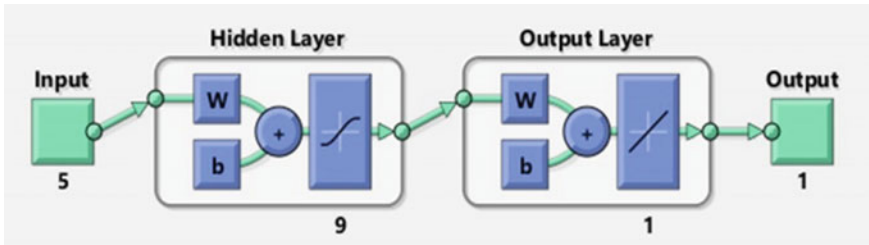
Fig. 3 Design of multilayer perceptron network in MATLAB

Table 1 Thermosphysical properties

Physical properties	Base fluid: Water	Nanoparticle: Single-walled carbon nanotube
$\rho\,(\mathrm{kg/m}^3))$	997	2600
$c_p\,(\mathrm{J/kg\ K})$	4179	425
$k\,(\mathrm{W/m\ K})$	0.613	6600
Pr	6.2	

Table 2 Performance of multilayer perceptron network

Number of neurons in hidden layer	Skin friction number Training dataset		Nusselt number Training dataset	
	Mean square error	Coefficient of regression	Mean square error	Coefficient of regression
4	1.74152E-3	9.82339E-1	2.6601E-4	9.99077E-1
5	3.48807E-3	9.69087E-1	9.25039E-5	9.99648E-1
6	3.13397E-3	9.72045E-1	6.41286E-5	9.99761E-1
7	2.80677E-3	9.70745E-1	1.52309E-5	9.94955E-1
8	3.01290E-3	9.64360E-1	1.54733E-6	9.99993E-1
9	**5.71663E-8**	**9.99999E-1**	**6.11120E-7**	**9.99998E-1**
10	5.88515E-4	9.93550E-1	4.91572E-5	9.99841E-1
11	2.86865E-3	9.68374E-1	1.24046E-5	9.99968E-1
12	3.05609E-5	9.62673E-1	1.38276E-4	9.99406E-1
13	1.23823E-5	9.99867E-1	4.18983E-5	9.99857E-1
14	2.80991E-3	9.72336E-1	5.52868E-4	9.98351E-1
15	2.87347E-3	9.69965E-1	1.60223E-5	9.99956E-1

minimum MSE and maximum R during the process of training. Additionally, it is seen that increment in the quantity of neuron in hidden layers may not be beneficial fundamentally.

Figures 4, 5, 6 and 7 depict linear regression plot for skin friction number between the target values and the predicted results acquired from neural network. The best

Fig. 4 Regression plot for training subset for skin friction number
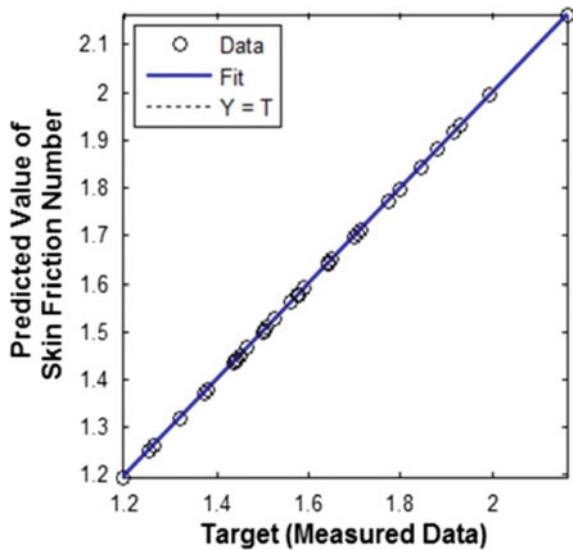
Fig. 5 Regression plot for testing subset for skin friction number
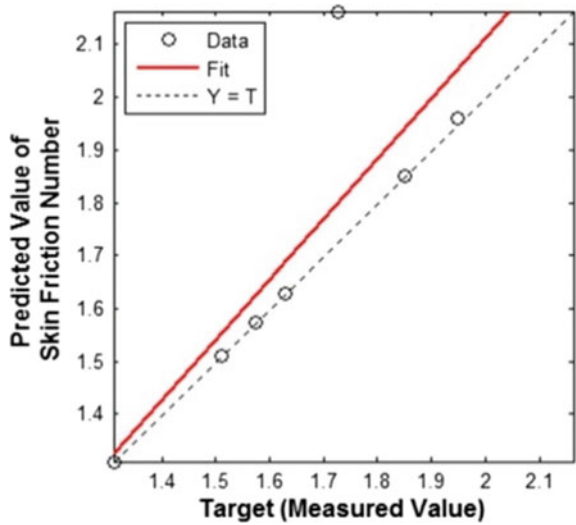
Fig. 6 Regression plot for validation subset for skin friction number
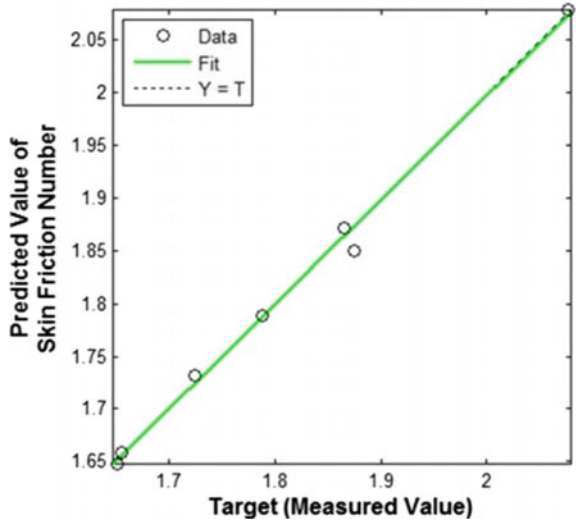
fit line exhibits exact fitness of the measured values with the predicted outcomes. It is noticed that the ANN model is trained properly and it is demonstrated in Fig. 4 that there is a remarkable correlation between measured and predicted results with value of R equal to 0.99999. The mutuality obtained between measured and predicted results for test dataset, validation dataset, and all data is represented in Figs. 5, 6, and 7, respectively. It is marked that value for coefficient of correlation R for test, validation, and all data is given as 0.83431, 0.99745, and 0.96366, respectively. The consequences uncover that the predicted outcomes are in remarkable compatibility

Fig. 7 Regression plot for all dataset for skin friction number
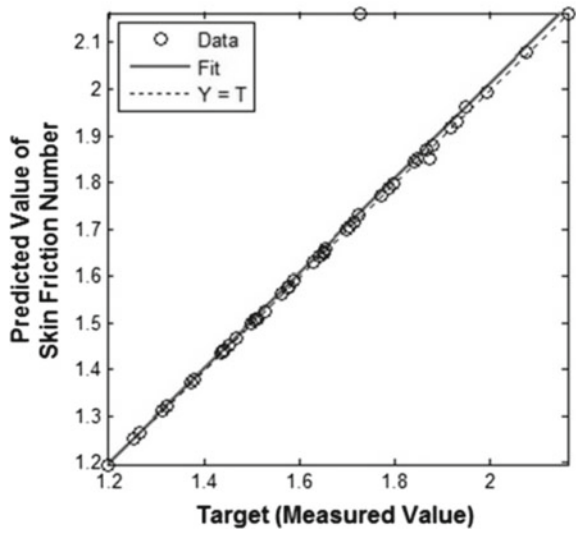
with the numerical data. Similarly, Figs. 8, 9, 10 and 11 represent linear regression plot for Nusselt number. The value for coefficient of correlation R acquired for the four subsets, namely training, testing, validation, and all data, is given as 0.99999, 0.99849, 0.99998, and 0.99976, respectively. This examination so far uncovers that by utilizing ANN model, Nusselt number, and skin friction number can be designed alternatively with viable precision. The outcomes acquired from the ANN model are in generally excellent concurrence with the numerical outcomes.

Fig. 8 Regression plot for training subset for Nusselt number
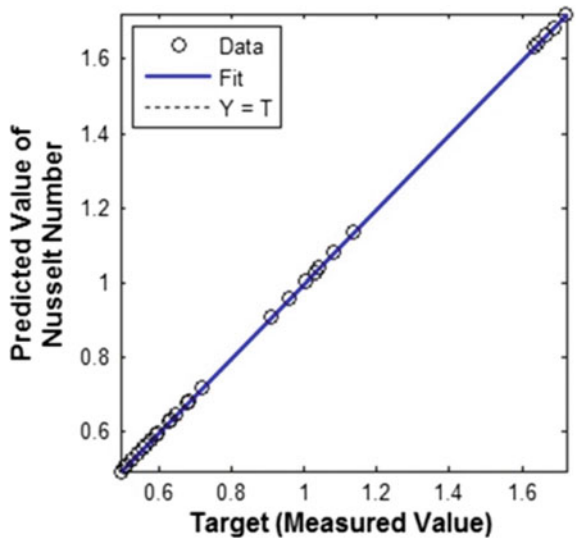
Fig. 9 Regression plot for testing subset for Nusselt Number
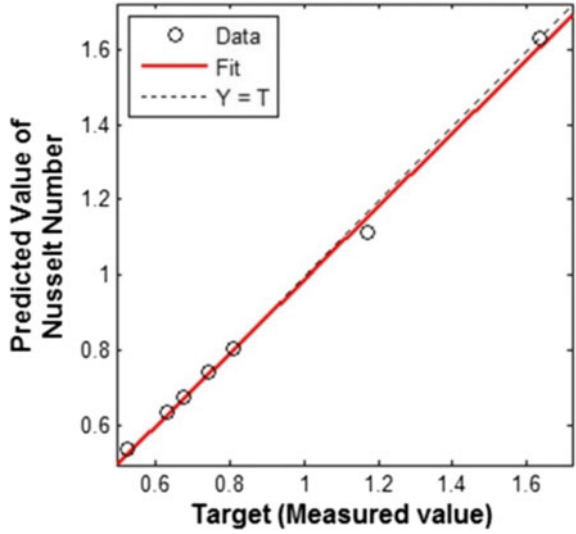
Fig. 10 Regression plot for validation subset for Nusselt number
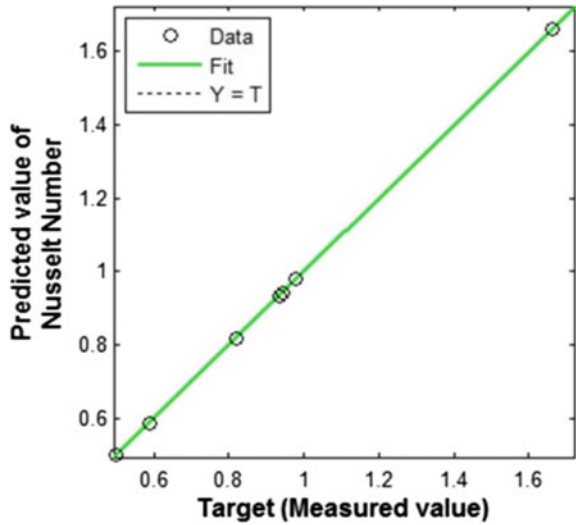
To evaluate the credibility and exactness of the suggested ANN technique, the numerically calculated values for the skin friction and Nusselt number are contrasted with the predicted outcomes by varying different parameters. The outcome of these quantities incorporating different pertinent parameters is well demonstrated in Tables 3 and 4. It is seen that the predicted outcomes are observed to be in fantastic agreement.

Figures (4, 5, 6, 7, 8, 9, 10 and 11) are illustrated below.

Fig. 11 Regression plot for all dataset for Nusselt number
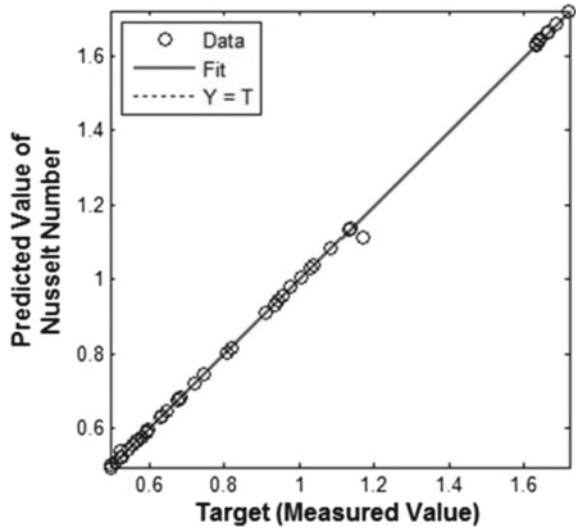
Table 3 Friction factor prediction

Ø	M	E_1	Nr	Bi	$-\frac{Re_x^{1/2}}{\sqrt{2}}C_f$ calculated	$-\frac{Re_x^{1/2}}{\sqrt{2}}C_f$ ANN
0.10	0	0.5	0.5	0.5	1.5755	1.573999
0.20	1	0.5	0.5	0.5	1.9480	1.941614
0.08	0.5	0.5	1	0.5	1.4997	1.497472
0.12	0.5	1.2	0.5	1	1.3720	1.374146
0.18	0.5	1	0.5	0.5	1.6507	1.694695

Table 4 Nusselt number prediction

Ø	M	E_1	Nr	Bi	$\frac{Nu_x l\sqrt{2}}{Re_x^{1/2} x}$ calculated	$\frac{Nu_x l\sqrt{2}}{Re_x^{1/2} x}$ ANN
0.05	0.1	0.5	0.5	0.5	0.5813	0.57867
0.04	0.5	0.5	1	0.5	0.7436	0.74347
0.06	0.5	0.5	0.5	2	1.6400	1.63920
0.03	1	0.5	0.5	0.5	0.6097	0.61270
0.02	0.5	0.5	0.5	1	1.0774	1.08050

5   Conclusions

A multilayer feed-forward neural network has been proposed to predict skin friction number and Nusselt number for electrical MHD boundary layer flow of nanofluid over an exponentially stretching sheet in presence of carbon nanotubes with convective boundary conditions. For this reason, a few numerical cases with union of input factors and output information are made. The coherence of the applied predicted techniques has been explored for various configurations to approve the viability so as to show the results with least reasonable error. The salient outcomes of the present examination are clarified as pursues:

- The composed ANN model with the configuration of 5-9-1 is found to be reliable due to remarkable accuracy during the training, testing, and validation. The proposed ANN model is proficient, precise, and efficient on the grounds that it includes substantially minimum effort and yields outcomes a lot quicker than the numerical techniques. Additionally, it is presumed that the postulated ANN model might be considered as an option and groundbreaking method for understanding the heat and mass transfer perspectives.
- For the training dataset, the friction factor predicted with R and MSE values of approximately 9.99999e-1 and 5.71663e-8, respectively. This estimation for R and MSE demonstrates the precision of the ANN model and its capacity to forecast the impact of different parameters on the behavior of proposed numerical model.
- It is also observed that the Nusselt number predicted from the ANN model manifests precise outcomes as numerical result. It is to be noted that the value of R and MSE obtained for training data set is 9.99998E-1 and 6.11120E-7, respectively.

References

1. Afrand, M., Nadooshan, A. A., Hassani, M., Yarmand, H., & Dahari, M. (2016). Predicting the viscosity of multi-walled carbon nanotubes/water nanofluid by developing an optimal artificial neural network based on experimental data. *International Communications in Heat and Mass Transfer, 77* 49–53.
2. Alnaqi, A. A., Hal, S. S. T., Aghaei, A., Soltanimehr, M., Afrand, M., & Nguyen, T. K. (2019). Predicting the effect of functionalized multi-walled carbon nanotubes on thermal performance factor of water under various Reynolds number using artificial neural network. *Physica A, 521,* 493–500.
3. Rabbi, K. M., Sheikholeslami, M., Shafee, A. K. A., Li, Z., & Tlili, I. (2019). Prediction of MHD flow and entropy generation by Artificial Neural Network in square cavity with heater-sink for nanomaterial. *Physica A*.
4. Ahmadi, M. H., Gharyehsafa, B. M., Gord, M. F., Jilte, R. D., Kumar, R., & Chau, K. W. (2019). Applicability of connectionist methods to predict dynamic viscosity of silver/water nanofluid by using ANN-MLP. *MARS and MPR algorithms, Engineering Applications of Computational Fluid Mechanics, 13*(1), 220–228.
5. Toghraie, D., Sina, N., Jolfaei, N. A., Hajian, M., & Afrand, M. (2019). Designing an Artificial Neural Network (ANN) to predict the viscosity of Silver/Ethylene glycol nanofluid at different temperatures and volume fraction of nanoparticles. *Physica A, 534* 122–142.

6. Akhgar, A., Toghraie, D., Sina, N., & Afrand, M. (2019). Developing dissimilar artificial neural networks (ANNs) to prediction the thermal conductivity of MWCNT-TiO2/Water-ethylene glycol hybrid nanofluid. *Powder Technology, 355,* 602–610.
7. Reddy, P. B. A., & Das, R. (2016). Estimation of MHD boundary layer slip flow over a permeable stretching cylinder in the presence of chemical reaction through numerical and artificial neural network modeling. *Engineering Science and Technology, an International Journal.*

Strengthening of Metal Matrix Composites

Vineet Tirth and **Parul Gupta**

Abstract This article presents the physical and metallurgical parameters, which affect the distribution of the discontinuous reinforcements in the matrix of metals or alloys fabricated by liquid state processing. The metal matrix composites (MMC) were developed using stir casting at a speed of 800 rpm, the temperature of 750 °C using a pitched blade stirrer. The strengthening mechanisms have been predicted using the classical continuum model and the factors affecting the load and stress distribution are discussed explicitly. For the prediction of elastic properties, two simple limiting models of the rule of mixtures are generally used. The rule of the mixture has been found most appropriate for the composites with continuous reinforcements. The iso-stress condition has given lesser error in the elastic modulus. In presence of the deformable particles, the composite may undergo extensive plastic deformation. The mathematical models and the empirical relationships suggested in this article will help the researchers and industries to design the discontinuously reinforced composite materials and to control the reinforcement distribution and matrix strengthening.

Keywords Metal matrix composites · Strengthening of composites · Dislocations · Plastic deformation

1 Introduction

In the past four decades, a diversity of fabrication methods has evolved to augment the microstructure and obtain desirable properties of composites made from metallic matrix. These processing techniques are reviewed from time to time by the

V. Tirth (✉)
Mechanical Engineering Department, College of Engineering, King Khalid University, Abha 61411, Kingdom of Saudi Arabia
e-mail: vtirth@kku.edu.sa

P. Gupta
Mechanical Engineering Department, Moradabad Institute of Technology, Moradabad 244001, UP, India
e-mail: parulgupta197@gmail.com

researchers [1–4]. The size of the reinforcement is of the order of 10–100 μ in such composites, and they are often referred to as macro-composites. However, to obtain the composites with fine reinforcement, of the order of one micron or lesser, reaction synthesis is employed. The matrix material in metal matrix composites (MMCs) may be solid; in the form of powder, film or sheet; liquid, as melted metal or alloy; and vapor, as superheated melted metal atomized to generate a spray. In the liquid state processing, there exists a linear relationship between the pressure and the freezing time. It was reported that the metallurgical parameters depend on the composition, temperature, and pressure at which the composites are prepared [5, 6].

2 Materials and Methods

2.1 Materials

In this article, the composites have been prepared with commercial 98.5% pure α-Al $(1,1,1)$ as the matrix and active Al_2O_3 particles (purity >99%) of size range ~100 microns as the reinforcement with a fixed weight percent of 7%.

2.2 Experimental Procedure

The metal matrix composites were developed using stir casting at a stirring speed of 800 rpm, the temperature of 750 °C, and using a pitched blade stirrer. Figure 1a shows the photo of the stirrer and Fig. 1b demonstrates the line diagram of the stir casting setup. The mechanical stirring was used to mix the Al_2O_3 particles in the superheated liquid Al. Stirring was done at fixed time of 60 s. The stirrer blade was made from mild steel and coated with zirconia particles suspended in acetone. A top loading electrical resistance-muffle furnace was used for melting and chromel–alumel thermocouples were used for temperature measurement.

Archimedes principle was used to estimate the density of the composites and the porosity was determined by the difference in volume of the composite and the sum of the volumes of the matrix and the reinforcement.
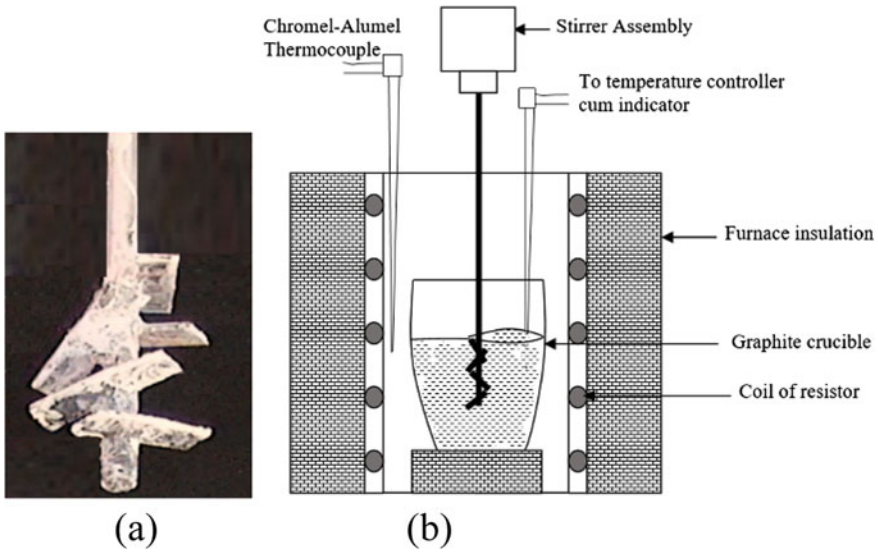
Fig. 1 a Photo of pitched blade stirrer used in the study. **b** Line diagram of the stir casting setup

3   Results and Discussion

3.1   Properties of Composites

A few mechanical properties experimentally determined for the Al-7 wt%Al$_2$O$_3$ composite are given in Table 1 and the density of the materials in Fig. 2. The ultimate tensile stress (UTS) and the 0.2% proof stress of the composite increased by 76% and 74.4%, respectively. In Al, the proof stress is 78.9% of the UTS and in composite, it is 81% of the UTS. The hardness has also shown improvement but the ductility of the composite has decreased by 25%. The density of Al$_2$O$_3$ is highest, being a ceramic, followed by the density of the composite and Aluminum.

For the prediction of elastic properties of a two-phase composite, two simple limiting models of rule of mixtures are generally used [7, 8]. The first one represents an iso-strain condition of the two phases and predicts the upper limit of the elastic modulus of the composite, which is given in Eq. (1).

Table 1 Mechanical properties of the materials

Material	Ultimate tensile stress [N/mm^2]	0.2% offset proof stress [N/mm^2]	Ductility [% Elongation]	Hardness [BHN]
Aluminum (Cast)	55.6	43.92	35.25	99.2
Al-7 wt%Al$_2$O$_3$ Composite	72.8	58.96	9.7	107.6
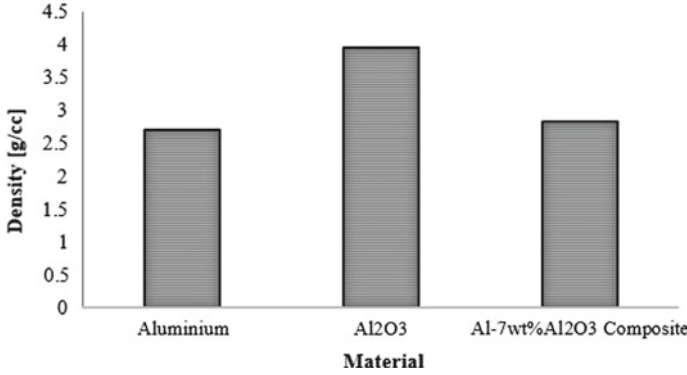
Fig. 2 Density of the materials in g/cc

$$E_c = E_f V_f + E_m V_m \tag{1}$$

Where E_m, E_c, and E_f are the modulus of elasticity of the matrix, composite, and reinforcement, respectively, and V_m and V_f are the volume portions of the matrix and reinforcement. The other expression is given in Eq. (2) represents an iso-stress condition of the two phases and predicts the lower limit estimate of the elastic modulus.

$$E_c = \frac{E_f E_m}{E_f V_m + E_m V_f} \tag{2}$$

The volume fraction of the composite and constituents has been estimated for validation of Eqs. (1) and (2) with the experimental results and are given in Table 2. The volume fraction of the Al_2O_3 particles is 3.84% and porosity is 0.95% in the composites.

The rule of the mixture has been found most appropriate for the composites with continuous reinforcements. However, it has also been modified for the composites of discontinuous reinforcement and is expressed by Eq. (3).

$$E_c = \frac{(1 + 2 A q V_f) E_m}{1 - q V_f} \tag{3}$$

Table 2 Volume fraction of the composite and its constituents

Material	Volume [cc]	Volume fraction [%]
Composite V_c	356.60	100
Matrix (Al) V_m	339.51	95.2
Reinforcement V_f	13.7	3.84
Porosity V_p	3.39	0.95

Fig. 3 Aspect ratio of
particle
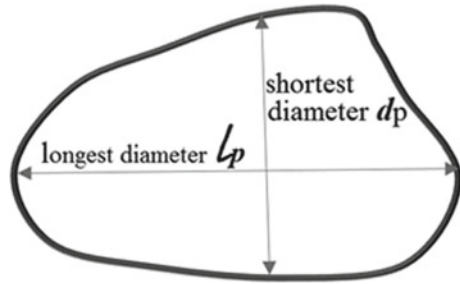
Table 3 Validation of iso-strain and iso-stress equation for Al-7 wt%Al$_2$O$_3$ composite

Material	E_c (Calculated from the equation) [GPa]	E_c (Experimentally determined) [GPa]	Error [%]
Iso-strain condition Eq. (1)	79.89	73.50	8.70
Iso-stress condition Eq. (2)	71.93	73.50	2.13

Where A is the aspect ratio (l_p/d_p) of the particle, represented by Fig. 3 and q may be estimated by Eq. (4).

$$q = \frac{E_f / E_m - 1}{E_f / E_m + 2A} \tag{4}$$

The iso-strain (Eq. (1)) and the iso-stress (Eq. (2)) equations are validated experimentally and the results are given in Table 3.

The elastic modulus of the composite was calculated by the both iso-strain and iso-stress equations and also determined experimentally by the slope of the stress–strain curve. A comparison of the values given in Table 3 shows that for the discontinuously reinforced composite (Al-7 wt%Al$_2$O$_3$), the iso-stress condition is more valid as it gives an error of 2.13% while the iso-strain condition given an error of 8.7%.

3.2 Strengthening of Composites

Numerous strengthening mechanisms have been proposed for discontinuously reinforced composite materials [10–12. The strength of a composite is reliant on the plastic behavior of its phases. Beyond the elastic limit of a composite, the matrix deforms plastically while the strengthening phase may deform elastically under the stress concentration imposed by the virtue of its continuity with the matrix. Thus, the strengt of composite material is to be considered from the perspective of deformable or non-deformable particles [13, 14]. In presence of the deformable particles, the composite may undergo extensive plastic deformation. The stress initiating gross plastic flow is independent of the volume concentration of the particles and their

mean free path. The yield stress of the composite, σ_{yc} under a matrix constraint, sufficient to develop stresses to deform the particle is expressed by Eq. (5) [5]. Where G_p and G_m are the shear moduli of the particle and matrix, respectively, b is Burger's vector of the dislocation pile up against the particle, and c is a constant depending upon the shear stress and shear strain.

$$\sigma_{yc} = \left[(G_m G_p b)/c \right]^{1/2} \tag{5}$$

The yield strength of non-deformable particles composite is expressed by Eq. (6) [6].

$$\sigma_{yc} = \left[(G_m G_p b)/c\,\lambda_1 \right]^{1/2} \tag{6}$$

where λ_1 is the inter-particle spacing expressed by Eq. (7) [6].

$$\lambda_1 = d_o[\sqrt{(2\pi/3V_f)} - \sqrt{(8/3)}]/2 \tag{7}$$

Where $d_o = \sqrt{(3/2l)}$, l is the mean linear intercept of random particle distribution, and V_f is the particle volume proportion.

Mileiko [14] was the first who developed a concept correlating the ductility and strength of two ductile constituents to the mechanical properties of the composite with fibers as reinforcement. It is centered upon the application of plastic unpredictability criteria. The criteria are applied under the following assumptions: (i) the bond amid the fiber and the matrix is perfect so that there exists equal strain in both the phases; (ii) the flow stress of the composite can be estimated by the law of mixture; and (iii) the association between the strain and stress of both the composite and the components follow a power law expressed by Eq. (8) [14].

$$\sigma_c = k_f\, \varepsilon_c^n \tag{8}$$

Where σ_c is the stress, ε_c is the critical strain, and k_f and n are constants. The constant k_f is used to account for the incompressibility of the material and the constant n is a number, which determines the critical value of the strain.

Classical composite strengthening (Models of continuum) are based on the assumption that there exist a load transfer and sharing mechanism between the reinforcement and the matrix, which undergoes a non-plastic deformation. Based on the same assumption, in shear-lag theory, the transmission of load transpires from the base matrix and the reinforcement having high aspect ratio through the shear stresses developed at the reinforcement–matrix interfaces. An adapted shear-lag theory also explains the transfer of load at the ends of the reinforcement to predict the composite yield stress, given in Eq. (9) [13]. Where σ_{yc} and σ_{ym} represent the yield stress of the composite and the un-reinforced alloy matrix, t and L represent the reinforcing particulate lengths parallel and perpendicular to the stress, respectively, A is the aspect ratio of particulate, and V_f is the volume proportion of particulates.

$$\sigma_{yc} = \sigma_{ym} V_f \left[1 + \frac{(L+t)A}{4L} \right] + \sigma_{ym}(1 - V_f) \tag{9}$$

In case of an equiaxed reinforcement particulate, Eq. (9) maybe reduced to Eq. (10).

$$\sigma_{yc} = \sigma_{ym}(1 + \alpha\, V_f) \tag{10}$$

Where α is a constant which has different values as reported by researchers given hereunder:

$\alpha = 1/2$ [13]

$\alpha = 4(DZ)^2/\pi^2$ [14]

Where Z is the average of reciprocal of section diameter of the plane and D is the average size of the particle.

$\alpha = -0.3$ [14, 15] in steel with dual phase.

It is noteworthy that Eq. (10) is linear; however, the increase in σ_{yc} is marginal in response to the increase in the volume proportion of the particle.

Dispersion strengthening-Orowan strengthening: Another possible explanation of the observed strengthening of particulate reinforced aluminum-based composite is based on the Orowan theory. The moving dislocations can adjust and bypass the reinforcement particulates, which are difficult to penetrate, leaving a footprint called Orowan loop. For polycrystalline materials, σ_{yc} of the composite may be estimated by Eq. (11) called an Orowan relationship.

$$\sigma_{yc} = \frac{0.83M\, G\, b}{2\pi\sqrt{1-\nu}} \frac{\ln(2r_s/r_o)}{\lambda} \tag{11}$$

Where λ represents the average inter-particle separation over the plane of slip, G represents shear modulus, M is a factor called Taylor factor, b is burger vector, r_o is cut-off radius, ν is the Poisson's ratio, and r_s is effective particulate radius.

Effects of dislocation density: It is a well-known phenomenon that the dislocations are generated in the composites during solidification and also during heat treatment due to the difference in the coefficient of thermal expansion between the reinforcement particulates, which are often ceramics in the metallic matrix. The thermal expansion coefficient of the later is much higher than the former. A few examples of such composites are $Al-Al_2O_3$, $Al-SiC$, $Al-MgO$, etc. The same philosophy is applicable to the fibers and platelets. With the increase in the number of dislocations, the dislocation density increases leading to an increase in the strength of the composite, which is a function of the dislocation density, which in turn depends on the strength of the matrix, the amount of reinforcement, and their size [16].

Multiple dislocations–Models of particle interaction: The metallic materials are normally polycrystalline with a single phase. Their yield stress σ_{yc} is phenomenally proportionate to the diameter of the grain, d_g, represented by the universal Hall–Petch expression given in Eq. (12).

$$\sigma_{yc} = \sigma_o + \frac{K_y}{\sqrt{d_g}} \tag{12}$$

In Eq. (12), K_y is the grain boundary's resistance to slip, also called a Hall–Petch gradient. The values of K_y at ambient temperature are (i) for face-centered cubic (fcc), in the range of 0.05-0.1 MPa-m$^{1/2}$; (ii) for body-centered cubic (bcc) metals, 0.3–1.8 MPa-m$^{1/2}$. A factor σ_o is used to rationalize the internal back stresses and the stress resistance due to friction, during the gliding motion of dislocation.

4 Conclusions

The theories of particle incorporation, rejection, and the strengthening of the composites have been reported and discussed in this article. Some theories have been applied to validate their applicability to the Al-7%Al$_2$O$_3$ composites prepared in this study. The following conclusions are drawn from the study.

1. The UTS and the 0.2% proof stress of the composite increased by 76% and 74.4%, respectively, compared with the Al. In Al, the proof stress is 78.9% of the UTS and in composite, it is 81% of the UTS. The hardness has also shown improvement but the ductility of the composite has decreased by 25%.
2. The volume fraction of the Al$_2$O$_3$ particles is 3.84% and porosity is 0.95% in the Al-7%Al$_2$O$_3$ composites.
3. The validation of the elastic modulus with experimental values revealed that for the discontinuously reinforced composites, the iso-stress condition gives more accurate results.

The deliberations of this study have given opportunities to validate the experimental results and theoretical estimations. The comparison of elastic modulus has been made in this study; similar approach may be used to validate the other properties. A better design of a composite material may be achieved with this methodology. A comparison of the predicted and experimentally determined strength of the composites processed with the other advanced processes like plasma sintering, powder metallurgy, and liquid melt infiltration, reactive synthesis, etc., may be another interesting study.

References

1. Miracle, D. B. (2005). Metal matrix composites-from science to technological significance. *Composites Science and Technology, 65,* 2526–2540.
2. Clyne, T. W. (2001). Metal Matrix Composites: Matrices and Processing In A. Mortensen (Ed.), *Encyclopedia of materials: Science and technology* (pp. 1–14). Elsevier.
3. Koczak, M. J., & Premkumar, M. K. (1993). Emerging technologies for the in-situ production of MMCs. *Journal of Materials Science, 45*(1), 44–48.

4. Tjong, S. C., & Ma, Z. Y. (2000). Microstructural and mechanical characteristics of in-situ metal matrix composites. *Materials Science and Engineering A, 29,* 49–113.

5. Tirth, V., & Arabi, A. (2020). Effect of liquid forging pressure on solubility and freezing coefficients of cast aluminum 2124, 2218 and 6063 alloys. *Archives of Metallurgy and Materials, 65*(1), 357–366. https://doi.org/10.24425/amm.2020.131738.

6. Broutman, L. J., Krock, R. H. (1967). Modern Composites Materials. Addison-Wesley Publishing Co., Inc.,7(8), 481–486.

7. Le Roy, G., Embury, J. D., & Edward, G. (1981). A model of ductile fracture based on the nucleation and growth of voids. *Acta Metallurgica, 29,* 1509–1522.

8. Arsenault, R. J. (1991). Strengthening of metal matrix composites due to dislocation generation through CTE mismatch. In R. K. Everett, R. J. Arsenault (Eds.), *Metal matrix composites: Mechanisms and properties* (pp. 101–132). San Diego, CA, USA: Academic Press Inc.

9. Arsenault, R. J., Wang, L., & Feng, C. R. (1991). Strengthening of composites due to microstructural changes in the matrix. *Acta Metallurgica et Materialis, 39,* 47–57.

10. Tirth, V. (2018). Dry sliding wear behavior of 2218 Al-Alloy-Al_2O_3(TiO_2) hybrid composites. *Journal of Tribology, 140*(2), 021603 1–9.

11. Tirth, V., Ray, S., Kapoor, M. L. (2009). Effect of squeeze pressure on aging and mechanical properties of AA2218-5 Wt. Pct. *Al_2O_3 (TiO_2) Composites, Metallurgical and Materials Transactions A, 40*A, 1246–1254.

12. Tirth, V., Algahtani, A., & Mahmoud, E. R. I. (2018). tribological characterization of stir cast 2218 alloy-5%-Alumina-Titania hybrid microcomposites developed by liquid forging. *Materials Expression, 8*(6), 475–488.

13. Ghosh, P. K., & Ray, S. (1986). Effect of porosity and alumina content on the mechanical properties of compocast aluminium alloy-alumina particulate composite. *Journal of Materials Science, 21,* 1667–1674.

14. Mileiko, S. T. (1969). The tensile strength and ductility of continuous fiber composite. *Journal of Materials Science, 4*(11), 974–981.

15. Aikin, R. M., Jr., & Christodoulou, L. (1991). The role of equiaxed particles on the yield stress of composites. *Scripta Metallurgica et Materialia, 25,* 9–14.

16. Prasad, P. R., Ray, S., Gaindhar, J. L., & Kapoor, M. L. (1985). Mechanical poperties of Al-10% Cu alloy particulate composites. *Scripta Metallurgica, 19,* 1019–1022.

17. Nath, S. K., Ray, S., & Kapoor, M. L. (2002). A single-particle model for theoretical estimation of tensile strength of two-phase metals. *Metals Materials and Processes, 14*(3), 241–254.

18. Aikin, R. M. (1997). The mechanical properties of in-situ composites. *Journal of Materials Science, 49*(8), 35–39.

Experimental Analysis of Hydrocarbon Refrigerant and CuO Nano-Particles Based Vapour Compression System

Rajneesh Kaushik, Rajeev Kamal Sharma, Mohit Kalsia, and Kundan Lal

Abstract An experimental study has been carried out to investigate the performance characteristics of a nano-refrigerant in a vapor compression refrigeration system. Experiments are conducted for two different fluids: (i) pure hydrocarbon (HC) refrigerant and (ii) nano-refrigerant. In this study, different concentrations of CuO nanoparticles (0.2, 0.3 and 0.4 g) were added in the base refrigerant. In order to conduct the experiments, some of the parameters were varied such as (i) heat supplied from 25 ~ 26 $^\circ$C, (ii) heat supplied from 35 ~ 36 °C. A significant enhancement in coefficient of performance (COP) is observed which is maximum with nanoparticles concentration of 0.4 g. The cooling speed becomes relatively higher compared to the base refrigerant and is found to be increasing with rise in nanoparticles concentration. In addition, this study also identifies the difficulties and scope for future research. These results may be also used in commercial refrigerators.

Keywords Nanoparticles · Nano-refrigerant · Cooling speed · COP

1 Introduction

Nanofluids are the colloids suspensions of nanoparticles and base fluid. The base fluids could be water, refrigerants, lubricants, and organic fluids and common nanoparticles are metal, metal oxide, metal carbide, and metal nitride. The induction

R. Kaushik (✉) · R. K. Sharma · M. Kalsia
Chitkara College of Applied Engineering, Chitkara University, Punjab, India
e-mail: rajneesh.kaushik@chitkara.edu.in

R. K. Sharma
e-mail: rajeev.sharma@chitkara.edu.in

M. Kalsia
e-mail: kalsiamohit.007@gmail.com

K. Lal
Mechanical Engineering, Thapar Institute of Engineering & Technology, Punjab, India
e-mail: kundanlalrana@thapar.edu

of the nanoparticles by the previous researches has shown a tremendous enhancement in the heat transfer characteristics and thermo-physical properties, which are the critical parameters in calculating the heat transfer rates [1–4]. The thermal transfer characteristics significantly improve because of relative Brownian motion present between base fluid and nanoparticles which carry heat along in the form of convection around nanoparticles with base fluid [5].Nanofluids found to possess a better coefficient of performance because of improved degree of conduction and convection heat transfer [6]. This leads to a better heat transfer properties and in energy savings in refrigeration and air conditioning applications [7]. Though, nanoparticles have better suspension in base fluid than microparticles, but the suspension of the nanoparticles can be improved further with addition of sodium dodecyl benzene sulfonate [8]. This improvement in thermal properties of nanolubricants also enhances the performance of the system [9]. The addition of nanoparticles in lubricants helps to work system efficiently and save energy consumption [10]. With increase in concentration of nanoparticles in base fluid and decrease in the thermal resistance with rise in temperature helps in improving the thermal transfer characteristics [11].Though the increase in particles size and concentration increases the aggregation behavior but it can be inhibited by increasing oil concentration [12]. By increasing the volume concentration of nanoparticles, other properties like the density and viscosity of nano-refrigerant also get affected. A significant increase in the thermal conductivity results in COP enhancement of the system [13]. Although, there are issues related to nanoparticles dispersion stability which primarily depends upon the hydrophilicity and dispersion behavior but dispersant augmentation and optimization treatment increases the dispersion situation markedly [14].The dispersion stability with fullerene C_{60-} nano oils is good for a week. The nanoparticles in mineral lubricants reduce the frictional coefficient especially for lower loads. The lower frictional coefficient increased the COP significantly with R600a and fullerene C_{60} compressors [15]. In the literatures, the studies have been conducted to check various parameters with different refrigerants. However, issues such as global warming, to develop an eco-friendly refrigeration system with less ozone depletion potential (ODP) and global warming potential (GWP) are the future challenges. This paper identifies the new area where research gaps could be brought down and by working and solving the challenges of the conventional refrigeration vapor compression cycle.

2 Methodology

The main objective of experimental verification was to determine the actual performance of nanorefrigerant in vapor compression refrigeration system. In this way, adequate data was obtained by varying the concentrations of nanoparticles. All the tests were conducted at 30 ± 2 °C which are close to tropical conditions. The tests were performed on the experimental set up which was fabricated in Thapar University laboratory as given in Fig. 1. The main parameters to be measured during the experiments were temperature and pressure at various points. These points were compressor

Fig. 1 Test rig

inlet, compressor outlet, expansion valve inlet, and outlet. These parameters were required to measure the system performance such as coefficient of performance and cooling speed. Firstly, tests were performed with pure hydrocarbon refrigerant and again they were repeated with hydrocarbon nanorefrigerant with same conditions and procedures. This test is done with three different concentrations of nanoparticles.

2.1 Testing Procedure

The tests were conducted on test rig based on vapor compression cycle with few additional components for proper working and some for recording of data. Key components required for the proper working were dryer, manual control valves, heater, agitator, and vacuum pump while for recording were thermometers, pressure gauges, voltmeter, ammeter, energy meter, rotameter, and weighing balance. To analyze the system performance, three basic tests were performed to find out cooling speed, coefficient of performance, and power consumption of the system. These all tests were performed with hydrocarbon refrigerant and then repeated with three different concentrations of CuO-based nanorefrigerant.

2.2 Procedure for Charging of the System

To charge the system, two manual valves were fixed at the compressor charging port. Initially, the system is evacuated with the help of vacuum pump to ensure the removal of any air and dirt particles. Once the system had enough negative pressure, vacuuming was stopped and charging of the pure refrigerant was done with manual control valve. By opening manual valve, the refrigerant is passed into the running system. After getting the cooling effect, valve was closed and charging line also disconnected. Measure the weight of cylinder. The total amount charged on the system was calculated by measuring the difference of refrigerant cylinder weight. For nanorefrigerant, nanoparticles had been added into the existing system with small straw fixed between the manual charging port and charging line.

2.3 Test Procedure to Calculate Cooling Speed

The basic purpose of the test is to find that how much time is being taken to cool the product for defined temperature range at standard testing conditions of 30 ± 2 °C. Initially, the cooling system was soaked at 30 ± 2 °C to have uniform temperature throughout the cooling system. After this, power was given to system till steady state and heater was started in order to get the water temperature 40 °C in the evaporator assembly. The heater was switched off and all the readings were noted down. Then cooling system was started and all the readings including time taken for every degree of cooling were noted till the temperature of evaporator reached at 25 °C.

2.4 Test Procedure for Heat Load Test

This test was conducted to check coefficient of performance of the system at various heat loads. This test was done at standard atmospheric conditions of 30 ± 2 °C. At first, the cooling system was soaked at 30 ± 2 °C so that all the parts have uniform temperature. After this, power was given to system until steady state. Once the system reached steady state, it was checked for two different heater loads at $25 \sim 26$ °C and $35 \sim 36$ °C. Afterwards data was recorded for every unit degree load and cooling of that load for three hours.

   These tests had been repeated four times. Firstly, it was for pure hydrocarbon refrigerant, secondly with hydrocarbon refrigerant mixed with 0.2 g of CuO nanoparticles, thirdly with hydrocarbon refrigerant mixed with 0.3 g of CuO nanoparticles and then with hydrocarbon refrigerant mixed with 0.4 g of CuO nanoparticles.

3   Results and Discussion

During the experimentation, pressure, temperature, and time readings were taken to find the COP and cooling speed. The experiments were performed on various concentrations of nanoparticles such as 0.2 g CuO, 0.3 g CuO, and 0.4 g CuO. The volume flow rate was kept 3.8 LPH and the readings were taken at different conditions. To find the cooling speed, the reading was noted under steady-state conditions which were obtained almost after two hours of continuous running of the system. After that, the heater was switched on, till the temperature of the evaporator rose above 40 °C. Then the heater was switched off, and the time and other reading were recorded for every drop in unit degree of temperature. This process continued till the temperature of the evaporator fell down to 25 °C. For the calculation of coefficient of performance, test was done at different flux load. Firstly, the temperature range was kept between 35 ~ 36 °C. During this test, the heating load was provided from 35 to 36 °C. Then, it was turned off automatically while keeping the compressor on. All the parameters were recorded to keep the temperature at 35 °C. The same test was repeated for the flux range of 25 ~ 26 °C.

3.1   Temperature Drop in Condenser

The condenser is used to dissipate the heat of refrigerant which is compressed and hot. To record temperature and pressure, two thermometers and two pressure gauges were fixed at the inlet and outlet of condenser. Temperature drop could be found by subtracting the temperature outlet from the temperature inlet. If the temperature drop in condenser is high, then it is considered to be very effective. In the experimental setup, the condenser temperature drop was measured for pure hydrocarbon refrigerant and for different concentrations of the nanoparticles at two heat loads. The different concentrations were 0.2, 0.3, and 0.4 g of CuO.

Figure 2 depicts condenser temperature drop with 3.8 LPH volume flow rate of nanorefrigerant during the steady heat load of 25–26 °C at surrounding temperature of 30 ± 2 °C. For pure hydrocarbon refrigerant, which is taken as reference for the comparison, the drop is 25 °C. With addition of nanoparticles concentration, there is considerate improvement in temperature drop which is 28.1, 29.3, 30.2 °C with 0.2 g of CuO, 0.3 g of CuO, and 0.4 g of CuO, respectively. Overall, there is minimum 12.72% increase in condenser temperature drop for 0.2 g of CuO concentration and maximum increase of 20.8% for concentration of 0.4 g of CuO nanorefrigerant. This significant increase in heat transfer is important parameter to conclude the overall improvement in overall effectiveness of the system.

Figure 3 is illustrating the condenser temperature drop at steady heat load of 35 ~ 36 °C. The results showed the same trend, which is observed in heat load at 25 ~ 26 °C with same testing condition of 30 ± 2 °C. The temperature drop in condenser for pure hydrocarbon refrigerant is taken as reference. For pure hydrocarbon refrigerant,
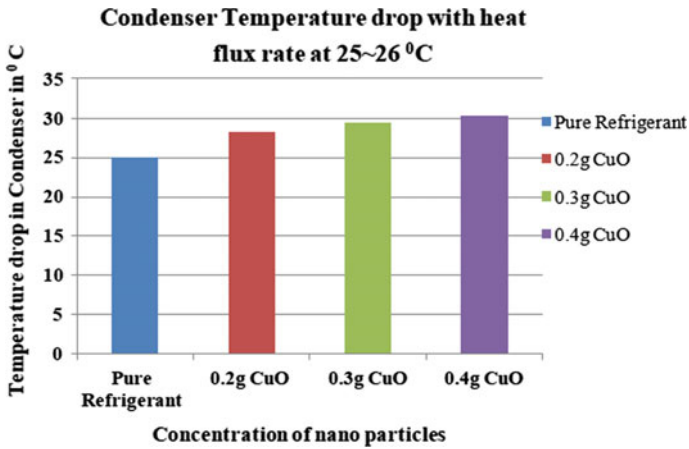
Fig. 2 Condenser temperature drop with 3.8 LPH volume flow rate of nanorefrigerant
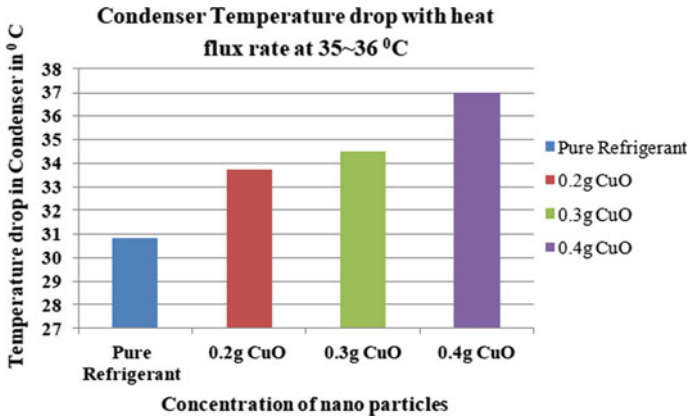
Fig. 3 Concentration of nanoparticles

temperature reduction in condenser temperature is 30.8 °C and with nanorefrigerant, temperature drop increased by 9.2, 11.8, 19.9% with 0.2 g CuO, 0.3 g CuO, and with 0.4 g CuO. This data is also showing a certain improvement in condenser temperature drop. So, it inferences that thermo-physical properties of hydrocarbon-based CuO nanorefrigerant enhance significantly. It could be due to improvement in heat transfer characteristics of nanorefrigerant.

3.2   Temperature Gain in the Evaporator

Evaporator is a heat exchanger, where cooling is obtained by absorbing the latent heat of vaporization. In evaporator, refrigerant enters at very low pressure in liquid form and absorbs heat which results the vaporization of the refrigerant which causes cooling in evaporator. In the experimental setup, the heat load is given to water by the heater. The refrigerant, which is at low temperature and low pressure, takes this heat from water. Hence, the refrigerant carries the heat along with it. So the net cooling effect is observed in the evaporator area. We have tried to find the temperature gain by the evaporator. The temperature gain is the difference in temperature between evaporator outlet and evaporator inlet. If the difference is large, then performance of the system would be better.

Figure 4 illustrates the evaporator temperature gain with constant flow rate of 3.8LPH at constant heat load at 25–26 °C.The ambient conditions may little vary and we consider it 30 ± 2 °C of temperature. The higher will be the temperature gain in the evaporator, better will be the system performance. To analyze the same, vapor compression system on hydrocarbon refrigerant base is checked for evaporator gain at constant heat load. Then on the same conditions, this test is repeated for the nanohydrocarbon refrigerant with concentration of nanoparticles of 0.2 g CuO, 0.3 g CuO, and 0.4 g CuO. The reference is taken with pure hydrocarbon and the evaporator temperature gain for the pure hydrocarbon refrigerant is obtained as 28.1 °C. With nanoparticles based refrigerant, the results obtained were on the better side. There is an evaporator temperature gain from 6.1 to 8.7% with different nanoparticles concentrations when compared with pure hydrocarbon refrigerant.

Figure 5 is showing the evaporator temperature gain at constant mass flow rate and at constant heat load of 35 ~ 36 °C. The conditions are kept same as the previous test except the heat load temperature. In this test, firstly, the parameters are checked
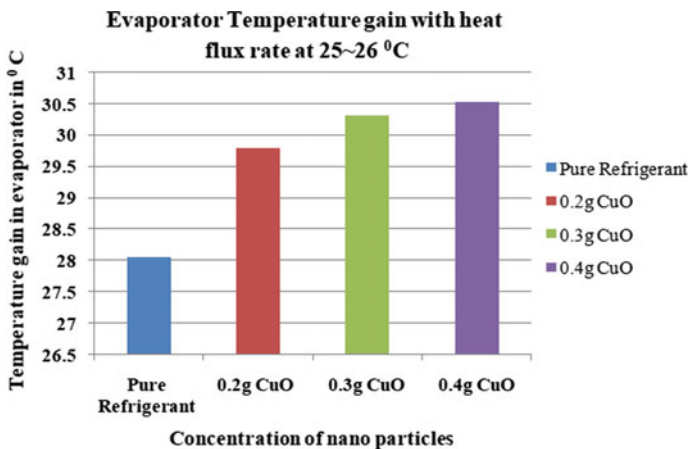
Fig. 4 Concentration at 25–26 °C

**Evaporator Temperature gain with heat
flux rate at 35~36 ⁰ C**
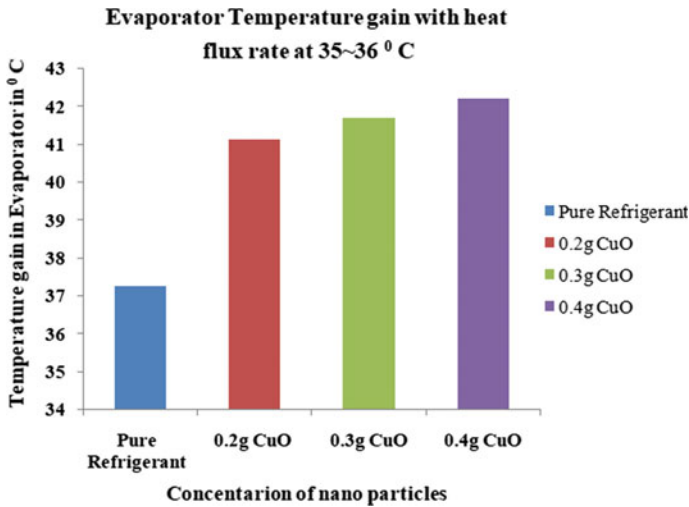
Fig. 5 Concentration at 35–36 °C

with pure hydrocarbon refrigerant and then it is being repeated with different concentrations of nanoparticles of CuO mixed with hydrocarbon refrigerant. The different concentrations are 0.2 g CuO, 0.3 g CuO, and 0.4 g CuO. It has been found in the experiments that there is a significant evaporator temperature gain with nanorefrigerant. The gain is between 10.3 ~ 13.2%, when it is compared with pure hydrocarbon refrigerant. This gain suggests the better refrigerant effect, which is desirable from the customer and manufacturer point of view. So all these results of temperature drop in condenser and temperature gain in evaporator is indicating performance enhancement with the use of nanorefrigerants.

3.3   Coefficient of Performance

It is the most important parameter which should be checked for refrigeration systems. Higher COP of the system is always desirable. It can be defined as the ratio of refrigeration effect to the power supplied to the system. COP depends on the ambient working conditions. In the experimental setup, refrigerant effect is obtained by the heating load. It is being measured by one of the energy meter. The power supply of the compressor is input supply and which is recorded by the second energy meter. In all of the experiments, the flow rate is kept constant at 3.8LPH. The COP is evaluated for different concentrations at steady heating load of 25 ~ 26 °C and 35 ~ 36 °C. For the 25 ~ 26 °C heat load, the COP of the system is increased with the increase of CuO nanoparticle in the hydrocarbon refrigerant. The trend was increasing sharply for 0.2 g of CuO. It continued to increase with subsequent concentrations of nanoparticles of CuO of 0.3 g and 0.4 g, but the rate is fallen.

The detailed graph is shown in above Fig. 6. The COP found with pure refrigerant is 1.25, which is increased with the presence of copper oxide nanoparticles. The increase of the COP is in the range of 4.7 ~ 11% when compared with pure hydrocarbon refrigerant. The highest COP is obtained for the concentration of 0.4 g of CuO mixed in the hydrocarbon refrigerant.

The same test is performed with constant volume flow rate to obtain the COP at heat load of 35 ~ 36 °C S shown in Fig. 7. In this test, the reference has been taken with pure hydrocarbon refrigerant. All COP with different concentrations of CuO nanoparticles are compared with reference. From the experiments, almost same trend is observed of improvement of COP with concentration of nanoparticles. This is because of the better thermo-physical properties of nanorefrigerants. It is quite
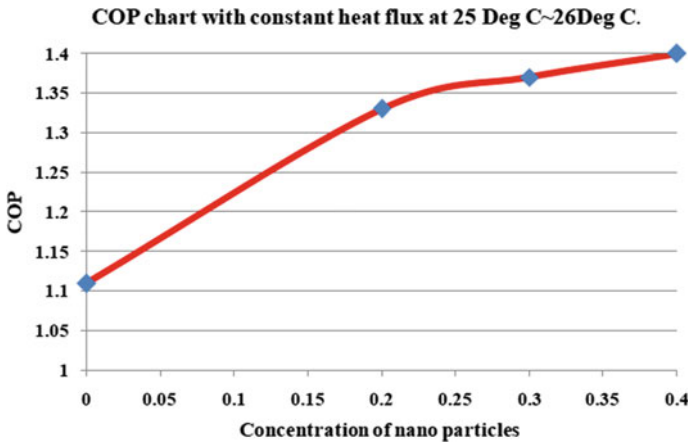
Fig. 6 COP chart
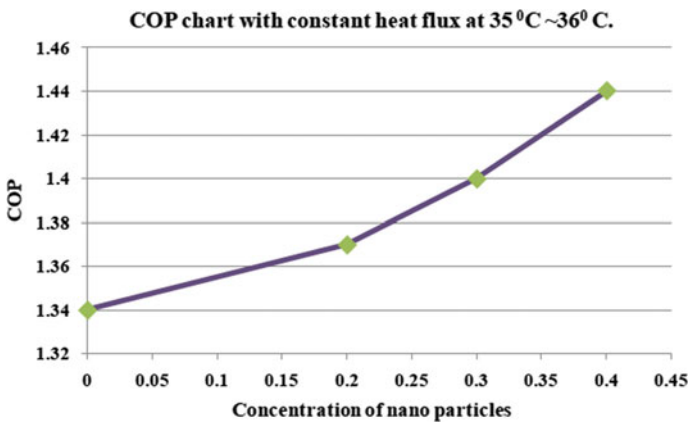
Fig. 7 COP chart

useful for the industry and customer point of view. The results show that there is rise in COP of the range of 2.2 ~ 7.4% with addition of nanoparticles.

3.4 Cooling Speed

It is defined as a rate of removal of heat with respect to time. It is time taken to cool the freezer compartment from 32 to 5 °C and in the fresh food compartment, from 32 to 15 °C. It is a very significant parameter. If the rate is higher, the system would be rated as a better appliance. In the present experimental setup, the cooling speed is found from 40 to 25 °C temperature in the freezer compartment.

Pure hydrocarbon refrigerant is taken as reference for the comparison of cooling speed with different concentrations of nanoparticles. The ambient temperature and mass flow are taken same as in the previous tests. It has been found that the cooling speed for pure refrigerant is 59 min for 15 ° of temperature drop from 40 to 15 °C. For the hydrocarbon with 0.20gm CuO refrigerant, the cooling speed obtained is 54 min. With 0.3 g CuO mixed in hydrocarbon refrigerant, the cooling speed obtained is 51 min. With 0.4 g CuO nano-refrigerant, cooling speed obtained is 51 min. Figure 8 is showing the cooling speed curve for all the concentrations together.

It can be concluded form the graph that cooling speed is improved up to 18% by the addition of 0.4 g of CuO nanoparticles in hydrocarbon-based refrigerant.
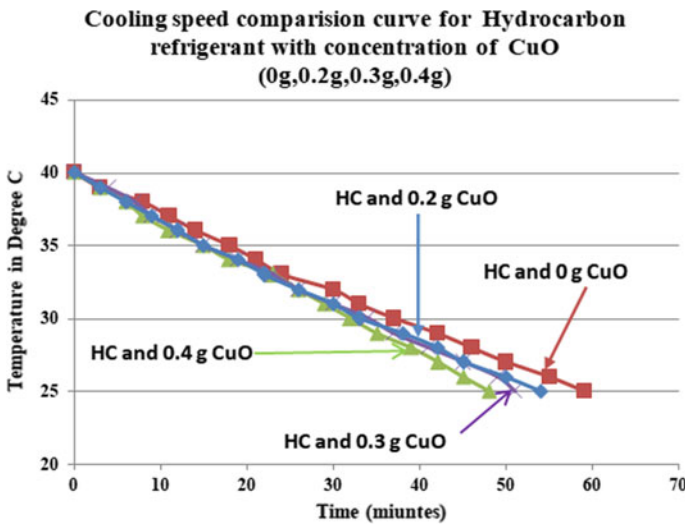
Fig. 8 Cooling speed

4 Conclusions

The present research work entitled "Nano refrigerants Based Vapour Compression System" was aimed at, to use copper oxide nanoparticles in combination with hydrocarbon refrigerant. The CuO nanoparticles of 40 nm size have been used. Various concentrations of nanoparticles were mixed with hydrocarbon refrigerant to explore the performance of a vapor compression system.

(i) The system was charged with nanorefrigerant hydrocarbon + CuO, 0.20 g mass, 0.30 g mass, and 0.40 g mass of nanoparticles.

(ii) All readings were observed at constant volume flow rate of 3.8LPH for cooling speed of the system of the system at ambient condition (30 ± 2 °C).

(iii) For COP calculation, readings are noted for two heat loads in evaporator at temperature 25–26 and 35–36 °C.

(iv) Temperature drop in condenser, temperature gain in evaporator, COP for the system, and cooling speed graph were studied for pure hydrocarbon refrigerant and nanorefrigerant at all concentrations.

(v) The experimental results showed that thermo-physical properties and HT characteristics enhance with adding of CuO nanoparticles to the hydrocarbon refrigerant.

(vi) It was observed that there is more temperature drop across the condenser for the nanorefrigerant (12.7–20.8%) compared to pure hydrocarbon refrigerant. Similarly, a gain of (6.1–8.7%) was obtained for evaporator temperature. An improvement in COP was also observed during the investigations (4.7–11%). This was achieved under evaporator constant load at 25–26 °C

(vii) The results were also observed when refrigeration system is operated at heat load 35–36 °C evaporator temperature.

(viii) The system works normally same as any conventional refrigeration system

(ix) Refrigerating effect enhances with the addition of nanoparticles (0.20–0.40gm) in refrigerant.

5 Future Scopes

The present research work was aimed at only one type of refrigerant, three concentrations of nanoparticles of CuO only. But there could be number of other parameters which can be varied to get the system performance.

(i) Nanoparticles with different concentrations can be used.

(ii) There are number of refrigerants other than refrigerant hydrocarbon which can be used to investigate the performance.

(iii) The performance may be evaluated with different mass flow rates, different size of nanoparticles, different heat loads and different working conditions.

(iv) The system can be evaluated at more controlled environment condition such as in testing chambers to get more accurate results.

(v) The evaporator load can be replaced with actual load.

References

1. Akhavan-Behabadi, M. A., Sadoughi, M. K., Darzi, M., et al. (2015). Experimental study on heat transfer characteristics of R600a/POE/CuO nano-refrigerant flow condensation. *Experimental Thermal and Fluid Science, 66*, 46–52.
2. Alawi, O. A., & Sidik, N. A. C. (2015). The effect of temperature and particles concentration on the determination of thermo and physical properties of SWCNT-nano-refrigerant. *International Communications in Heat and Mass Transfer, 67,* 8–13.
3. Alawi, O. A., & Sidik, N. A. C. (2014). Influence of particle concentration and temperature on the thermophysical properties of CuO/R134a nano-refrigerant. *International Communications in Heat and Mass Transfer, 58,* 79–84.
4. Zawawi, N. N. M., Sharif, M. Z., et al. (2017). Thermo-physical properties of Al2O3-SiO2/PAG composite nanolubricant for refrigeration system. *International Journal of Refrigeration, 80*, 1–10.
5. Pinto, R. V., & Fiorelli, F. A. S. (2016). Review of the mechanisms responsible for heat transfer enhancement using nanofluids. *Applied Thermal Engineering, 108*, 720–739.
6. Li, H., Yang, W., Zhixin, Y., & Zhao, L. (2015). The performance of a heat pump using nanofluid (R22 + TiO2) as the working fluid – an experimental study. *Energy Procedia, 75,* 1838–1843.
7. Azmi, W. H., Sharif, M. Z., et al. (2017). Potential of nanorefrigerant and nanolubricant on energy saving in refrigeration system – A review. *Renewable and Sustainable Energy Reviews, 69,* 415–428.
8. Yang, L., Jiang, W., et al. (2017). Dynamic characteristics of an environment-friendly refrigerant: Ammonia-water based TiO2 nanofluids. *International Journal of Refrigeration, 82,* 366–380.
9. Manoj Babu, A., Nallusamy, S., & Rajan, K. (2015). Experimental analysis on vapour compression refrigeration system using nanolubricant with HFC-134a refrigerant. *Nano Hybrids, 9,* 2234–9871.
10. Bi, S., Shi, L., & Zhang, L. (2008). Application of nanoparticles in domestic refrigerators. *Applied Thermal Engineering, 28*, 1834–1843.
11. Huminic, G., Huminic, A., Morjan, I., & Dumitrache, F. (2011). Experimental study of the thermal performance of thermosyphon heat pipe using iron oxide nanoparticles. *International Journal of Heat and Mass Transfer, 54,* 656–661.
12. Lin, L., Peng, H., & Ding, G. (2016). Experimental research on particle aggregation behaviour. In nano refrigerant–oil mixture. *Applied Thermal Engineering, 98*, 944–953.
13. Mahbubula, I. M., Saidur, R., & Amalina, M. A. (2013). Thermal conductivity, viscosity and density of R141b refrigerant based nanofluid. *Procedia Engineering, 56*, 310–315.
14. Yang, L., & Kai, D. (2013). An optimizing method for preparing natural refrigerant: Ammonia-water nano fluids. *An International Journal, 147*(1), 24–33.
15. Xing, M., Yu, J., & Wang, R. (2015). Application of fullerene C60 nano-oil for performance enhancement of domestic refrigerator compressors. *International Journal of Refrigeration, 40*, 398–403.

Composite Coating on Aluminum-Based Alloys Through Ni-P Electroless Plating Route

Naghma Jamal , **Shalini Mohanty** , **Sanu Raj** , **and Alok Kumar Das**

Abstract The present study deals with the deposition of a layer of Ni-P and Ni-MoS_2-Al_2O_3 composite coating by using different compositions of Al_2O_3 and MoS_2 powders in the electroless (EL) plating bath on Al-alloy substrate. The results are then compared to that of the samples coated without powders in the EL bath. The samples prepared with the addition of powders in the electroless bath show improved surface properties post coating. Various characterizations of the samples are done such as micro-hardness, coating thickness, compositional analysis through EDS and XRD, and surface morphology is seen through FESEM images. The micro-hardness of the powder-coated samples varies in the range of 122.56 HV to 202.42 HV whereas that of the substrate is 110.74 HV at 0.2 kgf loading condition. XRD results indicate the presence of MoS_2, Al_2O_3, Ni, NiAl, SiO_2, and NiO phases that contribute toward the improvement of both hardness and lubricating properties on the Al-substrate post coating.

Keywords Electroless · Micro-hardness · Coating thickness · Solid lubricant · Composite coating

N. Jamal · S. Mohanty (✉) · S. Raj · A. K. Das
Department of Mechanical Engineering, Indian Institute of Technology (IIT-ISM), Dhanbad, Jharkhand 826004, India
e-mail: shalinimohanty5@yahoo.com

N. Jamal
e-mail: njamal2510@gmail.com

S. Raj
e-mail: sanurajchandi123@gmail.com

A. K. Das
e-mail: eralok@yahoo.co.in

93

1   Introduction

Inherent lightness and high strength-to-weight ratio of aluminum and their alloys make them imperative engineering materials. In addition to low density, they possess good ductility, excellent thermal and electrical conductance, high mechanical strength, low operating cost, good reflectivity, and workability [1, 2]. Despite of such impressive properties, they are restricted to be used in severe operating conditions such as high temperature, abrasive, and corrosive environment as they are prone to failure. Therefore, to impart sufficient hardness and to improve corrosion resistivity, surface coating is the most liable option. To this regard, numerous methods are available for surface coatings like electro-deposition, electroless coating, chemical vapor deposition, thermal spraying, physical vapor deposition, etc. [3]. Of all the coating processes, electroless (EL) coating is widely used because of its cost-effectiveness and providing with incredible surface properties. As current is not employed in EL coating, deposit is uniform in nature as well as good wear and corrosion-resistant properties are obtained [2].

The EL plating process is a controlled chemical reduction reaction in which a reducing agent is introduced in a liquid solution of metallic salt which reduces metal atoms, resulting in deposition on a substrate. The advantage of this process is that it can process not only electrically conductive material but also non-conductive materials such as rubber and polymers. In this process, reduction of nickel occurs on the substrate by using reducing agents like sodium hypophosphite (for Ni-P) and sodium borohydride (for Ni-B) [2]. Most of the research work has been done on Ni-P/Ni-B coating alone [4–7]. However, with the increasing demand in the applications of EL coating, it has emerged as a leading growth area in surface engineering. As like the conventional plating method, in composite coating, Nickel-P basic bath is used but with added powders and out of certain chemical reaction between the ions generated from the bath and the substrate, a composite layer is formed. The added ingredient as suspended particles alters the surface properties of the substrate post coating. The co-deposited particulates or suspended matters are of two types. The first type includes metal oxides, nitrides, and carbides such as SiC, Al_2O_3, etc. whereas the second type includes lubricious and soft particles such as MoS_2, PTFE, BN, etc. [2]. Recent studies [2, 8, 9] show that EL composite coating has significantly improved micro-hardness, corrosion resistance, and wear resistance properties. Some composite coatings are Ni-P-Al_2O_3 [8], Ni-P-MoS_2 [9], Ni-P-Al_2O_3-ZrO_2 [2], etc. Hu et al. [10] studied the Ni-P-Al_2O_3 composite coating on magnesium alloy. Results obtained indicated that Ni-P-Al_2O_3 composite coating has improved corrosion resistance and micro-hardness as compared to Ni-P binary coating. Scanning electron microscope (SEM) was used to observe morphological growth of Ni-P-Al_2O_3 growth. Results from thermal shock test suggested that there is no effect of Al_2O_3 particles on adhesion of coating. Ranganatha et al. [11] compared the Ni-P binary coating, Ni-P-W ternary coating by variation of tungsten metal, and Ni-W-P ternary coating with WS_2 nano-particles on low carbon. The deposits were gone through XRD for surface analysis, SEM with EDS to investigate surface

Table 1 Chemical composition of Al6061

Elements	Al	Mg	Si	Cu	Zn	Cr	Mn
Content %	95.8	0.98	0.6	0.23	0.25	0.20	0.15

morphology. Micro-hardness of deposits was tested with Knoop's intender. Taye et al. [12] carried out Ni-Al_2O_3-WS_2 composite coating by EL process on aluminum studied the effect of variation in concentration of WS_2 and Al_2O_3 nano-powders. Coating surface morphology and the elements present in coating were analyzed by FESEM along with EDX. X-ray diffraction (XRD) was used to identify intermetallic compounds. Results indicated that the samples with Ni- Al_2O_3-WS_2 coating have improved micro-hardness compared to substrate and with 3 g/L Al_2O_3 and 1.4 g/L WS_2 maximum coating thickness was obtained.

Although a widespread use of EL plating has been reported but a less work has been explored with EL composite plating, i.e., using suspended nano-particles. So, in the present work, we have made an effort to plate aluminum alloy with Ni-P co-deposited with nano Al_2O_3 and MoS_2 powders. By varying the concentration of Al_2O_3 and MoS_2 powders, coating with different properties have been achieved and various characterization methods have been implemented to study the surface properties obtained post the coating.

2 Materials and Methods

2.1 Material Preparation

Aluminum alloy (Al-6061) cut into 7 mm × 7 mm × 5 mm through wire-cut electrical discharge machine was used for carrying out the experiments; the composition of which is given in Table 1. The samples were polished with SiC-based emery paper with grit size 2000 to obtain a smooth surface and cleaned with acetone in an ultrasonicator to make the surface contaminant-free (often required in the plating of titanium, magnesium, and aluminum alloys).

2.2 Experimental Procedure

The experimental setup for the EL coating is shown in Fig. 1. The sample was dipped into the Ni-P electroless bath placed in a beaker with the help of string tied to the supporting stand on a magnetic stirrer. The pH and temperature were maintained during process. To avoid oxidative reactions on aluminum, zincating is necessary before actual coating process. Double zincating process comprises of desmutting, etching, and zincating. A 50:50 concentration of nitric acid (69% pure) and water

Fig. 1 Experimental set-up
for the EL plating [12]

Supporting stand
String
Thermometer cum pH controller
Borosil glass beaker
Substrate
Stir bar/ flea
Magnetic stirrer
RPM controller
Temperature controller
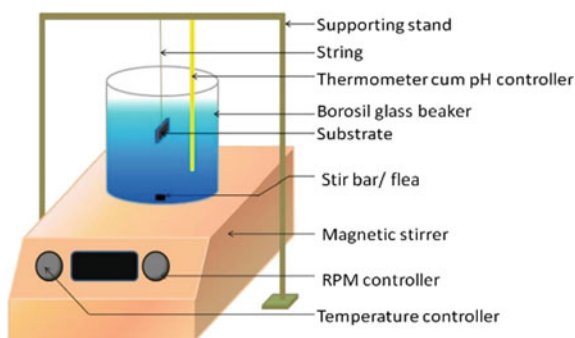
Table 2 Composition of zincate layer

Composition	ZnO	FeCl$_3$	NaOH
Concentration (g/L)	60	2	560

Table 3 Bath composition of electroless bath

Component	Concentration (ml/L)
Deionised water	740
Nifoss 2500 make up	200
Nifoss 2500 base	60

were used to prepare desmutting solution at room temperature. Etching solution was prepared by dissolving sodium hydroxide pellets into DI water in a beaker. Zincate layer bath was prepared with zinc oxide, sodium hydroxide, and ferric chloride with concentration as detailed in Table 2. After the zincating process, samples were directly immersed into Ni-P EL coating bath having composition shown in Table 3.

Throughout the experiments, pH was maintained between 4–4.8 and temperature was maintained between 70–80 °C. The magnetic stirrer was set at 600 rpm and the coating process was carried out for 30 min. A total ten experiments have been performed by varying concentration of Al$_2$O$_3$ and MoS$_2$ in the EL Ni-P bath, and samples are cleaned using ultrasonicator.

3 Characterization Methods

The coating thickness of the EL-plated samples was determined using the optical microscope (Model: Olympus) along the transverse section of the coated samples. The compositional study of the coating was evaluated by XRD (model: PANalytical) analysis with 2Θ value ranging from 0 to 120°. Further, the surface morphology was studied with the use of FESEM (model: Zeiss supra 55) with an accelerating voltage of 2 kV. Vickers hardness testing machine (Model: Economet VH-1 MD, Chennai

Metco, India) was used to measure the micro-hardness of the coated samples under a load of 0.2 kgf and dwell time of 10 s.

4 Results and Discussion

4.1 Composite Coating Thickness

The composite coating thickness was measured along cross-section after diamond polishing. Measurement was taken at four different sites as shown in Fig. 2 and an average value was recorded in Table 4. It can be observed from Fig. 3 that with increase in concentration of MoS_2 powder at a constant value of Al_2O_3, coating thickness first slightly decreases then increases. But with the increase of concentration
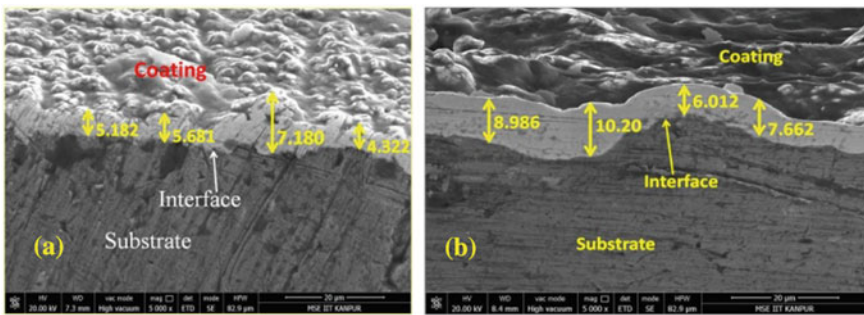
Fig. 2 Cross-sectional FESEM image of coated sample, **a** Al_2O_3 3 g/L and MoS_2 0.6 g/L **b** Al_2O_3 3 g/L and MoS_2 0.8 g/L in EL bath

Table 4 Observation table

Expt No.	Powder concentration		Coating thickness (µm)	Micro-hardness (HV)
	Al_2O_3	MoS_2		
1	0	0	14.00	115.12
2	1	0.4	11.20	185.08
3	1	0.6	10.72	182.04
4	1	0.8	12.22	153.43
5	2	0.4	11.97	202.42
6	2	0.6	11.62	185.64
7	2	0.8	14.94	159.05
8	3	0.4	6.27	163.71
9	3	0.6	5.64	161.89
10	3	0.8	8.62	122.56
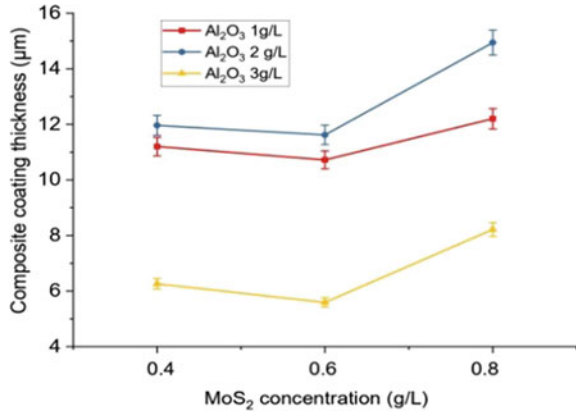
in Al_2O_3 coating thickness first increases then decreases rapidly. This may be due to the fact that Al_2O_3 particles being hard causes erosion of material from surface thereby degrading the coating thickness [12].

4.2 Coating Surface Morphology

The FESEM images of coated sample are shown in Fig. 4. Figure 4a shows the surface morphology of sample coated with Al_2O_3 2 g/L and MoS_2 0.4 g/L while Fig. 4b shows that of Al_2O_3 3 g/L and MoS_2 0.6 g/L. It is observed that more number of pores and cracks are seen in sample coated with 2 g/L Al_2O_3 and 0.4 g/L MoS_2 compared to that of 3 g/L Al_2O_3 and 0.6 g/L MoS_2. The reason may be the abrupt collision of particles in the EL bath that results in formation of micro-cracks and pores on the coated surface in the latter case. The FESEM images confirm the co-deposition Al_2O_3 and MoS_2 nanoparticles along with Ni-P matrix.
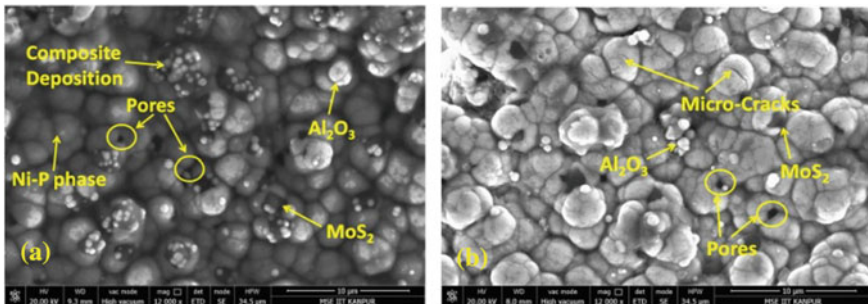
Fig. 4 Composite coating surface morphology, **a** Al_2O_3 2 g/L and MoS_2 0.6 g/L **b** Al_2O_3 3 g/L and MoS_2 0.8 g/L powder content in EL bath

Fig. 5 Variation of micro-hardness with concentration of Al_2O_3 and MoS_2
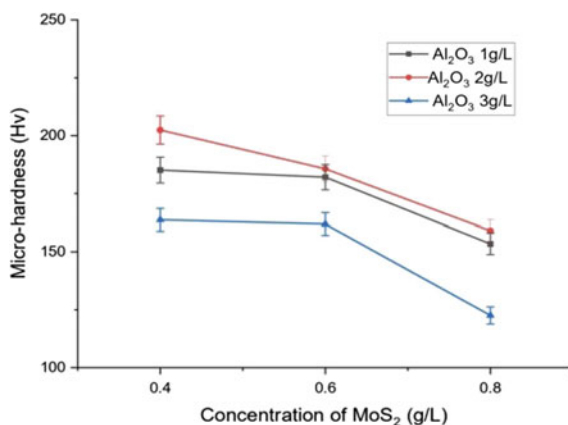
4.3 Micro-Hardness

The micro-hardness of the Ni-P sample is found to be 115.12 HV whereas in case of the coated samples prepared with mixing of powders in the bath, the micro-hardness varied from 122.56 HV to 202.42 HV which is more than that of the substrate (110.74). Figure 5 shows the variation of micro-hardness of composite coating with the Al_2O_3 and MoS_2 powder content in the Ni-P plating bath. It is evident from the graph that with an increase in MoS_2 concentration, the micro-hardness decreases. MoS_2, being a solid lubricant, is softer than Ni and its presence attributes to a decrease in crystal size of Ni- MoS_2 coating. The increase in grain boundaries due to change in crystal size may interrupt the dislocation mobility. Additionally, a drastic decrease in micro-hardness is observed from 0.6 g/L to 0.8 g/L MoS_2 content. This may be due to the degradation of the coating performance after a high weight fraction of MoS_2 (0.8 g/L) is considered. At this bath concentration, the particles collide with the matrix, degrade the uniformity of the coating surface leading to unfavorable performance of the composite layer [12]. Again an interesting trend is observed in Fig. 5 wherein an increase in Al_2O_3 content from 1 g/L to 2 g/L results in increase in micro-hardness. The reason being the presence of Al_2O_3 particles enhances the phase structure of the coating and thus improving their micro-hardness. However, as the Al_2O_3 content reaches 3 g/L, the composite coating micro-hardness decreases to 122.56 HV. This solely means that a higher concentration of Al_2O_3 may affect the Ni-P crystal structure thus degrading the performance of the coated surface [10].

4.4 Compositional Study

The energy dispersive spectrum (EDS) was done on composite-coated sample to evaluate the elemental composition. Figure 6 shows the EDS plot of composite
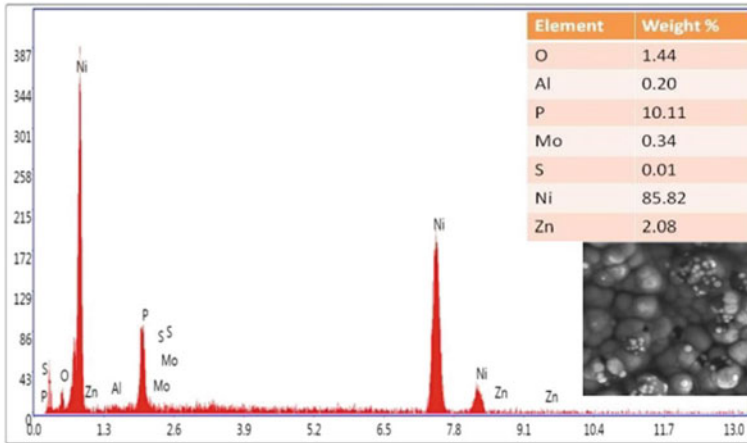
Fig. 6 EDS spectra of composite-coated sample prepared at Al$_2$O$_3$ 2 g/L and MoS$_2$ 0.8 g/L powder concentration in EL bath

coating (Al$_2$O$_3$ 2 g/L and MoS$_2$ 0.6 g/L) which clarifies the presence of element nickel, phosphorous, oxygen, aluminum, molybdenum, sulfur and zinc. It can be concluded that co-deposition of nanopowders has been achieved successfully and hence the composite coating.

X-ray diffraction analysis was used to determine the various phases in the EL coated surface. The data was fed to X'pert High Score Plus software and analysis was done. The plots as shown in Fig. 7 reveal that there is presence of Ni, Al, AlNi, SiO$_2$, MoS$_2$, NiO, and Al$_2$O$_3$. The presence of Ni, NiO, and AlNi peak marks the transfer of nickel ions to the Al-alloy substrate material effectively. The peaks of molybdenum disulphide and aluminum oxide affirm that there is improvement in hardness and lubricity properties of the coated sample prepared at 3 g/L Al$_2$O$_3$ and 0.6 g/L MoS$_2$ powder content.

Fig. 7 XRD plot for sample coated at 3 g/L Al$_2$O$_3$ and 0.6 g/L MoS$_2$ powder concentration in EL bath
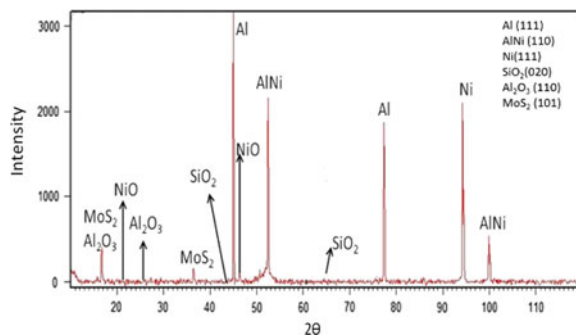
5 Conclusions

In this study, Ni-P and Ni-Al$_2$O$_3$-MoS$_2$ composite EL plating was successfully achieved on aluminum alloy substrate. A comparative study had been done between electroless Ni-P and Ni-Al$_2$O$_3$-MoS$_2$ composite coating. The conclusions obtained from this comparative study are briefed below.

The maximum composite coating thickness (14.94 µm) was observed at 2 g/L Al$_2$O$_3$ and 0.8 MoS$_2$ and minimum (5.64 µm) at 3 g/L Al$_2$O$_3$ and 0.6 MoS$_2$ powder concentration in EL bath. The micro-hardness of the composite-coated samples increased to up to 84% of that of the substrate material with the addition of powders in the bath. Formation of phases of Ni, AlNi, SiO$_2$, MoS$_2$, NiO, Al$_2$O$_3$, and AlPO$_4$ affirms the formation of a hard, temperature-resistant, and lubricating layer of the composite coating through EL plating method.

References

1. Saxena, V., Rani, R. U., & Sharma, A. K. (2006). Studies on ultra high solar absorber black electroless nickel coatings on aluminum alloys for space application. *Surface & Coatings Technology, 201*(3–4), 855–862.
2. Agarwala, R. C., & Agarwala, V. (2003). Electroless alloy/composite coatings: A review. *Sadhana., 28*(3–4), 475–493.
3. Mohanty, S., Bhushan, B., Das, A. K., & Dixit, A. R. (2019). Production of hard and lubricating surfaces on miniature components through micro-EDM process. *The International Journal of Advanced Manufacturing Technology, 105*(5–6), 1983–2000.
4. Zuleta, A. A., Correa, E., Castaño, J. G., Echeverría, F., Baron-Wiecheć, A., Skeldon, P., et al. (2017). Study of the formation of alkaline electroless Ni-P coating on magnesium and AZ31B magnesium alloy. *Surface & Coatings Technology, 321,* 309–320.
5. Zhang, J., Xie, Z. H., Chen, H., Hu, C., Li, L., Hu, B., et al. (2018). Electroless deposition and characterization of a double-layered Ni-B/Ni-P coating on AZ91D Mg alloy from eco-friendly fluoride-free baths. *Surface & Coatings Technology, 342,* 178–189.
6. Qin, T. N., Yan, Y. A., Cong, N. I., Zhao, X. Y., & Yi, D. I. (2011). An in situ measure method to study deposition mechanism of electroless Ni-P plating on AZ31 magnesium alloy. *Transactions of Nonferrous Metals Society of China, 21*(12), 7–2790.
7. Abdel-Gawad, S. A., Sadik, M. A., & Shoeib, M. A. (2019). Preparation and properties of a novel nano Ni-B-Sn by electroless deposition on 7075-T6 aluminum alloy for aerospace application. *Journal of Alloys and Compounds, 785,* 1284–1292.
8. Hu, R., Su, Y., Liu, Y., Liu, H., Chen, Y., Cao, C., et al. (2018). Deposition process and properties of electroless ni-p-al 2 o 3 composite coatings on magnesium alloy. *Nanoscale Research Letters, 13*(1), 198.
9. Li, Z., Wang, J., Lu, J., & Meng, J. (2013). Tribological characteristics of electroless Ni–P–MoS2 composite coatings at elevated temperatures. *Applied Surface Science, 264,* 516–521.
10. Hu, R., Su, Y., Liu, Y., Liu, H., Chen, Y., Cao, C., & Ni, H. (2018). Deposition process and properties of electroless Ni-P-Al 2 O 3 composite coatings on magnesium alloy. *Nanoscale Research Letters, 13*(1), 198.
11. Ranganatha, S., Venkatesha, T. V., & Vathsala, K. (2012). Electroless Ni–W–P coating and its nano-WS2 composite: preparation and properties. *Industrial and Engineering Chemistry Research, 51*(23), 7932–7940.

12. Taye, D., Mohanty, S., Das, A. K., & Singh, N. K. (2019). Electroless Ni–Al 2 O 3–WS 2 composite coating on aluminum substrate. *Transactions of the Indian Institute of Metals, 72*(9), 2281–2292.

Fabrication and Experimental Study of Mechanical Behavior of Hollow Glass Fiber-Based Self-healing Polymer Composite

Anuj Kumar Jain, Rajeev Kumar, and Pikesh Bansal

Abstract Self-healing property is now being pursued worldwide with avid interest as an alternative process in checking damages in materials. Incorporating self-repair elements inside hollow fibers is one such approach which is considered here along with study of damage occurrence and restoration of mechanical strength. In present work, hollow glass fiber reinforced self-healing polymer is fabricated, and mechanical response to tensile loading is studied. In our approach, hollow glass fibers of 200–300 micron inner diameter are fabricated and further utilized as fiber reinforcement for self-healing polymer composite. During curing process, initial setup consists of Bisphenol-A-based resin as material for matrix. Hollow glass fiber, which is filled with self-healing agents, is embedded uniformly within the matrix. Further, the material is tested for its tensile strength in the presence of healing agent. The result demonstrates weak fracture toughness of hollow glass fiber with regards to Bisphenol-A epoxy resin. This may be attributed to higher hollowness percentage of glass fiber.

Keywords Hollow glass fiber · Self healing composite · Tensile strength · Stress-strain response

1 Introduction

Under various loading situations, materials show phenomena of degradation, damage and failure. Henceforth, more research has been concentrated predominantly on design of new robust material, yet these designed engineering materials are failed

A. K. Jain (✉) · P. Bansal
ABES Engineering College, Ghaziabad, AKTU Lucknow, Ghaziabad, India
e-mail: anuj.jain@abes.ac.in

P. Bansal
e-mail: pikesh.bansal@abes.ac.in

R. Kumar
Pranveer Singh Institute of Technology, Kanpur, India
e-mail: rajeevnitwkhagoli@gmail.com

Fig. 1 Schematic of hollow
fiber self-healing system
used
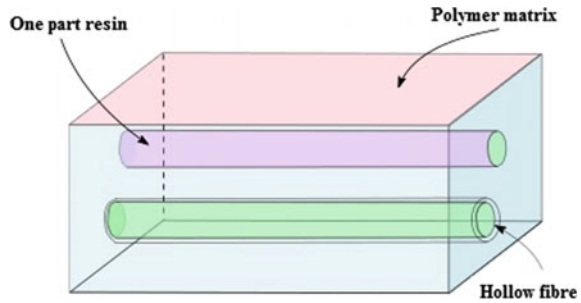
eventually. However, we do notice a number of biological materials to address this problem with more elegant way, which may be termed as self-healing property. This self-repairing property of material is the ability to repair the internal structure and functionality associated with it, if there occurs any damage. Hence, this approach may impart the material a safer and long working life of component by external or internal mode of recovery process.

This area was first completely overviewed by Zwaag [1] during 2007, which included complete spectrum of materials in regards to self-healing nature from polymer to metal and ceramics. Out of various approach of self-healing (capsule-based, vascular and intrinsic), we have focused on fiber reinforced polymer composite, as they exhibit a simpler mechanism of self-repair apart from offering ability to preserve functional self-repair elements and its integrity, Hossain et al. [2]. The hollow fiber embedded within a structure for exhibiting self-repair characteristics has been studied by Dry [3], Motoku et al. [4], Zako and Takano [5], Bleay et al. [6]. A functional hollow glass fiber self-healing technique generally highlights its structural form as fibers consisting of one part resin system or two part resin along with hardener system, Palleau et al. [7], Shepherd et al. [8], Acome et al. [9]. The schematic of above-said system is shown in Fig. 1.

2 Fabrication of Specimen

The requisite hollow glass fiber is fabricated at Glass Blowing Section, Indian Institute of Technology (IIT) Kanpur, with fiber diameter varying between 200 and 300 μm with hollowness of approximately 50–60% as shown in Fig. 2.

For imparting self-healing functionality, these hollow glass fibers are further embedded in uncured epoxy resin. While undergoing mechanical testing, like bending or tensile loading, these hollow fibers filled with healing liquids may fracture, thereby initiating the self-repair mechanism near the vicinity of failure zone in composite. In our setup, the healing agents are trapped using epoxy putty at the ends of glass fibers, and they function similar to bleeding mechanism in biological

Fig. 2 Bunch of hollow glass fibers fabricated at Glass Blowing Section, IIT Kanpur

organisms, Trask and Bond [10], Durabi et al. [11]. In order to have better fracture visualization inside the composite, generally a translucent glass/epoxy-based laminates are utilized.

2.1 Fabrication of Hollow Glass-Based Composite

For making a laminar structure, the matrix considered for composite is Bisphenol-A-based epoxy resin. The resin is cured with hardener in 80:20 ratios. Further, nearly 500 hollow glass fibers with inner diameter 200–300 μm and length 165 mm are embedded in matrix before curing process. The cured sample of composite lamina containing hollow glass fiber is shown in Fig. 3.

The fabricated composite plate measures 200 mm in length and 165 mm in width. In order to fabricate desired specimen for mechanical testing, the fabricated plate has undergone water jet machining at manufacturing lab, IIT Kanpur. Further, for tensile testing, a number of specimens are generated by machining the laminar composite to get final dog bone form as shown in Fig. 4.

Fig. 3 Plane composite having hollow glass fiber, after being cured

Fig. 4 Schematic of
intrinsic structure composite
containing HGF and
machined dog bone
specimen

Hollow glass reniforced composite plate
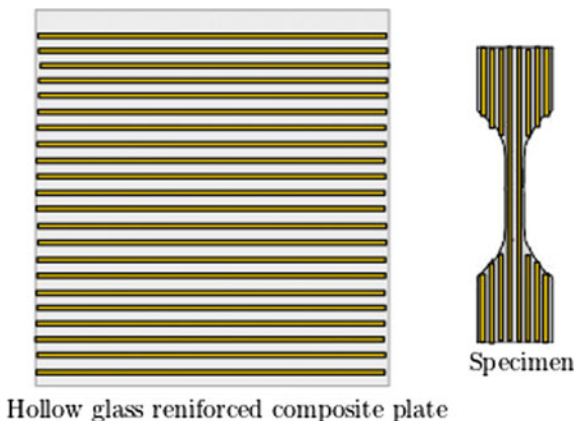
Specimen

Fig. 5 Tensile testing dog
bone specimen
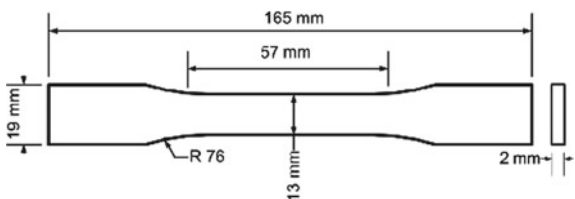
2.2 Fabrication of Dog Bone Specimen for Tensile Testing

The requisite dog bone specimen is shown in Fig. 5, with specified dimensions. These specimens are polished at ends, so that injection of self-healing chemical mixture can take place.

Further, under extreme precaution, self-healing agents are injected inside tensile specimen after the ends are reopened. The healing agents considered here are mixture of methacrylic acid, methyl methacrylate and nitro-benzene (mixed in proportion of 18:4:1). Further, in order to seal the ends of hollow glass fiber, a suitable epoxy putty (Silver PreCon Seal Powder Coating Epoxy Putty) is used. The self-healing chemical is injected inside each hollow glass fiber at 1.1 atmospheric pressure. This is to insure sufficient release of mixture during crack formation under failure.

3 Experimentation with Self-healing Composite

For tensile testing, the dog bone specimen is firmly placed at INSTRON-1195 UTM machine (rated with 100 kg load) available at MTL, ACMS, IIT Kanpur. Rate of application of tensile load is maintained at 0.005 mm/min. Five repeated tests are
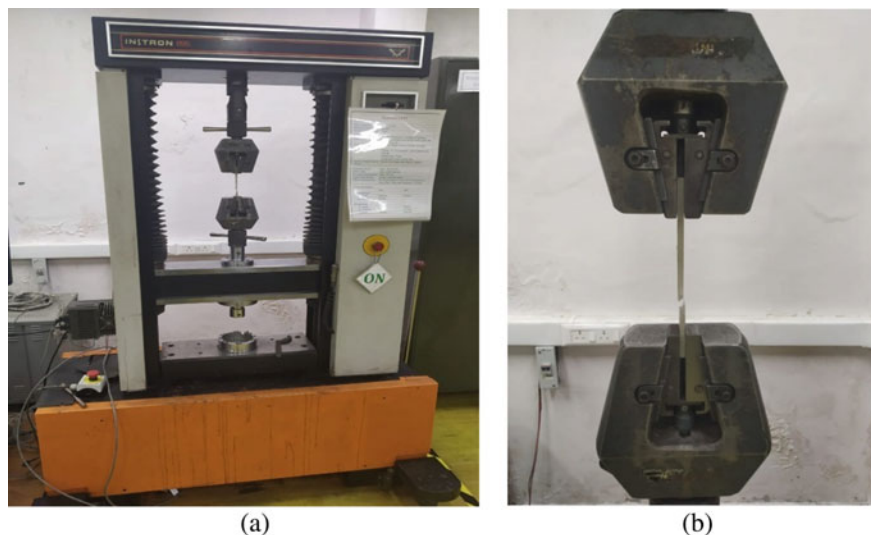
Fig. 6 **a** Tensile testing setup, **b** Specimen failure

performed for determining the tensile behavior of self-healed composite specimen. The experimental setup and failure specimen are shown in Fig. 6.

Corresponding load–displacement curve and stress–strain response are shown in Fig. 7.

The composite material showed following stress behavior while undergoing tensile testing.

S. No.	Variable	Value
1	Peak stress	16.025 MPa
2	Peak load	1.304 kN
3	0.2% yield stress	12.348
4	Yield strain	0.609%
5	Elongation at break(Using strain)	1.071%

4 Conclusions

The composite material exhibits brittle behavior, as observed by the nature of stress–strain response under uniaxial tensile loading. The steep drop of stress at ultimate stress indicates lower fracture toughness of hollow glass fiber with regards to strength of Bisphenol-A matrix. Further, nonlinear behavior of epoxy is also depicted in load–displacement curve. Due to 50–60% hollowness in glass fiber filled with healing
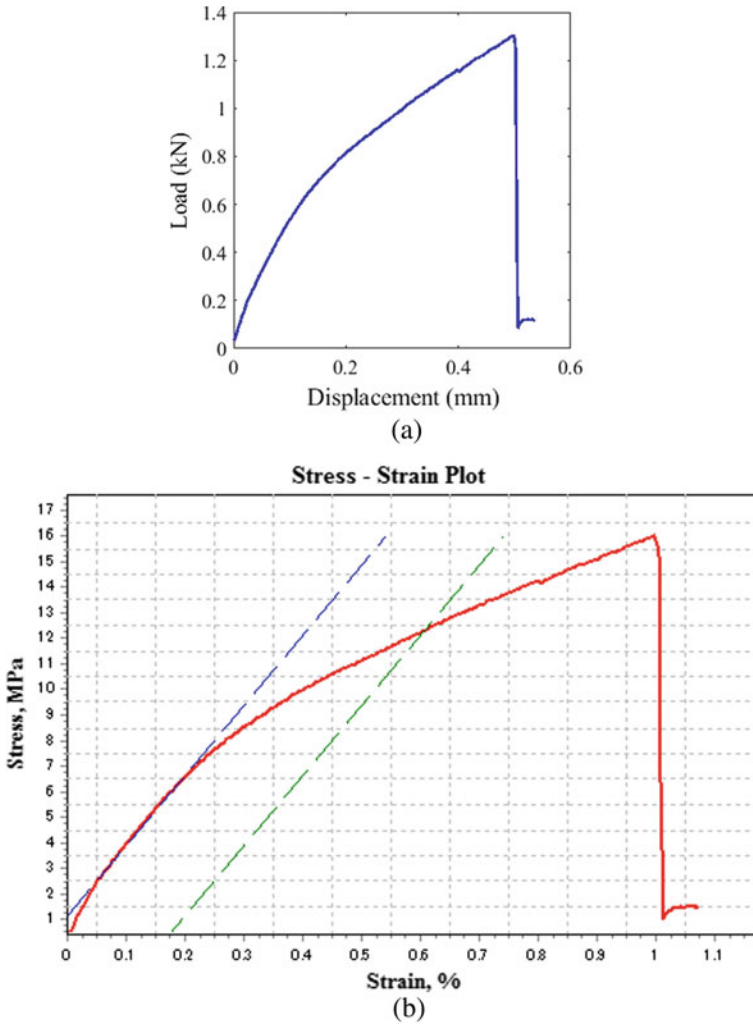
Fig. 7 **a** Load–displacement response, **b** Stress–strain response of self-healing composite under tensile testing

liquid, the reinforcement provided by glass is sufficient till ultimate stress, while load carrying capacity beyond this value drastically drops. If the specimen is applied with pre-crack at the middle span, healing phenomena would take place, resulting in local strengthening of composite. This may be further utilized to change the fracture toughness with healed and without healed conditions

From above experimentation, it may be concluded that, local strengthening may be beneficial during healing of composite. However, if the rate of loading is quite slow, healing property of composite can show remarkable results in repairing the failed composite.

References

1. Van der Zwaag, S. (2007). *Self healing materials: An alternative approach to 20 centuries of materials science*. Dordrecht: Springer.
2. Hucker, M., Bond, I. P., Foreman, A. & Hudd, J. (1999). Optimisation of hollow glass fibres and their composites. Adv. Compos. Lett. 8, 181–189.
3. Dry, C. (1996, July) Procedures developed for self repair of polymer matrix composites. *Composite Structures*, *35*(3), 263–269. https://doi.org/10.101/0263-8223(96)00033-5
4. Motoku, M., Vaidya, U. K., & Janowski, G. M. (1999). Parametric studies on self-repairing approaches for resin infused composites subjected to low velocity impact. *Smart Materials and Structures, 8,* 623–638. https://doi.org/10.1088/0964-1726/8/5/313.
5. Zako, M., & Takano, N. (1999). Intelligent materials systems using epoxy particles to repair microcracks and delamination in GFRP. *Journal of Intelligent Material Systems and Structures, 10,* 836–841. https://doi.org/10.1106/YE1H-QUDH-FC7W-4QFM.
6. Bleay, S. M., Loader, C. B., Hawyes, V. J., Humberstone, L., & Curtis, P. T. (2001). A smart repair system for polymer matrix composites. *Composites A, 32,* 1767–1776. https://doi.org/10.1016/S1359-835X(01)00020-3.
7. Palleau, E., Reece, S., Desai, S. C., Smith, M. E., & Dickey, M. D. (2013). Self-healing stretchable wires for reconfigurable circuit wiring and 3D microfluidics. *Advanced Materials, 25,* 1589–1592.
8. Shepherd, R. F., Stokes, A. A., Nunes, R. M., & Whitesides, G. M. (2013). Soft machines that are resistant to puncture and that self seal. *Advanced Materials, 25,* 6709–6713.
9. Acome, E., et al. (2018). Hydraulically amplified self-healing electrostatic actuators with muscle-like performance. *Science, 359,* 61–65.
10. Trask, R. S., & Bond, I. P. (2006). Biomimetic self-healing of advanced composite structures using hollow glass fibres. *Smart Materials and Structures, 15,* 704–710. https://doi.org/10.1088/0964-1726/26/15/3/005.
11. Darabi, M. A., et al. (2017). Skin-inspired multifunctional autonomic-intrinsic conductive, self healing hydrogels with pressure sensitivity, stretchability, and 3D printability. *Advanced Materials, 29,* 1700533.

Influence of Spindle Rotational Speeds on Pure Mg and 0.1GNP-3Al-Mg Alloy-Nanocomposite in Wire Electrical Discharge Turning Process

Pravir Kumar, Biplab Kumar Roy, Amitava Mandal, Ashis Mallick, and Manoj Gupta

Abstract In the present study, pure bulk Mg and 0.1GNP-3Al-Mg alloy-nanocomposite were synthesized through powder metallurgy followed by hot extrusion. The synthesized materials were characterized by XRD and EDX area mapping. The room temperature, micro-hardness, tensile, and compressive behavior of the pure Mg and the nanocomposite were studied and compared. The Vicker's hardness, ultimate tensile strength, and ultimate compressive strength of the 0.1GNP-3Al-Mg alloy-nanocomposite were observed improved by 46.15%, 17.6%, and 20.56%, respectively, corresponding to the pure Mg. The cylindrical specimens developed were then turned using wire electrical discharge turning (WEDT) process. The effect of spindle rotational speeds on various output parameters like material removal rate (MRR) and surface roughness (R_a, R_q, R_z) was studied and compared for the two materials. The MRR of the developed nanocomposite shows a lower MRR in comparison with the pure Mg at the same spindle rotational speed. However, the roughness values of both the pure Mg and the mg alloy-nanocomposite are close. Finally, FESEM images were taken, and detailed surface characteristics were discussed. It was observed that the Mg-3Al/0.1GNP nanocomposite contained lots of voids and micro-cracks and that the surface of pure Mg was relatively smoother.

P. Kumar (✉) · B. K. Roy · A. Mandal · A. Mallick
Department of Mechanical Engineering, Indian Institute of Technology (ISM),
Dhanbad 826004, India
e-mail: pravirkumar30@gmail.com

B. K. Roy
e-mail: r.biplabkumar@yahoo.com

A. Mandal
e-mail: amitava03@gmail.com

A. Mallick
e-mail: 123.ashis@gmail.com

M. Gupta
Department of Mechanical Engineering, National University of Singapore, Singapore 117576,
Singapore
e-mail: mpegm@nus.edu.sg

1 Introduction

Magnesium-based nanocomposites are considered as a potential candidate to be used in automobile, aerospace, sports, and electronic for structural application. Magnesium (Mg) exhibits an excellent combination of high specific strength, machinability, recyclability, castability, damping behavior, electromagnetic radiation resistance, and thermal stability [1]. The Mg is also biodegradable, and the modulus property of the magnesium is near to the human bone. Therefore, the magnesium-based nanocomposite is also seen as a potential replacement of non-degradable titanium alloy, stainless steel, or polymer-based materials for the implant material in the orthopedic application. It reduces stress shielding effects and helpful in bone regeneration [1, 2]. The alloying of Mg with aluminum (Al) improves the strength and percentage elongation of the alloy. Various Mg–Al alloys like AZ91D, AZ (Mg/Al/Zn), AE (Mg/Al/RE), AM60B, AM50A, AM (Mg–Al–Mn), AE42, and AS21 find application in aerospace and ground transportation. Further, the addition of graphene nano-platelets (GNP) improves the strength of the alloy-nanocomposite [3]. Graphene exhibits superior physiochemical properties like excellent thermal conductivity, high carrier mobility at room temperature, high Young's modulus of elasticity (1 TPa), intrinsic strength (130 GPa), good tribological property, a large specific surface area, and so on [4].

Mg-based material can be machined through conventional machining, although there are various challenges like burr-free surface, good surface integrity, chip ignition, tool wear, etc. The non-conventional machining process like electric discharge machining (EDM) is highly profitable over conventional machining processes as regards the absence of mechanical forces, less material wastage, and production of complex geometry. EDM is an economical and very popular manufacturing process to machine conductive metallic materials disregarding their hardness [2]. Wire electrical discharge machining (WEDM) is derived from the EDM process, where the tool is replaced by a continuously fed wire. The wire feed rate varies from 1–20 m/min, and the material is removed by continuous sparks arising between the wire electrode and the workpiece, resulting in melting and evaporation [5]. With WEDM, desired shape, profile, and tailored topography can be obtained that is favorable for the implant fixation. The change in surface integrity with better surface roughness, the formation of the recast layer, micro-cracks, etc., may improve biocompatibility by favoring cell adhesion and tissue growth for the orthopedic implant and corrosion behavior. Wire electrical discharge turning (WEDT) is a modification of typical WEDM, where an auxiliary rotary axis is attached to the existing setup. The workpiece rotates continuously, and the wire electrode moves perpendicular to the axis of rotation. A few researchers studied the consequences of process parameters on the output responses such as material removal rate (MRR), surface roughness, and the roundness [6–11]. However, the effect of the spindle rotational speed on these output

responses is contradictory. Some recent studies concerning WEDT are the fabrication of micro end mills [12], fabrication of micro electrode by creating a helical groove by WEDT [13], and optimization based on teaching-learning-based optimization (TLBO) algorithms [14]. This experimental study concentrates on the effect of spindle rotational speeds on MRR and surface roughness'. The reason for considering the three roughness variables is that R_a alone cannot differentiate between the peaks and valleys of the surface. Hence, three roughness parameters are taken into consideration. To the best of authors' knowledge, there are no previous studies of the WEDT process on Mg-based nanocomposites.

In this present study, the WEDT process was performed on synthesized bulk pure Mg and 0.1GNP-3Al-Mg alloy-nanocomposite and compared.

2 Materials and Methodology

The pure bulk Mg and 0.1GNP-3Al-Mg were synthesized through the powder metallurgy route, followed by hot extrusion. In the synthesis of alloy-nanocomposite, 3 wt% of Al, 0.1 wt% of graphene nano-platelet, and 96.9 wt% of Mg powders ($\geq$99.5% purity and 60–300 μm size-range) have been blended in the RETSCH PM-400 machine. The pure Mg powder and a mixture of the alloy-nanocomposite were cold compacted to form a cylindrical billet of size 40 mm length and 35 mm diameter. The billets were then sintered in a microwave furnace followed by hot extrusion to get the rod of 8 mm diameter. The details of the materials and synthesis process can be found in the author's other article [15]. The density, hardness, and the mechanical behaviors of the pure Mg and 0.1GNP-3Al-Mg alloy-nanocomposite are presented in Table 1.

The XRD result of the nanocomposite is presented in Fig. 1. The peaks of the intensities correspond to the Mg phase. There are no peaks of intensity corresponding to Al, and GNP is visible due to presence in lower weight percentages. The EDX area mapping of the 0.1GNP-3Al-Mg (Fig. 2) represents the distribution of Al and GNP in the base material Mg.

The experiments were performed on a commercial WEDM (Make: Electronica Maxicut-e). A rotary setup developed by the authors was mounted on the WEDM for rotating the workpiece (Fig. 3).

Table 1 Mechanical properties [15]

Sample name	Density (g/cm^{-3})	Vicker's hardness	Ultimate tensile strength (MPa)	Ultimate compressive strength (MPa)
Pure Mg	1.7402	39	202.76	287
0.1GNP-3Al-Mg	1.7601	57	238.44	346
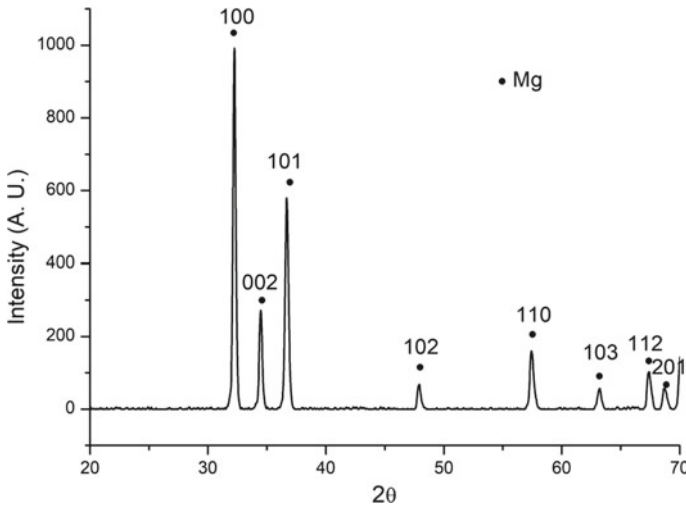
Fig. 1 XRD plot

A zinc-coated brass wire of diameter 250 µm was used as the wire electrode. Spindle rotational speeds were varied at four different levels (viz. 150, 300, 450, and 600 RPM), and its effect on MRR and surface roughness is studied. All other parameters were kept at constant levels and are recorded in Table 2. A length of 10 mm was turned for each specimen at a depth of cut of 2 mm. A roughness tester (Make: Mitutoyo SJ-210) was used to measure the surface roughness.

3 Results and Discussion

The pure bulk Mg and 0.1GNP-3Al-Mg were synthesized successfully through the powder metallurgy route and then hot extruded. The Vicker's hardness, ultimate tensile, and compressive strength of the 0.1GNP-3Al-Mg alloy-nanocomposite were improved by 46.15%, 17.6%, and 20.56%, respectively, in comparison with the pure Mg. The improvements of the mechanical properties of the 0.1GNP-3Al-Mg are due to alloying of Mg with stronger Al and reinforcing with stronger GNP particles. The various strengthening mechanism like dispersion strengthening, grain refinement, Orowan strengthening, CTE mismatch, elastic modulus mismatch. The results obtained from the WEDT experiment are plotted in the form of a graph.

From Fig. 4, it can be noticed that the MRR of pure Mg, as well as the Mg nanocomposite, increases with the increase in spindle rotational speed. However, the increment from 450 to 600 RPM is very negligible. Also, the MRR of the nanocomposite is lesser than that of the pure Mg at the same spindle rotational speed. This may be due to the requirement of greater energy to break the bonding strength of Mg-3Al/0.1GNP nanocomposite.
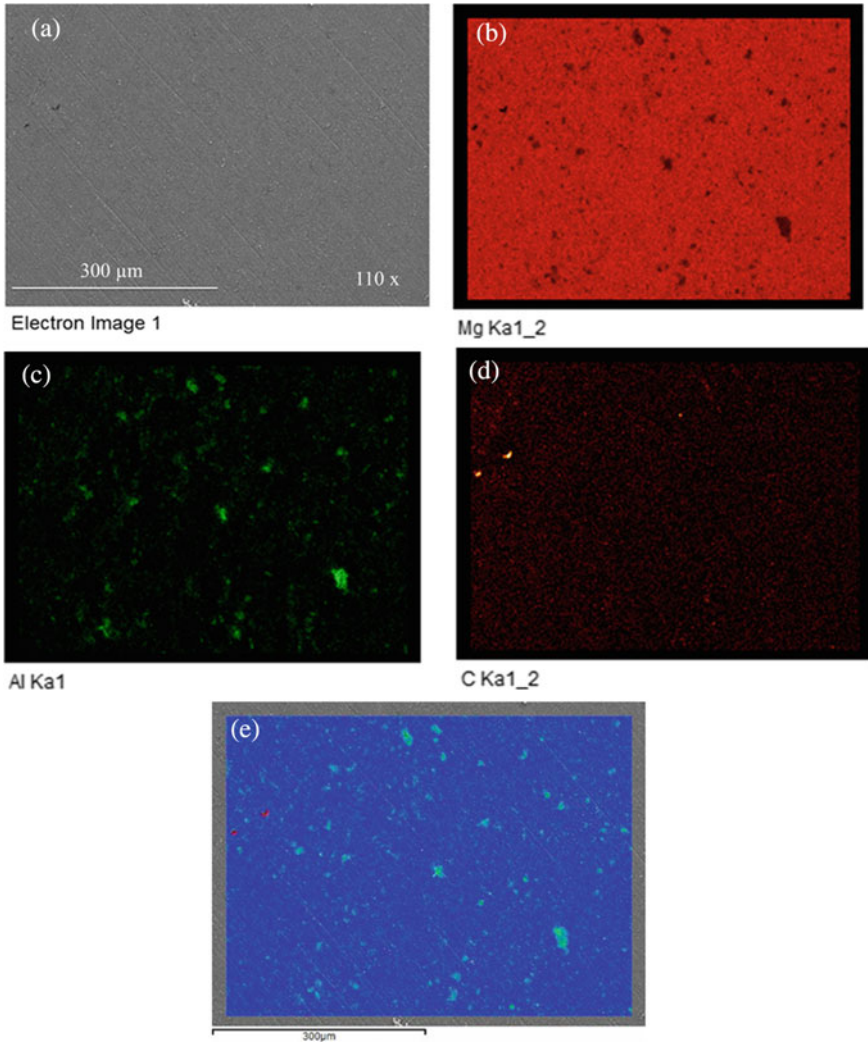
Fig. 2 EDX area mapping of the 0.1GNP-3Al-Mg nanocomposite **a** FESEM image, **b** magnesium, **c** aluminum, **d** carbon, and **e** elemental overlay

In this experimental study, three roughness parameters, namely roughness average (R_a), root mean square roughness (R_q), and the average peak to valley height (R_z), are selected. All three roughness parameters increase with increasing spindle rotational speeds. There is a negligible difference between the roughness values of pure Mg and the 0.1GNP-3Al-Mg nanocomposite at the same spindle rotational speed (Fig. 4).

The FESEM images (Fig. 5) show the effect of spindle rotational speed at 150 and 600 RPM on the 0.1GNP-3Al-Mg nanocomposite. It can be noticed that as the
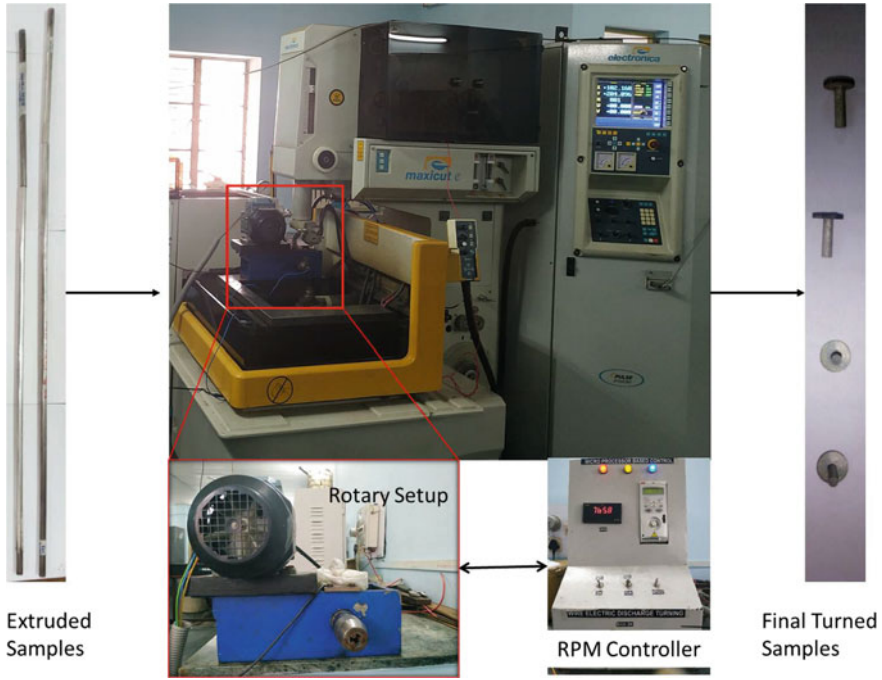
Fig. 3 Flowchart representing the extruded samples, the WEDM machine, the rotary setup, and the turned samples in IIT (ISM), Dhanbad

Table 2 Parameters kept at constant values

Parameters	Values
Pulse-on-time	1.10 µs
Pulse-off-time	190 µs
Gap voltage	40 V
Wire feed	1 m/min
Wire tension	600 kgf

spindle rotational speed increases, the surface degrades in the form of re-solidified molten metal, voids, and feed marks, which in turn results in higher roughness values.

Comparing the surface features of pure Mg and the 0.1GNP-3Al-Mg alloy-nanocomposite at 450 RPM (Fig. 6), it can be noticed that WEDT of pure Mg results in a relatively smoother surface. Numerous micro-cracks and micro-voids can be noted in the 0.1GNP-3Al-Mg nanocomposite.
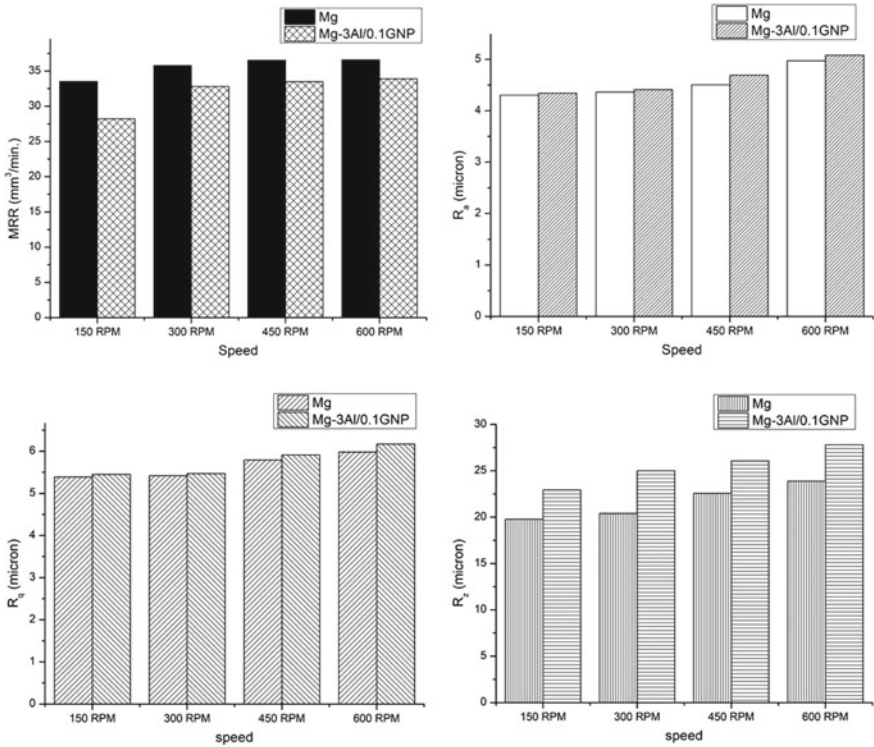
Fig. 4 MRR and roughness (R_a, R_q, and R_z) comparison of pure Mg and 0.1GNP-3Al-Mg nanocomposite
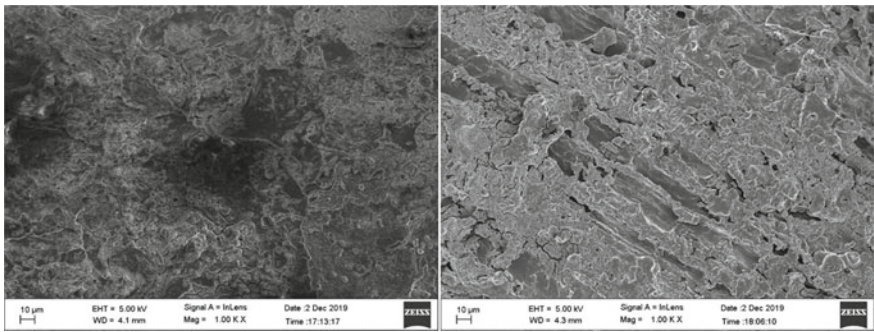
Fig. 5 FESEM image of Mg-3Al/0.1GNP nanocomposite at 150 and 600 RPM
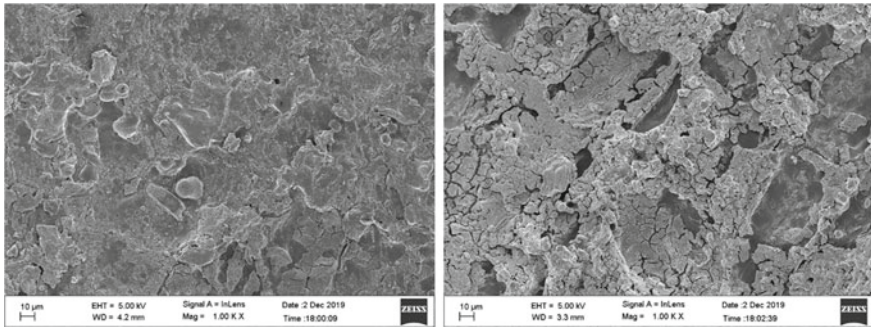
Fig. 6 FESEM image of pure Mg and 0.1GNP-3Al-Mg nanocomposite at 450 RPM

4 Conclusion

The pure bulk Mg and 0.1GNP-3Al-Mg alloy-nanocomposite were synthesized successfully through the powder metallurgy process aided with microwave sintering and then subjected to a hot extrusion process. The room temperature mechanical properties of the two compositions were evaluated and compared. The alloying of Mg with Al and the addition of GNP as reinforcement contributed to the improvement of the mechanical properties. The Vicker's hardness, ultimate tensile, and compressive strength of the 0.1GNP-3Al-Mg alloy-nanocomposite improved by 46.15%, 17.6%, and 20.56%, respectively, in comparison with the pure Mg. The WEDT operation was then performed on the extruded samples, and the effect of spindle rotational speeds on various output parameters like MRR and surface roughness was studied. It was observed that MRR improves with an increase in the spindle rotational speed, whereas the roughness deteriorates with an increase in the spindle rotational speed. Also, the MRR of pure Mg was better than that of the 0.1GNP-3Al-Mg nanocomposite at the same spindle rotational speed, but the roughness values of both the samples were pretty much close to each other. From the FESEM images, it was noticed that surface defects in terms of micro-cracks and voids were more in 0.1GNP-3Al-Mg, which resulted in a rougher surface.

Parametric study of other input parameters such as pulse-on-time, pulse-off-time, gap voltage, flow rate, wire tension, and wire feed rate can be done on pure bulk Mg and 0.1GNP-3Al-Mg alloy-nanocomposite to further improve the performance characteristics

References

1. Parande, G., Manakari, V., Kopparthy, S. D. S., & Gupta, M. (2018). Utilizing low-cost eggshell particles to enhance the mechanical response of Mg–2.5 Zn magnesium alloy matrix. *Advanced Engineering Materials*, *20*(5), 1700919 (2018).
2. Kumar, K., Gill, R. S., & Batra, U. (2018). Challenges and oppurtunities for biodegradegradble magnesium alloy implants. *Materials Technology, 33*(2), 153–172.
3. Kumar, P., Mallick, A., Kujur, M. S., Tun, K. S., Shabadi, R., & Gupta, M. (2018). Strength of Mg–3% Al alloy in presence of graphene nano-platelets as reinforcement. *Materials Science and Technology, 34*(9), 1086–1095.
4. Novoselov, K. S., Fal, V. I., Colombo, L., Gellert, P. R., Schwab, M. G., & Kim, K. A. (2012). Roadmap for graphene. *Nature, 490*(7419), 192 (2012).
5. Roy, B. K., & Mandal, A. (2019). Surface integrity analysis of Nitinol-60 shape memory alloy in WEDM. *Materials and Manufacturing Process. [Internet]. 34*(10), 1091–1102 (2019). Available from: https://doi.org/10.1080/10426914.2019.1628256.
6. Haddad, M. J., Alihoseini, F., Hadi, M., Hadad, M., Tehrani, A. F., & Mohammadi, A. (2010). An experimental investigation of cylindrical wire electrical discharge turning process. *International Journal of Advanced Manufacturing Technology, 46*(9–12), 1119–1132.
7. Hadad, M. (2014). Optimization of machining parameters on surface roughness and roundness in the cylindrical wire electrical discharge turning (CWEDT) of AISI D3 tool steel. *Rev. Tec. la Fac. Ing. Univ. del Zulia. 37*(2), 74–84 (2014).
8. Hadad, M., Bui, L. Q., & Nguyen, C. T. (2018). Experimental investigation of the effects of tool initial surface roughness on the electrical discharge machining (EDM) performance. *The International Journal of Advanced Manufacturing Technology, 95*(5–8), 2093–104 (2018).
9. Mohammadi, A., Tehrani, A. F., & Abdullah, A. (2013). Introducing a new technique in wire electrical discharge turning and evaluating ultrasonic vibration on material removal rate. *Procedia CIRP [Internet], 6*, 583–588 (2013). Available from: http://dx.doi.org/10.1016/j.procir.2013.03.005.
10. Mohammadi, A., Tehrani, A. F., Emanian, E., & Karimi, D. (2008). Statistical analysis of wire electrical discharge turning on material removal rate. *Journal of Materials Processing Technology, 205*(1–3), 283–289.
11. Mohammadi, H., Torkzadeh, K., & Teharani, A. R. F. (2009). Evaluation of surface roughness and material removal rate in CWEDM using DOE and ANN. *Iranian Conference on Manufacturing Engineering, 2009, 3*–5.
12. Sun, Y., Gong, Y. D., Wen, X. L., Yin, G. Q., & Meng, F. T. (2020). Micro milling characteristics of LS-WEDM fabricated helical and corrugated micro end mill. *International Journal of Mechanical Sciences*, *167* (October 2019) (2020).
13. Krupa, J. S., & Samuel, G. L. (2020). Fabrication and Characterization of Helical Grooved Cylindrical Electrodes Generated by WED Turning Process. In: Advances in Unconventional Machining and Composites, 437–449.
14. George, J., & Jose, R. M. (2019). Multi-objective optimization of roundness, cylindricity and areal surface roughness of Inconel 825 using TLBO method in wire electrical discharge turning (WEDT) process. *Journal* of the *Brazilian Society* of *Mechanical Sciences* and *Engineering* [Internet]. (2019). Available from: https://doi.org/10.1007/s40430-019-1880-y.
15. Kumar, P., Kujur, M., Mallick, A., Tun, K. S., & Gupta, M. (2018). Effect of graphenenanoplatelets on the mechanical properties of Mg/3wt% Al alloy-nanocomposite. In *IOP Conference Series: Materials Science and Engineering* 346 (1), 012001, IOP Publishing (2018).

Investigation of Laser-MIG Hybrid Welding Performances in al Alloys with Influence of Ar–He–Ne Mix Shielding

Kamal Lochan Sahu, Nehal Kumar, Alok Singh, Naveen Anand Daniel, and Umesh Kumar Vates

Abstract During the laser welding process, there is a drastic laser power wastage and keyhole fluctuation due to the shielding effect of dense plasma. Similarly, in the case of MIG welding, occurrence of porosity defects and burn-through defects are too common. Combining these two methods of welding can result in minimizing the defects. This study has shown that using the mixture of Ar–He–Ne shielding gas and selecting certain parameters in a range provides us with a good welded specimen with good strength and smooth surface finish. The study will be analysed, and the result concluded from this experiment will be compared with conventional welding processes. This experiment is emphasized to increase the knowledge regarding hybrid welding and foresee its future application based on the outcome.

Keywords Keyhole fluctuation · Shielding effect · Porosity defect · Shielding gas · Residual stress

1 Introduction

This laser-MIG hybrid welding shows a great use in automobiles, pressure vessels and shipbuilding, etc., since it consists of the deeper penetration depth and high welding velocity. This modern laser-MIG welding method is utilizer for the 7xxx (7th series) aluminium, which results in a reduction in welding residual stress and

K. L. Sahu (✉) · N. Kumar · A. Singh · N. A. Daniel · U. K. Vates
Department of Mechanical Engineering, Amity University, Noida, India
e-mail: kamalsahu83.ks@gmail.com

N. Kumar
e-mail: nehalkumar8294@gmail.com

A. Singh
e-mail: aloksingh.011998@gmail.com

N. A. Daniel
e-mail: nadaniel@amity.edu

U. K. Vates
e-mail: ukvates@amity.edu

distortion of the joints. Some studies have shown that laser leading mode exhibits higher strength compared to the MIG leading mode, in addition to that, it also has deeper penetration depth and less welding porosities. Using helium (He) with argon (Ar) in the shielding gas resulting in suppressing the weld porosity of aluminium alloy and the plume effect reduces due to the higher ionization potential of helium, not only that the welding rate was higher because a high energy arc was generated.

This paper deals with the major idea of using this hybrid welding method with a 6xxx (6th series) aluminium alloy 6063-T6 which is also known as the architectural alloy. These aluminium alloys have medium strength and high corrosion resistance. The typical application of this type is indoors, window frames, shop fittings, etc., with this process of hybrid welding, the production speed and the production quality will be enhanced.

2   Literature Review

The findings of the various research papers based on hybrid welding are summarized below. The research papers are diverse material with different parameters, and based on the following data and conclusion from the research papers, the experiment has been conducted.

The porosity defects are minimized to a great extent due to the use of the helium as a shielding gas [1]. As per the previous research papers by conducting the NDT on these hybrid welded specimens resulted in low porosity defects. As compared with argon, helium has a higher level of thermal conductivity which increases the level of energy absorption by the shielding gas during the welding process. References [2, 3] which in turn increases the molten pool temperature during the welding process. The experiment denotes that the hybrid weld specimens contain a large amount of weld metal than the laser weld bead [4]. It is advantageous in terms of gap tolerance and bead within the butt welding case. When the metal is melted with the focused laser, it results in a vapour above the metal surface, now the continuous irradiation on the vapour ionizes the vapour and forms plasma plume [5]. These plumes affect the penetration depth of the laser. This previous studies show that this effect of the plume was suppressed by optimizing the parameter of assist gas or combination of shielding gas. In the welding method, the liquid metal overdue the molten pool cools off and solidifies to convert to weld. The performance of the weld is greatly influenced by the solidified liquid metal. The liquid metal in the molten pool always starts to solidify from the boundary of the pool. The molten metal will start joining on the molecular level at the boundary of the pool and starts crystallizing. There are areas affected by the thermal cycle that is the semi-melted grain zone which leads to un-melted recrystallized grains. There are areas near weld spot which have small columnar crystals adjacent to semi-melted grains. These small columnar crystals can be observed growing randomly in any direction. But along the temperature gradient, the grains will struggle to grow and along with other directions, the growth of the

grain will be restrained and stopped. Along the temperature gradient, the slender columnar crystals grow which are towards the weld centre [6]. The restrained force round the molten metal is very small at the molten pool centre. During crystallization, it forms a snowflake-like columnar crystal, and it nucleates from inside of the liquid state. Laser-MIG welding results in serious grain growth due to the heat affected by both laser and arc. The hardness grows incessantly until it reaches the maximum of the whole joint hardness value as the hardness test spot moves towards the fusion line. The hardness value is maximum near the fusion line. The reason for this phenomenon is that the finer and small grains are of greater hardness and thus columnar grains adjacent to the fusion line are finer than coarse dendrite near centre of the weld line. The second reason is the element structure of the centre of the weld is different from the adjacent area around the fusion line. The area near the fusion line contains 0.47% Si which improves hardness compared to the weld centre which has no Si [7]. The lower part of the weld has a higher hardness value than the upper part. The reason is that the grain size in the lower part of the weld is smaller than the grain size in the upper weld part. The hardness is increased due to an increase in resistance to deformation of material and increase in microscopic hardness because of smaller grain size the grain boundaries increase for same size material and thus increase in obstacle to dislocation movement.

2.1 Need for LMHW

In this current scenario, the growth of technology in every sector is tremendous. In the welding sector too, today, laser welding is considered for various operations, and it has proved to be competent to fulfil all the required needs, still, there are some defects present in laser welding. The major need for laser-MIG hybrid welding (LMHW) is to overcome these defects, and this study will show, by altering some parameters for a specific need, we can get the best outcome. As per the study conducted till now, with a hybrid welding system, large parts can be welded easily even the parts with complex geometry. Most of the welding processes provide the end product with residual stresses, and these stresses are a major concern, if the product from the welding has to be used for bearing a heavy load, by combining some specific welding processes, these residual stresses can be alleviated.

This hybrid welding process also deals with other defects such as porosity defects and keyhole fluctuation. These defects are minimized with the use of shielding gases in a definite ratio. With the use of this hybrid arrangement, the production speed can be enhanced, which is an important aspect in industrial terms.

2.2 Change in Parameters of Laser-MIG Hybrid Welding

- **Laser power**

An expansion in laser power will by and large increment the weld entrance. In the instance of crossover laser-circular segment welding (as restricted with the laser-just procedure), this wonder is emphasized because the reflectivity of the workpiece metal is decreased when the metal is warmed by the circular segment [8, 9]. This property directly affects the heat zones which are formed during the welding process. It completely depends on the heat intensity which may cause thermal cracks.

- **Welding speed**

The welding speed in case of laser welding is defined as the velocity with which the welding on the specimen is done, and additionally, it improves the hole filling capacity by the filler wire [10]. An increase in the welding speed will result in faster production, which is an important factor if considered for the industrial aspect.

- **Joint gap**

For laser welding, holes up to 0.2 mm can be overseen. Holes bigger than this will lead to weld imperfections, for example, a deficient weld dab and undercut. The half breed laser-bend procedure enables us to get workpieces together with holes of 1 mm with no issue and much more extensive holes if the wire sustaining is set sufficiently high. This procedure is in this manner progressively tolerant to off base joint readiness and joint fit-up just as warm twisting of the workpiece during the welding procedure. It is likewise increasingly tolerant of a bar to hole misalignment.

3 Experimental Procedure

In this experiment based on the previous research so far, different parameters of laser and MIG welding will be selected, and specimens with hybrid laser and MIG welding will be fabricated, the relationship between the factors affecting the process and the output of the process will be determined. In simple terms, a design of experiment (DOE) will be formed. In addition to that, some specimens with only laser and MIG welding will also be fabricated.

Firstly, specimens will be passed through non-destructive testing (NDT) and then destructive testing (DT). Data on all the experiments will be noted and will be compared with other specimens and data present in previous papers.

Based on this data, a conclusion will be drawn about the efficiency of this hybrid welding procedure in case of this specific made of aluminium alloy (6063-T6).

The investigation of the experiment will be done by comparing the data from the reference surface modelling (RSM) software and physically experimenting. There

Table 1 Chemical compositions of aluminium alloy and filler wire (wt%)

Welding components	Elements								
	Si	Fe	Cu	Mn	Mg	Cr	Zn	Ti	Al
(Al - alloy) 6063-T6	0.2–0.6	≤0.35	≤0.1	≤0.1	0.45–0.9	≤0.1	≤0.1	≤0.1	≤97.5
(Wire) ER5356	4.5	≤0.60	≤0.30	≤0.15	≤0.20	–	≤0.10	≤0.15	–

Table 2 Standard values taken in the experiment

	Minimum	Medium	Maximum
(a) Pulse	5	6	7
(b) Frequency (Hz)	8	9	10
(c) Current (A)	100	110	120

will be a set procedure followed for the testing of each specimen. Non-destructive testing will be performed first since it will cause no damage to the specimen (Table 1).

3.1 Preparation of Specimens, the Parameters Considered Are

- Pulse
- Frequency (Hz)
- Current (A)

There are three levels of values which are taken as minimum, medium, and maximum. And a DOE for the experiment is created. According to which, 15 different specimens are created and will be tested with destructive testing and non-destructive testing (Table 2).

In the above table, three critical parameters are considered namely pulse, frequency, and current. Respective values for the critical parameters are taken as shown in the table such that the values are categorized into three parts minimum, medium, and maximum. These values will be utilized in forming the design of experiment (DOE). Further specimens will be fabricated based on the DOE, and the testing procedure will be conducted (Table 3).

3.2 Non-destructive Testing

This is the initial testing method which determines any contamination and any metallurgical defects in the specimen. The welded specimen needs to withstand various

Table 3 Design of experiment formed according to the table above

S no.	Pulse (Hz)	Frequency (Hz)	Current (A)	Tensile strength (MPa)
1.	7	10	110	231
2.	7	9	120	242
3.	7	9	100	206
4.	7	8	110	234
5.	6	9	110	230
6.	6	10	100	216
7.	6	10	120	256
8.	6	8	100	211
9.	6	8	120	245
10.	5	10	110	238
11.	5	8	110	248
12.	5	9	120	262
13.	5	9	100	202
14.	7	10	120	246
15.	5	8	100	217

loading conditions. To determine that non-destructive testing (NDT) is the best way without consuming the specimen.

The quality of the welded specimen can be compromised after the molten puddle cools down and solidifies [11]. This can happen due to wrong set-up and technique, human error, low temperature and moisture, high cooling rate, etc. NDT mainly depends on the ability of the inspector.

3.2.1 List of Non-destructive Tests to Be Conducted

- **Visual inspection**
- **Dye penetration test**
- **Eddy current test**
- **Ultrasonic testing**
- **Radiographic testing**

After non-destructive testing, a range of destructive testing will be conducted for the evaluation of the stress in the fabricated specimens.

3.3 Destructive Testing

- These tests are suggested by the design engineer considering the performance, service life, and application of the weld joint.
- Destructive testing is done after the non-destructive testing (NDT) is done on the specimen. NDT includes radiographic test, ultrasonic test, magnetic particle test, and die penetration test.
- Destructive testing is done by considering the stresses and loading condition of the weld joints during its life time.
- Location of the weld is considered, i.e. the specific requirements that are needed for the welded specimen for the particular location.
- Application of the joint, it refers to the application of the weld joint throughout its service lifetime.
- Destructive testing is done to analyse the technique used to perform the welded specimen.
- Atmospheric conditions throughout the service life of the welded specimen.
- Performance of the weld joint on application of various types of loads also how adequate is the design to survive various loading conditions is determined by destructive testing.

3.3.1 List of Destructive Testing to Be Conducted

- Guided bend test
- Charpy V-notch test
- Hardness test
- Tensile test

4 Conclusion

Metal inert gas (MIG) welding is also known as gas metal arc welding (GMAW). It is a basic welding procedure in which the electrode is fed into the specimen in the presence of shielding gas with the help of the current. In this current scenario, MIG welding is considered one of the major industrial procedures used in the fabrication of the product. There are many industries where MIG welding is the core of the production and fabrication of the product such as the automotive industry, construction, and infrastructure, railroads, and shipping. Hence, optimization of MIG welding with laser welding will be optimal for industrial purposes since this can result in faster production with higher strength and quality.

From the literature study conducted, it can be concluded that the improvement that can be attained by fusing MIG welding with LASER welding will result in better production and quality product. The main objective of the experiment is to improve

the tensile strength of the specimen. Which will be calculated by comparing the data collected by experimenting physically and the data collected through the reference surface modelling (RSM) software.

References

1. Pandian Pitchipoo, G. S. K. (2011). Assessment of MIG welding defects using omputer vision system.
2. Xiaoyi Yang, H. C. Z. Z. C. C. C. Z. (2019). Effect of shielding gas flow on welding process of laser-arc hybrid welding and MIG welding.
3. Giovanni Tani, G. C. A. F. A. A. (2007). The influence of shielding gas in hybrid LASER–MIG welding.
4. Yang Dongxia, L. H. D. N. Z. H. H. (2012). Optimization of weld bead geometry in laser welding with filler wire process using Taguchi's approach.
5. Stanciu Elena-Manuela, G. D. O. D. (2011). Mechanism of keyhole formation in laser welding.
6. Fuheng Nie, H. D. S. C. P. L. L. W. Z. Z. X. L. H. Z. (2016). Microstructure and mechanical properties of pulse MIG welded 6061/A356 aluminum alloy dissimilar butt joints. *Journal of Materials Science & Technology*.
7. Chenfeng Duan, S. Y. J. G. X. A. Y. W. (2019). Microstructure and ratcheting behavior of 6061 aluminum alloy laser-MIG hybrid welding joint.
8. Zhao Jiang, X. H. L. H. F. l. Y. Z. (2018). Double-sided hybrid laser-MIG welding plus MIG welding of 30-mm-thick aluminium alloy. *The International Journal of Advanced Manufacturing Technology*.
9. Mikhail Sokolov, A. S. (2014). Methods for improving laser beam welding efficiency.
10. Salminen, A. (2014). Improving laser beam welding efficiency.
11. Mark Willox, G. D., A brief description of NDT techniques.

Regression and Taguchi Analysis of TiO$_2$, MnO and CaF$_2$ on Brinell Hardness Number of Submerged Arc Welding Flux Using Red Mud

Shyam Sunder Sharma, Rishi Dewangan, Ashish Goyal, and Anurag Joshi

Abstract After applying the Bayer process, aluminium residue is generated which is called as "Red Mud". Globally, approximately 250 million tons red mud is produced every year during aluminium production. It persists some industrial compounds like: Fe$_2$O$_3$, TiO$_2$, MnO, CaO, SiO$_2$, Al$_2$O$_3$, etc. These compounds are important ingredient for developing submerged arc welding flux with other elements (CaF$_2$, CaO, TiO$_2$ and water glass as binder). In this paper, Brinell hardness is calculated on weld bead using develop flux. This process is optimized through regression and Taguchi analysis on numerous parameters, i.e. TiO$_2$, MnO and CaF$_2$. We have simulated the practical performance in computational environments using open source Python programming. The results are meeting at 95% of confidence level, and this can be further utilized for developing solution regarding experimentation of submerged arc welding flux.

Keywords Red mud · Computation analysis · Taguchi analysis · Regression analysis

1 Introduction

Aluminium is high strength lightweight material which also has good recyclable property. It plays an important role in various societies in various applications such as transportation, food, infrastructure, construction, electronics [1]. Aluminium is

S. S. Sharma (✉) · A. Goyal · A. Joshi
Manipal University Jaipur, Jaipur 303007, India
e-mail: shyamsunder.sharma@jaipur.manipal.edu

A. Goyal
e-mail: ashish.goyal@jaipur.manipal.edu

A. Joshi
e-mail: anurag.joshi@jaipur.manipal.edu

R. Dewangan
Amity University Rajasthan, Jaipur 302015, India
e-mail: rdewangan@jpr.amity.edu

produced from bauxite ore by two different process, i.e. hart Harold and Bayer process. Around 30–40% bauxite converted into red mud during aluminium production in Bayer process [2]. Nearly 2 billion tons red mud produced in every year which is gradually increased, it is harmful for environment due to alkaline nature disposal (pH 10.5–12) [2], and it also contains some industrial compound such as Fe_2O_3 (30–60 wt%), Al_2O_3 (10–20 wt%), SiO_2 (3–50 wt%), Na_2O (2–10 wt%), CaO (2–8 wt%) and TiO_2 (0–25 wt%) [3]. Many researcher uses red mud for various application like water treatment for removing toxic metals [4–7], construction materials [8, 9] adsorbents and catalysts [10, 11], developing flux [12], for determination of thermo processing behaviour on variable particle size [13, 14], used as coating material for improvement of mechanical properties of steel [15–17], and there are so less work done on the field of submerged arc welding, so different type of flux was produced by red mud by adding allowing compound like TiO_2, CaF_2, MnO in varying percentage. Bead on plate welding procedure was adopted for getting optimized weld bead, and then, it is further tested for different mechanical and chemical behaviour. This work is simulated through computational analysis under open source environment using Python programming. This programming suits the requirement to evaluate the scientific results for specific computation. Taguchi and regression analysis offer an efficient and systematic optimized design at lower cost [18]. Taguchi analysis simplifies the optimal procedure and shows its significance value and contribution on each parameter. There are some researchers used Taguchi analysis in various field such as to determin the welding process parameter [19], to check characteristics and contribution of die casting parameters [20] and to study erosion characteristics of fibre reinforced composites [21]. This research work focuses on improvement of experimental result by Taguchi and regression analysis on hardness value.

2 Experimentation

Submerged arc welding is commonly used in industrial application due to good mechanical property and narrower heat affected zone. In submerged arc welding, flux plays critical role in welding, approximately 50% cost is carried out by flux, and in this research work, flux preparation is the main objective before starting the submerged arc welding. In this research work, the flux is prepared using the agglomeration techniques based on red mud with some alloying elements. The composition of red mud that was used to prepare a basic material as mentioned below (Table 1).

Agglomeration techniques were used for flux preparation, here red mud chose as base ingredient, and CaF_2, TiO_2, CaO and water glass sieved and mixed for flux preparation, then this agglomerated mixture baked at 800 degree centigrade for 2 h in muffle furnace for removing its moisture content, and this baked flux further sieved to get granular optimized flux. Table 2 shows the composition chart of flux.

Submerged arc welding process works on constant voltage, and MIG works on constant current, so automated table arrangement developed where constant wire

Table 1 Red Mud composition

Sr. No.	Compound	Content (wt%)
1	Fe$_2$O$_3$	25–35
2	Al$_2$O$_3$	12–20
3	TiO$_2$	3–10
4	SiO$_2$	3–10
6	CaO	1–3
7	LOI	10–18

Table 2 Flux composition chart

Sr. no	Red Mud	TiO2	MnO	CaO	CaF2	Fe2O3	Water glass
1	30	10	15	10	5	5	25
2	30	10	12.5	7.5	5	10	25
3	30	15	10	10	5	5	25
4	30	15	7.5	7.5	5	10	25
5	30	15	10	7.5	2.5	10	25
6	30	10	15	7.5	2.5	10	25

is fed and MIG set-up replaces submerged arc welding set-up. Figure 1 shows the welding set-up picture.

Bead on plate welding procedure was used on mild steel substrate of size 50 mm × 20 mm × 5 mm shown in Fig. 2. So many welding runs are performed to get good and optimized weld bead which can be used for further testing procedure. Brinell hardness test was carried out on the specimen after welding process. This test was done by using 10 mm carbide ball indenter on 3000 kg load, and results were calculated.
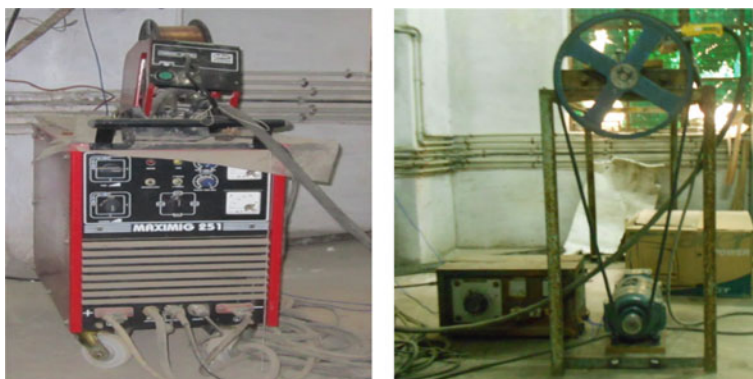
Fig. 1 Automated table welding set-up

Fig. 2 Weld bead

To establish the relationship in between input values and output values, regression analysis has been applied, and in regards of this, the following linear equation is utilized:

$$Z = p + q1Y1 + q2Y2 + q3Y3 + \cdots qnYn \tag{1}$$

Here, Z is the related component which is desired to estimate the results; Y1, Y2, Y3,…Yn are the given dynamic values, based on these, the estimation can be done, and p, q1, q2, q3,…qn are the constants, such values are assessed by a least squares process.

3 Result and Discussion

In this research work, agglomeration technique was used for development of flux, and bead on plate welding procedure was adopted to get optimized broad hip, and then, it is further tested for Brinell hardness, and its tabulated result which has been generated through computational analysis (using Python programming) represented through following graph (Fig. 3).

Above results were corrected by using regression and Taguchi analysis as follows:

$$BHN = 234 + 2.10\,TiO_2 - 1.41MnO - 13.0CaF_2 \tag{2}$$

Here: Fe_2O_3 and CaO are removed due to co-linearity.

Equation 2 comprises the resultant value of BHN. Here, BHN is tested in hardness specimen under payload of 10 KN. The BHN tabulated value is compared with value
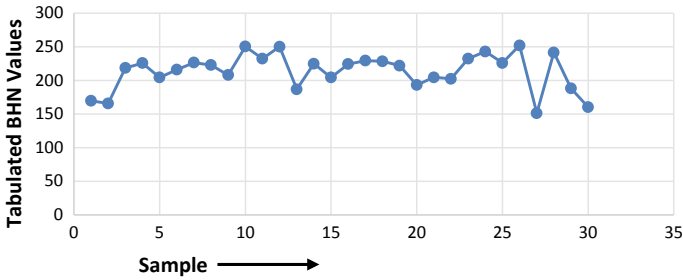
Fig. 3 Tabulated BHN calculations

Table 3 Anova table for flux composition

Source	DF	Seq SS	Adj SS	Adj MS	F	P	Contribution	Confidence level
TiO2	1	6060.6	836.6	836.6	11.18	0.003	28.80%	Significant
MnO	1	4593.8	366.6	366.6	4.9	0.037	21.82%	Significant
CaF2	1	7587.5	26	26	0.35	0.561	36.05%	Non-significant
TiO2*MnO	1	109.3	354.7	354.7	4.74	0.04	0.52%	Significant
MnO*CaF2	1	898.9	898.9	898.9	12.01	0.002	4.18%	Significant
Error	24	1795.9	1795.9	74.8			8.53%	
Total	29	21046						

of regression-BHN. After this comparison, it has been identified that resultant BHN has 5–7% error (Table 3).

Above results come through Anova, and the maximum contribution is put by CaF_2 which is not significant due the 95% confidence level of Anova. So, we can reduce its percentage in overall composition, and from previous research, it is found that higher percentage of CaF_2 leads to porosity and deficiency of mechanical properties. The second-best contribution result is TiO_2 which is also substantial that enhances the toughness and mechanical strength of weld material. All the results found to be significant, and it can be further reused for different submerged arc welding flux.

4 Conclusion

Currently, lots of work is happening worldwide regarding utilization of waste material.

- Waste material is utilized to reduce the negative impact on environment. Red mud is effectively utilized for developing the welding flux.

- Through statistical analysis, it has been identified that TiO2 and MnO component is more superior than other substance for developing the welding flux.
- In future, the similar kind of analysis can be carried out further in the form of SEM, XRD wear test, corrosion analysis, etc., to characterize the submerged arc welding flux using red mud.

References

1. Geetha, B., & Ganesan, K. (2015). Effects of red mud reinforcement on hardness, wear behaviour of cast Al–6Si–0.45 Mg alloy. *Applied Mechanics and Materials, 787,* 658–663.
2. Sharma, S. S., Shukla, D. D., & Sharma, B. P. (2019). Analysis of lean manufacturing implementation in SMEs: A "5S" technique. Advances in Industrial and Production Engineering. Lecture Notes in Mechanical Engineering. Springer, Singapore pp 469–476. Print ISBN: 978-981-13-6411-2. Online ISBN: 978-981-13-6412-9, https://doi.org/10.1007/978-981-13-6412-9_46.
3. Fayyad, E. M., Abdullah, A. M., Hassan, M. K., Mohamed, A. M., Jarjoura, G., & Farhat, Z. (2018). Recent advances in electroless-plated Ni-P and its composites for erosion and corrosion applications: A review. *Emergent Materials, 1*(1–2), 3–24.
4. Ding, X., Ahmed, S., Bao, N., Ding, J., Liu, R., & Yi, J. (2019). Clustering-induced high magnetization in Co-doped TiO 2. *Emergent Materials, 2*(3), 295–301.
5. Jamwal, A., Vates, U.K., Gupta, P., Aggarwal, A., & Sharma, B. P. (2019). Fabrication and characterization of Al_2O_3–TiC-reinforced aluminum matrix composites. Advances in Industrial and Production Engineering. Lecture Notes in Mechanical Engineering. Springer, Singapore. Pp 349–356. Print ISBN: 978-981-13-6411-2, Online ISBN: 978-981-13-6412-9. https://doi.org/10.1007/978-981-13-6412-9_33.
6. Şimşek, M., Aldemir, S. D., & Gümüşderelioğlu, M. (2019). Anticellular PEO coatings on titanium surfaces by sequential electrospinning and crosslinking processes. *Emergent Materials, 2*(2), 169–179.
7. Zouboulis, A. I., & Kydros, K. A. (1993). Use of red mud for toxic metal removal: The case of Nickel. *Journal of Chemical Technology and Biotechnology, 53,* 95–101.
8. Genç-Fuhrman, H., Tjell, J. C., & McConchie, D. (2004). Adsorption of arsenic from water using activated neutralized red mud. *Environmental Science and Technology, 38*(8), 2428–2434.
9. Gupta, V. K., & Sharma, S. (2002). Removal of cadmium and zinc from aqueous solutions using red mud. *Environmental Science and Technology, 36*(16), 3612–3617.
10. Daniel, N. A., Singh, N. K., Vates, U. K., Sharma, B. P., & Subramanian, S. (2019). Optimization of critical parameters of EDD steel in die cavity manufacturing. Advances in Industrial and Production Engineering. Lecture Notes in Mechanical Engineering. Springer, Singapore, pp. 357–363. Print ISBN: 978-981-13-6411-2, Online ISBN: 978-981-13-6412-9. https://doi.org/10.1007/978-981-13-6412-9_34.
11. Singh, M., Upadhayay, S. N., & Prasad, P. M. (1996). Preparation of special cements from red mud. *Waste Management, 16*(8), 665–670.
12. Tsakiridis, P. E., Agatzini-Leonardou, S., & Oustadakis, P. (2004). Red mud addition in the raw meal for the production of Portland cement clinker. *Journal of Hazardous Materials, 116*(1–2), 103–110.
13. Wang, S., Ang, H. M., & Tadé, M. O. (2008). Novel applications of red mud as coagulant, adsorbent and catalyst for environmentally benign processes. *Chemosphere, 72*(11), 1621–1635.

14. Sharma, B. P., Rao, G. S., & Vates, U. K. (2019). Powder metallurgy processing and mechanical characterization of iron-based composite reinforced with Alumina and Zirconium Diboride. Advances in Industrial and Production Engineering. Lecture Notes in Mechanical Engineering. Springer, Singapore, pp. 303–308. Print ISBN: 978-981-13-6411-2, Online ISBN: 978-981-13-6412-9. https://doi.org/10.1007/978-981-13-6412-9_28.

15. Singh, B., Khan, Z. A., Siddiquee, A. N., & Maheshwari, S. (2016). Effect of CaF$_2$, FeMn and NiO additions on impact strength and hardness in submerged arc welding using developed agglomerated fluxes. *Journal of Alloys and Compounds, 667,* 158–169.

16. Dewnangan, R., & Khan, M. (2012). Development of Submerged Arc Welding flux using Red Mud. In: International conference on Agile Manufacturing, IIT(BHU), Varanasi.

17. Puri, D., Tiwari, V., & Prakash, S. (2004). Some observations on the role of charge particle size in Alumino Thermic processing of red mud. *Journal of Indian Industrial Metallurgy*, *57*(2), 195–199.

18. Vates, U. K., Sharma, B. P., Kanu, N. J., Daniel, N. A., Subramanian, S., & Sharma, P. (2020). Optimization of process parameters of galvanizing steel in resistance seam welding using RSM. Proceedings of International Conference in Mechanical and Energy Technology. Smart Innovation, Systems and Technologies, vol 174, pp. 695–706. Springer, Singapore. Print ISBN: 978-981-15-2646-6, Online ISBN: 978-981-15-2647-3, https://doi.org/10.1007/978-981-15-2647-3_65.

19. Simatupang, P. H., Hanafi, R., Purwasasmita, B. S., Imran, I., & Pane, I. (2012). the study of red mud addition influences in metakaolinite-based geopolymer characteristics. *Advanced Materials Research, 450,* 281–285.

20. MohanDas, C. D., Ayyanar, A., Susaiyappan, S., & Kalimuthu, R. (2017). Analysis of the effects of fabrication parameters on the mechanical properties of Areca fine fiber-reinforced phenol formaldehyde composite using Taguchi technique. *Journal of Applied Research and Technology*, *15*(4).

21. Singh, S. (2017). Wear behavior of Al-6063/SiC metal matrix composites reinforced with different particles sizes using taguchi's methodology. *Materials Today: Proceedings, 4*(9), 1.

Chemical Treatment of Reinforced Fibers Used for Bio Composite: A Review

Shubhanshu Mishra and Vijay Chaudhary

Abstract Natural fibers reinforced polymer composites are extensively used to maintain ecological balance due to their bio-degradable nature. Natural fibers have lower weight, high strength, and biodegradable nature. Various chemical treatments are performed on natural fibers before reinforcement in composite to enhance their properties. Surface characteristics of natural fiber are playing the important role to obtained maximum adhesion between natural fiber and polymer matrix. When the natural fiber's surface holds substantial wax content, impurities, and other oily content, then it will have a poor level of adhesion with the matrix. Due to lacking of dryness and roughness of natural fibers, it losses the adhesion forces. While the natural fiber's surface is clean, non-oily, dry, and rough surface, it will positively have better adhesion property with the polymer matrix. Tensile properties of fiber improve due to brittle and ductile behaviors of fibers and reinforcements of natural fibers. Various chemical treatments are alkali treatment, silane treatment, acetylation, benzoylation, acylation, maleated coupling agents, isocyanates, permanganate, sodium bicarbonate treatment, sodium chlorite treatment, enzyme peroxide treatment, ozone treatment, etc. This paper discussed in depth knowledge on chemical treatment of natural fibers and the effect of chemical treatment on properties of developed natural fiber-reinforced polymer composites.

Keywords Fiber-reinforced composites · Natural fiber · Epoxy matrix · Chemical modifications · Surface treatments

S. Mishra (✉) · V. Chaudhary
Department of Mechanical Engineering, Amity University Uttar Pradesh, Noida 201313, India
e-mail: sbmishra1997@gmail.com

V. Chaudhary
e-mail: vijaychaudhary111@gmail.com

1   Introduction

Life cycles largely depend on the environment. The environment is faced with many issues of pollution such as plastic wastage and large consumption of synthetic plastic. Some environmental problems are solved when synthetic plastics are replaced by biodegradable plastics [1]. Synthetic fibers (glass, carbon, and aramid) have many issues that have an impact on environmental pollution in the form of synthetic wastages [2]. Biodegradable plastics are decomposed without any damaging effect on the environment as they are transformed into water and carbon dioxide. Biodegradable composites are a combination of natural fibers and biodegradable polymer matrix [1]. Biodegradable fibers are extracted by plant fibers, animal fibers, and mineral fibers. Source of plant fibers are grass (bamboo, rice), leaf (banana, apple), wood (softwood, hardwood), stems or bast (jute, nettle, flax), seed or fruits (cotton, coir, coconut). Some of the animal fibers are classified in silk, wool, and feathers. Some types of mineral or vegetable fibers are asbestos, basalt, and mineral wool. Biodegradable composites have potential applications in various industries such as automotive, medical, construction, and textile products [3–6]. Bio-degradable composites were fabricated by reinforced fibers and polymer matrix. Reinforced fibers provide the strengthening to the structure of composite and polymer matrix surrounds the reinforced fibers [7]. Sometimes developed bio-degradable has less strength, less interfacial fiber matrix adhesion, and low surface properties of natural fiber. To enhance the surface properties of natural fiber, chemical treatment of bio-degradable fibers are performed. Chemical treatment improves the properties of biodegradable fibers, which is comparable with synthetic fibers in terms of strength, thermal stability, tribological performance, damping capability, etc. [1–8] Some important chemical treatments that have been able to improve the properties of natural fibers are alkali treatment, silane treatment, acetylation, benzoylation, acylation, maleated coupling agents, isocyanates, permanganate, sodium bicarbonate treatment, sodium chlorite treatment, enzyme peroxide treatment, ozone treatment, etc.

Various authors carried out their research on chemical treatment of natural fibers and the effect of chemical treatment on the properties of developed bio-composites.

Chaitanya and Singh [6] developed sisal fiber-reinforced PLA composite. They treated fibers with sodium bicarbonate treatments. The authors concluded that developed composites showed maximum strengths in the terms of tensile strength, flexural strength, compression strength and tensile modulus, and flexural modulus after 72 h of treatment. Hossain et al. [7] developed alkali and chromium sulfate treatment of ladies finger plants fiber. Authors found that modulus of elasticity is increased, and with increases span lengths, tensile strength decreases in treated and untreated fibers. Thermal stability is similar in treated and untreated fibers. Hossain et al. [8] manufactured pine epoxy composites. The author concluded that treated and untreated composites have similar biodegradation properties, and after buried in soil, composites are reduced in thermal stability, tensile strength, and elastic modulus. Goud and Rao [9] fabricated composite with roystonea regia fiber and epoxy matrix. They

performed alkali and silane treatment of fibers. The author concluded that interfacial bonding between fibers and matrix enhanced after chemical treatments which improve the overall strength of the developed composites. Zahari et al. [10] manufactured ijuk fiber and polypropylene matrix reinforced composites. Fibers were treated with vinyltrimethoxy silane treatment. The author concluded that after silane treatment, tensile strength slightly increases with an increase in the weight percentage of fibers.

In this paper, a dense review of chemical treatments is discussed. Chemical treatment of fibers influences the properties of composites discussed by many researchers as given in Table 1. Table 2 shows the difference between properties and advantages between natural fibers and synthetic fibers.

2 Chemical Treatment of Natural Fibers

2.1 Sodium Bicarbonate Treatment

Sodium bicarbonate treatment enhances the properties and reduces the impurity of fibers. In this treatment, fibers were dipped into a mixture of $NaHCO_3$ and water [6]. During the treatment period, the fiber dipped mixture was stirred at 1 h regular intervals. The fibers were removed from the mixture at time intervals of 24, 72, 120, and 168 h. Dipped fibers are washed under running distilled water to get without sodium ions. After washing, treated fibers were dried by an air oven at 100 °C temperature for 8 h. and afterward cooled and stored before to processing. $NaHCO_3$ breaks down into hydroxide ions and carbonic acid in the presence of water. $NaHCO_3$ mixture took a longer time to react and achieve the desired results. After treatment, moisture susceptibility of the sisal fibers is continuously decreased with increasing treatment time. And thermal stability of fibers is enhanced with an increase in treatment time. Various authors carried out sodium bicarbonate treatment of natural fibers in their research. Fiore et al. [22] performed the sodium bicarbonate treatment of unidirectional fiber. The author concluded that tensile strength increases by 20% and modulus is improved 45% compared to untreated fibers. Raharjo et al. [23] performed the sodium bicarbonate treatment on zalacca fibers, which were treated with 10% $NaHCO_3$ solution for 24, 120, and 240 h. The morphological examination of the fiber surface is examined by SEM. The author concluded that the highest tensile strength and elastic modulus is at 120 h treated period. The treated surface shows a cleaner and rougher surface on fibers.

Table 1 Various types of chemical treatments of natural fibers

Sl. no.	Fibers	Matrix	Treatments	Results
1	Sisal fibers,	Poly-lactic acid (PLA)	Sodium bicarbonate	Higher tensile, flexural and compressive strengths and increases tensile, flexural modulus at 72 h treated fibers, but impact modulus is higher at 24 h treated fibers [6]
2	Ladies finger		Alkali, chromium sulfate, and combination of chromium sulfate and sodium bicarbonate	Young modulus increased, tensile strengths decreased, surface roughness increased [7]
3	Pine fiber	poly (hydroxybutyrate-co-hydroxyvalerate)	Alkaline treatments	Decomposition process is same as untreated fiber [8]
4	Roystonea regia	Epoxy	Alkaline and silane treatment	Tensile strengths are increased in silane treatments and higher impact strength in untreated fibers [9]
5	Ijuk fiber	Polypropylene matrix	Vinyltrimethoxy silane treatments	Tensile strength slightly increases with fiber weight ratio and decreasing the percentage of water absorption [10]
6	Sisal fiber		Silane treatment	The peaks at 1742 and 1249 cm − 1 seen in the untreated sisal fibers disappear after alkaline treatment, sisal fibers easily released hemicellulose and lignin components by NaOH treatment [11]

(continued)

Table 1 (continued)

Sl. no.	Fibers	Matrix	Treatments	Results
7	Pineapple leaf and kenaf fibers		Silane, alkali, and combined silane and alkali treatments	Treated KF and PLAF with NaOH show a very clean and smooth surface. It shows a very good effect of 6% concentration NaOH on KF. Tensile strengths and modulus both are increased in both cases [12]
8	Hemp, sisal, jute, and kapok		Caustic soda for alkalization, acetylene	NaOH concentration has reduced thermal resistance. Due to the exposure of the hydroxyl groups, enhance and facilitate mechanical interlocking and the bonding reaction [13]
9	Jute fiber	Phenolic resin matrix	(Methanol-soluble), CNSL-PF (5%) (water-soluble)	Higher tensile strength and flexural strength. Thickness swelling are also increased with time [14]
10	Waste jute fiber	–	Ozone treatment	Fiber tensile properties decreases continuously as a function of treatment time. Afterward ozone treatment crystallinity were changed. After certain time period, serval fibers loss the properties. It is green alternates of oxidation of cellulose [15]
11	Abaca fiber		Alkali treatment	NaOH (alkali) removes the hydroxyl ions (OH–) from the cell wall and increase the surface roughness [16]

(continued)

Table 1 (continued)

Sl. no.	Fibers	Matrix	Treatments	Results
12	Sisal fiber	Epoxy	Sodium bicarbonate	After 120 h of treatment, sisal fiber achieves the highest interfacial adhesion and mechanical properties with epoxy matrix [17]
13	Natural date palm fiber	Natural date palm fiber		Enhanced the properties such as thermal stability, hardness, tensile strength, tensile modulus, and morphology of the composites. The composites had good resistance to acids and alkalies [19]
14	Banana fiber	Polyester	Silane, NAOH	Chemical modification improves the storage modulus of banana-fiber-reinforced polyester composites. NaOH has resulted in the maximum increase of modulus values. The loss modulus curves are found to be flattened by the incorporation of fibers [20]

Table 2 Difference between natural fibers and synthetic fibers

Fibers	Advantages	Disadvantages
Natural fibers	Biodegradable, low density, low cost	Inhomogeneous quality, dimensional variability
Synthetic fibers	Wetness resistance good mechanical properties	Problematic in recycling, relatively higher cost

2.2 Alkali Treatments

In alkali treatment, bio-degradable fibers are treated with NaOH solution at 70°C. NaOH breaks the ester linkages of polyester. After alkali treatment, it enhanced the wetting and surface roughness property. It removed the alkali hydrophilic hemicellulose. Alkali treatment has advantage low cost, relieve, and not affected to decomposition. Mukhtar et al. [24] performed alkali treatment on sugar palm fiber (SPF) with 4% NaOH concentration and deep 250 g fibers in the 5 L aqueous solution for 1 h. The author concluded that tensile strength of treated fibers increases by 12.6% when compared with the untreated fibers. XRD shows the higher crystallinity index of the treated fibers. Oushabi et al. [25] performed the treatment on developed composites of date palm fibers polyurethane matrix. The author found experimental results that non-cellulosic materials are easily removed after treatments and enhance tensile strengths of DPFs and also find that the adhesive force is increased. Obi Reddy et al. [26] performed alkali treatments on borassus fibers, which extracted from borassus fruit. The author concluded that after 8 h of alkali treatment, the tensile properties such as strength, modulus, and % elongation of the fibers enhanced by 41, 69, and 40%, respectively. Fibrils could be clearly observed and an increase in surface roughness on the fiber surface. Due to alkali treatment for a longer period, during the dissolution of hemicelluloses and increasing the interfibrillar region of natural fibers. Consequently, adhesion force increases between the fiber–matrix interface in composites and also improves the aspect ratio which widely depends on the fiber diameter. The reduction of fiber's diameter increases the aspect ratio.

2.3 Acetylation

In this treatment, fibers are treated in four stages. In the first stage, fibers were treated in glacial acetic acid for 1 h at 20 °C. Afterward, it is treated with acetic anhydride having concentrated H_2SO_4 as a catalyst for 5 min. Then, fibers were washed with distilled water and dried. In the second stage, fibers were treated in acetic anhydride without an acid catalyst for 1 h at 20 °C and washed with distilled water and dried. In the last stage, fibers were treated in acetic anhydride without acid catalyst in a water soak measured at 70 °C for 1 h and 3 h, respectively. Then, fibers were washed with distilled water and dried before prior used [13]. The surface

topography of the fibers and their crystallographic structure are changed due to alkalization. Various authors carried out their work on acetylation. U Zaman et al. [27] performed acetylation treatment on banana empty fruit bunch fiber/polypropylene (PP) composites. The author concluded that composite showed higher interfacial shear strength and mechanical properties as compared to the untreated composites. The tensile strength could be increased due to the reduction of lignin and extractible, insignificant increase in cellulose content, and a partial portion of hemicellulose converting to acetylated hemicellulose. Acetylation removed waxy material from the surface of fibers and reduce polarity by covering hydroxyl groups. Tserki et al. [28] performed acetylation and propionylation treatments on flax, hemp, and wood fibers. The author concluded that hydrophilicity of the materials decreased by esterification with moisture absorption reduction increases of the amorphous portion, and fiber crystallinity was slightly decreased, due to the esterification reaction.

2.4   Ozone Treatments

Ozone treatment is eco-friendly and an alternative technique for the oxidation of natural fibers. During the ozone treatment process, the atmospheric air converted into oxygen through an oxygen concentrator and oxygen also converted into ozone gases through an ozone generator. To find a humid ozonized ecosystem, ozone reacts with water through a humidification system. Natural fibers are located in a humid ozonized ecosystem for changeable periods. The ozone analyzer examined the mass flow rate in mg/l with the help of outlet gases. Afterward, ozone gases are destroyed in oxygen via ozone destroyer [15]. After a certain period, fibers lose physical and chemical properties. Ozone treatments reduce lignin. It resolves the hemicellulose fraction and enhances the degree of crystallinity and size of crystallites. Cheng and Zhao [29] performed ozone treatment on natural rubber/short carbon fibers. The author concluded that ozone treatment having the number of oxygen-containing groups. SEM micrographs showed that after ozone modification, interfacial adhesion was enhanced of tensile fractured composites when the oxidized time was 2.5 h. During the preparation process of fibers by oil for enhancing carbon fiber strength and deterring fiber broken of incorporated, the chemical composition of fiber surface is especially oxygen, carbon, and a trace of silicon. It could be readily notable that the oxygen content and O/C ratio of carbon fiber surface increase upon subjection to ozone, while the carbon content has the reverse trend. The generation of oxygen which contains functional groups on the fiber surfaces improve the oxygen content and O/C ratio of carbon fibers [30]. Osman [31] performed ozone treatments on wool and silk fibers. The author concluded that wool and silk fiber's whiteness parameters decrease and yellowness parameters increase after ozone treatments. Wetting time of fibers reduced, and tensile strength and E-modulus increased in both fibers while % elongation decreased.

2.5 Silane Treatments

Silane treatments enhanced the degree of cross-linking in the interface region as well as rises the fiber surface area and improves bonding strengths between the fiber and matrix [20]. The fibers are dipping in a weak mixture of a silane diluted in a water/alcohol or water/ketone mixture. Silane breaks down into silane and alcohol in presence of water, and reacts with the OH groups of the cellulose in natural fibers. These are formed stable covalent bonds to the cell walls which are chemisorbed onto the fiber surface. In this treatments fibers dipped into 2% aminosilane in 95% -alcohol for 5 min at a pH value of 4.5–5.5 afterward fibers dried 30 min with air drying for hydrolyzing the coupling agent [21]. Water and ethanol mixture with a concentration of 0.033% and 1% was also carried for silane solutions. It improves thermal stability. Zhou et al. [11] performed silane treatment on sisal fibers. The author concluded that after chemical treatments, sisal fibers change the thermal degradation, surface topography, and surface chemical structure. Naveen et al. [32] performed silane treatments on sisal treatments. The author concluded that due to the silane treatment, the hydrological group, hemicellulose, impurities, and amount of lignin are removed and improved a better adhesion between fiber and matrix. The load-carrying properties of treated natural fibers increase. In the micrographs, it clearly shown the difference between raw fibers and treated fibers. The treated fiber surface is very rough surface comparatively with untreated fibers. Izod strength is achieved good impact after silane treatments compared to other mechanical strengths.

3 Conclusion

Therefore, chemical treatments improve many characteristic factor given below:

- Natural fibers are treated with various chemical treatments (alkaline, silane, ozone, acetylation, and sodium bicarbonate).
- Chemical treatment improves the surface properties of natural fibers.
- Treated natural fibers provide good mechanical properties such as tensile strengths, flexural strengths, impact strengths, and thermal stability of composites.
- Chemical treatments increase wettability of fibers with polymer matrix as well as increase the surface roughness, which supports to improve adhesion force between reinforced fibers and polymer matrix.
- Chemical treatments are not affected in decomposing process and similar behaviors found in treated and untreated fibers. Treated natural fiber composites follow eco-friendly behavior.

References

1. Bajpai, P. K., Singh, I., & Madaan, J. (2014). Development and characterization of PLA-based green composites: A review. *Journal of Thermoplastic Composite Materials, 27*(1), 52–81. https://doi.org/10.1177/0892705712439571.
2. Chaudhary, V., Rajput, A. K., & Bajpai, P. K. (2017). Effect of particulate filler on mechanical properties of polyester based composites. *Materials Today: Proceedings.*
3. Chaudhary, V., Bajpai, P. K., & Maheshwari, S. (2020). Effect of moisture absorption on the mechanical performance of natural fiber reinforced woven hybrid bio-composites. *Journal of Natural Fibers.*
4. Chaudhary, V., Bajpai, P. K., & Maheshwari, S. (2017). Studies on mechanical and morphological characterization of developed jute/hemp/flax reinforced hybrid composites for structural applications. *Journal of Natural Fibers.* https://doi.org/10.1080/15440478.2017.1320260.
5. Chaudhary, V., Bajpai, P. K., & Maheshwari, S. (2018). An investigation on wear and dynamic mechanical behavior of jute/hemp/flax reinforced composites and its hybrids for tribological applications. *Fibers and Polymers, 19*(2), 403–415. https://doi.org/10.1007/s12221-018-7759-6.
6. Chaitanya, S., & Singh, I. (2017). Sisal fiber-reinforced green composites: Effect of Ecofriendly fiber treatment. *Society of Plastics Engineers POLYMER COMPOSITES—2017.* https://doi.org/10.1002/pc.24511.
7. Hossain, S. I., Hasan, M., Hasan, Md. N., & Hassan, A. (2013). Effect of chemical treatment on physical, mechanical and thermal properties of ladies finger natural fiber. *Advances in Materials Science and Engineering*, Vol. 2013, Article ID 824274, 6 p. http://dx.doi.org/10.1155/2013/824274.
8. Beltrami, L. V. R., Bandeira, J. A. V., Scienza, L. C., & Zattera, A. J. (2014). Biodegradable composites: morphological, chemical, thermal, and mechanical properties of composites of poly(hydroxybutyrate-cohydroxyvalerate) with curaua fibers after exposure to simulated soil. *Journal of Applied Polymer Science.* https://doi.org/10.1002/app.40712.
9. Goud, G., & Rao, R. N. (2013). Combined effect of alkali and silane treatments on tensile and impact properties of roystonea regia natural fiber reinforced epoxy composites. *Applied Polymer Composites*, *1*(3),
10. Zahari, W. Z. W., Badri, R. N. R. L., Ardyananta, H., Kurniawan, D., & Nor, F. M. (2015). Mechanical properties and water absorption behavior of polypropylene / ijuk fiber composite by using silane treatment. *Procedia Manufacturing*, *2*, 573–578. https://doi.org/10.1016/j.promfg.2015.07.099.
11. Zhou, F., Cheng, G., & Jiang, B. (2014). Effect of silane treatment on microstructure of sisal fibers. *Applied Surface Science, 292,* 806–812.
12. Asim, M., Jawaid, M., Abdan, K., & Ishak, M. R. (2016). Effect of alkali and silane treatments on mechanical and fibre-matrix bond strength of Kenaf and pineapple leaf fibres. *Journal of Bionic Engineering*, *13*, 426–435.
13. Mwaikambo, L. Y., & Ansell, M. P. (1999). The effect of chemical treatment on the properties of hemp, sisal, jute and kapok for composite reinforcement. Die Angewandte Makromolekulare Chemie 272, 108–116 (Nr. 4753).
14. Mitra, B. C., Basak, R. K., & Sarkar, M. (1998). Studies on jute-reinforced composites, its limitations, and some solutions through chemical modifications of fibers. *Journal of Applied Polymer Science, 67,* 1093–1100.
15. Maqsood, H. S., Bashir, U., & Wiener, J., Puchalski, M., Sztajnowski, S., & Militky, J. (2017). Ozone treatment of jute fibers. Springer Science + Business Media Dordrecht Cellulose, *24*:1543–1553. https://doi.org/10.1007/s10570-016-1164-y.
16. Sinha, A. K., Narang, H. K., & Bhattacharya, S. (2017). Effect of alkali treatment on surface morphology of abaca fibre. *Materials Today: Proceedings*, *4*, 8993–8996.
17. Fiore1, V., Scalici, T., Nicoletti, F., Vitale, G., Prestipino, M., & Valenza, A. (2015). A new eco-friendly chemical treatment of natural fibres effect of sodium bicarbonate on properties of

sisal fibre and its epoxy composites. *Composites Part B* (2015). https://doi.org/10.1016/j.compositesb.2015.09.028.

18. Alsaeed, T., Yousif, B. F., & Ku, H. (2013). The potential of using date palm fibres as reinforcement for polymeric composites. *Materials and Design Materials and Design, 43,* 177–184. https://doi.org/10.1016/j.matdes.2012.06.061.

19. Noorunnisa Khanam, P., Al Maadeed, M. A. (2014). Improvement of ternary recycled polymer blend reinforced with date palm fibre. *Materials and Design Materials and Design, 60*, 532–539. http://dx.doi.org/10.1016/j.matdes.2014.04.033.

20. Pothan, L. A., Thomas, S., & Groeninckx, G. (2006). The role of fibre/matrix interactions on the dynamic mechanical properties of chemically modified banana fibre/polyester composites. *Applied Science and Manufacturing Composites: Part A*, *37*, 1260–1269. https://doi.org/10.1016/j.compositesa.2005.09.001.

21. Asumani, O. M. L., Reid, R. G., & Paskaramoorthy, R. (2012). The effects of alkali–silane treatment on the tensile and flexural properties of short fibre non-woven kenaf reinforced polypropylene composites. *Composites: Part A, 43*, 1431–1440. http://dx.doi.org/10.1016/j.compositesa.2012.04.007.

22. Fiore, V., Scalici, T., & Valenza, A., Effect of sodium bicarbonate treatment on mechanical properties of flax-reinforced epoxy composite materials. *Journal of Composite Materials Journal of Composite Materials*, 1–12 https://doi.org/10.1177/0021998317720009.

23. Raharjo, W. P., Soenoko, R., Purnowidodo, A., & Choiron, A. (2019). Characterization of sodium-bicarbonate-treated Zalacca fibers as composite reinforcements. *Evergreen Joint Journal of Novel Carbon Resource Sciences & Green Asia Strategy,6*(1), 29–38, March 2019.

24. Mukhtar, I.,. Leman, I., Zainudin, E. S., & Ridzwan Ishak, M., Effectiveness of alkali and sodium bicarbonate treatments on sugar palm fiber: mechanical, thermal, and chemical investigations. *Journal of Natural Fibers*, https://doi.org/10.1080/15440478.2018.1537872.

25. Oushabi, A., Sair1, S., Oudrhiri Hassani, F., Abboud, Y., Tanane1, O., & El Bouari, A. (2017). The effect of alkali treatment on mechanical, morphological and thermal properties of date palm fibers (DPFs): Study of the interface of DPF-Polyurethane composite. *South African Journal of Chemical Engineering* (2017). https://doi.org/10.1016/j.sajce.2017.04.005.

26. Obi Reddy, K., Uma Maheswari, C., Shukla, M., Song, J. I., & Varada Rajulu, A. (2013). Tensile and structural characterization of alkali treated Borassus fruit fine fibers. *Composites: Part B, 44*, 433–438 http://dx.doi.org/10.1016/j.compositesb.2012.04.075.

27. Zaman, H. U., & Khan, R. A., Acetylation used for natural fiber/polymer composites. *Journal of Thermoplastic Composite Materials*, 1–21. https://doi.org/10.1177/0892705719838000.

28. Tserki, V., Zafeiropoulos, N. E., Simon, F., & Panayiotou, C. (2005). A study of the effect of acetylation and propionylation surface treatments on natural fibers. *Applied science and Manufacturing Composites: Part A*, *36*, 1110–1118. https://doi.org/10.1016/j.compositesa.2005.01.004.

29. Cheng, J., & Zhao, S. (2016). Influence of ozone treatment on microstructure and mechanical properties of pitch-based short carbon fiber-reinforced natural rubber. *Journal of Elastomers & Plastics*, 1–17. https://doi.org/10.1177/0095244316644860.

30. Arséne, M.-A., Bilba, K., & Onésippe, C. (2017). Treatments for viable utilization of vegetable fibers in inorganic-based composites. *Sustainable and Nonconventional Construction Materials using Inorganic Bonded Fiber Composites*. http://dx.doi.org/10.1016/B978-0-08-102001-2.00004-8.

31. Benli, H., & İbrahim Bahtiyari, M. (2017). Combination of dyeing method and ozone after-treatment to apply natural dyes on to cotton fabrics. *Ozone: Science & Engineering*. http://dx.doi.org/10.1080/01919512.2017.1336926.

32. Naveen, E., Venkatachalam, N., Naveenkumaran, G., & Ramkumar, M. (2016). Silane chemical treatment to the surface modification for the natural fiber. *Advances in Natural and Applied Sciences, 10*(3), 224–231.

Parametric Appraisal for EDM of Inconel 825 Superalloy Using Cu and Cu–Ni Electrodes

Soni Kumari, Gobinda Chandra Behera, Santosh Kumar Sahu, Saurav Datta, Goutam Nandi, and Pradip Kumar Pal

Abstract Effects of tool electrode on electro-discharge machining (EDM) performance of '*difficult-to-cut*' aerospace superalloy Inconel 825 is studied in this paper. Electrodes used are copper and copper–nickel alloy (90% Cu and 10% Ni). Experiments are conducted at varied peak discharge current with constant settings of pulse-on/off duration, gap voltage, electrode gap distance, and flushing pressure. EDM performance is evaluated in purview of material removal efficiency, and electrode wear rate. In addition, morphology, and topographical features of the machined surface are carried out. Later includes study of surface roughness, surface crack density, and white layer thickness.

Keywords Electro-discharge machining (EDM) · Superalloy · Inconel 825 · Surface crack · White layer

S. Kumari · G. Nandi · P. K. Pal
Department of Mechanical Engineering, Jadavpur University, Kolkata 700032, India
e-mail: soni.1802@gmail.com

G. Nandi
e-mail: gnandi87@gmail.com

P. K. Pal
e-mail: pradippal54@yahoo.com

G. C. Behera · S. Datta (✉)
Department of Mechanical Engineering, National Institute of Technology, Rourkela 769008, Odisha, India
e-mail: sdattaju@gmail.com

G. C. Behera
e-mail: gobindaabehera@gmail.com

S. K. Sahu
Department of Mechanical Engineering, Veer Surendra Sai University of Technology, VSSUT Burla, Sambalpur 768018, Odisha, India
e-mail: sahunitrkl@gmail.com

1   Research Background

Inconel 825 is a nickel-based superalloy possessing excellent oxidation as well as corrosion resistance. This alloy can retain its strength at elevated temperatures (hot strength). Inconel 825 has wide range of applications which are different fields including aerospace industry, chemical and petrochemical industry, automotive as well as marine industry. This alloy belongs to the category of '*difficult–to-cut*' material due to peculiar characteristics like poor thermal properties (thermal conductivity: 11.1 W/m K), and strong work-hardening tendency [2]. Conventionally used machine tools often face challenges to produce intricate shape with desired surface finish at reasonable speed. When Inconel 825 is machined through conventional routes, due to direct contact between tool and workpiece, abrasive carbide particles of work material often stick at the tool face which promotes rapid tool wear, and deteriorates machined surface finish. Such problems can be overcome by adapting nontraditional machining techniques. EDM is an electro-thermal machining process and does not require tool-work direct contact, and the process is independent of any mechanical disturbance (vibration) [1]. Any electrically conductive material (irrespective of hardness and toughness) can be machined through EDM. Due to these benefits, EDM finds widespread applications like mold and die manufacturing industry, aircraft and aviation industry, and automotive industry [2, 3]. Dikshit et al. [4] reported EDM performance of Ni-based Hastelloy in purview of machined surface integrity. MRR and EWR exhibited nonlinear relationship with respect to pulse duration. Pulse-on duration was influenced machined surface morphology as well as surface metallurgical features. Recast layer and heat-affected zone (HAZ) were affected by the heat treatment process. Feng et al. [5] reported that parametric setting, properties of parent workpiece, and recast layer composition greatly influenced severity of surface cracking as observed on EDMed surface of Inconel 718. Non-homogeneous metallurgical phases, at the interfacial zone, restricted crack propagation beyond recast layer depth toward interior of the bulk material. In another reporting, [6] studied influence of pulse current, duty factor, sensitivity control, gap control, and flushing pressure on material removal efficiency, and surface roughness of EDMed surface of Inconel 718 produced through copper made tubular-shaped electrode. Authors evidenced significant influence of pulse current on sputtered layer thickness and length of crack developed over the machined surface. In the context of EDM of Inconel 718 using copper tool, [7] reported that peak current and pulse-on duration were the most influential parameter for material removal efficiency, tool wear rate, and surface roughness of the EDMed Inconel 718 end product. Kang and Kim [8] studied influence of peak current, duty factor, and pulse-on duration on material removal efficiency, surface roughness, radial overcut, and surface crack density during EDM of Inconel 825. In was concluded that for MRR, surface roughness, and radial overcut, peak current appeared as the most influential parameter. On the contrary, surface crack density was found greatly influenced by pulse-on duration. Authors applied gray relational analysis to obtain optimal parameters setting for desired EDM output. Karthikeyan and Arun [9] studied influence of peak current, pulse-on time, and pulse-off time

on form tolerances of EDMed product made off Inconel 718 and 625 superalloys. Karunakaran et al. [10] studied EDM performance of Inconel 600 in purview of material removal rate, electrode wear, and surface roughness. Authors considered current intensity (supplied by generator), duty cycle, pulse time, and polarity as process variables. It was evidenced that positive polarity led to improved MRR, while lower surface roughness (R_a) was achieved by negative polarity. Khan et al. [11] reported machining behavior of Inconel 718 during Wire EDM and sinking EDM using Cu-SiC tool electrode. It was evidenced that Cu-SiC electrode exhibited better performance for sinking EDM in purview of MRR, electrode wear, and surface roughness. As compared to conventionally used copper electrode, lower electrode wear attributed to Cu-SiC electrode was due to its higher melting temperature as well as fine microstructure. Kumar et al. [12] studied machinability of Inconel 800 during EDM with copper tool electrode. Based on full factorial design of experiment, authors analyzed direct as well as interactive effects of process parameters including peak current, pulse-on time, and pulse-off time on material removal efficiency, extent of electrode wear, and machined work part surface roughness. Kumari et al. [13] determined an optimal setting of EDM parameters toward minimizing surface crack density as well as recast layer thickness of machined Inconel 601 specimens. EDMed surface morphological features were critically analyzed and correlated with elemental analysis, residual stress, and microhardness test results. Li et al. [14] applied Taguchi-based gray relational analysis toward determining an optimal setting of process control parameters for desired MRR as well as surface finish, during EDM of Inconel 718 superalloy. Mohanty et al. [15] studied effects of variation of electrode material (graphite, tungsten, brass, and copper) on EDM performance of Inconel 825 in consideration with varied flushing condition (with and without flushing) of dielectrics. EDM performance was assessed in terms of material removal efficiency and topographical features of the EDMed surface including roughness, crack density, recast layer thickness, and microhardness. Muttamara et al. [16] developed empirical mathematical models representing parametric influence on material removal rate and surface roughness during EDM of Inconel 625. Through analysis of variance (ANOVA), it was concluded that MRR is dominated by peak current followed by pulse-on time. On the contrary, pulse-on time, followed by pulse-off time, greatly influenced machined work part surface roughness. Rahul et al. [17] reported improved performance of high-response frequency magnetic suspension spindle system (MSSS) EDM (as compared to conventional EDM) in purview of increased discharge percentage (~30%), improved MRR (~23%), and lower electrode wear rate (~43%) during micro-hole production on Inconel 718 workpiece. In addition, improved inlet/outlet micro-hole diameters with tiny recast layer were achieved through MSS EDM.

The main input parameters of EDM are: peak discharge current, gap voltage, pulse-on time, and pulse-off time (electrical parameters) [18]. Non-electrical parameters include electrode material, dielectric type, flashing pressure, etc. In general, performance of EDM operation is evaluated in purview of material removal efficiency, tool wear rate, and surface integrity of the machined work part. Selection of

tool electrode plays an important role to achieve sound EDM performance. EDM electrode should possess the following properties: thermal and electrical conductivity, very high melting point, low wear rate, corrosion resistance, and resistance to deformation (form stability/shape retention capability) [19].

Reference [20] studied parametric effects on material removal rate, diameteral overcut, tool wear, and surface roughness during EDM of En-31 tool steel. Authors also studied effects of electrode material (copper, copper tungsten, brass, and aluminum) using varied pulse current at reverse polarity. It was concluded that with increase in pulse current, EDM responses were increased. Copper as well as aluminum electrodes provided the best machining rate. Authors concluded that discharge energy greatly influenced machined surface characteristics. It was evidenced that AgW electrode offered superior surface quality (smooth and defect-free nano-surface) among three electrodes used. On the contrary, CuW electrode caused the highest material removal efficiency followed by AgW. Rajesha et al. [21] reported effects of electrode material on EDM performance of alumina ceramics.

To this end, the present work examines performance of tool electrode (Cu and Cu–Ni) during EDM of Inconel 825 workpiece. EDM performance is evaluated in purview of material removal rate (MRR) and electrode wear rate (EWR). In addition, morphology and topographical measures of EDMed surface including machined work part surface roughness (R_a), surface crack density, and depth of white layer are studied in perspective of varied peak discharge current as well as electrode material.

2 Experimental Details

Experiments are carried out on electrical discharge machine (ED30 ZNC, Excetek Technologies Co. Ltd., Taiwan) on Inconel 825 flat plates (50 × 50 × 5) mm^3. Chemical constituents of Inconel 825 are as follows (wt%): Ni: 38-46; Fe: 22 (min); Cr: 19.5-23.5; Cu: 1.2–3; Mo: 2.5-3.5; Ti: 0.6-1.2; Mn: 1.0 (max); C: 0.05 (max); S: 0.03 (max); Al: 0.2 (max); Si: 0.5 (max). Two different electrodes are used: copper and Cu–Ni alloy (also called cupronickel alloy with 90% Cu and 10% Ni) having diameter of 15 mm. Conventional EDM oil is chosen as dielectric media.

Before experiments, initial masses of workpiece as well as tool electrodes are recorded using digital balance. Workpiece is fitted on work table, and electrode is fitted with tool holder. Experiments are performed at varied peak current (8A, 16A, 24A, 32A, and 40A). Remaining parameters are maintained at constant values. Constant parameter settings are: gap voltage (~230 V), pulse-on time (~1500 μs), pulse-off time (~500 μs), electrode gap distance (~50 μm), and dielectric circulation flushing pressure (~0.5 bar). Each trial experiment is continued up to 0.5 mm machined depth, and subsequent machining time is recorded. After every run, final masses of workpiece, as well as electrode, are measured. By using mass loss criteria, material removal rate and tool wear rate are computed. After machining, worn out electrode (edge) is viewed through optical microscopy. Surface roughness of the

EDMed specimen is measured using surface roughness tester (Talysurf). Morphology and topographic features of EDMed surface are analyzed through scanning electron microscopy.

3   Results and Discussion

For copper as well as Cu–Ni electrode, with increase in peak discharge current, MRR is increased. High discharge current leads to increase in localized temperature due to supply of high spark energy. Such temperature rise results in enormous melting and vaporization of work material, causing high amount of material removal. As compared to copper electrode, cupronickel electrode causes lower MRR due to its lower thermal conductivity. Copper corresponds to thermal conductivity of 401 W/m K. On the contrary, Cu–Ni alloy possesses thermal conductivity value of 40 W/m K. It is also seen that at low discharge current, both the electrodes exhibit approximately similar material removal efficiency, but with increased of peak current, effects of electrode material become prominent; hence, difference in MRR values obtained for two electrodes gets increased.

For copper as well as Cu–Ni electrode both, EWR is increased with respect to increased peak discharge current. However, Cu electrode experiences lower tool wear when compared to Cu–Ni electrode. EWR depends of mass loss of electrode during machining. Greater extent of carbon deposition is attributed to the bottom surface/edge of Cu electrode when compared to Cu–Ni electrode. Migration of carbon is due to decomposition of the dielectric media. Such transfer of carbon atoms onto the electrode surface causes formation of hard carbides while reacting with tool/work material. In case of Cu electrode, higher amount of carbon deposition decreases mass loss of electrode and hence, results in lower EWR value.

For copper and Cu–Ni electrode both, with increase in peak discharge current, EDMed surface finish appears increasingly disappointing; surface roughness value is increased. Higher discharge current results in huge temperature rise and thus, causes more melting as well as vaporization of work material. This further leads to increased crater dimension. Higher energy input leads to increased crater depth which causes higher value of surface roughness. Cupronickel electrode causes higher surface roughness due to its high electrode wear rate.

EDMed surface is produced by using Cu electrode and Cu–Ni electrode, respectively at 24A peak discharge current. In general, crack density is computed on top surface of the EDMed specimen. Initially, specimen area is viewed through scanning electron microscopy, and subsequently, total crack length is computed using *PDF-XChange Viewer* software. Crack density is referred as total crack length divided by the micrograph area. EDMed surface produced by using Cu electrode exhibited lower crack density as compared to the case of Cu–Ni electrode. Since Cu possesses higher thermal conductivity than Cu–Ni, heat energy can easily be transferred through Cu electrode; this further results in uniform deposition of molten material. Uniform deposition of molten material causes evolution of less residual stresses, which reduces
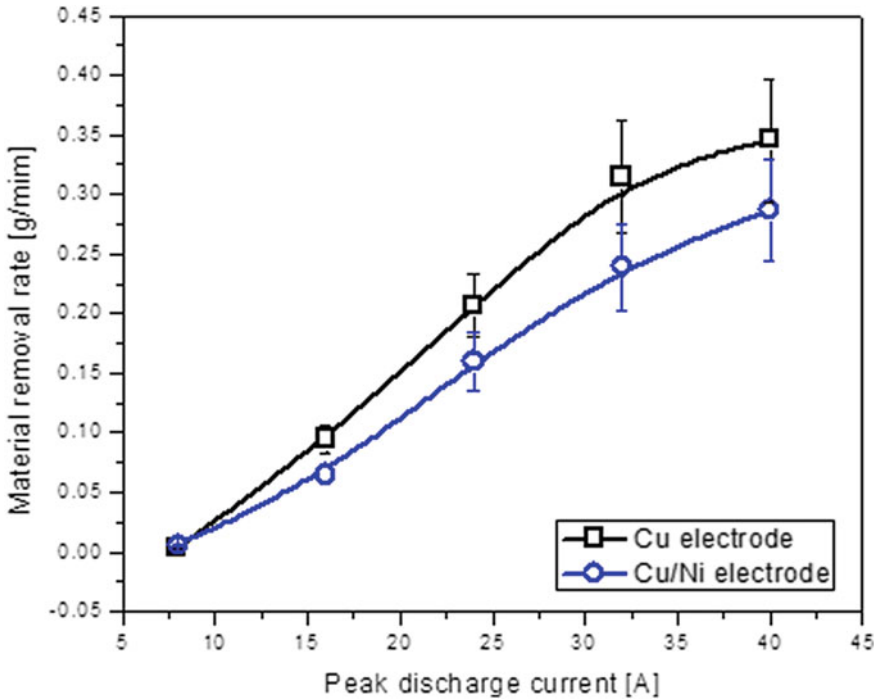
Fig. 1 MRR as a function of peak current

crack density [22]. In case of Cu–Ni electrode, due to its lower thermal conductivity, heat transfer gets restricted to somewhat and results in accumulation of intense heat energy at the machining zone. Subsequently, work surface experiences huge thermal stress which promotes surface cracking [23]. Surface cracking takes place when induced stress exceeds ultimate tensile strength of the work material [24–27]. In addition to surface cracks, EDMed surface exhibits poor surface morphology characterized by pockmarks and globules of debris. Globules of debris are formed due to rapid cooling of expelled molten material with dielectric fluid, or it may be due to insufficient flushing pressure. Pockmarks are formed, while entrapped gases are released from part of molten pool during solidification [28–30].

Figure 6 compares white layer thickness developed over EDMed surface produced by using Cu electrode and Cu–Ni electrode, respectively, at 24A peak discharge current. White layer is also termed as recast layer or re-hardened layer. During pulse-off duration, white layer develops due to re-solidification of molten material over machined surface, which is not flushed away by the dielectric media. As compared to Cu–Ni electrode, thicker white layer is obtained in case of Cu electrode. This is due to higher heat dissipation capacity of Cu electrode. With increase in heat transfer rate, molten material gets cooled uniformly at a faster rate and gets deposited over the machined surface. Deposition of molten material increases thickness of white
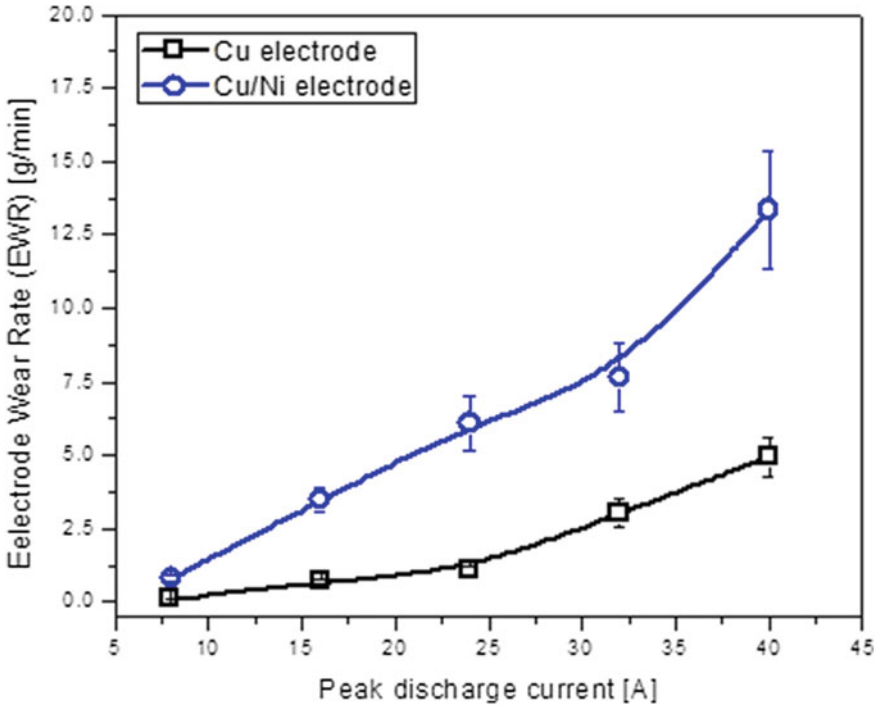
Fig. 2 EWR as a function of peak current
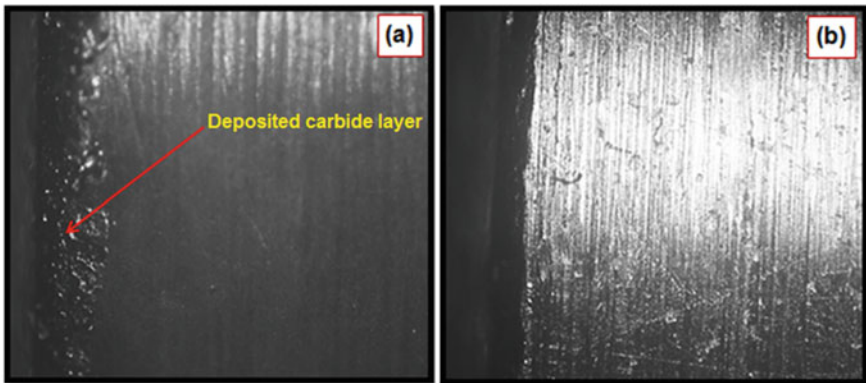
Fig. 3 Carbide layer deposited over electrode's bottom surface: (a) Cu electrode, and (b) Cu-Ni elec-trode
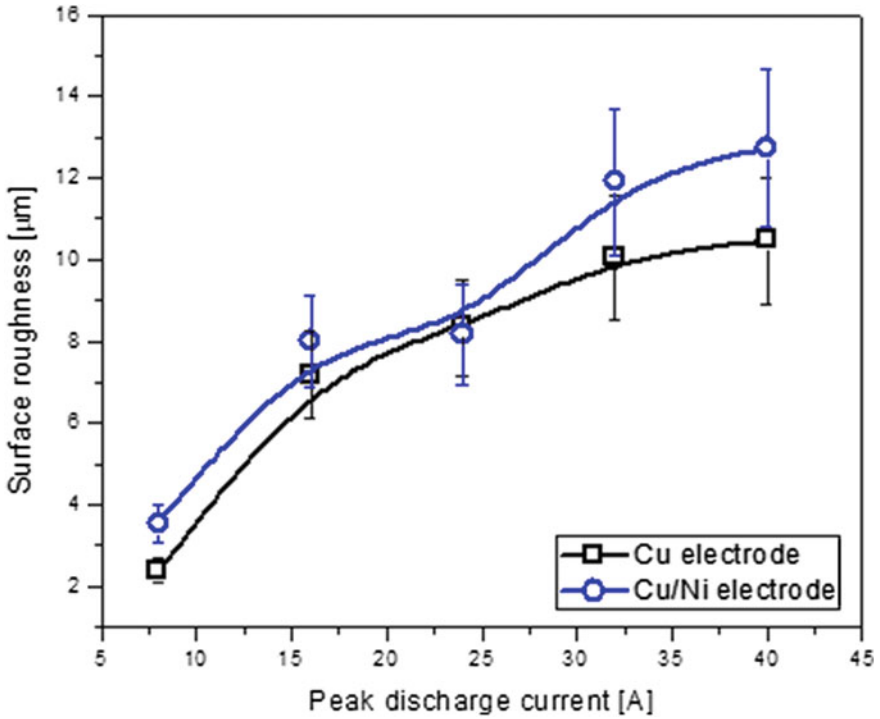
Fig. 4 Machined work part surface roughness (R_a) as a function of peak current
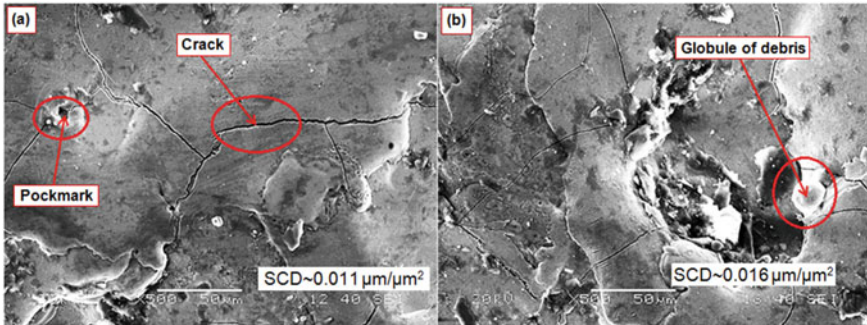
Fig. 5 Crack density as computed for EDMed surface produced by using (a) Cu electrode, and (b) Cu-Ni electrode at 24 A peak current

layer. White layer corresponds to altered metallographic structure when compared with base material. This layer is very hard (carbide-rich) and fine grained. Higher white layer thickness, in case of Cu electrode, may be due to higher material removal rate when compared to Cu–Ni electrode.
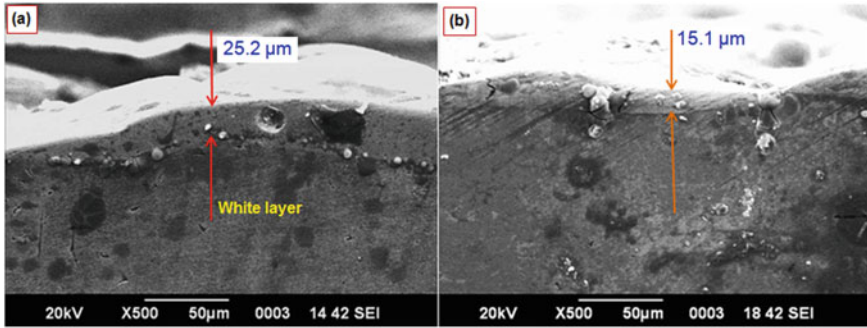
Fig. 6 Thickness of white layer developed over EDMed surface produced by using (a) Cu electrode, and (b) Cu-Ni electrode at 24 A peak current

4 Conclusions

- Cu electrode causes higher MRR than Cu–Ni electrode.
- Higher EWR is experienced in case of Cu–Ni electrode when compared to that of Cu electrode.
- Cu electrode produces better surface finish than Cu–Ni electrode.
- EDMed surface produced by using Cu electrode exhibits thicker white layer than Cu–Ni electrode.
- Severity of surface cracking appears relatively more for the EDMed surface obtained by using Cu–Ni electrode when compared to Cu electrode.

References

1. Abbas, N. M., Solomon, D. G., & Bahari, M. F. (2007). A review on current research trends in electrical discharge machining (EDM). *International Journal of Machine Tools and Manufacture, 47*(7–8), 1214–1228.
2. Ahmad, S., & Lajis, M. A. (2013). Electrical discharge machining (EDM) of Inconel 718 by using copper electrode at higher peak current and pulse duration. *IOP Conference Series: Materials Science and Engineering, 50*(1), 012062.
3. Dhanabalan, S., Sivakumar, K., & Narayanan, C. S. (2014). Analysis of form tolerances in electrical discharge machining process for Inconel 718 and 625. *Materials and Manufacturing Processes, 29*(3), 253–259.
4. Dikshit, M. K., Anand, J., Narayan, D., & Jindal, S. (2019). Machining characteristics and optimization of process parameters in die-sinking EDM of Inconel 625. *Journal of the Brazilian Society of Mechanical Sciences and Engineering, 41,* 302. https://doi.org/10.1007/s40430-019-1809-5.
5. Feng, Y., Guo, Y., Ling, Z., & Zhang, X. (2019). Micro-holes EDM of superalloy Inconel 718 based on a magnetic suspension spindle system. *International Journal of Advanced Manufacturing Technology, 101*(5–8), 2015–2026.
6. Hasçalık, A., & Çaydaş, U. (2007). Electrical discharge machining of titanium alloy (Ti–6Al–4 V). *Applied Surface Science, 253*(22), 9007–9016.

7. Jahan, M. P., Wong, Y. S., & Rahman, M. (2009). A study on the fine-finish die-sinking micro EDM of tungsten carbide using different electrode materials. *Journal of Materials Processing Technology, 209*(8), 3956–3967.

8. Kang, S. H., & Kim, D. E. (2003). Investigation of EDM characteristics of nickel-based heat resistant alloy. *KSME International Journal, 17*(10), 1475–1484.

9. Karthikeyan, P., & Arun, J. (2014). Machining characteristics analysis on EDM for Inconel 718 material using copper electrode. *International Journal of Research in Engineering and Technology, 3*(11), 309–311.

10. Karunakaran, K., & Chandrasekaran, M. (2017). Machineability study on die sinking EDM of Inconel 800 with electrolyte copper electrode. *ARPN Journal of Engineering and Applied Sciences, 12*(8), 2407–2411.

11. Khan, M. A. R., Rahman, M. M., & Kadirgama, K. (2015). An experimental investigation on surface finish in die-sinking EDM of Ti-5Al-2.5 Sn. *The International Journal of Advanced Manufacturing Technology, 77*(9–12), 1727–1740.

12. Kumar, A., Kumar, V., & Kumar, J. (2016). Surface crack density and recast layer thickness analysis in WEDM process through response surface methodology. *Machining Science and Technology, 20*(2), 201–230.

13. Kumari, S., Datta, S., Masanta, M., Nandi, G., & Pal, P. K. (2018). Electro-discharge machining of Inconel 825 super alloy: Effects of tool material and dielectric flushing. *Silicon, 10*(5), 2079–2099.

14. Li, L., Li, Z. Y., Wei, X. T., & Cheng, X. (2015). Machining characteristics of Inconel 718 by sinking-EDM and wire-EDM. *Materials and Manufacturing Processes, 30*(8), 968–973.

15. Mohanty, A., Talla, G., & Gangopadhyay, S. (2014). Experimental investigation and analysis of EDM characteristics of Inconel 825. *Materials and Manufacturing Processes, 29*(5), 540–549.

16. Muttamara, A., Fukuzawa, Y., Mohri, N., & Tani, T. (2009). Effect of electrode material on electrical discharge machining of alumina. *Journal of Materials Processing Technology, 209*(5), 2545–2552.

17. Rahul, Datta, S., Biswal, B. B., & Mahapatra, S. S. (2017). Electrical discharge machining of Inconel 825 using cryogenically treated copper electrode: Emphasis on surface integrity and metallurgical characteristics. *Journal of Manufacturing Processes, 26*, 188–202.

18. Jamwal, A., Aggarwal, A., Gautam, N., & Devarapalli, A. (2018). Electro-discharge machining: Recent developments and trends. *International Research Journal of Engineering and Technology, 5,* 433–448.

19. Kakkar, K., Rawat, N., Jamwal, A., & Aggarwal, A. (2018). Optimization of surface roughness, material removal rate and tool wear rate in EDM using taguchi method. *International Journal of Advance Research, Ideas and Innovations in Technology, 4*(2), 16–24.

20. Rajesha, S., Sharma, A. K., & Kumar, P. (2010). Some aspects of surface integrity study of electro discharge machined Inconel 718. In: S. Hinduja, L. Li (Eds.) *Proceedings of the 36th International MATADOR Conference*, Springer, London (2010).

21. Rajesha, S., Sharma, A. K., & Kumar, P. (2012). On electro discharge machining of Inconel 718 with hollow tool. *Journal of Materials Engineering and Performance, 21*(6), 882–891.

22. Singh, S., Maheshwari, S., & Pandey, P. C. (2004). Some investigations into the electric discharge machining of hardened tool steel using different electrode materials. *Journal of Materials Processing Technology, 149*(1–3), 272–277.

23. Torres, A., Luis, C. J., & Puertas, I. (2015). Analysis of the influence of EDM parameters on surface finish, material removal rate, and electrode wear of an INCONEL 600 alloy. *International Journal of Advanced Manufacturing Technology, 80*(1–4), 123–140.

24. Upadhyay, C., Datta, S., Masanta, M., & Mahapatra, S. S. (2017). An experimental investigation emphasizing surface characteristics of electro-discharge-machined Inconel 601. *Journal of the Brazilian Society of Mechanical Sciences and Engineering, 39*(8), 3051–3066.

25. Yang, C. B., Lin, C. G., Chiang, H. L., & Chen, C. C. (2017). Single and multiobjective optimization of Inconel 718 nickel-based superalloy in the wire electrical discharge machining. *International Journal of Advanced Manufacturing Technology, 93*(9–12), 3075–3084.

26. Şimşek, M., Aldemir, S. D., & Gümüşderelioğlu, M. (2019). Anticellular PEO coatings on titanium surfaces by sequential electrospinning and crosslinking processes. *Emergent Materials, 2*(2), 169–179.

27. Mandal, S., Das, V. V., Debata, M., Panigrahi, A., Sengupta, P., Rajendran, A., et al. (2019). Study of pore morphology, microstructure, and cell adhesion behaviour in porous Ti-6Al-4 V scaffolds. *Emergent Materials, 2*(4), 453–462.

28. Ding, X., Ahmed, S., Bao, N., Ding, J., Liu, R., & Yi, J. (2019). Clustering-induced high magnetization in Co-doped TiO_2. *Emergent Materials, 2*(3), 295–301.

29. Cooke, K. O., & Khan, T. I. (2018). Effect of thermal processing on the tribology of nanocrystalline Ni/TiO_2 coatings. *Emergent Materials, 1*(3–4), 165–173.

30. Fayyad, E. M., Abdullah, A. M., Hassan, M. K., Mohamed, A. M., Jarjoura, G., & Farhat, Z. (2018). Recent advances in electroless-plated Ni-P and its composites for erosion and corrosion applications: A review. *Emergent Materials, 1*(1–2), 3–24.

Aerodynamically Generated Noise Investigation Using Hybrid Approach

Sunil V. Hangargekar and S. Ravikumar

Abstract This work reports to study and analyze the noise generated by turbulent flow though duct by numerical simulation. Experimental work is already done in the previous publications. This paper majorly focused on correct methodology development in Actran solver to correlate the simulation and experimental results. Numerical simulations are done considering the compressible Navier–Stokes code and Lighthills analogy. First, computational fluid dynamics simulations are done using Navier–Stokes equations and exported the fluctuating components of velocity to acoustic solver for calculation of noise source generation and propagation using Lighthills analogy. This approach is called as hybrid approach. Numerical results compared with experimental work are already done in the previous publication. This work also shows new hybrid approach presented in detail to study any aeroacoustics problems early in the design phase of products.

Keywords Aeroacoustics · Turbulence · Aerodynamics · Broadband noise · Lighthills analogy

1 Introduction

1.1 Aeroacoustics Theory

Aeroacoustics is the branch of acoustics which deals with noise generation by turbulent flows also called as aerodynamically generated noise.

Over the last several years, duct noise is the serious problem. The past several year's works are going on to reduce the duct outlet flow noise level which is coming from the HVAC duct. Noise generation mechanism here has three possibilities,

S. V. Hangargekar (✉) · S. Ravikumar
Amrita School of Engineering, Department of Mechanical Engineering, Amrita Vishwa
Vidyapeetham-Coimbatore, Coimbatore, India
e-mail: hangargesunil30@gmail.com

S. Ravikumar
e-mail: s_ravikumar_cb@amrita.edu

Fig. 1 A typical HVAC duct system
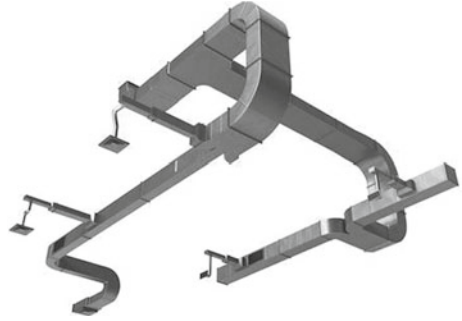
(a) Noise generated at the inlet of the duct because of fan rotation;
(b) Several bends and obstacles in the duct;
(c) Duct vent outlet.

Flow generated noise is more dominant in the duct. Flow is started from the duct inlet and travels across through several bends, obstacles and the outlet of the duct. Major sources of noise are nearby the bends and obstacles. A typical duct system is shown (see Fig. 1).

Early in 1952 Lighthill [1] reported the phenomena of sound generated by aerodynamically. Curle et al. [2] studied the wave propagation equation which he considered solid boundary effects. Ffowcs Williams and Hawking's [3] considered solid boundaries and convection effect. Ribner et al. [4] proposed aerodynamic source terms which are proportional to the first derivative of pressure fluctuations. Stephane Caro et al. [5] studied and investigated experimentally duct noise with DES as a flow turbulence model and Lighthills analogy as a hybrid approach for aeroacoustics model.

The main objective of this paper is to develop the correct methodology in Actran to correlate the results with experimental results. Experimental setup is shown in this paper, and more detail can be found in Ref. [5].

2   Mathematical Modelling

2.1   *Lighthills Analogy and Hybrid Technique*

The hybrid technique is the implementation of Lighthills analogy in finite element method approach (FEM). The equation which governs the sound propagation in fluid medium which is combination of mass and momentum conservation equations of fluid dynamics is called a wave equation which contains Right-side terms as noise sources coming from flow, and left-side terms contain sound propagation is given by,

$$\frac{\partial^2 p}{\partial t^2} - c^2 \frac{\partial^2 p}{\partial x^2} = \frac{\partial^2 T_{ij}}{\partial x_i \partial x_j} \tag{1}$$

where p is the acoustic pressure, c is the speed of sound and T_{ij} is the Lighthills stress tensor which is given by,

$$T_{ij} = \rho u_i u_j + (p - c^2 \rho) \delta_{ij} - \tau_{ij} \tag{2}$$

where the mean density of air is ρ, u is the fluid velocity vector, δ_{ij} is the delta function, τ_{ij} is the viscous stress tensor. For the low Mach number flows, Eq. 2 reduces to, $T_{ij} = \rho u_i u_j$.

The variational formulation of Lighthills analogy in the frequency domain is given as follows:

$$\int \left(-k^2 \omega \delta p + \frac{\partial \omega}{\partial x_i} \frac{\partial \delta p}{\partial x_i} + \frac{1}{c^2} \frac{\partial T_{ij}}{\partial x_j} \frac{\partial \delta p}{\partial x_i} \right) d\Omega = 0 \forall \delta p \tag{3}$$

where Ω is the computational volume, δp is the test function used in the finite elements, ω is the angular frequency and k is the wave number which is defined as,

$$k = \frac{\omega}{c}$$

Details can be found in Actran manual Caro et al. Source term T_{ij} is represented as the divergence of Lighthills tensor in the frequency domain; this quantity is computed using pressure, density and velocity fields by FLUENT. This quantity is first computed in the time domain, and then, Fourier transform will be used for the needful field for the aeroacoustics simulations in ACTRAN.

2.2 Mapping of Source on Acoustics Nodes

Source mapping is necessary because sources calculated in CFD domain should be mapped on the acoustic domain. The calculated values of divergence of Lighthills tensor are then integrated on the right-hand side of variational formulation and are given by,

$$RHS_\alpha^0 = \int N_\alpha \left(\frac{\partial^2 \rho u_i u_j}{\partial x_i \partial x_j} \right)_{CFD} d\Omega \tag{4}$$

where N is an appropriate test function and α is the considered node, using the Gauss divergence theorem, and integration by parts equation leads to,

$$RHS_\alpha^1 = \int N_\alpha \left(\frac{\partial \rho u_i u_j}{\partial x_j} \right)_{CFD} n_i dS - \int \frac{\partial N_\alpha}{\partial x_i} \left(\frac{\partial \rho u_i u_j}{\partial x_j} \right)_{CFD} d\Omega \qquad (5)$$

This can be further simplified as,

$$RHS_\alpha^1 = - \int \frac{\partial N_\alpha}{\partial x_i} \left(\frac{\partial \rho u_i u_j}{\partial x_j} \right)_{CFD} d\Omega \qquad (6)$$

Considering that the values of CFD are constants over their cells, acoustic right-hand side can be calculated by summing up the contributions of different CFD cells belonging to the elements surrounding node α

$$RHS_\alpha^1 = \int N_\alpha \left(\frac{\partial \rho u_i u_j}{\partial x_j} \right)_{CFD} n_i dS - \sum_k \Omega_k \sum_g w_k^g \frac{\partial N_\alpha}{\partial x_i} (x_k) \left(\frac{\partial \rho u_i u_j}{\partial x_j} \right)_{CFD}^k \qquad (7)$$

where Ω_k is the volume of kth CFD cell and w_k^g is the weight associated with the gth integration point of cell k. CFD source field is constant such that only one integration point is required for each CFD cell.

$$\therefore w_k = 1$$

3   Duct Aeroacoustics

3.1   Experimental Setup

In this section, experimental setup is shown in Fig. 2 which is carried out by Stephane Caro et al. He studied and reported the acoustics behaviour of the duct system. Duct placed in anechoic room and inlet velocity of 7.5 m/s is given by the rotation of the fan at the inlet of the duct. Flow direction is from reverberant room to anechoic room. Mufflers are used to damp out the acoustic waves coming from fan, and sound pressure level is measured at the receiver placed in the anechoic room. In simulation, duct and anechoic room are only modelled (see Fig. 3).

3.2   Flow Modelling

The 3D CFD simulations are done in FLUENT of the HVAC duct of a square cross-sectional dimension of 60×60 mm and the domain of rectangular cavity dimensions

Reverberant Chamber

Anechoic Chamber

Sealing

Variable Speed Fan   Muffler 1   Muffler 2   Adaptor with   BL Startup Duct   HVAC Duct
                                                      Turbulence Tripping   (3m long)
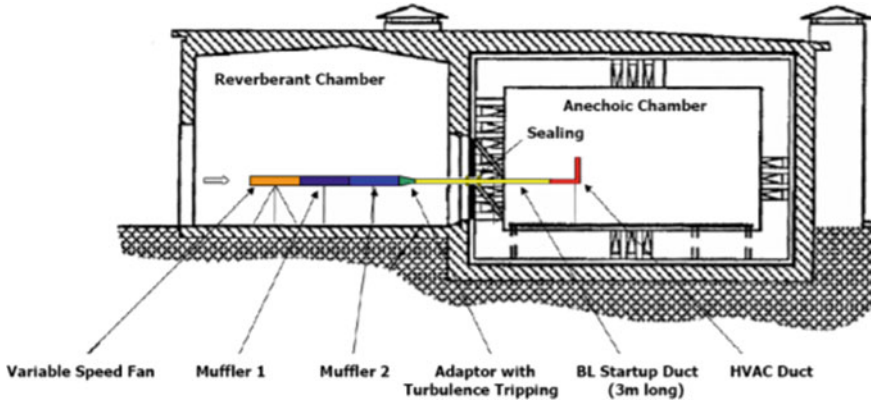
Fig. 2 Complete experimental setup

Fig. 3 Simulated region
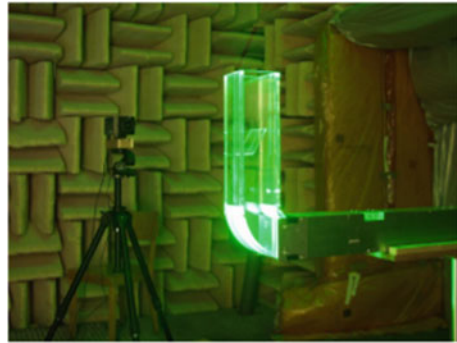
of 2000 × 2000 × 1600 mm shown in Fig. 4 and the duct cross section dimension is shown in Fig. 5. This domain is represented by two boundary conditions as follows:

(a)   Duct inlet as velocity inlet with a velocity of 7.5 m/s;
(b)   Duct outlet at rectangular cavity as pressure outlet from all five sides (see Fig. 4).

Meshing is done with 3D Hex dominant element type with the total number of elements or cells which are 2.31×10^6 Transient simulation is performed using detached eddy simulation (DES) with the Spalart–Allmaras turbulence model. The fluid is incompressible flow with a constant density of $\rho = 1.225$ kg/m^3 and kinematic viscosity of $\upsilon = 1.7 \times 10^{-5}$ m^2/s.

Input given is represented in Table 1.

Fig. 4 CAD model of the
duct (side view)
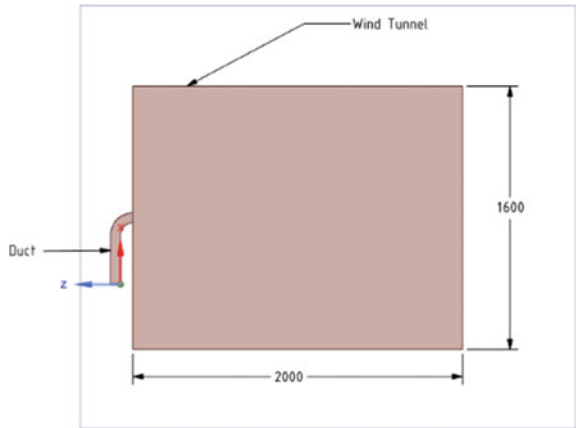
Fig. 5 Cross section of duct
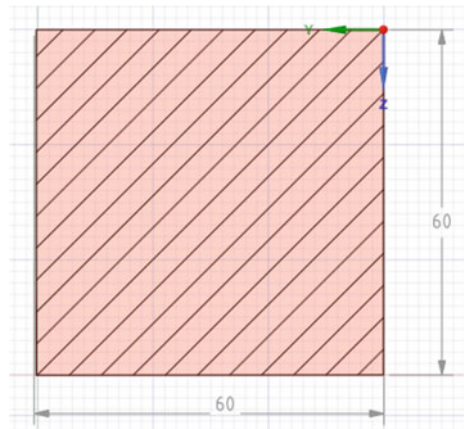
Table 1 Inputs for CFD
computation

Parameter	Value/model
Step size (Δt)	0.0005 s
Number of steps (N)	400
Flow time (t)	0.2 s
Turbulence model	DES (Spalart–Allmaras)
Fluid	Incompressible (air)
Solution type	Transient

3.3 Acoustic Modelling

3D acoustics simulation is done. One more domain is created closing the source domain (CFD domain) for the acoustics propagation shown in Fig. 6 There are a total of three domains created for aeroacoustics analysis as follows:

(a) Source domain or CFD domain (3D domain);
(b) Propagation domain (3D domain);
(c) Infinite layer (2D domain).

Meshing is done with 3D TET elements with the total number of elements of 2×10^5 for capturing the frequency bandwidth of 2000 Hz, and 12323 2D triangular element set is created for the infinite layer which acts as a non-reflecting boundary condition (see in Fig. 6). The microphone has placed at a 1-metre distance from the duct outlet for capturing the acoustic data.

Aeroacoustics computation procedure followed using a hybrid approach as follows in four steps,

(a) CFD results such as pressure, density and velocity computation in FLUENT:
(b) Extraction of CFD results and import to ACTRAN software;
(c) Noise sources computation using ICFD solver;
(d) Noise propagation or radiation computation using direct frequency response (DFR) solver.

Lighthills volume is assigned as a boundary condition which calculates the volume sources.
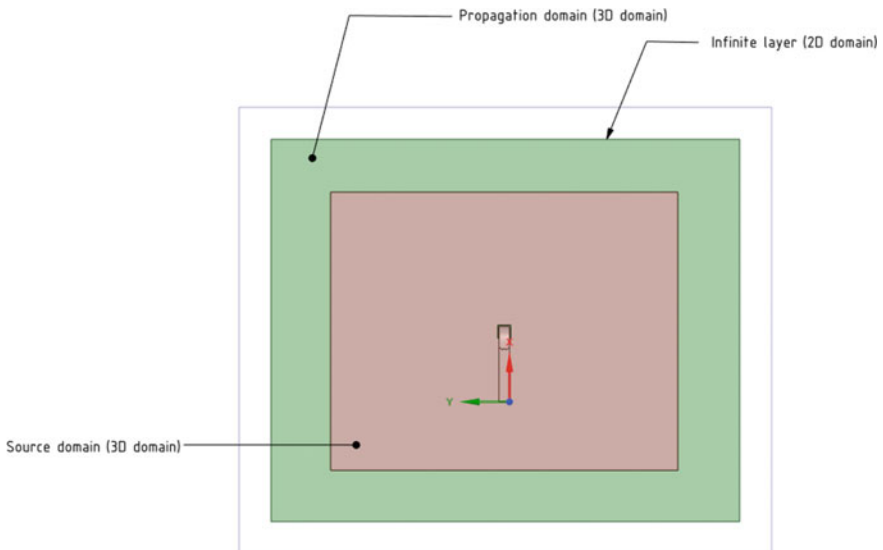
Fig. 6 Acoustic CAD model

Table 2 Inputs for acoustics computation

Parameter	Value
Total signal time (t)	0.2 s
Time resolution (Δt)	0.00025 s
Frequency bandwidth ($f = 1/\Delta T$)	4000 HZ
Frequency resolution ($\Delta f = 1/t$)	5 HZ

ACTRAN software computes divergence of the Lighthills tensor which is computed in FLUENT, and then, it takes the Fourier transform of the pressure–time signal converted to the frequency spectrum. Frequency width depends upon the acoustic mesh element size. Meshing should contain a minimum of eight elements per wavelength so that it captures all the frequencies. Mesh convergence study is not done here. Inputs required to solve the acoustics part is shown in Table 2.

4   Results and Discussion

4.1   CFD Results

CFD simulations were performed, and velocity fluctuations and vorticity magnitudes are observed. In the velocity contour plot, it can be seen more velocity fluctuations near vicinity of the duct bend (see Fig. 7). Also, vorticity is more when flow separates from the duct (see Fig. 8)

Fig. 7 Velocity vectors
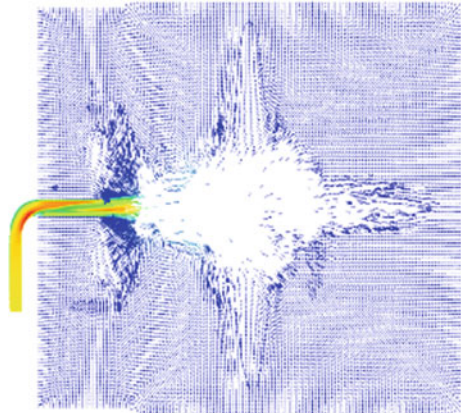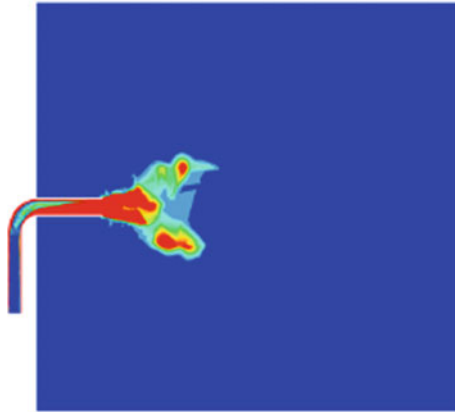
Fig. 8 Vorticity magnitude

4.2 Acoustic Results

CFD results were mapped over acoustic mesh as described above. It has been observed here that from the frequency spectrum, the noise is purely broadband noise (see Fig. 9) Sound characteristics are compared with experimental data, showing good agreement. There is some offset at lower frequencies the reason is yet unknown we are investigating that may be because of mesh size or source truncation that we do not know will investigate that why it is happening this offset rest of all frequencies modes showing good match with experiment, you can refer the experiment results in the Stephane Caro et al. Paper under Ref. [5] for more detail.

The acoustics mode shapes are also represented at 10 Hz, 100 Hz, 490 Hz and 1501 Hz (see Fig. 10). It is showing that at lower frequencies, noise levels are higher
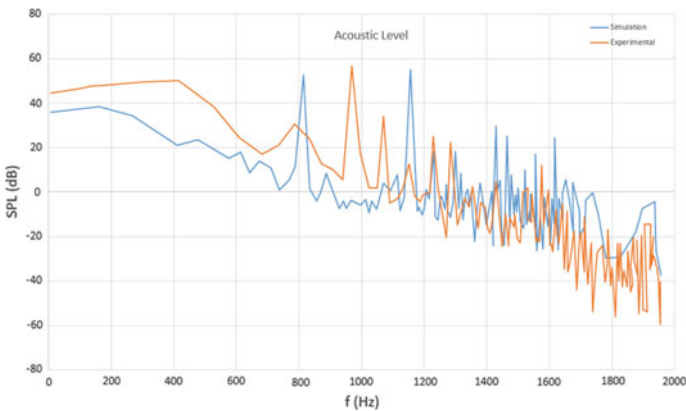
Fig. 9 Sound spectrum measured at microphone location

(a) 10 Hz (b) 100 Hz (c) 490 Hz (d) 1501 Hz
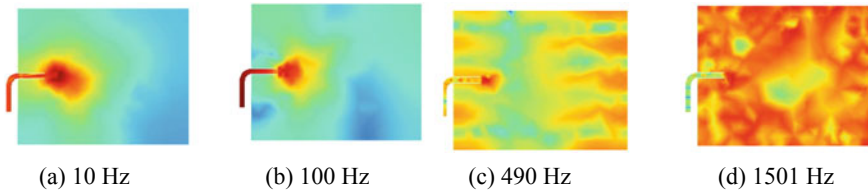
Fig. 10 Acoustics mode shapes (**a–d**)

and then higher frequencies which are also called as pseudo-noise in the literatures. As the frequency increases, noise becomes broadband in nature as can be seen in maps below. At 5 Hz it is showing axial mode and as frequencies increases like at 1501 Hz showing random modes as its broadband noise.

Total time taken for CFD simulation in FLUENT is 12 h in 10 core machine, and for acoustics, simulation in Actran is 3 h. Preprocessing and meshing time are not included in this computational time.

5 Conclusion

Aerodynamically generated sound from the duct has been studied numerically. These results are well compared with the experimental results of Caro et al. [5]. Overall sound pressure level is 50 dB experimentally, and it is 54 dB by simulation. Overall 8% deviation is observed between test and simulation. This deviation might be the cause of unmodelled muffler part in simulation and needs to understand the absolute level difference. Mid-range frequencies show good agreement with experiment. Higher frequency region shows fair agreement with experiment and can be understand with mesh sensitivity analysis in future studies. A major source of the sound generation is nearby the duct inlet, and bends in the duct and instabilities in flow generate flow sound at the duct outlet. Frequency characteristics are broadband spectra from which it is concluded as a broadband noise.

References

1. Lighthill, M. J. (1952). Sound generated by aerodynamically. I. General theory. Proceedings of the Royal Society (London) A-Mathematical, Physical, *211*(1107), 564–587.
2. Curle, N. (1995). Influence of solid boundaries upon aerodynamic sound. Proceedings of the Royal Society (London) A-Mathematical, Physical, *231*(1187), 505–514.
3. Williams, J. F., & Hawkings, D. L. (1969), Sound generated by turbulence and the surfaces in arbitrary motion. Philosophical Transactions of the Royal Society A, *264*(1151), 321–342.
4. Ribner, H. S. (1959). New theory of the jet noise generation, directionality and spectra. *The Journal of the Acoustical Society of America, 31*(2), 245–246.

5. Caro, S., Detandt, Y., Manera, J., Toppinga, R., & Mendonça, F. (2009), Validation of a New Hybrid CAA strategy and application to the noise generated by a flap in a simplified HVAC Duct. AIAA Paper, 9.

Characterization Techniques and Evolution of Natural Polymer Nanofiber Composites (NPNFCs): An Extensive Study

H. Jeevan Rao, S. Singh, P. Janaki Ramulu, and Basant K. Agarwal

Abstract The twenty-first century witnessed the emergence of renewable resources—the application of composites in aerospace industry enhanced with carbon, glass, kevlar, etc. However, these materials are not biodegradable and environment-friendly. To solve this issue, studies were being carried out on natural composites which are biodegradable. The intent of this study is to present a comprehensive review of the biodegradable composites and matrix materials used in the aerospace industry. Since an aerospace vehicle has to operate under critical weather conditions at variable altitudes, the main problems with the existing materials are related to crash resistance, crack propagation rate growth, self-healing properties, and mechanical properties along with the additional problem of environmental pollution. The alternatives to synthetic fibers, thermoplastics, and thermosetting resins are biopolymers, natural fibers and natural fiber nanocomposites (NFNCs). NFNCs are already implemented in the automotive and aerospace industry because of their biodegradability. However, the type of reinforcement can predominantly alter the dynamic behavior of natural cellulose fiber—nanoparticle-embedded composites (NFNRCs). Similarly, the reinforcement surface-area-to-volume ratio is a key parameter for aerospace applications. Based on the type of reinforcement, nanofiller-based natural composites can display various effective enhancements in desirable properties (like an impact tolerance, fatigue strength, tensile and flexural strength), rheological properties, electrical conductive properties, optical properties, enhanced material

H. Jeevan Rao (✉) · S. Singh · B. K. Agarwal
Amity Institute of Aerospace Engineering, Amity University Uttar Pradesh, Sector 125, Noida 201313, Uttar Pradesh, India
e-mail: jeevan.rao14@gmail.com

S. Singh
e-mail: ssingh10@amity.edu

B. K. Agarwal
e-mail: bkagarwal@amity.edu

P. Janaki Ramulu
School of Mechanical, Chemical and Materials Engineering, Adama Science and Technology University, Adama Post Box: 1888, Ethiopia
e-mail: srirama309@gmail.com

173

durability, energy absorption rate, and shock/impact resistance that make these materials crucial for aerospace application. Based on this, a comprehensive study has been studied on NFNRCs.

Keywords Bio-composites · Natural nanofiber · NFRNCs · Cellulose fiber · Surface modifications · XRD · FTIR · SEM

1 Introduction

The investigation of natural polymer nanocomposites is mandatory if it has to be extensively applied in the industries. The current aircraft components and interior parts are built from synthetic polymer composites—most commonly, carbon, glass, and kevlar. Currently, the developed materials have advantages and disadvantages on sustainability. The demand for recyclable, eco-friendly, durable, and biodegradable material blends arise in the aerospace industry and has motivated several studies at developing biodegradable composites due to its availability and its flexibility [1]. Suggested that the unique properties of natural fibers make them easy replacements for manmade or synthetic fibers [2]. Stated that the hazardous effects can be avoided by using fibers extracted from natural sources, and that the inherent physical behavior of natural cellulose fiber polymer composites is superior to manmade fibers [3]. Stated that natural fiber can be identified and extracted from barks, leaves, and fruits, due to their properties. Several natural fiber applications have been recorded in composites create dosing flax, banana, sisal, jute, vakka, abaca, pineapple, coconut sheath, cotton, rice, bamboo, grewia, and wood as reinforcements [4–6]. Suggested a high reliability of natural fibers, and that their composites were biodegradable and alternative to synthetic fibers also reducing pollution while decomposition and mentioned that green composites exhibited better mechanical properties and tribological properties and also, explained that the properties of natural polymer composites change with respective to major factor. Chemical treatment improves the properties of natural fiber compared to untreated fibers and promotes better inter-laminar adhesiveness among the fiber wall-surface and the suitable matrix that results in the reinforcements exhibiting better bonding and thereby enhancing the impact toughness and fatigue strength [7]. The strength of natural fiber embedded or blended polymers was mainly altered by the adhesive bonding between continuous phase matrix and the load carrying fibers [8]. In general, impact and damage properties of the natural cellulose fiber-reinforced polymer composites greatly increase with the fiber content. However, the Young's modulus of cellulose fiber polymer blend composites enhanced with gradual increment of fiber percentage. Based on mathematical modeling, rule of mixture (ROM) provides the ratio of fiber to matrix. To evaluate the stress–strain relationship between the composites, a Halpin–Tsai equation predicted to be the most adequate for different cellulose–natural fibers polymer composites [9, 10]. Investigated the relation between recycling ability and biodegradability and how it affects the mechanical properties in polymer hemp/sisal fibers composites [11]. Studied and

recognized the advantages and applications of nanotechnology in modern warfare as well as in the aerospace industry, such as the impact of nanomaterials like graphene, CNTs, titanium nanoparticles, etc. The authors also discussed the weight reduction, strength increment, and the effects of NFNCs on the thrust areas of an aircraft propulsive system, lightning protection system, and aircraft de-icing system.

Essential advantages and disadvantages of cellulose–natural fibers [12–15] are as follows: Natural fibers have high strength and stiffness with low density which produced naturally minimum amount of time required grow and which can involve the process of absorption of CO_2 and releasing of oxygen. Natural fiber production rate and cost are very lesser than synthetic fibers. Manufacturing process of natural cellulose fibers is easy, and they are non-carcinogenic. Subjected to temperature variations, they produced minimum amount of toxic fumes and extracts. Damage effects on cutting tools and machining equipment are very less compared to synthetic fibers. They are environment protectors as well as bio-degradable.

Compared to synthetic fibers, natural fibers are low durable, but it is feasible to enhance the properties by doing suitable saline chemical treatments according to the composition. NFs can easily absorb the moisture content in the atmosphere; due to that the reaction rate in the molecules, layers are high. It will be affecting on the physical behavior and impact and damage properties of the fiber. Temperature processing limits are low because the section criteria of matrix material will become important. Natural fibers show a different variety of properties in different aspects (Fig. 1 and Table 1).

Based on available natural resources on the globe and with effectiveness of farmers on farming every year, the production of natural fibers is mentioned above; primarily, sugarcane production is high in India, Brazil, and Europe, since availability of various natural fibers is creating scope for replacement of synthetic fibers [16] (Table 2).
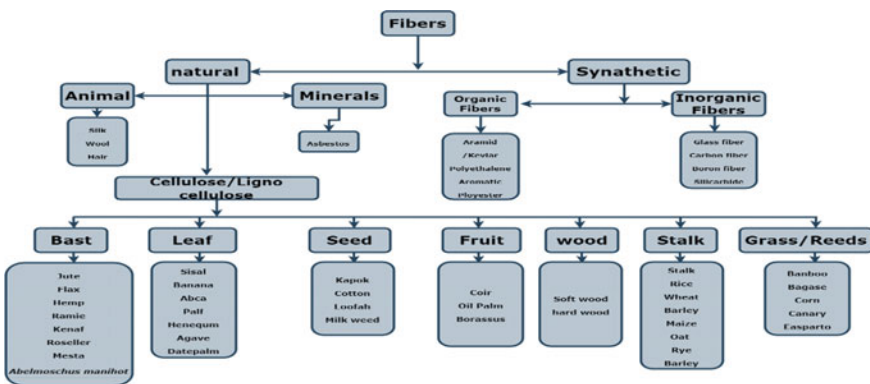
Fig. 1 Tree of notable natural and synthetic fibers

Table 1 Worldwide natural cellulose fiber production [9]

Source fiber	Production rate (10^3 ton)
Maximum bamboo	30.000
Sugarcane bagasse	75.000
(W/T)Jute	2300
Kenaf	970
Linseed—Flax	830
Grass	700
Agave—Sisal	375
Industrial hemp	214
Ramie	100
Cocunut—Coir	100
Banana—Abaca	70

Table 2 Available chemical composition of mostly used natural fibers [9]

Fiber	Natural cellulose (wt%)	Hemicellulose (wt%)	Lignin (wt%)	Waxes (wt%)
Banana–Abaca	56–63	20–25	7–9	3
Sc-Bagasse	55.2	16.8	25.3	–
Bamboo	26–43	30	21–31	–
Cocunut—Coir	32–43	0.15–0.25	40–45	–
Linseed—Flax	71	18.6–20.6	2.2	1.5
Industrial hemp	68	15	10	0.8
Jute	61–71	14–20	12–13	0.5
Kenaf	72	20.3	12–13	0.5
Ramie	68.6–76.2	13–16	0.6–0.7	0.3
Sisal	65	12	9.9	2
Oil palm	65	–	29	–
Pineapple(PALF)	81	–	12.7	–
Curaua	73.6	9.9	7.5	–
Wheat straw	38–45	15–31	12–20	–
Rice husk	35–45	19–25	20	14–17
Rice straw	41–57	33	8–19	8–38

2 Research Implications

It is time to realize the problems facing by mother Earth and imbalance due to extraction of non-renewable sources, Research is the backbone of the future generation and only way to recognize the renewable source to fill the gap created by the

non-renewable sources like petrochemicals, etc. Currently, worldwide, an awareness created by researchers on renewable resources [16, 17]. Stated that the twenty-first century could be called as cellulose century because of the utilization of natural fibers and natural resources like plant fiber, animal fiber, minerals asbestos and various nanomaterials for advanced applications as the aerospace industry, automobile, architecture, marine, space applications, etc. The applications of natural sources are globally increased, and industries are looking to produce a natural fiber with polymer matrix material application and have been looking with the combination of biopolymers [18]. Addressed the major issues and difficulties in development of natural fiber composites and ways to enhance the mechanical and physical properties of NFCMs and explained about best chemical treatment methods to enhance outer surface treatment and suitable procedures to developing the NFCMs [19], based on their extensive work explained, the behavior and application of natural fibers in the aerospace industry and specific aircraft structural components.

2.1   Factor Affecting Mechanical Properties of Natural Fibers

The most important parameter is fiber selection criteria, based on type of fiber, time required for harvesting, refinement of fiber extraction method, length–diameter ratio, chemical treatment and fiber content, matrix material selection, inter-laminar bonding strength, fiber dispersion and direction of orientation, specific technique of composite manufacturing, porosity, and void content in the composite [16].

From Table 3, many authors understand the maximum tensile properties, Young's modulus, elongation, and density of various natural fibers. As for dwarf natural fibers, deciding their orientation is critical. Dwarf natural fibers are randomly oriented; composite specimen exhibits the property in brittle nature, and it is going for sudden failure, and the long fibers are flexible to control their orientation and exhibit its ductile behavior, and load carrying capacity can increase.

2.2   Surface Modification Techniques of Biodegradable Natural Composites

Based on the literature noticed that the compatibility between the natural fiber and resin is low compared to synthetic fibers. To enhance the interfacial bonding between these surfaces, modification treatment is required.

Table 3 Mechanical behavior of mostly used and available natural fibers [9]

Type fiber tensile property (MPa) (GPa)	Young's modulus E- (GPa)	Elongation (%)	Density [g/cm3]
Banana—Abaca 400	12	03–10	1.50
Cocunut—Coir 175	4–6	30	1.20
Curaua 500–1150	11.8	3.7–4.3	1.40
Linseed—Flax 345–1035	27.6	2.7–3.2	1.50
Industrial hemp 690	70	1.6	1.48
Jute fibe 393–773	26.5	1.5–1.8	1.3
Kenaf fibe 930	53	1.6	–
Agave—Sisal 511–635	9.4–22	2.0–2.5	1.5
Ramie fiber 560	24.5	2.5	1.5
Oil palm 248	3.2	25	0.7–1.55
PALF 400–627	1.44	14.5	0.8–1.6
SC-Bagasse 290	17	–	1.250
Bamboo 140–230	11–17	–	0.6–1.1

2.2.1 Corona Treatment Method

It is one of the most versatile processes to treat surface, unique approach for material surface decay activation. This approach displays the face adhesion improvement of the natural fibers. This process on biodegradable natural cellulose fibers and listed polymer matrix was suitable for the enhancement of the compatibility among the listed hydrophilic cellulose fibers and a hydrophobic matrix material [9].

2.2.2 Plasma Treatment Method

It is the most used physical technique and is quite identical to corona treatment. The variation of plasma in this method introduces phenomenal modifications on the surface of a biodegradable cellulose natural fiber. Different surface alterations can be displayed based on the chemical reaction of the chemical fluids utilized. It can made some sensible free radical groups can be developed and divided, also the volumetric energy levels can be accelerate or decelerate, bonding and cross-linking among the elements can be progress for various polymers [9].

2.2.3 Alkaline Treatment Method

It is the famous chemical method (to extract the quantity of lignin, wax, and additional oils available in the surface walls of the natural cellulose fiber cells) for an application of cellulose natural fibers when used as reinforcement with polymers

Table 4 Notable physical parameters of natural fibers (diameter and moisture content) [20–22]

Fibers	Diameters (µm)	EMC (%)
Oil palm fronds	19.7	–
Oil palm EFB	19.1–25.0	–
Banana	12–30	15
Agave—Sisal	7–200	11
Pineapple leaf	20–80	13
Ramie	18–80	9
Coconut husks	100–450	10
Bagasse	10–34	–
Jute	5–200	12
Industrial hemp	10–500	9
Linseed—Flax	5–600	7
Aloe	–	12
Various woods	–	12
Banana—Abaca	–	9.5
Cotton	10–45	8
Kapok fruit fiber	–	10

matrix. Perfect surface bonding enhancement can be observed with different alkaline processes which are the bonding disorder of the hydrogen element in the frame network of the biodegradable natural cellulose fiber, therefore enhancing the surface roughness and interfacial bonding.[9]

From Table 4 and 5, it was observed that many authors studied the suitable polymers for natural fibers, suitable nanofillers for biodegradable composites, and the physical parameter—diameter, density, and moisture content—for various natural fibers. Biodegradable polymers such as PLA, PVA, TBR, TPS, PHBV, and soy-based resin [55–58] have reported for the use as matrix for the natural fiber reinforcement.

2.3 Processing Technologies for Natural Fibers

Fabrication techniques are selected based on the type of polymer material, it may thermosetting resin or thermoplastic resin.

2.3.1 Techniques for Natural Fibers with Thermosetting Resins

There are various techniques available to process the natural fiber with thermosetting resin composites and NFNCs, and the main disadvantage is curing time and

Table 5 Polymer matrix material for natural fibers

Polymer matrix + nanofiller for natural fibers	References
PA-11-Polyamide 11 + nanominerals	[21–23]
e-Caprolacta + organo-minerals	[24]
PA-6-Polyamide + montmorillonite clay (MMT)	[25]
PA-6-Polyamide + organically modified clay MMT (OMMT)	[26–28]
PA-6-Polyamide + iron oxide particles	[29]
PU-Polyurethanes + carbon nanotube (CNT)	[30]
PSU-Polyaniline and sulfonated urethane + carbon nanotube(CNT)	[31]
PP-Polypropylene + nanomineral clays	[32]
PP-Polypropylene + nano-carbon fiber	[33]
PP-Polypropylene + nano clays	[34]
PE-Poly(ethylene) + carbon nanotube	[35]
UHMWPE -Ultra-high MW poly(ethylene) + carbon nanotube	[36]
PS-Polystyrene + carbon nanotube	[37]
PS-Polystyrene + carbon nanotube	[38]
PEEK -Poly(ether ether ketone) + nanoparticles of SiO_2	[39]
PEEK -Poly(ether ether ketone) + carbon nanofibers CNFs	[40]
PEEK -Poly(ether ether ketone) + organo-alkoxysilanes	[41]
PEEK -Poly(ether ether ketone) + SiC nanoparticles.	[42, 43]
PI-Phenylethynyl-terminated imide + multi-walled carbon nanotube	[44]
PAA -Polyarylacetylene + carbon fiber	[45]
PAA -Polyarylacetylene + carbon fiber/LiAlH4	[46]
PAA Polyarylacetylene + carbon fiber	[47]
PBO-Poly p-phenylenebenzobisoxazole + SWNT (single-walled nanotubes)	[48]
ER- Epoxy resin + Coir-fiber nanofiller	[49]
PLA-Polylactic acid + PALF	[48, 49]
TPR-Tapioca-based bioplastic resin + PALF	[50]
TPS-Thermoplastic starch + PALF	[51]
PHB-Poly hydroxy butyrate – co hydroxyvalerate + PALF	[52, 53]
Soy-based resin + PALF	[54]

temperature; they require hand lay-up and spraying, resin transfer molding, injection molding, vacuum bag molding, pultrusion, vacuum-assisted resin transfer molding, casting injection molding, and polyurethane foam molding.

2.3.2 Techniques for Natural Fibers with Thermoplastic Resins

The common fabrication methods used for processing the natural fiber with thermoplastic resins are extrusion, thermoforming, cold pressing compression, filament winding, compression injection molding, foam molding, compression injection heating, direct long-fiber-reinforced thermoplastics, rotational molding, calendaring, and co-extrusion [9].

2.4 Applications

From the past couple of decades, the technology perspective of automobiles, aircrafts, ships, and other vehicle models had been enhanced. It was started in Europe encouraged by government legislation and then in North America and has featured the applications of natural fiber-reinforced polymers(NFRPs) in door panels, package trays, hat racks, instruments panels, internal engine covers, sun visors, boot liners, oil/air filters progressing to more structurally demanding components such as seat backs and exterior underfloor paneling. Now, all of the main international automotive and aerospace industry manufacturers use these materials, and their use is expected to increase in this area [17]. 3D woven fiber composites were developing for aerospace applications [56], and the aerospace industry has been selecting the NFCs & NFNCs for interior applications due to its biodegradable property [50]. Many researchers are suggesting RTM technique for natural fiber-reinforced polyester turbine blades to be an effective replacement for those reinforced with glass fiber obtained recognition by way of the Asia 2013 Innovation Award from the JEC composites group for the world's first functional natural fiber–flax composite wind turbine propeller blade [51]. Properties and applications of PALF natural fiber are studied [57].

3 Materials and Characterization Methods

Figure 2 describes the materials used in the aerospace industry applications of various films, foams, foils, non-woven, coatings, and adhesives [54]. Natural fibers are collected from various plants, fruits, leaves, roots, and, seeds. The properties of fibers depend on plant age, region, and climatic conditions. However, the fiber properties vary with respect to extraction process and chemical treatments. Based on the above-mentioned parameters, it is necessary to study the characteristics of the fiber [9, 17, 51]. Based on the available literature, various instruments are available to determine the properties. After extraction of fiber, they have to carry out the physical analysis, fiber mechanical properties analysis, and chemical analysis.
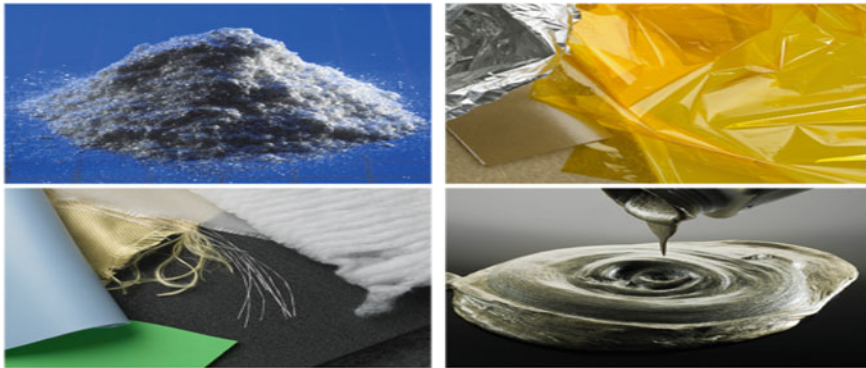
Fig. 2 Raw materials used in industries [54]

3.1 Various Techniques

Fourier transform infrared (FTIR) spectrum analysis is the right method to determine and display the chemical and functional groups existed in various natural fibers. The specimen should be in pellet form for this analysis. X-ray diffraction (XRD) analysis is a suitable method to find out the crystalline structure in natural fiber. Thermogravimetric analysis (TGA) is very useful to find the thermal stability of natural fiber for various applications. Differential scanning calorimeter analysis (DSC) determines the thermal transition of the materials and natural fiber polymer composites. However, it determines the transition, crystalline, and melting temperature of the materials. By using scanning electron microscopy (SEM), we can identify the surface morphology of natural fiber and materials. Hence, the surface roughness is the deciding factor of composite life. Energy-dispersive X-ray spectroscopy analysis can display the elements existing on the surface of natural fiber (C, O, N, Cl, Si, etc.) in terms of percentage. Atomic force microscopy can provide the accurate data of surface roughness of natural fiber, and this displays accurate images of surface. NMR spectroscopy is helpful to identify the anisotropic interfaces in natural fiber.

4 Summary

Based on the literature survey, natural fiber composites (NFCs) and natural fiber nanocomposite materials (NFNCs) are the most required sources for the industries to develop biodegradable materials. Based on their good sound absorbing properties and effective energy management on applications of green fiber technological manufacturing effect on environmental pollution can be reduced, the earth can easily take back biodegradable debris. Based on the survey the point out the advanced application of aerospace, space technology, automobile industry, and marine industry. The

natural fibers can be used as reinforcement materials for lightweight applications. The observation of surface roughness and morphology of natural fibers is more flexible for interfacial bonding with thermoplastics and thermosetting resins. The main objective of the study identified is NFCs which are very cost effective than synthetic fibers.

References

1. Madhu, P., Sanjay, M. R., Senthamaraikannan, P., Pradeep, S., Saravanakumar, S. S., & Yogesha, B. (2019). A review on synthesis and characterization of commercially available natural fibers: Part-I. *Journal of Natural Fibers, 16*(8), 1132–1144.
2. Bledzki, A. K., Sperber, V. E., & Faruk, O. (2002). Natural and wood fibre reinforcement in polymers (Vol. 13). iSmithers Rapra Publishing.
3. Burkart, A. (1976). A monograph of the genus Prosopis (Leguminosae subfam. Mimosoideae). *Journal of the Arnold Arboretum*, 450–525.
4. Santos, C. V. D., Leiva, D. R., Costa, F. R., & Gregolin, J. A. R. (2016). Materials selection for sustainable executive aircraft interiors. *Materials Research, 19*(2), 339–352.
5. Sanjay, M. R., Madhu, P., Jawaid, M., Senthamaraikannan, P., Senthil, S., & Pradeep, S. (2018). Characterization and properties of natural fiber polymer composites: A comprehensive review. *Journal of Cleaner Production, 172,* 566–581.
6. Şimşek, M., Aldemir, S. D., & Gümüşderelioğlu, M. (2019). Anticellular PEO coatings on titanium surfaces by sequential electrospinning and crosslinking processes. *Emergent Materials, 2*(2), 169–179.
7. Mandal, S., Das, V. V., Debata, M., Panigrahi, A., Sengupta, P., Rajendran, A.,… & Basu, S. (2019). Study of pore morphology, microstructure, and cell adhesion behaviour in porous Ti-6Al-4 V scaffolds. Emergent Materials, 2(4), 453–462.
8. Ding, X., Ahmed, S., Bao, N., Ding, J., Liu, R., & Yi, J. (2019). Clustering-induced high magnetization in Co-doped TiO 2. *Emergent Materials, 2*(3), 295–301.
9. Cooke, K. O., & Khan, T. I. (2018). Effect of thermal processing on the tribology of nanocrystalline Ni/TiO$_2$ coatings. *Emergent Materials, 1*(3–4), 165–173.
10. Fayyad, E. M., Abdullah, A. M., Hassan, M. K., Mohamed, A. M., Jarjoura, G., & Farhat, Z. (2018). Recent advances in electroless-plated Ni-P and its composites for erosion and corrosion applications: a review. *Emergent Materials, 1*(1–2), 3–24.
11. Lee, B. H., Kim, H. J., & Yu, W. R. (2009). Fabrication of long and discontinuous natural fiber reinforced polypropylene biocomposites and their mechanical properties. *Fibers and Polymers, 10*(1), 83–90.
12. Li, X., Tabil, L. G., & Panigrahi, S. (2007). Chemical treatments of natural fiber for use in natural fiber-reinforced composites: a review. *Journal of Polymers and the Environment, 15*(1), 25–33.
13. Mehta, G., Mohanty, A. K., Thayer, K., Misra, M., & Drzal, L. T. (2005). Novel biocomposites sheet molding compounds for low cost housing panel applications. *Journal of Polymers and the Environment, 13*(2), 169–175.
14. Faruk, O., Bledzki, A. K., Fink, H. P., & Sain, M. (2014). Progress report on natural fiber reinforced composites. *Macromolecular Materials and Engineering, 299*(1), 9–26.
15. Al-Oqla, F. M., & Sapuan, S. M. (2014). Natural fiber reinforced polymer composites in industrial applications: feasibility of date palm fibers for sustainable automotive industry. *Journal of Cleaner Production, 66,* 347–354.
16. Mansor, M. R., Nurfaizey, A. H., Tamaldin, N., & Nordin, M. N. A. (2019). Natural fiber polymer composites: Utilization in aerospace engineering. In Biomass, Biopolymer-Based Materials, and Bioenergy (pp. 203–224). Woodhead Publishing.

17. Majeed, K., Jawaid, M., Hassan, A. A. B. A. A., Bakar, A. A., Khalil, H. A., Salema, A. A., et al. (2013). Potential materials for food packaging from nanoclay/natural fibres filled hybrid composites. *Materials and Design, 46,* 391–410.

18. Rowell, R. M. (2008). Natural fibres: types and properties. Properties and performance of natural-fibre composites. Woodhead publishing, pp. 3–66.

19. Liu, T., Lim, K. P., Tjiu, W. C., Pramoda, K. P., & Chen, Z. K. (2003). Preparation and characterization of nylon 11/organoclay nanocomposites. *Polymer, 44*(12), 3529–3535.

20. Usuki, A., Kawasumi, M., Kojima, Y., Okada, A., Kurauchi, T., & Kamigaito, O. (1993). Swelling behavior of montmorillonite cation exchanged for ω-amino acids byϵ-caprolactam. *Journal of Materials Research, 8*(5), 1174–1178.

21. Lincoln, D. M., Vaia, R. A., Wang, Z. G., & Hsiao, B. S. (2001). Secondary structure and elevated temperature crystallite morphology of nylon-6/layered silicate nanocomposites. *Polymer, 42*(4), 1621–1631.

22. Fornes, T. D., & Paul, D. R. (2003). Crystallization behavior of nylon 6 nanocomposites. *Polymer, 44*(14), 3945–3961.

23. Li, L., Bellan, L. M., Craighead, H. G., & Frey, M. W. (2006). Formation and properties of nylon-6 and nylon-6/montmorillonite composite nanofibers. *Polymer, 47*(17), 6208–6217.

24. Liang, Y., Xia, X., Luo, Y., & Jia, Z. (2007). Synthesis and performances of Fe2O3/PA-6 nanocomposite fiber. *Materials Letters, 61*(14–15), 3269–3272.

25. Chen, W., Tao, X., & Liu, Y. (2006). Carbon nanotube-reinforced polyurethane composite fibers. *Composites Science and Technology, 66*(15), 3029–3034.

26. Poulin, P., Vigolo, B., & Launois, P. (2002). Films and fibers of oriented single wall nanotubes. *Carbon, 40*(10), 1741–1749.

27. Roy, S., Lu, H., Vengadassalam, K., & Hussain, F. (2004). Compressive Strength Enhancement of Pultruded Thermoplastic Composites Using Nanoclay Reinforcement. In 45th AIAA/ASME/ASCE/AHS/ASC Structures, Structural Dynamics & Materials Conference (p. 1778).

28. Jamwal, A., Vates, U. K., Gupta, P., Aggarwal, A., & Sharma, B. P. (2019). Fabrication and characterization of Al 2 O 3–TiC-reinforced aluminum matrix composites. In Advances in industrial and production engineering (pp. 349–356). Springer, Singapore.

29. Zhang, X., Huang, Y., Wang, T., & Liu, L. (2007). Influence of fibre surface oxidation–reduction followed by silsesquioxane coating treatment on interfacial mechanical properties of carbon fibre/polyarylacetylene composites. *Composites Part A Applied Science and Manufacturing, 38*(3), 936–944.

30. Ruan, S. L., Gao, P., Yang, X. G., & Yu, T. X. (2003). Toughening high performance ultrahigh molecular weight polyethylene using multiwalled carbon nanotubes. *Polymer, 44*(19), 5643–5654.

31. Ruan, S., Gao, P., & Yu, T. X. (2006). Ultra-strong gel-spun UHMWPE fibers reinforced using multiwalled carbon nanotubes. *Polymer, 47*(5), 1604–1611.

32. Ji, Y., Li, B., Ge, S., Sokolov, J. C., & Rafailovich, M. H. (2006). Structure and nanomechanical characterization of electrospun PS/clay nanocomposite fibers. *Langmuir, 22*(3), 1321–1328.

33. Qian, D., Dickey, E. C., Andrews, R., & Rantell, T. (2000). Load transfer and deformation mechanisms in carbon nanotube-polystyrene composites. *Applied Physics Letters, 76*(20), 2868–2870.

34. Jen, M. H. R., Tseng, Y. C., & Wu, C. H. (2005). Manufacturing and mechanical response of nanocomposite laminates. *Composites Science and Technology, 65*(5), 775–779.

35. Sandler, J., Werner, P., Shaffer, M. S., Demchuk, V., Altstädt, V., & Windle, A. H. (2002). Carbon-nanofibre-reinforced poly (ether ether ketone) composites. *Composites Part A Applied Science and Manufacturing, 33*(8), 1033–1039.

36. Schmidt, H. (1994). Multifunctional inorganic-organic composite sol-gel coatings for glass surfaces. *Journal of Non-Crystalline Solids, 178,* 302–312.

37. Jamwal, A., Prakash, P., Kumar, D., Singh, N., Sadasivuni, K. K., Harshit, K., et al. (2019). Microstructure, wear and corrosion characteristics of Cu matrix reinforced SiC–graphite hybrid composites. *Journal of Composite Materials, 53*(18), 2545–2553.

38. Wang, Q. H., Xue, Q. J., Liu, W. M., & Chen, J. M. (2000). The friction and wear characteristics of nanometer SiC and polytetrafluoroethylene filled polyetheretherketone. *Wear, 243*(1–2), 140–146.

39. Ogasawara, T., Ishida, Y., Ishikawa, T., & Yokota, R. (2004). Characterization of multi-walled carbon nanotube/phenylethynyl terminated polyimide composites. *Composites Part A Applied Science and Manufacturing, 35*(1), 67–74.

40. Fu, H. J., Huang, Y. D., & Liu, L. (2004). Influence of fibre surface oxidation treatment on mechanical interfacial properties of carbon fibre/polyarylacetylene composites. *Materials Science and Technology, 20*(12), 1655–1660.

41. Zhang, S., Hull, T. R., Horrocks, A. R., Smart, G., Kandola, B. K., Ebdon, J.,… & Hunt, B. (2007). Thermal degradation analysis and XRD characterisation of fibre-forming synthetic polypropylene containing nanoclay. Polymer degradation and stability, 92(4), 727–732.

42. Pratheep Kumar, A., & Pal Singh, R. (2007). Novel hybrid of clay, cellulose, and thermoplastics. I. Preparation and characterization of composites of ethylene–propylene copolymer. *Journal of Applied Polymer Science*, *104*(4), 2672–2682.

43. Sen, A., & Kumar, S. (2010). Coir-fiber-based fire retardant nano filler for epoxy composites. *Journal of Thermal Analysis and Calorimetry, 101*(1), 265–271.

44. Ogasawara, T., Ishida, Y., Ishikawa, T., & Yokota, R. (2004). Characterization of multi-walled carbon nanotube/phenylethynyl terminated polyimide composites. *Composites Part A: applied science and manufacturing*, *35*(1), 67–74.

45. Shah, D. U., Schubel, P. J., & Clifford, M. J. (2013). Can flax replace E-glass in structural composites? A small wind turbine blade case study. *Composites Part B Engineering, 52,* 172–181.

46. Lin, Z., Ye, W., Du, K., & Zeng, H. (2001). Homogenization of functional groups on surface of carbon fiber and its surface energy. *Journal of Huaqiao University*, *22*(3), 261–3.

47. Zhang, S., Hull, T. R., Horrocks, A. R., Smart, G., Kandola, B. K., Ebdon, J., ... & Hunt, B. (2007). Thermal degradation analysis and XRD characterisation of fibre-forming synthetic polypropylene containing nanoclay. *Polymer degradation and stability*, *92*(4), 727–732.

48. Pratheep Kumar, A., & Pal Singh, R. (2007). Novel hybrid of clay, cellulose, and thermoplastics. I. Preparation and characterization of composites of ethylene–propylene copolymer. *Journal of Applied Polymer Science*, *104*(4), 2672–2682.

49. Sen, A., & Kumar, S. (2010). Coir-fiber-based fire retardant nano filler for epoxy composites. *Journal of Thermal Analysis and Calorimetry*, *101*(1), 265–271.

50. Rao, H. J., Ramulu, P. J., Vardhan, M. V., & Chandramouli, C. H. (2016, September). Failure prediction in fiber metal laminates for next generation aero materials. In IOP Conference Series: Materials Science and Engineering (Vol. 149, No. 1, p. 012102). IOP Publishing.

51. Shah, D. U., Schubel, P. J., & Clifford, M. J. (2013). Can flax replace E-glass in structural composites? A small wind turbine blade case study. *Composites Part B: Engineering*, *52*, 172–181.

52. Ramli, S. N. R., Fadzullah, S. H. S. M., & Mustafa, Z. (2017). The effect of alkaline treatment and fiber length on pineapple leaf fiber reinforced poly lactic acid biocomposites. Jurnal Teknologi, 79(5–2).

53. Munawar, R. F., Jamil, N. H., Shahril, M. K., Rahim, S. A., Muhammad, S., Abidin, Z.,… & Lau, K. T. (2015). Development of green composite: pineapple leaf fibers (palf) reinforced polylactide (pla). In Applied Mechanics and Materials (Vol. 761, pp. 520–525). Trans Tech Publications.

54. Mathivanan, D., Norfazilah, H., Siregar, J. P., Rejab, M. R. M., Bachtiar, D., & Cionita, T. (2016). The study of mechanical properties of pineapple leaf fibre reinforced tapioca based bioplastic resin composite. In MATEC Web of Conferences (Vol. 74).

55. Smitthipong, W., Tantatherdtam, R., & Chollakup, R. (2015). Effect of pineapple leaf fiber-reinforced thermoplastic starch/poly (lactic acid) green composite: Mechanical, viscosity, and water resistance properties. *Journal of Thermoplastic Composite Materials, 28*(5), 717–729.

56. Kalambettu, A., Damodaran, A., Dharmalingam, S., & Vallam, M. T. (2015). Evaluation of biodegradation of pineapple leaf fiber reinforced PVA composites. *Journal of natural fibers, 12*(1), 39–51.

57. Kaewpirom, S., & Worrarat, C. (2014). Preparation and properties of pineapple leaf fiber reinforced poly (lactic acid) green composites. *Fibers and Polymers, 15*(7), 1469–1477.
58. Liu, W., Misra, M., Askeland, P., Drzal, L. T., & Mohanty, A. K. (2005). 'Green'composites from soy based plastic and pineapple leaf fiber: fabrication and properties evaluation. *Polymer, 46*(8), 2710–2721.

Experimental Analysis on Wear Behavior of Luffa–Date Leaves–Sawdust Hybrid Natural Fiber Composites

Shreoshi Das Gupta, D. N. Mahto, Niharika Kumari, Kamal Prasad, and M. K. Paswan

Abstract In the present day, natural fibers are a popular choice for researchers for creating various polymer composites because not only are they sustainable but also eco-friendly too. In the present world where there is an overuse of single-time use plastics and the usage of non biodegradable materials, natural fiber composites find itself in a vital role in various applications and research of engineering. It is very hard to choose an appropriate fiber for an application because the characteristics of the individual natural fiber depend on a large set of various properties which include where the fiber is harvested and the conditions at which it was harvested or even the fertilizers used for its growth and much more. The natural fibers which have been used in making the specimen are luffa fibers, saw dust, and date leaves which were reinforced with epoxy resin LY 556 matrix; the specimen fabricated was developed by hand lay-up technique, the natural fibers were dried in the sun for 36 h, and the fibers were mixed in different volume fractions in the ratios of 5(luffa): 3(date leaves): 2(sawdust), 4:5:1 and 6:3:1, respectively. The prepared sample is tested for flexural strength and tensile strength, and the result is shown graphically. Volume fraction of fibers is in the ratios of 5(luffa): 3(date leaves): 2(sawdust), 4:5:1 and 6:3:1, respectively.

S. Das Gupta (✉) · D. N. Mahto
Department of Physics, Kolhan University, Chaibasa, Jharkhand, India
e-mail: shreoshidasgupta@gmail.com

D. N. Mahto
e-mail: dn.mahato08@gmail.com

N. Kumari · K. Prasad
Department of Physics, T N B Bhagalpur, Bihar, India
e-mail: niharika.kumari108@gmail.com

K. Prasad
e-mail: kprasad65@gmail.com

M. K. Paswan
Department of Mechanical Engg, NIT Jamshedpur, Jamshedpur, Jharkhand, India
e-mail: manikant.nit@gmail.com

1 Introduction

Presently, researchers are finding materials for structural use which has a very high strength but are also lightweighted, and at the same time, it must be cost effective for getting the necessary results which are high strength and less weight. To obtain a composite material, two or more materials are combined. When the materials are combined, the so-formed composites have properties which are superior to the properties of the original individual components. There are cases when such properties are not even present in their parent materials.

The increase in the consciousness for the environment and how shifting to a sustainable source led to the thinking of materials other than synthetic fibers like an eco-friendlier product which has the required or more than the required properties. Also, the consumer's cognitive values have been changed by various green marketing and promotions of recycling and social influence

Daimler Benz for their Mercedes G class cars used door panels that were made from natural fibers. Construction materials are made from natural fibers which are renewable resources which would be embedded in biopolymers bring about economically and ecologically acceptable manufacturing technologies [1–11].

Vignesh [12] state that in polyester resins reinforced with coconut shells and coir fiber, the friction at contact surface of the material and at the rotating disk increases when the load is applied at an increasing rate.

Acharya et al. [13] had done a research on the wear behavior of cylindrical untreated luffa fiber and glass fabric-reinforced epoxy composite. From his studies, it could be concluded that the erosive wear behavior of natural fiber composites can be very much improved by adding it with synthetic fiber glass.

Panneerdhass et al. [14] have studied the flexural, compressive, tensile, impact energy and water absorption capacity of luffa fiber and ground nut-reinforced epoxy polymer.. The optimum mechanical properties were obtained at 40% of fiber volume fraction of treated fiber.

Ventateshwaran et al. [15] have studied the tensile strength and modulus of short, randomly oriented hybrid natural fiber composite and predicted using rule of hybrid mixture (RoHM). Hybrid composites were prepared using banana/sisal fibers of 40:0, 30:10, 20:20, 10:30, and 0:40 ratios, while overall fiber volume fraction was fixed. The comparison between experimental and RoHM showed that they are in good agreement.

2 Experiment

The processes are mentioned in below procedure that are required in various stages for completing the research work

  (i)   The fibers were cut in the following manner, each specimen 22.5 cm × 12 cm (luffa fibers); 22.5 cm × 1.5 cm (date leaves) and 10 μm (sawdust).
 (ii)   Recording and labeling each test specimen to its respective matrix ratios.
(iii)   Resin 9 (epoxy): 1 (fiber) in ratio.
 (iv)   Pouring of resin per each fiber layer, forming the composite using hand layup technique.
  (v)   After 24 h, the load of 50 kg is removed, and the top and bottom cells are repeeled off.
 (vi)   Cutting and reducing the size (22.5 cm × 24 cm) as per ASTM standard

2.1 Raw Materials

Natural fibers—luffa fibers, date tree leaves and sawdust.

In luffa fibers, the fibrous cords are arranged in various directions forming a natural mat. In this set/system of natural fibers, they are glued together with a natural resinous material.

Panneerdhass [14] states that the tensile strength of a 40% luffa fiber to epoxy composite has 18.7 MPa and the tensile strength and 42 Joules for a 30% luffa fiber epoxy composite as the impact strength.

2.2 Fabrication of the Composite

The sample specimens were fabricated in the following percentages of individual fiber ratios and epoxy ratios that were taken which have been mentioned in the table below. The hand layup test specimen was of the dimension of 25 cm × 25 cm (Table 1).

The natural fibers obtained were thoroughly dried for 5 days, and the composites were prepared in the percentages mentioned in the above table. The composites were flattened in a UTM to straighten out and give structure to it (Figs. 1 and 2).

Table 1 Composition of the composites

Sl. no	Luffa fiber %	Date leaf %	Saw dust %
1	50	30	20
2	40	50	10
3	60	30	10

Fig. 1 Raw materials—fibers

Fig. 2 Raw materials—epoxy, hardener and silicone spray

2.3 Experimental Procedure

The prepared composites were set out with a curing time of 24 h, and then, the test specimen was cut and placed in sunlight for removing the moisture present in the specimens and was tested using the universal testing machine and pin-on-disk setup.

All the raw materials of different composites with certain percentage of resins poured and built using the hand lay-up system and hand rolled up to 10 min. The whole test specimen is tightened up with 50 kg load for a time period of 24 h. The following are the test specimens used in the experiment (Figs. 3 and 4).

2.4 Experimental Setup

The wear test was conducted in the pin-on-disk-type friction and wear monitored. After laying out the test specimens of the natural fibers with epoxy resins mixed uniformly in their respective matrix ratios onto the hand lay-up hard cell with bottom

Fig. 3 Initial specimens (before cutting and shaping) front and back view

Fig. 4 Prepared test specimen

and top cover rolled manually by hand roller for about 25 times in forward and backward directions on the top of the layup machine. After that it was loaded with 50 kg load for 24 h. We have observed that when the sliding distance increases proportionately, wear rate also increases. There is a direct relationship between the sliding distance and wear rate.

2.5 Applications of Various Other Fiber Composites

The luffa fiber–date leaves–sawdust (6:3:1) composite can be used as wood substitute; that is, this composite could be used in building fake ceilings, door panels, tables and various other products (Figs. 5, 6 and Table 2).

Fig. 5 In-car products

Fig. 6 Door substitute

Table 2 Various applications of other natural fibers

SL. no.	Fibers	Application
1	Oil palm fiber	Building materials such as windows, door frames, structural insulated panel building systems, siding, fencing, roofing, decking and other building materials
2	Sisal fiber	In construction industry such as panels, doors, shutting plate and roofing sheets; also, manufacturing of paper and pulp
3	Rice husk fiber	Building materials such as building panels, bricks, window frame, panels, decking, railing systems and fencing
4	Flax fiber	Window frame, panels, decking, railing systems, fencing, tennis racket, bicycle frame, fork, seat post, snowboarding and laptop cases
5	Hemp fiber	Construction products, textiles, cordage, geo—textiles, paper and packaging, furniture, electrical, manufacture bank notes and manufacture of pipes

3 Results and Discussion

There are numerous applications of natural composite materials, and each day, these applications are discovered due to it being recyclable, biodegradable and eco-friendly. Natural fiber composites with similar load carrying capacity of alloy materials and metals would be revolutionary. In the current study of luffa fibers–date leaves–sawdust composites, specimens which were created using ASTM standards and tests were carried out universal testing machine, and the observed results are mentioned below.

(i)   Tensile Test Analysis

Using the UTM and generating the stress v/s strain curve which was plotted by the data from the machine during tensile loading for each of the test specimens. From the data, we can conclude that specimen 3 (6:3:1; L: D: S) has the highest tensile strength of the test (Figs. 7, 8 and Tables 3, 4).
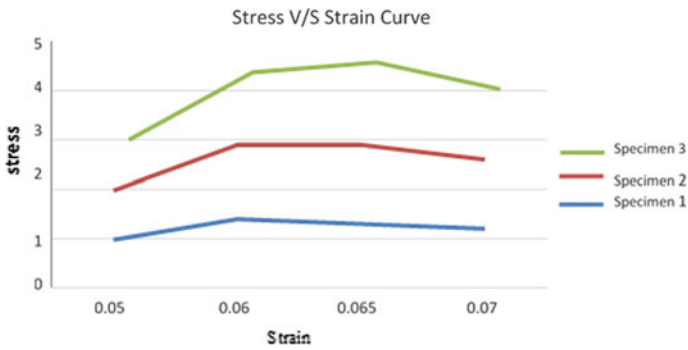
Fig. 7 Graph 1. Stress V/S strain curve
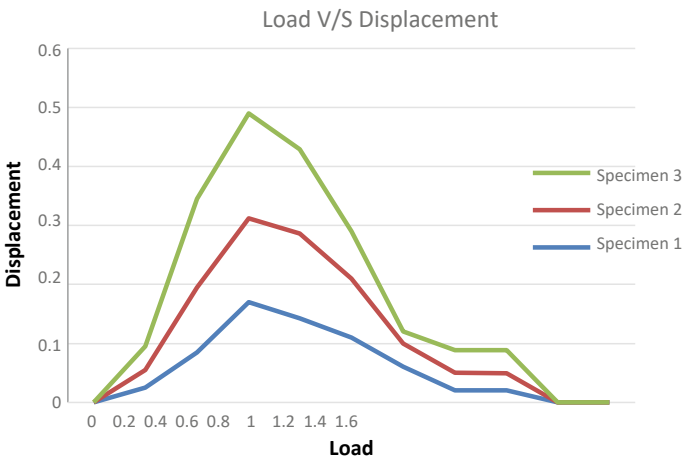
Fig. 8 Graph 2. Load V/S displacement graph

Table 3 Stress V/S strain for each of the specimens

Specimen strain	Specimen1 (gpa)	Specimen2 (gpa)	Specimen3 (gpa)
0.05	0.98	1	1.04
0.06	1.4	1.5	1.5
0.065	1.3	1.6	1.7
0.07	1.2	1.4	1.45

Table 4 Load V/S displacement for various specimens

Load	Specimen 1 (mm)	Specimen 2 (mm)	Specimen 3 (mm)
0	0	0	0
0.2	0.025	0.03	0.04
0.4	0.085	0.11	0.15
0.6	0.17	0.142	0.178
0.8	0.143	0.143	0.143
1	0.11	0.1	0.08
1.2	0.06	0.04	0.02
1.4	0.02	0.03	0.038
1.6	0.02	0.029	0.039

(ii)   Flexural Test Analysis

The load v/s displacement curve plotted from the data of the specimens which were tested was observed specimen 3 (6:3:1; L: D: S) is the better of the three samples.

4   Conclusion

From the experimental investigation of luffa–date leaf–sawdust fiber-reinforced hybrid composites, the following conclusions have been arrived that.

- The luffa–date leaf–sawdust was successfully fabricated using minimal cost, making it lightweight and more importantly eco-friendly.
- The results demonstrate that there is a direct relationship between the sliding distance and wear rate as the sliding distance increases proportionately, wear rate also increases.
- The maximum flexural strength of 20.2 N/mm^2 was recorded from the third test specimen of the luffa fiber–date leaf–sawdust composite with the ratio (6:3:1; L:D:S), whereas minimum flexural strength was recorded from specimen 1 of the composite ratio (5:3:2; L:D:S) 9.35 N/mm^2.

- From the above data, it can be observed that luffa fiber–date leaf–sawdust composite could be used as an alternative for synthetic fiber-reinforced composite material.

References

1. Harikrishna, M., Ajeeth, K., Ranganatha, S., & Thiagarajan, C. (2018). Fabrication and mechanical properties of hybrid natural fiber composites. *International Journal of Pure and Applied Mathematics, 19*(15), 685–696.
2. Chandu, K. V. P. P., Gopala Krishna, S. V., Subrahmanyam, B. V., Venkateswar Rao, K., experimental analysis on wear behaviour of banana—pineapple hybrid natural fiber composites. *International Journal of Engineering Science Invention* ISSN (online) 2319–6734 pp. 14–2.
3. Shalwan, A., & Yousif, B. F. (2013). In state of art: Mechanical and tribological behaviour of polymeric composites based on natural fibres. *Materials & Design, 48*, 14–24.
4. Srinivasababu, N., Kumar, J. S., & Reddy, K. V., Manufacturing and characterization of long palmyra palm/Borassus flabellifer petiole fiber reinforced polyester composites. *Procedia Technology, 1*(14), 252–259.
5. Verma, D., Gope, P. C., Shandilya, A., Gupta, A., & Maheshwari, M. K. (2013). Coir fiber reinforcement and application in polymer composites. *Journal of Materials and Environmental Science, 4*(2), 263–276.
6. Santhosh, J., Balanarasimman, N., Chandrasekar, R., & Raja, S. (2014). Study of properties of banana fiber reinforced composites. *International Journal of Research in Engineering and Technology, 3*(11), 144–150.
7. Mani, P., Dellibabu, G. V., Anilbasha, K., & Anbukarsi, K. (2014). Tensile and flexural properties of Luffa fiber reinforced composite material. *International Journal of Engineering Research and Technology*, 1882–5.
8. Venkatakrishnan, R., Senthilvelan, T., & Vijayakumar, T. (2015). Fabrication and mechanical properties of hybrid natural composite. In *Applied Mechanics and Materials* (Vol. 813, pp. 57–61). Trans Tech Publications.
9. . Verma D, Gope P. The use of coir/coconut fibers in composites. Faruk-Biofiber Reinforcements in Composite Materials. 2015:285–320.
10. Pujari, S., Ramakrishna, A., & Kumar, M. S., Comparison of jute and banana fiber composites: A review. *International Journal of Current Engineering and Technology, 2*(2), 121–126.
11. Kumar, S. S., Duraibabu, D. A., & Subramanian, K. (2014). Studies on mechanical, thermal and dynamic mechanical properties of untreated (raw) and treated coconut sheath fiber reinforced epoxy composites. *Materials and Design, 1*(59), 63–69.
12. Vignesh, Wear behaviour of coconut shell powder and coir fiber reinforced polyester composites. *IOSR Journal of Mechanical and Civil Engineering* (IOSR-JMCE) e-ISSN: 2278– 1684, p-ISSN: 2320-334XPP 53-57.
13. Acharya, N. et al. (2010). Effect of fiber content on abrasive wear of lantana camera fiber reinforced polymer matrix composite. *Indian Journal of Engineering and Material Science, 17*, 219–223.
14. Panneerdhass, R., Gnanavelbabu, A., & Rajkumar, K. (2014). Mechanical properties of luffa fiber and ground nut reinforced epoxy polymer hybrid composites. *Elsevier, Procedia Engineering, 97,* 2042–2051.
15. Venkateshwaran, N., Elayaperumal, A., & Sathiya, G. K. (2012). Prediction of tensile properties of hybrid-natural fiber composites. *Elsevier Journal*, Part B-43, 793–796, (2012).

Analysis of Mechanical Properties and Environmental Effect on Composite Sandwich Structure by Varying the Face Sheet Thickness

Arun Kumar Gaur, Anil Kumar, and Aman Aggarwal

Abstract In this study, composite sandwich panels were fabricated by vacuum-assisted hand lay-up method. Carbon fiber is used as face sheet material, and Nomex™ PN1 honeycomb is used as core material. Three panels were fabricated of different configurations; thickness of core took 8 mm remains the same in all three panels, but total thickness of face sheet took 0.4 mm, 0.8 mm and 1.2 mm for different panels. After fabrication, the specimens were prepared as per ASTM standards available for different tests and carried out various tests like compression test, three-point bending test, water absorption test, acid attack resistance test and soil degradation test on all panels and then analyzed the effect of varying face sheet thicknesses. The results showed that when specimen thicknesses were 8.4 mm, 8.8 mm and 9.2 mm, then compression strengths were 16.43 N/mm^2, 103.86 N/mm^2 and 571.65 N/mm^2, respectively and deflections were 2 mm(approx), 2.5 mm(approx) and 3 mm(approx), respectively; so increasing the face sheet thickness of structure increases the compression strength and deflection. For acid attack resistance test, when specimen thicknesses were 8.4 mm, 8.8 mm and 9.2 mm, then changes in weight were +50.20%, +27.08% and +20.92%, respectively so that effect of acid was less when the face sheet thickness increases. When specimen thicknesses were 8.4 mm, 8.8 mm and 9.2 mm, then changes in their weight for water absorption test were +8.98%, +6.08% and +9.92%, respectively, and changes in their weight for soil degradation test were +3.41%, +0.55% and +0.79%, respectively, so water absorption and soil degradation tests showed that increasing the face sheet thickness was better, but it should not be over thick.

A. K. Gaur (✉) · A. Aggarwal
Department of Mechanical Engineering, GITAM, Visakhapatnam, India
e-mail: arunjamdagni@gmail.com

A. Aggarwal
e-mail: aman_aggarwal38@rediffmail.com

A. Kumar
Department of MAE, G.B. Pant Engineering College, New Delhi, India
e-mail: anilritu84@gmail.com

1   Introduction

The composite structures are made by combination of two different materials; the materials may be metallic or non-metallic [1, 2]. In composite sandwich structure, two layers (one above and one below) of same or different materials are bonded with the middle layer of different materials [3, 4]. Nowadays, composite sandwich panel's use is increasing day by day in the industry due to its weight to stiffness and strength ratio [5]. The stiffness is the most important feature of the composite panels so that whenever we want to make new composite material with different combinations of materials, then every combination should be tested for stiffness before its use [6, 7]. The composite materials are used in various types of industries, so they work in different environmental conditions so that some necessary test should be carried out on them like water absorption test, acid attack resistance test, soil degradation test, etc., before using them in any structure [8, 9]. The ASTM standards are maximum acceptable all over world so that all the test should be tried to be carried out as per ASTM standards. Composite sandwich panels are mainly used in aerospace and transportation industry.

2   Literature Review

The sandwich composite structures are manufactured by two components; one is core and another is face sheet. A lot of research has been done to achieve a good composite sandwich panel by varying the core and face sheet materials and their shapes and sizes. During the research, composite structures are analyzed under various types of loading conditions. The given below literature review is related to the study of composite structures.

Pehlivan et al. [10] in this work, various types of carbon fiber-reinforced polymer honeycomb were studied under the compressive load. They conclude that thickness of cell wall was very important in crushing, and hexagonal honeycomb has much strength in crushing as compared to square and circular honeycombs [10].

Liu et al. [11] in this work, Nomex™ honeycomb sandwich structure is studied under the three-point bending load. The results are verified and compared by Abaqus and numerical. They concluded that effect of increasing face sheet thickness on ultimate strength is higher when core shear rigidity is higher [11].

Dinesh et al. [12] in this study, sandwich composite structure of foam and aluminum honeycomb core materials with carbon fiber face sheet is studied. They concluded that foam-based structure had better tensile and compressive strength, and aluminum core had better flexural strength [12].

Kumar et al. [13] in this work, they laminate the carbon fiber as face sheet and Nomex™ as core and then analyze the properties of laminate [13].

Takagi et al. [14] in this study, various parameters like foil thickness, cell size and specimen dimensions of honeycomb structures are studied. They concluded that honeycomb core is buckled before reaching the yield point [14].

Liu et al. [15] in this work, de-bonding of the face sheet from core material is studied. Sandwich under the flat-wise compression is observed and concluded that de-bonding occurred when adhesive was not strong and area of bonding was large [15].

Tamilarasan et al. [16] in this study, carbon fiber as face sheet and aluminum as core is used. Various tests are performed like tensile, flexural and impact as per ASTM standards. Then, scanning electron microscope analysis was done to investigate the structure [16].

Xiong et al. [17] in this study, carbon fiber face sheet and pyramidal honeycomb core are studied under the in-plane compression load. Various types of situations are observed and compared with FEM analysis [17].

Nia et al. [18] in this study, the effect of strain rate on compressive strength of bare and foam-filled honeycomb structure is studied. They concluded that crushing strength depends on strain rate for bare honeycomb structure, but in case of foam-filled honeycomb structures, the strain rate effect is negligible [18].

Zakeri et al. [19] in this study, honeycomb structure under various load conditions is studied. Effect of core and face material is also studied experimentally, analytically and by FEM. They concluded that flexural strength depends on face sheet, and compression strength depends on core [19].

3 Problem Formulation

The literature review shows that lots of research have been done related to composite sandwich structures, and many research papers have been published. But there has not been done much work on varying the face sheet thickness of carbon fiber with same core thickness of Nomex™ in sandwich composite structures. So, there could be a possibility of analysis of varying the face sheet thickness on the compression strength, deflection of structure, water absorption capacity, soil degradation capacity and effect of acid.

4 Methodology

- Carbon fiber is used as face sheet material; thickness of face sheet for each panel is different, which varies from 0.4 mm–1.2 mm.
- Nomex™ is used as core material, and core thickness remains same for each panel that is 8 mm.

Table 1 Fiber properties of the carbon fiber used in sandwich composite

	Type (C fiber)	Density (g/cm^3)	Tensile strength (Mpa)	Tensile modulus (Gpa)	Elongation (%)	Filament diameter (μ)	Size compatibility
Warp	3 K	1.8	3450	240	1.7	7	Epoxy
Weft	3 K	1.8	3450	240	1.7	7	Epoxy

Table 2 Properties of resin and hardener used in the sandwich of composite

Property	Appearance	Color	Specific gravity	Viscosity
Resin	Clear liquid	Max 2	1.1–1.2	1000–1500
Hardener	Clear liquid	Max 4	0.98–1.04	50–150

- Vacuum-assisted hand lay-up method is used for panel's fabrication.
- Prepared specimens as per required ASTM standards.
- Flat-wise compression test as per ASTM C365, three-point bending test as per ASTM C393, water absorption test as per ASTM D570, soil degradation test and acid degradation test.
- Analysis of the environmental effect and physical strengths of specimens.

5 Experimental Work

The composite sandwich panels were made by vacuum-assisted hand lay-up method. The core was made of Nomex™ PN1, and face sheets were made of carbon fiber. Core and face sheet are bonded by adhesive and hardener. The properties of material used for the fabrication of sandwich panels are given below in Tables 1 and 2.

Technical Data sheet (200 GSM 2*2 Twill Woven Carbon Fabrics)

Three panels of different configurations of composite sandwich structure are fabricated by vacuum-assisted hand lay-up method. 8 mm thickness of Nomex™ honeycomb is used as core, and 0.4 mm, 0.8 mm and 1.2 mm thickness carbon fiber is used as face sheet. After fabrication, specimens were prepared as ASTM standards.

6 Results and Discussion

To analyze the effect of varying face sheet thickness, the following test has been performed as per the ASTM/ISO standards.

6.1 Compression Test (ASTM C365)

To analyze the compression strength, specimen is prepared as per ASTM C365 standards. Two specimens took from each panel, and UTM is used for the compression test (Fig. 1 and Table 3).

6.2 Calculations for Deflection Using Three-Point Bending Test

The specimens were prepared as per ASTM C393, and three-point bending test has been performed (Fig. 2 and Table 4).
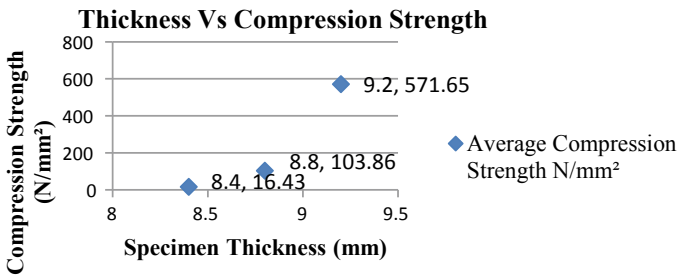
Fig. 1 Graph between thickness and compression strength for three panels

Table 3 Results of compression test

Specimen type	Specimen thickness (mm)	Specimen No.	Peak load (KN)	Elongation (mm)	Compression strength N/mm^2	Average compression strength N/mm^2
Total face sheet thickness 0.4 mm	8.4	1C1	4.6	2.3	21.904	16.43
	8.4	1C2	2.3	9.2	10.952	
Total face sheet thickness 0.8 mm	8.8	2C1	21.1	11.7	95.91	103.86
	8.8	2C2	24.6	8.4	111.82	
Total face sheet thickness 1.2 mm	9.2	3C1	116.9	4.1	560.26	571.65
	9.2	3C2	134.1	7.2	583.04	
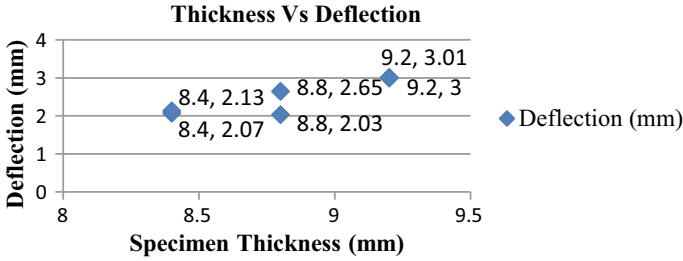
Fig. 2 Graph of thickness versus deflection for flexural test

Table 4 Results of three-point bending test

	Specimen 1		Specimen 2		Specimen 3	
Specimen thickness (mm)	8.4	8.4	8.8	8.8	9.2	9.2
Specimen width (mm	29.39	39.28	29.76	39.65	30.32	39.75
Peak load (N)	239	405	429	575	722	926
Deflection (mm)	2.07	2.13	2.03	2.65	3	3.01

6.3 Water Absorption Test (ASTM D570)

The specimens were prepared as per ASTM standards. The specimens were kept in water for 144 h, and during the test procedure, weight of each specimen was checked after an interval of 24 h. Analysis of percentage weight change is given by formula as (Fig. 3, Table 5),

$$W\% = \left\{ \frac{W\tau - W_\circ}{W_\circ} \right\} * 100$$

where $W\%$ = Percentage of water absorbed
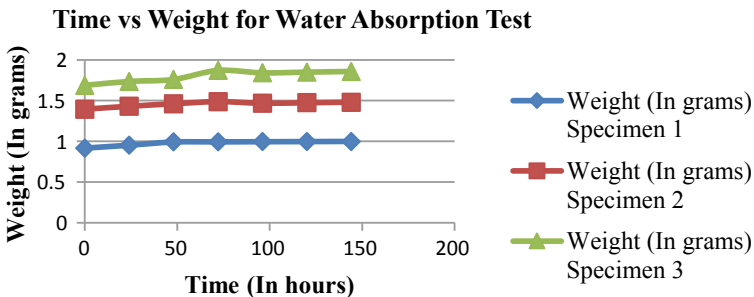
Fig. 3 Graph of time versus weight for water absorption test

Table 5 Water absorption test results (weight change with time)

S. No.	Time (in hours)	Specimen 1	Specimen 2	Specimen 3
1	0	0.9169	1.3959	1.6883
2	24	0.9528	1.4308	1.736
3	48	0.992	1.462	1.7601
4	72	0.9938	1.4877	1.8715
5	96	0.9956	1.4685	1.8417
6	120	0.9974	1.475	1.8507
7	144	0.9992	1.4808	1.8587
	% Change	**+8.98**	**+6.08**	**+9.92**

$W\tau$ = Weight of specimen after time,
W_o = Initial weight of specimen

- Overall, we can say that under water working conditions, higher the face sheet thickness is better for composite structures, but it should not be over thick.

6.4 Acid Attack Resistance Test

The specimens are prepared and kept in 50% sulfuric acid solution for 144 h and check the weight after 24 h interval regularly. Difference between the final and initial weight showed the effect of acid (Fig. 4 and Table 6).
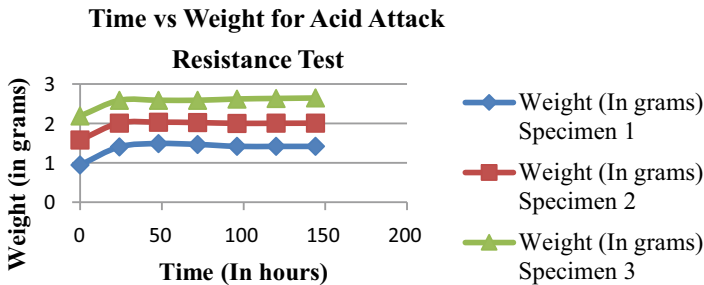
Fig. 4 Graph of time versus weight for acid attack resistance test

Table 6 Acid attack resistance test results (weight change with time)

S. no.	Time (in hours)	Specimen 1	Specimen 2	Specimen 3
1	0	0.9428	1.5785	2.1877
2	24	1.4052	2.0084	2.5859
3	48	1.4882	2.0314	2.5869
4	72	1.4665	2.0206	2.5869
5	96	1.4172	2.0013	2.6203
6	120	1.4166	2.0038	2.6338
7	144	1.4161	2.006	2.6453
	% Change	**+50.20**	**+ 27.08**	**+20.92**

- Overall, we can say that higher the face sheet thickness results in less effect of acid.

6.5 Soil Degradation Test

This test is required to analyze the effect of environment on the composite structure. For this test, specimens were prepared as per standards and check initial weight and then kept under soil which has more than 25% moisture for 8 days. After 8 days withdrawn the specimens, then clean thoroughly and weight them. Difference between the final and initial weight is considered as effect of soil (Table 7 and Fig. 5).

Table 7 Soil degradation test results (weight change with days)

S. no.	Time (in days)	Specimen 1	Specimen 2	Specimen 3
1	0	1.0425	1.5918	2.0614
2	8	1.0781	1.6006	2.0777
	% Change	**3.41**	**0.55**	**0.79**
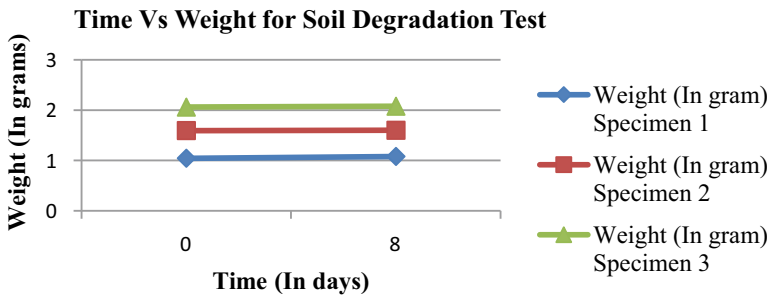
Fig. 5 Graph of time versus weight for soil degradation test

- The final results show that higher the face sheet thickness is better for composite structures, but it should not be over thick.

7   Conclusions

- Nomex™ PN1 and carbon fiber used hybrid composite sandwich panels were fabricated by vacuum-assisted hand lay-up method.
- Nomex™ PN1 is used as core and core thickness of 8 mm remains same for all the panels.
- Carbon fiber is used as face sheet, and total face sheet thicknesses were 0.4 mm, 0.8 mm and 1.2 mm for three different panels.
- Compression, three-point bending, water absorption, acid attack resistance and soil degradation tests have been carried out to analyze the effect of these tests on varying the face sheet thickness of panels.
- For the compression test, when specimen thicknesses were 8.4 mm, 8.8 mm and 9.2 mm, then compression strengths were 16.43 N/mm^2, 103.86 N/mm^2 and 571.65 N/mm^2, respectively, so the results showed that compression strength increases when the face sheet thickness increases.
- For the three-point bending test, when specimen thicknesses were 8.4 mm, 8.8 mm and 9.2 mm, then deflections were 2 mm(approx), 2.5 mm(approx) and 3 mm(approx), respectively, so the results showed that deflection increases when the face sheet thickness increases.
- For acid attack resistance test, when specimen thicknesses were 8.4 mm, 8.8 mm and 9.2 mm, then changes in weight were +50.20%, +27.08% and +20.92%, respectively, so the results showed that higher the face sheet thickness results in less effect of acid.
- For the water absorption and soil degradation tests, when specimen thicknesses were 8.4 mm, 8.8 mm and 9.2 mm, then changes in their weight for water absorption test were +8.98%, +6.08% and +9.92%, respectively, and changes in their weight for soil degradation test were +3.41%, +0.55% and +0.79%, respectively, so the results showed that higher the face sheet thickness is better, but it should not be over thick.

References

1. Composite, N. À. P., & Al, K. I. M. E. T. (2014). 3D optical printing of piezoelectric materials. *ACS Nano, 10*, 9799–9806.
2. Cholleti, E. R. (2018). A review on 3D printing of piezoelectric materials. *IOP Conference Series: Materials Science and Engineering, 455*(1).

3. Naficy, S., Gately, R., Gorkin, R., Xin, H., & Spinks, G. M. (2017). 4D printing of reversible shape morphing hydrogel structures. *Macromolecular Materials and Engineering*, *302*(1), 1600212.

4. Cooke, K. O., & Khan, T. I. (2018). Effect of thermal processing on the tribology of nanocrystalline Ni/TiO$_2$ coatings. *Emergent Materials, 1*(3–4), 165–173.

5. Fayyad, E. M., Abdullah, A. M., Hassan, M. K., Mohamed, A. M., Jarjoura, G., & Farhat, Z. (2018). Recent advances in electroless-plated Ni-P and its composites for erosion and corrosion applications: A review. *Emergent Materials, 1*(1–2), 3–24.

6. Ge, Q., Qi, H. J., & Dunn, M. L. (2013). Active materials by four-dimension printing. *Applied Physics Letters*, *103*(13).

7. Yu, K., Ritchie, A., Mao, Y., Dunn, M. L., & Qi, H. J. (2015). Controlled sequential shape changing components by 3D printing of shape memory polymer multimaterials. *Procedia IUTAM*, *12*, 193–203.

8. Şimşek, M., Aldemir, S. D., & Gümüşderelioğlu, M. (2019). Anticellular PEO coatings on titanium surfaces by sequential electrospinning and crosslinking processes. *Emergent Materials, 2*(2), 169–179.

9. Tibbits, S., McKnelly, C., Olguin, C., Dikovsky, D., Hirsch, S. (2014). 4d printing and universal transformation. ACADIA 14 Design Agency: Proceedings of the 34th Annual Conference of the Association for Computer Aided Design in Architecture, pp. 539–548.

10. Pehlivan, L., et al. (2019). An experimental study on the compressive response of CFRP honeycombs with various cell configurations. *Elsevier, Composites Part B: Engineering, 162,* 653–661.

11. Liu, Y., et al. (2019). Mechanical responses of a composite sandwich structure with Nomex honeycomb core. *Journal of Reinforced Plastics and Composites*, *38*(13).

12. Dinesh, S. et al. (2018). Experimental testing on mechanical properties of sandwich carbon fibers reinforced composites. *ICAME-IOP Publishing Conf. Series: Materials Science and Engineering,* vol. 402, 012180.

13. Kumar, S., et al. (2017). Experimental Investigations on Carbon-Nomex T410 reinforced polymer matrix composite for enhanced mechanical and tribological properties. *AIP Conference Proceedings, 1859,* 020089.

14. Takagi, K. et al. (2017). Compression characteristics of honeycomb sandwich panels to improve their impact resistances. *AMMSE- IOP Publishing Conf. Series: Materials Science and Engineering*, vo. 269, 012080.

15. Liu, L., et al. (2015). The flat wise compressive properties of Nomex™ honeycomb core with debonding imperfections in the double cell wall. *Elsevier, Composites Part B: Engineering, 76,* 122–132.

16. Tamilarasan, U., et al. (2015). Mechanical properties evaluation of the carbon fiber reinforced aluminum sandwich composites. *Material Research, 18*(5), 1029–1037.

17. Xiong, J., et al. (2014). Mechanical behaviors of carbon fiber composite sandwich columns with three dimensional honeycomb cores under in-planes compression. *Composites Part B Engineering, 60,* 350–358.

18. Alavi Nia, M. G., et al. (2013). An experimental investigation on effect of strain rate on the behavior of bare and foam filled aluminum honeycomb. *Materials and Design, 52,* 748–756.

19. Zakeri, A. A., et al. (2010). Experimental study on mechanical properties of aircraft honeycomb sandwich structures. *EPJ Web of Conferences, 6,* 24003.

Vibrational Characterization of Graphene Nano-ribbon Resonator

Saumil Desai , **Ankur Pandya** , **and Mitesh B. Panchal**

Abstract Nowadays, the attention-seeking characteristics of graphene material used for making nano-resonator, in particular, the capability of atomic level sensing, have unlocked new dimensions to develop the bio/nano-sensing technologies. Graphene in pristine form is non-piezoelectric material. To stimulate piezoelectricity into grapheme, a point or line defect, adatoms or mechanical/thermal strain can be applied. Natural frequency is an important aspect of piezoelectric resonator. In the present work, lithium adatoms are introduced onto the surface of graphene mono-layer nano-resonator. The present work deals with the different boundary conditions onto natural frequency of graphene nano-ribbon (GNR) resonator. Two boundary conditions including beam clamped at both ends and cantilevered are considered to illustrate the vibrational behaviour of mono-layer graphene nano-ribbon piezoelectric resonator. Due to size of nano-ribbon, Euler–Bernoulli beam theory is used to model the GNR.

Keywords Graphene nano-ribbon (GNR) · Natural frequency · Mode shape

1 Introduction

The decrease in physical dimensions of electromechanical systems (EMS) seem to have capabilities of working at high frequency range which is attention seeking in the recent time. Due to state-of-the-art manufacturing technology available, it has become possible to produce devices at nano-scale level. Modality ranging

S. Desai · M. B. Panchal
Department of Mechanical Engineering, Institute of Technology, Nirma University, Ahmedabad 382481, Gujarat, India
e-mail: saumil.desai@nirmauni.ac.in

M. B. Panchal
e-mail: mitesh.panchal@nirmauni.ac.in

A. Pandya (✉)
Department of Electronics & Communication Engineering, Institute of Technology, Nirma University, Ahmedabad 382481, Gujarat, India
e-mail: ankur.pandya@nirmauni.ac.in

from submicron sized resonators, switches and valves have already been used in various fields of engineering and science such as information processing, molecular/biological operation and detection, precision measurements to investigate the properties of a matter at a submicron level. The fundamental electromechanical system is a nano-scale resonator, i.e. a beam of material that oscillates to an applied force [1, 2]. It can be stated as a mechanical system in conjunction with an electronics control element to sense the perturbations persuaded to it to sense and results in the form of electrical signal, i.e., frequency at giga hertz level which was not attainable in micro-electromechanical system. NEMS possess fascinating features in terms of high-quality factors in terms of 10–1000 and its sensor-based technologies for active mass and force detection at an atto-newton level, gas molecular level mass detection, virus detection, and heat capacities far below a yoctocalorie These remarkable features make NEMS versatile for applications such as sensors related to force sensitivity, chemical, biology and ultra-high frequency resonators [3–6].

Generally, cantilevers and doubly clamped configurations of the beams are used as active components in nano-scaled resonator which eventually vibrate at high fundamental frequency in terms of GHz [7–9]. There are various materials available for manufacturing of these nano-scaled resonator like ZnO, lead zirconate titanate (PZT), SiO_2, GaAs, and graphene. Out of these materials, graphene possesses Young's modulus of elasticity approximately 1 TPa, poisson's ratio of 0.14, and density is $2200 \, kg/m^3$ [10, 11]. Though structure of graphene is two-dimensional, mono-atomic layer material, still it owns Young's modulus about 1 TPa, and it can be strained up to 25% [12] further than any other two-dimensional layered material used for NEMS resonator. Despite with excellent mechanical properties, graphene in its pristine form is not piezoelectric in nature due to its symmetry. To make graphene piezoelectric, symmetry must be broken by generating point and line defect, mechanical/thermal strain, and adatoms. This piezoelectric aspect with mechanical feature of bearing high external force with admirable electronic transport properties [10, 13] advocate graphene a chosen material for building of two-dimensional (due to high surface area to volume ratio) [14] NEMS that can be tuned to high dynamic range of frequency used in radio frequency communications and biological/molecular level detection using deformation technique. In addition to this, graphene is a virtually massless. This property is used to develop electrode made of graphene to avoid damping in number of implementations which include optoelectronics, nano-electronics and energy devices [15]. Another area of interest in the recent time is to detect the organic vapour and organic compound at molecular level with graphene. The sensors made of graphene have been experimented for on-site detection of glucose in blood (University of Minnesota), Escherichia coli (Indian Institute of Science, Bangalore) and organic vapours (Case Western Reserve University) [16].

2 Literature Review

Recent investigations on nano-resonators made of graphene sheets have opened a new area which promises ultrasensitive sensors. By experimenting nano-electromechanical systems made of mono-layer graphene sheet and multilayer graphene sheets. Bunch et al. [17] observed that the high Young's modulus close to 1 TPa, extremely low mass and the planar geometry of sheets make these nano-resonators ideal candidates for mass sensors. This graphene sheet in its folded form which is known as carbon nano-tube (CNT) has proven its applicability in separating the atoms and molecules under torsional loading. Arash and Wang [18] proposed a technique for an effective molecular separation. They concluded that separation is very sensitive to the value of torsion angle. They applied an impulse waves propagating along CNT to change the Vander-Wal force between the wall of nanotube and molecules inside the nanotube. Variation in Vander-Wal force induces the separation of molecules from the nano-tube wall and thus impels the motion of molecules to generate the molecular transfer phenomena inside the nano-tube across its length. This phenomenon is used for uninterrupted circulation of blood despite presence of the excessive lipid clots. Mahdvi et al. [19] studied the nonlinear vibration of single wall CNT imbedded in polymer matrices. In the work, a nonlinear deflection is considered to model the Vander-Wal forces between CNT and matrix for the nano-tube. They derived the relation between amplitudes and natural frequencies of the nano-tubes which is observed sensitive to the end conditions and aspect ratios of the tube. Arash et al. [20] probed the free vibration of single wall CNTs and double wall CNTs with different end conditions using molecular dynamics (MD) simulation at ambient temperature. The outcomes from their simulation direct that fundamental resonant frequency of a doubly clamped single wall CNT is inversely proportional to the aspect ratio of the tube. From their simulation results, it is also observed that the end conditions of the resonator have strong influence on resonant frequency of CNTs. The fundamental resonant frequency of a CNT with doubly clamped condition is the highest than simply supported and cantilever boundary conditions. Duan et al. [21] studied the free vibration of single walled CNT using molecular dynamics simulation and the non-local Timoshenko beam model. They studied the effect of boundary conditions and the aspect ratio of the nano-tube onto the natural frequencies of the single walled CNT and observed that the resonant frequency is influenced to both parameters, i.e., boundary conditions and aspect ratio.

Motivated by these information, the present work includes the graphene resonator in the form of nano-ribbon with lithium adatoms. In this work, two boundary conditions of nano-resonators are considered to obtain the vibration characteristics in the form of natural frequencies and mode shape. The boundary conditions are as follows: (1) doubly clamped and (2) cantilever.

3   Methodology

In this paper, the size of graphene nano-ribbon (GNR) is considered as follows: breadth, $b = 100$ nm, and thickness of monolayer, $t = 0.335$ nm, and length, L = 1000 nm. Two boundary conditions namely doubly clamped and cantilever beams are considered for nano-sized resonator to analyse the natural frequencies and their mode shapes. For the resonator working as piezoelectric sensor, it is important to know the natural frequency. There are various approaches available like Rayleigh–Ritz method, Hamilton's principle, Euler–Bernoulli thin beam theory, S. P. Timoshenko thick beam theory, etc. As for graphene nano-ribbon, the lateral dimensions are very small compared to longitudinal dimension, and effect of rotary inertia and shear are neglected due to mono-layer resonator, the Euler–Bernoulli thin beam theory is considered.

The equation of motion for the transverse vibration of beams is in the form of fourth-order partial differential equations with two boundary conditions at each end. For thin beams, a Euler–Bernoulli thin beam theory is expressed as follows:

$$\frac{\partial^2}{\partial x^2}\left(EI\frac{\partial^2 w}{\partial x^2}\right) + \rho A\frac{\partial^2 w}{\partial t^2} = 0 \tag{1}$$

where E = Modulus of elasticity of GNR, 1.1 TPa, I = Polar moment of Inertia, 0.310×10^{-36} m^4, ρ_{3D} = Density of GNR, 2200 kg/m^3, density of lithium atom, ρ_{3D} = 534 kg/m^3 and A = cross-sectional area of GNR, 33.5×10^{-18} m^2. Lithium atoms are adatoms on the surface of mono-layer GNR. Hence, the density of lithium atom is added to density of graphene.

For thin beam with uniform cross section, Eq. (1) is expressed as follows:

$$\left(EI\frac{\partial^4 w}{\partial x^4}\right) + \rho A\frac{\partial^2 w}{\partial t^2} = 0 \tag{2}$$

Using variables separation method, Eq. (2) can be written as two equations:

$$\left(\frac{d^4 y(x)}{dx^4}\right) + \frac{\rho A\omega^2}{EI}y(x) = 0 \tag{3}$$

$$\left(\frac{d^2 T(t)}{dt^2}\right) + \omega^2 T(t) = 0 \tag{4}$$

A solution of Eq. (3) is

$$y(x) = A\cosh(\beta x) + B\sinh(\beta x) + C\cos(x) + D_4\sin(x) \tag{5}$$

where A, B, C and D are coefficients which can be determined using boundary conditions of beam configuration and β is a constant equal to $\sqrt[4]{\frac{\rho A\omega^2}{EI}}$. While, a

solution of Eq. (4) is

$$T(t) = A_1\cos(\omega t) + B_1\sin(\omega t) \tag{6}$$

where A_1 and B_1 are constants which can be determined from the initial conditions.

The natural frequencies of the beam can be determined as follows

$$\omega = (\beta L)^2\sqrt{\frac{EI}{\rho AL^4}} \tag{7}$$

Equation (5) is known as mode shape function of the beam with natural frequency of vibration, ω. A beam is continuous system. Therefore, a beam can be discretized into 'n' masses with one natural frequency associated with each mass. If a discretized mass is designated with 'i', the corresponding frequency of resonance is designated as ω_i and associated normal mode is designated with W_i accordingly. So, the total free vibration of the beam be obtained by summing up all normal mode shapes as follows:

$$w(x,\ t) = \sum_{i=1}^{\infty} W_i(x)[A_1\cos(\omega t) + B_1\sin(\omega t)] \tag{8}$$

Using above equations, the natural frequencies with mode shapes have been determined for all the configurations.

For Doubly Clamped Beam

In this configuration, both ends are fixed, i.e., clamped. So displacement in transverse direction and slope of transverse direction are zero. Mathematically, it can be expressed as follows:

At one clamped end, i.e., $x = 0$, $y = 0$ and $\frac{dy}{dx} = 0$

At another clamped end, i.e., $x = L$, $y = 0$ and $\frac{dy}{dx} = 0$

So, the natural frequency can be found as follows:

$$\omega_n = (\beta_n L)^2 (EI/\rho AL^4)^{1/2} \tag{9}$$

Mode shape is obtained as follows:

$$W_n(x) = C_n\left[(\cos(\beta_n x) - \cosh(\beta_n x) - \frac{[\cos(\beta_n L) - \cos h(\beta_n L)][\sin(\beta_n x) - \sin h(\beta_n x)]}{\sin(\beta_n L) - \sin h(\beta_n L)}\right] \tag{10}$$

For Cantilever Beam,

In this configuration, one end is fixed, and another end is free. So, displacement in transverse direction and slope of transverse displacement are zero. At free end,

bending moment and shear force are zero. Mathematically, it can be expressed as follows: At clamped end, i.e., x = 0, y = 0 and $\frac{dy}{dx} = 0$

At free end, i.e., x = L, $EI\frac{d^2y}{dx^2} = 0$ and $EI\frac{d^3y}{dx^3} = 0$

So, the natural frequency can be found as follows:

$$\omega_n = (\beta_n L)^2 (EI/\rho AL^4)^{1/2} \tag{11}$$

Mode shape is obtained as follows:

$$W_n(x) = C_n\left[(cos(\beta_n x) - cosh(\beta_n x)\frac{[\cos(\beta_n L) - \cos h(\beta_n L)][\sin(\beta_n x) - \sin h(\beta_n x)]}{\sin(\beta_n L) - \sin h(\beta_n L)}\right] \tag{12}$$

4 Results

Table 1 summarizes the first six natural frequencies obtained for doubly clamped and cantilever configurations of GNR based high-frequency resonating system, using analytical and finite element method-based approaches. The error in the natural frequency obtained using analytical approach and finite element models is within $\pm 8\%$ which is considerable. Thus, the obtained results using finite element method-based simulation approaches are in agreement with the analytical results.

Figure 1 shows the natural frequency of resonator for doubly clamped and cantilever configurations of the resonator for the first six modes. The obtained results

Table 1 Natural frequency of the first six nodes for cantilever and doubly clamped configurations

Configuration	Mode	Natural frequency (Hz)		Error in %
		Analytical approach	Finite element approach	
Doubly clamped	1	6.86×10^6	6.93×10^6	-1.02041
	2	19.1×10^6	19.10×10^6	-0.52632
	3	37.3×10^6	37.46×10^6	-0.42895
	4	48.8×10^6	46.65×10^6	4.405738
	5	61.7×10^6	61.95×10^6	$-4.05E\text{-}01$
	6	92.2×10^6	92.5×10^6	-0.32538
Cantilever	1	1.08×10^6	1.05×10^6	3.543302
	2	6.85×10^6	6.81×10^6	0.583942
	3	19.05×10^6	19.08×10^6	-0.15748
	4	24.30×10^6	22.76×10^6	6.337449
	5	37.34×10^6	37.41×10^6	-0.18747
	6	61.72×10^6	61.87×10^6	-0.24303
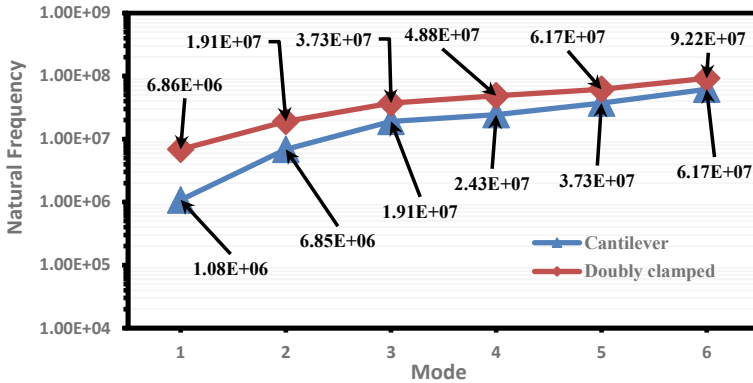
Fig. 1 Variation in natural frequency in GNR for considered doubly clamped and cantilever configurations for different modes of vibrations

state that natural frequency depends on the configuration of nano-resonator. From the results obtained, natural frequency for doubly clamped configuration is higher than cantilever configuration for dimensions considered of graphene nano-ribbon. Such results show that GNR with doubly clamped condition is more sensitive than the cantilever configuration. Similar results have been observed by many researchers [19–21].

Figure 2 shows the first six mode shapes obtained for both the considered boundary conditions of GNR (1000 nm × 100 nm) based high-frequency resonating systems namely cantilevered and doubly clamped. Figure 2 (a, c, e, g, i, k) show the modal analysis performed for GNR which is cantilever while Fig. 2 (b, d, f, h, j, l) show the modal analysis for doubly clamped GNR. The analyses for both configurations have been performed using ANSYS software. To find out the fundamental mode of frequency, the geometry has been constructed using design modeller. Here, GNR is considered as a beam element. As per the configuration, boundary conditions are applied. Two fixed boundary conditions are applied at the ends of GNR in doubly clamped configuration while in cantilever configuration, one end is clamped and another end is free. Using the boundary conditions, the displacement is zero at the ends in doubly clamped configuration while it is zero at fixed end and maximum at free end for all the modes of vibration as shown in figure.

5 Conclusion

In the present analysis, the natural frequency for the doubly clamped and cantilever configurations of GNR have been obtained using Euler-Bernoulli thin beam theory. The obtained results depict that the doubly clamped configuration of GNR is more sensitive than the cantilever boundary condition. If the percentage of decrease

(a)

(b)

(c)

(d)

(e)

(f)
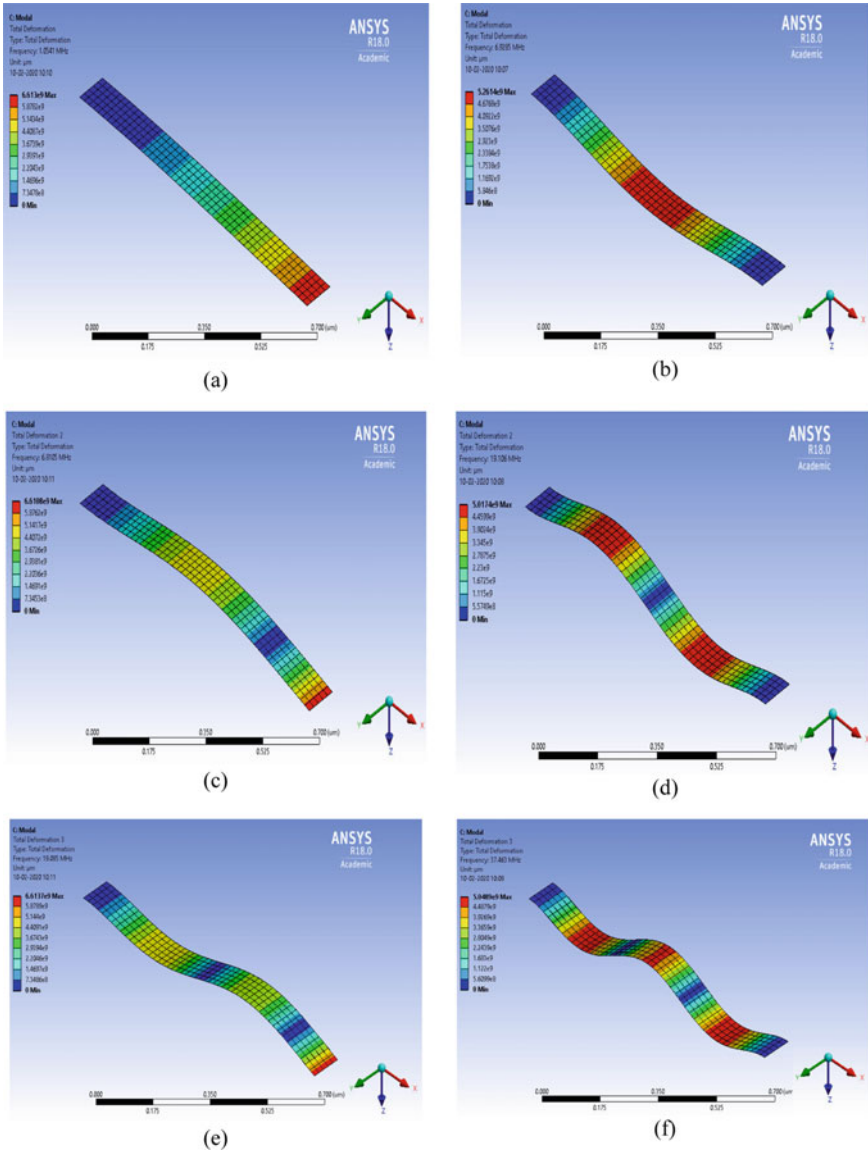
Fig. 2 (**a**, **c**, **e**, **g**, **i**, **k**) Mode shapes of GNR (1000 nm X 100 nm) for cantilever con-figuration and (**b**, **d**, **f**, **h**, **j**, **l**) Mode shapes of GNR (1000 nm X 100 nm) for doubly clamped configuration

(g)

(h)

(i)

(j)

(k)

(l)
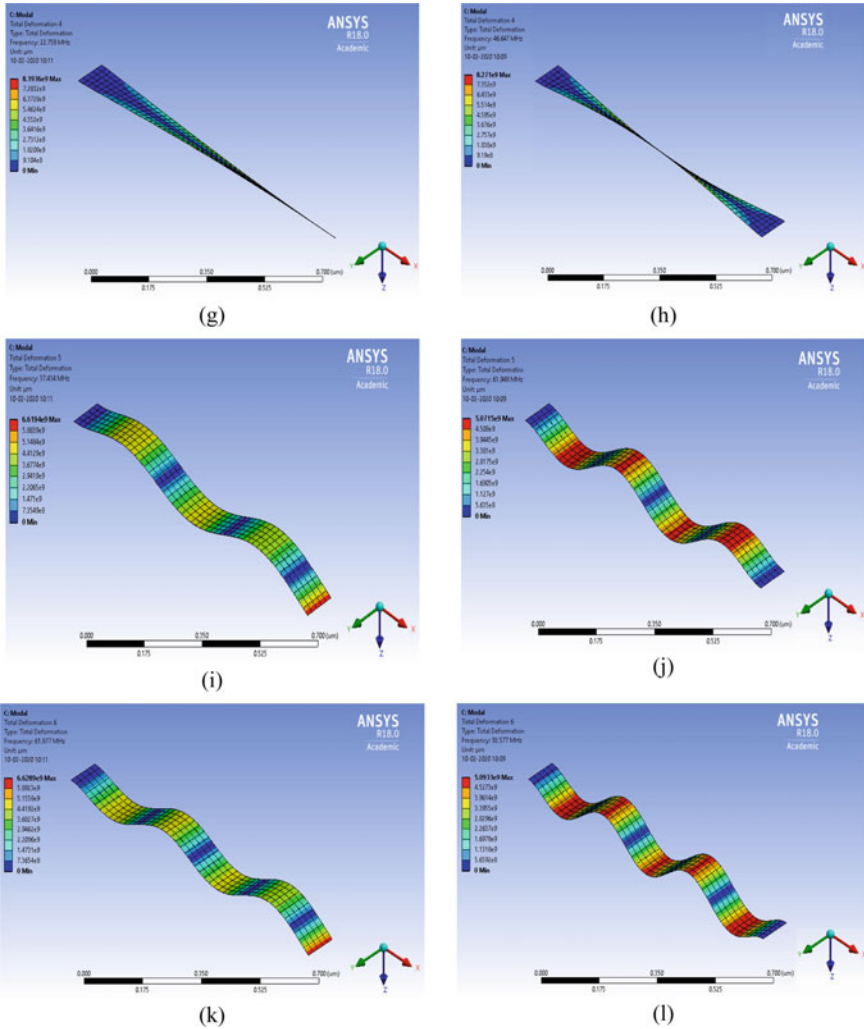
Fig. 2 (continued)

is measured using frequency obtained though analytical method, the frequency decreases from 84% to 33% for cantilever configuration. Based on this, it can be concluded that, the natural frequency is sensitive to the boundary conditions which is helpful to adopt the configuration while designing the nano-sensor based on the sensitivity. Also the mode shape analysis has been performed for doubly clamped and cantilever boundary conditions of GNR for first six modes of frequency. The error in the natural frequency for all the modes lies within $\pm 8\%$ using which it can be considered that the results obtained using analytical approach are satisfactory with the result obtained through finite element method. The performed analysis can be

useful for the practical realization of GNR based nano-mechanical resonator system as different possible sensing devices, which can be tuned to for higher dynamic range of frequency.

References

1. Verbiest, G. J., Kirchhof, J. N., Sonntag, J., Goldsche, M., Khodkov, T., & Stampfer, C. (2018). Detecting ultrasound vibrations with graphene resonator. *ACS, 18,* 5132–5137.
2. Craighead, H. (2000). Nanoelectromechanical systems. *Science, 290,* 1532–1535.
3. Cleland, A., & Roukes, M. (1996). Fabrication of high frequency nanometer scale mechanical resonators from bulk Si crystals. *Applied Physics Letters, 69,* 2653–2655.
4. Roukes, M. (1999). Yoctocalorimetry: phonon counting in nanostructures. *Physica B: Condensed Matter, 263,* 1–15.
5. Rueckes, T., Kim, K., Joselevich, E., Tseng, G., Cheung, C., & Lieber, C. (2000), Carbon nanotube-based non-volatile random access memory for molecular computing. *Science, 289,* 94–97.
6. Ilic, B., Craighead, H., Krylov, S., Senaratne, W., Ober, C., & Neuzil, P. (2004). Attogram detection using nanoelectromechanical oscillators. *Journal of Applied Physics, 95,* 3694–3703.
7. Liu, C., Qian, D., Qingmei, G., Chicheng, Ma., & Shuchang, Y. (2017). Axial control for nonlinear resonances of electrostatically actuated nanobeam with graphene sensor. *Applied Mathematics and Mechanics, 38*(4), 527–542.
8. Panchal, M. B., & Upadhyay, S. H. (2012). Doubly-clamped single walled boron nitride nanotube based nanomechanical resonators: a computational investigation of their behavior. *Journal of Nanotechnology in Engineering and Medicine, 3*(4).
9. Desai, J. A., & Panchal, M. B. (2019). Vibrational characterization of wavy atomic structures of single walled boron nitride nanotubes. *The European Physical Journal Plus, 134,* 136.
10. Qian, Z., Hui, Y., Liu, F., Kang, S., Kar, S., & Rinaldi, M. (2016). Graphene–aluminum nitride NEMS resonant infrared detector. *Microsystems & Nanoengineering, 2,* 1–7.
11. Weaver, W. Jr., Timoshenko, S., & Young, D. (1990). Vibration problems in engineering, Fifth Edition. Wiley.
12. Ong, M., & Reed, E. (2012). Engineered piezoelectricity in graphene. *ACS Nano, 6*(2), 1387.
13. Akita, S., Nakayama, Y., Mizooka, S., Takano, Y., Okawa, T., Miyatake, Y., & Nosaka, T. (2001). Nanotweezers consisting of carbon nanotubes operating in an atomic force microscope. *Applied Physics Letters, 79*(11), 1691–1693.
14. Pandya, A., & Jha, P. (2017). Electron Transport Parameters Study for Transition Metal Doped armchair graphene nanoribbon via Acoustical Phonon Interactions. *Journal of Electronic Materials, 46,* 2340–2346.
15. Kim, P., & Lieber, C. (1999). Nanotube nanotweezers. *Science, 286,* 2148–2150.
16. Bogue, R. (2014). Graphene sensors: A review of recent developments. *Sensor Review, 34,* 233–238.
17. Bunch, J. S., Van Der Zande, A. M., Verbridge, S. S., Frank, I. W., Tanenbaum, D. M., Parpia, J. M., Craighead, H. G., & McEuen P. L. (2007). Electromechanical resonators from graphene sheets. *Science, 315*(5811), 490–493.
18. Arash, B., Jiang, J. W., & Rabczuk, T. (2015). A review on nanomechanical resonators and their applications in sensors and molecular transportation. *Applied physics reviews, 2*(2), 021301.
19. Mahdavi, M. H., Jiang, L. Y., & Sun, X. (2009). Nonlinear vibration of a single-walled carbon nanotube embedded in a polymer matrix aroused by interfacial van der Waals forces. *Journal of Applied Physics, 106*(11), 114309.
20. Arash, B., & Ansari, R. (2010). Evaluation of nonlocal parameter in the vibrations of single-walled carbon nanotubes with initial strain. *Physica E: Low-dimensional Systems and Nanostructures, 42*(8), 2058–2064.

21. Duan, W. H., Wang, C. M., & Zhang Y. Y. (2007). Calibration of nonlocal scaling effect parameter for free vibration of carbon nanotubes by molecular dynamics. *Journal of applied physics, 101*(2), 024305.

Effect of Feed Rate on Bead Dimensions in TIG Welding

Rudra Pratap Singh, Abhishek Chauhan, Ashu Kumar Verma, and Abhishek Mishra

Abstract In every industry, some types of machines are used, and generally, the parts of machines are connected to each other with joints. The joints should be strong enough to bear the applied load to the structure. Welding is an important method of joining. In any welding process, the mechanical properties of the weld are closely related to the dimensions of the bead. In this investigation, the real experiments were performed with tungsten inert gas welding process to analyze the effect of feed rate on the dimensions of the bead. The input variables except the feed rate were fixed, as the current at 200 A, voltage at 10.5 V, travel speed or welding speed at 4.19 mm/s for whole the experimentation period. Only the rate of feed of electrode wire was varied, and the effect of this variation on weld width, depth of penetration, and reinforcement height was studied. Total 6 pairs of mild steel plates of dimensions 75 mm × 50 mm × 5 mm were welded for six variations of feed rate. The results were tabulated and were expressed in three diagrams one for depth of penetration, one for reinforcement height, and one for weld width. This study explains the sensitivity analysis of the effect of the feed rate on the three dimensions of the weld bead.

Keywords Tungsten inert gas welding · Feed rate · Weld bead · Input process parameters · Reinforcement height

R. Pratap Singh · A. Chauhan (✉) · A. K. Verma · A. Mishra
Department of Mechanical Engineering, GLA University, Mathura 281406, India
e-mail: abhishek.chauhan_me17@gla.ac.in

R. Pratap Singh
e-mail: rudra.singh@gla.ac.in

A. K. Verma
e-mail: ashu.verma_me17@gla.ac.in

A. Mishra
e-mail: abhishek.mishra_me17@gla.ac.in

1 Introduction

Joining of different parts of any structure is often required to work efficiently. These parts may be of dissimilar metals [1]. A large number of problems occur in dissimilar welding which may cause cracking and reduction in strength and other properties of weld. To overcome this problem, the study is required for welding process parameters and their effect on mechanical properties of the weld. Mechanical properties of the weld are related to the dimensions of the weld [2]. The weld width should be optimum, and if it is more or less than the optimum value, the mechanical properties may be lacking. The reinforcement height is the height up to which the weld is extended over the surface of the base plate. If we talk as a mechanical engineer, it should be zero as if it is any positive or negative value there will be stress concentration which is dangerous for the structures as it will reduce the mechanical properties of the weld [3]. If we talk as a metallurgical engineer, reinforcement height should be as much as possible; because during welding some properties degrade so cross-sectional area should be high enough to bear the load [4]. The depth of penetration is the distance up to which under the work pieces the mixing of base metal and electrode material takes place. The value of depth of penetration should be as much as possible, but the volume of weld material in a particular condition is fixed. This indicates that the product of depth of penetration, reinforcement height, and weld width is fixed in any particular condition, so if depth of penetration is large, the product of weld width and reinforcement height will be decreased, this can be explained similarly for other dimensions also. For better strength, the optimum values of depth of penetration, reinforcement height, and weld width are desired [5]. There are several input parameters which affect the dimension of the weld bead. In these input parameters current, voltage, speed of welding, feed rate, electrode diameter, etc., are very important. Feed rate was considered for the study in this work. The welding process for this study was taken as tungsten inert gas (TIG) welding. TIG process uses non-consumable tungsten electrode in the torch with a constant current welding power supply. Current generally used is in the range of 3–300 A, and the voltage used in general is in between 10 and 35 V. it may be manual or semi-automatic [6]. Filler metal may or may not be used. Argon helium mixture is generally used as shielding gases to protect the weld from atmospheric contamination [7]. Several materials ferrous and non-ferrous can be welded by TIG process [8]. A stronger weld can be achieved for sensitive materials like aluminum, magnesium, and copper alloys also. The sensitive metals react rapidly with air to form contaminations in other processes of welding. If shallow weld is desired, direct current electrode positive is used. If high current of about 600A is used for welding, then water cooling is required, otherwise air cooling is preferred [9]. Inside diameter of nozzle is kept about three times the diameter of electrode for the better performance of the tungsten inert gas welding process.

2 Experimental Procedure

TIG welding process is an arc welding process in which non-consumable electrodes are used with or without filler metals. Mild steel plates of dimensions 75 mm × 50 mm × 5 mm were used for making the weld. The plates were cut with the help of hack saw. The power source is a rectifier from which the power is supplied to the work pieces with the help of a torch and tungsten electrode. An electric arc is created in between the work piece and the tungsten electrode. The energy is conducted through the arc and a column of highly ionized gas and metal vapors. The temperature of about twenty thousand degree centigrade is produced in this process. This high heat is used to melt the material and to form the joint. The schematic diagram of a TIG welding system is shown in Fig. 1. The experimental setup of TIG welding is shown in Fig. 2, and the sound weld is shown in Fig. 3.

To investigate the effect of feed rate on the dimensions of weld bead, 12 mild steel plates of dimensions of 75 mm × 50 mm × 5 mm were cut from a long plate with the help of a power hack saw. These pieces were rubbed with emery paper to remove rust dust, etc., so that after welding, the contaminants should be out of the weld portion. The welding current was fixed as 200 A, the voltage was fixed at 10.5 V, and travel speed of welding was fixed as 4.19 mm/s. There were total six welded joints developed to study the effect of feed rate. The feed rate were taken as 2.12 mm/s, 4.23 mm/s, 10.58 mm/s, 12.70 mm/s, 16.93 mm/s, and 21.17 mm/s, respectively. The weld beads were sectioned transversely at two surfaces in such a way that middle portion containing 1 mm thick complete portion containing weld, heat-affected zone, and base metal were selected for investigation. The welds are generally not proper at start and at the end of the work pieces due to several reasons, so these portions are not proper for the study hence these portions are removed. The sectioned parts were ground with the help of emery belt grinders of grades 0, 2, and 3, so that weld width, depth of penetration, and reinforcement height become clear and visible. The ground portions were polished with double disk polishing machine. Etching process was done to the polished pieces with the help of a mixture of 2% nitric acid and 98% ethyl alcohol solution. The weld width, depth of penetration, and reinforcement

Fig. 1 Schematics diagram of TIG welding system

Fig. 2 Experimental setup

Fig. 3 Weld bead produces
using TIG welding process
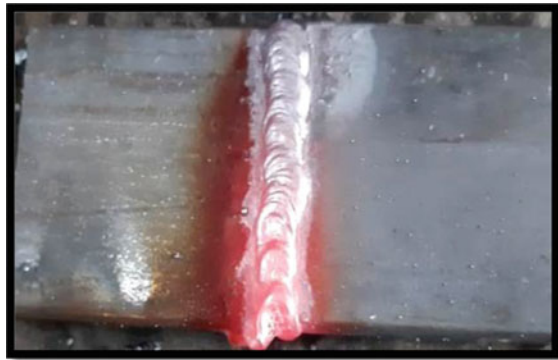
height were measured for every weld with the help of digital sliding calipers and
given in Table 1. The effect of feed rate was studied with the help of the data of the
table showing the relation between feed rate with weld width, reinforcement height,
and depth of penetration.

Table 1 Variation of weld bead, depth of penetration, and reinforcement height

SN	A	V	S (Travel speed) (mm/s)	F (Feed rate) (mm/s)	W W(mm)	DOP (mm)	RH (mm)
1	200	10.5	4.19	2.12	6.64	1.51	0.21
2	200	10.5	4.19	4.23	8.00	1.50	0.34
3	200	10.5	4.19	10.58	7.86	1.06	0.59
4	200	10.5	4.19	12.70	8.12	1.11	0.69
5	200	10.5	4.19	16.93	8.66	0.72	0.82
6	200	10.5	4.19	21.17	8.75	0.55	0.94

3 Result and Discussion

3.1 Effect of Feed Rate on Weld Width

Figure 4 shows the effect of feed rate on depth of penetration. The other input variables were kept at fixed values as the current at 200 A, welding voltage at 10.5 V, and speed of welding at 4.19 mm/s. At the feed rate of 2.12 mm/s, the weld width was 6.64 mm. When the feed rate was increased from 2.12 to 4.23 mm/s, the weld width increased from 6.64 to 8.00 mm. If the feed rate was increased from 4.23 to 10.58 mm/s, the weld width decreased from 8.00 to 7.86 mm. If the feed rate was increased from 10.58 to 12.70 mm/s, the weld width increased from 7.86 to 8.12 mm. If the feed rate was increased from 12.70 to 16.93 mm/s, the weld width increased from 8.12 to 8.66 mm. If the feed rate was increased from 16.93 to 21.17 mm/s, the weld width increased from 8.66 to 8.75 mm.

The variation of weld width with feed rate is according to the normal principles of physics. The feed rate is the length of electrode wire consumed per unit time. As the current and voltage were fixed, so the input power was fixed, but more mass of electrode was deposited if feed rate was increased. This indicates that the temperature
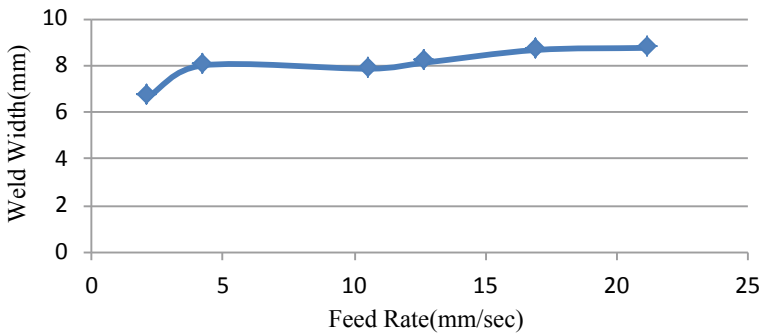
Fig. 4 Effect of feed rate on weld width

of molten part will be less which is the indication of low depth of penetration and more mass on the surface. The product of depth of penetration, reinforcement height, and weld width is proportional to the molten volume, so if depth of penetration is reduced the product of reinforcement height and weld width will be increased. The effect of feed rate on the reinforcement height is less, but it is increasing in normal condition. If feed rate was increased from 4.23 to 10.58 mm/s, the weld width decreased slightly which indicates that reinforcement height increased more in this region.

3.2 Effect of Feed Rate on Depth of Penetration

Figure 5 shows the effect of feed rate on depth of penetration. The other input variables were kept at fixed values as the current at 200 A, welding voltage at 10.5 V, and speed of welding at 4.19 mm/s. At the feed rate of 2.12 mm/s, the depth of penetration was 1.51 mm. When the feed rate was increased from 2.12 to 4.23 mm/s, the depth of penetration reduced from 1.51 to 1.50 mm. If the feed rate was increased from 4.23 to 10.58 mm/s, the depth of penetration decreased from 1.50 to 1.06 mm. If the feed rate was increased from 10.58 to 12.70 mm/s, the depth of penetration increased from 1.06 to 1.11 mm. If the feed rate was increased from 12.70 to 16.93 mm/s, the depth of penetration decreased from 1.11 to 0.72 mm. If the feed rate was increased from 16.93 to 21.17 mm/s, the depth of penetration decreased from 0.72 to 0.55 mm.

The variation of depth of penetration with feed rate is according to the normal principles of physics. Normally, the depth of penetration decreases with increase in feed rate. The feed rate is the length of electrode wire consumed per unit time. As the current and voltage were fixed, so the input power was fixed, but more mass of electrode was deposited if feed rate was increased. This indicates that the temperature of molten part will be less which is the indication of low depth of penetration and more mass on the surface. The product of depth of penetration, reinforcement height, and weld width is proportional to the molten volume, so if depth of penetration is reduced, the product of reinforcement height and weld width will be increased. The effect of feed rate on the reinforcement height is more, but it is increasing in normal condition
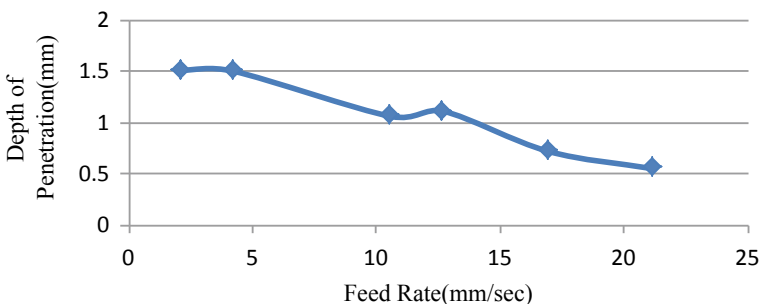
Fig. 5 Effect of feed rate on depth of penetration

if feed rate is increased. If feed rate was increased from 10.58 to 12.70 mm/s, the depth of penetration increased slightly, which indicates that reinforcement height or weld width decreased more in this region.

3.3 Effect of Feed Rate on Reinforcement Height

Figure 6 shows the effect of feed rate on reinforcement height. The other input variables were kept at fixed values as the current at 200 A, welding voltage at 10.5 V, and speed of welding at 4.19 mm/s. At the feed rate of 2.12 mm/s, the reinforcement height was 0.21 mm. When the feed rate was increased from 2.12 to 4.23 mm/s, the reinforcement height increased from 0.21 to 0.34 mm. If the feed rate was increased from 4.23 to 10.58 mm/s, the reinforcement height increased from 0.34 to 0.59 mm. If the feed rate was increased from 10.58 to 12.70 mm/s, the reinforcement height increased from 0.59 to 0.69 mm. If the feed rate was increases from 12.70 to 16.93 mm/s, the reinforcement height increased from 0.69 to 0.82 mm. If the feed rate was increased from 16.93 to 21.17 mm/s, the reinforcement height increased from 0.82 to 0.94 mm.

The variation of reinforcement height with feed rate is according to the normal principles of physics. The feed rate is the length of electrode wire consumed per unit time. As the current and voltage were fixed, so the input power was fixed, but more mass of electrode was deposited if feed rate was increased. This indicates that the temperature of molten part will be less which is the indication of low depth of penetration and more mass on the surface. The product of depth of penetration, reinforcement height, and weld width is proportional to the molten volume, so if depth of penetration is reduced, the product of reinforcement height and weld width will be increased. The effect of feed rate on the reinforcement height is large and is increasing in normal condition if feed rate is increased. The whole graph has this normal behavior.
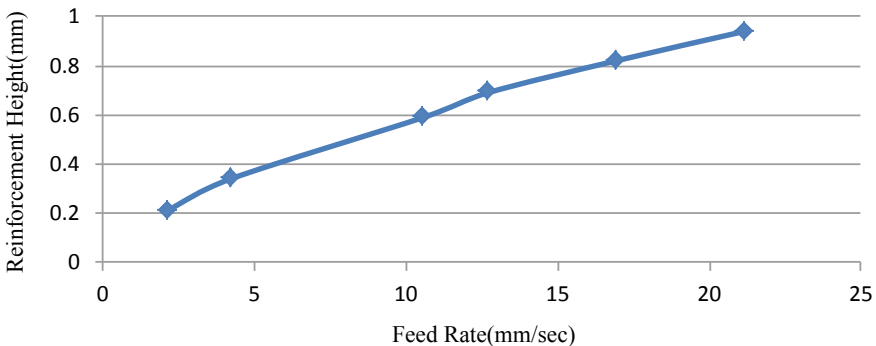
Fig. 6 Effect of feed rate on reinforcement height

4 Conclusions

The shape of weld bead in case of a welded joint ascertains the mechanical properties of the joint. Weld joint can be designed having optimum mechanical properties with some bead dimensions, which can be recognized with the help of some experiments. This work was aimed to recognize the effect of feed rate on the bead dimensions, which can be used to determine the mechanical properties of the weld. In this work, the relationships of feed rate with weld width, reinforcement height, and depth of penetration are represented with the help of some diagrams. The experimental results obtained indicate that:

1. With increasing in feed rate from 2.12 to 21.17 mm/s, the general trend of the weld width was found to increase from 6.64 to 8.75 mm but once it was opposite to its nature also. For feed rate increment from 4.23 to 10.58 mm/s, the weld width slightly decreased as the reinforcement height compensated it.
2. With increasing in feed rate from 2.12 to 21.17 mm/s, the general trend of the depth of penetration was found to decrease from 1.51 to 0.55 mm but once it was opposite to its nature also. For feed rate increment from 10.58 to 12.70 mm/s, the depth of penetration increased from 1.06 mm to 1.11 mm, and this was due to the product of weld width and reinforcement height reduced to compensate the depth of penetration.
3. With increasing in feed rate from 2.12 to 21.17 mm/s, the general trend of the weld width was found to increase from 0.21 to 0.94 mm. The trend was followed throughout the range of experimentation without any exception.
4. The optimum value of feed rate can be selected as per requirement of weld width, depth of penetration, and the reinforcement height with the help of this work.

References

1. Yuri, T., Ogata, T., Saito, M., & Hirayama, Y. (2000). Effect of welding structure and δ-ferrite on fatigue properties for TIG welded austenitic stainless steels at cryogenic temperatures. *Cryogenics, 40,* 251–259.
2. Xi-he, W., Ji-tai, N., Shao-kang, G., Le-jun, W., & Dong-feng, C. (2009). Investigation on TIG welding of SiCp-reinforced aluminum–matrix composite using mixed shielding gas and Al–Si filler. *Materials Science and Engineering A, 499*(1), 106–110.
3. Mandal, S., Das, V. V., Debata, M., Panigrahi, A., Sengupta, P., Rajendran, A.,… & Basu, S. (2019). Study of pore morphology, microstructure, and cell adhesion behaviour in porous Ti–6Al–4V scaffolds. *Emergent Materials*, *2*(4), 453–462.
4. Hussain, A. K., Lateef, A., Javed, M., & Pramesh, T. (2010). Influence of Welding Speed on Tensile Strength of Welded Joint in TIG Welding Process. International Journal of Applied Engineering Research, Dindigul, 1(3), 518-527.
5. Şimşek, M., Aldemir, S. D., & Gümüşderelioğlu, M. (2019). Anticellular PEO coatings on titanium surfaces by sequential electrospinning and crosslinking processes. *Emergent Materials, 2*(2), 169–179.
6. Tseng, K. H., & Hsu, C. Y. (2011). Performance of activated TIG process in austenitic stainless steel welds. *Journal of Materials Processing Technology, 211*(3), 503–512.

7. Narang, H. K., Singh, U. P., Mahapatra, M. M., & Jha, P. K. (2011). Prediction of the weld pool geometry of TIG arc welding by using fuzzy logic controller. International Journal of Engineering, Science and Technology, 3(9), 77-85.
8. Karunakaran, N. (2012). Effect of pulsed current on temperature distribution, weld bead profiles and characteristics of GTA welded stainless steel joints. *International Journal of Engineering and Technology, 2*(12).
9. Raveendra, A., & Kumar, B. R. (2013). Experimental study on pulsed and non-pulsed current TIG welding of stainless steel sheet (SS304). *International Journal of Innovative Research in Science, Engineering and Technology, 2*(6).

A Review of Effect of Welding Parameters on the Structure and Properties of the Weld in Shielded Metal Arc Welding Process

Rudra Pratap Singh, Abhishek Mishra, Abhishek Chauhan, and Ashu Kumar Verma

Abstract The shielded metal arc welding (SMAW) is one among the most common welding processes that is generally used in the fabrication process in industries to join components, as its operation is easy. Shielded metal arc welding is a prominent process of metal fabrication which finds its best usage in shipbuilding operations, construction, and metal structure industries. This paper investigates the descriptions and findings of different researchers. Several researchers performed experiments on SMAW and investigated the effect of rate of welding heat input on the structure and properties of the materials. The heat rate is the function of welding speed, welding current, and welding voltage. The properties of the materials are affected by welding current, welding voltage, and welding speed. This review research paper includes the selected important research papers which describe the effect of current, voltage, and speed of welding on the effect of mechanical and microstructural properties. The joints produced by shielded metal arc welding process have enough strength, and when these joints are compared with any other joints, the cost is relatively low.

Keywords Shielded metal arc welding · Polarity · Welding current · Weld · Strength · Process · Heat rate

R. Pratap Singh · A. Mishra (✉) · A. Chauhan · A. K. Verma
Department of Mechanical Engineering, GLA University, Mathura 281406, India
e-mail: abhishek.mishra_me17@gla.ac.in

R. Pratap Singh
e-mail: rudra.singh@gla.ac.in

A. Chauhan
e-mail: abhishek.chauhan_me17@gla.ac.in

A. K. Verma
e-mail: ashu.verma_me17@gla.ac.in

1 Introduction

Welding is a joining process in which two or more faying surfaces are joined together permanently to form one surface. Welding is a very reliable, "high-tech," and cost-effective process for materials to be joined. Manufacturers prefer welding process over any other technique to join the metals and their alloys efficiently. Welding is used in several constructional applications like buildings, bridges, computers, vehicles, etc., and some of these applications cannot be completed without applying the welding process. Many varieties of materials and products are used in welding process by using advanced developed technologies including laser and plasma arcs. Shielded metal arc welding process is one such process that finds its usage in small-scale industries; it is one of the most widely used welding processes in the world. It requires a human welder to weld and is often termed as manual metal arc welding process since it is not automated and is difficult to use in large-scale industries. It is also known as flux shielded arc welding process or stick welding process. In the process of shielded metal arc welding, a consumable electrode containing flux is used. The main advantage of the flux is to avoid the contact of atmospheric gases with the weld zone by providing a layer of slag. An electric arc is generated in between the work and the tip of the electrode using either the direct current or alternating current from a power source. There are several important terms in shielded metal arc welding process like arc voltage, welding current, welding speed, heat input, electrode, weld heat-affected zone, power supply, and polarity.

2 Literature Review

Molleda et al., performed the experiment on the mild steel welding with SMAW process and noticed spattering at the time of welding which was the result of the liquid metal droplets that are thrown out from the weld pool due to the action of tiny droplets from the electrode. They took the covered electrode and produced a resulting weld on the base metal. They found that the spatter particle welds to the base material and transfers heat very quickly to it and produces a very thin re-crystallized region in the heat-affected zone [1].

Ravindra Kumar et al., examined a low carbon steel ASTM SA210 GrA1 weld using shielded metal arc welding process. On HAZ, base metal, and the weld metal, the oxidation studies were made after the plates were exposed to air under cyclic conditions at 900 °C. Kinetics of oxidation was developed using the technique called the thermo-gravimetric technique. The analysis on the oxidation products was performed using scanning electron microscopy/energy dispersive and X-ray diffraction (XRD). The result made from XRD analysis was that the high intensity of Fe_2O_3 was formed as the base metal oxidizes in air and when compared at 900 °C, thicker oxide scale is formed on the base metal rather than the weld metal [2].

Goyal et al., noticed that the initial heating by arc which is having double ellipsoidal nature is the primary heat that is being transferred to the weld pool. They developed an analytical model. They used the different analytical techniques and considered two sources of heat which are not similar in nature and estimated the distribution of temperature in the region of HAZ and the weld pool. They told that the base metal which melts under the sway of two dissimilar heat sources can lead to the estimation of the profile of weld pool by evaluating the weld isotherms [3].

Tabatabaeipour et al., compared two different arc welding processes, the first one shielded metal arc welding process, and the second as gas tungsten arc welding processes. They performed the ultrasonic testing of these two welding processes and used the technique of time-of-flight diffraction (ToFD). B-scan images that were collected by using ToFD technique revealed that the specimen that was made from SMAW is much easier as compared to that of the specimen prepared by GTAW process, because waves are scattered to a greater extent in the latter case [4].

Gurpreet Singh Sidhuet al., studied the effect of consumable electrodes on the properties of a weld due to the intermixing of the weld metal from consumable electrode used in shielded metal arc welding process. They found that to attain the high productivity, high weld quality, economy, and strong weld, the flux is intermixed, and the chemical compositions of the electrode is changed to obtain the required cost-effective process and robust product structures [5].

Izzatul Aini Ibrahim et al., measured the hardness and microstructural changes as a consequence of using different process parameters of welding for mild steel with a thickness of 6 mm. They used welding speed, welding current, and voltage as the variables, performed hardness test, and studied the microstructure. They used current from 90 to 210 A and concluded that on increasing the current the depth of penetration increases. They also told that the depth of penetration is a function of arc voltage [6].

Pravinkumar et al., examined a material to find out the tensile strength using the vibration concept. They used stirring of the molten metal before its solidification. The conclusion that was derived reveals that as the molten metal is stirred, it increases the material strength [7].

Maridurai et al., investigated the tensile properties of carbon steel P91. They welded the root pass by three different processes namely tungsten inert gas welding process, submerged arc welding process, and shielded metal arc welding process. They studied the characteristics of fracture, impact strength, and tensile strength of the weld and the base metal in the three processes. They used crack tip opening displacement for their study [8].

Olawale et al., established correlation between heat treatment and some mechanical properties in shielded metal arc welding process. They selected carbon steel as the material and the AWS E6013 as electrode for their investigations. They kept the voltage as constant and the current as varying and subjected the heat treatment to work piece at different temperatures. They concluded that the hardness and ultimate tensile strength both increase with the increase of current before heat treatment, but after heat treatment these values decrease if current is increased [9].

Praveen Kumar et al., selected welding voltage, welding current, welding speed, and electrode angle as welding parameters for shielded metal arc welding process. They used ANOVA and conducted the experiments to analyze with orthogonal array [10].

Rohitjha et al., investigated two different weld designs. V grooved and flat surface welding joints were obtained with the help of SMAW process. They evaluated the mechanical properties like tensile strength, yield strength, and percentage elongation of weld metal for different welding current and welding speeds. They found that V joint has maximum ultimate tensile and yield strengths [11].

Rajeev Ranjan et al., tested the optimization of different welding process parameters which include the welding current, voltage, welding speed by evolving a mathematical model for a mild steel specimen for a sound weld deposit. They used various process parameters and the factorial design to disclose that there is a direct variation in the weld deposited area with the welding current and the welding voltage. Their study also revealed that the welding speed and the weld deposited area have an inverse relationship [12].

Rohitjha et al., investigated the effect of welding parameter, welding current, voltage, and heat input on mechanical properties like UTS of mild steel in SMAW process and evaluated the optimum welding current. The UTS of weld metal is to be investigated by using tensile testing machine, and the welding current is varying. They found that at 120 A, the tensile strength of weld metal is high, and after optimum value, if the current is increased, the value of UTS decreases [13].

Kchaou et al., used shielded metal arc welding process for two stainless steel plates and investigated the microstructure and mechanical properties of the weld. They found that the ductility decreases in weld metal in comparison with the base metal. They told that due to the rapid cooling of weld metal the microhardness of weld metal increases [14].

Olga Liskevych et al., measured the thermal efficiency and the heat input and developed a method which can be used for the determination of the metallurgical aspects using shielded metal arc welding process. They found that the results depend on the welding parameters, environmental conditions, the dimensions of the sample work, and the base metal. They used these parameters for the estimation of amount of heat loss from the surface of the welded plates [15].

Brajesh Kumar Singh et al., studied how the weldment properties are affected with the variations in the design of joints. They used samples for the study on IS 2062:E250 plates of mild steel with the help of shielded metal arc welding process. They used the variation in the geometry of the joint and studied and compared the effects of these variables on the properties of the plates of mild steel for different geometries. They concluded that double 'V' joint is more effective and superior to other joints in terms of the mechanical properties [16].

Abhishek et al., used FEM and ANSYS software to investigate the effect of temperature distribution in weld joint on residual stresses and distortion. They found that the distortion and residual stresses can be minimized by optimizing current, voltage, and speed of welding in shielded metal arc welding process [17].

Dutta et al., used optical and scanning electron micrograph to investigate the different regions of the weld and found that the peak temperature in the case of shielded metal arc welding process is lower than that in gas tungsten arc welding process by about 75 °C, and the duration of peak temperature is also less in the case of SMAW process [18].

Bbodule et al., compared shielded metal arc welding process with oxy-acetylene welding process using low carbon steel as the base material. They found that if heat input is increased, the yield strength, ultimate tensile strength, and hardness values decrease, and the 'V' grooved weld has better mechanical properties in comparison with that of the straight edged surface welds. They told that if toughness is increased, the hardness and tensile strength values decrease [19].

Deogade et al., performed thermal analysis of the heat-affected and weld zones of ferrite stainless plates welded by shielded metal arc welding process. The simulation was done by using ANSYS and three-dimensional finite element analyses. They analyzed the residual stress distribution with the temperature and warned that the higher heat input rates become dangerous for residual stresses in thin plates [20].

Raffi Mohammad et al., tried to matchup the mechanical and the microstructural changes of high stainless steel, which is free of nickel, by using different welding processes such as shielded metal arc welding, gas tungsten arc welding, and electron beam welding. They found that the weld obtained by shielded metal arc welding process is the cheapest of all but beneficial for general joining work [21].

Pengfei Baia et al., developed a sensing method, completely based on the arc voltage to sense the depth of penetration. In their method to imitate the beginning of the process, the work piece was made to act upon by a stationary arc for about 2 s. They used peak current and fluctuating voltage to describe the penetration status [22].

Vijayesh Rathi et al., used shielded metal arc welding process to establish relationship between microhardness and input welding parameters like heat input, voltage, current, and welding speed for weld and heat-affected zones. They found that at low heat input, the microhardness of weld metal decreases, but it increases for the heat-affected zone. They also concluded that in shielded metal arc welding process at lower heat input, better impact strength and hardness values are obtained. They told that at higher heat input, the cooling rate becomes higher; and hence, the cracks are developed in heat-affected zone and weld metal [23].

Shukla et al., analyzed the effect of different input welding parameters on depth of penetration for shielded metal arc welding process. They used AISI 1020 plates for welding and applied surface response method and concluded that welding current is the main input parameter which has very large effect on depth of penetration [24].

Chen et al., used S 690 Q grade steel to form butt weld and studied the effect of this steel on tensile strength of the weld. They found that S 690 Q grade increases tensile strength of the welded joint, but the relation in between these two cannot be established easily written with any equation but can be approximated by using some other tools [25].

Zhang et al., studied the weld of 12 Cr_2Mo_1R heat-resistant steel. They formed butt joint using arc welding process. They added different amount of phosphorous in

different welds and analyzed the variation of microstructure and impact strength of the weld with phosphorous and found that phosphorous makes the size of microstructure small which increases the impact strength of the weld. They found phosphorus to be highly depleted in the δ phase, which inhibits δ-phase precipitation by reducing δ-phase nucleation and growth in the weld [26].

Kumar et al., had experiments for performance of electrodes with arc welding process. They utilized probability density distribution and signal-processing technique in their work. They concluded that probability density distribution is a very good method to obtain almost actual value of the output for the given input values. They also found that different electrodes provide the property of their constituents, and also if current is constant, then smaller diameter electrode has greater energy density and larger depth of penetration [27].

Sumardiyanto and Sushilowati experimented low carbon steel, API5L using shielded metal arc welding process. They analyzed the effect of input welding parameters on mechanical properties of the weld. They used three different electrodes E 6010, E 7016, and E 7018 and two values of current as 90 and 100 A and concluded that depth of penetration increases with current and electrodes also have effect on mechanical properties of weld [28].

3 Conclusion

Ongoing through the investigations done by the selected researchers, some conclusions can be derived for input–output process parameters for the structure and properties of the weld obtained through shielded metal arc welding process. These can be summarized as below:

1. The mechanical properties of the weld have strong relation with the macro and microstructure of the weld obtained by shielded metal arc welding process.
2. If number of passes of weld is more, then complete transformation of delta ferrite to austenite is not possible due to the existence of differential heating and cooling rates in passes. This develops superior quality of weld having more tensile strength and hardness.
3. If arc voltage or welding current is increased, the hardness increases, but tensile and impact strength values decrease.
4. If voltage is increased, the weld width increases.
5. The microstructures of weld zone and heat-affected zone are entirely different.
6. Manganese, silicon, sulfur, etc., are alloyed to increase some specific properties of the weld.

4 Scope for Further Work

1. Little work is reported on metal transfer influencing chemical composition, bead geometry, strength, and metallurgy of weld in submerged arc welding process.
2. Transient study of current voltage in shielded metal arc welding requires more work, as it is the least searched area.
3. The optimum values of input output welding variables are not searched yet; it should be tried by utilizing MATLAB and ANN, etc., to simulate properly.
4. Application of magnetic field can be utilized properly to distribute the input heat of welding on the weld surface, so serious work over this area is needed.
5. The process is slow as after electrode consumption, new electrode rod requires some time in adjusting it with the electrode holder. Methods should be searched to have continuous feeding of electrode rod to work.
6. The process can be made semi-automatic by using some other arrangements like lathe machine in which lead of screw of lathe machine can be utilized to provide speed of welding as automatic.

References

1. Molleda, F., Mora, J., Molleda, J. R., Mora, E., & Mellor, B. G. (2007). The importance of spatter formed in shielded metal arc welding. *Materials Characterization, 58*, 936–940.
2. RavindraKumar, V. K., & Tewari, S. P: (2009). Oxidation behavior of base metal, weld metal and HAZ regions of SMAW weldment in ASTM SA210 GrA1 steel. *Journal of Alloys and Compounds, 479*, 432–435.
3. Goyal, V. K., Ghosh, P. K., & Saini, J. S. (2009). Analytical studies on thermal behaviour and geometry of weld pool in pulsed current gas metal arc welding. *Journal of Materials Processing Technology, 209*, 1318–1336.
4. Tabatabaeipour, S. M., & Honarvar, F. (2010). A comparative evaluation of ultrasonic testing of AISI 316L welds made by shielded metal arc welding and gas tungsten arc welding processes. *Materials Processing Technology, 210*, 1043–1050.
5. Sidhu, G. S., & Chatha, S. S. (2012). Role of shielded metal arc welding consumables on pipe weld joint. *International Journal of Emerging Technology and Advanced Engineering, 2*(12), 746–750.
6. Ibrahim, I. A., Mohamat, S. A., Amir, A., & Ghalib, A. (2012). The effect of gas metal arc welding (GMAW) processes on different welding parameters. *Procedia Engineering, 41*, 1502–1506.
7. Praveen Kumar, B. S., & Vijaykumar, Y. (2012, May). Optimization of shielded metal arc welding parameters for welding of pipes by using Taguchi approach, 4(5). ISSN 0975-5462.
8. Thirupathy, M., Rai, S., Sharma, S., & Palanisamy P. (2012, May–August). Analysis of tensile strength and fracture toughness using root pass of tig welding and subsequent passes of SMAW and saw of P91 material for boiler application. *International Journal of Mechanical Engineering and Technology (IJMET), 3*(2), 594–603. ISSN 0976-6359.
9. Olawale, J. O., Ibitoye, S. A., Oluwasegun, K. M., Shittu, M. D., & Ofoezie, R. C. (2012). Correlation between process variables in shielded metal-arc welding (SMAW) process and post weld heat treatment (PWHT) on some mechanical properties of low carbon steel welds. *Journal of Minerals and Materials Characterization and Engineering, 11*, 891–895. Published Online September 2012.

10. Praveen Kumar, B. S., & Vijayakumar, Y. (2012, September–October). Selection of optimum process parameters of shielded metal arc welding (SMAW) to weld steel pipes by design of experiments. *International Journal Of Engineering Research And Applications (IJERA), 2*(5), 377–381. ISSN: 2248-9622.

11. Rohit Jha, A. K. J. (2014, April). Investigating the effect of welding current on the tensile properties of SMAW welded mild steel joints. *International Journal of Engineering Research & Technology (IJERT), 3*(4). ISSN: 2278-0181.

12. Rajjevranjan. (2014, September). Parametric optimization of shielded metal arc welding processes by using factorial design approach. *International Journal of Scientific and Research Publications, 4*(9). ISSN 2250-3153.

13. Rohit Jha, A. K. J. (2014, June). Influence of welding current and joint design on the tensile properties of SMAW welded mild steel joints. *International Journal of Engineering Research and Applications, 4*(6) (Version 4), 106–111. ISSN: 2248-9622.

14. Kachaou, Y., Haddar, N., Henaff, G., & Elleuch, K. (2014, November). Micro structural, compositinal and mechanical investigation of shielded metal arc welding (SMAW) welded super austenitic UNS N08028 (Alloy 28) stainless steel. *Materials and Design.* Impact Factor: 3.5. https://doi.org/10.1016/j.matdes.2014.06.014.

15. Liskevych, O., & Scotti, A. (2015). Determination of the gross heat input in arc welding. *Journal of Materials Processing Technology, 225*, 139–150.

16. Singh, B. K., Jha, A. K., Singh, P. K. (2015). Effects of joint geometries on welding of mild steel by shielded metal arc welding (SMAW). *International Research Journal of Engineering and Technology*, 95–100.

17. Abhishek, B. P., Anil Kumar, G,. & Madhusudhan, T. (2015, May). Experimental and finite element analysis of thermally induced residual stresses for stainless steel 303grade using GMAW pocess. *International Research Journal of Engineering and Technology (IRJET), 2*(2). ISSN: 2395-0056.

18. Dutta, J., Pranith Kumar Reddy, P. (2015). Thermo mechanical and metallurgical analysis of SMA and GTA welded low carbon steel butt joints. *World Academy of Science, Engineering and Technology International Journal of Chemical, Molecular, Nuclear, Materials and Metallurgical Engineering, 9*(7).

19. Bodude, M. A., & Momohjimoh, I. (2015). Studies on effects of welding parameters on the mechanical properties of welded low-carbon steel. *Journal of Minerals and Materials Characterization and Engineering, 3*, 142–153. Published Online.

20. Deogade, S. R., Ambade, S. P., Patil, A. (2015, March–April). Finite element analysis of residual stresses on ferritic stainless steel using shield metal arc welding. *International Journal of Engineering Research and General Science, 3*(2). ISSN 2091-2730.

21. Raffimohammed, G., Reddy, M., & Srinivasa Rao, K. (2016). Welding of nickel free high nitrogen stainless steel: Microstructure and mechanical properties. Received 29 April 2016; revised 6 June 2016; accepted 7 June 2016.

22. Baia, P., Wanga, Z., Hua, S., Maa, S., & Liang, Y. (2017). Sensing of the weld penetration at the beginning of pulsed gas metal arc welding. *Manufacturing Processes, 28*, 343–350.

23. Rathi, V., & Hunny. (2018). Analyzing the effect of parameters on SMAW process. *International Journal of Emerging Research in Management &Technology, 4*(6). ISSN: 2278-9359.

24. Shukla, A. A., Joshi, V. S., Chel, A., & Shukla, B. A. (2018). Analysis of Shielded metal arc welding parameter on depth of penetration on aisi 1020 plates using response surface methodology. *ScienceDirect,* 239–246.

25. Chen, C., Chiew, S.-P., Zhao, M.-S., Lee, C.-K., & Fung, T.-C. (2019). Welding effect on tensile strength of grade S690Q steel butt joint. *Journal of Constructional Steel Research, 153,* 153–168.

26. Zhang, J., Chen, H., Fan, D., Huang, J., Yu, X., Feng, W., et al. (2019). Effects of phosphorus impurity on the microstructure and impact toughness of weld joint for the 12Cr2Mo1R heat resistant steel. *Journal of Manufacturing Processes, 38,* 453–461.

27. Kumar, V., Albert, S. K., & Chandrasekhar, N. (2019). Signal processing approach on weld data for evaluation of arc welding electrodes using probability density distributions. *Measurement, 133,* 23–32.
28. Sumardiyanto, D., & Susilowati, S. E. (2019). Effect of welding parameters on mechanical properties of low carbon steel API5L shielded metal arc welds. *American Journal of Materials Science, 9*(1), 15–21.

Thermal Cycling Effects on Microstructural Evolution and Hardness of Martensite 13wt.%Cr–4wt.%Ni Steel

Jai Singh and S. K. Nath

Abstract Martensitic 13wt.%Cr–4wt.%Ni steel (13-4 MSS) is widely used in underwater applications where it is exposed to severe fluid velocity. The severe service conditions cause its erosion which leads to a reduction in efficiency and large economic losses. To develop the erosion resistance steel, this is an attempt to strengthen the 13-4 MSS by processing a new heat treatment called thermal cycling treatment (TCT). The as-received steel (as-received) was subjected to TCT by using a thermomechanical simulator (Gleeble 3800). The microstructural characterization of as-received and the microstructural evolution due to TCT was analyzed by optical, electron microscopy, and XRD analysis. The microhardness of each phase and the bulk material hardness were determined to characterize the TCT. The progressive dissolution and the fragmentation of delta ferrite caused the removal of delta ferrite content from 12.7% (for as-received) to 6.3% (for treated). The bulk material hardness was found to be the function of the microhardness of martensite and the volume fraction of the delta ferrite. A 42% increase in the bulk material hardness was obtained by the present TCT.

Keywords Stainless steel · Thermal cycling treatment · Microstructure · Microhardness · Hardness

1 Introduction

Martensitic 13wt.%Cr–4wt.%Ni steel (13-4 MSS) is chiefly used to fabricate the hydro-turbine blades due to its good mechanical properties, and moderate erosion resistance [1]. But still, this undergoes a severe problem of erosion (slurry and cavitation) due to the silt present in the water and the flow conditions. So, attempts are

J. Singh
Centre of Nanotechnology, IIT Roorkee, Roorkee 247667, UK, India
e-mail: jsingh@nt.iitr.ac.in

S. K. Nath (✉)
Department of Metallurgical and Materials Engineering, IIT Roorkee, Roorkee 247667, UK, India
e-mail: indiafmt@iitr.ac.in

being made to increase its hardness, so that it can withstand for longer life. These attempts include different heat treatments [2], coatings [3], cladding [4], thermo-mechanical processing (TMP) [5], etc. The erosion performance is governed by the bulk properties, but some techniques improve only the surface properties. The other conventional heat treatments performed in literature are time-taking treatments. TMP treatments are difficult to experiment with.

Thermal cycling treatment (TCT) is a type of heat treatment in which repeated heating and cooling around critical temperature is provided [6]. The TCT has been tested on many grades of the steels by taking different sets of parameters [7, 8]. The present work performed the thermal cycling treatments on 13-4 MSS using Gleeble 3800. The TCT was performed at 1000 °C for 1, 3 cycles. The microstructural phase analysis of the as-received and the evolved microstructure was performed by optical, electron microscopy, and the XRD analysis. The microhardness and the bulk material hardness were determined to characterize the performed TCT.

2 Experimental Methods

A lath martensite steel ASTM A743 CA-6NM (Martensitic 13 wt%Cr–4 wt%Ni steel (13-4 MSS)) was selected for the research in the present study. This material was provided by Bharat Heavy Electricals Limited (BHEL), Haridwar, India, for research purposes. The spectroscopy of as-received 13-4 MSS (as-received) was performed by Thermo Jarrell ash spark emission spectroscope to detect the chemical composition. The as-received steel was found to have 13.51% Cr, 3.35% Ni, 0.07% C, 0.62% Mn, 0.64% Si, 0.32% Mo, 0.01% P, 0.06% Cu, 0.02% S by wt., and rest Fe.

The TCT was performed on a thermal–mechanical simulator, Gleeble 3800. A photographic image of Gleeble 3800 is shown in Fig. 1a. The selected temperature of the TCT (1000 °C) falls in the austenitic range of the as-received which was verified from the phase diagram in [1]. Other parametric details of the TCT are shown in Fig. 1b. The specimen used for conducting the TCT was cylindrical having 30 mm length and 10 mm diameter. The specimens were taken out after conducting 1 (1000-1c), and 3 (1000-3c) cycles.

The microstructures of as-received and thermal cycling treated specimens were examined by following the standard metallographic techniques. Small specimens were cut and polished with emery papers of 320, 800, 1200, and 1500 grit size. For the treated specimens, microstructures were taken randomly on the cross section just below the thermocouple which was welded in the mid of the length to record the temperature. After the paper polishing, cloth polishing using a 0.5 μm diamond paste was done to finally finish the specimens. The chemical etching, using Villela's reagent (100 ml ethanol + 1 g picric acid +5 ml HCL), was used to take the microstructures. Microstructural images were taken on an optical microscope; LOM DMI-5000 M. To examine the microstructure more closely, the scanning electron microscope (SEM) micrographs were recorded using a FESEM. X-ray study was performed by XRD peaks which were obtained from Rigaku SmartLab X-ray diffractometer. The XRD
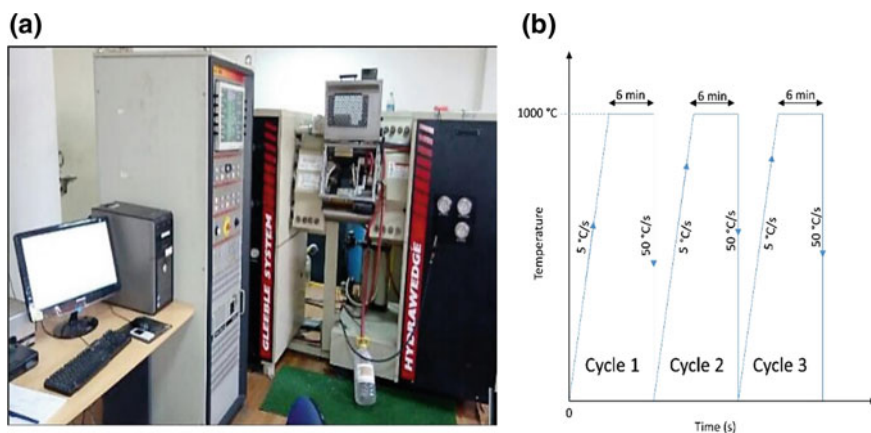
Fig. 1 **a** Photographic image of Gleeble 3800 and **b** parametric details of thermal cycling treatment having three cycles

was done at a rate of 2°/min from 30° to 120°. The XRD spectra were inspected using X'pertHighScore Plus having PDF4 database. The specimens having a 10 mm diameter and 10 mm height were used for SEM and XRD analysis for both as-received and treated specimens.

The microhardness of each constituent of the microstructure and the hardness of bulk material were tested to characterize the TCT. The microhardness was tested on UHL VMHT microhardness tester at 50 g load for 15 s dwell time. The average of five readings is reported. The bulk hardness was tested on FIE VM50 Vickers hardness tester at a 10 kg load for 15 s dwell time. For bulk hardness, an average of ten readings is reported. Due care was taken in maintaining the minimum gap of five times the diagonal of the indenter between any two indentations.

3 Results and Discussion

3.1 Microstructure

The optical microstructure for as-received is shown in Fig. 2a, and the evolved microstructures due to TCT are shown in Fig. 2b and c. It can be observed that the martensite exists in the form of parallel laths while the other phase, delta ferrite, is in small and large irregular shaped colonies. It can also be seen that a progressive dissolution of delta ferrite has been taken place to fragment the delta ferrite colonies. Due to the short duration holding of the specimen at the TCT temperature (1000 °C), the complete dissolution of delta ferrite does not take place. To ensure this, the quantitative assessment of the delta ferrite content was done using quantitative metallography in ImageJ software. Five images were taken for each specimen
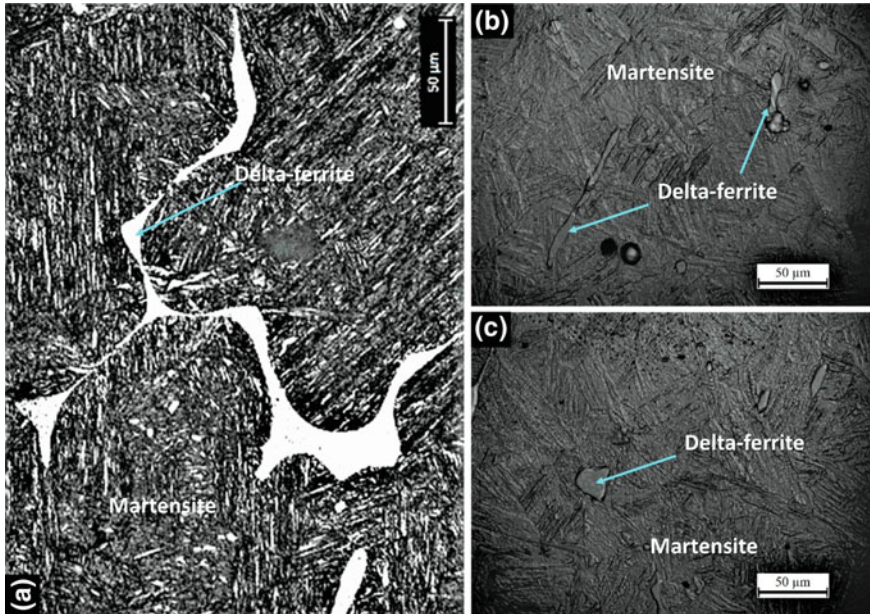
Fig. 2 Optical micrographs illustrating the constituent phases (at 500X) **a** of as-received, **b** 1000-1c, and **c** 1000-3c specimens

to ensure the reliability and the reproducibility of the calculated results. The calculated volume fractions of delta ferrite are given in Table 1. From the table, it can be observed that significant removal of delta ferrite (from 12.7 to 6.3%) took place from the microstructure due to the TCT. This is a big achievement of this TCT because delta ferrite, once formed, is very difficult to remove by any conventional treatment [9]. Delta ferrite is undesired due to its low hardness in lath martensite steels [10].

Figure 3 shows the XRD spectra for as-received and thermal cycling treated (1000-1c, and 1000-3c) specimens. It can be observed that retained austenite vanished from the XRD peaks of the treated specimens. The reduced peak intensities indicate a reduction in the delta ferrite content for the treated specimens. So, XRD analysis also supports the observation made in the previous explanation. The closer examination of the microstructure is done by SEM micrographs which are illustrated in Fig. 4. From Fig. 4a, it can be noticed that there exists a long arrangement of parallelism among the laths of the as-received, while it breaks after some gaps in the case of 1000-3c specimen as shown in Fig. 4b. This break in the parallelism was caused by the repeated transformation of martensite into austenite which causes the increase

Table 1 Volume contents of delta ferrite in as-received and thermal cycling treated specimens

	As-received	1000-1c	1000-3c
Volume content of delta ferrite (%)	12.7 ± 0.2	8.1 ± 0.4	6.3 ± 0.3
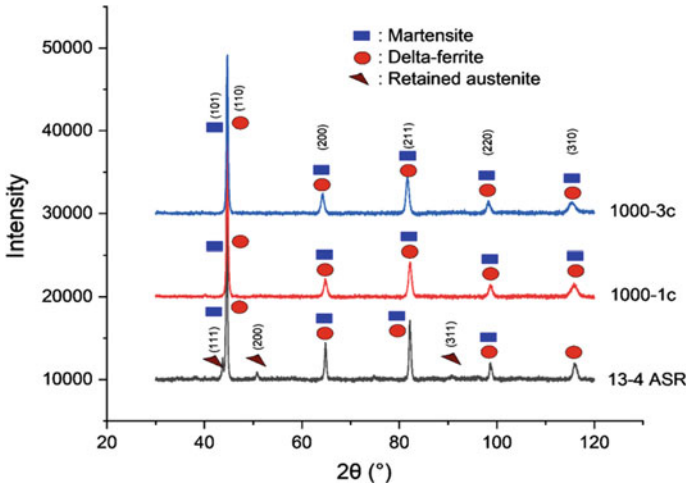
Fig. 3 XRD patterns in as-received and the thermal cycling treated specimens (1000-1c, and 1000-3c)
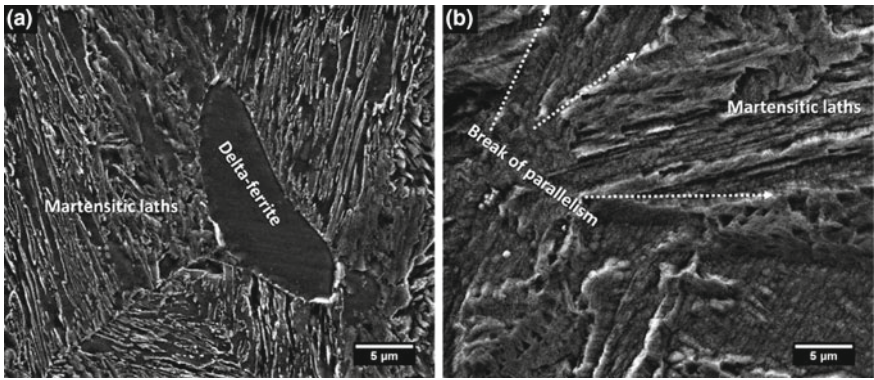
Fig. 4 SEM micrographs illustrating the lath martensite (at 4000X): **a** of as-received and **b** 1000-3c specimens

in the block boundary density [11]. The increased block boundary density leads to the block refinement. The martensite blocks are considered equivalent grain size in the lath martensite steel [12]. The grain (block) refinement was not assessed quantitatively in this study.

3.2 Microhardness and Bulk Hardness

Figure 5 illustrates the variation of microhardness of each phase and the bulk material hardness due to the TCT. It can be seen that the microhardness of both the constituents (delta ferrite and martensite) increased due to the TCT as compared to the counterpart of as-received. Also, there is a significant rise in the hardness (bulk) of the thermal cycling treated specimen. The hardness (bulk) is a function of microhardness of its constituents, and the volume fraction of delta ferrite. Here, due to the small content, the microhardness of delta ferrite is not of that much significance as compared to the counterpart of martensite. As delta ferrite is soft, it decreases the bulk hardness. The present TCT decreased the delta ferrite from 12.7% (for as-received) to 6.3% (1000-3c). This is the major reason for the increased bulk hardness of treated specimens from 273HV (for as-received) to 358HV for 1000-1c and 388HV for 1000-3c. The microhardness of martensite increased from 330HV (for as-received) to 384HV (for 1000-1c) and 409HV (for 1000-3c). The factors responsible behind this include block refinement, lath size, and the dislocation densities. The refinement in the blocks can be anticipated from Fig. 4. The quantitative assessment of block and lath sizes and dislocation densities requires a separate extensive study.
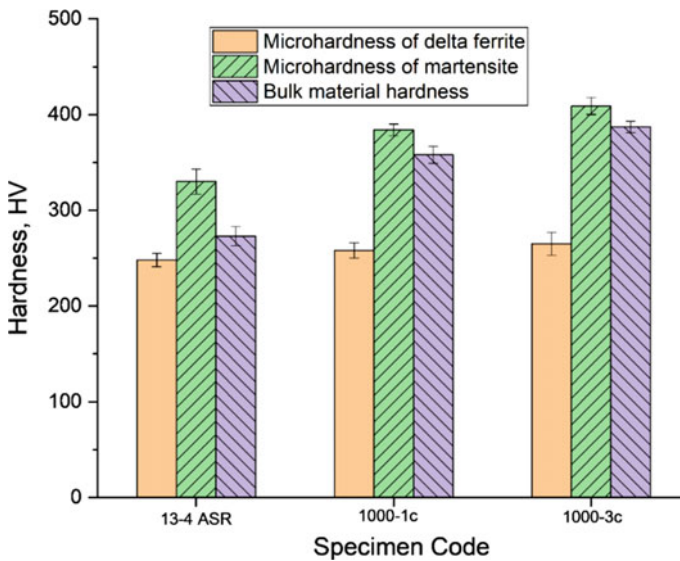
Fig. 5 Variation of microhardness and the bulk hardness due to thermal cycling treatment

4 Conclusions

- The dissolution and the fragmentation of delta ferrite caused the removal of delta ferrite content from the microstructure of the thermal cycling treated specimens. The volume fraction of delta ferrite reduced from 12.7% (for as-received) to 6.3% (1000-3c).
- The parallelism of laths broke after some gap due to the repeated transformation of martensite into austenite during thermal cycling treatment. This increases the block boundary density.
- The bulk hardness was found to be a function of the microhardness of martensite (the major constituent) and the content of delta ferrite. The bulk hardness increased from 273HV (for as-received) to 388HV (for 1000-3c). Apart from this, mechanical properties like impact toughness, tensile properties fracture strength, etc., should also be characterized for the treated specimens which were not done in this study.

References

1. Singh, J., & Nath, S. K. (2020). Effects of cyclic heat treatment on microstructure and mechanical properties of 13%Cr–4%Ni martensitic stainless steel. *Journal of Materials Engineering and Performance, 29,* 2478–2490. https://doi.org/10.1007/s11665-020-04787-w.
2. Amarendra, H. J., Kalhan, P., Chaudhari, G. P., Nath, S. K., & Kumar, S. (2012). Slurry erosion response of heat treated 13Cr–4Ni martensitic stainless steel. *Materials Science Forum, 710,* 500–505. https://doi.org/10.4028/www.scientific.net/MSF.710.500.
3. Nath, G., & Kumar, S. (2018). Studies on slurry erosion behavior of HVOF applied Y2O3-added WC–10Co–4Cr cermet on 13-4 martensitic stainless steel. *Metallography, Microstructure Analysis, 7,* 133–142. https://doi.org/10.1007/s13632-018-0426-5.
4. Minhaj, M., Singh, B., & Zafar, S. (2020). Slurry erosion performance of Ni + B$_4$C microwave composite clads. *Journal of Tribology, 142,* 1–11. https://doi.org/10.1115/1.4045770.
5. Kishor, B., Chaudhari, G. P., & Nath, S. K. (2016). Slurry erosion of thermo-mechanically processed 13Cr4Ni stainless steel. *Tribology International, 93,* 50–57. https://doi.org/10.1016/j.triboint.2015.08.048.
6. Mishra, A., Saha, A., & Maity, J. (2016). Development of high strength ductile eutectoid steel through cyclic heat treatment involving incomplete austenitization followed by forced air cooling. *Materials Characterization, 114,* 277–288. https://doi.org/10.1016/j.matchar.2016.03.001.
7. Mishra, S., Mishra, A., Show, B. K., & Maity, J. (2017). Simultaneous enhancement of ductility and strength in AISI 1080 steel through a typical cyclic heat treatment. *Materials Science and Engineering A, 688,* 262–271. https://doi.org/10.1016/j.msea.2017.02.003.
8. Ravi Kumar, B., Sharma, S., Kashyap, B. P., & Prabhu, N. (2015). Ultrafine grained microstructure tailoring in austenitic stainless steel for enhanced plasticity. *Materials & Design, 68*, 63–71. https://doi.org/10.1016/j.matdes.2014.12.014.
9. Wang, P., Lu, S. P., Xiao, N. M., Li, D. Z., & Li, Y. Y. (2010). Effect of delta ferrite on impact properties of low carbon 13Cr–4Ni martensitic stainless steel. *Materials Science and Engineering A, 527,* 3210–3216. https://doi.org/10.1016/j.msea.2010.01.085.

10. Kitahara, H., Ueji, R., Tsuji, N., & Minamino, Y. (2006). Crystallographic features of lath martensite in low-carbon steel. *Acta Materialia, 54,* 1279–1288. https://doi.org/10.1016/j.act amat.2005.11.001.
11. Kim, H. J., Kim, Y. H., & Morris, J. W. (1998). Thermal mechanisms of grain and packet refinement in a lath martensitic steel. *ISIJ International, 38,* 1277–1285. https://doi.org/10.2355/isijinternational.38.1277.
12. Morito, S., Yoshida, H., Maki, T., & Huang, X. (2006). Effect of block size on the strength of lath martensite in low carbon steels. *Materials Science and Engineering A, 440,* 237–240. https://doi.org/10.1016/j.msea.2005.12.048.

A Review on Wire Arc Additive Manufacturing: Effect of Process Parameters on the Build Material Properties

Meet Gor, Harsh Soni, Gautam Singh Rajput, Honey Shah, and Pankaj Sahlot

Abstract Wire arc additive manufacturing (WAAM) has attracted more attention in recent years, due to its ability to create large components with high material deposition rate and low cost of equipment. It is getting more popular nowadays because it provides high strength at low cost, high deposition rate, faster build time, and optimum heat input. In this article, a comprehensive literature review has been covered to show the effect of different process parameters on mechanical and microstructural properties. Primarily, aim is to provide information about accuracy of WAAM manufactured part in correlation with change in different processes parameters such as heat input, current, voltage, wire feed rate, and travel speed. This paper also gives an idea about which parameters can be used to get desired mechanical and microstructural properties. It also provides information about challenges that lead to abnormal results and remedies to overcome with heterogeneous and anisotropic properties of materials. Selection of process parameters help to optimize the WAAM process to obtain the desired geometry with required properties.

Keywords Additive manufacturing · Wire arc additive manufacturing · Processes parameters · Mechanical properties · Microstructural properties

M. Gor · H. Soni · G. S. Rajput · H. Shah · P. Sahlot (✉)
Mechanical Engineering, School of Technology, Pandit Deendayal Petroleum University, Gandhinagar 382007, Gujarat, India
e-mail: pankaj.sahlot@sot.pdpu.ac.in

M. Gor
e-mail: meet.gmtmm19@sot.pdpu.ac.in

H. Soni
e-mail: harsh.smtmm19@sot.pdpu.ac.in

G. S. Rajput
e-mail: gautam.rmtmm19@sot.pdpu.ac.in

H. Shah
e-mail: honey.smc16@sot.pdpu.ac.in

247

1 Introduction

In past many years, additive manufacturing (AM) has achieved great heights of success. An AM process is to create three-dimensional and complex build parts in a layer by layer deposition which result in less material waste [1]. For a metal additive manufacturing process, several methods have been developed such as laser beam, electron beam, plasma beam, GTAW, and GMAW [2]. Laser is a high power and high-energy source to generate high energy density beam of photons focused on a particular small spot area to heat that region and to melt metal. It generates beam powers of very high watts (in thousands) and beam can focus to millimeters spot sizes [3]. In electron beam, instead of beam of photons, electron beam is used to get high energy density as same as laser beam. Plasma arc jet is highly focused beam with intense heat to localize small region and use inert gas as shielding [3]. Laser and electron beam-based additive manufacturing is more popular because of its dimensional accuracy, but at the same time, it is more time-consuming process as well as specific set up is required for this process [4]. The AM processes based on fusion has low deposition rate, increasing lead times; hence, there is a need of one AM process which gives higher strength and high deposition rate, based on this requirement. Researchers developed wire arc additive manufacturing (WAAM) in 1920 to achieve high strength, high productivity, low cost, lower cycle time, and no requirement of specific tooling [5]. WAAM required an electric arc as a heat source and wire continuously feed from feedstock. WAAM process for GMAW is with special purpose machine, where the MIG torch is used as a heating source. In this processes, variety of materials and process parameters can be used to achieve required properties [6]. As this process is based on arc, the parameter of arc generation like current, voltage, travel speed, and deposition rate influences the build material attributes like bead width and height, surface roughness, and build properties like tensile strength and hardness [7]. Hence, it is necessary to study the effect of process parameters during WAAM process. The main aim of this paper is to show recent advancement related to effect of processes parameters on the build material properties. This paper also includes future visions of WAAM process.

2 Effect of Process Parameters

Selection of processes parameter plays an important role in WAAM to produce complex 3D shape, desired property, and quality components. Different parameters like heat input, current, voltage, wire feed rate, travel speed, etc., control the quality of 3D fabricated components [8]. The effect of different processes variables on deposition of layers for Inconel 625 by GMAW-WAAM is examined [9]. The effect of heat input, current, welding speed, shielding gas on tensile strength, hardness, and roughness are observed as given in Table 1. Four different experiments

Table 1 Effect of different process parameters on tensile strength, hardness, and surface roughness for GMAW-WAAM [9]

Wall	Heat input (kJ/cm)	Current (A)	Welding speed (cm/min)	Shielding gas	Tensile strength (MPa)	Hardness (Vickers) (HV)	Roughness—RMS (mm)
a	3.024	138–130	38	97.5%Ar, 2.5%CO_2	751.94	223.13	0.187
b	2.906	133–119	38	95.5% Ar, 3% He, And1.5% H_2	698.13	213.06	0.162
c	2.965	130–121	36	(95% Ar, 5% H_2)	699.88	202.38	0.116
d	2.899	131–123	38	99.999% Ar	698.99	200.38	0.101

(wall number a, b, c, and d) were performed to examine the effect of these parameters. Heat input influences the tensile strength, and strength decreases with decrease in heat input. Hardness also increases with increase in the heat input. As observed in results, higher macrohardness was observed more for (wall a) with 97.5% Ar, 2.5% CO_2 shielding gas, whereas minimum for 95.5% Ar, 3% He and 1.5% H2 (Wall b). Figure 1 shows influence of process variables on roughness of deposited surface. The surface roughness decreases with decrease in heat input [9]. Maximum wall roughness is obtained for wall a and minimum for wall d. Chakkravarthy and Jerome investigated the effect of torch angle on the topology, orientation, and texture of a component built by WAAM-CMT (cold metal transfer) process. Two different values of torch angles (5° and 15°) were used to perform experiments. The proposed model suggested that weaving motion has an influence on the texture, grain refinement, and
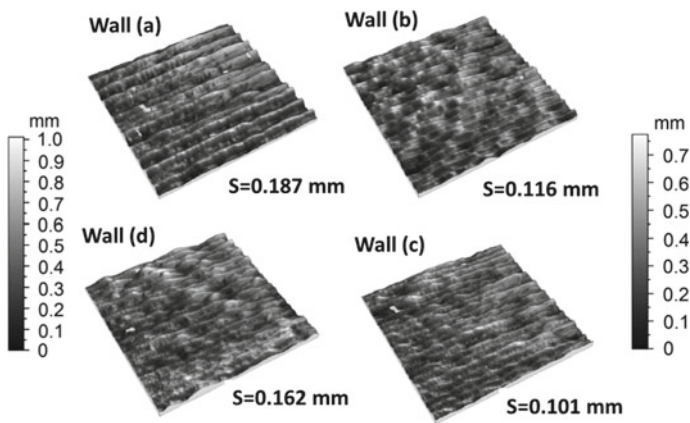
Fig. 1 Influence of process parameters on surface roughness [9]

topology. Waving motion was more effective as torch angle increased. The surface roughness in case of 15° was fine up to 59 nm which improves corrosion resistance. Therefore, with the high angle, component can be built with minimum requirement of post-processing [10].

Researchers have also investigated effect of process variables on heat input and weld bead geometry for all the six experiment perform with different parameters like current, voltage, travel speed, and wire feed as shown in Fig. 2. They found that heat input decreases as speed rate increases for constant voltage. However, heat input increases as increment in the voltage for constant speed rate. In addition, the best result is achieved in case of first experiment for lesser speed rate and voltage as shown in Fig. 2 [11]. Fang et al. examined that minimum temperature of the build material does not depend on the deposition length during the deposition pass. However, as the width and thickness increase, minimum temperature decreases in beginning due to strengthening effect of the deposited part by his conduction. Heat conduction was enhanced within a short time and leads increase in minimum temperature [12]. Figure 3 shows the travel speed effect on the bead geometry with steady current and wire speed rate for WAAM processes. The ratio of feed rate to travel speed was set

Fig. 2 Deposited layer at various parameter [11]
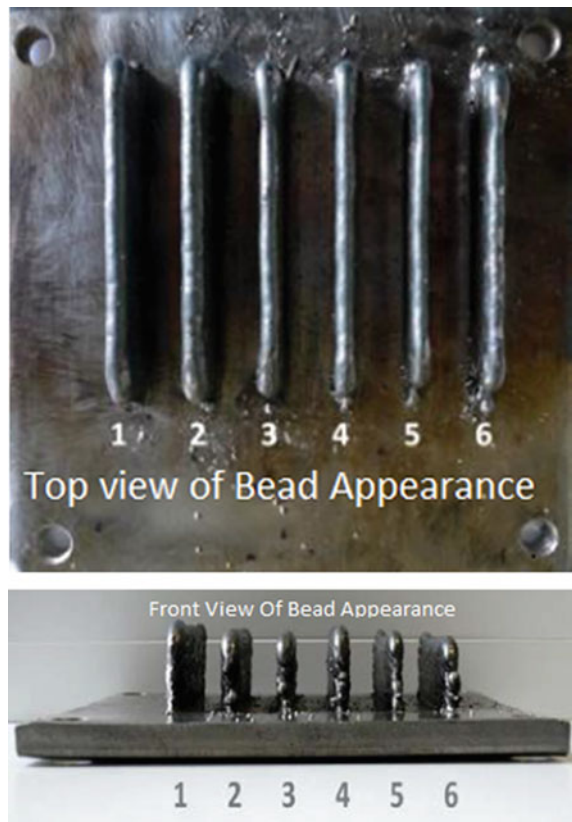
Fig. 3 Effect of travel speed on deposited layer [13]
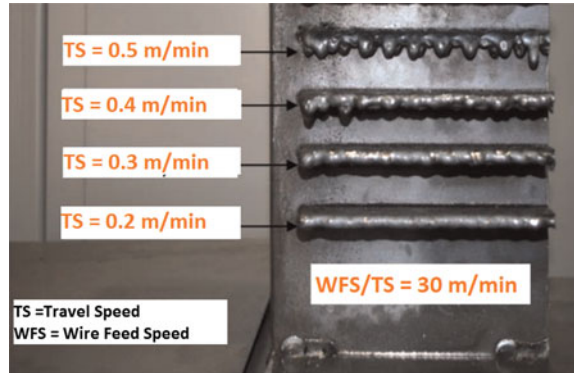
on 30, and travel speed was varied in a range of 0.2–0.5 m/min. They found smooth weld bead for lower travel speed of 0.2 m/min as compared with higher travel speed of 0.5 m/min due to formation of globular spatter at higher speed [13].

During GMAW-WAAM, distance between nozzles and deposited material plays a crucial role in deciding the arc current, voltage, and deposition rate. Yang et al. performed various experiments to observe effect of current on the build characteristic for GMAW-WAAM. The mean bead increases with increase in current. However, standard deviation deceases up to 80A after that it increases again the surface texture during process also increases with increase in current [14]. In GMAW-WAAM usually, the work plate is moved down in predefined value after every layer. However, it was observed that movement is not constant every time, and it affects the deposition rate [15]. The variation in deposition rate increases with increase in deposited layer. Figure 4 shows the effect of current on the bead geometry during GMAW-WAAM. The weld bead decreases with increase in the current. In addition to this, surface roughness increases as the current increases as shown in Fig. 4 [14]. Malinet al. performed WAAM using super duplex filler wire to develop walls with different heat input. All the build components were defect free with different process parameter. Yield strength of build component was lower than that of base metal (i.e., 100–160 MPa). Notch toughness was around 100 J at 20 °C. The secondary intermetallic phase was formed due to multiple heating and cooling during layer deposition. Lower mechanical properties have been observed due to lower ferrite contain [16].

Dinovitzer et al. studied the influence of different process variables on build material characteristic of nickel-based alloy by GTAW based wire arc additive manufacturing. They concluded that bead width and wetting angle decrease and bead height increased as wire feed rate is increased [17]. In MIG-WAAM, it was observed that weld attempts are successful as well as unsuccessful with change in travel speed. Unsuccessful weld attempts are due to superficial porosity melting, discontinuities, and collapsing [18]. When researchers have observed higher tensile and hardness with speed arc WAAM as compared to speed pulse WAAM due to finer solidification structure [19]. The strength of heat treated alloys declined with the arrangement
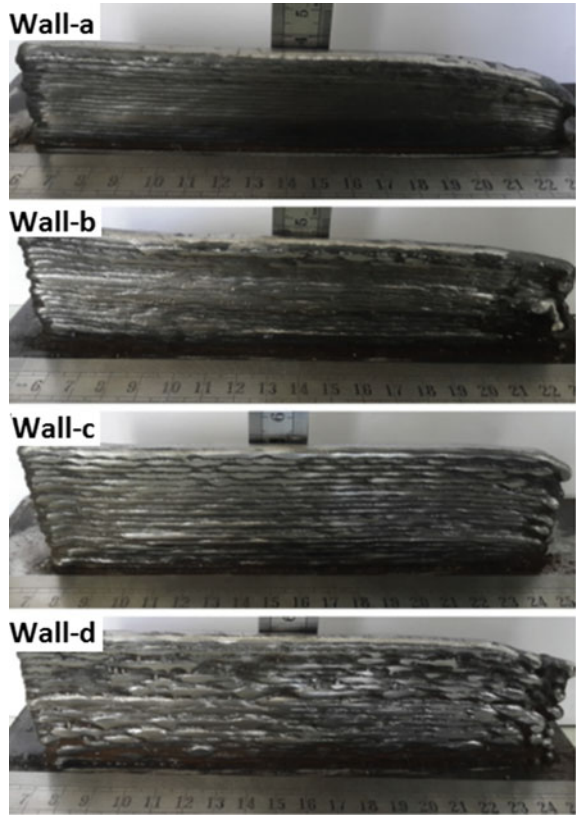
temperature while the ductility increment till 1473 K and scopes to its greatest estimation at value of 1.56% and then start decreasing as solution temperature approaches to 1543 K [20]. The microhardness drops significantly as Al content increased with estimated value 510.3 HV0.2 and 335.5 HV0.2 for Ti-45Al and Ti-35Al, and Ti-55Al samples value is 250.9 HV0.2, respectively [21]. Surface waviness of high-speed low-alloy (HSLA) steel decreases with increase in heat due to good wettability of the layers over the previously deposited [22]. Researchers also observed short build stress relief at 653 K for 2 h, and it gives 30% higher ductility without getting larger grain size for Ti–6Al–4V material [23]. Hot iso-static pressing is effective technique to eliminate the porosity; though in the ductility and strength, there was no major improvement. The static tensile strength properties were compared and found different uniform elongation [24]. Fatigue strength observed regarding the maximum applied stress at around 10 million cycles was 600 MPa and 400 Mpa, respectively. The tensile strength in the CMT mode is observed maximum as compared to the arc mode and wrought alloy. The CMT mode of variable polarity transfer columnar grain effectively in the form of equi-axed grain; therefore, grain size will be refined that improves the mechanical performance [25]. As wire feed rate increases, bead

width and wetting angle decrease. However, bead height increases. The variation in frequency affects also the narrowed bead shape and the quality of surface texture [26, 27].

3 Conclusion

The WAAM technique is widely adopted by industries because of its capability to build a component with bare minimum wastage of materials, faster build rate also with freedom of any customize design. In this technique, process parameters play a crucial role to obtain the complex geometry and desired properties. This paper gives a comprehensive literature to examine the effect of process parameters on the build material properties. Effect of process variables like Current, Voltage, feed rate, heat input, and wire feed on build material properties for various WAAM processes are discussed. Current and voltage influence the heat input, process time, deposition rate, as per the heat input equation current and voltage are directly proportional to the heat input so as the current increases the heat input also increases. Travel speed is contrarily proportional to the heat input, so with increasing the travel speed, the heat input lessens. Additional heat input affects the appearance of the molten pool, because as the heat input is low, then the width of the layer decreases and height of the layer increases. As the heat input increments, the appearance of layer becomes rough, so as the heat input increments, the roughness value (RMS) will also increase and the reason for this is because of the spread ability increases with more heat. In mechanical property, tensile strength and hardness are essential properties because these influenced by travel speed, current and voltage. This means that the higher heat input makes a strong bond with the layer to increase the strength. More hardness is obtained at high heat input due to high cooling rate which lead to finer structure. WAAM technology has an inherent capability to build a complex component for automobiles that is difficult to building with the conventional methods. This advantage of WAAM techniques specially helps in build the unique designs every time with low cost rather than establishing a steady production line. This process has been widely used for developing an automobile prototype because of its rapidness and lower cost.

References

1. Majeed, A., Ahmed, A., Lv, J., Peng, T., & Muzamil, M. (2020). A state-of-the-art review on energy consumption and quality characteristics in metal additive manufacturing processes. *The Journal of the Brazilian Society of Mechanical Sciences and Engineering, 42*(5). https://doi.org/10.1007/s40430-020-02323-4.
2. Kumar, M., Sharma, A., Mohanty, U. K., & Kumar, S. S. (2019, Janaury). *Additive manufacturing with welding*.

3. Prevorovsky, Z., Krofta, J., & Kober, J. (2017, October). *NDT in additive manufacturing of metals* (vol. 2017).

4. Fang, Z. C., Wu, Z. L., Huang, C. G., & Wu, C. W. (2020). Review on residual stress in selective laser melting additive manufacturing of alloy parts. *Optics & Laser Technology, 129*(15), 106283. https://doi.org/10.1016/j.optlastec.2020.106283.

5. Wu, B., et al. (2018). A review of the wire arc additive manufacturing of metals: properties, defects and quality improvement. *Journal of Manufacturing Processes, 35*(August), 127–139. https://doi.org/10.1016/j.jmapro.2018.08.001.

6. Rodrigues, T. A., Duarte, V., Miranda, R. M., Santos, T. G., & Oliveira, J. P. (2019). Current status and perspectives on wire and arc additive manufacturing (WAAM). *Materials (Basel), 12*(7). https://doi.org/10.3390/ma12071121.

7. Knezovi, N., & Topic, A. (2018, January). *New technologies, development and application* (vol. 42, pp. 0–7). https://doi.org/10.1007/978-3-319-90893-9.

8. Cunningham, C. R., Flynn, J. M., Shokrani, A., Dhokia, V., & Newman, S. T. (2018). Invited review article: Strategies and processes for high quality wire arc additive manufacturing. *Additive Manufacturing, 22*(June), 672–686. https://doi.org/10.1016/j.addma.2018.06.020.

9. Jurić, I., Garašić, I., Bušić, M., & Kožuh, Z. (2019). Influence of shielding gas composition on structure and mechanical properties of wire and arc additive manufactured inconel 625. *JOM Journal of the Minerals Metals and Materials Society, 71*(2), 703–708. https://doi.org/10.1007/s11837-018-3151-2.

10. Chakkravarthy, V., & Jerome, S. (2020). Printability of multiwalled SS 316L by wire arc additive manufacturing route with tunable texture. *Materials Letters, 260*(xxxx), 126981. https://doi.org/10.1016/j.matlet.2019.126981.

11. Liberini, M., et al. (2017). Selection of optimal process parameters for wire arc additive manufacturing. *Procedia CIRP, 62,* 470–474. https://doi.org/10.1016/j.procir.2016.06.124.

12. Fang, X., et al. (2019). Effect of characteristic substrate parameters on the deposition geometry of CMT additive manufactured Al-6.3%Cu alloy. *Applied Thermal Engineering, 162*(99), 114302. https://doi.org/10.1016/j.applthermaleng.2019.114302.

13. Kazanas, P., Deherkar, P., Almeida, P., Lockett, H., & Williams, S. (2012). Fabrication of geometrical features using wire and arc additive manufacture. *Proceedings of the Institution of Mechanical Engineers, Part B: Journal of Engineering Manufacture*, *226*(6), 1042–1051. https://doi.org/10.1177/0954405412437126.

14. Yang, D., He, C., & Zhang, G. (2016). Forming characteristics of thin-wall steel parts by double electrode GMAW based additive manufacturing. *Journal of Materials Processing Technology, 227,* 153–160. https://doi.org/10.1016/j.jmatprotec.2015.08.021.

15. Xiong, J., & Zhang, G. (2014). Adaptive control of deposited height in GMAW-based layer additive manufacturing. *Journal of Materials Processing Technology, 214*(4), 962–968. https://doi.org/10.1016/j.jmatprotec.2013.11.014.

16. Lervåg, M., et al. (2020). Additive manufacturing with superduplex stainless steel wire by cmt process. *Metals (Basel), 10*(2), 5–12. https://doi.org/10.3390/met10020272.

17. Dinovitzer, M., Chen, X., Laliberte, J., Huang, X., & Frei, H. (2019). Effect of wire and arc additive manufacturing (WAAM) process parameters on bead geometry and microstructure. *Additive Manufacturing, 26,* 138–146. https://doi.org/10.1016/j.addma.2018.12.013.

18. Venturini, G., Montevecchi, F., Bandini, F., Scippa, A., & Campatelli, G. (2018). Feature based three axes computer aided manufacturing software for wire arc additive manufacturing dedicated to thin walled components. *Additive Manufacturing, 22,* 643–657. https://doi.org/10.1016/j.addma.2018.06.013.

19. Wang, L., Xue, J., & Wang, Q. (2019). Correlation between arc mode, microstructure, and mechanical properties during wire arc additive manufacturing of 316L stainless steel. *Materials Science and Engineering A, 751*(February), 183–190. https://doi.org/10.1016/j.msea.2019.02.078.

20. Wang, J., Pan, Z., Wei, L., He, S., Cuiuri, D., & Li, H. (2019). Introduction of ternary alloying element in wire arc additive manufacturing of titanium aluminide intermetallic. *Additive Manufacturing, 27*(March), 236–245. https://doi.org/10.1016/j.addma.2019.03.014.

21. Wang, J., Pan, Z., Cuiuri, D., & Li, H. (2019). Phase constituent control and correlated properties of titanium aluminide intermetallic alloys through dual-wire arc additive manufacturing. *Materials Letters, 242,* 111–114. https://doi.org/10.1016/j.matlet.2019.01.112.
22. Rodrigues, T. A., Duarte, V., Avila, J. A., Santos, T. G., Miranda, R. M., & Oliveira, J. P. (2019). Wire and arc additive manufacturing of HSLA steel: Effect of thermal cycles on microstructure and mechanical properties. *Additive Manufacturing, 27*(March), 440–450. https://doi.org/10.1016/j.addma.2019.03.029.
23. Bermingham, M. J., Nicastro, L., Kent, D., Chen, Y., & Dargusch, M. S. (2018). Optimising the mechanical properties of Ti–6Al–4V components produced by wire + arc additive manufacturing with post-process heat treatments. *Journal of Alloys and Compounds, 753,* 247–255. https://doi.org/10.1016/j.jallcom.2018.04.158.
24. Biswal, R., et al. (2019). Criticality of porosity defects on the fatigue performance of wire + arc additive manufactured titanium alloy. *International Journal* of *Fatigue*, *122*(September 2018), 208–217. https://doi.org/10.1016/j.ijfatigue.2019.01.017.
25. Zhang, C., Li, Y., Gao, M., & Zeng, X. (2018). Wire arc additive manufacturing of Al-6Mg alloy using variable polarity cold metal transfer arc as power source. *Materials Science and Engineering A, 711*(August 2017), 415–423. https://doi.org/10.1016/j.msea.2017.11.084.
26. Silwal, B., & Santangelo, M. (2018). Effect of vibration and hot-wire gas tungsten arc (GTA) on the geometric shape. *Journal of Materials Processing Technology, 251,* 138–145. https://doi.org/10.1016/j.jmatprotec.2017.08.010.
27. Guo, J., Zhou, Y., Liu, C., Wu, Q., Chen, X., & Lu, J. (2016). Wire arc additive manufacturing of AZ31 magnesium alloy: Grain refinement by adjusting pulse frequency. *Materials (Basel)*, *9*(10). https://doi.org/10.3390/ma9100823.

Tribological Aspect of Nano-lubricant Based on Carbon Nanotubes (CNTs) and Graphene—A Review

Prayag Narayan Singh, Ankit Saxena, and Swati Gangwar

Abstract In the present time, heat dissipation is one of the major concerns for any mechanical system sustention. The principal reason for the breakdown in any mechanical system is found due to the wear and tear of its mechanical parts. This problem can be solved by many methods; effective lubrication is one of them. Effective lubrication is based upon the selection of base oil/lubricants mixing with nanoparticles. These nanoparticles are present in scattered form in base oil named as 'nano-lubricants'. This research review article represents a useful overview of significant research advancement on carbon nanotubes (CNTs) and graphene to be used as nanoparticles to synthesize nano-lubricants. The main reason for using these two as nanoparticle is because they have the similar surface characteristics and coalesce electronic structure. It is observed that graphene flakes have been inspected as an improver for lubricants due to their exceptional thermo-physical and tribological characteristics. On the other hand, nano-lubricants prepared with carbon nanotubes are likely to hold improved heat transfer properties because of the non-spherical shape of the CNTs. This comprehensive review could be useful for future in the research area of nano-lubrication because, in present time energy demands, precision manufacturing and mechanical losses are progressively rising that shows a need for an efficient lubricant for any mechanical system survival.

Keywords Tribology · Nano-lubricant · Carbon nanotubes · Graphene

P. N. Singh · A. Saxena · S. Gangwar (✉)
Mechanical Engineering, Madan Mohan Malaviya University of Technology, Gorakhpur, India
e-mail: sgme@mmmut.ac.in

P. N. Singh
e-mail: prayagsingh19bbau@gmail.com

A. Saxena
e-mail: saxena01ankit@gmail.com

1 Introduction

The progressively rising energy demands, precision manufacturing, and mechanical losses show a need for efficient lubricants. Lubricants are employed primarily to decrease wear and friction of machine components. The accumulation of additives has been a recognized preparation to improve the tribological and thermal performance of lubricants. Numerous additives are used to increase thermal conductivity [1], viscosity [1] or can be utilized as anti-wear agents [1], anti-friction agents [1], extreme-pressure agents [1] and to provide resistance from oxidation [1]. Graphene is basically a 2D monolayer of the carbon atoms that are packed into an identical honeycomb structure. The carbon atoms are arranged in a sp2 hybridized linkage with three adjacent neighbours, each at approx. 1.42 Å distance, leaving one hybridized half-filled p-orbital which is at right angles for each carbon to the graphene-plane. The rhombus unit cell contains two atoms from two dissimilar sublattices which makes graphene a mutual lattice. Graphene may be presumed as parental substance for the allotropes of carbon of the other dimensions as shown in the following Fig. 1.

Carbon nanotubes (CNTs) have cylindrical structures up to few micrometres in length and hundreds of nanometres in diameter. The structure of CNTs can be seen from following Fig. 2. CNTs are highly anisotropic, and both single-walled carbon nanotubes (SWCNTs) as well as multi-walled carbon nanotubes (MWCNTs) have a high value of thermal conductivity in axial direction while their transverse conductivity is expected to lower values [3].
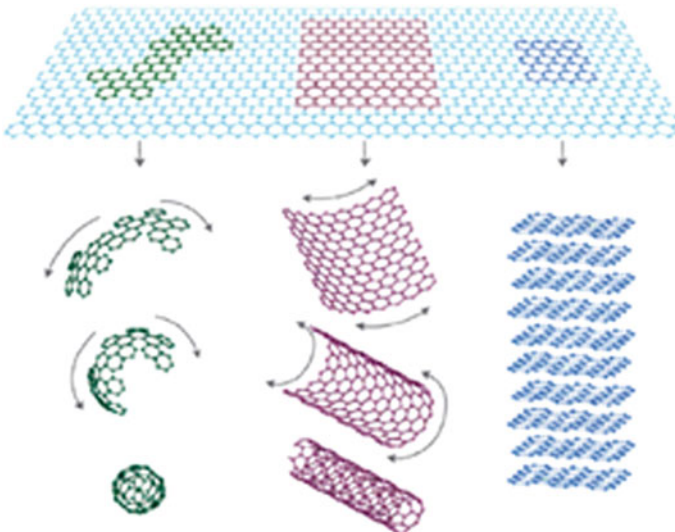
Fig. 1 Graphene: a 2D building material for carbon materials [1]
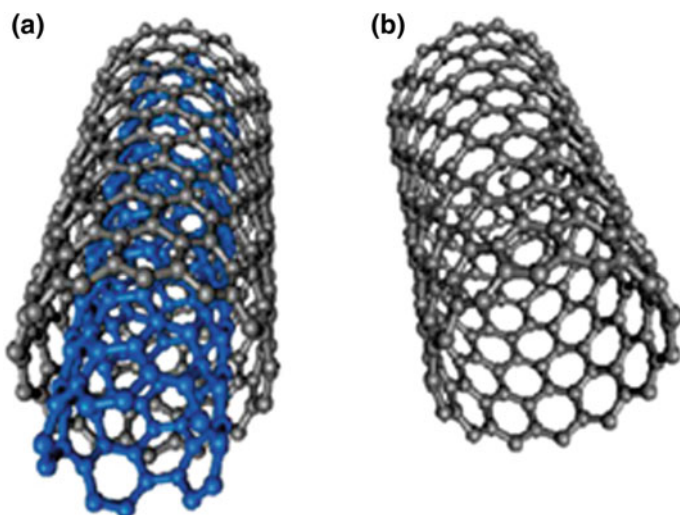
Fig. 2 Structures of carbon nanotubes: **a** Multiwall carbon nanotube (MWCNT), **b** Single-wall carbon nanotube (SWCNT) [4]

2 Material, Properties, and Applications

2.1 Graphene

Graphene can be assumed as the basic building block material for the allotropes of carbon of other dimensionalities. Graphene nano-flakes are prepared by one layer of atomic carbon with excellent properties as presented in Table 1. The atoms of carbon of graphene are settled in a monolayer indicating a lattice which is look alike as hexagonal honeycomb as shown in following Fig. 3. The rhombus unit cell contains two atoms from two diverse sublattices which makes graphene a bipatite lattice [5]. Generally, graphene can be found either in the form of a single layer which is acquired from 'pyrolytic graphite' which is highly ordered through micromechanical

Table 1 Graphene's various properties [1, 2]

Sr. no.	Properties	Values
1	Thermal conductivity	~5000 Wm^{-1} K^{-1}
2	Thermal resistance (at interface)	4×10^{-8} Km^{2}W^{-1} (rGr–SiO$_2$)
3	Specific surface area	2600 m^2 g^{-1}
4	Young's modulus	~1 TPa
5	Fracture strength	130 GPa
6	Melting point	4125 k (predicted value)
7	Fracture toughness	4 M Pa$\sqrt{}$/m

Fig. 3 Shaded region shows rhombus unit cell with two sublattice points with lattice of graphene [5]
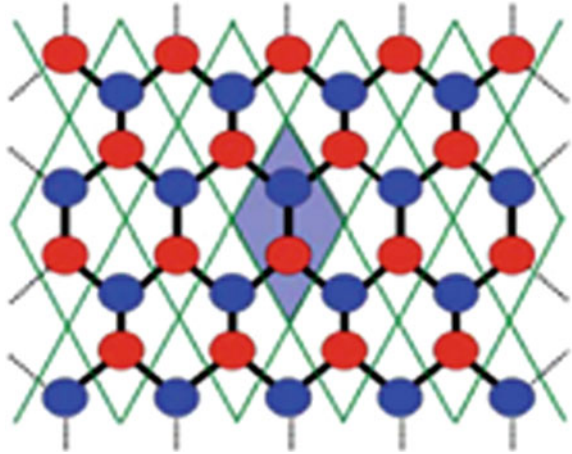
cleavage process [1] or in the form of multilayers, and it has two-dimensional structure. Furthermore, graphene comes across atomic vacancies, non-sp2 carbon defects, structural defects, and many other defects. Graphene is known as 'miracle material' or 'super material' due to its tremendous properties [2]. Graphene provides exclusive friction and wear properties due to its two-dimensional layered structure. In addition, graphene is used as a lubricating agent since it contains exceptional properties like easy shear capability, high chemical inertness, and it is impermeable to gases as well as liquids. The outstanding mechanical strength of graphene provides protection from wear [2], while the impermeability helps it to prevent oxidation and corrosion nature of the substrate [2]. On the other hand, the limitations of graphene are its uneconomical production and stability of dispersion in conventional lubricants. Researchers have found that single-layer graphene has a superior thermal conductivity value than multi-layer graphene.

2.2 Carbon Nanotubes

The nanotubes contain numerous tens of graphitic shells having diameters of size ~1 nm and a large ratio of length with its diameter [6]. The formation of nanotubes can be seen from following Fig. 4. CNTs may be labelled as a sheet of graphite that is rolled up into a nanoscale-tube (i.e., single-wall carbon nanotubes (SWCNTs)), or maybe additional tubes of graphene about SWCNT core (i.e., multi-wall CNTs (MWCNTs)) [7, 8]. In the case of CNTs, both ends are capped generally by fullerene-like structures, and they have lengths of an order of numerous centimetres while range of their diameter remains between portions of nanometres and tens of nanometres. MWNTs and SWNTs are formed mostly using these three techniques: catalytic growth, arc discharge, and laser ablation [6]. The samples of produced nanotube are
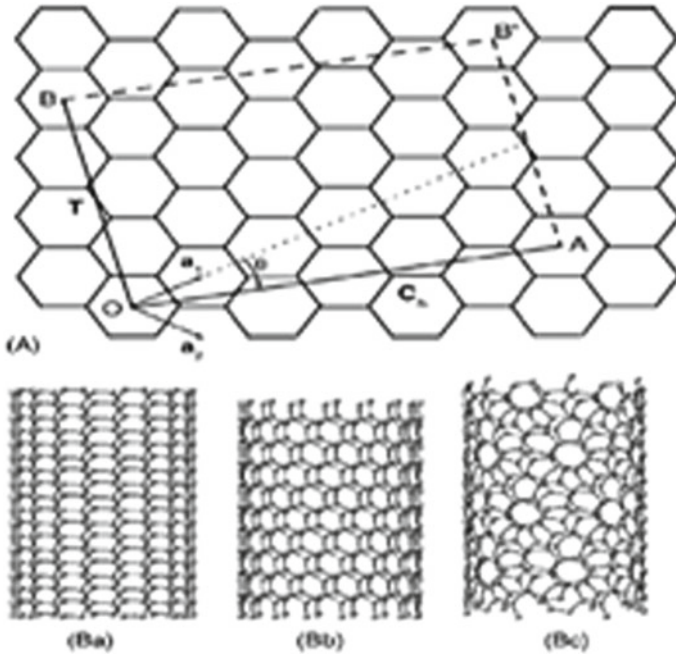
Fig. 4 Creation of a nanotube by rolling-up graphene [6]

characterized by using electronic, optical, and Raman spectroscopies. The synthesis of carbon nanotubes can also be done by process of chemical vapour deposition. Nickel is used as a catalyst for achieving MWCNT while cobalt is used for achieving SWCNT; furthermore, a quartz tube is utilized to grow of CNTs. The value of Young's modulus for SWCNT is about 5 TPa, while for MWCNTs, it is about 1.8 TPa, and bending strength for MWCNT is about to 14.2 GPa [9]. Researchers found that CNTs are an appropriate choice for production of composites because of their extraordinary tensile strength and Young's modulus values [6]. Generally, CNTs have an inert structure which means that CNT walls have a tendency of not to be reactive, but tips similar to fullerene of CNTs are acknowledged to be extra reactive [8].

2.3 Tribology of Graphene

Singh et al. [10] have studied the wear and friction response of synthesized graphene on GCr15 bearing steel by utilizing a ball-on-disc type tribometer. They found the mean value of friction coefficient as 0.15 during 800 cycles of friction test, and further, they found that the decreased values of wear track from 428.69 to 89.21 μm and wear scar from 545.03 μm to 125.88 μm, respectively, by utilizing coating of graphene on steel. These reductions in the coefficient of friction as well as in wear

are achieved due to strong force of adhesion between the surface and graphene and also due to the lower shear strength of interlayers.

Ren et al. [11] have estimated the anti-wear and anti-friction properties of nanoparticles of ZnO@graphene core-shell by utilizing a four-ball friction-wear testing machine according to the ASTM D2783 standard and found that when 0.5–1 wt.% of nanoparticles are suspended, then wear scar diameter is decreased by 20% while the coefficient of friction is decreased by 25%.

Jinshan et al. [12] tested numerous samples of modified graphene platelets (MGP) dispersions (0.015, 0.035, 0.055, 0.075, 0.095 and 0.105 wt.%) and modified natural flake graphite (MNFG) dispersions and found when concentration of 0.075 wt.% of MGP is dispersed in base oil, then enhancement in load-carrying capacity is achieved from a value of 418.5 N to a value of 627.2 N. In case of oil with modified natural flake graphite (MNFG), this value is up to 523 N. It indicates that load-carrying capacity has a larger value in case of base oil with modified graphene platelets (MGP) than base oil with MNFG or base oil alone. Wu et al. [13] have dispersed the graphene oxide (GO) sheets in bio-oil at 0.2, 0.4, 0.5, 0.6, 0.8 and 1 wt.% concentrations, their tribological properties were tested on a multifunctional end-face tribometer, and the minimum value of coefficient of friction is obtained as nearly 0.15 at a concentration of 0.4 wt.% GO, while the minimum value of wear loss is obtained as nearly 3.5 mg at a concentration of 0.6 wt.% GO.

Huang et al. [14] have prepared a nano-lubricant by dispersing alumina (Al_2O_3) and GO nanoparticles in deionized water, the tribological properties of above nano-lubricant was investigated by utilizing the block-on-ring friction test, they found that coefficient of friction was reduced by 47%, and enhancement in surface roughness was achieved by 60% for a quantity of 0.12 wt.% 1:1 GO-Al_2O_3 in comparison of 0.06 wt.% GO, similarly, coefficient of friction was reduced by 64% and enhancement in surface roughness was achieved by 63% for a quantity of 0.12 wt.% 1:1 GO-Al_2O_3 in comparison of 0.06 wt.% Al_2O_3.

Xie et al. [15] have prepared a nano-lubricant by dispersing graphene and nano-SiO_2 in water, the tribological properties of above nano-lubricant was investigated by a ball-on-plate configuration, and they found that when 0.4 wt.% concentration of graphene and 0.1 wt.% concentration of nano-SiO_2 were dispersed in water, then wear volume is decreased by 79% and coefficient of friction is decreased by 48.5%. Meng et al. [16] have prepared nano-lubricant by dispersing Cu nanoparticles decorated graphene oxide in liquid paraffin, their tribological testing was done by a four-ball tribometer, and they found that when 0.05 wt.% concentration of above dispersion was used, then reduction in wear by 52.7% and coefficient of friction by 27% were achieved.

2.4 Tribology of Carbon Nanotubes

Singh et al. [17] have formed a nano-lubricant by dispersing MWCNTs in the SN 500 grade base oil and performed tribological test by using the pin-on-disc tribometer with

grey CI and EN31 discs and Al6061-SiC-C pins. They found wear rate of MWCNTs dispersed base oil for AMMC-CI equal to $(1.09 \pm 0.008) \times 10^{-4}$ mm^3/m, while for base oil alone wear rate was $(6.32 \pm 0.014) \times 10^{-4}$ mm^3/m. Similarly, wear rate of MWCNTs dispersed base oil for AMMC-EN3 was $(0.008 \pm 0.001) \times 10^{-4}$ mm^3/m, while base oil alone it was $(0.04 \pm 0.008) \times 10^{-4}$ mm^3/m.

Jeyaprakash et al. [18] dispersed 0.3, 0.5, 0.7, 1.0 and 1.3 wt.% concentrations of MWCNTs nodular cast iron contacts steel in SAE 15 W-40 CF-4 diesel engine oil, and they performed tribological test with the pin-on-disc tribometer and found that coefficient of friction was reduced by 32.25% for 0.3 wt.%, 35.48% for 0.5 wt.%, 41.93% for 0.7 wt.%, 51.61% for 1.0 wt.% and 38.70% for 1.3 wt.% of MWCNTs. Khalil et al. [19] dispersed 0.1, 0.5, 1 and 2 wt.% concentrations of MWCNTs nanoparticles in paraffinic mineral oils and Mobil gear 627 and done tribological test with four-ball tribotester according to ASTM D-5183, ASTM D-2596 and ASTM D-2783 standards and found that the addition of MWCNTs in paraffinic mineral oils causes a reduction in coefficient of friction by nearly 49% and reduction in wear by 39%, while MWCNTs in Mobil gear 627 oil causes reduction in coefficient of friction by nearly 57% and reduction in wear by 68%.

Sun et al. [20] have done oxidation of MWCNTs and prepared partially exfoliated multi-walled carbon nanotubes (Px-CNTs), they dispersed the Px-CNTs into water and after the tribological testing by using a UMT-2 ball-plate machine, they found that 0.5 wt.% of dispersed Px-CNTs into water causes decrease in friction force up to 66.4% in comparison with graphene oxide nanoribbons (GONRs) and CNTs-COOH dispersed in water, similarly 0.5 wt.% of Px-CNTs in water causes reduction in friction force by 13.82 and 19.82% in comparison with 0.3 wt.% of GONRs and MWCNTs with water.

Ye et al. [21] prepared alkyl functional MWCNTs (AMWCNTs) and oxygen functional MWCNTs (OMWCNTs) additives and dispersed them in liquid paraffin (LP) and water, respectively, in different proportions. Their tribological testing was done by the SRV-5 friction tester, and they found that when the OMWCNTs are added in pure water, then coefficient of friction is reduced to 0.17 from a value of 0.28, and similarly when AMWCNTs are added in LP, then coefficient of friction is reduced to 0.10 from a value of 0.21.

Su et al. [22] dispersed MWCNTs in LB2000 vegetable-based oil in an optimum concentrations of 0.05%, and they studied the tribological properties of above nano-lubricant by using a pin-on-disc friction and wear tester and found that at the normal force of 10 N, the wear scar depth of discs was decreased by 15.69% while coefficient of friction was decreased by 23.89%, similarly for a normal force of 2 N, the wear scar depth of discs was decreased by 14.36%, while coefficient of friction was decreased by 24.71%. Min et al. [23] fabricated 'fluorinated carbon nanotubes' by using the facile hydrothermal method, the tribological tests was performed at a value of 3–7 N of applied load and 200–400 rpm rotational speed, and they found that 0.15 wt.% of urea-modified fluorinated carbon nanotubes decrease the coefficient of friction by 80.86%, wear rate by 96.70% and wear scar width by 75%.

Singh et al. [24] have synthesized water-based lubricant by dispersing graphene nano-platelets and MWCNTs in 0.05 wt.%, 0.2 wt.%, 0.4 wt.%, 0.6 wt.%, 0.8 wt.%

and 1 wt.%. Their tribological characteristics have been investigated by using a rotary type pin-on-disc tribotester. The results have showed that at the optimum concentration of 0.8 wt.% of nanoparticles, the wear rate decreased by 61.80% and the friction coefficient decreased by 58.4% at the sliding speed of 20 m/min.

Dovjuu et al. [25] have synthesized MWCNT–nano-cellulose and graphene–nano-cellulose nano-fluids in mass ratios of 1:1, 1:2 and 2:1; they further investigated the thermal conductivity by utilizing Lambda system and found that for the optimum mass ratio of 2:1 of graphene–nano-cellulose, the highest increment in thermal conductivity is 3.77% at the temperature of 40 °C.

Baskar et al. [26] have synthesized CNT based nano-fluid by dispersing CNTs in 0.1, 0.2, 0.3 and 0.4% concentrations of volume in water and ethylene glycol and found that at the volume concentration of 0.3%, the coefficient of heat transfer increased by nearly 34.74%, while at 0.15% of volume, the coefficient of heat transfer increased by nearly 30%.

2.5 Application of Graphene

Graphene is highly useful in the production of biological as well as chemical sensors, Multi-layer sheets of graphene is used in electrochemical sensors which can detect urea [27, 28], also they are able to detect tenacious hydrocarbons, hormone disruptors, medicinal contaminants and pesticides [27]. Graphene-based TiO_2 photocatalysts are used as a photodegrader of biological and organic impurities [27, 29]. Also, the strength of polymeric membranes can be enhanced by graphene nanomaterials. Graphene has a great potential to be used as an absorbent for capturing gaseous pollutants like CO_2 and H_2 since it possesses layered structure, tunability of functional groups and high surface area [27, 29]. Graphene oxide has extraordinary material properties like layer number, surface area and lateral dimensions [30] which are utilized in carrying various types of therapeutics such that proteins, small drug molecules, antibodies and genes and in protection of DNA [30]. Graphene holds exclusive optical property to absorb near-infrared (NIR) light [30].

2.6 Application of Carbon Nanotubes

CNTs are utilized to produce detection devices like biosensors, electrochemical detectors and gas sensors. They are also utilized in the electrochemical stripping method [8]. Piezoelectric detection of volatile analytics can be done by using sorption properties of CNTs. CNTs are also be utilized in production of gas sensors and can detect ammonia, hydrogen, nitrogen dioxide and inorganic vapour by using their electrical property variations [8]. Electrodes containing CNTs can be used as a component in fuel cells and sensors [31]. CNTs can be used in electrochemical double-layer capacitors (EDLCs) which are assumed as a greater substitute for

lithium batteries. Moreover, CNTs can also be used in filters and membranes, catalysis, actuators and biomedical applications [31]. CNTs are used for vaccine delivery in a large scale for treatment of different infectious diseases and also for treatment of cancer because it possesses low toxicity, vivo stability, ability of attachment with numerous copies of antigens and lack of inherent immunogenicity [32], and also due to enriched mechanical properties, CNTs improve formation of tissues and the scaffold properties [32].

3 Conclusion

The above article represents a review of various applications and modifications in tribological properties of nano-lubricant if graphene and carbon nanotubes used as nanoparticles. It can be seen that both the graphene as well as carbon nanotubes have a huge impact on tribological performances (reduction in wear and friction) of nano-lubricants as well as in improvement of heat transfer properties of different type of nano-fluids. They are highly recommended nano-materials for reducing wear and friction of various machine components since their discovery. On the other hand, they are also useful in different types of sensors, filters, electrodes as well as biomedical applications and many more applications.

References

1. Rasheed, K., Khalid, M., Rashmi, W., Gupta, T. C. S. M., & Chan, A. (2016). Graphene based nanofluids and nanolubricants—Review of recent developments. *Renewable and Sustainable Energy Reviews, 63*, 346–362.
2. Paul, G., Hirani, H., Kuila, T., Murmu, N. C. (2019). Nanolubricants dispersed with graphene and its derivatives: An assessment and review of the tribological performance. *Nanoscale, 11*(8), 3458–3483.
3. Marquis, F. D. S., & Chibante, L. P. F. (2005). Improving the heat transfer of nanofluids and nanolubricants with carbon nanotubes. *JOM, 57*(12), 32–43.
4. Dehghani, M. H., Kamalian, S., Shayeghi, M., Yousefi, M., Heidarinejad, Z., Agarwal, S., & Gupta, V. K. (2019). High-performance removal of diazinon pesticide from water using multi-walled carbon nanotubes. *Microchemical Journal, 145*, 486–491.
5. Dutta, S., & Pati, S. K. (2010). Novel properties of graphene nanoribbons: A review. *Journal of Materials Chemistry, 20*(38), 8207–8223.
6. Popov, V. N. (2004) Carbon nanotubes: Properties and application. *43*, 61–102.
7. Soundarrajan, P., Patil, A., & Dai, L. (2003). Surface modification of aligned carbon nanotube arrays for electrochemical sensing applications. *Journal of Vacuum Science & Technology A: Vacuum, Surfaces, and Films, 21*(4), 1198–1201.
8. Trojanowicz, M. (2006). Analytical applications of carbon nanotubes: A review. *TrAC—Trends in Analytical Chemistry, 25*(5), 480–489.
9. Treacy, M. M. J., Ebbesen, T. W., & Gibson, J. M. (1996). Exceptionally high young's modulus observed for individual carbon nanotubes. *Nature, 381*, 678.

10. Singh, S., Xinchun, C., Chenhui, Z., Gautam, R. K., Tyagi, R., & Luo, J. (2020). Nickel-catalyzed direct growth of graphene on bearing steel (GCr15) by thermal chemical vapor deposition and its tribological behavior. *Applied Surface Science, 502,* 144135.

11. Ren, B., Gao, L., Xie, B., Li, M., Zhang, S., Zu, G., & Ran, X. (2019). Tribological properties and anti-wear mechanism of ZnO@graphene core-shell nanoparticles as lubricant additives. *Tribology International, 144,* 106114.

12. Jinshan, L., Wang, L., & Chen, G. (2011). Modification of graphene platelets and their tribological properties as a lubricant additive. *Tribology Letters, 41*(1), 209–215.

13. Wu, D., Xu, Y., Yao, L., You, T., & Hu, X. (2018) Tribological behaviour of graphene oxide sheets as lubricating additives in bio-oil. *Industrial Lubrication and Tribology, 70*(8), 1396–1401.

14. Huanga, S., Hea, A., Yunb, J.-H., Xuc, X., Jiangd, Z., Jiaoe, S., & Huanga, H. (2019). Synergistic tribological performance of a water based lubricant using graphene oxide and alumina hybrid nanoparticles as additives. *Tribology International, 135*(February), 170–180.

15. Xie, H., Dang, S., Jiang, B., Xiang, L., Zhou, S., Sheng, H., Yang, T., & Pan, F. (2018). Tribological performances of SiO_2/graphene combinations as water-based lubricant additives for magnesium alloy rolling. *Applied Surface Science, 475*(October), 847–856.

16. Meng, Y., Su, F., & Chen, Y. (2011). Synthesis of nano-Cu/graphene oxide composites by super-critical CO_2-assisted deposition as a novel material for reducing friction and wear. *Chemical Engineering Journal, 281,* 11–19. Elsevier B.V.

17. Singh, H., & Bhowmick, H. (2018). Tribological behaviour of hybrid AMMC sliding against steel and cast iron under MWCNT-oil lubrication. *Tribology International, 127,* 509–519.

18. Jeyaprakasha, N., Sivasankaranb, S., Prabuc, G., Yanga, C.-H., Alaboodi, A. S. (2019, December). Enhancing the tribological properties of nodular cast iron using multi wall carbon nanotubes (MWCNTs) as lubricant additives, 37–41.

19. Khalil, W., Mohamed, A., Bayoumi, M., & Osman, T. A. (2016). Tribological properties of dispersed carbon nanotubes in lubricant. *Fullerenes Nanotubes and Carbon Nanostructures, 24*(7), 479–485.

20. Sun, X., Zhao, M., Han, B., Kang, H., Fan, Z., Liu, Y., et al. (2017). Frictional reduction with partially exfoliated multi-walled carbon nanotubes as water-based lubricant additives. *Journal of Nanoscience and Nanotechnology, 18*(5), 3427–3432.

21. Ye, X., Songfeng, E., Fan, M. (2019). The influences of functionalized carbon nanotubes as lubricating additives: Length and diameter. *Diamond and Related Materials, 100,* 107548.

22. Yu, S., Tang, Z., Wang, G., & Wan, R. (2018). Influence of carbon nanotube on the tribological properties of vegetable based oil. *Advances in Mechanical Engineering, 10*(5), 1–11.

23. Min, C., He, Z., Liu, D., Zhang, K., & Dong, C. (2019). Urea modified fluorinated carbon nanotubes: Unique self-dispersed characteristic in water and high tribological performance as water-based lubricant Additives. rsc.li/njc.

24. Singh, R. K., Dixit, A. R., Sharma, A. K., Tiwari, A. K., Mandal, V., & Pramanik, A. (2018). Influence of graphene and multi-walled carbon nanotube additives on tribological behaviour of lubricants. *International Journal of Surface Science and Engineering, 12*(3), 207.

25. Dovjuu, O., Kim, S., Lee, A., Kim, J., Noh, J., Huh, S., et al. (2020). A simple approach for heat transfer enhancement of carbon nanofluids in aqueous media. *Journal of Nanoscience and Nanotechnology, 20*(4), 2337–2343.

26. Baskar, S., Chandrasekaran, M., Vinod Kumar, T., Vivek, P., & Karikalan, L. (2018). Experimental studies on convective heat transfer coefficient of water/ethylene glycol-carbon nano tube nanofluids. *International Journal of Ambient Energy,* 1–4.

27. Perreault, F., de Faria, A. F., & Elimelech, M. (2015). Environmental applications of graphene-based nanomaterials. *Chemical Society Reviews, 44*(16), 5861–5896.

28. Srivastava, R. K., Srivastava, S., Narayanan, T. N., Mahlotra, B. D., Vajtai, R., Ajayan, P. M., & Srivastava, A. (2012). Functionalized multilayered graphene platform for urea sensor, *6,* 168–175.

29. Ghosh, A., Subrahmanyam, K. S., Krishna, K. S., Datta, S., Govindaraj, A., Pati, S. K., & Rao, C. N. R. (2008). Uptake of H_2 and CO_2 by graphene. *Journal of Physical Chemistry C, 112*(40), 15704–15707.

30. Wu, S.-Y., Soo, S., An, A., Hulme, J. (2015). Current applications of graphene oxide in nanomedicine. *International Journal of Nanomedicine, 10*, 9–24.
31. Schnorr, J. M., & Swager, T. M. (2011). Emerging applications of carbon nanotubes. *Chemistry of Materials, 23*(3), 646–657.
32. Prajapati, S. K., Malaiya, A., Kesharwani, P., Soni, D., & Jain, A. (2020). Biomedical applications and toxicities of carbon nanotubes. *Drug and Chemical Toxicology*, 1–16.

Review of Recent Progresses in Thermoelectric Materials

Jitendra Mohan Giri and Pawan Kumar Singh Nain

Abstract Thermoelectric (TE) technology facilitates the direct conversion of heat into electricity and vice versa. Thermoelectric materials attract researchers since they facilitate a promising green energy solution in the form of solid-state cooling and power generation. However, the low energy conversion efficiency restricts the use of TE materials in real-world applications. Developing highly efficient thermoelectric materials is necessary to benefit the environment as well as the economy. The performance of a particular TE material is generally evaluated by the dimensionless figure of merit (*ZT*). Recent years have witnessed progress with new techniques in maximizing the *ZT* values of various thermoelectric materials. In this review, we summarize recent development in thermoelectric materials for a specific temperature range, which has been developed to improve their maximum *ZT* value up to 95% at the same temperature.

1 Introduction

The environmental issues resulting from unsustainable consumption of fossil fuels are well known. Thermoelectric (TE) devices are compact, noiseless, and environmentally friendly and exhibit a leading potential for sustainable development. The thermoelectric module is a p-type and n-type semiconductor element-based solid-state device that converts the thermal energy with temperature difference into electric power (known as Seebeck effect) and also capable of converting electrical energy into temperature gradient (known as Peltier effect). Based on the directions of energy

J. M. Giri (✉) · P. K. S. Nain
Galgotias University, Greater Noida 201312, India
e-mail: jitendra.giri@galgotiasuniversity.edu.in

P. K. S. Nain
e-mail: pawan.kumar@galgotiasuniversity.edu.in

conversion, these devices are termed as thermoelectric coolers (TEC) and thermo-electric generator (TEG). Thermoelectric generators allow obtaining electricity from any heat source, which shows fantastic application potential. From micro-scale appli-cations to large-scale applications, thermoelectric coolers offer a futuristic role in cooling systems as they work without any moving element involving working fluid.

2 Background

Thermoelectricity is based on two primary thermoelectric effects; the Seebeck effect and the Peltier effect. According to the Seebeck effect, an electromotive force emerges through the electrical circuit consisting of p-type and n-type semiconductor materials and connected in series when contacts are maintained at different temperatures. According to the Peltier effect, if the electric current passes through the circuit of p-type and n-type semiconductor materials, interconnected in series, heat flows from one side to the other side. So, one side of the thermoelectric module is cooled while the other side gets heated.

The performance of any thermoelectric material is generally recognized by the figure of merit (Z). Z depends on three essential material parameters: Seebeck coef-ficient (S), electrical conductivity (σ), and thermal conductivity (κ) and usually expressed in the dimensionless form at an absolute temperature (T). The dimen-sionless figure of merit (ZT) is defined as $ZT = S^2 \sigma T/\kappa$. Alternatively, ZT is also defined as ($S^2/\rho\kappa$) T, where ρ is the electrical resistivity. A large power factor (S^2/ρ) is required to enhance thermoelectric performance. A good thermoelectric material should possess a large Seebeck coefficient (S), low thermal conductivity (σ), and high electrical conductivity (κ). The conversion efficiency of TE devices is directly related to the dimensionless figure of merit of their constituting materials. Thus, a high value of the figure of merit is highly desirable.

3 Recent Progresses to Enhance *ZT* of Thermoelectric Materials

In recent years, researchers applied new approaches and techniques in maximizing the *ZT* values of various thermoelectric materials. The available thermoelectric mate-rials exhibit varying performance in the different temperature ranges. Improvement in each available thermoelectric material is a focused goal of researchers for a sustain-able alternative of conventional energy converters. Earlier, the performance of the semiconductors used in TE applications was dependent on the available pure and perfect single crystals. However, these materials can be doped by adding small quan-tities of impurities. These impurities act as the electron donor for the parent materials. Most traditional semiconductors have cubic structures, whereas anisotropic crystals

are used for TE applications. The task of designing high-performance thermoelectric materials is to adjust the physical parameters of interconnected S, σ, and κ for a crystalline structure. Thermoelectric transport includes the flow of thermal energy and charge. The energy of phonons (vibrational waves of atoms) represents the thermal energy. Electron scattering on phonons creates electrical resistance. Through incorporating some new scattering mechanisms, nanostructures provide an opportunity to sever the connection between electric and thermal transport. The lattice thermal conductivity needs to be reduced for improvement in TE performance. Mass fluctuations increase through vacancies, and interstitial atoms result in higher phonon scattering that can lead to better TE performance. Sintering of bulk materials and melting production are the techniques used for research efforts to get improved TE materials. This work summarizes recent approaches to enhance the ZT of various thermoelectric materials. There is a wide variety of elements and compounds which can be categorized as thermoelectric materials. It is to be noted that every thermoelectric material exhibits different performance at different temperatures. Hence, it is not possible to recommend a single TE material that is suitable for all practical ranges of temperature in real-world applications. Thus in the present study, the authors have classified the TE materials based on their suitability for low-, medium-, and high-temperature applications.

3.1 Low-Temperature Thermoelectric Materials (300–500 K)

Bi_2Te_3 and its alloys with ZT values of around 0.9–1.0 are considered prominent TE materials at room temperature and widely used for practical thermoelectric applications [1, 2]. Hu et al. demonstrated that the porous structure affects thermoelectric performance [3]. As porosity increased, electrical and thermal conductivity decreased significantly. Reducing thermal conductivity compensates for the deterioration in electrical conductivity and improves the ZT value. A sample premixed with five wt percent NH_4HCO_3 was reported with 1.1 value of maximum ZT at temperature 343 K. This was around 20% better than that of the entirely dense sample with 0.92 value of ZT. Bi-containing Sb_2Te_3 and the related alloys with a high thermoelectric figure of merit can be futuristic options to use in thermoelectric devices. $Sb_{2-x}Bi_xTe_3$ samples were milled, pressed, and annealed under vacuum for 3 h at 250 °C by Adam et al. [4]. Bi was added to the binary Sb_2Te_3 system. An increased Seebeck coefficient and power factor were obtained for $Sb_{1.65}Bi_{0.35}Te_3$ with the reduced value of thermal conductivity. Subsequently, a high ZT of 1.14 at 400 K was achieved. The sample composition of $(Bi_2Te_3)_{0.15} + (Sb_2Te_3)_{0.85}$ was prepared to shift maximum ZT to the high-temperature zone by Madavali et al. [5]. The maximum ZT values of 1.3 and 1.07 were reported at 400 K and 300 K, respectively.

Tellurium is the prevailing thermoelectric material utilized in low to medium range of temperature. However, it contains an inferior thermoelectric efficiency with a low value of ZT. An enhancement in the performance of amorphous silicon has

been reported by Banerjee et al. [6]. They applied the method of arsenic ion implantation. The low-temperature dopant activation was done. It was observed that the *ZT* value of amorphous silicon (a-Si) thin films could be enhanced by seven orders at room temperature. Arsenic doping at low-temperature results in the enhancement of electrical conductivity. Empowering a-Si as a conspicuous TE material may be useful for sustainable energy applications at room temperature with maximum *ZT* up to 0.77. The magneto-thermoelectric figure of merit (*ZT*) in 3-D Dirac semimetal Cd_3As_2 crystal was reported by Wang et al. [7]. The magnetic field very effectively reduces electric conductivity and thermal conductivity. A maximum *ZT* value of 1.1 was obtained at 350 K temperature under 7 T of the magnetic field.

A hypothesis of thermoelectric transport properties in 2-D semiconducting quantum well structures is built up by Yelgel et al. [8]. Within the temperature range 50–600 K, computations are performed for n-type 0.1 wt% CuBr-doped $Bi_2Se_3/Bi_2Te_3/Bi_2Se_3$ and also for p-type 3 wt% Te-doped $Sb_2Te_3/Bi_2Te_3/Sb_2Te_3$ quantum well frameworks. It is discovered that diminishing the well thickness pronouncedly affects upgrading the *ZT* value. At 350 K temperature, the maximum *ZT* value of 0.97 is obtained for $Bi_2Se_3/Bi_2Te_3/Bi_2Se_3$. At 440 K temperature, the maximum *ZT* value of 1.945 is obtained for $Sb_2Te_3/Bi_2Te_3/Sb_2Te_3$. $CaMnO_3$ has a generally high Seebeck coefficient; however, the electrical conductivity (σ) is quite low (within the temperature range 300–1000 K). Hence, an un-doped material brings a low power factor ($S^2\sigma$). The bismuth doping of $Ca_{1-x}Bi_xMnO_3$ has been reported by Paengson et al. [9]. With x range of 0-0.05, TE materials were setup. The solid-state reaction and hot pressing techniques were used. Bi doping increased carrier concentration for all samples with different x. The electrical resistivity diminished with expanding bismuth content. The maximum *ZT* value of 0.065 at 473 K was found for $Ca_{0.97}Bi_{0.03}MnO_3$. It is worth mentioning that the *ZT* value was increased by 95% at the same temperature compared to $CaMnO_3$. Bi_2Te_3 and the family of similar compounds potentially satisfy the thermoelectric efficiency levels at low temperatures. However, the dimensionless figure of merit values decreases severely at a temperature over 450 K. The bulk $Bi_{1.9}Lu_{0.1}Te_3$ samples with diverse micro-grained particles were fabricated using cold isolated pressing (CIP) with annealing at high temperature and secondly by spark plasma sintering (at 653 and 683 K) by Yaprintsev et al. [10]. The maximum *ZT* ~ 0.9 for 450–500 K range of temperature range is obtained.

The summary of recent *ZT* improvements of thermoelectric materials at low temperatures discussed in this study is presented in Table 1.

3.2 Medium-Temperature Thermoelectric Materials (500–900 K)

CuAgSe exhibits excellent potential due to its fantastic carrier mobility. It also has low thermal conductivity. To prepare monodisperse CuAgSe nanocrystals, a scalable

Table 1 Summary of recent ZT improvements of TE materials at low temperatures

Researchers	Year	Thermoelectric material	Method for properties enhancement	Impact on ZT performance
Hu et al.	2020	$Bi_{0.4}Sb_{1.6}Te_3$	Pre-mixing with NH_4HCO_3	• Max. Dimensionless figure of merit (ZT_{max}) of 1.11 at 343 K • 20% increment in ZT_{max} as compared with fully dense material
Adam et al.	2020	Sb_2Te_3	Bi-containing	ZT_{max} value of 1.14 at 400 K for Sb_2Te_3
Madavali et al.	2018	$(Bi_2Te_3)_x + (Sb_2Te_3)_{1-x}$	Increasing Sb_2Te_3 content	• ZT_{max} value of 1.3 at 400 K • ZT_{max} value of 1.07 at 300 K
Banerjee et al.	2018	Amorphous silicon	Arsenic doping	ZT around ~0.64 ± 0.13 at room temperature
Wang et al.	2018	Cd_3As_2	Enhancement by the magnetic field	ZT_{max} value of 1.1 at 350 K
Yelgel and Srivastava	2014	$Bi_2Se_3/Bi_2Te_3/Bi_2Se_3$ and $Sb_2Te_3/Bi_2Te_3/Sb_2Te_3$	By varying the well thickness+	$ZT_{max} = 0.97$ at 350 K for $Bi_2Se_3/Bi_2Te_3/Bi_2Se_3$ and $ZT_{max} = 1.945$ at 440 K for $Sb_2Te_3/Bi_2Te_3/Sb_2Te_3$
Paengson et al.	2017	$CaMnO_3$	Bi doping and hot pressing of $CaMnO_3$	• ZT_{max} value of 0.065 at 473 K for $Ca_{0.97}Bi_{0.03}MnO_3$ • 95% increment in ZT_{max} as compared with un-doped material
Yaprintsev et al.	2017	$Bi_{1.9}Lu_{0.1}Te_3$	Fabrication by cold isostatic pressing and SPS	ZT_{max} value ~0.9 for 450–500 K

colloidal synthesis has been reported by Zuo et al. [11]. The gathered powder test was cleaned by a non-sulfur substance of $NaNH_2$. It was done to expel the organic ligands from the surface. After that, annealing process was also done. A 0.68 value of maximum ZT at 566 K was obtained. The obtained material shows the potential of TE applications for mid-range temperatures. The material before annealing exhibits a temperature- controlled transition from n-type toward p-type. This makes it suitable for thermal control transistor applications. $CoSb_3$ skutterudite is considered potential TE material for power generation. La Filler atoms are used to minimize lattice thermal conductivity for the skutterudite to get better TE performance [12, 13]. Bashir et al. reported a high ZT value of 1.15 at 692 K with La and In as the $In_{0.3}La_{0.5}Co_4Sb_{12}$ skutterudite [14]. BiCuSeO contains low thermal conductivity and an average power

factor. BiCuSO was doped with Pb and effectively synthesized by high pressure by Zhu et al. [15]. BiCuSeO doped with Pb increases the carrier concentration. This Pb doping improves the power factor. The thermal conductivity is smothered by Pb doping. At 700 K temperature, the maximum ZT of 0.14 is achieved. Synthesization with feasible high-pressure and high-temperature techniques can increase the TE performance of Cu_2Se bulk materials. At 723 K, a high ZT value of 1.19 was reported for Cu_2Se synthesized at 3 GPa by Xue et al. [16]. Recently, GeTe and its derivatives have gained considerable attention as promising thermoelectric materials. Perumal et al. [17] reported a maximum ZT value of 2.1 for In and Bi co-doped GeTe at 723 K.

The synthesization of a group of TiNiSn-based alloys has been performed by Chen et al. [18]. It was done by way of an easy solid-state reaction followed by the SPS method. The amount and mixture of the heterogeneous phase were precisely managed, which results in a successful decrement of thermal conductivity (up to 2.3–3.0 $Wm^{-1}K^{-1}$). Besides, TE figure of merit was enhanced up to 0.49 at 750 K temperature. Silicon–germanium-based alloys are appealing. For radioisotope thermoelectric power generation at an excessive temperature (more than 1000 °C), they offer a good choice of TE material. On the other side, mesostructured $In_{0.25}Co_4Sb_{12}$ and $In_{0.25}Yb_{0.05}Co_4Sb_{12}$ samples have been synthesized by Benyahia et al. [19]. The samples were fabricated through melting and annealing. Then, the ball-milling procedure was applied to minimize size and sintered through the SPS method. With a mean grain size of 400 nm, a maximum dimensionless figure of merit of 1.4 at 750 K temperature is obtained. It was achieved in the BM $In_{0.25}Co_4Sb_{12}$ + 0% CeO_2. TiNiSn-based half-Heusler (HH) alloys are widely studied. These thermoelectric materials show a high-temperature stabilization. However, the thermal conductivity is constantly enormously high, and hence, further ZT enhancement is difficult. SiC nanoparticles were brought into the matrix of $Pb_{0.98}Na_{0.02}Te$ doped with SrTe by Ai et al. [20]. The increased Seebeck coefficient and decreased electrical conductivity resulted in a remarkable peak ZT of 1.73 at 750 K.

Copper selenide is a promising thermoelectric material because of its fantastic electrical properties. A hydrothermal technique to incorporate astounding β-$Cu_2Se_{1-x}I_x$ nanopowder with a cost-effective minimum consumption of energy is reported by Wang et al. [21]. The nanopowder with different levels of doped iodine was used. Utilizing this straightforward and modest methodology, an improved ZT of 1.13 is obtained at a temperature of 773 K in iodine-doped Cu_2Se ($x = 0.03$) pellets after hot squeezing. Recently, the synthesis of p-type SiGe with boron using varied proportion is reported by Murugasami et al. [22]. The material was sintered through the spark plasma sintering technique. Doped with $B_{1.5}$ at.% synthesized SiGe alloy exhibits the enhanced ZT of 0.525 at 800 °C temperature. A considerable improvement of approximately 9.38% is obtained. Recently, the enhancement of skutterudite performance is reported by Yang et al. [23]. Tellurium-doped skutterudite has been shown to have promising TE properties using nano-micro-level pores. Cobalt, antimony, and tellurium powders were utterly blended with a nominal composition of $Co_4Sb_{11.5}Te_{0.5}$. Then, the material was stacked into carbon cauldrons and kept inside quartz tubes below vacuum for heating. The acquired ingots were ground into powders utilizing two successive methods, first by a mortar and then

by ball milling below vacuum. The two powders (without ball milling and with ball milling) with different proportions were blended, and after that, sintered using spark plasma sintering technique. The annealing process below vacuum was also done on the obtained bulk material. The authors reported that annealed nanoparticles carry some randomly allotted nanopores with a range of sizes from 200 nm to 2 μm. The development of these nanosized pores is due to strain during sintering. The thermal conductivity drops drastically which is a desired effect. A 1.2 value of the maximum dimensionless figure of merit is obtained for the annealed material at a temperature of 800 K. A significant increment of approx. 35% was reported. The thermoelectric properties of n-type-doped Mg_2 $(Si_{0.4}Sn_{0.6})_{1-y}$ Bi_y solid solutions are investigated theoretically by Yelgel [24]. From 300 to 800 K temperature range, the selected y range is 0.005–0.06 for doping Bi with available experimental data. It was found that an appropriate y can increase ZT. The maximum ZT is obtained with y = 0.03 at 800 K and values 1.82.

The graphene nanoplate incorporated into Cu_2Se samples has been fabricated by Li et al. [25]. The ball-milling technique was applied. Then, sintering through the SPS method was done. The homogeneous dispersion of the carbon phase reduced the Cu_2Se particles to form an excellent dense construction. Maximum ZT reached a high 1.7 value at 873 K. This gives an appropriate technique to use carbon engineering to maximize TE performance for Cu_2Se and family compounds. The deliberate actuated dislocations and vacancies are compelling in diminishing the thermal conductivity of polycrystalline SnS, as reported by Asfandiyar et al. [26]. Low thermal conductivity and high electrical conductivity $Sn_{0.99}Ag_{0.005}S$ sample were obtained at 877 K. Ag doping brings high power factor, and an enhanced ZT of 1.1 at 877 K was recorded for $Sn_{0.99}Ag_{0.005}S$. N-type half-Heusler NbCoSn performs well in TE performance, but p-type performs poorly. Replacing Sc at Nb site may change the n-type NbCoSn to a p-type semiconductor as reported by Yan et al. [27] by changing the Fermi level, indicating that Sc is a suitable p-type dopant. ZT_{max} value of 0.13 at 879 K has been reported.

The summary of recent ZT improvements of thermoelectric materials at medium temperatures discussed in this study is presented in Table 2.

3.3 High-Temperature Thermoelectric Materials (>900 K)

Lead selenide (PbSe) displays a temperature-dependent Seebeck coefficient, low thermal conductivity, and low electrical resistivity. Further, it has resolved the issue that emerges to get both n- and p-type legs. A simultaneous advancement of thermal and electrical properties of p-type PbSe has been reported by Zhao et al. [28]. The density hypothesis for estimations of valence band energy levels was used. Between lead selenide and nanostructures of $CdS_{1-x}Se_x/ZnS_{1-x}Se_x$, appropriate valence band alignments were introduced. A highly enhanced dimensionless figure of merit of 1.6 at 923 K was attained at $Pb_{0.98}Na_{0.02}Se + 3\%Cds$. Due to its high TE efficiency, Si-Ge alloys are considered valuable TE materials operating at high temperatures. The effect

Table 2 Summary of recent ZT improvements of TE materials at medium temperatures

Researchers	Year	Thermoelectric material	Method for properties enhancement	Impact on ZT performance
Zuo et al.	2018	CuAgSe	Colloidal synthesis of monodisperse CuAgSe NCs	ZT_{max} value of 0.68 at 566 K
Bashir et al.	2018	$CoSb_3$	La and In filling	ZT_{max} value of 1.15 at 692 K
Zhu et al.	2018	BiCuSO	Doping with Pb	ZT_{max} value of 0.14 at 700 K
Xue et al.	2019	Cu_2Se	Synthesis with high pressure	ZT_{max} value of 1.1 at 723 K
Perumal et al.	2019	GeTe	In and Bi doping	ZT_{max} value of 2.1 at 723 K
Chen et al.	2017	TiNiSn-based half-Heusler (HH) alloys	Synthesis with solid-state reaction	ZT_{max} value of 0.49 at 750 K
Benyahia et al.	2018	$In_{0.25}Co_4Sb_{12}$	Synthesis by a melting–annealing–ball-milling–SPS method	ZT_{max} value of 1.4 at 750 K
Ai et al.	2020	PbTe	SiC dispersing and SrTe doping	ZT_{max} value of 1.73 at 750 K for $Pb_{0.98}Na_{0.02}Te$/4 mol%SrTe composite
Wang et al.	2019	Cu_2Se	Synthesis of Cu_2Se alloys doped with iodine	ZT_{max} value of 1.13 at 773 K for $Cu_2Se_{1-x}I_x$ (x = 0.03)
Murugasami et al.	2019	SiGe	Synthesis of SiGe alloys doped with Boron	ZT_{max} value of 0.525 at 800 °C for doped with $B_{1.5}$
Yang et al.	2019	Te-doped skutterudite ($Co_4Sb_{11.5}Te_{0.5}$)	Nanomicroporous structure in $Co_4Sb_{11.5}Te_{0.5}$ materials via annealing the nano-$Co_4Sb_{11.5}Te_{0.5}$/$Co_4Sb_{11.5}Te_{0.5}$ composites	• Max. Dimensionless figure of merit (ZT_{max}) of 1.2 at 800 K for annealed sample (N10–A100) • 33.7% increment in ZT_{max} as compared with dense material (N0)
Yelgel	2016	$Mg_2Si_{0.4}Sn_{0.6}$	Mg_2 $(Si_{0.4}Sn_{0.6})_{1-y}$ Bi solid solutions	ZT_{max} value of 1.82 at 800 K
Li et al.	2018	Cu_2Se	By graphene nanoplate incorporation	ZT_{max} value of 1.7 at 873 K
Asfandiyar et al.	2020	SnS	Intentional-induced dislocations and vacancies and Ag doping	ZT_{max} value of 1.1 at 877 K for $Sn_{0.99}Ag_{0.005}S$
Yan et al.	2020	NbCoSn	Sc substitution at the Nb site	ZT_{max} value of 0.13 at 879 K

Table 3 Summary of recent *ZT* improvements of TE materials at high temperatures

Researchers	Year	Thermoelectric material	Method for properties enhancement	Impact on *ZT* performance
Zhao et al.	2013	PbSe	Integration of band structure with hierarchical structuring	ZT_{max} value of 1.6 at 923 K
Muthusamy et al.	2020	Si–Ge–Au	Boron doping	ZT_{max} value of 1.63 at 973 K
He et al.	2014	Cu_2S	Cu deficiency	ZT_{max} value of 1.7 at 1000 K
Fu et al.	2015	FeNbSb	Hf doping	ZT_{max} value of 1.5 at 1200 K
Wille et al.	2019	$Yb_{14}ZnSb_{11}$	Containing RE	ZT_{max} value of 0.7 at 1275 K

on thermoelectric properties of B-doped Si-Ge-Au nanocomposites was investigated, taken as $Si_{65-x}Ge_{31}Au_4B_x$ by Muthusamy et al. [29]. At 973 K, a maximum *ZT* value of 1.63 was reported at x = 3. The phonon-liquid electron-crystal concept for copper sulfide with reduced thermal conductivity and higher thermoelectric performance has been proposed by He et al. [30]. A high *ZT* value of 1.7 was reported at 1000 K by using copper deficiency as $Cu_{2-x}S$ with x = 0.03.

Half-Heusler compounds are increasingly attracting attention because of their strong mechanical and electrical properties at high temperatures. At 1200 K, through heavier Hf doping the p-type FeNbSb heavy-band half-Heusler alloys with 1.5 value of high *ZT* was reported by Fu et al. [31]. $Yb_{14}ZnSb_{11}$ is considered for intermediate valence interest. With rare earth (RE) solution as $Yb_{14-x}RE_xZnSb_{11}$ was investigated by Wille et al. [32]. The dimensionless figure of merit was reported as high as 0.7 at 1275 K with x = 0.5.

The summary of recent *ZT* improvements of thermoelectric materials at high temperatures discussed in this study is presented in Table 3.

4   Conclusion

Exploring advancement in thermoelectric materials for sustainable energy solutions is the contemporary area of interest. The *ZT* value of thermoelectric materials should be enhanced for a broad range of potential applications of thermoelectric devices. From this study, it can be highlighted that:

- In the recent past, material researchers are successfully applying new approaches to upgrade the performance of available materials for a particular temperature range.

- A promising new approach is to create nanolevel and macro-level pores in tellurium doped skutterudite to enhance *ZT* by approximately 35%.
- Another interesting approach is introducing a facile method for colloidal synthesis of copper-silver selenide. With ZT_{max} value of 0.68 at temperature 566 K, this resulted as a promising candidate for TE research in the intermediate temperature range.

The significant outcomes of researchers will boost the applicability of TE devices contribution to the present world's green energy solutions. For greater commercialization of thermoelectric applications, improved materials with high values of *ZT* are required at prevailing operating temperatures. This will boost the manufacture of better performing TE modules. These advancements in *ZT* values could close the gap in performance between conventional bismuth-tellurium-based materials and newer materials. The costs to invent newer thermoelectric materials are quite different from the production cost of those materials. The costs of candidate materials, costs to process those materials into TE elements, and cost to compensate the material loss are significant for the real commercial applications of newly researched materials. The non-availability of the requisite raw materials might result in holding the production of TE devices. More extensive work on that would be useful.

References

1. Witting, I. T., Chasapis, T. C., Ricci, F., Peters, M., Heinz, N. A., Hautier, G., & Snyder, G. J. (2019). The thermoelectric properties of bismuth telluride. *Advanced Electronic Materials, 5*, 1800904. https://doi.org/10.1002/aelm.201800904.
2. Goldsmid, H. J. (2014). Bismuth telluride and its alloys as materials for thermoelectric generation. https://doi.org/10.3390/ma7042577.
3. Hu, X., Hu, J., Fan, X., Feng, B., Pan, Z., Liu, P., Zhang, Y., Li, R., He, Z., Li, G., & Li, Y. (2020). Artificial porous structure: An effective method to improve thermoelectric performance of Bi_2Te_3 based alloys. *Journal of Solid State Chemistry, 282.* https://doi.org/10.1016/j.jssc.2019.121060.
4. Adam, A. M., El-Khouly, A., Novitskii, A. P., Ibrahim, E. M. M., Kalugina, A. V., Pankratova, D. S., Taranova, A. I., Sakr, A. A., Trukhanov, A. V., Salem, M. M., & Khovaylo, V. (2020). Enhanced thermoelectric figure of merit in Bi-containing Sb_2Te_3 bulk crystalline alloys. *Journal of Physics and Chemistry of Solids, 138*, 109262. https://doi.org/10.1016/j.jpcs.2019.109262.
5. Madavali, B., Kim, H. S., Lee, C. H., Kim, D.-S., & Hong, S. J. (2019). High thermoelectric figure of merit in p-type $(Bi_2Te_3)_x - (Sb_2Te_3)_{1-x}$ alloys made from element-mechanical alloying and spark plasma sintering. *Journal of Electronic Materials, 48*, 416–424. https://doi.org/10.1007/s11664-018-6706-7.
6. Banerjee, D., Vallin, Ö., Samani, K. M., Majee, S., Zhang, S. L., Liu, J., & Zhang, Z. B.: Elevated thermoelectric figure of merit of n-type amorphous silicon by efficient electrical doping process. *Nano Energy, 44*, 89–94.
7. Wang, H., Luo, X., Chen, W., Wang, N., Lei, B., Meng, F., Shang, C., Ma, L., Wu, T., Dai, X., Wang, Z., & Chen, X. (2018). Magnetic-field enhanced high-thermoelectric performance in topological Dirac semimetal Cd_3As_2 crystal. *Science Bulletin, 63*, 411–418.

8. Yelgel, Ö. C., & Srivastava, G. P. (2014) Thermoelectric properties of $Bi_2Se_3/Bi_2Te_3/Bi_2Se_3$ and $Sb_2Te_3/Bi_2Te_3/Sb_2Te_3$ quantum well systems. *Philosophical Magazine, 94*, 2072–2099. https://doi.org/10.1080/14786435.2014.903340.

9. Paengson, S., Pilasuta, P., Singsoog, K., Namhongsa, W., Impho, W., & Seetawan, T. (2017). Improvement in thermoelectric properties of $CaMnO_3$ by Bi doping and hot pressing. In: *Materials today: Proceedings* (pp. 6289–6295). https://doi.org/10.1016/j.matpr.2017.06.129.

10. Yaprintsev, M., Lyubushkin, R., Soklakova, O., & Ivanov, O. (2018). Microstructure and thermoelectric properties of $Bi_{1.9}Lu_{0.1}Te_3$ compound. *Rare Metals, 37*, 642–649.

11. Zuo, Y., Liu, Y., He, Q. P., Song, J. M., Niu, H. L., & Mao, C. J. (2018). CuAgSe nanocrystals: Colloidal synthesis, characterization and their thermoelectric performance. *Journal of Materials Science, 53*, 14998–15008. http://doi.org/10.1007/s10853-018-2676-7.

12. Bao, S., Yang, J., Zhu, W., Fan, X., Duan, X., & Peng, J. (2006). Preparation and thermoelectric properties of La filled skutterudites by mechanical alloying and hot pressing. *Materials Letters, 60*, 2029–2032. https://doi.org/10.1016/j.matlet.2005.12.074.

13. Liu, K., Dong, X., & Jiuxing, Z. (2006). The effects of La on thermoelectric properties of $La_xCo_4Sb_{12}$ prepared by MA-SPS. *Materials Chemistry and Physics, 96*, 371–375.

14. Bashir, M. B. A., Said, S. M., Sabri, M. F. M., Miyazaki, Y., Shnawah, D. A., Shimada, M., Salleh, M. F. M., Mahmood, M. S., Salih, E. Y., Fitriani, F., & Elsheikh, M. H. (2018). In-filled $La_{0.5}Co_4Sb_{12}$ Skutterudite system with high thermoelectric figure of merit. *Journal of Electronic Materials, 47*, 2429–2438.

15. Zhu, H., Su, T., Li, H., Hu, Q., Li, S., & Hu, M. (2018). Thermoelectric properties of BiCuSO doped with Pb. *Solid State Communications.* https://doi.org/10.1016/j.ssc.2018.04.013.

16. Xue, L., Zhang, Z., Shen, W., Ma, H., Zhang, Y., Fang, C., Jia, X. (2019). Thermoelectric performance of Cu_2Se bulk materials by high-temperature and high-pressure synthesis. *Journal of Materiomics, 5*, 103–110. http://doi.org/10.1016/j.jmat.2018.12.002.

17. Perumal, S., Samanta, M., Ghosh, T., Shenoy, U. S., Bohra, A. K., Bhattacharya, S., Singh, A., Waghmare, U. V., & Biswas, K. (2019). Realization of high thermoelectric figure of merit in gete by complementary co-doping of Bi and In. *Joule, 3*, 2565–2580. https://doi.org/10.1016/j.joule.2019.08.017.

18. Chen, J. L., Liu, C., Miao, L., Gao, J., Zheng, Y. Y., Wang, X., Lu, J., & Shu, M. (2018). Improved thermoelectric performance achieved by regulating heterogeneous phase in half-heusler TiNiSn-based materials. *Journal of Electronic Materials* (2018).

19. Benyahia, M., Ohorodniichuk, V., Leroy, E., Dauscher, A., Lenoir, B., & Alleno, E. (2018). High thermoelectric figure of merit in mesostructured $In_{0.25}Co_4Sb_{12}$ n-type skutterudite. *Journal of Alloys and Compounds.* http://doi.org/10.1016/j.jallcom.2017.11.195.

20. Ai, X., Hou, D., Liu, X., Gu, S., Wang, L., & Jiang, W. (2020). Enhanced thermoelectric performance of PbTe-based nanocomposites through element doping and SiC nanoparticles dispersion. *Scripta Materialia, 179*, 86–91.

21. Wang, J., Liu, B., Miao, N., Zhou, J., & Sun, Z. (2019). I-doped Cu_2Se nanocrystals for high-performance thermoelectric applications. *Journal of Alloys and Compounds* (2019). https://doi.org/10.1016/j.jallcom.2018.08.291.

22. Murugasami, R., Vivekanandhan, P., Kumaran, S., Suresh Kumar, R., & John Tharakan, T. (2019). Simultaneous enhancement in thermoelectric performance and mechanical stability of p-type SiGe alloy doped with Boron prepared by mechanical alloying and spark plasma sintering. *Journal of Alloys and Compounds* (2019). https://doi.org/10.1016/j.jallcom.2018.09.029.

23. Yang, H., Wen, P., Zhou, X., Li, Y., Duan, B., Zhai, P., & Zhang, Q. (2019). Enhanced thermoelectric performance of Te-doped skutterudite with nano-micro-porous architecture. *Scripta Materialia.* http://doi.org/10.1016/j.scriptamat.2018.09.015.

24. Yelgel, Ö. C. (2016). Theoretical study of thermoelectric properties of n-type doped $Mg_2Si_{0.4}Sn_{0.6}$ solid solutions. *Philosophical Magazine.* https://doi.org/10.1080/14786435.2016.1143128.

25. Li, M., Kazi Nazrul Islam, S. M., Dou, S., & Wang, X. (2018). Significantly enhanced figure-of-merit in graphene nanoplate incorporated Cu_2Se fabricated by spark plasma sintering. *Journal of Alloys and Compounds* (2018). https://doi.org/10.1016/j.jallcom.2018.07.353.

26. Asfandiyar, Cai, B., Zhao, L. D., & Li, J. F. (2020). High thermoelectric figure of merit ZT > 1 in SnS polycrystals. *Journal of Materiomics, 6*, 77–85.

27. Yan, R., Xie, W., Balke, B., Chen, G., & Weidenkaff, A. (2020) Realizing p-type NbCoSn half-Heusler compounds with enhanced thermoelectric performance via Sc substitution. *Science and Technology of Advanced Materials, 21*, 122–130.

28. Zhao, L. D., Hao, S., Lo, S. H., Wu, C. I., Zhou, X., Lee, Y., Li, H., Biswas, K., Hogan, T. P., Uher, C., Wolverton, C., Dravid, V. P., & Kanatzidis, M. G.: High thermoelectric performance via hierarchical compositionally alloyed nanostructures. *Journal of the American Chemical Society*. https://doi.org/10.1021/ja403134b.

29. Muthusamy, O., Ghodke, S., Singh, S., Delime-Codrin, K., Nishino, S., Adachi, M., Yamamoto, Y., Matsunami, M., Harish, S., Shimomura, M., & Takeuchi, T.: Enhancement of the thermoelectric performance of Si-Ge nanocomposites containing a small amount of Au and optimization of boron doping. *Journal of Electronic Materials, 49*, 2813–2824. https://doi.org/10.1007/s11664-019-07857-5.

30. He, Y., Day, T., Zhang, T., Liu, H., Shi, X., Chen, L., & Snyder, G. J. (2014). High thermoelectric performance in non-toxic earth-abundant copper sulfide. *Advanced Materials, 26*, 3974–3978. https://doi.org/10.1002/adma.201400515.

31. Fu, C., Bai, S., Liu, Y., Tang, Y., Chen, L., Zhao, X., & Zhu, T.: Realizing high figure of merit in heavy-band p-type half-Heusler thermoelectric materials. *Nature Communications, 6*, 1–7. https://doi.org/10.1038/ncomms9144.

32. Kunz Wille, E., Grewal, N., Bux, S., & Kauzlarich, S.: Seebeck and figure of merit enhancement by rare earth doping in $Yb_{14-x}RE_xZnSb_{11}$ (x = 0.5). *Materials, 12*, 731. https://doi.org/10.3390/ma12050731.

Experimental Investigation on Surface Characteristics of Nickel-Based Super Alloy Inconel-600 in Powder Mixed Electric Discharge Machining by Using Response Surface Methodology

Satish Kumar and **Sanjeev Kumar**

Abstract Present work considers the experimental study of the surface properties of Inconel-600 through transfer of material mechanism using electrical discharge machining (EDM) with powder mixed dielectric. Different process variables such as tool material (copper, copper-chromium, graphite), powder particles (tungsten carbide, cobalt and boron carbide), peak current, pulse-on time (T_{on}) and pulse-off time (T_{off}) have been analyzed on surface roughness (SR). Response surface methodology (RSM) with Box–Behnken design technique has been used for the experiments. Experimental results indicated that the current, T_{off}, and tool material significantly affect the surface roughness while among the three powder particles, boron carbide significantly affects the surface integrity of the Inconel-600 material. Also during the study of surface characteristics of selected machined samples with a scanning electron microscope, microcracks, craters, debris and pockmarks were noticed. Machined specimen also analyzed with the help of energy-dispersive X-ray spectrometer (EDX).

Keywords Powder Mixed Electrical Discharge Machining (PMEDM) · Surface Roughness (SR) · Response Surface Methodology (RSM)

1 Introduction

Inconel-600 has expanded in many areas, namely gas turbines, submarines, nuclear reactors, petroleum plants and rocket engines. Due to the unique properties of this material, it has an ability to keep high strength and outstanding surface stability. The machining that is commonly performed on this material is EDM, but researchers with traditional EDM have faced many restrictions, such as high tool wear rates, low material removal rates (MRR) and rough surfaces texture. The above-mentioned

---

S. Kumar (✉) · S. Kumar
Department of Mechanical Engineering, Chandigarh Engineering College, Landran, Punjab, India
e-mail: satish.4310@cgc.edu.in

S. Kumar
e-mail: dr.sanjeevsharma.cecme@cgc.edu.in

restrictions of normal EDM process and many new techniques have been tried out such as a hybrid EDM process, i.e., EDM combined with other process, use of P/M electrodes, powder is mixed with dielectric. To mend the surface qualities and machining effectiveness, a new machining method is used, i.e., PMEDM. Huge literature based on surface modification by with powder or additives in dielectric medium has been discussed in detail.

Antar et al. [1] Investigate the surface integrity effects and indicated that, with the same Ra values, it was feasible to shrink the friction coefficient by 60%, compared to samples using standard EDM settings. Rajesh et al. [11] explored the effect of EDM process variables on MRR and surface quality while machining the Inconel-718 and developed a mathematical model for MRR and SR by using ANOVA. It has been revealed that high flushing pressure with low value of T_{off} improved the SR as well as MRR. Muthukumar et al. [8] on Inconel-800 material with copper electrode and reported that voltage and current are vital parameters, for the response. Habib [3] studied the input variables, i.e., T_{on}, gap voltage, I_p and SiC percentage for the response parameters, i.e., MRR, gap size, EWR and SR. Revealed that SR hikes with the hike of T_{on}, gap voltage and I_p. Yan et al. [13] detected the effect of abrasive EDM on SKD 61 and improved the surface hardness with the use of proper concentration of powder additives in EDM oil. Tzeng and Chen [12] studied the effect of additive powder, i.e., aluminum, Sic and chromium on the surface eminence of EDMed SKD-11. It has been concluded that small powder particles having range 70–80 µm produced an ultimate finishing surface. Kansal et al. [4] used the Taguchi method for optimization of input parameters for powder mixed EDM and concluded that the aluminum powder as an additive, improved the SR and reduced the recast layer. Klocke et al. [5] investigating the effect of Al and Si powder particles having size <30 µm on Inconel-718. It has been revealed by the analysis of machined surface that with the aluminum powder particles enhance the surface finish. Kumar et al. [7] Ti–6Al–4V was machined with the help of EDM with process parameters. With the help of optimization technique, analyze the impact of process parameter on MRR and SR and found that both are directly propositional to the current. Optimized value which they observed is: discharge current 18 amp, Ton 100 µm and voltage 40 V. Papazoglou et al. [10] investigate and proposed semi-empirical relations between process and performance parameters to describe them. After experimentation, they revealed that MRR and mean machining power are proportional to each other, and SR depends upon discharge energy.

From the literature review, it is clear that less work has been done on PMEDM of Inconel-600. The preceding work exposed the machinability of die steel, titanium, composite matrix element, etc. but a very limited work has been explored on Inconel-600 material. Therefore, it was needed to extend the present research work for Inconel-600 with machining process variables, i.e., peak current, T_{on}, T_{off}, tool material.

2 Materials and Methods

Die sinking EDM machine is used for pilot experimentation and the results indicated that at a powder concentration of 6 g/l, better SR has been achieved. Schematic diagram and experimental setup for EDM machine of Inconel-600 as shown in Fig. 1a and b. Hence, for further experimentation, powder concentration has been taken as 6 g/l. Copper, copper-chromium and graphite were selected as tool electrodes. Tables 1 and 2 show the chemical composition of work specimen and tool materials.

On the bases of pilot experimentation, machining process variables, i.e., I_p, T_{on}, T_{off}, tool material and powder particles were selected to examine their effects on the surface integrity of Inconel-600. The work material has been taken in the form of rectangular plates with dimensions $150 \times 15 \times 6$ mm.

Five rectangular plates of such dimension were taken to complete the experiments. The measurements of SR were taken an average of three times and measured in μm. The process parameters, i.e., work material (Inconel-600), tool diameter (ø 12 mm), tool length (40 mm), dielectric temperature (20–25 °C), +ve polarity, machining depth (0.5 mm) and flushing from side way, were kept constant during experimentation. The machining process variables and their levels are shown in the Table 3. The experiments have been performed using Box–Behnken design of RSM.
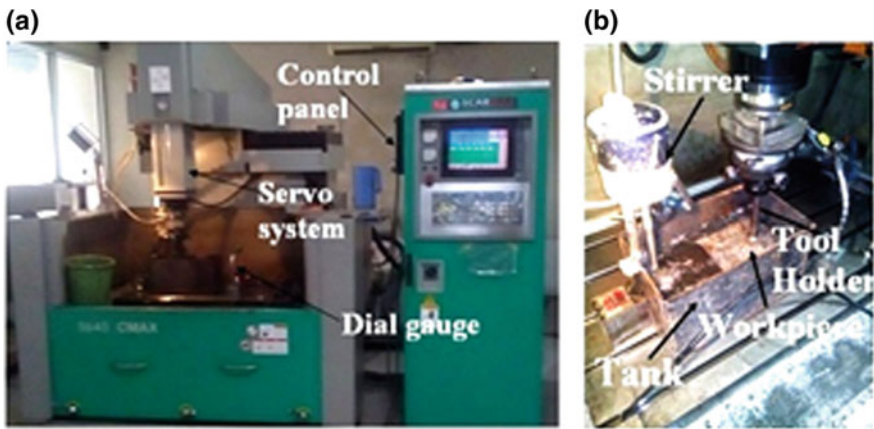
Fig. 1 **a**, **b** Schematic diagram and experimental setup for EDM machine of Inconel-600

Table 1 Chemical composition of Inconel-600 material

Element	Ni	Fe	Cr	C	Mn	S	Si	Cu
%	Base material	7.78	14.56	0.15	1.0	0.015	0.5	0.5

Table 2 Chemical analysis (wt%) of electrode materials

Elements	Copper	Copper–Chromium
Cu	99.7	98.4
Zn	0.0148	<0.0050
Pb	0.0206	0.0118
Sn	0.0356	<0.0050
Mn	0.005	0.006
Fe	0.109	0.0319
Ni	0.0083	0.0104
Si	<0.0050	<0.0050
Cr	0.0061	1.36
Al	<0.0020	<0.0020
S	<0.0020	<0.0020
Bi	<0.0050	<0.0050
Sb	<0.0050	0.0072

Table 3 Machining process variables and their levels

S. no	Symbols	Input factors	Level			Units
			I	II	III	
1	A	Current (I_p)	4	8	12	Ampere
2	B	T_{on}	60	90	120	μs
3	C	T_{off}	30	45	60	μs
4	D	Tool material	Cu	Cu–Cr	Graphite	ø 12 mm
5	E	Powder particles	Tungsten carbide	Cobalt	Boron carbide	gram

2.1 Response Surface Methodology (RSM)

RSM explores the relationships between different input process parameters and one or more response parameters. It analyzes the data by plotting the plots for accuracy and response curves. Box–Behnken design does not contain fractional factorial design to find out the best response. Therefore, in the present work RSM has been used for deriving the relationship between input process variables and the response, i.e., SR. To study the effects of the PMEDM parameters, second-order polynomial surface models have been developed. The response surface is described by an equation [8]:

$$y_u = \alpha_0 + \sum_{i=1}^{L} \alpha_i x_i + \sum_{i=1}^{L} \alpha_{ii} x^2 i + \sum_{i<1} \alpha_{ij} x_i x_j \cdots\cdots, \qquad (1)$$

where y_u is the response, and the x_i (1, 2, …, L) are coded levels of L process variables, the terms α_0, α_i, α_{ii}, α_{ij} are the second-order regression coefficients.

3 Results and Discussions

3.1 Analysis of Surface Roughness

To examine the effect of input variables for SR, Design-Expert 6.0 software has been used and the relevant data from Table 4.

From one factor plots based on Fig. 2a revealed that whenever current is increased from 4 to 12 amp, SR also hikes from 4.06 to 9.52 µm. When T_{off} falls from 60 to 30 µs and T_{on} hikes from 60 to 120 µs displayed the effect on SR, i.e., 7.16–8.15 µm and 7.59–8.03 µm as illustrated in Fig. 2b and c. The results are in excellent agreement as reported by [2]. From Fig. 2d, it has been observed that surface roughness increased while using graphite as a tool material. Among the three powder form, boron carbide significantly affected SR as shown in Fig. 2e. The optimum input parameter combination for SR is current = 4A, T_{on} = 60 µs, T_{off} = 60 µs, Cu–Cr as a tool material and boron carbide as a powder additive. Figure 2f shows the perturbation plot, i.e., just like a one factor plot at time experimentation. This assistance is to compare the effect of all the facts at a specific point in the design area. Basically, it provides silhouette views of the response surface. Factors A, C, D and E show the slope means the response is sensitive to that factor.

Based on ANOVA, terms A, C, D, E and interaction terms, AC, BC, BE and CD are vital terms, i.e., peak current, T_{on}, T_{off}, tool material and interaction effects of peak current with T_{off}, T_{on} with T_{off}, T_{on} with powder particles and T_{off} with the tool material has a significant effect. The value of R^2

(R^2) is 0.9503, Pred-R^2 = 0.8911 and Adj-R^2 = 0.9322. "Pred R^2" of 0.8911 is an acceptable contract with the "Adj R^2" of 0.9322. The p-value for lack of fit is 0.1003 suggesting that this model adequately fits the data. Figure 3a shows the contour plot for factor A and E. Normal plots of residuals of the developed model as shown in Fig. 3d. It is noticed from the figure that all results are very near to the expected values. The results are in good contract as reported by [2].

Errors are usually allocated that a tumble on a straight line. From the 3D plots, it can be noticed that current and powder particles have significantly affect the SR also T_{on} has very little bit effect on SR as shown in Fig. 3b and c.

After the removal of non-vital terms, a final equation for SR can be obtained as (Table 5).

Equation for SR in coded factors:

$$\text{Surface roughness (SR)} = +7.74 + 2.56 \times A + 0.35 \times B - 0.56 \times C + 0.39 \times D - 0.055 \times E - 1.10 \times A^2 + 0.43 \times D^2$$

Table 4 Design of experiments and results

| Input factors | | | | | Response | | | |
| Run No. | Current (Amp) | Pulse-on time (Ton) (µs) | Pulse-off time (Toff) (µs) | Tool material | Powder | Surface roughness (Ra) | | | Mean value |
	(A)	(B)	(C)	(D)	(E)	R-1	R-2	R-3	
1	4	90	60	Cu–Cr	Co	4.503	4.504	4.511	4.506
2	8	90	45	Cu–Cr	Co	7.918	7.92	7.952	7.93
3	8	90	60	Gr	BC	6.45	6.482	6.466	6.466
4	8	90	45	Cu	WC	9.89	9.892	9.876	9.886
5	8	90	30	Cu–Cr	BC	7.156	7.206	7.406	7.256
6	8	120	30	Cu–Cr	Co	9.16	8.95	9.67	9.26
7	8	90	60	Cu–Cr	BC	5.9	6.11	6.65	6.22
8	8	90	60	Cu	Co	8.88	8.78	9.1	8.92
9	4	90	45	Cu	Co	4.01	4.81	4.41	4.41
10	8	90	45	Cu–Cr	Co	7.718	7.72	7.752	7.73
11	8	90	45	Cu–Cr	Co	7.7	7.76	7.82	7.76
12	8	90	45	Gr	WC	8.333	8.38	8.616	8.443
13	8	90	30	Gr	Co	9.68	9.699	9.769	9.716
14	12	90	30	Cu–Cr	Co	11.715	11.698	10.256	11.223
15	8	90	30	Cu	Co	6.15	6.1	6.2	6.15
16	12	90	45	Cu–Cr	BC	9.175	9.187	9.217	9.193
17	12	90	60	Cu–Cr	Co	6.435	6.475	8.096	7.002
18	8	120	45	Cu–Cr	WC	8.56	8.56	8.569	8.569
19	4	90	45	Gr	Co	5.1	5.1	5.28	5.16

(continued)

Table 4 (continued)

| Input factors | | | | | | Response | | | |
| Run No. | Current (Amp) | Pulse-on time (Ton) (µs) | Pulse-off time (Toff) (µs) | Tool material | Powder | Surface roughness (Ra) | | | Mean value |
	(A)	(B)	(C)	(D)	(E)	R-1	R-2	R-3	
20	12	90	45	Gr	Co	10.58	10.602	10.627	10.603
21	8	120	60	Cu–Cr	Co	7.11	7.1	7.15	7.12
22	4	90	45	Cu–Cr	BC	3.702	3.701	3.706	3.703
23	8	90	45	Gr	BC	8.88	8.882	8.887	8.883
24	8	120	45	Cu	Co	9.45	8.42	7.63	8.5
25	12	60	45	Cu–Cr	Co	9.55	10.5	11.66	10.57
26	8	90	45	Cu–Cr	Co	7.33	7.32	7.34	7.33
27	8	90	60	Cu–Cr	WC	7.84	7.84	7.87	7.85
28	4	90	30	Cu–Cr	Co	3.67	3.67	3.679	3.673
29	12	90	45	Cu	Co	9.9	9.7	9.8	9.8
30	4	120	45	Cu–Cr	Co	4.56	4.562	4.567	4.563
31	8	120	60	Cu–Cr	Co	6.6	6.61	6.65	6.62
32	12	90	45	Cu–Cr	WC	8.984	8.983	8.991	8.986
33	8	90	45	Cu	BC	5.505	5.505	5.508	5.506
34	8	90	45	Cu–Cr	Co	8.3	8.31	8.38	8.33
35	8	60	45	Cu–Cr	WC	7.031	7.032	7.036	7.033
36	12	120	45	Cu–Cr	Co	9.092	9.091	9.096	9.093

(continued)

Table 4 (continued)

Input factors						Response				
						Surface roughness (Ra)				
Run No.	Current (Amp)	Pulse-on time (Ton) (μs)	Pulse-off time (Toff) (μs)	Tool material	Powder	R-1	R-2	R-3	Mean value	
	(A)	(B)	(C)	(D)	(E)					
37	8	120	45	Gr	Co	8.025	8.025	8.028	8.026	
38	8	120	45	Cu–Cr	BC	7.4	7.35	7.6	7.45	
39	8	90	45	Cu–Cr	Co	7.71	7.707	7.812	7.743	
40	8	90	30	Cu–Cr	WC	9.28	9.275	9.234	9.263	
41	8	60	60	Cu–Cr	Co	7.88	7.81	7.998	7.896	
42	4	60	45	Cu–Cr	Co	2.801	2.795	2.735	2.777	
43	8	60	45	Cu–Cr	BC	7.443	7.493	7.693	7.543	
44	8	60	45	Gr	Co	8.5	8.6	9.09	8.73	
45	8	60	45	Cu	Co	7.73	7.69	6.348	7.256	
46	4	90	45	Cu–Cr	WC	4.001	4.009	4.029	4.013	
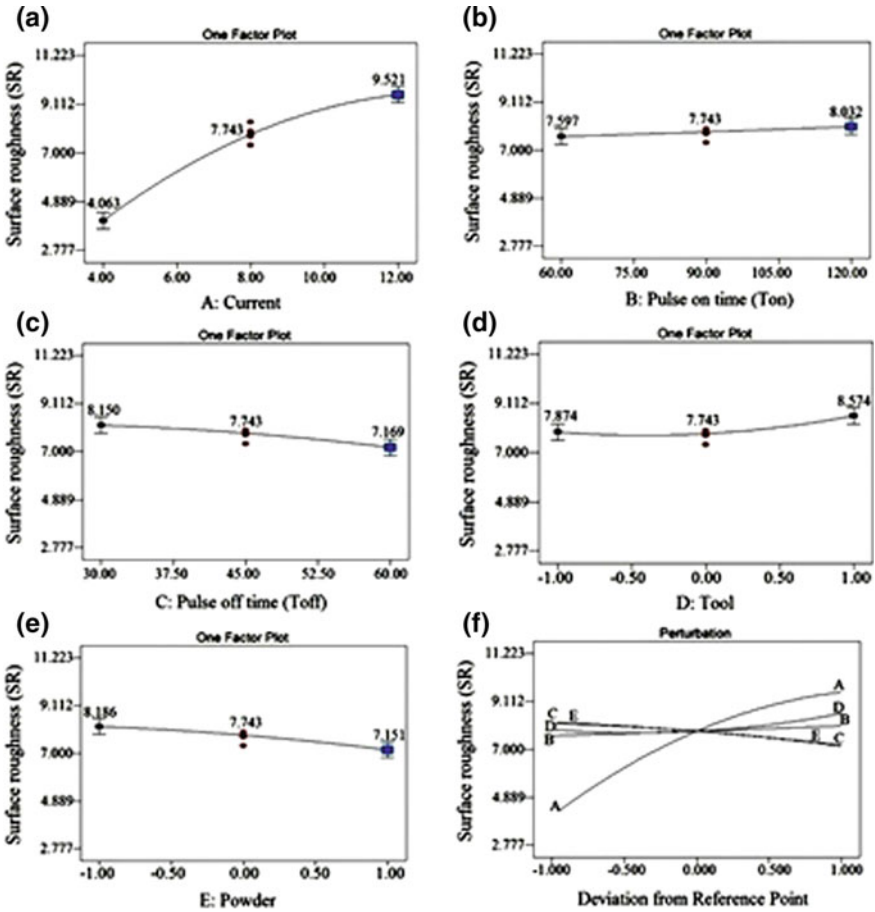
Fig. 2 One factor plots for surface roughness

$$- 1.52 \times A \times C - 0.98 \times B \times C - 0.74$$
$$\times B \times D - 0.66 \times B \times E - 1.43 \times C \times D$$

Equation for SR in actual factors:

$$\text{Surface roughness (SR)} = +7.738 + 2.564 \times \text{Current} + 0.351 \times T_{on} - 0.561 \times T_{off}$$
$$+ 0.393 \times \text{Tool} - 0.055 \times \text{Powder} - 1.103 \times \text{Current}^2$$
$$+ 0.434 \times \text{Tool}^2 - 1.515 \times \text{Current} \times T_{off} - 0.979$$
$$\times T_{on} \times T_{off} - 0.737 \times T_{on} \times \text{Tool} - 0.655 \times T_{on}$$
$$\times \text{Powder} - 1.430 \times T_{off} \times \text{Tool}.$$
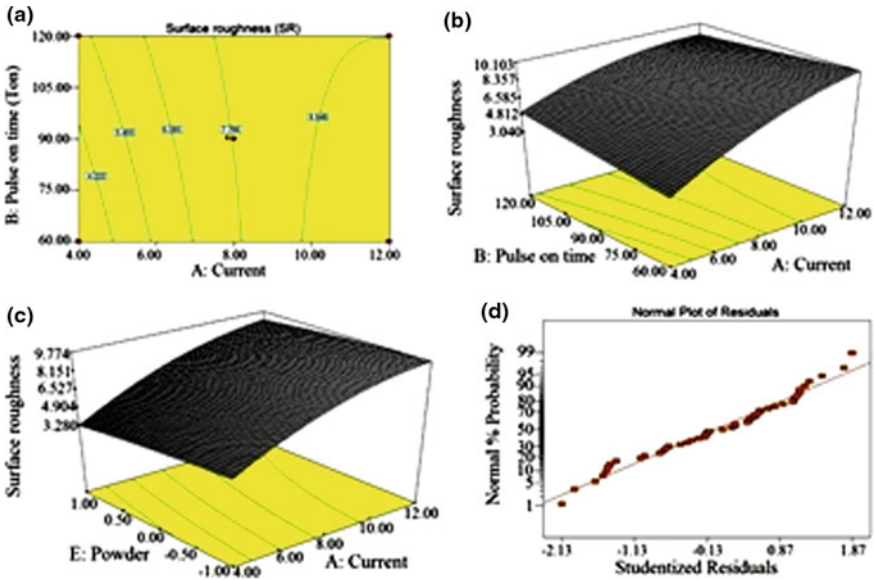
Fig. 3 Response surface plots: **a** contour plot for surface roughness; **b** and **c** 3D surface plot **d** normal probability residual plot for surface roughness

4 SEM Micrograph Analysis

The surface structure of the samples was investigated with the SEM, EDS analyzer incorporated with the model; ZEISS, Ultra Plus, Serial no. 43. Current, Ton, workpiece material and tool, powder mixed dielectric medium are the main factors which are accountable for affecting the surface quality of machined specimen during the machining with EDM. With the increase in current, high discharge energy is transferred to the machining area so that melting and evaporation takes place, resulting in the formation of a small pit on the surface. In addition, due to huge energy, impulsive force also hikes, which play an important role in the formation of bigger pit size which causes uneven finish. For the intent of scrutiny, three trials for current setting, namely (i) 4A, (ii) 8A and (iii) 12A along with three different tool material and three powder particles, were analyzed in detail.

Figure 4 shows the SEM images with the magnification of 500 X and 2.00 KX, respectively. From one factor plot, it is observed that T_{on} has very little bit effect on surface integrity so T_{on} is kept constant during the structure analysis of selected samples.

SEM micrograph of Inconel-600 machined with tool as a Cu in boron carbide as a additive at 8A current, 90 μs T_{on} and 60 μs T_{off} is shown in Fig. 4a and d. Figure 4a shows the formation of microcracks on the surface, but with higher magnification,

Table 5 Analysis of variance for surface roughness (after elimination)

Source	Sum of squares	DF	Mean square	F-value	Prob > F	
Model	169.98	12	14.17	52.54	<0.0001	Significant
A	119.16	1	119.16	442.03	<0.0001	
B	0.69	1	0.69	2.56	0.1189	
C	3.55	1	3.55	13.17	0.0009	
D	1.96	1	1.96	7.27	0.011	
E	4.29	1	4.29	15.91	0.0003	
A2	9.4	1	9.4	34.88	<0.0001	
D2	2.21	1	2.21	8.18	0.0073	
AB	2.66	1	2.66	9.87	0.0035	
AC	6.39	1	6.39	23.69	<0.0001	
BC	1.79	1	1.79	6.64	0.0146	
CD	9.06	1	9.06	33.61	<0.0001	
DE	5.81	1	5.81	21.54	<0.0001	
Residual	8.9	33	0.27			
Lack of fit	8.24	27	0.31	2.8	0.1003	Not significant
Pure error	0.65	6	0.11			
Cor total	178.88	45				
R^2	0.9503		Adj R^2	0.9322		
Pred R^2	0.8911		Adeq precision	29.873		

subsurface cracks can be noticed on the surface as illustrated in Fig. 4d. Figure 4b and e show the micrograph of Inconel-600 with machining conditions at copper-chromium electrode, tungsten carbide as a powder additive, 4A current, 90 µs T_{on} and 30 µs T_{off}. Micro-pores and crater are noticed on the surface, but no cracks are formed when current reduced to 4A, pulse-on time is same as 90 µs and T_{off} reduced to 30 µs. Due to low current and T_{off}, SR is reduced, which can be seen in Fig. 4b also with higher magnification along with the same machining conditions, subsurface crack is observed as shown in Fig. 4e. Figure 4c and f shows the micrograph of Inconel-600 with machining conditions at graphite electrode, cobalt as a powder additive, 12A current, 90 µs T_{on} and 45 µs T_{off}. During the critical assessment of the machined sample, surface defects such as pockmarks, debris particles are observed which affect the surface finish because of high temp, material will melt with the huge heat transfer to the machined surface [6].
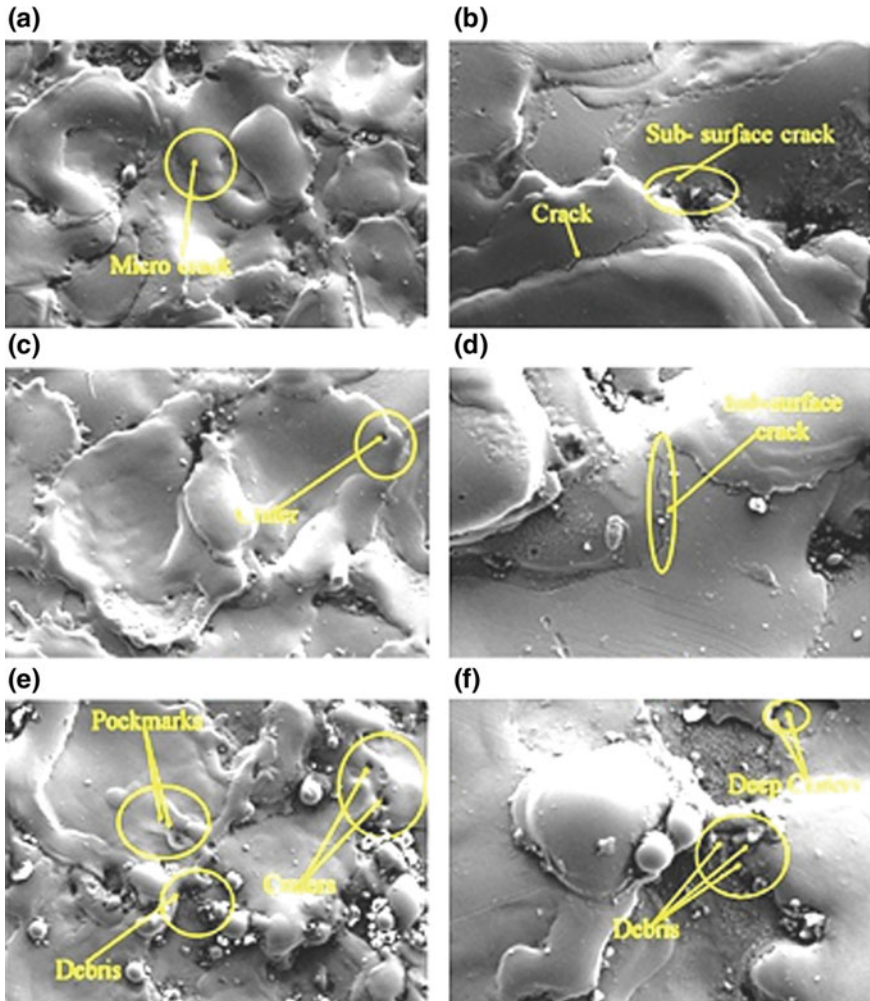
Fig. 4 SEM micrographs (500 × and 2.000 KX): **a** and **d** Run No. 8, **b** and **e** Run No. 13, **c** and **f** Run No. 16

4.1 EDX Analysis

To identify the elemental composition of the machined specimen, an analytical technique, i.e., energy-dispersive X-ray analysis (EDX) is used. This method confirmed the existence of parent metal and shifted particles from tool material and dielectric fluid, as illustrated in Figs. 5a–d. This technique typically shows heights corresponding to energy levels for which the most X-rays were obtained. Prior to machining, the weight % of elements is C = 11.6, O = 3.51, Cr = 13.61, Fe = 8.92 and Ni = 62.36 as shown in Fig. 5a. With PMEDM at different machining

(a) (b) (c) (d) EDX spectra panels.
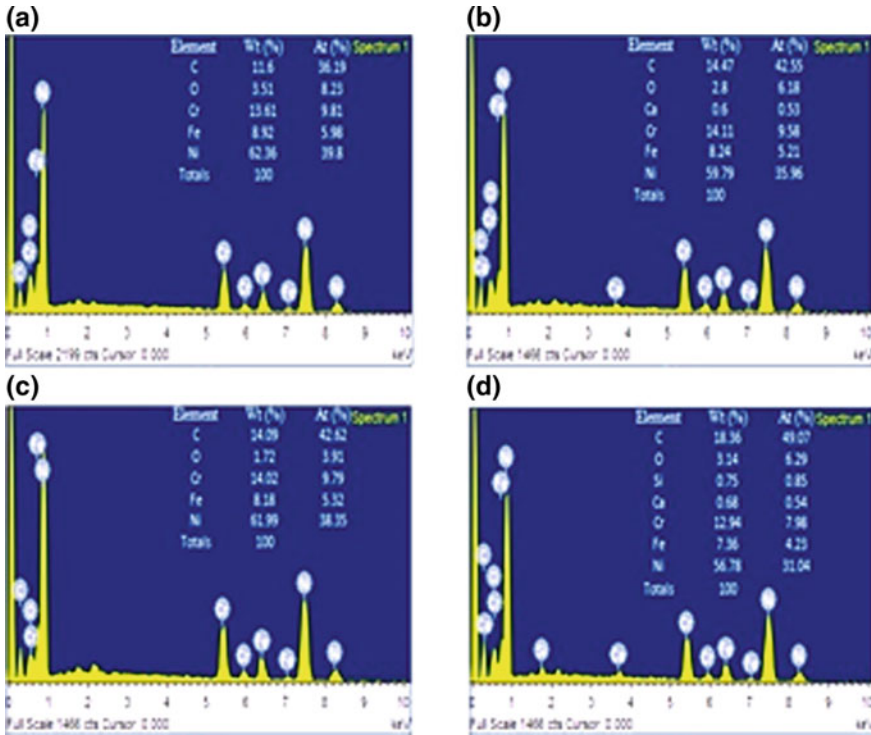
Fig. 5 EDX analysis of Inconel-600 **a** before machining; **b** Run No. 8, at $I_p = 8$ A, $T_{on} = 90$ μs, $T_{off} = 60$ μs, tool Cu in boron carbide as powder additive; **c** Run No. 13 and **d** Run No. 16

conditions, weight % of a component changes to C = 14.09–18.36, O = 1.72–3.14, Cr = 12.94–14.11, Fe = 7.26–8.24 and Ni = 56.78–61.99 as highlighted in Fig. 5b–d. From the EDX analysis, silicon and calcium were also identified. This may be due to the fusion, re-solidification and evaporation of the tool material and may be shifted to the work material. EDX results also indicated that carbon and oxygen also present in Inconel-600.

5 Confirmation Experiment

The three confirmation experiment has been performed for surface roughness. For the confirmation test, values of selected process variables must lie within the ranges for which the formula were derived [4, 9].

The data for the confirmation run and prediction designed for SR are set out in Table 6 and conclude that the calculated error is small, within −5.15–6.58%. Clearly, this confirms the ability to better reproduce the experimental findings.

Table 6 Confirmation test and comparison of results

Machining conditions						Surface roughness (μm)		
S. No	Current, A (amp)	Ton, B (μs)	Toff, C (μs)	Tool material, D	Powder, E	Exp. value	Predicted value	Error (%)
1	4	90	45	Gr	Co	5.16	4.82	6.58
2	8	60	45	Cu–Cr	BC	6.99	7.35	−5.15
3	12	120	45	Cu	WC	9.46	8.93	5.60

6 Conclusions

Based on experimental study, results indicated that SR obtained was ranged from 4.063 to 9.521 μm. The SR was most significantly affected by current, T_{off}, tool material and powder particles. The minimum SR was obtained, when the parameters are set as $I_p = 4$ amp, $T_{on} = 60$ μs, $T_{off} = 60$ μs, Tool material as a copper-chromium and boron carbide as a powder particles. Surface roughness improves when T_{off}, copper–chromium as a tool electrode and boron carbide is used as a powder particles while SR increased with the increase of current. T_{on} has little bit effect on SR. Values of R^2, adj. R^2 and pred. R^2 for SR is 0.9503, 0.9322 and 0.8911. "Pred R^2" of 0.8911 is in an acceptable contract with the "Adj R^2" of 0.9322. The confirmation test showed that the error between the expected and experimental value of SR is −5.15–6.58%, respectively. This confirms validation of results for predicted values and experimental values. It was noticed that due to peak current resulting in the creation of microcracks, craters, pockmarks and debris.

Declaration of Competing Interests The author confirms that he has no competing interest.

References

1. Antar, M., Hayward, P., Dunleavey, J., & Butler-Smith, P. (2018). Surface integrity evaluation of modified EDM surface structure. *Procedia CIRP, 68,* 308–312.
2. Banerjee, S., Mahapatro, D., & Dubey, S. (2009). Some study on electrical discharge machining of ({WC + TiC + TaC/NbC}–Co) cemented carbide. *The International Journal* of *Advanced Manufacturing Technology, 43,*1177–1188.
3. Habib, S. S. (2009). Study of the parameters in electrical discharge machining through response surface methodology approach. *Applied Mathematical Modelling, 33,* 4397–4407.
4. Kansal, H. K., Singh, S., & Kumar, P. (2005) Application of Taguchi method for optimization of powder mixed electrical discharge machining. *International Journal of Manufacturing Technology* and *Management,* 7(2/3/4), 39–341.

5. Klocke, F., Lung, D., Antonoglou, G., & Thomaidis, D. (2004). The effects of powder suspended dielectrics on the thermal influenced zone by electro discharge machining with small discharge energies. *Journal of Materials Processing Technology, 149,* 191–197.
6. Kumar, A., Kumar, V., & Kumar, J. (2013). Multi-response optimization of process parameters based on response surface methodology for pure titanium using WEDM process. *International Journal of Advanced Manufacturing Technology, 170,* 4861–4869.
7. Kumar, R., Roy, S., Gunjan, P., Shaoo, A., Sarkar, D. D., & Das, R. K. (2018). Analysis of MRR and surface roughness in machining Ti–6Al–4V ELI Titanium alloy using EDM Process. *Procedia Manufacturing, 20,* 358–364.
8. Muthukumar, V., Rajesh, N., Venkatasamy, R., Sureshbabu, A., & Senthilkumar, N. (2014). Mathematical modeling for radial overcut on electrical discharge machining of incoloy 800 by response surface methodology. *Procedia Mater Sci, 6,* 1674–1682.
9. Patil, G. N., & Brahmankar, P. K. (2010). Some studies into wire electro-discharge machining of alumina particulate-reinforced aluminum matrix composites. *International Journal of Advanced Manufacturing Technology, 48,* 537–555.
10. Papazoglou, E. L., Markopoulos, A. P., & Manolakos, D. E. (2018). Experimental research on EDM of AISI 01 tool steel and study of the surface white layer formation. *Procedia structural integrity, 10,* 235–242.
11. Rajesh, S., Sharma, A. K., & Kumar, P. (2012). On electro discharge machining of inconel 718 with hollow tool. *Journal of Materials Engineering and Performance, 21*(6), 882–890.
12. Tzeng, Y. F., & Chen, F. C. (2005). Investigation into some surface characteristics of electrical discharge machined SKD-11 using powder-suspension dielectric oil. *Journal of Materials Processing Technology, 170*(1–2), 385–391.
13. Yan, B. H., Lin, Y. C., Huang, F. Y., & Wang, C. H. (2001). Surface modification of SKD 61 during EDM with metal powder in the dielectric. *Materials Transactions, 42,* 2597–2604.

Effect of Various Aspects on Mechanical Properties of High Entropy Alloys: A Review

Rohan Onattu and Pankaj Sahlot

Abstract The research effort in high entropy alloys (HEAs) has intensified in the recent years. This is due to the fact that HEAs have a wide range of compositions based on elements used, the number of different elements in a system and the sheer number of compatible elements that exist. HEAs exhibit broader range of superior mechanical and microstructural properties, and this fact points toward many potential applications. The aim of this research is to unify and present the multiple streams of research efforts which have impacted the understanding of HEAs. The information has been included based on its dominant focus areas. Article has been categorized into important aspects based on its effect on the mechanical properties of the alloys. The effect of element compositions, treating conditions and processes on microstructural and mechanical properties has been also considered. In future, better methods and newer technologies will definitely result in better and more reliable materials which will supersede some of the previously existing materials.

Keywords High entropy alloys · Strength · Fatigue · Annealing · Cryogenic

1 Introduction

High entropy alloys were first proposed by Yeh et al. [1] aiming to mix multiple metals into one single alloy. The resulting high mixing entropy causes the entire crystal structure to stabilize. Alloys with interesting combination of properties were never seen before. The mixing gives rise to four major strengthening mechanisms; severe lattice distortion, sluggish diffusion, high entropy and cocktail effects are famously known as four core effects. Since then the research efforts on multi principal element alloys

R. Onattu · P. Sahlot (✉)
Mechanical Engineering, School of Technology, Pandit Deendayal Petroleum University, Gandhinagar 382007, Gujarat, India
e-mail: pankaj.sahlot@sot.pdpu.ac.in

R. Onattu
e-mail: onattu.smc16@sot.pdpu.ac.in

have grown and diversified into many various fields. The original HEA has diversified into interstitial high entropy alloys (IHEA) which had minimal strength-ductility trade-off [2]. Refractory high entropy alloys (RHEAs) investigation for effects of various manufacturing techniques, material addition and composition was studied [3–7]. Dual-phase high entropy alloys (DPHEAs) and effects like high strength and work hardenability were also reported [2, 8, 9]. These new breeds of HEAs show different behavior and strengthening mechanisms as a result of the modifications subjected. It is of great interest due to applications span from structural components to nuclear radiation shields. The versatility of HEAs is unparalleled because of the sheer number of combination and its distinct properties which can be engineered to suit specific requirements but in a broad field of applications. This study throws light on the mechanical properties and variety of different studies undertaken. The hardness and strength, percentage elongation and ductility observed in these HEAs were subject to different circumstances such as effects of annealing, fatigue, properties at cryogenic temperatures. The literature referred has multiple unique focus areas in its nature and methodology. This work aims to discuss recent research efforts in mechanical properties. Recent developments of annealing effects and cryogenic effects on HEA have also been summarized.

2 Effect on Mechanical Properties

2.1 Hardness and Strength

HEAs exhibit superior material properties in all fronts compared to normal alloys or pure metals without the usual trade-off between the properties [12, 15]. The effects of specific pre and post as well as in-fabrication processing and various evolving mechanisms of HEAs have been cataloged. The synthesis of HEA results in inherently higher UTS and YS, thus making it superior compared to any of its individual components [10]. Furthermore, the effects of various processes and parameters on the UTS and YS are mentioned under those specific effects and conditions ahead. Figure 1 shows the strength and hardness for different HEA systems. Maximum strength and hardness are observed for AlCrFeNiV, while minimum is observed for AlCoCrCuFeNiSi. The variation arises due to difference in manufacturing and crystal structures of different HEAs [10]. This kind of data helps to select the appropriate material for required applications.

Figures 2 and 3 show the range of yield strength and percentage ductility for various engineered materials. The data for various principal metal alloys, ceramics, bulk metallic glasses (BMG's), composites with HEAs have been compiled and presented. The variation is due to constituent elements, microstructures and manufacturing processes [11–14]. This information helps to select the material with moderate strength and ductility.
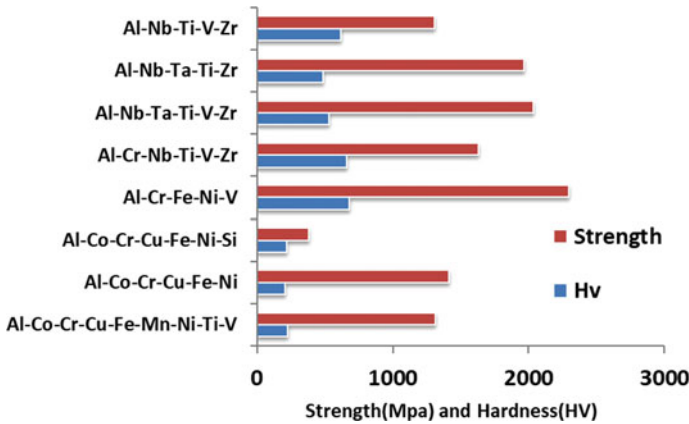
Fig. 1 Compilation of hardness and strength values for various compositions of HEAs [10]
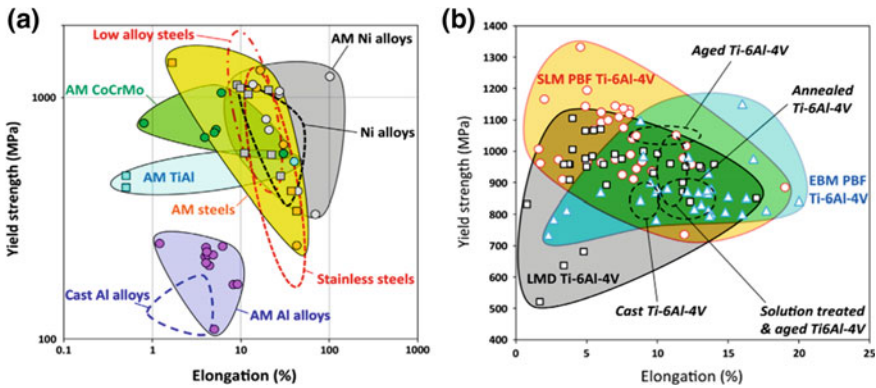
Fig. 2 Yield strength as a function of elongation for various engineering materials [12]

2.2 Effects of Annealing

The effects of annealing have been studied by performing experiments which aim to see its effects on the hardness and structure of the alloys. However, change was observed in its crystal structure and increase in its hardness values due to precipitation of one of its elements. The microhardness was raised from 370 to 500 HV after aging (600 °C for 10 h) in the homogenized condition. The precipitation of the Hf, Ta-rich HCP particles and the hardening in the BCC matrix of the alloy was related [16]. Another study also found that some degree of trade-off between yield strength and elongation values after undergoing annealing cold rolling strengthened the alloy as increase in annealing temperature led to gradual softening. The yield strength correspondingly decreased, whereas total elongation increased [17]. Multiple crystal structures simultaneously exist with FCC and BCC where addition
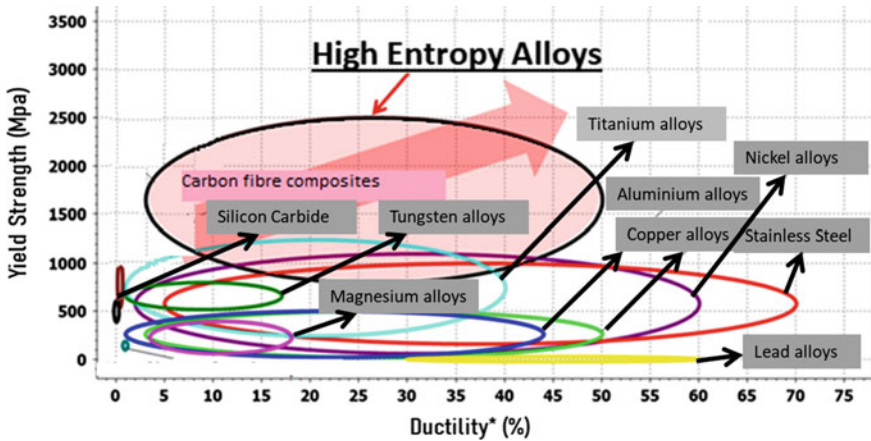
Fig. 3 Yield strength as a function of ductility for different engineering alloys [15]

of one component is better for its magnetic properties. The resulting alloy had a simple solid solution consisting of FCC with a BCC phase. The addition of Al in Mn containing HEAs is good for its magnetic characteristics. However, post annealing, the value of magnetization decreased [18]. Figure 4 shows effect of temperature and grain size on engineering stress and strain for CoCrFeMnNi HEA. The effect is visible in the form of change in curve profiles and area under the curve. The strength is more at low temperature and decreases with increase in temperature. The strength also increases with decrease in grain size.
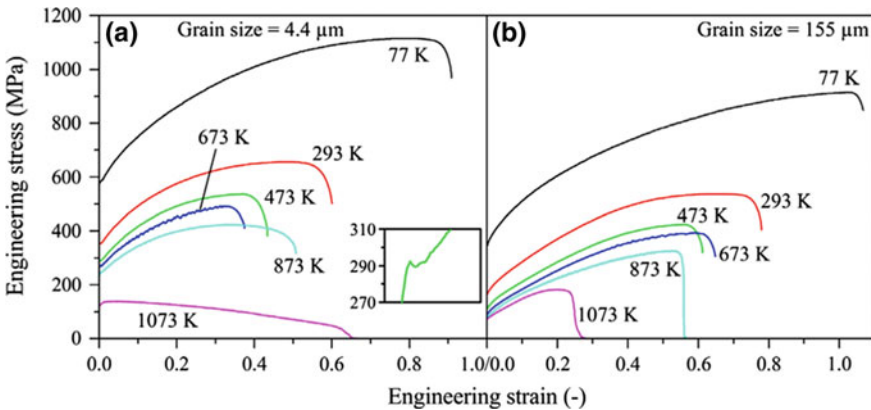
Fig. 4 Stress versus Strain plots for CoCrFeMnNi HEA at varying temperatures: **a** fine and **b** coarse grained [14]

2.3 Fatigue Properties of HEA

Fatigue is found in nearly all applications, and to sustain it, materials must be necessarily fabricated. HEAs undergo low and high cycles of fatigue in many studies aiming to quantify its properties and performance. In one study, it was found that strain and stress amplitude when increased lead to damage at the grain boundaries and decreases low cycle fatigue. An increase in strain amplitude gives rise to the formation of higher misorientation increasing to the accumulation of damage near grain boundaries and a decrease in low cycle fatigue life. The fatigue life decreases, when the applied stress amplitude increases, before crack initiation. Nano-twinning is a prime deformation mechanism and occurs during fatigue crack propagation. Nano-twinning formation results in strengthening [19, 20]. Another study pointed out that defect in HEAs affects fatigue resistance, but the nano-twinning effect strengthens it and increases fatigue endurance. The defects of the HEA-fatigue samples influence the fatigue resistance. Nano-twinning bolsters HEAs' fatigue resistance with higher fatigue-endurance limits. HEAs show greater fatigue-endurance limits, fatigue-crack-growth properties and fatigue ratio [21]. The fatigue test also produced a combination of BCC and FCC phases which revealed both ductile and brittle failure features on its fracture surface HEA alloys produced displayed a combination of bcc as well as FCC phases. Fracture-surface examinations of toughness tests revealed a mixture of brittle and ductile/dimpled features [22]. Fatigue crack initiation is also delayed due to BCC phase present. The monotonic load bearing capacity of EHEA is higher than its as-cast EHEA counterpart, and fatigue crack initiation of EHEA is delayed due to (BCC)B2 precipitates which hinder the path of PSBs [23].

2.4 Properties at Cryogenic Temperatures

Metals being used in cryogenic applications must possess relevant properties to be used safely and effectively. Thus, studies were carried out on HEAs at cryogenic temperatures. Laser AM parts had large number of dislocation giving it strength but also at cryogenic temperatures deformation twinning takes place under large strains which impede the dislocation and thus strengthens it. LAM introduces abundant dislocations which increase the yield strength. Dislocation glide and deformation twinning appear under cryogenic conditions at large strain levels. Impediment of this dislocation motion by twinning mechanism strengthens the bulk HEA sample [24]. There was also an increase in the yield strength (YS) and ultimate tensile strength (UTS) with minimal loss of ductility, and at cryogenic temperatures, the deformation mechanisms switch to stacking fault energy controlled modes rather than dislocation. Comparing single-phase FeCoNiCr HEA to its precipitation-strengthened FeCoNiCrTi0.2 HEA counterpart, a significant increase in YS and UTS with slight sacrifice

of ductility was observed. The decrease in temperature from 293 to 77 K caused deformation mechanisms to change from dislocation-dominant to SF-controlled modes, indicating reduced SFE with decreasing temperature [25].

3   Conclusion

This work has covered various important aspects of mechanical properties for HEAs. Hardness and strength variations are due to different compositions, effects of fatigue loading and interactions with deformation mechanisms, effects of annealing and cryogenic temperatures on properties of HEAs. Different HEA system results in variation in the mechanical properties due to difference in crystal structure. Al–Cr–Fe–Ni–V system shows maximum ultimate tensile strength of around 2000 MPa and 700 HV hardness. Annealing processes affect the properties of HEAs. Annealing shows some degree of trade-off between strength and elongation of HEAs. The crystal structure also undergoes changes in exhibiting multiple structures simultaneously. Fatigue loading creates a FCC-BCC mix phase and corresponding fracture surfaces in the HEA samples. The damage mostly occurs at the grain boundaries. Nano-twinning being the dominant deformation mechanism impedes the fatigues crack propagation and thus strengthens it. LAM HEA samples for cryogenic temperatures have a large number of dislocations in them. These dislocations result in high strength. HEAs have shown promising results in its mechanical properties.

References

1. Yeh, J. W., et al. (2014). Nanostructured high-entropy alloys with multiple principal elements: Novel alloy design concepts and outcomes. *Advanced Engineering Materials, 6*(5), 299–303.
2. Li, Z., Pradeep, K. G., Deng, Y., Raabe, D., & Tasan, C. C. (2016). Metastable high-entropy dual-phase alloys overcome the strength-ductility trade-off. *Nature, 534*(7606), 227–230.
3. Guo, W., et al. (2019). Microstructures and mechanical properties of ductile NbTaTiV refractory high entropy alloy prepared by powder metallurgy. *Journal of Alloys and Compounds, 776,* 428–436.
4. Seol, J. B., et al. (2018). Boron doped ultrastrong and ductile high-entropy alloys. *Acta Materialia, 151,* 366–376.
5. Lee, C., et al. (2018). Lattice distortion in a strong and ductile refractory high-entropy alloy. *Acta Materialia, 160,* 158–172.
6. Dobbelstein, H., Gurevich, E. L., George, E. P., Ostendorf, A., & Laplanche, G. (2019). Laser metal deposition of compositionally graded TiZrNbTa refractory high-entropy alloys using elemental powder blends. *Additive Manufacturing, 25,* 252–262.
7. Zhang, H., Zhao, Y., Huang, S., Zhu, S., Wang, F., & Li, D. (2019). Manufacturing and analysis of high-performance refractory high-entropy alloy via selective laser melting (SLM). *Materials (Basel), 12*(5).
8. Nene, S. S., Frank, M., Liu, K., Mishra, R. S., McWilliams, B. A., & Cho, K. C. (2018). Extremely high strength and work hardening ability in a metastable high entropy alloy. *Scientific Reports, 8*(1), 1–8.

9. Jumaev, E., et al. (2019). Chemical evolution-induced strengthening on AlCoCrNi dual-phase high-entropy alloy with high specific strength. *Journal of Alloys and Compounds, 777,* 828–834.

10. Lyu, Z., Lee, C., Wang, S. Y., Fan, X., Yeh, J. W., & Liaw, P. K. (2019). Effects of constituent elements and fabrication methods on mechanical behavior of high-entropy alloys: A review. *Metallurgical and Materials Science A*, *50*(1).

11. Chen, S., Tong, Y., & Liaw, P. K. (2018). Additive manufacturing of high-entropy alloys: A review. *Entropy, 20*(12), 712–724.

12. Gorsse, S., Hutchinson, C., Gouné, M., & Banerjee, R. (2017). Additive manufacturing of metals: A brief review of the characteristic microstructures and properties of steels, Ti–6Al–4V and high-entropy alloys. *Science and Technology of Advanced Materials, 18*(1), 584–610.

13. Chen, S., Tong, Y., & Liaw, P. K. (2018). Additive manufacturing of high-entropy alloys: A review. *Entropy, 20*(12).

14. Pickering, E. J., & Jones, N. G. (2016). High-entropy alloys: A critical assessment of their founding principles and future prospects. *International Materials Reviews, 61*(3), 183–202.

15. Tang, Z., et al. (2013). Aluminum alloying effects on lattice types, microstructures, and mechanical behavior of high-entropy alloys systems. *JOM Journal of the Minerals Metals and Materials Society, 65*(12), 1848–1858.

16. Stepanov, N. D., Yurchenko, N. Y., Zherebtsov, S. V., Tikhonovsky, M. A., & Salishchev, G. A. (2018). Aging behavior of the HfNbTaTiZr high entropy alloy. *Materials Letters, 211,* 87–90.

17. Klimova, M. V., et al. (2019). Recrystallized microstructures and mechanical properties of a C-containing CoCrFeNiMn-type high-entropy alloy. *Materials Science and Engineering A, 740–741,* 201–210.

18. Mishra, R. K., Sahay, P. P., & Shahi, R. R. (2019). Alloying, magnetic and corrosion behavior of AlCrFeMnNiTi high entropy alloy. *Journal Materials Science, 54*(5), 4433–4443.

19. Bahadur, F., Biswas, K., & Gurao, N. P. (2020). Micro-mechanisms of microstructural damage due to low cycle fatigue in CoCuFeMnNi high entropy alloy. *International Journal of Fatigue, 130,* 105258.

20. Tang, Z., Yuan, T., Tsai, C. W., Yeh, J. W., Lundin, C. D., & Liaw, P. K. (2015). Fatigue behavior of a wrought Al0.5CoCrCuFeNi two-phase high-entropy alloy. *Acta Materialia, 99,* 247–258.

21. Chen, P. Y., et al. (2018). Fatigue behavior of high-entropy alloys: A review. *Science China Technological Sciences, 61*(2), 168–178.

22. Seifi, M., Li, D., Yong, Z., Liaw, P. K., & Lewandowski, J. J. (2015). Fracture toughness and fatigue crack growth behavior of as-cast high-entropy alloys. *JOM Journal of the Minerals Metals and Materials Society, 67*(10), 2288–2295.

23. Shukla, S., Wang, T., Cotton, S., & Mishra, R. S. (2018). Hierarchical microstructure for improved fatigue properties in a eutectic high entropy alloy. *Scripta Materialia, 156,* 105–109.

24. Qiu, Z., Yao, C., Feng, K., Li, Z., & Chu, P. K. (2018). Cryogenic deformation mechanism of CrMnFeCoNi high-entropy alloy fabricated by laser additive manufacturing process. *International Journal of Lightweight Materials and Manufacture, 1*(1), 33–39.

25. Tong, Y., et al. (2019). Outstanding tensile properties of a precipitation-strengthened FeCoNiCrTi0.2 high-entropy alloy at room and cryogenic temperatures. *Acta Materialia, 165,* 228–240.

Comparative Analysis of Different Composites for Ankle Foot Orthosis: A Review

Neelesh Kumar Dubey and Swati Gangwar

Abstract In ancient times, orthosis was made up of woods which were easily available and easy to fabricate; later, it replaced by metal and leather because of various properties such as high strength, tear resistant, but these orthoses were generally bulky, heavy and less comfortable to the wearers. After industrial revolution, composite materials such as carbon fiber composite, polymer composite, replaced the conventional materials. Its several physical and mechanical properties such as high strength-to-weight ratio, high strength and modulus, corrosion resistance, low density, etc., which makes them most suited material for ankle foot orthosis. Nowadays, composite materials are widely used in the field of medicals; various medical devices are made up of composite material. Carbon fiber is quite expensive, making it less economical for general patient uses, whereas plastic materials have less strength compared to carbon fiber, and it is also not eco-friendly. The purpose of this study is to investigate the potential of natural fiber composites for the application of ankle foot orthosis. The discussion will be on ankle foot orthosis, manufacturing process used, comparing the mechanical properties of natural fiber to the currently used materials. In this research, it was concluded that natural fibers possess desirable mechanical properties for ankle foot orthosis, and it has almost similar mechanical properties to polypropylene and are very cheap as compared to other material such as carbon fiber that could be beneficial for future ankle foot orthosis material application.

Keywords Ankle foot orthosis · Natural fibers · Composites · Mechanical properties

N. K. Dubey · S. Gangwar (✉)
Department of Mechanical Engineering, Madan Mohan Malviya University of Technology, Gorakhpur 273010, India
e-mail: sgme@mmmut.ac.in

N. K. Dubey
e-mail: n.dubey028@gmail.com

1 Introduction

Orthoses are external device which are prescribed to disabled person to improve their structural and functional characteristics of body. Orthoses are used to control, assist a body part, aid rehabilitation from fracture, restrict motion of body part in particular direction during injuries. Orthosis device does not completely replace the body part; it only improves the proper working of body part with some kind of deformities. Orthosis device should have some ideal specification such as light in weight, durable, high tensile and compressive strength, comfortable to wearer and cheap [1]. Orthosis devices can be divided according to anatomy of human body into three parts: upper limb orthosis, spinal orthosis and lower limb orthosis [2]. Upper limb orthosis is prescribed to the patient suffering from arthritis, hemiplegia, rheumatoid and other deformities. Upper limb orthosis covers upper part of body which is shoulder, arm, wrist, elbow and hand. Spinal orthosis is used to support the spin prevent it from curving and keeps it straight. Lower limb orthosis covers foot, knee, hip and ankle. Lower limb orthosis prescribed to the patient suffering from cerebral palsy, paralysis, rickets, bow legs, knocked knee, arthritis and flat foot [1]. Orthosis nomenclatures according to anatomy of human body are given below [2].
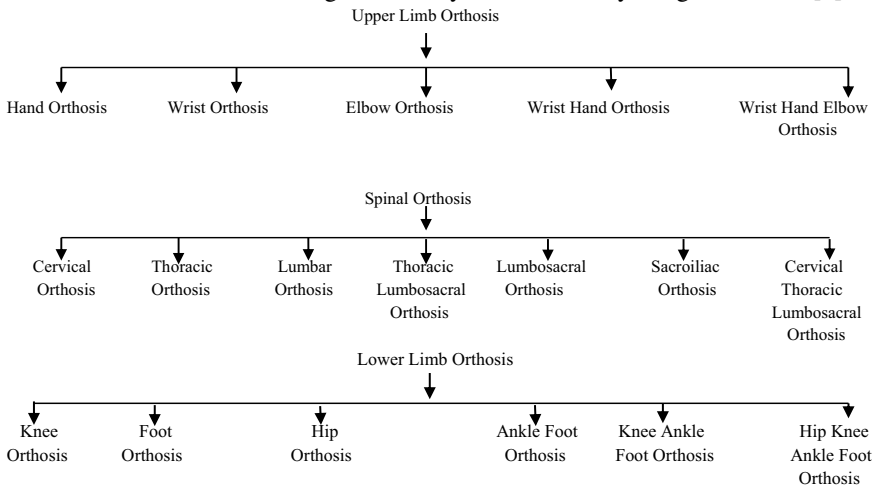
2 Ankle Foot Orthoses (AFOs)

Ankle foot orthosis is a kind of lower limb orthosis which is used to correct the foot drop and other deformities of ankle joint. It provides stability, support and control to ankle joint and improves gait movement by providing assistive torque (dorsiflexion or plantar flexion) at the joint [3].

Typical AFO design comes in L shape, vertical part of AFO covers the calf portion, and horizontal portion comes below the foot. AFOs can be divided into three type
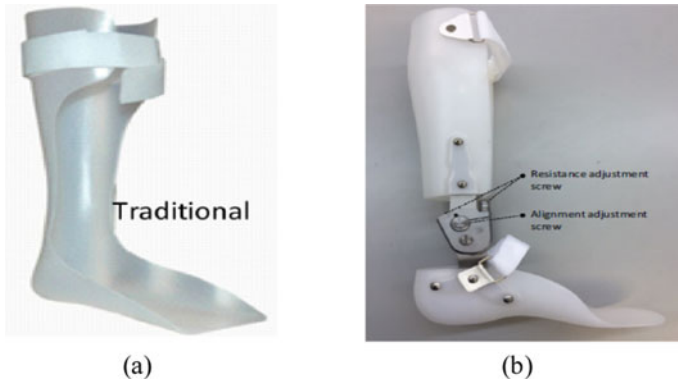
Fig. 1 **a** Passive AFO [2] and **b** active or articulate AFO [4]

which are active, passive and semi-active. The passive or non-articulated AFOs are rigid; it provides fixed support to the body due to fix stiffness of device so that patient is not able to move their ankle. Passive AFOs do not contain any electronic component, sensor, actuators and power supply. Generally, these are made up of thermoplastic materials, simple in design and cheaper than active AFOs [1, 3].

Semi-active and active or articulated AFOs are incorporated with actuators, control system, electronic sensors, etc. These AFOs are flexible which provide flexibility in motion to the ankle joint and improve gait movement. Passive and active AFOs are shown in Fig. 1. Active AFOs provide active control and torque to the ankle joint by means of actuators. These AFOs are much efficient than passive AFOs, but only limitation is that they are bulky, heavy and costly than passive AFOs [1, 3].

3 Different Fabrication Techniques of Ankle Foot Orthosis (AFOs)

Since ancient period, orthoses were made up of wood and leather, after industrial revolution metals were used in the place of wood and leather. Now due to rapid change in technologies, manufacturing techniques, materials, and due to development of new machines orthosis materials also rapidly changing and now composite materials are used due to its various advantages over conventional materials. Earlier, AFOs are made up of conventional materials like wood, metal and leather made manually. AFOs can be made by one of the following methods [5].

3.1 Thermoforming Technique

Thermoplastic materials like polypropylene are used in thermoforming of AFOs. In the thermoforming process, material is heated and formed on plaster cast impression. Thermoplastics have unique property that it softens upon heating. This property helps in easy molding of polypropylene in required shape and size as per the requirement of patient. There are some factors which need to be considered for proper thermoforming of polypropylene.

(a) Temperature up to which material is heated (heating temperature).
(b) Time duration of heating.
(c) Uniform distribution of temperature in oven.
(d) Teflon sheet condition.

Papi et al. have provided a novel methodology to determine load and strain carried by AFO during walking. AFO used in this study was fabricated using polypropylene by thermoforming method [8].

Zou et al. used polypropylene material for fabrication of AFO using thermoforming technique. They have performed finite element analysis to predict the mechanical behavior of ankle foot orthosis [9].

Amerinatzi et al. have designed a new AFO using thermoforming technique. They have used NiTi alloy-based hinged spring to provide more normal ankle joint movement during walking [12].

3.2 Pre-preg Technique

Pre-preg is a technique in which reinforcement fiber is pre-impregnated in matrix material in required ratio. This method is generally used with carbon fiber to produce high-quality, strong orthosis compared to tradition hand lay-up technique. It is possible to achieve more than 50% reinforcement in pre-preg technique which is not possible in tradition hand lay-up technique.

Mungia and dalgarno have explored the possibilities of generating modular AFO elements. They used pre-preg carbon fiber for footplate and strut which results in lower cost production and optimized design compare to tradition method [5].

Zou et al. have used finite element analysis to predict mechanical behavior of carbon fiber ankle foot orthosis. In this study, AFO was fabricated using pre-preg technique [9].

Takhash and abbas have fabricated ankle foot orthosis using pre-preg carbon fiber sheet. They have concluded in their study that carbon fiber AFO has superior mechanical properties than polypropylene AFO [19].

Major reasons of using pre-preg technique are it produces less waste, requires less curing time, cost effective and provides better mechanical properties.

3.3   3D Printing Techniques

3D printing is an additive manufacturing technique in which 3D objects are fabricated layer by layer using 3D model of object. 3D model of objects is generated by computer-aided design software. 3D printing techniques of orthosis manufacturing have several advantages over conventional fabrication techniques such as high production rate, better quality control, repeatability, compact equipment and easy to develop a new product [31].

Faustini et al. have mentioned steps involve in additive manufacturing of orthosis given below:

Step 1:   Scanning of body part using 3D scanner.
Step 2:   3D scanner creates complete geometrical data of body part.
Step 3:   Development of 3D model using computer-aided design software.
Step 4:   Manufacturing of orthosis using 3D printer.

Fantini et al. have produced a foot orthosis made up of acrylonitrile butadiene styrene and polylactic acid by fused deposition modeling. They have concluded that process produces less waste and consumes less production time [11].

Ielapi et al. have conducted a study to create a standardized framework for evaluating the ankle stiffness of 3D-printed AFOs. In this study, AFOs were fabricated using CFRP and polyamide 12 materials by 3D printing technique [16].

Faustini et al. have used selective laser sintering technology to produce three different AFOs. Materials used in fabrication of AFOs were dura form PA, dura form GF and rilsan d80 [17].

Ielapi et al. have conducted a study to create a standardized framework for evaluating the ankle stiffness of 3D-printed AFOs. In this study, AFOs were fabricated using CFRP and polyamide 12 materials by 3D printing technique [16].

4   Reported Work on Material Used in Fabrication of Ankle Foot Orthosis (AFOs)

Over the past several years, ankle foot orthosis materials have gradually evolved from wood, metal and leather, plastics and carbon fiber reinforcement composite. Currently, most researchers are using plastics and carbon fiber materials. Table 1 shows different research works on AFOs, carbon fiber composites have most superior mechanical properties among all available material for AFOs, but it is also most expensive, whereas plastics are less expensive, but its mechanical properties are very less compared to carbon fiber composites.

Table 1 Overview of materials and techniques used for ankle foot orthosis (AFOs)

Authors	Objective	Body part	Materials	Fabrication technique	Results
Cha et al. [6]	Design and build an AFO by 3D printing technique	Ankle foot	Thermoplastic polyurethane	3D printing	AFO results in increase in gait speed
Alam et al. [7]	Computer integrated design approach to build an AFO	Ankle foot	Side bar and foot plate–aluminum alloy 6061-T6 Calf part-PLA	Rapid prototyping	AFO was light weight AFO was comfortable and easy to use
Papi et al. [8]	Establish a methodology for quantification of AFO moment during walking	Ankle foot	Polypropylene	Thermoforming polymer sheets	Method provided could be used to determine load and strain carried by AFO during walking
Zou et al. [9]	To predict the mechanical behavior of AFOs by finite element analysis	Ankle foot	Three AFOs Two made up of carbon fiber and one made up of polypropylene	Thermoforming for PP Pre-preg carbon fiber with resin	FEA model could be used to predict mechanical behavior of AFO
Dombroski et al. [10]	Manufacture a custom-made orthosis using a low-cost 3D scanning and printing tool	Ankle foot	Arcylonitrile butadiene styrene	3D printing	3D printing method results in a higher arch index (AHI) than shod condition
Fantini et al. [11]	Methodological study of foot orthosis using rapid manufacturing	Foot	Acrylonitrile butadiene styrene Polylactic acid	Fused deposition modeling	Less invasive process Reduction in waste material
Amerinatzi et al. [12]	Build and design an AFO which provides more normal ankle joint movement	Ankle foot	NiTi alloy for hinged spring	Thermoforming polymer sheet	Higher ankle moment and normal walking due to use of NiTi spring

Table 1 (continued)

Authors	Objective	Body part	Materials	Fabrication technique	Results
Barries-Muriel et al. [13]	Establish a standard procedure to perform the skin strain analysis and to calculate lines of non-extensions	Ankle foot	Nylon 12PA	3D printing	Skin strain analysis LoNES improves and optimizes the wearable device Reduction in friction between skin and device
Bartonek et al. [14]	Design and build a spring orthosis for children with plantar flex or weakness	Ankle foot	Carbon fiber composite	Autoclave technique	Positive ankle work increased Ankle power absorption and generation increased
Deckers et al. [15]	Design and produce an AFO using alternate method which is laser sintered as shaping technology and compare with traditional method	Ankle foot	Calf and foot part –Polyamide 12 Two carbon fiber rods	Laser sintering	Less time required for patient fitting compared to tradition method
Ielapi et al. [16]	Create and validate a standardized framework for the evaluation of ankle stiffness of 3D printed AFOs	Ankle foot	Rods-CFRP Foot and calf part-polyamide 12	3D printing	Result revealed a better indication of AFO stress distribution and stiffness
Faustini et al. [17]	Manufacturing of ankle foot orthosis by SLS technique	Ankle foot	Dura form PA Dura form GF Rilsan D80	Selective laser sintering	Better mechanical damping High energy dissipation

Table 1 (continued)

Authors	Objective	Body part	Materials	Fabrication technique	Results
Liu et al. [18]	Investigate the feasibility of AFO fabrication by additive manufacturing	Ankle foot	Polyamide 12	3D printing	AFOs are light in weight have good mechanical property Improvement in gait of patient
Takhash and Abbas [19]	Build a knee ankle foot orthosis using carbon fiber composite and compare the mechanical properties with polypropylene AFO	Ankle foot	Bars-stainless steel Carbon fiber with c-orthocryl laminated resin as matrix	Pre-preg carbon fiber sheet	Carbon fiber AFO has superior mechanical properties than polypropylene
Walbran et al. [20]	Present a new method for 3D-printed AFOs that customize the fit and also allow variable stiffness of ankle joint	Ankle foot	Carbon fiber pre-impregnated with an epoxy matrix	3D printing	Automation could be easily achieved for 3D-printed segment which reduces the labor cost

5 Natural Fiber Composite as an Alternate Material for Ankle Foot Orthosis (AFOs)

From the earlier literature review in this paper, it can be concluded that composite materials are best suited for AFO material. An ideal AFO design required to be light in weight, comfortable to the patient, strong and have better aesthetic design. Most common materials used for AFO are carbon fiber, plastics, wood and metal. Table 2 shows the different materials and their mechanical properties used in fabrication of AFO by different researchers.

Common materials such as carbon fiber, glass fiber are more expensive than wood, metals and plastics. Metal AFOs are heavier and bulky than carbon and glass fiber AFOs. Thus, natural fibers such as kenaf, jute, hemp, sisal, flax are turned out to be better alternative of current AFO materials. Natural fibers are obtained from various parts of plants such as the seeds, stems and leaves. They are light in weight, cheap, recyclable, easily available, eco-friendly and biocompatible which are the desirable properties of an ideal AFO material.

Table 2 Mechanical properties of AFO material made up of different synthetic fiber

Authors	Materials	Tensile properties (MPa)	Tensile modulus (GPa)	Poisson's ratio	Rotational stiffness (N-m/°)
Faustini et al. [17]	Rilsan D80	45	1.4	–	10.18
Faustini et al. [17]	Duraform PA	44	1.6	–	10.47
Faustini et al. [17]	Duraform GF	38.1	5.9	–	11.03
Takhas and Abbas [19]	Polypropylene	35.74	1.25	–	–
Chen et al. [21]	Polypropylene	33	1.1	0.45	39.1
Chen et al. [21]	PC-ABS	41	1.9	0.39	67.7
Chen et al. [21]	ULTEM	72	2.5	0.36	89
Zou et al. [9]	Carbon fiber	437	–	0.50	–
Zou et al. [9]	Polypropylene	30	2.4	0.43	–

Table 3 shows the different types of natural fiber and their mechanical properties presented by researchers over the past several years. There are several methods for improving the properties of natural fiber composite such alkali treatment, chemical treatment, hybridizing with other fiber. Natural fibers are flexible in design, and it can easily moldable in any size and shape as per the requirement of the design. Strength and other properties can be improved by changing fiber orientation, matrix material and additives so that its properties are compatible with the currently used materials.

Natural fiber composites have good specific properties, but limitations with natural fibers are that there is variation in their properties. These limitations could be improved by advancement in processing and hybridization with two or more fiber. In few decades, natural fiber composites are emerging very rapidly and have capability to replace the convention material such as metals and ceramics in the field of construction materials, automobile, sporting goods, and electronic components, marine and aerospace parts [32].

Table 4 shows different type of natural and synthetic fiber, their mechanical and physical properties and cost. Cost of natural fiber less than that of synthetic fiber. Mechanical properties of natural fiber is lower than that of synthetic fiber, but properties of natural fiber can be improved by different methods and can be used as an alternative material for AFO while reducing the cost of product.

It can be conclude form Tables 2, 3 and 4 that mechanical properties such as tensile strength, tensile modulus, etc., of natural fiber and currently used material such as plastic are compatible. Though the mechanical properties of carbon fibers are much higher than natural fiber, its low cost, availability, biocompatibility can be considered

Table 3 Mechanical properties of some composite materials made up of natural fibers

Authors	Composite materials	Tensile strength (MPa)	Young's modulus (GPa)
Saba et al. [22]	Kenaf + Epoxy + Magnesium Hydride	39.36	4.76
Sepe and Bollino [23]	Untreated Hemp Fiber + Epoxy	80.74	5.336
Paduzi et al. [24]	Kenaf + Kelvar + Epoxy	54.18	6.90
Sosiati et al. [25]	Kenaf + Polypropylene + NaOH	44	1.80
Pawar et al. [26]	Epoxy + Jute (40%) + Granite (16%)	32.50 ± 0.51	1.355 ± 0.524
Bakhori et al. [27]	Jute + Epoxy	46.268	1.207
Gupta and Srivastava [28]	Jute (75%) + Sisal (25%) + Epoxy	100.65 ± 9.92	1.69 ± 0.17
Nimanpure and Hashmi [29]	Sisal (15%) + Kenaf (15%) + Polyester resin	77.36	4.89

Table 4 Cost, density and mechanical properties of natural and synthetic fibers [1, 30]

Fiber	Density (gm/cc)	Tensile strength (MPa)	Tensile modulus (GPa)	Cost ($/kg)
Flax	1.5	345–1035	27.6	0.40–0.55
Hemp	1.4	690	35	0.40–0.55
Jute	1.3	393–773	26.5	0.40–0.55
Sisal	1.5	511–635	9.4–22	0.40–0.55
E-glass	2.5	2000–3500	70	2.0
S-glass	2.5	4570	86	2.0
Carbon	1.8	4900–7010	230.3–324.1	32–36
Cotton	1.5–1.6	287–597	5.5–12.6	0.40–0.55
Pineapple	1.53	413–1627	39.5–82.5	0.40–0.55

as an alternate to the carbon fiber. Natural fibers could fulfill all needed properties for an ideal AFO material by improving its strength by different enhancement method. In addition, natural fibers have property of absorption of liquid so it can absorb the sweat produced between body and enclosed portion of AFO.

6 Conclusion

This paper discussed on ankle foot orthosis, different material used for it, different processing technique for fabrication of AFO. There are several conclusions that can be derived from this study are summarized as follows:

1. Existence of orthosis can be seen from ancient period in form of simple design, as industrial revolution comes new materials, improved technology drives the simple design of orthosis to the more complex and better design to improve the functionality of device, improve gait movement, increases the comfort among the wearer by using various kind of sensors, hinges, computer-assisted design.
2. Currently existing materials for ankle foot orthosis are wood, metal and leather, carbon fiber composite, plastics such as polylactic acid (PLA), acrylonitrile butadiene styrene (ABS), Duraform PA, Duraform GF, polypropylene. It can be concluded from this review that carbon fiber has superior mechanical property in comparison to other material which makes it most suitable for ankle foot orthosis material, but due to its high fiber cost makes it uneconomical for industries so plastic materials are used instead carbon fiber.
3. In manufacturing of ankle foot orthosis, there are mainly three processes which are generally used for fabrication which are pre-preg technique for carbon fiber, thermoforming plastic and 3D printing. Among these processes, 3D printing is most efficient and requires less fabrication time, but 3D printing requires material in filament form so there are only few material which are available to be used in 3D printing.
4. By going through existing researches on natural fiber, it can be seen that natural fiber has similar mechanical properties to the some of the plastic materials such as polypropylene, etc. By using natural fiber cost of ankle foot orthosis will be reduced while maintaining the desirable properties such low weight, good strength and high stiffness.
5. Natural fibers such as kenaf, sisal, jute, hemp are light in weight, eco-friendly, biocompatible, cheaper, easily recyclable and provide desirable mechanical properties for ankle foot orthosis.

References

1. Shahara, F. S., Sultana, M. T. H., Lee, S. H., Jawaid, M., Shaha, A. U. M., Safri, S. N. A., & Sivasankaran, P. N.: A review on the orthotics and prosthetics and the potential of kenaf composites as alternative materials for ankle-foot orthosis. *Journal of the Mechanical Behavior of Biomedical Materials, 99*, 169–185.
2. Chen, R. K., Jin, Y., & Wensman, J., Smith, A.: Additive manufacturing of custom orthoses and prostheses—A review. *Additive Manufacturing, 12*, 77–89.
3. Ulkir, O., Akgun, G., & Kaplanoglu, E. (2018). Mechanical design and analysis of a pneumatic ankle foot orthosis. In: *2018 Electric Electronics, Computer Science, Biomedical Engineerings Meeting, EBBT* (pp. 1–4).

4. Kobayashi, T., Orendurff, M. S., Hunt, G., et al. (2017). An articulated ankle–foot orthosis with adjustable plantarflexion resistance, dorsiflexion resistance and alignment: A pilot study on mechanical properties and effects on stroke hemiparetic gait. *Medical Engineering & Physics, 44,* 94–101.

5. Munguia, J., & Dalgarno, K. (2013). Ankle foot orthotics optimization by means of composite reinforcement of free-form structures. In: *24th International Solid Freeform Fabrication Symposium—An Additive Manufacturing Conference, SFF 2013* (pp. 766–776).

6. Cha, Y. H., & Lee, K. H., et al. (2017). Ankle foot orthosis made by 3D printing technique and automated design software. In: *Applied bionics and biomechanics* (vol. 2017).

7. Alam, M., Choudhury, I. A., & Mamat, A. B. (2014). Custom aided design and fabrication of a custom articulated ankle foot orthosis. *Journal Of Mechanics In Medicine and Biology, 15*(4), 2015.

8. Papi, E., Maclean, J., & Bowers, R. J., et al. (2015). Determination of loads carried by polypropylene ankle-foot orthoses: A preliminary study. *Proceedings of the Institution of Mechanical Engineers, Part H: Journal of Engineering in Medicine,* 40–51.

9. Zou, D., He, T., Dailey, M., et al. (2014). Experimental and computational analysis of composite ankle foot orthosis. *Journal of Rehabilitation Research and Development, 51,* 1525–1536.

10. Dombroski, C. E., Balsdon M. E., & Froats, A. (2014). The use of a low cost 3D scanning and printing tool in the manufacture of custom made foot orthoses: A preliminary study. In *BMC Research Notes* (Vol. 7, pp. 443).

11. Fantini, M., & De Crescenzio, F., et al. (2017). Design and rapid manufacturing of a customized foot orthoses: A first methodological study. In: *Advanced on Mechanics, Design Engineering and Manufacturing.* Lecture Notes in Mechanical Engineering. Springer Internation Publishing.

12. Amerinatanzi, A., & Zamanian, H., et al. (2016). On the advantages of superelastic NiTi in ankle foot orthoses. In *Conference On Smart Material, Adaptive Structures And Intelligent System. Proceesings of ASME.*

13. Barrios-Muriel, J., Romero Sánchez, F., Alonso, F. J., et al. (2018). Design of semi rigid wearable devices based on skin strain analysis. *Journal of Biomechanical Enineering., 141,* 021008.

14. Bartonek, A., Eriksson, M., et al. (2007). A new carbon fiber spring orthosis for children with planterflexor weakness. *Gait & Posture, 25,* 652–656.

15. Deckers, J. P., Vermandel, M., et al. (2018). Development and clinical evaluation of laser-sintered ankle foot orthoses. *Plastics, Rubber and Composites, 47*(1), 42–44.

16. Ielapi, A., & Lammens, N., et al. (2019). A validated computational framework to evaluate the stiffness of 3D printed ankle foot orthoses. *Computer Methods in Biomechanics and Biomedical Engineering.*

17. Faustini, M. C., & Neptune, R.R., et al. (2008, February). Manufacture of passive dynamic ankle foot orthoses using selective laser sintering. *IEEE Transaction on Biomedical Engineering, 55*(2).

18. Liu, Z., & Zhang, P., et al. (2019). Additive manufacturing of specific ankle foot orthoses for persons after stroke: A preliminary study based on gait analysis data. *Mathematical Bioscience & Engineering, 16*, 8134–8143.

19. Takhakh, A. M., & Abbas, S. M. (2018). Manufacturing and analysis of carbon fiber knee ankle foot orthosis. *International Journal of Engineering and Technology, 7,* 2236.

20. Walbran, M., Turner, K., et al. (2016). Customized 3D printed ankle foot orthosis with adaptable carbon fiber composite spring joint. *Cogent engineering, 3,* 1227022.

21. Chen, R. K., & Chen, L., et al. (2014). Additive manufacturing of personalized ankle foot orthosis. In: *Preceedings of NAMRI/SME* (vol. 42).

22. Saba, N., Alothman, O. Y., Almutairi, Z., et al. (2019). Magnesium hydroxide reinforced kenaf fibers/epoxy hybrid composites: Mechanical and thermomechanical properties. *Construction and Building Materials, 201,* 138–148.

23. Sepe, R., Bollino, F., Boccarusso L., Caputo F. (2017). Influence of chemical treatment on mechanical property of hemp fiber reinforced composite. In: *Composite Part B.*

24. Muhamad Paudzi, M. K. F., Abdullah, M. F., & Ali, A. (2018). Fatigue analysis of hybrid composites of kenaf/kevlar fibre reinforced epoxy composites. *Journal of Engineering,* 1–8.
25. Sosiati, H., Anugrah, R., & Binangun, Y. A., et al. (2019). Characterization of tensile properties of alkali-treated kenaf/polypropylene composites. In: *AIP Conference Proceeding* (Vol. 2097, pp. 030113).
26. Pawar, M. J., Patnaik, A., & Nagar, R. (2015). Investigation of mechanical and thermo-mechanical properties of granite powder filled treated jute fiber reinforced epoxy composite. In: *Wiley Online Library, Polymer composites-2015*.
27. Bakhori, S. N. M., & Zuikafy, S. N. F., et al. (2017). Tensile properties for MWCNT filled jute-epoxy composite. *Journal of Advanced Research in Applied Mechanics 31*(1), 16–21.
28. Gupta, M. K., & Srivastava, R. K. (2016, August). Mechanical, thermal and water absorption properties of hybrid sisal/jute fiber reinforced polymer composite. *India Journal of Engineering & Material Science, 23*, 231–238.
29. Nimanpure, S., & Hashmi, S. A. R. (2017). Mechanical electrical and thermal analysis of sisal fibril/kenaf fiber hybrid polyster composite. In: *Wiley Online Library, Polymer composites-2017*.
30. Nath, S., & Jena, H., et al. (2016). Analysis of mechanical properties of jute epoxy composite with cenosphere filler. *Silicon*, *11*, 659.
31. Pallari, J. H. P., & Dalgarno, K. W., et al. (2010). Design and additive fabrication of foot and ankle-foot orthoses. In: *Proceedings of 21st Annual International Solid Freeform Fabrication Symposium* (pp. 834–845).
32. Sanjay, M. R., Arpitha, G. R., et al. (2016). Applications of natural fibers and its composites: An overview. *Natural Resources, 7,* 108–114.

Structural, Wear and Thermal Behavior of Copper Metal Matrix Composites: A Review

Prateek Mittal, Vaibhav Raghav, Dinesh Chawla, Jimmy Mehta, Mani Kant Paswan, and Pallav Gupta

Abstract Materials have always been a prime area of research in the development and advancement of new technologies. Metal matrix composites have gained importance due to their low weight and high strength, low coefficient of thermal expansion, good wear resistance and capability to withstand high temperatures. Various researchers have undertaken wide variety of research works in the field of copper matrix composites involving diverse fabrication techniques and varied reinforcement. This paper presents a comprehensive review of selected research works undertaken in the field of copper matrix composites wherein phase analysis, microstructure, hardness, wear and thermal behavior are discussed.

Keywords Metal matrix composites · Copper matrix based composites · Composite materials · Hybrid composites

---

P. Mittal (✉) · D. Chawla · J. Mehta
Department of Mechanical Engineering, Manav Rachna International Institute of Research and Studies, Faridabad, India
e-mail: prateekmittal.fet@mriu.edu.in; prateekme@gmail.com

D. Chawla
e-mail: dineshchawla.fet@mriu.edu.in

J. Mehta
e-mail: jimmy.fet@mriu.edu.in

P. Mittal · P. Gupta
Department of Mechanical Engineering, A.S.E.T, Amity University, Noida, Uttar Pradesh, India
e-mail: pgupta7@amity.edu

V. Raghav
Shri Vishwakarma Skill University, Gurugram, India
e-mail: vaibhavraghav2012@gmail.com

M. K. Paswan
Department of Mechanical Engineering, National Institute of Technology, Jamshedpur, India
e-mail: mkpaswan.me@nitjsr.ac.in

1 Introduction

Metal matrix composites (MMCs) have gained considerable popularity in the past two decades due their extraordinary properties like high strength-to-weight ratio, low coefficient of thermal expansion, high resistance to wear, exceptional corrosion resistance, good resistance to fatigue loading and ability to withstand heat [1, 2]. Pure copper finds its application in various thermal and electrical applications due to its high thermal and electrical conductivity. However, addition of ceramic reinforcement improves the properties of pure copper which consequently makes it suitable for a wide range of applications [3]. Hybrid and single-reinforcement MMCs both have been worked upon in the past, and hybrid composites have been found to have better mechanical properties subject to the correct selection of reinforcement and appropriate composition (wt%) [4]. In general, ceramics are used as reinforcement as they enable the pure metal to withstand high temperatures and provide good hardness and resistance to wear. However, in case of copper due to its poor wetting capability this dispersion of reinforcement particles is sometimes improper which leads to significant variation of mechanical properties at different locations within the material [5–6]. One major challenge in mass production of MMCs is their production cost which is high in most cases except stir casting [7]. As far as tribological properties of the MMCs are concerned, the wear properties of the composites have been found to improve to a great extent on addition of ceramic particles as reinforcement [8, 9]. Copper matrix composites reinforced with ceramics wear are mainly due to abrasion wherein breakage of asperities is the main contributor to the removal of material during sliding [10–11]. The compressive strength of the MMCs on addition of harder reinforcement is found to increase considerably unless some soft component like graphite is added which eventually lowers the hardness due to its soft and lubricating nature [12]. The microstructure of the composites as reported in previous studies depends on the fabrication technique to a great extent. The density of the composite materials with pure metal as the matrix and ceramic particles as reinforcement is found to decrease as the content of reinforcement increases due to the hard nature of ceramic particles [13–14]. However, if the form of the material is changed during fabrication like in bending, rolling or extrusion, the hardness and density are found to increase; this increase may be attributed to strain hardening [15]. Various researchers have analyzed different properties and behavior of the materials under different conditions in order to find its applicability in a specific area of concern [16–17]. There are several techniques for synthesis of composites which can be classified on the basis of phase in which processing is done. Prominent techniques are stir casting [18, 19], powder metallurgy [3], in situ fabrication [20], infiltration process [21], sintering [18], etc.

2 Behavior of Cu Composites

2.1 Phase

Kang and Kang [22] prepared copper composites using cold spray and plasma spray wherein tungsten/copper composite powder was sprayed on mild steel substrate [22]. Oxides of copper were found in X-ray diffraction (XRD) peaks of the samples prepared by plasma spraying; however, no oxides were seen in composites with cold spray process. Daoush et al. [23] fabricated CNT/Cu nano-composites using multi-walled carbon nano-tubes (CNTs). The XRD patterns indicated the peak pertaining to grapheme structure of CNTs at around 25° 2Θ value [23]. XRD patterns of pure copper and pure CNT were shown to clearly demarcate them from the XRD pattern of the prepared composite. Shehata et al. [24] prepared alumina nano-particle reinforced copper matrix composite by in situ processing. Two ways of preparation of samples were adopted first wherein aqueous solution of alumina was used and second in which aqueous solution of copper was used. The XRD pattern of the prepared composite samples indicated the presence of a third-phase $CuAlO_2$ which occurs as a result of reaction between Cu_2O and alumina [24]. Samples prepared through both the routes were found to contain the third-phase $CuAlO_2$ apart from the oxide of copper. Alam and Singh [25] prepared copper matrix-based composites with class and silicon carbide as reinforcement. The composites were fabricated by cold compaction followed by sintering. The peaks obtained in XRD pattern of copper milled for long duration after heat treatment showed the presence of oxides CuO and Cu_2O [25]. Yusoff et al. [26] WC reinforced copper-matrix-based composites through mechanical alloying and sintering. XRD patterns of the prepared samples indicated that at some places, the peaks of W were higher than Cu because of the weak atomic scattering factor of Cu under X-rays as compared to that of W [26].

2.2 Microstructure

Grzonka et al. [27] prepared a composite material containing Cu0.8Cr alloy and diamond powder through pulse plasma sintering carried out at around 900 °C. The SEM image revealed that there were no cracks or voids. The interface was distinctly identifiable and was about 200 nm thick. The interface region was found to have high concentration of chromium and copper. The analyses of different phases found in the interlayer region indicated the presence of Cr_3C_2 in the binding phase [27]. Silvain et al. [28] prepared the copper matrix composites reinforced with continuous graphite fibers. The resulting composite was found to have uniform mechanical properties due to homogeneous distribution of fiber. Fairly less porosity was obtained in the composite (less than 2%). In some interface regions, weak bonding was evident due to peeling of fibers from copper. However, no chemical reaction between graphite fibers and copper matrix was observed [28]. Kim et al. [29] prepared multi-layer

graphene (MLG)/Cu matrix using a combination of ball milling and rolling (equal speed and differential speed). 0.5 and 1.0 vol.% reinforcement content composites were prepared to achieve better mechanical properties. The powders of Cu and graphene were subjected to strong compressive forces exerted during ball milling resulting in transformation of powders to flakes. Composites prepared by equal speed rolling were found to contain fine MLG particles which were elliptical or strip-like in shape [29]. Chen et al. [30] prepared copper matrix composites reinforced with graphene nano-platelets (GNPs). Graphene was suspended in the alcoholic solution of copper ion. The GNPs were found to be uniformly distributed between Cu_2O nano-particles. The investigation of microstructure revealed that graphene was covered on either side by copper nano-particles [30]. Liu et al. [31] prepared graphite flake/copper composites using electroless plating of copper on graphite flakes followed by spark plasma sintering of composite powders. The orientation of graphite flakes was in the direction normal to the direction in which pressing action took place. The TEM image indicated that the interface was continuous [31]. Tian et al. [32] fabricated oxide dispersion-strengthened copper (ODSC)-based composites. Dispersion-distributed alumina particles were used, and powder metallurgy was adopted as the manufacturing route with internal oxidation. The TEM image showed that alumina particles were distributed uniformly in the matrix [32]. Travitzky [33] fabricated Al_2O_3/Cu composites through pressure-less and gas pressure-assisted infiltration. Plasma sprayed alumina preforms were used as reinforcement. In the SEM images after fracture of material, copper was found to deform plastically. A copper oxide covering around the alumina grains was found which tended to ease the crack propagation [33]. Singh and Gautam [34] fabricated the copper matrix-based hybrid composite reinforced with WC, alumina and chromium through stir casting route. The micrographs indicated homogeneous distribution of reinforcement within the matrix. However, it was found that at higher fractions of reinforcement (wt%) the dispersion tended to be some-what non-homogeneous and mild agglomeration of ceramic particles was seen [34].

2.3   Hardness

Upadhyaya and Upadhyaya [35] prepared Cu-alumina composite through blending and mechanical alloying (0–3 wt% alumina). The hardness of composites fabricated by mechanical alloying showed an increasing trend with the increase in alumina content. However, hardness of composites fabricated by blending was observed to be high at 2 wt% alumina content [35]. Rajkumar et al. [36] assessed the hardness of copper-CNT composites fabricated through microwave sintering on Vickers hardness test rig. The hardness of composites was found to be higher than pure sintered copper. The highest hardness was recorded in composites containing 15 vol.% reinforcement (126 HV). Composites manufactured through microwave sintering showed better hardness than conventional sintering and spark plasma sintering [36]. Jenei et al. [37] prepared multi-walled copper nano-tube/copper composites through cold

pressing followed by high-pressure torsion at room temperature and 373 K and reported the microhardness of samples as a function of distance from the center [37]. Fathy et al. [12] tested the hardness of copper–alumina nano-composite powders prepared by thermochemical techniques. Sample containing 12.5 wt% Al_2O_3 exhibited the highest hardness of 99.4 HB. The hardness was found to increase with increase in alumina content [12]. Abu-Oqail et al. [38] fabricated W–Cu net shape composite wherein wet powders of copper and tungsten were used to create the net shape composite (20–30 wt% Cu). The hardness was found to increase with tungsten content. The values of microhardness obtained after two hours of sintering were found to be considerably higher than after one hour. Highest value of hardness, i.e., 250 HB, was obtained for W-20 wt% Cu [38]. Chandrakanth et al. [39] fabricated Cu-TiC-Graphite hybrid metal matrix composite through microwave sintering route. The hardness of Cu-10%TiC-5% graphite was obtained for various depths and sintering times. Hardness of 20 min sintered composite at 2 mm depth from surface was found to be highest, i.e., around 83 HV [39].

2.4 Wear

Moustafa et al. [40] observed the wear rates of Cu-graphite composites manufactured through cold pressing followed by sintering. Wear rates for coated and uncoated composites were found to be almost same. 20 wt% coated and uncoated composites showed the best wear resistance at the loads ranging from 100 to 450 N [40]. Tjong and Lau [41] performed the wear test on TiB_2-reinforced copper matrix composites prepared by isostatic pressing. The variation in volume loss with sliding distance was almost negligible except for pure copper. Least loss in volume was observed for 20 vol.% TiB_2 composite [41]. Larionova et al. [42] observed the tribological and wear behavior of copper–carbon nano-fiber composites prepared by chemical vapor deposition (CVD). The wear in Cu-33 vol.% CNFs was found to be less than half of Cu-33vol.% graphite composites. High hardness as compared to graphite composites and steady grain boundaries were the primary reason for better wear properties of CNF composites [42]. Deshpande et al. [43] investigated the wear behavior of Cu-WC composites prepared by infrared infiltration technique. The composite samples were found to wear out at faster rate when wear stress increased beyond 0.6 MPa [43]. Fathy et al. [12] observed the wear rates of Cu-Al_2O_3 composites at different velocities. The composites containing 12.5 wt% alumina showed better wear resistance at all sliding speeds. The wear rates of composites were found to increase with the increase in applied load and sliding speed [12]. Winzer et al. [44] reported that wear mechanism in 1–15 μm copper ligament diameter composites was found to be a mix of adhesive and oxidative wear. 30 μm copper ligament diameter composites showed the highest wear resistance wherein a mix of abrasive and oxidative wear mechanism was predominant [44].

2.5 Thermal Behavior

Schubert et al. [45] fabricated copper/carbon composites through powder metallurgy route. Diamond grit of different mesh was used as reinforcement to assess the effect on thermal properties of Cu matrix. Composites containing 65 vol.% diamond showed the highest thermal conductivity of 700 W/mK [45]. Firkowska et al. [46] observed the thermal properties of copper-CNT composites. Considerable difference between theoretical and practical observations of thermal conductivity was seen and was attributed to the assumptions made in the calculation of theoretical thermal conductivity. An optimum value of CNT length and wt% is suggested for obtaining high thermal conductivity [46]. Yoshida and Morigami [47] studied the thermal behavior of diamond/Cu composites with 50–80 vol.% of diamond. The thermal conductivity was found to increase with the increase in diamond particle size (20–110 μm), and the coefficient of thermal expansion was found to decrease with the increase in vol.% of diamond. The highest thermal conductivity was obtained for the sample containing 70 vol.% diamond of about 800 W/mK [47]. The comprehensive study reveals that hybrid composites show better mechanical and thermal properties than conventional composites [18]. Table 1 represents the summary of prominent research works.

Table 1 Summary of reviewed works pertaining to microstructure, wear and thermal behavior

Matrix	Reinforcement	Processing route	Behavior	References
Cu	Cr and diamond	Pulse plasma sintering	Structural	[27]
Cu	Graphite fibers	Diffusion bonding	Structural	[28]
Cu	MLG	Milling and rolling	Structural	[29]
Cu	Graphene	Spark plasma sintering	Structural	[30]
Cu	Graphite flakes	Electroless plating	Structural	[31]
Cu	Aluminum oxide	P/M	Structural	[32]
Cu	Aluminum oxide	Infiltration	Structural	[33]
Cu	WC	Stir casting	Structural	[34]
Cu	Graphite	Cold pressing	Wear	[40]
Cu	TiB$_2$	Isostatic pressing	Wear	[41]
Cu	Carbon Nano-fiber	CVD	Wear	[42]
Cu	WC	Infrared infiltration	Wear	[43]
Cu	Alumina	Gas-pressure infiltration	Wear	[44]
Cu	Diamond	P/M	Thermal	[45]
Cu	CNT	Oxidation and reduction	Thermal	[46]
Cu	Diamond	Sintering	Thermal	[47]

3 Concluding Remarks

Based on the findings of research works reviewed in this paper, following conclusions can be drawn:

- Stirring time and stirring speeds affect the mixing of reinforcement phase in the matrix;
- Preheating of ceramic reinforcement increases the chances of urm dispersion;
- Wetting agents like magnesium may be added to improve the wettability of copper;
- Differential solidification and intermittent cooling must be avoided to reduce the chances of defects in the composite.

References

1. Garg, P., Jamwal, A., Kumar, D., Sadasivuni, K. K., Hussain, C. M., & Gupta, P. (2019). Advance research progresses in aluminium matrix composites: manufacturing & applications. *Journal of Materials Research and Technology, 8*(5), 4924–4939.
2. Hossain, S., Rahman, M. M., Jamwal, A., Gupta, P., Thakur, S., & Gupta, S. (2019, September). Processing and characterization of pine epoxy based composites. In: *AIP conference proceedings* (Vol. 2148, No. 1, p. 030017). AIP Publishing LLC.
3. Schubert, T., et al. (2008). Interfacial design of Cu-based composites prepared by powder metallurgy for heat sink applications. *Materials Science and Engineering: A, 475*(1–2), 39–44.
4. Jamwal, A., Prakash, P., Kumar, D., Singh, N., Sadasivuni, K. K., Harshit, K., et al. (2019). Microstructure, wear and corrosion characteristics of Cu matrix reinforced SiC–graphite hybrid composites. *Journal of Composite Materials, 53*(18), 2545–2553.
5. Zhan, Y. Z., & Guoding, Z. (2003). The effect of interfacial modifying on the mechanical and wear properties of SiCp/Cu composites. *Materials Letters, 57*(29), 4583–4591.
6. Jamwal, A., Seth, P. P., Kumar, D., Agrawal, R., Sadasivuni, K. K., & Gupta, P. (2020). Microstructural, tribological and compression behaviour of Copper matrix reinforced with Graphite-SiC hybrid composites. *Materials Chemistry and Physics*, 123090.
7. Hossain, S., Rahman, M. M., Chawla, D., Kumar, A., Seth, P. P., Gupta, P., et al. (2020). Fabrication, microstructural and mechanical behavior of Al-Al$_2$O$_3$-SiC hybrid metal matrix composites. *Materials Today: Proceedings, 21,* 1458–1461.
8. Zhan, Y., & Zhang, G. (2004). Friction and wear behavior of copper matrix composites reinforced with SiC and graphite particles. *Tribology Letters, 17,* 91–98.
9. Zhan, Y., & Zhang, G. (2006). The role of graphite particles in the high-temperature wear of copper hybrid composites against steel. *Materials & Design, 27*(1), 79–84.
10. Gupta, P., et al. (2018). Dependence of wear behavior on sintering mechanism for iron-alumina metal matrix nanocomposites. *Materials Chemistry and Physics, 220,* 441–448.
11. Akhlaghi, F., & Zare-Bidaki, A. (2009). Influence of graphite content on the dry sliding and oil impregnated sliding wear behavior of Al 2024–graphite composites produced by in situ powder metallurgy method. *Wear, 266*(1–2), 37–45.
12. Fathy, A., Shehata, F., Abdelhameed, M., & Elmahdy, M. (2012). Compressive and wear resistance of nanometric alumina reinforced copper matrix composites. *Materials and Design, 36,* 100–107.
13. Bandil, K., et al. (2019). Microstructural, mechanical and corrosion behaviour of Al–Si alloy reinforced with SiC metal matrix composite. *Journal of* Composite *Materials, 53*(28–30), 4215–4223.

14. Sohag, A. Z., et al. (2020). Effect of ceramic reinforcement on the microstructural, mechanical and tribological behavior of Al–Cu alloy metal matrix composite. *Materials Today: Proceedings, 21*, 1407–1411.

15. Gupta, P., Kumar, D., Jha, A. K., & Prakash, O. (2016). Effect of height to diameter (h/d) ratio on the deformation behaviour of Fe–Al_2O_3 metal matrix nanocomposites. *Bulletin of Materials Science, 39*(5), 1245–1258.

16. Prasanna Kumar, U. J., Gupta, P., & Jha, A. K., et al. (2017). Closed die deformation behavior of cylindrical iron–alumina metal matrix composites during cold sinter forging. *Journal of The Institution of Engineers (India): Series D, 98*(1), 155.

17. Gong, T., et al. (2019). Microstructure and tribological behavior of interfaces in Cu-SiO_2 and Cu–Cr metal matrix composites. *Journal of Alloys and Compounds, 786*, 975–985.

18. Jamwal, A., Mittal, P., Agrawal, R., Gupta, S., Kumar, D., Sadasivuni, K. K., et al. (2020). Towards sustainable copper matrix composites: Manufacturing routes with structural, mechanical, electrical and corrosion behaviour. *Journal of Composite Materials, 54*(19), 2635–2649.

19. Mittal, P., Paswan, M. K., Sadasivuni, K. K., & Gupta, P. (2020). Structural, wear and thermal behaviour of Cu–Al2O3–graphite hybrid metal matrix composites. *Proceedings of the Institution of Mechanical Engineers, Part L: Journal of Materials: Design and Applications, 234*(8), 1154–1164.

20. Bannan, J., Temple, R. I., & Jones, R. (2003). In situ fabrication of titanium carbide reinforced copper MMC. *Materials Science and Technology, 19*(8), 1148–1150.

21. Carreno-Morelli, E., et al. (1998). Processing and characterization of aluminium-based MMCs produced by gas pressure infiltration. *Materials Science and Engineering A, 251*(1–2), 48–57.

22. Kang, H.-K., & Kang, S. B. (2003). Tungsten/copper composite deposits produced by a cold spray. *Scripta Materialia, 49,* 1169–1174. https://doi.org/10.1016/j.scriptamat.2003.08.023.

23. Daoush, W. M., Lima, B. K., Moa, C. B., Nama, D. H., & Honga, S. H. (2009). Electrical and mechanical properties of carbon nanotube reinforced copper nanocomposites fabricated by electroless deposition process. *Materials Science and Engineering A, 513–514,* 247–253.

24. Shehata, F., Fathy, A., Abdelhameed, M., & Moustafa, S. F. (2009). Preparation and properties of Al_2O_3 nanoparticle reinforced copper matrix composites by in situ processing. *Materials and Design, 30*(7), 2756–2762.

25. Alam, S. N., & Singh, H. (2014). Development of copper-based metal matrix composites: An analysis by SEM. *EDS and XRD. Microsc Anal, 28,* 8–13.

26. Yusoff, M., et al. (2011). Mechanical alloying and sintering of nanostructured tungsten carbide-reinforced carbon composite and its characterization. *Materials and Design, 32,* 3293–3298.

27. Grzonka, J., Kruszewski, M. J., Rosiński, M., Ciupiński, Ł., Michalski, A., & Kurzydłowski, K. J. (2015). *Materials Characterization, 99*, 188–194.

28. Silvain, J. F., et al. (1994). Elastic moduli, thermal expansion and microstructure of coppermatrix composite reinforced by continuous graphite fibres. *Composites, 25*(7), 570–574.

29. Kim, W. J., Lee, T. J., & Han, S. H. (2014). Multi-layer graphene/copper composites: Preparation using high-ratio differential speed rolling, microstructure and mechanical properties. *Carbon, 69,* 55–65.

30. Chen, F., Ying, J., Wang, Y., Du, S., Liu, Z., & Huang, Q. (2016). Effects of graphene content on the microstructure and properties of copper matrix composites. *Carbon, 96,* 836–842.

31. Liu, Q., He, X. B., Ren, S. B., Zhang, C., Liu, T. T., & Qu, X. H. (2014). Thermophysical properties and microstructure of graphite flake/copper composites processed by electroless copper coating. *Journal of Alloys and Compounds, 587,* 255–259.

32. Tian, B., Liu, P., Song, K., Li, Y., & Ren, F. (2006). Microstructure and properties at elevated temperature of nano-Al_2O_3 particles dispersion-strengthened copper base composite. *Materials Science and Engineering A, 435–436,* 705–710.

33. Travitzky, N. A. (1998). *Materials Letters, 36,* 114–117.

34. Singh, M. K., & Gautam, R. K. (2017). Synthesis of copper metal matrix hybrid composites using stir casting technique and its mechanical, optical and electrical behaviours. *Transactions of the Indian Institute of Metals, 70,* 2415–2428. https://doi.org/10.1007/s12666-017-1103-0.

35. Upadhyaya, A., & Upadhyaya, G. S. (1995). Sintering of copper–alumina composites through blending and mechanical alloying powder metallurgy routes. *Materials and Design, 16,* 41–45.
36. Rajkumar, K. A. S. (2011). Tribological studies on microwave sintered copper-carbon nanotube composites. *Wear, 270*(9–10), 613–621.
37. Jenei, P., Yoon, E. Y., Gubicza, H. S. Kim, J., Lábár, J. L., & Ungár, T. (2011). *Materials Science and Engineering A, 528*(13–14), 4690–4695.
38. Abu-Oqail, A., et al. (2012). Effects of processing parameters of tungsten–copper composites. *International Journal of Refractory Metals & Hard Materials, 35,* 207–212.
39. Chandrakanth, R. G., et al. (2010). Fabrication of copper–TiC–graphite hybrid metal matrix composites through microwave processing. *International Journal of Advanced Manufacturing Technology, 48,* 645–653.
40. Moustafa, S. F., El-Badry, S. A., Sanad, A. M., & Kieback, B. (2002). *Wear, 253,* 699–710.
41. Tjong, S. C., & Lau, K. C. (2000). Abrasive wear behavior of TiB_2 particle reinforced copper matrix composites. *Materials Science and Engineering A, 282,* 183–186.
42. Larionova, T., et al. (2014). Friction and wear of copper–carbon nanofibers compact composites prepared by chemical vapor deposition. *Wear, 319,* 118–122.
43. Deshpande, P. K., & Lin, R. Y. (2006). Wear resistance of WC particle reinforced copper matrix composites and the effect of porosity. *Materials Science and Engineering A, 418,* 137–145.
44. Winzer, J., Weiler, L., Pouquet, J., & Rödel, J. (2011). Wear behaviour of interpenetrating alumina copper composites. *Wear, 271,* 2845–2851.
45. Schubert, T., Weißgärber, T., & Kieback, B. (2009). *Fabrication and properties of Copper/Carbon composites for thermal management applications* (Vol. 59). Advanced Materials Research. Trans Tech Publications Ltd.
46. Firkowska, I., Boden, A., Vogt, A. M., & Reich, S. (2011). *Journal of Materials Chemistry, 21,* 17541.
47. Yoshida, K., & Morigami, H. (2004). Thermal properties of diamond/copper composite material. *Microelectronics Reliability, 44*(2), 303–308.
48. Jamwal, A., Vates, U. K., Gupta, P., Aggarwal, A., & Sharma, B. P. (2019). Fabrication and characterization of Al_2O_3–TiC-reinforced aluminum matrix composites. In Advances in industrial and production engineering (pp. 349–356). Springer, Singapore.
49. Liu, Q., Castillo-Rodríguez, M., Julio Galisteo, A., de Villoria, R. G., & Torralba, J. M. (2019). Wear behavior of copper-graphite composites processed by field-assisted hot pressing. *Journal of Composites Science, 3*(1), 29.
50. Zhan, Y., & Zhang, G. (2004). Friction and wear behavior of copper matrix composites reinforced with SiC and graphite particles. *Tribology Letters, 17*(1), 91–98.
51. Kumar, A., Yeasin Arafath, M., Gupta, P., Kumar, D., Mustansar Hussain, C., & Jamwal, A. (2019). Microstructural and mechano-tribologicalbehavior of Al reinforced SiC-TiC hybrid metal matrix composite. *Materials Today: Proceedings.*
52. Towhidul Islam Nayim, S. M., et al. (2020). Effect of CNT and TiC hybrid reinforcement on the micro-mechano-tribo behaviour of aluminium matrix composites. *Materials Today: Proceedings, 21,* 1421–1424.
53. Gupta, P., Kumar, D., Prakash, O., & Jha, A. K. (2013). Structural and mechanical behaviour of 5% Al_2O_3-reinforced Fe metal matrix composites (MMCs) produced by powder metallurgy (P/M) route. *Bulletin of Materials Science, 36*(5), 859–868.

Parametric Analysis of Electric Discharge Machining of Hybrid Composite Materials

Gurpreet Singh Matharou and Basanta Kumar Bhuyan

Abstract This study is an attempt to investigate the influences of input variables like voltage (V), current (I), pulse on time (T_{on}), pulse off time (T_{off}) and spark gap (S_g) on the response parameters such as material removal rate (MRR) of the electrodischarge machining (EDM) of Al-SiC-B_4C-Mg as a hybrid composite workpiece material using copper electrode as a tool material. The hybrid composite material has been developed by stir casting route with 84%(wt) Aluminum 6063, SiC of micron size 45 µm in 10%(wt), B_4C of micron size 52 µm in 5%(wt) and Mg in 1%(wt). The trend of graph advocates that MRR increases with increase in voltage, current and pulse on time, but MRR decreases with increase of pulse off time. Moreover, it has also been observed that the highest value of MRR was found in pulse off time at 3 µs and current at 13 A and the lowest MRR was obtained at 40 V.

Keywords Electric discharge machining · Material removal rate · Aluminum composite · Current · Voltage · Workpiece

1 Introduction

In the last few years, there has been a considerable shift in research materials from traditional materials to newly devised composites. The industry today requires materials with enhanced strength, less weight, high hardness, low densities, etc. Composite materials to a greater extend had fulfill the requirement of industry [1]. The new composites had reported to be lighter in weight, stronger in strength, less expensive as compared to traditional materials. Hybrid metal matrix composites (HMMCs) place a vital role for the manufacturing industry today. The new novel HMMC is Al-SiC-B_4C-Mg which has got lots of demand in elaborative applications in automobiles, mineral processing industries, aerospace, etc. [2] To machine the HMMC

G. S. Matharou (✉) · B. K. Bhuyan
Mechanical Engineering Department, FET- MRIIRS, Faridabad, India
e-mail: gsmatharou1@gmail.com

B. K. Bhuyan
e-mail: bkbhuyan.fet@mriu.edu.in

material, conventional machining can be used along with various non-conventional methods like laser beam machining (LBM), electron beam machining (EBM) and electrochemical machining (ECM), etc. which have offered more MRR, less surface roughness (R_a) and high electrode wear rate (EWR). To cope up the above processes, the well-known process called as die sinking electrodischarge machining (EDM) has been employed for better outcomes during the machining of HMMC workpiece. The die sinking EDM is also capable to machine conductive material irrespective of their chemical composition and physical properties and comparatively better results in terms of high MRR, less EWR and good surface finish can be achieved [3–5].

Sahu et al. [5] had attempted on electrodischarge machining of Nimonic alloy using copper electrode to study the effect of current and T_{on} on MRR, EWR and R_a. They reported that with variation of current and $T_{on,}$ MRR and EWR increase. Dikshit et al. [6] had conducted investigation on Inconel 625 super alloy by forming empirical model for R_a and MRR as output variables. They concluded that MRR is influenced by current and then by T_{on} and R_a is greatly influenced by T_{on} then T_{off}. Choudhary et al. [7] had investigated the influence on MRR and R_a while they had machined Hastelloy C-4 material using list of input parameters that includes current, T_{on} and T_{off} and conducted the experiments using Taguchi's L_{18} orthogonal array. They concluded that better R_a was achieved using cryogenic treated electrode then normal electrode. Muthuramalingam et al. [8] had predicted the residual stress, while machining silicon steel using different electrode made up of copper, brass and tungsten carbide tools and with different pulse generator (transistor pulse and iso-energy type). The input variables chosen were voltage, current and duty factor. They concluded that lower cracks are obtained using iso-energy pulse generator and residual stress dependency on electrodes electrical conductivity. Wei et al. [9] had concluded that small duty factor and high gap voltage are required for efficient MRR of silicon-carbide-based composite. Jithin et al. [10] had developed a single as well as multi-spark model to predict the average R_a for electrodischarge texturing. They attempted on both single and multi-spark models and had simulated the profile of surface and concluded through parametric study that at low values of current and T_{on}, denser distribution of peaks and valleys visible while thinner distribution at high values of both the input parameters. Zhang et al. [11] had studied the input variables (polarity, geometry of tool, spark gap, dielectric type and depth of immersion on impulse force) using an EDM with single-pulse generator. They analyzed and concluded that high impact force generated when polarity is made positive, electrode contact surface was made flat, spark gap increased, immersion depth increased and less impact force generated when air is being used as dielectric medium. Lin and Lin [12] had used gray relational approach for the optimization of performance characteristics (MRR, EWR, R_a) while machining glass fiber using EDM process. They had taken workpiece polarity, T_{on}, T_{off}, duty factor, voltage and current as input parameters.

Singh et al. [13] had used dry EDM and argon as a dielectric medium on high-chromium high-carbon die steel material to check the effects of current, duty cycle, T_{on}, tool rotation and gas pressure during discharge to evaluate the R_a. They concluded T_{on} and current had direct influence on the R_a. Paswan et al. [14] had compared steam and kerosene-based dielectric medium while electrodischarge

machining of Al-MMC using copper electrode to find out the effects on MRR, recast layer and R_a. They reported improvement in recast layer by 37%, decline in MRR and R_a by around 6 and 1.5 times respectively and cost saving by 80% while using steam-based dielectric. Guu and Hocheng [15] had studied the effect of workpiece rotation during EDM of AISID2 tool steel material with copper electrode. They maintained the identical conditions of machining during EDM of rotary tool and stationary tool and aftereffects were compared. Mazarbhuiya et al. [16] had attempted reverse EDM machining of carbon fiber-reinforced polymer (CFRP) composite using tungsten carbide and copper mixed electrode made through powder metallurgy. They had investigated through surface morphology using XRD and EDS analyses, the characteristics of surface by depositing powder made up of tungsten and copper on the workpiece surface. Ahmed et al. [17] had conducted experiment to machine Ti-6Al-4 V material using different set of electrode materials with negative polarity (graphite, copper, brass and aluminum) with current and T_{on} as input variables to find the effect on MRR and R_a. They concluded that material removal and current are directly related. Graphite gives best MRR, and aluminum gives least surface roughness. Kong et al. [18] had made an experimental analysis of effect of ablation process by using a blend of oxygen and nitrogen for machining Ti-6AL-4 V in an EDM. They suggested that with addition of nitrogen with oxygen had reduced the oxide formation during ablation which causes explosive tendency. A ratio of 5:1 (O_2:N_2) has been recommended for stable and efficient machining of deep blind hole in the material. The machining efficiency is about 8 times than in air medium and about 4 times in liquid medium. Gaikwad et al. [19] had analyzed the effect of gap, current, T_{on}, electrical conductivity (Taguchi L_{36} orthogonal array) on MRR using EDM process during the machining of NiTi alloy, and copper was used as a tool material. They had concluded that MRR is affected by parameters such as spark gap, current, T_{on} and electrical conductivity of NiTi. Jahan et al. [20] had investigated that while machining microholes on NiTi SMA and Ti-6Al-4 V the surface roughness at the center and edges are different and the reason suggested is due to a higher concentration of spark at the center compared to the edges. During the operation, the tool electrode became hemispherical and tapered resulting higher spark at the center.

Kumar et al. [21] had analyzed the effect of current and T_{on} on Ti-5AL-2.5Sn which had been cryogenically treated to find performance measures in terms of MRR, EWR and surface roughness. They concluded that there had been significant improvement in machining characteristic of cryogenic treated material compared to untreated. MRR had increased with increase in current and T_{on}. Also they suggested that due to deposition of carbon on the metal at high temperature there had been noticeable effect on the machining properties of the alloy. Rahul et al. [22] had made a comparative study on the metallurgical characteristics and surface integrity of EDM of Ti-6Al-4 V, A_2 tool steel and Inconel 601. Severe cracks, non-uniform deposition of molten material and white layer formation were reported more on Ti-6Al-4 V surface compared to other two. Fluoro-ethylene carbonate (F_eC) precipitates and carbon enrichment were observed on A_2 tool steel surface [23, 24].

From the available literature review, it has been found that machining of Al 6063-SiC-B_4C-Mg is still under experimental stage during EDM process which enhances

the various aspects and application of the aforesaid composite materials in different Industries. Further, the experimental studies were carried out by varying various input parameters of EDM on MRR during the machining of hybrid metal matrix composite material (Al 6063-SiC-B$_4$C-Mg).

2 Details of Experimental Work

2.1 Fabrication of Hybrid Metal Matrix Composite

The conventional stir casting route has been employed since it has advantages in terms of cost, suitability for mass production and simple operation. The stir casting procedure has been employed for the fabrication of required Aluminum 6063 HMMC with SiC micron size 45 μm in 10%(wt), B$_4$C micron size 52 μm in 5%(wt) and Mg in 1%(wt). The reinforced material SiC has got capability to withstand high temperature and has low density with high hardness. B$_4$C has neutron-absorbing properties with good mechanical strength [21]. Firstly, the reinforced materials SiC and B$_4$C are preheated at about 900–1050 °C to remove any moisture in them and to oxidized their surfaces. The Aluminum 6063 pieces were taken in new crucible and firstly heated to 480–500 °C for around 2 h before melting.

After that the aluminum is heated beyond melting temperature at 700–750 °C so that it completely melts. Now for around 15–20 min, SiC and B$_4$C are being added manually and stirrer motor is operated in between at 400–500 rpm to mix the contents and to achieve the best consistency possible. After stirring operation, the melt was poured in the rectangular mold to give a brick of size length 140 mm, breadth 60 mm and height 30 mm. The brick is further cut into smaller size of 50 mm X 25 mm X 20 mm for experimentation on die sinking EDM. Figure 1 shows the sample of workpiece and the pure copper electrode with 20 mm cutting diameter. Table 1 shows mechanical properties of hybrid composite materials.

2.2 Experimentations

JOEMARS EDM AZ50 series Taiwan make has been used for conduct of the experiment. The EDM used has three-phase power input with maximum current of 50Amp. The machine unit JM 320 has been connected to the power supply unit. With direct polarity, a pure copper electrode of 20 mm diameter has been used for experimentation. Figure 2 shows the actual photograph of JOEMARS EDM.

The most key input variables such as voltage (V), current (I), pulse on time (T$_{on}$), pulse off time (T$_{off}$) and spark gap (S$_g$) and a most predominant response characteristics like MRR have been selected based on deep study of literature review and exhaustive pilot experiments. Table 2 represents the different input variables

Fig. 1 Prepared composite samples with copper cutting tool

Table 1 Mechanical properties of hybrid composite materials [25]

Hybrid metal matrix composite material	Tensile strength (N/mm^2)	Yield strength (N/mm^2)	Density (Kg/m^3)	Brinell hardness (HB)	Break load (KN)
84wt% Al–10wt% SiC–5 wt% B$_4$C	120.32	98.75	2537.5	71.58	9.45
	Maximum displacement (mm)	Elongation (%)	Flexural break load (KN)	Flexural maximum deflection (mm)	Flexural strength (MPa)
	9.7	7.53	3.68	5.6	214.12

Fig. 2 JOEMARS EDM

Table 2 Input variables and corresponding ranges

Input parameters	Units	Range value
Current (I)	Ampere	5, 7, 9, 11, 13
Pulse on time (T_{on})	μs	40, 50, 60, 70, 80
Pulse off time (T_{off})	μs	3, 4, 5, 6, 7
Spark gap (S_g)	mm	4, 5, 6, 7, 8
Voltage (V)	Volt	40, 50, 60, 70, 80
Flushing speed	Kg/cm^2	1.2
Machining time	Min.	15 min per sample

with ranges. Machining time is kept constant at 15 min per sample. A digital weight balancer of accuracy 0.1 mg has been used for taking specimens weight before and after machining. The MRR was calculated using the following relation,

$$\frac{w_b - w_a}{\rho X t} \qquad (1)$$

where w_b and w_a = Initial and final weight of samples in gm

ρ = Density of workpiece material in gm/cm^3

t = Time of machining in minutes

3 Results and Discussion

The effect of various input parameters like voltage, current, pulse-on time, pulse-off time and spark gap on output parameter MRR was studied using EDM process during the machining of Al6063-SiC-B$_4$C and tool used as a copper material. The experiments were carried out with varying one input parameter, while keeping other parameters remains constant. The following trends of graph has been illustrated and elaborated in different sections.

3.1 Effect of Voltage (V) on MRR (mm^3/min)

The effect of applied voltage and spark gap on MRR in EDM process, keeping other parameters constant, is illustrated in Fig. 3. It can be observed that MRR increases with increase in applied voltage for three different values of spark gap (4, 5, 6) mm. It was observed that MRR is lowest with voltage 40 V and spark gap 4 mm, whereas highest value of MRR has been observed at voltage 80 V and spark gap of 5 mm. The phenomenon of such action can be explained as voltage increases; a huge number of bubbles are generated thereby higher discharge energy per spark causing more
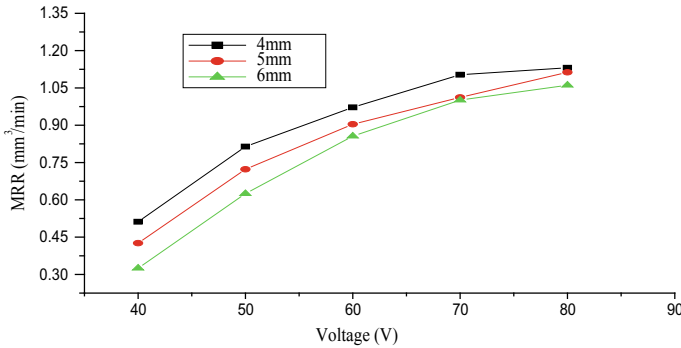
Fig. 3 Effect of voltage on MRR

heat generation at the localized area of influence resulting in more MRR. In addition to that, at high voltage the electrolysis process is accelerated resulting in formation and accumulation of hydrogen gas bubbles at the electrode tip and thereby causing increase in discharge energy from the electrode.

3.2 Effect of Current (I) on MRR (mm³/min)

The effect of current and spark gap on MRR in EDM process, keeping other parameters constant, is illustrated in Fig. 4. It can be observed that as current increases, the MRR also increases proportionately. This phenomenon is because of the fact that with increase in current, the energy in spark and erosion action also increases and thus the MRR. The maximum MRR can be observed at 13 amps at 4 mm spark gap. Minimum value of MRR was observed at I = 5 Amp with 6 mm spark gap.
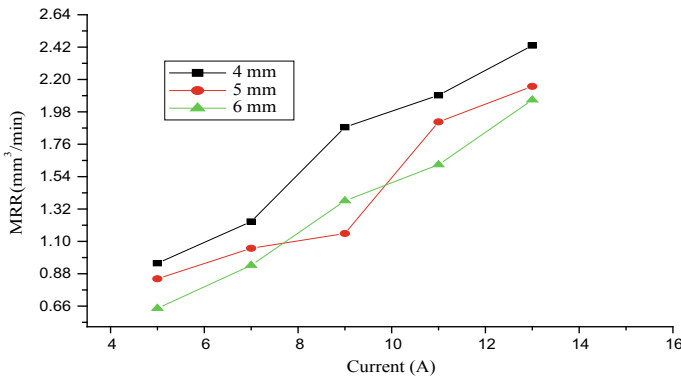
Fig. 4 Effect of current on MRR
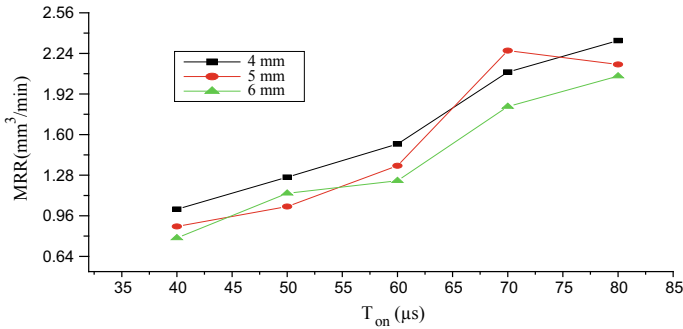
Fig. 5 Effect of T_{on} on MRR

3.3 *Effect of Pulse on Time (T_{on}) on MRR*

The effect of pulse on time and spark gap on MRR in EDM process, keeping other parameters constant, is illustrated in Fig. 5. The pulse on time (T_{on}) has direct influence on MRR. The T_{on} values in the experiment ranges from (40–85) μs. With increase in T_{on}, the interaction time of electrode on workpiece increases causing increase in efficiency of dissolution. The current intensity also increases. The maximum value of MRR can be observed at T_{on} value of 70 μs at 4 mm spark gap and minimum at T_{on} value of 40 μs at 6 mm spark gap. The MRR increases till 70 μs, and after that a slight decline can be observed. This could be because of generation of high heat energy near the subsurface of the workpiece.

3.4 *Effect of Pulse off Time (T_{off}) on MRR*

The effect of pulse off time and spark gap on MRR in EDM process, keeping other parameters constant, is illustrated in (Fig. 6). The T_{off} values 3–7 μs have been considered for the experimentation. Less MRR has been observed at high value of T_{off}, due to interaction time reduction. It has been observed that as T_{off} values increases the cooling effect of dielectric medium increases causing the workpiece surface to cool down a little, resulting in more energy requirement to form a conductive channel and thus reducing the spark formation and thus reduction in MRR. The highest value of MRR can be seen at T_{off} value of 3 μs with spark gap of 4 mm. The lowest value of MRR is found out at T_{off} value of 7 μs with spark gap of 6 mm.

Fig. 6 Effect of T_{off} on MRR
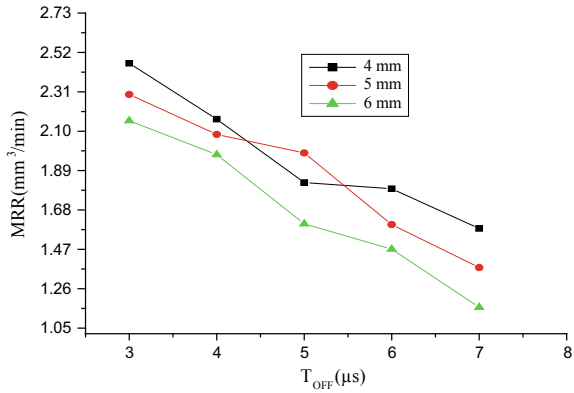
4 Conclusions

The Al 6063-SiC-B$_4$C-Mg, hybrid metal matrix composite, has been successfully prepared using stir casting method. During EDM of the HMMC, following observations were made:

1. With the increase in voltage, current and T_{on} the MRR increases due to high discharge of spark energy from the electrode.
2. It has been observed from the graph that the MRR reduces gradually with the variation of T_{off}.
3. The current and T_{on} were found to be the most influential input parameters on which the MRR depends directly.
4. It has been obtained that MRR decreases beyond 70 µs of T_{on}, at spark gap of 5 mm.
5. The trends of the graphs demonstrate that spark gap of 4 mm was depicted with the higher MRR as compared to spark gap at 5 and 6 mm.

References

1. Chawla, K. K. (1998). *Composite materials science and engineering*. Newyork: Springer.
2. Gopala, K. A., & Prasad, D. V. (2009). Empirical modeling and optimization of wire electrical discharge machining. *International Journal of Advanced Manufacturing Technology, 43,* 914–925.
3. Zhang, Y., Liu, Y., & Shen, Y. (2013). Die-sinking electrical discharge machining with oxygen-mixed water-in-oil emulsion working fluid. *Proceedings of Institution of Mechanical Engineers, Part B: Journal of Engineering Manufacture, 227,* 109–118.
4. Khan, A. A., Ali, M. Y., & Haque, M. M. (2009). A study of electrode shape configuration on the performance of die sinking EDM. *International Journal of Mechanical and Material Engineering, 4*(1), 19–23.

5. Sahu, D., Sahu, S. K., Jadam, T., & Datta, S. (2019). Electro-discharge machining performance of nimonic 80A. An experimental observation. *Arabian Journal for Science and Engineering, 44*, 10155–10167.

6. Dikshit, M. K., Anand, J., Narayan, D., & Jindal, S. (2019). Machining characteristics and optimization of process parameters in die-sinking EDM of Inconel 625. *Journal of the Brazilian Society of Mechanical Sciences and Engineering, 41*(7), 412–419.

7. Choudhary, R., Garg, H., Prasad, M., & Kumar, D. (2017). Effect of cryogenic treatment of tool electrode on the machining performance and surface finish during electrical discharge machining of hastelloy C-4. *Materials Today: Proceedings, 4*(2), 1158–1166.

8. Muthuramalingam, T., Mohan, B., & Vignesh, S. (2018). Performance analysis of pulse generators on residual stress of machined silicon steel using the EDM process. *Silicon, 10*(5), 1785–1792.

9. Wei, C., Zhao, L., Hu, D., & Ni, J. (2013). Electrical discharge machining of ceramic matrix composites with ceramic fiber reinforcements. *International Journal of Advanced Manufacturing Technology, 64,* 187–194.

10. Jithin, S., Bhandarkar, U. V., & Joshi, S. S. (2020). Multi-spark model for predicting surface roughness of electrical discharge textured surfaces. *The International Journal of Advanced Manufacturing Technology*. https://doi.org/10.1007/s00170-019-04841-5.

11. Zhang, M., Zhang, Q., Zhu, G., Liu, Q., & Zhang, J. (2016). Effects of some process parameters on the impulse force in single pulsed EDM. *Proceedia CIRP, 42*(1), 627–631.

12. Lin, J. L., & Lin, C. L. (2002). The use of the orthogonal array with grey relational analysis to optimize the electrical discharge machining process with multiple performance characteristics. *International Journal of Machine Tools and Manufacture, 42*(2), 237–244.

13. Singh, N. K., & Singh, Y. (2019). Experimental investigation and modeling of surface finish in argon-assisted electrical discharge machining using dimensional analysis. *Arabian Journal for Science and Engineering, 44*(6), 5839–5850.

14. Paswan, K., Pramanik, A., Chattopadhyaya, S., Basak, A. K. (2019) A novel approach towards sustainable electrical discharge machining of metal matrix composites (MMCs). *The International Journal of Advanced Manufacturing Technology, 106*(6).

15. Guu, Y. H., & Hocheng, H. (2001). Effects of workpiece rotation on machinability during electrical discharge machining. *Materials and Manufacturing Processes, 16*(1), 91–101.

16. Mazarbhuiya, R. M., Dutta, H., Debnath, K., & Rahang, M. (2020). Surface modification of CFRP composite using reverse-EDM method. Surfaces and Interfaces SURFIN 100457. https://doi.org/10.1016/j.surfin.2020.100457.

17. Ahmed, N., Ishfaq, K., Rafaqat, M., Pervaiz, S., Anwar, S., & Salah, B. (2019). EDM of Ti-6Al-4 V: Electrode and polarity selection for minimum tool wear rate and overcut. *Materials and Manufacturing Processes, 34*(7), 769–778.

18. Kong, L., Liu, Z., Han, Y., & Qiu, M. (2018). Research on the efficient and stable sinking electrical discharge machining ablation process of Ti-6Al-4 V. *The International Journal of Advanced Manufacturing Technology, 97*(5), 2151–2161.

19. Gaikwad, V., & Jatti, V. K. S. (2018). Optimization of material removal rate during electrical discharge machining of cryo-treated NiTi alloys using Taguchi's method. *Journal of King Saud University, 30*(3), 266–272.

20. Jahan, M. P., Kakavand, P., & Alavi, F. (2017). A comparative study on micro-electro discharge-machined surface characteristics of Ni-Ti and Ti-6Al-4 V with respect to biocompatibility. *Procedia Manufacturing, 10*(2), 232–242.

21. Kumar, S., Batish, A., Singh, R., & Singh T. P. (2017) Machining performance of cryogenically treated Ti-5Al-2.5Sn titanium alloy in electric discharge machining a comparative study. *Proceedings of the Institution of Mechanical Engineers, Part C: Journal of Mechanical Engineering Science, 231*(11), 2017–2024.

22. Rahul, Datta, S., Masanta, M. (2018). Surface integrity and metallurgical characteristics of the EDMed work surfaces of A2 tool steel (SAE 304SS), Inconel 601 and Ti-6Al-4V a comparative analysis. *Silicon 10*(4), 1557–1572.

23. Shorowordi, K. M., Haseeb, A. S. M. A., & Celis, J. P. (2006). Tribo-surface characteristics of Al–B4C and Al–SiC composites worn under different contact pressures. *Wear, 261*(5–6), 634–641.
24. Kalaiselvan, K., Muruganand, N., & Siva, P. (2011). Production and characterization of AA6061-B$_4$C stir cast composite. *Materials and Design, 32,* 4004–4009.
25. Qudeiri, J. E., Mourad, A. H., Ziout, A., Abidi, M. H., & Elkaseer, A. (2018). Electric discharge machining of titanium and its alloys: Review. *International Journal of Advanced Manufacturing Technology, 96*(4), 1319–1339.

A Literature Review for Development of Advanced Composites Materials by Reinforcement of Epoxy Composites with Graphene and Natural Silk

K. N. Sanjeev Kumar, Sanjeev Sharma, Abdel-Hamid I. Mourad, and P. B. Sharma

Abstract Penetration of composites in the wind and aerospace sector is very critical for sustainable business growth. The primary focus is toward a reduction in composite weight and thereby the cost of the material. Further, advancement in the improvement of the mechanical strength of the composites can lead to the development of lightweight high-performance composites which is imperative for these growing market sectors. This review focus on various ongoing researches on graphene and natural silk being used as nano reinforcement in the epoxy composites that have shown significant potential to enhance the mechanical properties and thereby result in reducing the weight of the structural members used in wind turbine and aircraft. Also, this review explores the novel concept of graphene and natural silk fiber being used as combined reinforcement materials for the development of high-performance epoxy composite materials.

Keywords Graphene · Natural silk · Epoxy composites · Advanced composite materials

K. N. S. Kumar (✉) · S. Sharma · P. B. Sharma
Mechanical Engineering Department, ASET, Amity University, Haryana, Gurugram, India
e-mail: knsanjeev@gmail.com

S. Sharma
e-mail: ssharma26@ggn.amity.edu

P. B. Sharma
e-mail: pbsharma@ggn.amity.edu

A.-H. I. Mourad
Mechanical Engineering Department, College of Engineering, United Arab Emirates University, Abu Dhabi, UAE
e-mail: ahmourad@uaeu.ac.ae

1 Introduction

The global composite market is projected to reach USD 152.98 billion by 2027, at a CAGR of 8.05% from 2019 to 2027. Composites have made deep penetrations into the wind and aero sectors and are inseparable now. In the prevailing competitive market, both wind and aero industries look for low-weight high-performance composite materials for industry survival. Composites provide higher tolerance to temperature extremes, have higher wear and corrosion resistance, and thereby, resulting in the higher impact of reducing the product life cycle cost which has made them make profound applications in the industry. However, the greater push from the aero and wind market for fuel economy and efficiency, respectively, has made lightweight the highest prerogative in these sectors.

Multifunctional composites have made a notable impact by providing the means to reduce the material weight which not only reduces the operational costs but also reduces the fuel consumption in aircrafts and improves the power curve in the case of wind turbines. Composite is a combination of two or more distinctly different components—one or more reinforcement fiber fillers and a matrix material. The resultant new material has properties significantly different from that of individual components. Fibers show relatively high tensile strength than matrix material like polymer resins which in turn are extremely tougher and malleable than fibers. Hence, their combinations result in the formation of new material with properties complementary to each other. This means the resultant new material has relatively better tensile strength, toughness, and malleability than that of individual components.

Due to the uncertainty of the material behavioral characteristics in extreme conditions, the design engineer either takes the additional factor of safety in terms of more weight than is required or misjudge to inadequately size the component leading to the failure. More importantly, wider variations in terms of geometries, constituents, and production process make it critical for the design engineer to have advanced knowledge on the material behaviors especially on static strength, fatigue failure to design the system to provide assurance both on short-term performance and long-term product life cycle. This advanced knowledge during the design of the system is vital for the improvement of the economics in case of the wind turbine for increasing their range of use through improved material properties.

In wind and aero sectors, there is a directed predicament for applied research on advancement in the design of wind blades and aircraft wings with materials of economically lightweight for lower operating loads for longer life with higher operational performance than that of existing blades/wings being used. Further, there is a growing need for driving product cost out through the development of advanced high-performance composites for meeting the highly demanding industrial applications. Any research in the development of lightweight high-performance composites is imperative for these growing market sectors like wind and aero which would be affable by them.

This review paper highlights the various researches on graphene and natural silk being used as nano-reinforcement in the epoxy composites which have shown significant potential to improve mechanical properties and thereby reducing the weight of the structural members used in wind turbine and aircraft. Further, this review paper concentrates on the research gap through combined reinforcement of the matrix composite with graphene and natural silk which can result in a high-performance composite in terms of lightweight, superior mechanical properties than that being currently used in the industry. A literature review was carried out covering the above discussions on the scope of the advancement of the composite materials and is presented in Sect. 2.

2 Literature Survey

A comprehensive literature study was carried out to understand the current mechanical properties of epoxy resin composites being used in wind and aero industry applications. Further, the literature survey was focused on the study on the impact on mechanical properties of the epoxy resin composites by reinforcement either with graphene or silk fiber. In specific, it was researched to understand whether there have been combined reinforcements of the epoxy resins composite with both graphene and silk fibers as reinforcement medium and possible application to enhance the properties of composite materials.

Several reputed research journals were reviewed for research papers related to the application of graphene and natural silk fiber in the composite applications from the period 2000–2019. These related research papers cited for the research proposal are listed in the reference section. Critical feedbacks and data point on the research through this literature survey study are presented in the following sections:

Composites consist of fibers that serve as the backbone, and matrix, which holds the fibers together. The advantages of composites are their high strength and stiffness, along with low density which results in reduced weight of the component [1]. Every combination does not work out, and each combination of materials has its own pros and cons. The main composition of a composite consists of a matrix and reinforcement. Reinforcement can be of different types. Based on their shapes, they can be fibers, particulate, flakes, skeletal or laminar. Matrix is the binding material which holds the fiber together in the composite, providing it support and protection [1]. It also helps to evenly distribute the load that falls on the composite onto the fibers. Some of the most commonly used matrix materials are epoxy, polyester, nylon, PVC, and polyethylene. A comparison between their properties is shown in Table 1.

Epoxy resin is the first choice material vastly used due to its characteristic properties – High amenability with dimensional stability, good adhesion, chemical resistance, higher temperature extreme tolerance, high strength-to-weight ratio, low moisture absorption along with fair mechanical properties at low cost [3–12]. They find significant applications in electronics, wind, aerospace and civil engineering. Also, they are compatible with all common reinforcements, fatigue strength superior to

Table 1 Properties of common matrix materials [2]

Material	Density (kg/m^3)	Moduli of elasticity tensile Et (GPa)	Ultimate strength σt (MPa)	Ultimate strength σc (MPa)	Poisson's ratio v	Coefficient of thermal expansion α (10^{-6}/^{0}C)
PVC	1400	2.8	58	–	–	50
Polyester	1200–1400	2.5–4.0	45–90	100–250	0.37–0.40	100–200
Epoxy	1100–1350	3.0–5.5	40–100	100–200	0.38–0.40	45–65
Nylon	1140	2.8	70	–	–	100
Polyethylene	960	1.2	32	–	–	120

Table 2 Mechanical properties of epoxy [2]

Properties of Epoxy Resin	
Modulus of elasticity E (GPa)	5.0
Flexural strength (MPa)	60
Tensile strength (MPa)	73
Maximum elongation (%)	4
Viscosity at 25 degree Celsius (cP)	12000–13000
Density (g/cm^3)	1.16

aluminum alloy and are used in the temperature range up to 175 degree Celsius [13, 14]. Hence, epoxy resin is used as the dominant matrix composite material for the above cited reasons. However, its inherent brittleness, delamination, high cross-link density and low fracture toughness have limited its usage for structural component applications leading to the research on usage of natural fibers as reinforcement fillers to enhance its impact strength and toughness [13–16]. Increasing the temperature of epoxy leads to a significant drop in flexural strength. Hence, it implies that flexural strength varies inversely with temperature [17]. It is observed from Table 2 that the values and epoxy's mechanical properties are not very exceptional and contribute to its brittleness in the solid state.

Graphene is one more reinforcement material which has shown the greater potential to improve their mechanical performance. Graphene is perhaps one of the most inspiring discoveries in the field of science and technology since its potential applications are limitless due to its admirable properties. Extensive research on graphene has led to produce novel materials with enhanced properties [18–21]. It is an allotrope of carbon, a single layer of atoms bonded in a honeycomb lattice. Among the various other nanofillers, graphene has been used to reinforce epoxy which can be then further strengthened with other natural fibers or alumina.

2.1 Use of Graphene for Reinforcement in Composites

Graphene's excellent thermal, mechanical, and electronic properties make it one of the most favored reinforcement materials for filling agents in composite materials and its applications. Graphene provides higher reinforcement than carbon nanotubes, and graphene fillers in the epoxy resin matrix increase the impact strength and toughness, thereby aids for a wide range of applications [17–24]. Graphene nanocomposites show marked enhancements in their multifunctional aspects at low loading, in comparison with conventional composites and materials [2]. This enables it to be lighter with simple processing, as well as increased mechanical strength for various applications (Fig. 1).

The physical and chemical properties of the host matrix are upgraded upon embedding due to the exceptional properties of graphene. This leads to the enhancement of strength and bonding between graphene layers and the host matrix [25]. In the study by [26], characteristic properties of nanocomposites were measured at lower content of graphene addition as filler material. The results showed that Young's modulus of the nanocomposite was around 31% more than pristine epoxy, 40% increase in tensile strength, and 53% increase in fracture toughness. The graphene dispersion in the matrix material is a critical factor and has a direct characteristic impact on the composite material [27, 28]. Further, when compared with CNT, graphene's higher specific surface area aids to disperse graphene into the matrix without surface modification [28]. It is also relatively easy to produce, inexpensive and potentially has less health hazards compared to CNT.

A study conducted by [29], test results over the glass fiber graphene epoxy composite which was prepared using bi-directional glass fiber along with epoxy resin (LY 556) and graphene and hardener (HY 951) showed when graphene increased from 1 to 2% in an epoxy along with acetone as the dispersion medium, stress increased from 186 to 195 MPa. It was found to be a 5% improvement in strength due to the addition of graphene. Further increase of graphene from 2% to up to 8% resulted in decrease in the strength of the laminate. From the flexural result, when

Fig. 1 A rendering of graphene's uniform structure at the molecular scale [2]
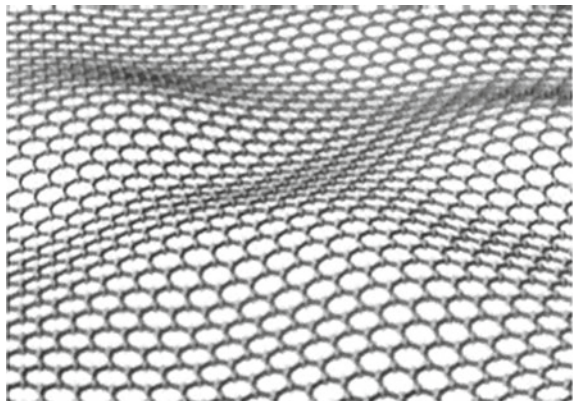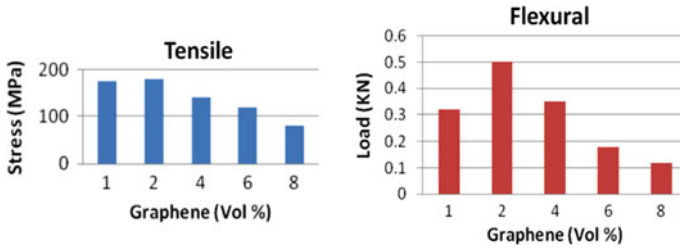
Fig. 2 Tensile flexural values for different ratios of graphene [29]

graphene increased from 1 to 2%, the load increased from 0.32 to 0.5 kN. Further increase of graphene from 2% to up to 8% resulted in decrease in the strength of the laminate [29] (Fig. 2).

However, when higher volume fraction of graphene is used, the non- uniform dispersion of the graphene and resultant voids in the matrix results in lower tensile and flexural strength [29]. Test results from the study [30] revealed that polymer beams were reinforced with graphene and carbon fibers had better properties than that of plain control beams (Table 3). High surface area of reinforcement fillers enables for distribution of load over a large surface resulting in better performance.

In another study [31], a hybrid CF/GO/epoxy composite was prepared by reinforcing epoxy with GO and then impregnated over the carbon fiber using compression molding. The test results confirmed bending strength and Young's modulus going up 66% and 72%, respectively. The shear strength between the laminated surface (ILSS) rose by 25% at 0.3% of GO addition, due to the interlocking and bonding. From the results of the study [32], it was evident that hot set laminate strength was better than that of cold setting laminate.

From the research examples cited in this paper, it is to be noted that graphene with a higher surface area and of few layers of thickness would be the best choice for the reinforcement. It is to be noted that it is important to have a homogenous

Table 3 Test results for CFs and graphene reinforced in epoxy composites bean subjected to the 3-point loading test: Ultimate load and maximum deformation [30]

Sl. No.	Specimen reference	Ultimate load in (KN)	Maximum deformation in (mm)
1	Plain epoxy (PE)	0.5	3.9
2	PE + Graphene (GA)	0.77	5.696
3	PE + Carbon Fiber (CF)s	0.8	4.53
4	PE + GA + CFs	0.82	4.376

Note: 2,3,4 weight% is w.r.to epoxy

Fig. 3 Impact strength of a wide range of polymer composites [34]
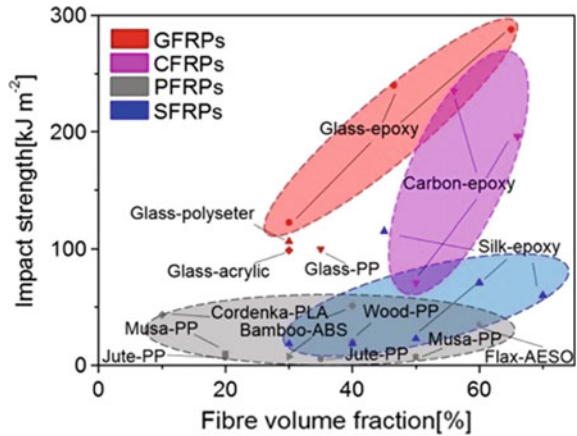
state of dispersion of filler to avoid the formation of aggregates which would act as failure points during impact testing. During the selection of the filler materials, care should be taken to ensure filler materials do not have limitations in terms of wrinkles, impurities, or defects. Also, the matric-filler bonding needs to be strong to have effective stress transfer. These are crucial factors in the development of successful advanced composite materials. In order to counterbalance some of the non-desired properties of graphene in composites is through the use of hybrid fillers through a combination of graphene and an organic or inorganic filler [33].

2.2 Use of Natural Fibers for Reinforcement of Composites

In the study [34], the impact strength vs fiber volume fraction for polymer composites (Fig. 3) has been plotted. Test results show that carbon, glass, and silk fibers provide higher impact strength than natural fibers in the epoxy resin matrix. Silk fibers are the only natural reinforcements to provide such high impact strength [34–38]. From Fig. 3, it is clear that the impact strength of plant fiber-reinforced polymer (PFRP) is not dependent on the volume fraction, whereas glass fiber-reinforced polymer (GFRP) and carbon fiber-reinforced polymer (CFRP) are dependent. In the case of silk reinforcement, impact strength varies between 30 and 70% volume fraction which permits for higher volume fraction reinforcement which makes it a good reinforcement medium [39].

Further to be noted is that structurally distinct silks, namely domestic B.mori/Bm and the wild A.pernyi/Ap silkworms, were used in fabric forms. The toughening effects on silk-epoxy composites (SFRPs) were noted (from Fig. 4) to be dependent on the silk species and the volume fraction of silk. Ap silk had the profound toughening effect at 60 vol.% and displayed tensile and flexural strength of three times and impact strength of eight times, as compared to pure epoxy resin. The
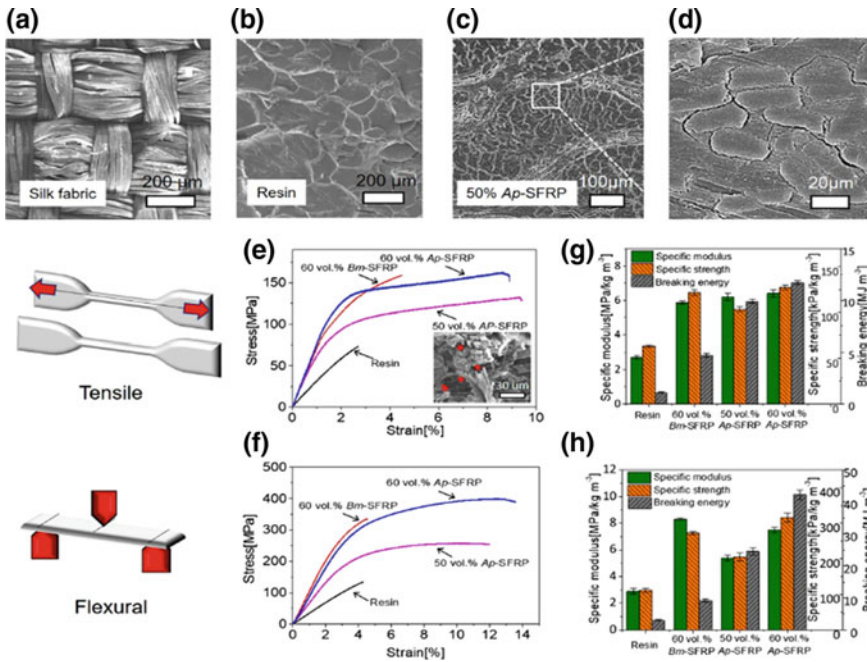
Fig. 4 Scanning electron microscopy images of the microstructure and comparison of stress–strain curves [34]

findings demonstrated both marked toughening and strengthening effects for epoxy composites from natural silk reinforcements. These results show opportunities for mechanically superior and "green" structural composites.

The study by [40] showed comparison of toughness and modulus with respect to materials containing silk fibers, materials containing graphene oxide and silk fiber nanocomposites (GO-SF) (Fig. 5). Results show the modulus, ultimate stress, and toughness of the GO-SF nanocomposite membranes are superior with outstanding mechanical properties than others.

3 Research Gap and Impact of the Research Work

Literature survey has silently shown that a lot of research on graphene and natural silk fiber reinforced individually in polymer composites, but there has been no combined reinforcement for the development of epoxy-based composite at a lower cost. Mechanical properties of the composites have seen significant improvement when reinforced either with graphene or silk fiber. The various researches discussed

Fig. 5 Comparison of mechanical properties [40]
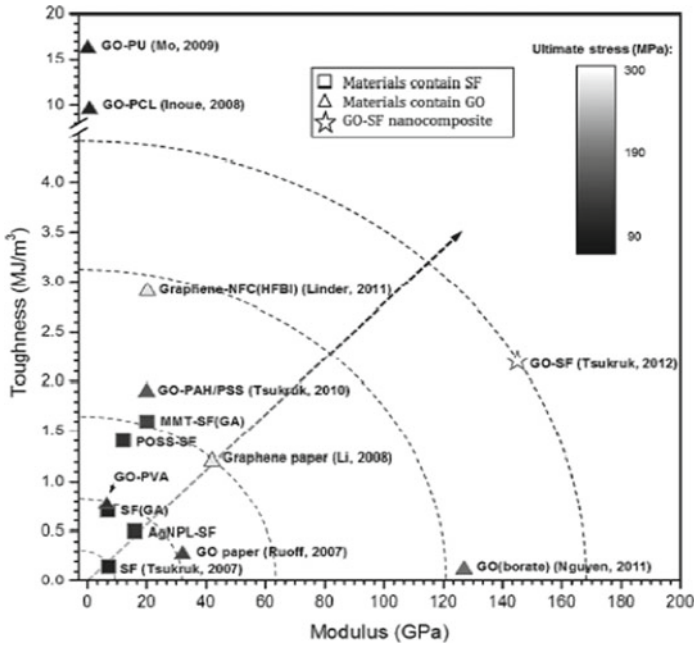
Abbreviations	
PVA: poly(vinyl alcohol)	PSS: poly(sodium 4-styrene sulfonate)
PU: polyurethane	NFC: Native nanofi brillated cellulose
PCL:poly(ε -caprolactone)	HFBI: Hydrophobin
PAH: poly(allylamine hydrochloride)	GA:Glutaraldehyde
AgNPL: silver nanoplatelets	POSS: polyhedral oligomeric silse squioxane
MMT: montmorillonite.	GO: Graphene Oxide

in the literature survey have shown that there is a distinct enhancement of the mechanical property of the epoxy resin composite when reinforced either with graphene or with natural silk fibers.

From the research data collected and presented in this paper, it is to be noted that the best-quality graphene with a higher aspect ratio with few layers of thickness and homogeneous dispersion of filler to avoid the formation of aggregates are crucial factors in the development of successful advanced composite materials. In the study [34], silk reinforcement impact strength varies between 30 and 70% volume fraction which permits for higher volume fraction reinforcement. Further, the study by [40] had shown that GO-silk fibroin nanocomposites outstanding mechanical properties—modulus, ultimate stress, and toughness than composite materials either reinforced with graphene or silk only. From the work of [41], graphene/glass fiber/epoxy composites can be prepared by directly spraying graphene onto glass fibers or by infiltrating graphene into an epoxy resin matrix with very low weight fractions of

Fig. 6 Ashby plot of specific strength and stiffness (normalized by density) of different materials [42]
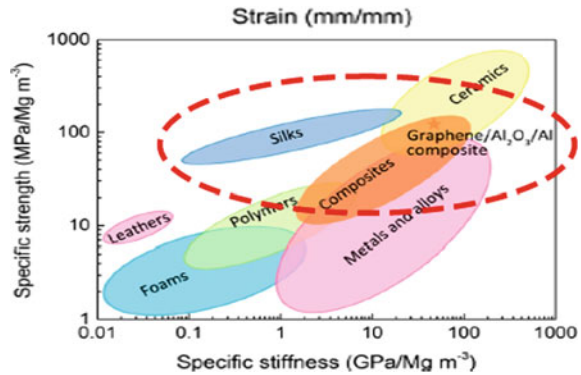
graphene. This method can be used for graphene/silk/epoxy composite development either by direct spraying graphene onto silk fabrics or by infiltrating graphene into epoxy resin and then applying this mixture over silk fabrics to create composite laminates.

Hence, there is additional scope to further study the extent of enhancing the mechanical properties of epoxy resin composite by combined modulation of reinforcement of silk and graphene to the matrix composite, which has not been explored yet. As shown in Fig. 6, it is evident that there are scope exits to do further research and development by combined modulation of graphene, silk, and composites to understand the impact on the mechanical properties of composites. There is a greater need to ascertain various avenues for further improvement or enhancement of the mechanical properties of the composites which can lead to the development of the lightweight high performance composites for wider applications outside wind and aero industry like in bullet-proof vest development in military operations, auto industry and as well making of lightweight personal protective equipment for working personnel in any industrial sector.

4   Conclusion

There is a high demand for advanced composite materials with lightweight high-performance composite for wind, aero, auto, and ancillary sectors. The billion USD turnover composite market itself is a high driver for enabling wider research on advanced composite materials which are lightweight and can provide enhanced mechanical, electrical and thermal properties. There is additional scope to further study the extent of enhancing the mechanical characterization of epoxy resin composite by combined modulation of reinforcement of silk and graphene to the matrix composite. This has not been explored in detail yet, and hence, this research review paper identifies this definite scope to develop advanced composite materials by combined modulation of reinforcement of silk and graphene to the epoxy matrix

composite for lightweight but improved mechanical strength to sustain the same operational stresses. It is to be noted that there is a huge demand for such lightweight high-performance composites and will get absorbed by the composite industries to support wider applications in the wind, aero, and automotive sectors.

References

1. Mukhopadhyay, M. (2005). *Mechanics of composite materials and structures.* Universities Press (India) Limited.
2. Divakara Shetty, S., & Nagaraja, S. (2019). A literature review on processing and testing of mechanical properties of hybrid composites using graphene/epoxy with alumina. *International Journal of Mechanical Engineering and Technology, 10*(3), 1263–1274.
3. Harke (2006). Epoxy Resin Systems for Composites. Harke Chemical GmbH, Thailand, pp. 1–20.
4. Maureen, A. B., Cary, J. M., John, D. N. Epoxy resin, Hexcel Corporation.
5. Wang, Y., Zhang, B., & Ye, J. (2011). Microstructures and toughening mechanisms of Organoclay/ polyethersulphone/epoxy hybrid nanocomposites. *Material Science Engineering. A, 528,* 7999–8005.
6. Ghaemy, M., & Riahi, M. H. (1996). Property-structure relationships in epoxy resin systems. *Polymer Journal, 2*(2), 119–126.
7. Thomas, R., Yumei, D., Yuelong, H., Le, Y., Moldenaers, P., Weimin, Y. et al. (2008). Miscibility, morphology, thermal, and mechanical properties of a DGEBA based epoxy resin toughened with a liquid rubber. *Polymer 49,* 278–294.
8. Jain, P., Choudhary, V., & Varma, I. K. (2003). Effect of structure on thermal behaviour of epoxy resins. *European Polymer Journal, 39,* 181–187.
9. Mimura, K., & Ito, H. (2002). Characteristics of epoxy resin cured with in situ polymerized curing agent. *Polymer, 43,* 7559–7566.
10. Zhang, X., Min, Y., & Hua, Z. (2014). Epoxy-based electronic materials containing nitrogen heterocyclic ring: Flame retardancy. *Progress in Chemistry, 26,* 1021–1031.
11. Zhou, H., Zhao, S., Yu, W., Jiang, H., Guo, C., Li, Y. (2013). Research on performance of flame-retardant epoxy resin electronic packaging materials. In *Advanced Materials Research 2013*, pp. 117–120.
12. Toldy, A., Szolnoki, B., & Marosi, G. (2011). Flame retardancy of fibre-reinforced epoxy resin composites for aerospace applications. *Polymer Degradation and Stability, 96,* 371–376.
13. Dirlikov, S., Frischinger, I., Chen, Z. (1996). phase separation of two-phase epoxy thermosets that contain epoxidised triglyceride oils', In *Advances in Chemistry Series Toughened Plastics II Novel Approaches in Science and Engineering.* Washington DC, American Chemistry Society, pp. 95–103.
14. Oh, P. S., Kim, H. S., Ma, P. (1996). Effect of rubber on stress-whitening in epoxies cured with 4, 4 diamino diphenyl sulphone. In *Advances in Chemistry Series Toughened Platics II Novel Approaches in Science and Engineering.* Washington DC: American Chemical society, pp. 111–1119.
15. Lu, J., & Youngblood, J. P. (2015). Adhesive bonding of carbon fiber reinforce composite using UV-curing epoxy resin. *Composites Part B, 82,* 221–225.
16. Ibrahim, H., Farag, M., Megahed, H., & Mehanny, S. (2014). Characteristics of starch-based biodegradable composites reinforced with date palm and flax fibres. *Carbohydrate Polymers, 101,* 11–19.

17. Reis, J. M. L. (2012). Effect of temperature on the mechanical properties of polymer mortars. *Materials Research, 15*(4), 645–649.
18. Sharma, M., Gao, S., Mäder, E., Sharma, H., Wei, L. Y., & Bijwe, J. (2014). Carbon fiber surfaces and composite interphases. *Composites Science and Technology, 102,* 35–50. https://doi.org/10.1016/j.compscitech.2014.07.005.
19. Wei, J., Vo, T., & Inam, F. (2015). Epoxy/graphene nanocomposites–processing and properties: A review. *RSC Adv., 5,* 73510–73524. https://doi.org/10.1039/c5ra13897c.
20. Atif, R., Shyha, I., & Inam, F. (2016). Mechanical, thermal, and electrical properties of graphene-epoxy nanocomposites—A review. *Polymers, 8,* 281. https://doi.org/10.3390/polym8080281.
21. Phiri, J., Gane, P., & Maloney, T. C. (2017). General overview of graphene: production, properties and application in polymer composites. *Materials Science and Engineering B, 215,* 9–28. https://doi.org/10.1016/j.mseb.2016.10.004.
22. Gao, S., Zhou, X., Ding, Y. (2007). Effective thermal and electrical conductivity of carbon nanotube composites. *Chemical Physics Letters*, *434*(4–6), 297–300.
23. Ma, J., Xu, J., Ren, J.-H., Yu, Z.-Z., & Mai, Y.-W. (2003). A new approach to polymer/montmorillonite nanocomposites. *Polymer, 44*(16), 4619–4624.
24. Ma, J., Xiang, P., Mai, Y.-W., & Zhang, L.-Q. (2004). A novel approach to high performance elastomer by using clay. *Macromolecular Rapid Communications, 25*(19), 1692–1696.
25. Kuilla, T., Bhadra, S., Yao, D., Kim, N. H., Bose, S., & Lee, J. H. (2010). Recent advances in graphene based polymer composites. *Progress in Polymer Science, 35*(11), 1350–1375.
26. Rafiee, M. A., Rafiee, J., Wang, Z., Song, H., Yu, Z. Z., Koratkar, N. (2009). Enhanced mechanical properties of nanocomposites at low graphene content. ACS Nano, *3*(12).
27. Ma, J., Yu, Z.-Z., Kuan, H.-C., Dasari, A., & Mai, Y.-W. (2005). A new strategy to exfoliate silicone rubber/clay nanocomposites. *Macromolecular Rapid Communications, 26*(10), 830–833.
28. Fan, Yuchi. (2010). Lianjun Wang and Jianlin, preparation and electrical properties of graphene nano sheet/AL2O3 composites. *Carbon Science, 48*(10), 1743–1749.
29. Annamahesh, A., Sunitha, K., Rangarajan, S. (2019) Study on mechanical behavior of graphene based polymer composites. *International Journal of Innovative Technology and Exploring Engineering (IJITEE)*, *8*(4). ISSN: 2278-3075.
30. Shankar, A., Hallada, b., Nagaraj, R., Banapurmatha, b,∗, Anand, M., Hunashyala et.al. (2017). Experimental investigation for graphene and carbon fibre in polymer-based matrix for structural applications. *Journal of Applied Research and Technology 15*, 297–302.
31. Pathak, A. K., Borah, M., Gupta, A., Yokozeki, T., & Dhakate, S. R. (2016). Improved mechanical properties of carbon fiber/graphene oxide-epoxy hybrid composites. *Composites Science and Technology, 135,* 28–38.
32. Mahendra, G., Srividya, K., Reddy, C.K., Kavitha, E. Hygrothermal degradation studies on e-glass woven rovings- epoxy composite. *International Journal of Engineering Sciences & Research Technology*.
33. Papageorgiou, Dimitrios G., Kinloch, Ian A., & Young, Robert J. (2017). School of materials and national graphene institute, the university of Manchester, UK "Mechanical properties of graphene and graphene-based nanocomposites". *Progress in Materials Science, 90,* 75–127.
34. Yang, K., Wu, S., Guan, J., Shao, Z., & Ritchie, R. O. (2017). Enhancing the mechanical toughness of epoxy-resin composites using natural silk reinforcements. *Scientific Reports, 7*(11939).
35. Mader, A., Kondor, A., Schmid, T., Einsiedel, R., & Müssig, J. (2016). Surface properties and fibre-matrix adhesion of man-made cellulose epoxy composites-Influence on impact properties. *Composites Science and Technology, 123,* 163–170.
36. Gironès, J., et al. (2011). Biocomposites from Musa textilis and polypropylene: Evaluation of flexural properties and impact strength. *Composites Science and Technology, 71,* 122–128.
37. Santulli, C. (2007). Impact properties of glass/plant fibre hybrid laminates. *Journal Materials Science, 42,* 3699–3707.

38. Wambua, P., Ivens, J., & Verpoest, I. (2003). Natural fibres: Can they replace glass in fibre reinforced plastics? *Composites Science and Technology, 63,* 1259–1264.
39. Shah, D. U., Porter, D., & Vollrath, F. (2014). Can silk become an effective reinforcing fibre? A property comparison with flax and glass reinforced composites. *Composites Science and Technology, 101,* 173–183.
40. Hu, K., Gupta, M. K., Kulkarni, D. D., & Tsukruk, V. V. (2013). Ultra-Robust graphene oxide-silk fibroin nanocomposite membranes. *Advanced Materials, 25,* 2301–2307.
41. Yavari, F., Rafiee, M., Rafiee, J., Yu, Z.-Z., Koratkar, N. (2010). Dramatic increase in fatigue life in hierarchical graphene composites. *ACS applied materials & interfaces, 2*(10), 2738–2743.
42. Zhang, Yunya, & Li, Xiaodong. (2017). Bioinspired-Graphene/Al2O3 doubly reinforced aluminum composites with high strength and toughness. *Nano Letters, 17,* 6907–6915.

Hybridization of Natural Fibers to Develop the Polymeric Composite Materials: A Review

Dhruv Bhardwaj, Ayush Gupta, Vijay Chaudhary, and Sumit Gupta

Abstract In recent years, study on natural fiber-reinforced polymer composites has been extensive due to their strength and reduced weight. Natural fibers are also eco-friendly, have a reduced carbon footprint in the environment, biodegradable, low cost of production and are cheap as compared to synthetic fibers. Reuse of the waste natural fiber is a sustainable option for the environment. Although these properties make natural fiber a substitute in practical applications above synthetic fibers, their affinity toward water and improper matrix interface bonding is a major concern toward their use in many applications. Due to the above reasons, the use of synthetic fiber comes into play. Synthetic fibers do not encounter these problems but are non-biodegradable and cost more than natural fibers. Therefore, a lot of time has been spent on research and development of hybrid composites. These hybrid composites utilize both natural and synthetic fibers in such a way to get best possible solutions. Present work focuses on these hybrid composites, their production, properties and where they lack.

1 Introduction

A composite material is made up of two or more distinct materials that show significant difference in their physical and chemical properties that, when combined with each other, create a material that shows properties different to the two materials used.

D. Bhardwaj · A. Gupta · V. Chaudhary · S. Gupta (✉)
Amity School of Engineering and Technology, Amity University, Sector-125, Noida 201301, Uttar, India
e-mail: sumitgupta2007@gmail.com

D. Bhardwaj
e-mail: dhruvsanjay97@gmail.com

A. Gupta
e-mail: ayush.gupta19@s.amity.edu

V. Chaudhary
e-mail: vchaudhary2@amity.edu
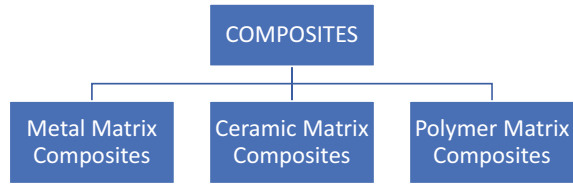
A composite consists of a continuous and discontinuous phase, with the latter being harder and stronger, thus gets embedded in the continuous phase. The discontinuous phase is called the reinforcement, while the continuous phase is called the matrix which can either be metallic, polymeric or ceramic. If the matrix is in polymeric form, then the composite is called a polymer matrix composite (PMC). The fibers used as reinforcement can be fibrous or non-fibrous (particulate) in nature. If the fibers are derived from natural plant or other living species, then they are natural fibers, if they are made from non-biodegradable substances, they are synthetic fibers and the combinations of the two are called hybrid composites (Fig. 1).

Vijaya Ramnath et al. [1] showed in his studies that abaca-GFRP composite has the ability to be used in automotive industry due to its greater flexural and impact strength than the abaca-jute-GFRP hybrid composite. Although the abaca-jute-GFRP composite showed better tensile strength and strain failure, the hybrid composite is better in other general applications.

Afzaluddin et al. [2] performed an experiment where the overall mechanical properties of the sugar palm fiber (SPF) and glass fiber hybrid composite were better with the addition of SPF content.

Kalagi et al. [3] experimented the use of natural fiber and synthetic fiber hybrid composites to be used in the production of energy sector. Hybrid composite can be a potential candidate where they can replace the conventional material systems of wind industry. These materials can be introduced for the manufacturing of various sections of a wind turbine. Use of coconut coir has become common practice to make either hybrid composite or natural fiber-reinforced composites. Shrivastava et al. [4] showed E glass woven fabric with coconut coir give better mechanical properties than that of pure coir/epoxy composites. Synthetic fibers can be introduced with natural fibers to enhance composite properties.

In recent studies done on Kevlar fiber hybrid composites, Singh et al. [5] experimentally showed that the bagasse–Kevlar homogeneous hybrid composite can be used in application where wear is more and increases with loading. The fiber is biodegradable and cost effective. These are important factors for the hybrid composites and provide many interesting facts regarding fiber length and its orientation. Naveen et al. [6] also worked on Kevlar fiber mixed with cocos nucifera sheath, to give a hybrid composite with similar properties to pure epoxy/Kevlar composite. Fiber content based on weight percentage showed that Kevlar (75%)/cocos nucifera sheath (25%) has overall impressive properties to replace pure epoxy/Kevlar composites (Fig. 2).
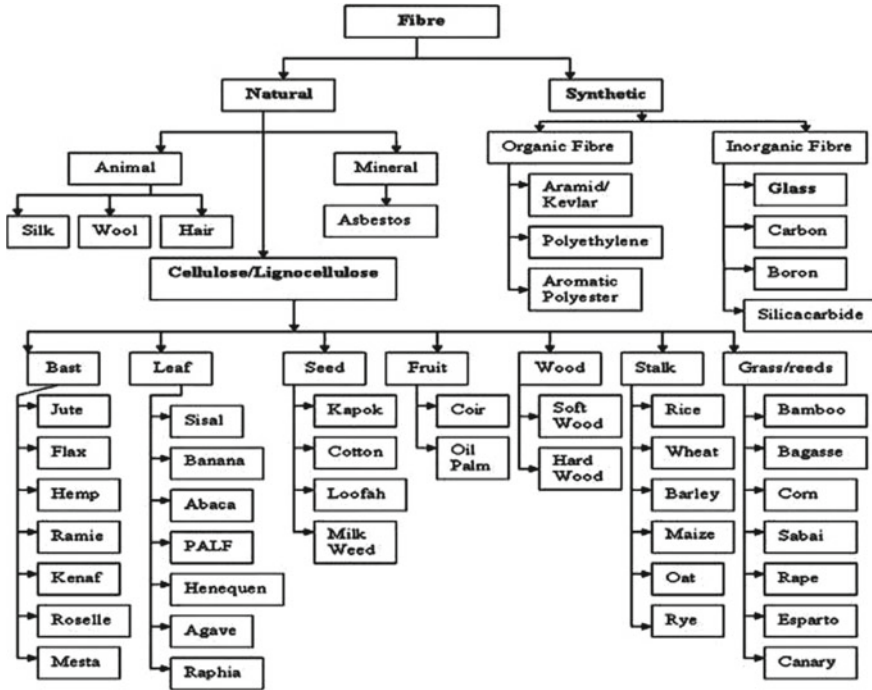
Fig. 2 Classification of natural and synthetic fibers retrieved from cellulosic/synthetic fiber-reinforced polymer hybrid composites [6]

Treatment of natural fibers is important to make composites, as it removes dirt and other particles that may hamper its properties. Vijayakumar et al. [7] provided treated caryota and bamboo fiber with glass fiber reinforcement hybrid composite of good enough property to replace pure glass/epoxy composite. The properties were compared to glass/epoxy, bamboo/epoxy and caryota/epoxy, all of which showed better properties in one area or the other. The use of plant leaves and various other parts has become common business for natural fiber-reinforced composites as well as the hybrid composites and the hybrid banana–pineapple–glass fiber composite show such properties that they can be used in many applications such as automotive, electrical parts and packaging, structural building, etc. as shown by Venkata Deepthi et al. [8]. Similar study introduced jute fibers instead of banana leaves and showed increased strength with increase in fiber content done by Indra Reddy et al. [9].

Sansevieria trifasciata fibers are also plant species which gives good properties when combined with carbon fibers. Borukati et al. [10] showed that overall cost of production decreased with increase in fiber content and 40% by weight content of STCFRP hybrid composite shows good enough properties to be used in automobile and aerospace applications. Plant fibers are also very commonly used in place of leaves for the development of natural composites. Banana–glass hybrid composite

exhibits better properties than pure epoxy and can replace pure epoxy composite in many applications. The introduction of glass enhances tensile and flexural properties to great extent. Vijaya kumar et al. [11]

Many NFRP composites show better mechanical qualities than many synthetic composites. Coconut coir when used in right fiber length and orientation after treatment with NaOH simply is a good alternative to many synthetic fibers. Marimuthu et al. [12] used treated waste coconut coir and glass fibers to make a glass–coconut hybrid fiber. The addition of coconut coir gave enhanced mechanical properties to the hybrid composite and showed that it can be used in the place of epoxy glass fiber composite due to it being semi-biodegradable, cost effective and environmentally friendly.

The recent increase in fumes and problems with waste management has started a revolution for researchers to start preparing composites that are recyclable and reusable to certain extent, and many studies have been done on NFRP composites regarding this. Hybrid composites made up of natural fibers have started a trend where more than one kind of natural fiber are used in place of one fiber. They also remove synthetic-natural hybrid composites by exhibiting similar properties. The study done by Chaudhary et al. [13] showed natural hybrid composites observed better mechanical properties than simple NFRP composites, Jute/hemp/flax/epoxy hybrid composite showed the highest tensile strength, modulus and impact strength. Jute/hemp/epoxy hybrid composite achieved the maximum flexural strength. Use of hybrid composites hence can provide good alternatives in future.

Balachandar et al. [14] provided hybrid composites made up of human hair-sisal-bamboo which was a comparative study on length of human hair and its effect on composite properties. This study gave an insight on future technology, waste management and use of natural fibers to be used in place of many synthetic fibers. Similarly, Krishnakumari et al. [15] showed a natural hybrid between luffa and boerhavia diffusa roots which focused on matrix and fiber compatibility. The study showed better compressive properties but lower tensile and flexural properties.

Khandai et al. [16] experimented with natural, synthetic and hybrid composites that showed that although the synthetic fibers cannot be directly replaced with natural fibers due to their mechanical properties, hybrid between the two can be suitable for many applications such as automotive and aerospace. Their combined properties make them a good alternative. The experiment provided a glass-natural hybrid composite with properties similar to glass fibers which can be replaced in near future.

2 Materials and Method

As time moves, we all can say that not only non-renewable resources scarce but also dependent upon natural sources. With renewable resources now becoming more and more our requirement, it is inevitable that hybrid composites will soon become the most largely used materials everywhere. The materials which show good mechanical

properties and are biodegradable to some extent will serve the purpose of people. The use of plants and their leaves as reinforcement have become common, and synthetic fibers like glass, carbon, Kevlar, etc. are being used for quite some time. To make a hybrid material, the use of both layer by layer or with some other configuration is done.

Fiber source

The plants, which produce natural fibers, are classified as primary and secondary depending on their utilization. Primary plants are those grown for their fiber content, while secondary plants are plants in which the fibers are produced as a by-product. Jute, hemp, kenaf, and sisal are examples of primary plants. Pineapple, oil palm and coir are examples of secondary plants. There are six basic types of natural fibers. They are classified as follows: best fibers (jute, flax, hemp, ramie and kenaf), leaf fibers (abaca, sisal and pineapple), seed fibers (coir, cotton and kapok), core fibers (kenaf, hemp and jute), grass and reed fibers (wheat, corn and rice) and all other types (wood and roots).

Synthetic fibers are produced by manmade efforts which generally include extruding of fiber forming materials through spinnerets, making a fiber. Glass fibers are comprised of silica-based formulation or other glass formulation and then extruded into fibers of required length. This process of heating and extruding is called millennia which is been recently used in textile industry. Before this, glass fibers were used in small lengths or staples. To produce a carbon fiber, the carbon atoms are bonded together in crystals that are more or less aligned parallel to the long axis of the fiber as the crystal alignment gives the fiber high strength-to-volume ratio (in other words, it is strong for its size). Several thousand carbon fibers are bundled together to form a tow, which may be used by itself or woven into a fabric.

Matrixes for Polymer Composites

Matrix materials or resins in case of composites are classified based on their chemical base, i.e., thermosets and thermoplastic. Although thermoplastics are tougher, resilient and corrosion resistant, they have a fundamental disadvantage over thermosetting resins, which is that they have to be molded at elevated temperatures. Thermoplastic resins mainly used are unsaturated polyesters due to their lower cost but are not as strong as the thermosetting resin like epoxy. Hence, the main research effort is concentrated on thermosetting plastics. Thermosetting plastics or thermosets are formed with a network molecular structure of primary covalent bonds. Some thermosetting resins maybe cross-linked at higher temperature or a combination of pressure and temperature. Others are cross-linked at room temperature due to the chemical reaction.

Thermosetting matrix

The main advantages of thermosetting polymer matrix materials are melted with low-temperature melting point and also easily mixed with fibers prior to curing. The important limitation of thermosetting polymer matrix is irreversible. In general, polyesters are highly usable thermosetting matrix FRP composites, because of

handling flexibility, dimension wise stable, ease of handling, dimensional stability, excellent mechanical strength, electrical resistance, chemical properties and available at low cost. They are commonly applied in hand lay-up and spray-up processes.

Epoxy

Epoxy resins are the most commonly used thermoset plastic in polymer matrix composites. Epoxy resins are a family of thermoset plastic materials which do not give off reaction products when they cure and so have low cure shrinkage. They also have good adhesion to other materials, good chemical and environmental resistance, good chemical properties and good insulating properties. The epoxy resins are generally manufactured by reacting epichlorohydrin with bisphenol. Different resins are formed by varying proportions of the two: As the proportion of epichlorohydrin is reduced, the molecular weight of the resin is increased. The excellent properties of epoxy (good adhesion, mechanical properties, low moisture content, little shrinkage, and processing ease) make it one of the best matrix materials for composites.

Thermoplastic matrix

In recent trend, the usage of thermoplastics matrix materials is widely increased than the thermoset matrix material, due to the faster processing and curing. On the other hand, thermoplastics do not undergo a chemical reaction on application of heat. They simply melt on application of heat and pressure to form a component. Thermoplastics are softened, and they undergo large and rapid change in viscosity with variation in temperature. Thermoplastics are repeatedly softened by heating and hardened by cooling (Figs. 3 and 4).
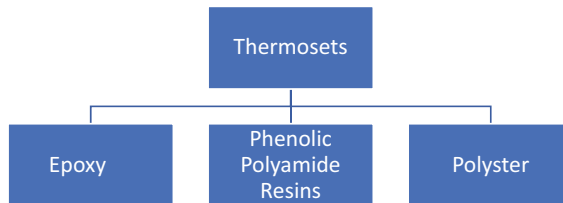
Fig. 3 Types of thermoset polymers
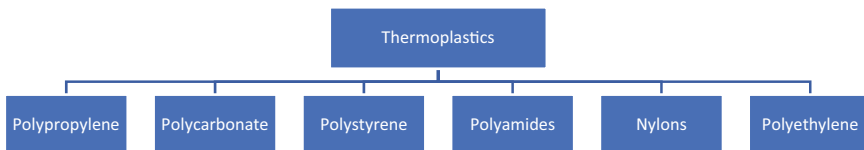
Fig. 4 Types of thermoplastic polymers

3   Mechanical Properties

The addition of synthetic fibers into natural fibers increased mechanical properties to greater extent. Hybrid composites when compared to natural fiber-reinforced polymer composites showed overall better qualities in terms of impact strength, tensile strength and flexural properties. However, when compared with synthetic fibers, hybrid composites lack the properties but make it up due to their lower cost of production, manufacturing and being biodegradable and environmentally friendly.

These properties are largely dependent upon fiber orientation, characteristics, length and treatment in case of natural fibers and fiber orientation, length and characteristics (unidirectional or bidirectional) in case of synthetic fibers. In order to expand the use of hybrid fibers, the study of fibers is very important and essential.

- The addition of synthetic fibers enhances properties of NFRP composites to more than 100%.
- Addition of natural fibers on the other hand increases biodegradability and renewability in case of synthetic fibers.
- The more the fiber content, the better the properties will become but only to certain extent as water absorption and wet ability comes into question.
- Fiber orientation, characterization and length are important during manufacturing of hybrid fibers as they are directly related to its properties.

4   Applications

The study to find alternatives to non-renewable resources is becoming larger every day, and to find materials that can effectively replace synthetic fibers and have better mechanical and physical properties than natural fibers is a big task. Many authors have made significant efforts to this field of study and have found good alternatives to replace synthetic fibers. Due to their ease of fabrication, lower cost and superior mechanical properties, fiber-reinforced polymer composites are being widely considered for use in many applications such as automobile market. Hybrid polymers offer a different type of solution to many problems as they are cost effective, environmentally friendly and have properties very similar to synthetic composites. Hybrid composites have been effectively used in wind turbine blades as existing material used for the production of wind energy is still non-biodegradable and needs to be disposed after end of life in service; due to this problem, finding an environmentally friendly material is very important. Hybrid materials are also used in electronic packaging and in building construction due to lower cost of production and biodegradability. Today, the main research has been on making these hybrid polymer composites more sustainable and environmentally friendly due to global warming and climate change. These sustainable options can be recycled using many techniques like pyrolysis, where we can extract reusable compounds and reduce unnecessary

waste. Hybrid composites provide overall better sustainability and give lesser problems during recycling processes and hence can be used in place of synthetic fiber composites.

5   Conclusions

In the present work, the fabrication, process parameters, mechanical properties and applications of hybrid polymer composites have been studied and reported. Hybrid polymer composites not only reduce cost of production of composites but also solve the problems related to environment. The addition of synthetic fibers as reinforcement into the natural fibers showed great changes in terms of mechanical and chemical properties. While the addition of natural fibers to synthetic fibers to make hybrid composites greatly reduces cost of production and makes the composite semi biodegradable. As the popularity of hybrid composites increases in the automobile as well as civil industry, its future scope is enormous.

- Mechanical and chemical properties vary from the content of fiber added to the composite.
- The addition of synthetic fibers like glass, Kevlar and carbon increases tensile, impact and flexural strengths.
- Natural fibers when combined to synthetic composites give lower production cost and make the composite biodegradable to certain extent.
- The curing of natural fibers increases the mechanical properties of the composites.

References

1. Vijaya Ramnath, B., Junaid Kokan, S., Niranjan Raja, R., Sathyanarayanan, R., Elanchezhian, C., Rajendra Prasad, A., & Manickavasagam, V. M. (2013). Evaluation of mechanical properties of abaca–jute–glass fibre reinforced epoxy composite. *Materials & Design*, *51*, 357–366.
2. Afzaluddina, A., Jawaid, M., Salit, M. S., & Ishak, M. R. (2019). Physical and mechanical properties of sugar palm/glass fiber reinforced thermoplastic polyurethane hybrid composites. *Journal of Materials Research and Technology*, *8*(1).
3. Kalagi, G. R., Patil, R., & Nayak, N. Experimental study on mechanical properties of natural fiber reinforced polymer composite materials for wind turbine blades. *Materials Today: Proceedings*, *5*(1), Part 32018, 2588–2596.
4. Shrivastava, R., Telang, A., Rana, R. S., & Purohit, R. (2017). Mechanical properties of coir/glass fiber epoxy resin hybrid composite. *Materials Today: Proceedings 4*(2), Part A 2017, 3477–3483.
5. Singh, T., Gangil, B., Singh, B., Verma, S. K., & Fekete, G. (2019). Natural-synthetic fiber reinforced homogeneous and functionally graded vinyl ester composites: Effect of bagasse-Kevlar hybridization on wear behaviour. *Journal of Materials Research and Technology*, *8*(6), 5961–5971.

6. Naveen, J., Jawaid, M., Zainudin, E. S., Sultan, M. T. H., & Majid, M. S. A. (2019). Thermal degradation and viscoelastic properties of Kevlar/Cocos nucifera sheath reinforced epoxy hybrid composites. *Composite Structures*, *2191*, 194–202.

7. Vijayakumar, S., & Palanikumar, K. (2019). Mechanical property evaluation of hybrid reinforced epoxy composite. *Materials Today: Proceedings*, *16*, Part 2, 430–438.

8. Venkata Deepthi, P., Sita Rama Raju, K., & Indra Reddy, M. (2019). Dynamic mechanical analysis of banana, pineapple leaf and glass fibre reinforced hybrid polyester composites. *Materials Today: Proceedings*, *18*, Part 6, 2114–2117.

9. Indra Reddy, M., Anil Kumar, M., & Rama Bhadri Raju, Ch. (2018). Tensile and flexural properties of jute, pineapple leaf and glass fiber reinforced polymer matrix hybrid composites. *Materials Today: Proceedings*, *5*(1), Part 1, 458–462.

10. Borukati, S. R., Durga Prasad, B., & Ramesh, A. (2019). Development and characterization of natural fiber/carbon fiber reinforced hybrid composite material. *Materials Today: Proceedings, 18*, Part 7, 5394–5399.

11. Vijaya Kumar, N., Sai Krishna, B., & Sai Chandrika, N. (2019). Evaluation of properties of glass-banana-fiber reinforced hybrid fiber polymer composite. *Materials Today: Proceedings, 18*, Part 6, 2137–2141.

12. Prakash Marimuthu, K., Mohan Kumar, S., Ravi Kumar, V., & Govindaraju, H. K. (2019). Characterization of mechanical properties of epoxy reinforced with glass fiber and coconut fiber. *Materials Today: Proceedings, 16*, Part 2, 661–667.

13. Chaudhary, V., Bajpai, P. K., & Maheshwari, S. (2017). Studies on mechanical and morphological characterization of developed jute/hemp/flax reinforced hybrid composites for structural applications. *Journal of Natural Fibers*. https://doi.org/10.1080/15440478.2017.1320260.

14. Balachandar, M., Vijaya Ramnath, B., Ashok Kumar, S., & Siva Sankar, G. (2019). Experimental evaluation on mechanical properties of natural fiber polymer composites with human hair. *Materials Today: Proceedings, 16*, Part 2, 1304–1311.

15. Krishnakumari, A., Devaraju, A., & Saravanan, M. (2018). Evaluation of mechanical properties of hybrid rootfiber reinforced polymer composites. *Materials Today: Proceedings, Volume 5*(6), Part 2, 14560–14566.

16. Khandai, S., Nayak, R. K., Kumar, A., Das, D., & Kumar, R. (2019). Assessment of mechanical and tribological properties of flax/kenaf/glass/carbon fiber reinforced polymer composites. *Materials Today: Proceedings, 18*, Part 7, 3835–3841.

Underwater Friction Stir Welding of AA6082-T6: Thermal Analysis

Mohd Atif Wahid, Pankul Goel, Zahid Akhtar Khan, Krishna Mohan Agarwal, and Etkaf Hasan Khan

Abstract Underwater friction stir welding (UFSW) is a variant of friction stir welding (FSW) in which the workpiece is totally inundated in water during the welding. In this study, a 3D nonlinear thermal model is developed to estimate the temperature distribution of the joint produced by FSW and UFSW using ANSYS Workbench 15. The thermal model is made in transient thermal module, and the temperature distribution is ascertained utilizing numerical simulation. The FSW/UFSW experiments are performed on aluminum alloy AA-6082- T6 at same parametric combination to discover the temperature distributions in inundated water state and normal air. The obtained results revealed that the temperature distribution acquired during the experiment is in immense agreement with the temperature attained employing numerical simulation. It is found that the peak temperature in UFSW remains significantly less than the temperature encountered during FSW. For UFSW, the heat-affected zone (HAZ) area is noticeably narrowed, and the thermal gradient is effectively controlled distinguishing it from FSW.

Keywords Aluminum · Friction stir welding (FSW) · Temperature distribution · Thermal modeling · Underwater friction stir welding (UFSW)

M. A. Wahid (✉) · E. Hasan Khan
Department of Mechanical and Automation Engineering, DTC, Greater Noida, India
e-mail: wahidatif89@gmail.com

E. Hasan Khan
e-mail: e.khan@delhitechnicalcampus.ac.in

P. Goel
Department of Mechanical Engineering, IMS Engineering College, Ghaziabad, India
e-mail: pankul.goel@imsec.ac.in

Z. A. Khan
Department of Mechanical Engineering, Jamia Millia Islamia, New Delhi, India
e-mail: zakhan@jmi.ac.in

K. M. Agarwal
Department of Mechanical Engineering, Amity University, Noida, India
e-mail: profkmagarwal@gmail.com

Nomenclature

μ	Friction coefficient
ρ	Density
c_p	Heat capacity utilize
κ	Coefficient of thermal conductivity
T	Temperature
T_{amb}	Ambient temperature
T_0	Initial temperature
q	Heat flux

1 Introduction

The fusion welding (FW) processes involve melting and solidification of base materials (BMs) which leads to large number of welding defects such as porosity, cavity, and slag inclusion [1]. These defects have been overcome using a solid-state welding process; FSW which was originated at TWI, UK during 1991 [2]. FSW is a proven technology to yield excellent joints in aluminum alloys (AAs). During the process, a tool (non-consumable) with a profiled probe and shoulder is embedded into the centerline of the two BMs and afterward traversed along the abutting edges. This process involves heat generation due to friction between tool and BMs followed by plastic deformation due to continuous stirring of probe. Moreover, extra heat is produced by viscoplastic scattering of mechanical energy at high strain rates due to interaction among BMs and the tool [3]. This heat causes thermal softening of the BMs, and these softened materials are mixed and extruded from the front to the back end of the probe due to tool traversing. Subsequently, softened material solidifies and consolidated into a weld joint. [4]. In FSW, the quality of joint exclusively depends on amount of heat generation. Higher heat input results in decrease of mechanical properties of joint [5, 6]. These high heat thermal cycles can be controlled using various coolants namely water, liquid nitrogen, etc. [1, 7]. UFSW is one such process in which water is used to normalize the temperature prevailing in joints [1]. The welding is performed underwater which can be stagnant or in a state where it is constantly flowing across the surface of the samples to be welded. The coarsening and dissolution of precipitates are restricted due to far-reaching circulation and excellent heat-captivating ability of the water. In recent years, UFSW joints have also offered improved mechanical performance and fewer defects as compared to FSW joints [1]. The water cooling suppresses inter-mixing of the dissimilar metals, grain structural coarsening, and the kinetics of intermetallic compound (IMC) formation [10]. In this regard, several researchers have investigated UFSW. Fratini et al. [8] improved joint strength and hardness by attaining low peak temperature using water during UFSW of AA 7075. Zhang et al. [9] conducted UFSW on 2219-T6 aluminum alloy. They enhanced mechanical properties and microstructures in heat-affected zone (HAZ) via

controlling the thermal cycles. Liu et al. [6] performed UFSW on Al 2219 and impro-vised elasticity of the joint by varying welding temperature. Using liquid nitrogen, Benavides et al. [10] conducted FSW on AA 2024. They decreased BM temperature to −30 °C from 30 °C and improved the hardness of HAZ significantly. Thermal modeling of underwater FSW of AA 2219-T6 was conducted by Benavides et al. [11] using MSC MARC software. They reported that the high-temperature distribution region in UFSW joint remains less compared to normal FSW joint.

In spite of several benefits of UFSW over FSW, few researches have been performed using UFSW. The researches available are on 2xxx and 7xxx AAs with minor studies on marine-grade 6xxx AAs. The accessible literature also discloses limited research related to thermal modeling and simulation of UFSW. Being motivated from these research gaps, this research was systematically planned and conducted to achieve the following aims (i) to conduct finite element simulation for anticipating temperature development during UFSW of AA 6082-T6 (ii) to explore the cooling effect of UFSW in comparison with normal FSW. The novelty of this work is that it demonstrates the application of FEM to model a novel solid-state welding process, i.e., UFSW, especially for marine-grade AAs.

2 Finite Element Modeling

The thermal modeling is used to estimate the transient temperature distribution in the BM during welding process. The experimental limitations are the measurement of temperature along the weld line as well as the quantity of areas at which temperature could be estimated (involves high cost of experimentation). It is as such important to anticipate numerically the temperature profile during FSW/UFSW. In this study, a three-dimensional, nonlinear thermal model is developed to estimate the tempera-ture distribution of joints using ANSYS Workbench. The thermal model is made in transient thermal module.

In thermal modeling, temperature distribution T is function of time (t) and spatial coordinates (x, y, z), estimated by three-dimensional heat transfer Eq. (1)

$$\rho c_{\mathrm{p}} \frac{\partial T}{\partial t} = \frac{\partial}{\partial x}\left(kx \frac{\partial T}{\partial x}\right) + \frac{\partial}{\partial y}\left(ky \frac{\partial T}{\partial y}\right) + \frac{\partial}{\partial z}\left(kz \frac{\partial T}{\partial z}\right) + q(x, y, z, t) \quad (1)$$

where k_x, k_y, k_z is the thermal conductivity, C_p is the heat capacity, q(x, y, z, t) is internal heat generation rate, and the density ρ [12, 13].

Assumptions Some assumptions made during modeling are:

- BM is considered homogeneous and isotropic.
- During welding, there was no melting of workpiece.
- Symmetrical boundary conditions were considered along the weld line.
- There is no heat loss due to clamping from the workpiece.

Table 1 Thermal properties of AA 6082-T6

Density (g/cm3)	Thermal conductivity (W/mK)	Modulus of elasticity (GPa)	Thermal expansion (μm/m-K)	Melting point (°C)	Specific heat (J/Kg K)
2.7	180	70	23.1	555	900

- No cyclic load was involved, so effect of creep was not taken.
- Tilt angle of the tool is zero.
- Heat losses due to radiation are neglected.
- Friction coefficient is constant throughout process, 0.5 and 0.65 for FSW and UFSW, respectively.

2.1 Meshing of Workpiece

Meshing is produced using default meshing module of ANSYS Workbench which automatically generates mesh around the plate. Fine mesh is appeared near the center which becomes coarse away from the weld line. Fine mesh bears the number of nodes and elements 20209 and 9821, respectively.

2.2 Material Properties

Thermal properties of AA6082-T6 are given in Table 1.

A noteworthy issue during modeling of heat flow is getting an accurate value of the input energy or heat flux. This is due to the varying friction coefficient throughout the whole process. In previous published work, friction coefficient values were taken in the range 0.3–0.85 [12, 13]. In this paper, friction coefficient value for air and water is taken as 0.5 and 0.65, respectively.

2.3 Boundary Conditions

Initially, some boundary conditions were considered for both processes as follows:

$$T(x, y, z, t) = T_0 = 45°C \tag{2}$$

Boundary condition for heat flux between workpiece and tool is given by:

$$k\frac{\partial T}{\partial n} = q \tag{3}$$

Boundary condition for convective heat transfer from all work surfaces is:

$$k\frac{\partial T}{\partial n} = h\,(T - T_{amb}) \tag{4}$$

where h is the convection coefficient, T_{amb} is the ambient temperature, and n is the normal direction vector of the boundary. In this paper, ambient temperature (air temperature) is considered as 45 °C. In earlier works, convection coefficient (h) for all surfaces exposed to atmosphere was assumed to 10–30(W/m^{2}C), and convection coefficient between backing plate and workpiece was 200–1000(W/m^{2}C) [12–14]. As such, convection coefficient for FSW is taken as 10 W/m^{2}C and 200(W/m^{2}C) between backing plate and workpiece. From previous researches, it is found that during UFSW, the water in and around the tool consists of two parts. One is the water that is boiling near the tool leading to high amount of heat transfer with respect to workpiece, and other is the non-boiling water away from the tool. Convective coefficient near boiling water is taken as 3000(W/m^{2}C), and for non-boiling region, it is 850(W/m^{2}C) based on trial experiments and previous research [11–13].

2.4 Heat Flux Input

The heat due to friction is quantified by defining transient heat flux Q. Using Eq. (5) of Chao et al. [15], total heat flux is given by

$$Q = \pi\,\omega\,\mu(r_o^2 + r_o r_i + r_i^2)\,/45(r_o + r_i) \tag{5}$$

where μ is the frictional coefficient between plates and workpiece, ω is the tool rotational speed, F is the downward force on tool, and r_0 and r_i are the radii of the shoulder and pin of tool. The frictional heat rate q(r) is understood to be increasing linearly along radius according to Eq. 6 and applied to model using tabular boundary condition. Cylindrical coordinate system is used for movement of FSW tool and calculating heat flux for each time step.

$$q\,(r) = 3Qr\,/2\pi\left(r_o^3 - r_i^3\right)\text{ for } r_i \leq r \leq r_o \tag{6}$$

3 Experimental Procedure

The BM is selected as 3 mm thick AA-6082 T6 plate with 200 mm × 50 mm dimensions. FSW experiments were executed in two different conditions, i.e., in air (FSW) and under water (UFSW). Cam-shaped probe of 20 mm shoulder dia with
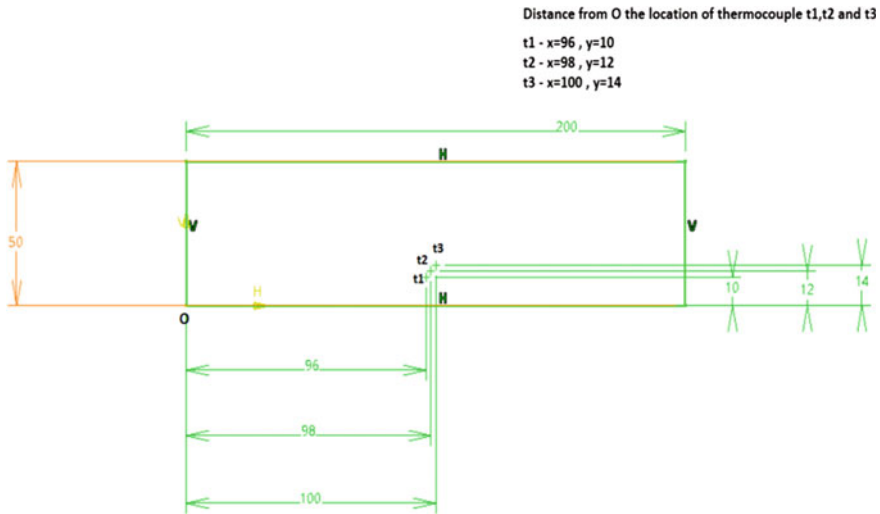
Fig. 1 Location of various K-type thermocouples

height and pin dia of 2.7 mm and 6 mm, respectively, was used. A solitary run with 2^0 tilt angle and 0.25 mm plunge depth was performed normal to the rolled direction. The welding speed and rotational speed are mutual for FSW and UFSW, i.e., 80 mm/min and 900 rpm, respectively. These parameters were chosen as maximum tensile strength was obtained at this parametric combination.

The temperature of various locations is measured using K-type thermocouple. The position of the thermocouple is given in Fig. 1.

4 Simulation Result and Discussion

4.1 Model Validation

FSW of material AA 6082-T6 is simulated and contrasted to experimental results. The dimensions of workpiece, material, rotational speed, tool dimension, and welding speed is same as used during experiment. The temperature calculated by various thermocouples in FSW and UFSW are denoted by t_1, t_2, and t_3 and T_1, T_2, and T_3, respectively, for easy understanding. Figures 2 and 3 depict the comparison of temperature variation between experimental and simulated results. The temperature and time is measured in Celsius and seconds, respectively. The outcomes are in great concurrence with experimental results.

In simulation, the peak temperature during FSW is obtained 9.48% higher as compared to experiment. However, little variation (less than 5%) in temperature is found during UFSW. During modeling, the temperature of air is set as (45 °C);

Fig. 2 Comparison of experimental and simulated result for thermocouple 1 in FSW (t_1)
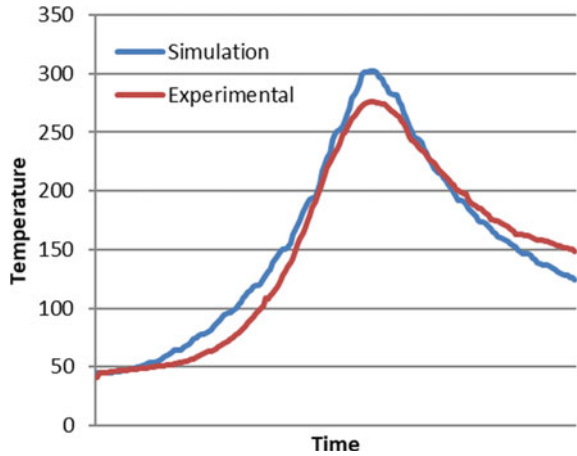
Fig. 3 Comparison of experimental and simulated result of thermocouple 1 in UFSW (T_1)
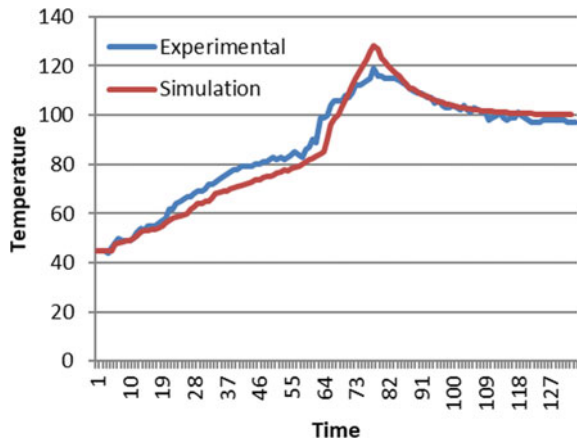
however, real air temperature close to the workpiece is expanded as a result of the continuous aggregation of heat input. Due to this heat dissipation near the work piece is weakened compared to practical situation. Another contributing factor during simulation, coefficient of friction is presumed to be constant in FSW and UFSW; however, coefficient of friction changes with temperature in both cases. Similar trend was also observed for thermocouple location 2 and 3. Figs. 4 and 5 depict the comparison of temperature variation between experimental and simulated results for location 2. The peak temperature found at this location (Figs. 4 and 5) was lower than the location 1 (Figs. 2 and 3). The peak temperature reduces due to heat dissipation as the distance from the weld center increases [7].

Fig. 4 Comparison of
experimental and simulated
result for thermocouple 2 in
FSW (t$_2$)
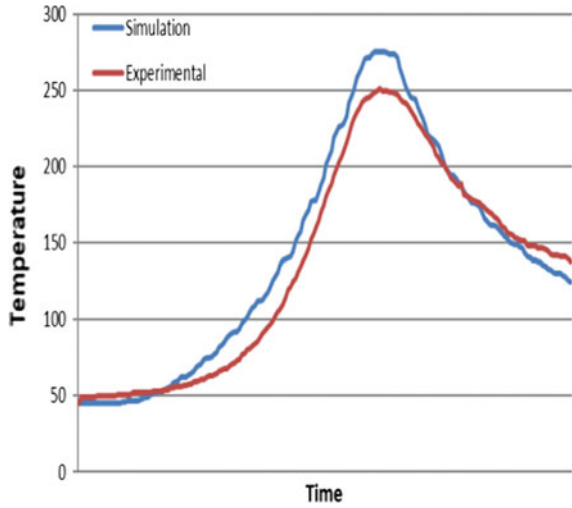
Fig. 5 Comparison of
experimental and simulated
result for thermocouple 2 in
FSW (T$_2$)
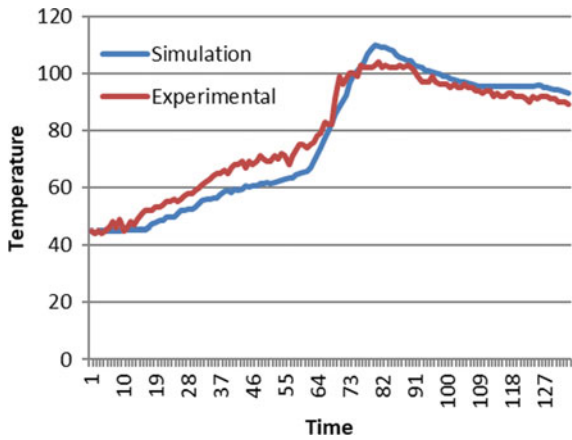
4.2 Effect of Cooling

The peak temperature measured in experimentation during FSW and UFSW at location 1 is 276 °C and 116 °C, respectively, which occurred at near about 65 s. The thermal gradient is observed low during UFSW. The maximum temperature in FSW and UFSW during simulation is measured as 302.12 °C and 128.38 °C. The cooling rate increases due to water which lowers the peak temperature during UFSW. Low peak temperature and thermal gradient observed in UFSW limits the coarsening of precipitates and causes improvement in strength [1, 5, 7]. The simulation profiles based on these results are shown in Figs. 6 and 7.
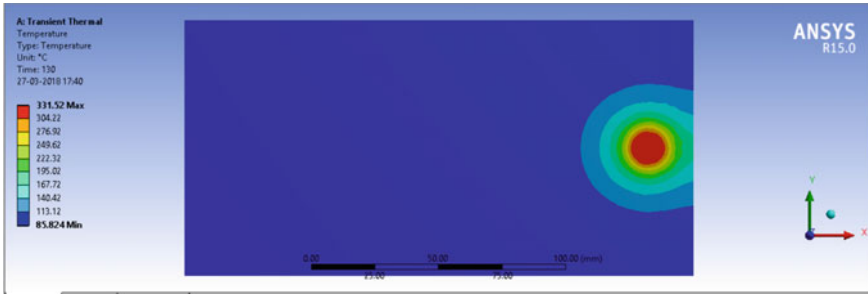
Fig. 6 Temperature distribution in welding process of UFSW (at z = 0)
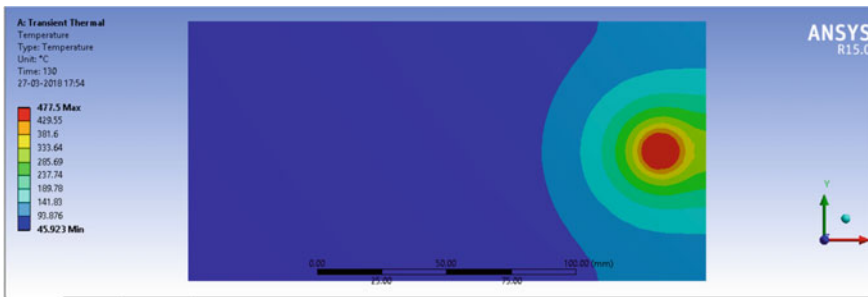
Fig. 7 Temperature distribution in welding process of FSW (at z = 0)

It is clear from results that HAZ is narrow in UFSW which attribute to lower level of material and heat flow in UFSW. This can be due to greater heat convection of boiling water relatively to free convection of air which causes rapid heat dissipation from work piece during UFSW. Another perception is that temperature rise and drop in UFSW is sharp, while in FSW, it is continuous, and this can be attribute to the fact that heat transfer rate within in workpiece in water is lower due to water cooling, so temperature is not ascending till apparatus is close to the thermocouples. When the tool comes close to thermocouples, sharp ascent in temperature is observed because of boiling water close to the tool.

5 Conclusions

- The temperature at different locations is predicted using finite element simulation, and it is experimentally validated. The outcomes of simulation results are in occurrence with the experimental results.
- The maximum peak temperature of FSW joint is significantly higher than the UFSW joints.

- For FSW and UFSW the duration of time required for both was found to be approximately similar for reaching peak temperature.
- The heat-affected zone for UFSW is narrow compared to FSW.
- The temperature rise and drop of FSW is found as gradual, while for UFSW, it is observed as sharp.

Some of the future suggestions may be joining of dissimilar material combination using UFSW, development of computational and analytical model for understanding the material flow, evaluation of fracture toughness and corrosion, joining of thick plates using UFSW, etc.

References

1. Wahid, M. A., Khan, Z. A., & Siddiquee, A. N. (2018). Review on underwater friction stir welding: A variant of friction stir welding with great potential of improving joint properties. *Transactions of Nonferrous Metals Society of China, 28*(2), 193–219.
2. Goel, P., Khan, N. Z., Khan, Z. A., Ahmari, A., Gangil, N., & Abidi, M. H., et al. (2019). Investigation on material mixing during FSW of AA7475 to AISI304. *Materials and Manufacturing Processes, 34,* 192–200.
3. Lienert, T. J., Stellwag, W. L., Grimmett, B. B., & Warke, R. W. (2003). Friction stir welding studies on mild steel. *Welding Journal, 82*(1), 1S–9S.
4. Goel, P., Mohd, A. W., Sharma, N., Siddiquee, A. N., & Khan, Z. A. (2019). Effects of welding parameters in friction stir welding of stainless steel and aluminum. In K. Shanker, R. Shankar, R. Sindhwani (Eds.), CONFERENCE 2018, FLAME, *Advances in industrial and production engineering. Lecture notes in mechanical engineering* (pp. 815–823). Springer, Singapore.
5. Wang, K., Wu, J., & Wang, W., et al. (2012). Underwater friction stir welding of ultrafine grained 2017 aluminum alloy. *Journal of Central South University, 19*, 2081–2085. https://doi.org/10.1007/s11771-012-1248-2.
6. Liu, H. J., Zhang, H. J., Huang, Y., & L. (2009). Mechanical properties of underwater friction stir welded 2219 aluminum alloy. *Transactions of Nonferrous Metals Society of China 20*, 1387–1391.
7. Wahid, M. A., Sharma, N., Goel, P., Khan, Z. A., & Siddiquee, A. N. (2019). Temperature and traverse force analysis during underwater friction stir welding. In A. Prasad., S. Gupta., R. Tyagi (Eds.), CONFERENCE 2018, FLAME, *Advances in engineering design. Lecture notes in mechanical engineering* (pp. 41–49). Springer, Singapore.
8. Fratini, L., Buffa, G., & Shivpuri, R. (2010). Mechanical and metallurgical effects of in process cooling during friction stir welding of AA7075–T6 butt joints. *Acta Materialia, 58,* 2056–2067.
9. Zhang, H. J., Liu, H. J., & Yu, L. (2011). Effect of water cooling on the performances of friction stir welding heat- zone. *JMEPEG, 21,* 1182–1187.
10. Benavides, S., Li, Y., Murr, L. E., Brown, D., & McClure, J. C. (1998). Low temperature friction-stir welding of 2024 aluminum. *Scripta Materialia, 41,* 809–815.
11. Benavides, S., Li, Y., & Murr, L. E., et al. (1998). Low-temperature friction-stir welding of 2024 aluminum. *Scripta Materialia, 41*(8), 809–815.
12. Zhang, H. J., Liu, H. J., & Yu, L. (2013). Thermal modeling of underwater friction stir welding of high strength aluminum alloy. *Transactions of Nonferrous Metals Society of China, 23,* 1114–1122.
13. Zhu, X. K., & Chao, Y. J. (2004). Numerical simulation of transient temperature and residual stresses in friction stir welding of 304L stainless steel. *Journal of Materials Processing Technology, 146*(2), 263–272.

14. Chao, Y. J., & Qi, X. (1998). Thermal and thermo-mechanical modeling offriction stir welding of aluminum alloy 6061-T6 [J]. *Journal of Materials Processing and Manufacturing Science, 7*(2), 215233.
15. Chao, Y. J., Qi, X., & Tang, W. (2003). Heat transfer in friction stir welding-Experimental and numerical studies. *Journal of Manufacturing Science and Engineering-Transactions of the ASME, 125*(1), 138–145.

Hybrid Metal Matrix Composite Development by Stir Casting and Environmental Concerns

Gurpreet Singh Matharou and Basanta Kumar Bhuyan

Abstract In the last few decades, the demand for composite materials is on increasing trend. As an engineering supply material, the composites have already been replacing iron/bronze-based alloys. A composite material, generally has two or more, different materials with entire different compositions in terms of physical and chemical characteristics. By suitable mixing methods such as open and closed molding, cast molding produces a new material with characteristics entire different from the parent materials. Around fifty thousand different materials are available to today's engineers, which needs to be explored. Such new composites because of their advantageous position in terms of strength, hardness, weight, etc., find considerable demand in today's automobile, aeronautical, and other mechanical sectors. This paper addresses the detailed development stages of Al 6063-10%w SiC-5%w B_4C with 1%w of Mg hybrid metal matrix composite (HMMC) through stir casting route. During stir casting process, the melting action of material emits out certain gases and residual apart from the required composite. The residuals have certain environmental concerns, which need to be addressed, since some of the gases and solid waste can cause adverse affects to the environment in terms of air and soil pollution. The severe affects have been addressed of such residuals on the environment.

Keywords Hybrid metal matrix composite (HMMC) · Stir casting · Silicon carbide · Boron carbide · Composite materials

1 Introduction

In the last few years, the demand for metal matrix is on a rise. The demand for new composites materials as new composites has got high specific properties. Hybrid metal matrix composites (HMMCs) are a type of composite materials in which a

G. S. Matharou (✉) · B. K. Bhuyan
Mechanical Engineering Department, FET- MRIIRS, Faridabad, India
e-mail: gsmatharou1@gmail.com

B. K. Bhuyan
e-mail: bkbhuyan.fet@mriu.edu.in

parent material is in major matrix form and reinforcement/s are being added into it to improve its mechanical and thermal properties. Short fibers, particulates, and whiskers are the form of reinforcements which can be added to the main metal. HMMC's are the composite materials that are generally composed of two phases, matrix, and dispersed phase. They generally have better strength, wear resistance, and damping capacity as compared to alloys without the reinforcement materials. The reinforcement material is embedded into the matrix. It has been observed during composite development that right selection of parent material to be made along with reinforcement materials with correct %weight of each constituent. A slight change in % content drastically affects the properties of a new composite. Nowadays, different techniques have been developed to develop HMMC's out of which stir casting process is the most used technique due to its cost-effectiveness and simpler operation. Stir casting is a method in which the parent material is heated to its melted, and reinforcements are being added manually and mechanical stirring operation is being performed. The consistency needs to be of top order. The mixture was then poured into dies and the molten composite was left to solidify.

2   Stir Casting Method

In this method, a crucible made generally of ceramic or graphite is being used to melt the parent metal in a furnace. A motorized stirrer with graphite impeller, rotation speed of around 150–800 rpm is being employed generally to agitate the melt occasionally. The reinforcement materials need to be preheated so as to remove the moisture contents, which helps in wettability during stirring. Sable [1] had suggested a maximum limit of 30% of reinforcement for stable composites. During stir casting, non-homogeneous mixture formation has been a concern; this tendency is because of improper segregation of reinforcement due to improper process parameters (rotation of stirrer, angle of stirring application, condition of wetting, density, etc.) steps followed. The material properties also have been reported to alter the quality of the homogeneous mixture.

In stir casting method, the main metal matrix is melted to achieve molten state by heating it above to its liquid temperature. The preheated reinforcement materials were added slowly to it as semi-solid state is being achieved. Again the entire mix was heated to achieve molten state and in between stirring is being done so that the best possible consistency can be achieved. The efficiency of stir casting procedure largely depends on the following three characteristics.

2.1   Stirring Speed

It has been addressed by several authors that uniform distribution of the reinforcement materials in the parent metal is essential for the improvement in the properties of the

HMMCs like stiffness, toughness, tensile strength, etc. The stirrer with low rpm has been reported to apply ineffective shearing force on the main metal matrix leaving no space for reinforcement materials to uniformly distribute in it [2]. At slow rpm of mixing, cluster formation and agglomeration tendency have been reported. The stirrer is used at high rpm considerable and helps in formation of required composite, since at high rpm, the shear force helps the reinforced material to get the passage inside the metal matrix dispersed phase and get bonding action with metal matrix deep inside it, thereby creating a consistent mixture [2]. It has been also reported that at increased stirrer speed, porosity tendency can be increased since there had been chances of gas particles to move inside the matrix.

2.2 Stirring Duration

Stirring time also affects the distribution of dispersion into the metal matrix [5]. Clustering of the material has been observed at lower stirring time and also non-uniform mixture with fewer inclusions of reinforcement materials.

2.3 Stirring Temperature

With increase in temperature of the matrix metal, the viscosity was found to decrease causing effect in the reinforcement materials distribution. In addition, the chemical reaction was also reported to increase with increase in temperature of the molten material [5].

3 Metal Matrix and Reinforcements

HMMC (AL-10SiC-5B$_4$C-1 Mg) consists of 84%(wt) Aluminum 6063, SiC of micron size 45 μm in 10%(wt), B$_4$C of micron size 52 μm in 5%(wt), and Mg in 1%(wt).

3.1 Metal Matrix Aluminum-6063

Aluminum 6063 is fairly durable and is moderately strong. It is widely used as a general purpose alloy for many engineering purposes [3, 6]. It has been reported to have usage in automobile sector covering junction box, gear boxes, and tooling industry. Both types of thin and thick castings can be formed from aluminum castings (Table 1).

Table 1 Thermal properties of Al-6063

Coefficient of thermal expansion (per °C)	0.000022
Thermal conductivity (cal/cm^2/cm/celcius at 25 °C)	0.285
Electrical conductivity (% copper standard at 20 °C)	33
Density (g/cm^3)	2.65
Freezing range (°C) approx	625–525

Table 2 Physical properties of B$_4$C

Properties	Value
Melting point (K)	2783
Density (g/cm$^{3)}$	2.55
Thermal conductivity (W/mk)	17–42

Table 3 Physical properties of SiC

Properties	Value
Coefficient of thermal expansion °C	4
Specific heat J/Kg	750
Thermal conductivity (W/mk)	120

3.2 Reinforcement Material/s

Boron carbide (B$_4$C) is one of the toughest materials available. Above 1250 °C, it has been reported to be harder than cubic boron nitride and diamond. (Table 2) B$_4$C ceramics have mechanical properties in contrast to those of SiC ceramics but have even greater wear resistance.

Silicon carbide (SiC) is composed of tetrahedra of silicon and carbon atoms with strong bonds in the crystal lattice. The SiC material has less thermal expansion, high strength, and thermal conductivity of higher order and has been reported to have thermal shock resistant (Table 3).

4 HMMC Development

The stir casting setup used for fabricating Al-10% SiC-5% B$_4$C-1% Mg is shown in Fig. 1. It consists of furnace with temperature range up to 1400 °C for heating the materials, mechanical stirrer and motor for mixing of materials in a graphite crucible [4–6].

Wt measurement of the constituents is done using electronic balancer (Fig. 2). The silicon carbide and boron carbide particles were preheated at 850–900 °C so as to remove any traces of moisture and oxidizes their surface forming silicon oxide (SiO$_2$) layer. This layer improves the wettability of the composite [7–12].

Fig. 1 Electric furnace (up to 1400 °C)

Fig. 2 Digital weight balancer (0–500 gm)
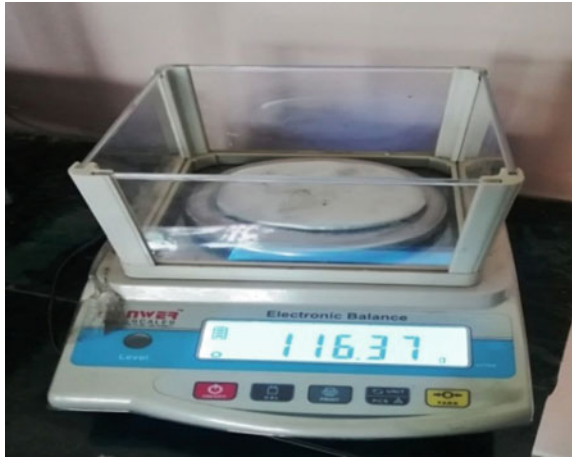
Al 6063 billets were taken into fresh crucible and furnace was switched on till a uniform temperature of 700–750 °C was attained. The flux is being added to the alloy to prevent oxidation [13] (Fig. 3).

The molten metal was then cooled naturally to semi-solid state at around 550–600 °C and slowly preheated SiC and B_4C were added to the melt in fragments and mechanical stirring was being done (Fig. 4).

Less than 1% wt of magnesium (Mg) was also added to improve wettability of the mixture [14]. The mixture was then stirred for 5 min continuously and the consistent mixture was poured into the die (Fig. 5).

The solidified HMMC bar is taken out from the die and is processed and cut into suitable identical pieces (50 × 20 × 10 mm) further for the experimentation on Electro Discharge Machine. The properties of the developed HMMC are shown in Table 4.

Fig. 3 Aluminum billets melting in furnace

Fig. 4 Motorized stirring of HMMC

Fig. 5 Graphite die with HMMC brick

Table 4 Physical properties of developed HMMC

Hybrid metal matrix composite material	Tensile strength (N/mm^2)	Yield strength (N/mm^2)	Density (Kg/m^3)	Brinell hardness (HB)	Break load (KN)
84wt% Al–10wt% SiC–5 wt% B_4C	120.32	98.75	2537.5	71.58	9.45
	Maximum displacement (mm)	Elongation (%)	Flexural break load (KN)	Flexural maximum deflection (mm)	Flexural strength (MPa)
	9.7	7.53	3.68	5.6	214.12

5 Environmental Concerns

The stir casting process requires melting the metal at around 800–1000 °C. The metal matrix used is Aluminum 6063 with boron carbide (B_4C) and silicon carbide (SiC) as reinforced materials. The melting action develops certain unwanted gases and residual waste which needs to be addressed. The list of some of the unwanted gases/residual waste and their affects on environment and human health are shown in Table 5 [15].

6 Conclusion

The fabrication of hybrid metal matrix composite with Aluminum 6063 as a matrix material, with silicon carbide (SiC) and boron carbide (B_4C) as reinforced materials through stir casting process has been discussed in detail. The melting action develops certain unwanted gases and residual waste has severe implications on human health and the environment. Aluminum hydroxide may cause nausea and vomiting; aluminum oxides cause toxicity; aluminum sulfate causes severe irritation to intestines and stomach; boron oxides have certain fatal consequences if exposure is chronic in nature; fly ash considerably increases the PM 2.5 and PM 10 levels; magnesium oxide causes irritation to eyes and nose. The future researches should work in the direction of reducing the pollutant formation while formation of hybrid metal matrix composites.

Table 5 List of unwanted gases/residual waste/affects on environment

Sr. no	Unwanted gases/residual waste	Environmental concerns and human health
5.1	Aluminum hydroxide	The exposure of aluminum hydroxide may cause repulsion, vomiting, hyperacidity, pungency, low blood phosphates (hypophosphatemia), distaste, causticity leading to bowel obstruction, and fecal impaction [16]
5.2	Aluminum oxides	Indicative toxicity has been reported, followed by chronic inhalation of the aluminum oxides. Long-term aluminum oxide inhalation may cause pneumoconiosis with cold and exertion and a restrictive pattern of rib cage function. In severe cases, death has been reported due to respiratory failure [17]
5.3	Aluminum sulfates	Eating or gulping aluminum sulfate produces serious disturbance to the digestive organs and stomach. An influenced individual may encounter retching, queasiness, and the runs, adding water to aluminum sulfate can make sulfuric acid structure. The sulfuric acid may cause soil damage by reducing its constituents
5.4	Boron oxides	1. Acute health effects the following short-term health effects may occur immediately after exposure to boron oxide. Contacts can aggravate the skin and eyes. Breathing in boron oxide can bother the nose and throat causing hacking and wheezing. Introduction to boron oxide may cause heaving wooziness, cerebral pain, sickness, and so forth
		2. Chronic health effects the accompanying long haul well-being influences may happen after some time getting introduction to boron oxide and can keep going for months to years [16]. Boron oxide may make permanent damage to kidney and livers
5.5	Silicon dioxide	Silicon dioxide exists naturally on earth and on our bodies. No evidence has been reported to advocate its implication on human health, but more research is required to ascertain its role on the body. Inhalation of silica dust may cause diseases related to breathing. [15]
5.6	Fly ash particles	It can get placed in the deepest part of the lungs, where they may cause asthmatic attack, inflammation, and immunological reactions. They contribute to particulate matter 2.5 and 10 [15]

(continued)

Table 5 (continued)

Sr. no	Unwanted gases/residual waste	Environmental concerns and human health
5.7	Magnesium oxide	Breathing magnesium oxide can cause irritation to both eyes and nose. Exposure to magnesium oxide can cause "metal fume fever." A symptom in which the patent has got metallic taste in the throat with headache, sneezing symptoms, and cold symptoms [17, 18]

References

1. Sable, A. D., & Deshmukh, S. D. (2012). Preparation of MMCs By stir casting method. *IJMET, 2*(5), 16–21.
2. Aqida, S. N., Ghazali, M. I., & Hashim, J. (2014). The effects of stirring speed and reinforcement particles on porosity formation in cast MMC. *International Journal of Modern Manufacturing, 1*(6), 124–128.
3. Kumar, Rajesh, & Parshuram, M. (2013). Preparation of aluminum matrix composite by using stir casting method. *IJEAT, 3,* 56–62.
4. Hashim, J., & Looney, L. (1999). Metal matrix composites: Production by the stir casting method. IJEAT.
5. Mathur, S., & Barnawal, A. (2013). Effect of process parameter of stir casting on metal matrix composites. *International Journal of Science and Research 2*(12), 395–398.
6. Clyne, T. W., & Withers, P. J. (2010). *An introduction to metal matrix composites* (1st ed.). Cambridge: Cambridge University Press.
7. Bhuyan, B. K. , Gupta L., & Garg C. (2020) Design and development of tabletop electrochemical grinding setup *Materials Today: Proceedings*, *21*(3) , 1479–1482 (SCOPUS, Published by Elsevier, UK and ISSN: 2214-7853)
8. Khattri, K., Choudhary, G., Bhuyan, B. K., & Solekar, A. (2018). A review on parametric analysis of magnetic abrasive machining process. *Materials Science and Engineering*, *330*, 1–9. (SCOPUS, Published by IOP Science, UK and ISSN: 1757-899X)
9. Bhuyan, B. K., Bhuyan, P., & Mishra, S. (2020). Modeling and response optimization of traveling wire electro-chemical spark machining of borosilicate glass using hybrid approach. *Journal of Advanced Manufacturing Systems*, *19*(3), 425–447. (SCOPUS, WoS Published by World Scientific, Singapore and ISSN: 1793-6896)
10. Bansal, A., Gupta, S., & Bhuyan, B. K. (2019). A review on wear behavior of cutting tools during machining of inconel, nimonic, and hastelloy. *Indian Journal of Science and Technology*, *12*(41), 1–8. (SCOPUS, WoS, EBSCO and ISSN: 0974-5645)
11. Sharma, B. P., Junaid, M., Akhil, D., Rao, G. S., & Vates, U. K. (2019). Mechanical behavior of stir-casted Al + ZrB2 + Al2O3 metal matrix composites. In *Advances in interdisciplinary engineering. Lecture notes in mechanical engineering*. Springer, Singapore, pp. 71–77. Print ISBN: 978-981-13-6576-8, Online ISBN: 978-981-13-6577-5. https://doi.org/10.1007/978-981-13-6577-5_8.
12. Sharma, B. P., Rao, G. S., & Vates, U. K. (2019). Powder metallurgy processing and mechanical characterization of iron-based composite reinforced with alumina and zirconium diboride. In *Advances in industrial and production engineering. Lecture notes in mechanical engineering*. Springer, Singapore, pp. 303–308. Print ISBN: 978-981-13-6411-2, Online ISBN: 978-981-13-6412-9. https://doi.org/10.1007/978-981-13-6412-9_28.
13. Bodukuri, A. K., Eswaraiah, K., Rajendar, K., & Sampath, K. (2016). Fabrication of Al–SiC–B4C metal matrix composite by powder metallurgy technique and evaluating mechanical properties. *Perspectives on Science, 8,* 428–431.

14. Bains, P. S., Sidhu, S. S., & Payal, H. S. (2016). Fabrication and machining of metal matrix composites: A review. *Materials and Manufacturing Processes, 31*(5), 553–573.
15. Gopalakannan, S., Senthilvelan, T., & Ranganathan, S. (2012). Modeling and optimization of EDM process parameters on machining of Al7075-B4C MMC using RSM. *Procedia Engineering, 38,* 685–690.
16. Bahrami, A., Soltani, N., Pech-Canul, M. I., & Gutiérrez, C. A. (2015). Development of metal-matrix composites from industrial/agricultural waste materials and their derivatives. *Critical Reviews in Environmental Science and Technology, 46*(2), 143–208.
17. Oxide (2009). *Hazardous Substance Fact Sheet Synonyms, Boric Anhydride*; Diboron Trioxide Chemical Name: Boron Oxide (B_2O_3) BORON OXIDE, 1–800.
18. New Jersey Department of Health and Senior Services (2007). "Magnesium Oxide Hazard Summary," no. January 2007.

Mechanical, Chemical and Thermal Recycling of Bio-Composites: A Review

Partha Pratim Das and **Vijay Chaudhary**

Abstract In a wide variety of uses, such as the automobile, aerospace and renewable energy industries, composite materials are used. But due to their inherent nature of heterogeneity, they were not properly recycled, especially for the polymer composites based on thermosets. The current and future legislation on waste management and the environment mandates that all engineering materials from end-of-life (EOL) items such as cars, wind turbines and aircraft be adequately recovered and recycled. Ultimately, recycling can lead to a saving of money and electricity. Various technologies have been developed, mainly based on fiber reinforcement and yet to be commercialized: mechanical recycling, chemical and thermal treatment. It is anticipated that new separation and recycling technologies for composite materials recycling will be available through collaborative efforts from design, manufacturing and end-of-life management, and that more easily recyclable composite materials will be produced in the future. A thorough analysis of the different methods of reuse of bio-composites is addressed in this paper.

Keywords Polymer composites · Reuse · Recycling · Renewable · Bio-composites

1 Introduction

In recent decades, enormous changes have been uncovered on the planet as far as the use of materials in different fields, transformations grumbled so uncommon necessities of pinnacle regions and progressively enhanced prerequisites identified with shopper product generation and also not least usually all ecological necessities [1]. Composite materials are widely considered materials designed [2] that can replace non-ferrous or iron oxide materials. There in an alternative option in manufacturing industry, polymer composite materials are of potentially huge interest, for

P. P. Das (✉) · V. Chaudhary
Department of Mechanical Engineering, Amity University Uttar Pradesh, Noida 201313, India
e-mail: das1.parthapratim@gmail.com

V. Chaudhary
e-mail: vijaychaudhary111@gmail.com

example, electrical designing, hardware, building and structural building, rail, street and marine, aviation strategy and aeronautical and so on [3]. Composite materials consist of reinforcement material (glass fiber, carbon fiber, Kevlar, etc.) and a frame (polyester gum, epoxy sapphire, etc.). Fiber glass is the reinforcement materials that are used most. They have several attributes: high elasticity, high synthetic reinforcement, minimum effort. In order to achieve minimal cost or to offer high properties to a composite, we can understand for a material to help the framework, such as: coupling operators, impetus, colors and agents to accelerate [4]. The potential and reuse of waste composite materials are a major issue we see these days. Composite parts can very well be seen in the use and composite waste occurred due to multiple forms of generation that consume impressive capacity fields. Over time the processing of such materials will trigger the assembling organizations' significant problems. Since the enthusiasm for recreating or reusing answers is exceptionally low, the set of composite materials wasting in time is extremely noteworthy [5]. We can acquire a wealthy material in glass fiber by squandering the composite materials. Thus, a truly important fortification can be embedded in different materials or used for the acquisition of polymer reinforced materials. The recuperation and reusing of polymeric composite materials have encountered a significant worry in the most recent years. Examines committed to innovations for reusing composite materials were started and did by various researchers, [6]. Mixtures of cement with sand and wasted fiberglass are classified [7].

2 Recycling of Bio-Composites

Automotive and electrical and electronics projects are the main source of polymer composite waste sources, and the composites of waste have interesting monetary incentives for reuse. Over the past two decades, a wide range of reusing procedures were adopted: mechanical (mostly granulating), pyrolysis and other warm procedures, and solvolysis. Some of them, especially pyrolysis have even reached a technical scale and are exploited industrially: for example, in the UK, ELG Carbon Fiber Ltd. (ELGCF) used pyrolysis, in the USA, Adherent Technologies Inc. (ATI) [8] used a wet compound breakdown of composite lattice gums to recover fibrous gums. Pyrolysis is the most boundless invention in the material market, since it is a demonstrated and widely used technique. Nevertheless, as the fibers degrade at high temperatures, forms of solvolysis have attracted increased interest, particularly over the last decade. Despite the fact that the main recycling method developed for plastics as shown in Fig. 1, the procedures which are presently practicable for polymer composites are restricted to the recovery of materials by chemical forms, the mixture of regrind during compounding and the rehabilitation of vitality through incineration [9].
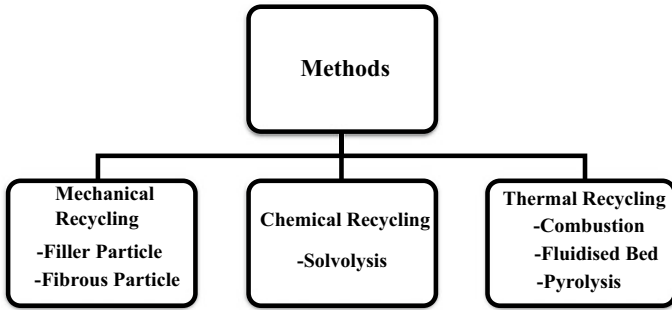
Fig. 1 Various recycling methods

2.1 Recycling Through Mechanical Process

Usually known as physical recycling, this recycling technique is one of the most commonly used reuse techniques for fiber-reinforced polymer composites. Mechanical recycling is the most common process for recycling plastic waste [10]. In this technique, the composites of polymers are grounded, reprocessed and compounded to create another item or rough material to supply another item indicated for the similar or other use [11]. This procedure involves various steps, starting with the underlying decrease in piece measurement through a devastating procedure is illustrated in Fig. 2. The procedure involves the use of a low-speed slicing or pulverizing plant to lower the larger material into smaller parts in the range of 50–100 mm [12]. The reduction in size evacuates the metal parts contained in the composites and, if necessary, assists transport. The subsequent stage of mechanical reuse is a further reduction in size using a sled plant or other strong factories, whereby the products are further squashed into better pieces. The last advance involves ordering the corresponding recycling components in various tests based on their own sizes utilizing violent winds and strainers. Now and then chip recyclates are even gotten. Mechanical reuse approaches are best suited if the composite waste materials are decently good and unpolluted, even though their origin is known. By and relatively wide, there is a greater scope for reuse among the distinctive types of recycled, powdered and stringy recycled compared to different types of recyclates [12]. Those reflect the fact they cannot be reused in thermoset mixes due to the low mechanical consistency due to the lower thickness of powdered recyclates. Meanwhile, making a bond with the polymer is troublesome for stringy recyclates, and the larger size of recyclates includes pressure and goes about as locations for starting disappointment. Even stringy recyclates do not perform well in this way as equivalent reinforced materials to the raw materials.

Rowell et al. [13] examined the recyclability of polypropylene composites reinforced with jute and found that during nine reprocessing attempts, the tensile and flexural capacities were substantially improved. Most of the polymeric materials currently in use are thermoplastics; this term involves plastics that melt and flow

Collection

↓

Manual sorting

↓

Baling

↓

Crushing

↓

Washing

↓

Regeneration

↓

Semi-finite Products

↓

End Products

Fig. 2 Steps involved in mechanical recycling
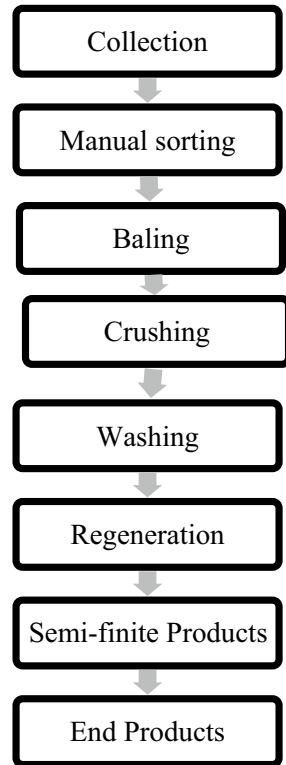
while molding or controlling the temperature and pressure. According to Luz et al. [14], the use of an additive preserved or even improved the tensile strength of the original composite compared to that of the non-additive recycled material. Importantly, a high-intensity thermo-kinetic mixer was used to subject these reprocessed composites to further mixing. Although this process typically results in excessive breakdown and thermal degradation, the use of additives prevented these outcomes. Figure 2 shows the steps involved in mechanical recycling process.

2.2 Recycling Through Chemical Process

Chemical recycling, also referred to as feedstock recycling, is characterized as the procedure aimed at chemical debasement of polymer leftovers into their monomers or other essential synthetic compounds.

The results of this procedure could be reprocessed in the petroleum enterprises as crude materials for all the generation of new polymers or for the creation of various synthetic compounds or as an elective fuel. Synthetic recyclables are considered to stand out as one of the most prudent forms of reuse of superior composites [15]. This

method may be used as low-sub-atomic volume hydrocarbons to separate the polymer from important filaments. These filaments can be reused as filler material for other plastic structures, and the hydrocarbons can be reused as synthetic or energizing compounds. The synthetic reuse method will reuse completely different types of polymer composite materials in a theoretical and monetary way [16]. There is only one restriction related to this reusing procedure, i.e., it also can cause water and air contamination across the board which is an unsafe well-being hazard to the devoted people who reuse such items. The chemical recycling process (solvolysis) for CF-reinforced composites was investigated by Hernanz et al. [17] using alcohols as reactive extraction medium. EP was weakened in the presence of this solution and CFs were collected at 85–99% of strength compared to virgin fibers. Pimenta et al. [18] studied the current state of CF-reinforced polymer recycling methods, focusing on processes for fiber recovery and re-manufacturing, including marketing and future recycled product applications. Fundamentally, it is used to depolymerize build-up polymers, such as PET, PA, PMMA and PC, and certain expansion polymers, such as polyurethanes, into oligomers and unique monomers that could then be depolymerized into raw materials. Figure 3 shows the steps involved in chemical recycling.

Low temperature chemical recycling or solvolysis occurs under normal atmospheric pressure, at less than 200 °C. Acid or other solvents are used to break down

Fig. 3 Steps involved in chemical recycling
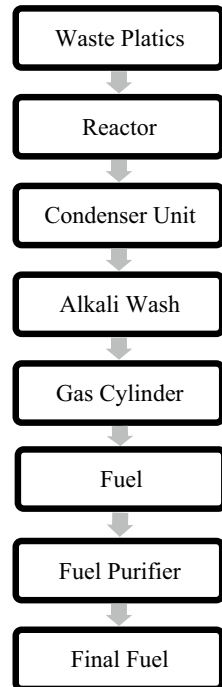
the chemical bonds that make up the polymer matrix [19]. In acid solvolysis, pre-treatment must be used to accelerate the process of breakdown of the polymer's chemical chain, particularly in the processing of FRP, which consists of many laminas, so it is easier to split up. Eight-layer FRP waste, for example, can be recycled within an hour if pre-treatment has been applied, in which 15 h of recycling is required [20]. The reuse of feedstock is connected to the polymer system and it can be isolated onto four classifications: solvolysis, oxidative processes, thermal decomposition and comparative forms of warm deterioration and reduction. Solvolysis is a conventional term that includes glycolysis, methanolysis, alcoholysis, ammonolysis and hydrolysis for dissolvable responses.

Based on their chemical composition the consistency of the recycled glass fibers used in this study differed from one another. The consistency of the recycled fibers is determined by the amount of soluble compounds that they produce in the solvolysis material. Fibers that contain more soluble Al_2O_3 and CaO compounds lose 60% of their initial weight over a long period of time [21]. Use a broad range of temperatures from 230 to 500 °C [22], the chemical FRP waste processing methods with supercritical gas, applied to different liquids have been studied in general.

Many liquids, such as methanol, ethanol, propanol, acetone or glycol, are used as catalysts for supercritical water solvolysis and are also used as key substances for supercritical solvolysis. In several studies [23], in which these fluids were used as the main solvolysis material, very good results were obtained in terms of the consistency of recycled fibers, both carbon and glass fiber.

2.3 Recycling Through Thermal Process

Thermal processing can be assembled into three forms: combustion, pyrolysis with a fluidized bed and pyrolysis. These three methodologies emphasize the recovery of a wide spectrum of strands, fillers and various enhancements to the disadvantage of the significant system. This is in view of the fact that the polymer cross section in all of these methodologies is volatilized into polymers and gas of low atomic weight, such as greenhouse gases, hydrogen, methane and an oil element. Depending on the structure of the polymer's sub-nuclear heap, the method's working temperature occurs within 450–700 °C zone [24]. Polymers, for example, prefer lower temperatures for polyester tars, whereas epoxies or thermoplastics are operated at elevated temperatures. In solid stoves, where the polymer composite wastes are converted to relative unimportance and other unrefined materials (fillers and strands) for solid formation, high temperature preparation is done to a large extent.

Decomposing resin using optimal thermal conditions is not as effective for GF as CF, but recycled glass fiber (rGF) post-chemical treatments help to some degree to restore their properties [25]. Like CF, GF thermal recycling in high-heat operating conditions (300–600 °C) decreases the strength of the resulting GF by up to 80% and is difficult to reuse due to its low capacity for reinforcement [26]. Only 10% of the fuel commitment to a bonding stove can be replaced with polymer composites reinforced

Table 1 Summary of the three recycling methods

Methods	Advantages	Challenges	References
Mechanical recycling	Cost effective, effective and well known	Deterioration of products properties, pre-treatment	[29]
Chemical recycling	Operation of PET, i.e., (polyethylene terephthalate), simple technology	Mainly limited to condensation polymers	[29, 31]
Thermal recycling	Generates considerable amount of energy from polymers	Not ecological acceptable	[30]

with glass filaments in any case. The advantage of warm reuse procedures over reuse via chemical means is that the former is tolerant of more contaminated material scarp. Shi et al. [27] researched the mechanical properties of rCF using pyrolysis under superheated steam. They found that the recycled fibers had a significant amount of char on the surface of the rCF which prevented the fibers from being fully reusable.

In an effort to preserve optimum tensile strength in recycled fibers, Ye et al. [28] produced an optimized method of steam thermolysis combining vacuum pyrolysis with mild gasification to recycle CFRP waste. In laboratory and semi-industry scales, the device maintained 90% of tensile power (Table 1) [29–30].

3   Conclusions

In the present study, a dense review is done on various recycling method used for bio-composites. The following conclusions are made from the review study are:

- Various methods are adopted for recycling of bio-composites, viz: mechanical, chemical and thermal recycling routes.
- The trash of polymer composite is viewed to be an important end-of-life waste disposal approach for scarp plastic products.
- The recovery fiber is one of important tasks of all too many studies within this area. Chemical recycle offers the best maximum performance fibers (relative to pure material) among the three major types of recycling processes.
- Mechanical recycling provides the high-strength fibers, then followed by recycling route thermal processes.
- It has also been observed that heat energy and economic research of bio-composite recycling deserve much serious attention to hold a greater value.
- Among the following recycling approaches, chemical recycling is the only technique suitable under the principles of sustainable growth, as this approach contributes to the development of the polymer monomers.
- The primary goal of most studies in this field of recycling is fiber recovery.

References

1. Das, P. P., & Chaudhary, V. (2020). Tribological and dynamic mechanical analysis of bio-composites: A review. *Materials Today: Proceedings, 25,* 729–734.
2. Chaudhary, V., Rajput, A. K., & Bajpai, P. K. (2017). Effect of particulate filler on mechanical properties of polyester based composites. *Materials Today: Proceedings, 4*(9), 9893–9897.
3. Ribeiro, M. C. S., Fiúza, A., Ferreira, A., Dinis, M. D. L., Meira Castro, A. C., Meixedo, J. P., et al. (2016). Recycling approach towards sustainability advance of composite materials' industry. *Recycling, 1*(1), 178–193.
4. Bourmaud, A., Duigou, A. L., & Baley, C. (2011). What is the technical and environmental interest in reusing a recycled polypropylene/ hemp fiber composite? *Polymer Degradation & Stability.*, *96*(10), 1732–1739. https://doi.org/10.1016/j.polymdegradstab.2011.08.003.
5. Faruk, O., Bledzki, A. K., Fink, H. P., & Sain, M. (2012). Biocomposites reinforced with natural fibers: 2000–2010. *Progress in Polymer Science, 37*(11), 1552–1596.
6. Faruk, O., Bledzki, A. K., Fink, H. P., & Sain, M. (2012). Biocomposites reinforced with natural fibers: 2000–2010. *Progress in Polymer Science*, *37*, 1552–1596.
7. Barbero, E. J. (1998). *Introduction to Composite Materials Design* (336 p.). USA: West Virginia University. ISBN 97e8-1-4200-7915-9.
8. Liu, Y., Meng, L., Huang, Y., & Du, J. (2004). Recycling of carbon/epoxy composites. *Journal of Applied Polymer Science, 94*(5), 1912–1916.
9. Piñero-Hernanz, R., Dodds, C., Hyde, J., García-Serna, J., Poliakoff, M., Lester, E., et al. (2008). Chemical recycling of carbon fibre reinforced composites in nearcritical and supercritical water. *Composites Part A Applied Science and Manufacturing, 39*(3), 454–461.
10. Arvanitoyannis, I. S., & Bosnea, L. A. (2001). Recycling of polymeric materials used for food packaging: current status and perspectives. *Food Reviews International*, *17*, 291–346.
11. Henshaw, J. M., Han, W., & Owens, A. D. (1996). An overview of recycling issues for composite materials. *Journal of Thermoplastic Composite Materials, 9,* 4–20.
12. Akesson, D., Fuchs, T., Stoss, M., Root, A., Stenvall, E., & Skrifvars, M. (2016). Recycling of wood fiber-reinforced HDPE by multiple reprocessing. *Journal of Applied Polymer Science, 133.*
13. Rowell, R. M., Sanadi, A. R., Caulfield, D. F., & Jacobson, R. E. (1997). Utilization of natural composites: problems and opportunities. In A. L. Leão, F. X. Carvalho, & E. Frollini (Eds.), *Lignocellulosic: plastics composites* (pp. 23–52). São Paulo: Universidade de São Paulo.
14. Luz, S. M., Del Tio, J., Rocha, G. J. M., Gonçalves, A. R. & Del'Arco, A. P. Jr. (2008). Cellulose and cellulignin from sugarcane bagasse reinforced polypropylene composites: Effect of acetylation on mechanical and thermal properties. *Composites. Part A, Applied Science and Manufacturing, 39*(9), 1362–1369.
15. Fleischer, J., Teti, R., Lanza, G., Mativenga, P., Möhring, H.-C., & Caggiano, A. (2018). Composite materials parts manufacturing. *CIRP Annals, 67,* 603–626. https://doi.org/10.1016/j.cirp.2018.05.005.
16. Gharde, S., & Kandasubramanian, B. (2019). Mechanical, thermal and chemical recycling methodologies for the Fiber Reinforced Plastic (FRP). *Environmental Technology & Innovation*, *14*, 100311. https://doi.org/10.1016/j.eti.2019.01.005.
17. Piñero Hernanz, R., García Serna, J., Dodds, C., Hyde, J., Poliakoff, M., Cocero, M., et al. (2013). Chemical recycling of carbon fiber composites using alcohols under subcritical and supercritical conditions. *Journal of Supercritical Fluids The.* 83–92. https://doi.org/10.1016/j.supflu.2008.02.008.
18. Pimenta, S., & Pinho, S. T. (2011). Recycling carbon fiber reinforced polymers for structural applications: Technology review and market outlook. *Waste Management, 31,* 378–392.
19. Meng, F., McKechnie, J., & Pickering, S. J. (2018). An assessment of financial viability of recycled carbon fiber in automotive applications. *Composites Part A: Applied Science and Manufacturing, 109,* 207–220. https://doi.org/10.1016/j.compositesa.2018.03.011.

20. Pinero-Hernanz, R., Dodds, C., Hyde, J., García-Serna, J., Poliakoff, M., Lester, E., et al. (2008). Chemical recycling of carbon fiber reinforced composites in near critical and supercritical water. *Composites: Part A (Applied Science and Manufacturing), 39,* 454–461.
21. Ding, X., Ahmed, S., Bao, N., Ding, J., Liu, R., & Yi, J. (2019). Clustering-induced high magnetization in Co-doped TiO 2. *Emergent Materials, 2*(3), 295–301.
22. Fayyad, E. M., Abdullah, A. M., Hassan, M. K., Mohamed, A. M., Jarjoura, G., & Farhat, Z. (2018). Recent advances in electroless-plated Ni-P and its composites for erosion and corrosion applications: A review. *Emergent Materials, 1*(1–2), 3–24.
23. Francis, R. (2016). *Recycling of polymers: methods, characterization and applications.* Hoboken, NJ, USA: Wiley.
24. Asmatulu, E., Twomey, J., & Overcash, M. (2014). Recycling of fiber-reinforced composites and direct structural composite recycling concept. *Journal of Composite Materials, 48,* 593–608.
25. Oliveux, G., Dandy, L. O., & Leeke, G. A. (2015). Current status of recycling of fiber reinforced polymers: review of technologies, reuse and resulting properties. *Progress in Materials Science, 72,* 61–99.
26. Bachmann, J., Hidalgo, C., & Bricout, S. (2017). Environmental analysis of innovative sustainable composites with potential use in aviation sector—a life cycle assessment review. *Science China Technological Sciences, 60,* 1301–1317.
27. Shi, J., Kemmochi, K., & Bao, L. (2012). Research in recycling technology of fiber reinforced polymers for reduction of environmental load: Optimum decomposition conditions of carbon fiber reinforced polymers in the purpose of fiber reuse (Vols. 343–344, pp. 142–149). Advanced Materials Research. Switzerland: Trans Tech Publications. https://doi.org/10.4028/www.scientific.net/AMR.343-344.142.
28. Ye, S. Y., Bounaceur, A., Soudais, Y., et al. (2013). Parameter optimization of the steam thermolysis: A process to recover carbon fibers from polymer-matrix composites. *Waste Biomass Valorization, 4,* 73–86.
29. Hopewell, J., Dvorak, R., & Kosior, E. (2009). Plastics recycling: Challenges and opportunities. *Philosophical Transactions of the Royal Society B: Biological Sciences, 364,* 2115–2126.
30. Singh, N., Hui, D., Singh, R., Ahuja, I., Feo, L., & Fraternali, F. (2017). Recycling of plastic solid waste: A state of art review and future applications. *Composites Part B: Engineering, 115,* 409–422.
31. Karayannidis, G. P., & Achilias, D. S. (2007). Chemical Recycling of Poly(ethylene terephthalate). *Macromolecular Materials and Engineering, 292,* 128–146.

Testing of Material for Disc Brake Rotor

Manish Kumar Chauhan, Animesh Garg, Aditya Syal, and Manmeet Singh

Abstract The vehicle disc is part of a rear-wheel drive or suspension steering wheel while travelling at a specific speed. All considered brake rotor material is a solid metal that consumes a ton of fuel due to its high display power. The objective of this paper is to make an alternate material for disc brake rotors. Two systems for building materials were introduced, for example, cost per unit area and modern location system. Material requirements were analysed and the selected processes were combined between solid steel, aluminium amalgam, titanium mixing, dissolved creams and composites. The mechanical properties including compressive quality, adequate kicks, square coating, thermal mobility and gravity at approximately cost were used as key parameters in the material validation stages. The appraisal combined with the aluminium iron cross-component composite as the most suitable for the brake disc system.

Keywords Composite materials · Rotor disc brake · Thermal analysis

1 Introduction

In automotive applications, achieving low fuel consumption in the same way as removing ozone-damaging substances is a very important issue. To reduce car weight and improve the beauty of the area, the automotive business has expanded the use of aluminium in light vehicles from late. Aluminium blend-based iron system composites (MMCs) with the help of complex materials have shown good validation for such applications. These low-quality materials and high thermal delivery in the case

M. K. Chauhan (✉) · A. Garg · A. Syal · M. Singh
Mechanical Engineering Department, A.S.E.T, Amity University, Noida, Uttar Pradesh, India
e-mail: mkumar17@amity.edu

A. Garg
e-mail: animesh.garg2008@gmail.com

A. Syal
e-mail: syal.aditya@yahoo.in

M. Singh
e-mail: manmeetsingh.3254@gmail.com

of unreasonably high related time-consuming deductions used to hear scepticism about metals are subject to achieving 50–60% weight loss in closing instruments. In addition, these used items work better under unprecedented levels of help praying for high speed, high quality, etc., which have great potential with respect to current vehicles. Since the brake or rotor plate is an integral part from the developing point of view, the material used to move the rear parts should have reliable and strong coverage and wear areas under varying weight conditions, speed, temperature and condition are maximum [1].

There are a few elements that will be identified when designing a flat plate material. The most important idea is the importance of the brake drift material to overcome high strokes and undesirable wear [1]. Another requirement is to tolerate high temperatures designed to be lowered. The weight, the cutting process and the cost alike of those basic components should be considered over the course of the work. In the phase of optical decisions, recycling of iron is available unless CO_2 enhancement during reperfusion has to be taken into consideration. The binding circle should have enough warm care to maintain the final strength or to be separated from the warm concern until the glimmer can disperse. This is not particularly colossal at a particular stop, but it is largely due to the repeated times that arise from the values of dynamic operation. The motive behind this paper is to develop new standard materials with low-grade ceramic brake material without negative impact. In this sense, they were rearranged the four distinct nuances of the coconut fibre research area, breaking down exchange rates, thermal substances and intensive treatments using the powder metallurgy system. Properties considered being obesity, hardness, hardness, mechanical properties, adequate cargo testing, weight loss, wind testing and deterioration strength [2]. An object selection graph is a very useful tool for looking at various objects in a conceptual framework through which basic relationships can be identified between the intangible physical properties and used to derive the optical properties of a particular application for inserting the plug.

2   Material Selection Method

Only materialism has a few ways of progressing to the virtual world. The process of consolidation can be done in such a way that the general purpose in any case made by different manufacturers is often conveyed by different materials and by different collection structures. Alternatively, choosing an effective combination of item and technique are undoubtedly a quicker assignment than a small piece during the strategic planning at various stages of item verification.

2.1 Factors Affecting the Disc

The braking system is a basic security part of ground-based transportation framework along these lines the assistant materials utilized in brakes ought to have a mix of properties, for instance, extraordinary compressive quality, higher scouring coefficient, wear sheltered, lightweight, incredible warm cut-off and financially achievable [3].

2.2 General Material Performance Requirements

Disc brake accessories enable the brake force to cut the cushion brakes on the rotor mounted on the interior. The top piece of machinery for a weight room is operated by a mechanical engineer. It allows the power of small adjustable insert in the handlebar to be converted into a large grip force on the driver's seat. This large assist force compresses the rotor through material filters and passes through the control of the binding. When the maximum contact level reaches the maximum, the brake power will be transmitted. Not enough strokes can move under the type of material used for a rocket robot. Combination brakes are usually emphasized in the performance of more than one stroke or the coefficient of the scan test when the vehicle is moving.

All disc brakes structures rely upon brake cushions pushing on the different sides of a brake rotor to grow the moving obstacle and moderate the vehicle down. The proportion of frictional force is found by increment the force, driving the pad into the rotor and by the coefficient of contact of the pad.

The force moving back the brake plate or rotor is moving. The power hindering the plate is processed as,

$$F_{Rotor} = 2C_{f,Pad} \times F_{Pad} \qquad (1)$$

The slowing mechanism is a crucial security part of ground-based transportation frameworks; henceforth, the basic materials utilized in brakes ought to have forces a mix of properties, for example, great compressive strength, economically viable, wear resistant and better thermal capacity.

3 Rotor Design and Dimension

Geometric model of disc rotor is prepared on the SOLIDWORKS 2017 software (Fig. 1) and the desired dimensions were chosen for designing the rotor as shown in Table 1.

Fig. 1 Design of disc brake rotor
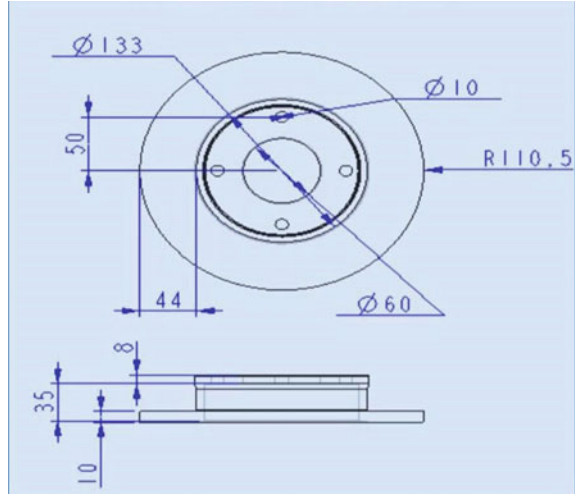
Table 1 Dimensions of rotor used

Parameter name	Parameter value
Outer diameter of the rotor disc	221 mm
Inner diameter of rotor disc	133 mm
Hole diameter	60 mm
Thickness of the rotor disc	10 mm
Calliper piston diameter	44 mm
Mass of disc	2.9 kg

Table 2 Material properties which have been synthesized

Material	Hardness (HV5)	0.2% yield strength (MPa)	UTS (MPa)	E (GPa)	EL (%)	Porosity (%)
Al-4% Cu	50.5	81	118	73.9	3.04	3.04
Al-4% Cu-6% TiC	71.7	100.6	147	89.6	2.87	3.17
Al-7% Si	59.5	114	167	78	3.03	2.01
Al-7% Si-5% Ti B2	71.12	168	189	91.3	2.68	2.13

4 Materials Selected

After studying the current materials being used for disc brake rotor, we have selected Al-Cu-TiC and Al–Si-TiB2 on basis of following properties (Table 2) [2, 4].

5 Testing of Materials

The different tests have been performed on two selected materials.

5.1 Pin on Disc Test

The pin on disc test is delineated in the figure above. The stationary pin is pressed against turning disc under the given load. The pin can be of any shape, be that as it may, the most well-known shapes are round or barrel-shaped because of simplicity of arrangement of such pins (flat pins are normally dependent upon certain misalignment which can prompt non-uniform stacking and challenges for hypothetical investigation). During the test, the frictional force, wear and temperature are persistently observed.

5.2 Scanning Electron Microscopy (SEM)

The SEM checks a drew in electron pillar over a surface to make an image. The electrons in the pole help out the example, making various signs that can be used to procure information about the surface attributes. Figure 2a and b shows the SEM results for Al-Cu-TiC and Al–Si-TiB2.

5.3 Vickers Hardness Test

The Vickers procedure relies upon an optical estimation system. The microhardness test methodology, ASTM E-384, decides an extent of light loads using a jewel indenter to make space which is then used to give hardness esteem. Figure 3a and b shows the hardness test results for Al-Cu-TiC and Al–Si-TiB$_2$, respectively.

5.4 Atomic Force Microscopy (AFM)

An atomic force microscope is a kind of high resolution examining test magnifying instrument that has a resolution that you can quantify in portions of a nanometre. Atomic force microscopy utilizes a cantilever with a sharp probe that checks the surface of the sample. Figure 4a and b shows the AFM results for Al-Cu-TiC and Al–Si-TiB2, respectively.

(a)
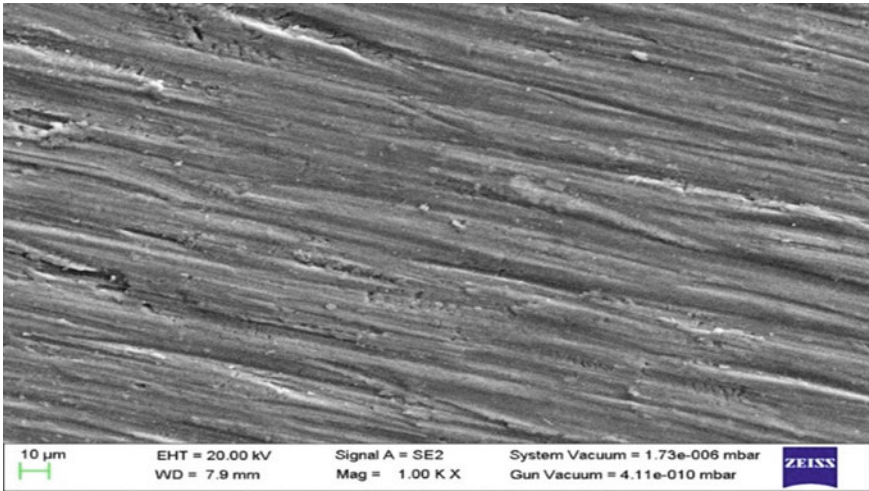
(b)
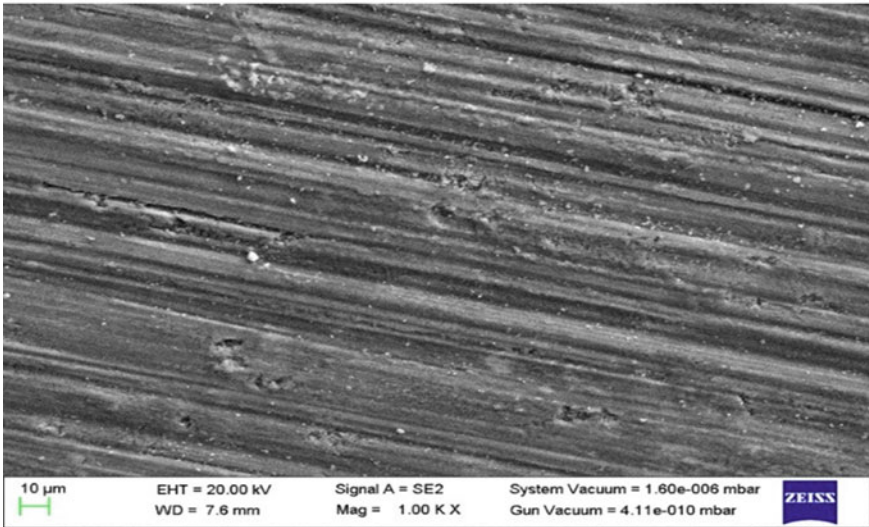
Fig. 2 **a** SEM result for Al-Cu-TiC, **b** SEM result for Al–Si-TiB$_2$

6 Results and Discussion

3-D model is prepared in SOLIDWORKS software for brake disc which is saved as IGES type file and after that it is imported in ANSYS R17.1 workbench simulation module. Virtual analysis of disc brake is performed to test the model virtually under the application of hypothetical loads and conditions. The ANSYS analysis is

(a) (b)
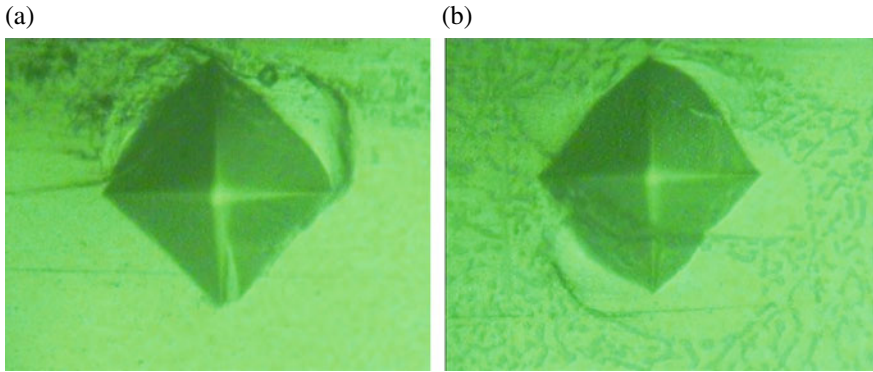
Fig. 3 **a** Hardness result for Al-Cu-TiC, **b** hardness result for Al–Si-TiB$_2$

(a) (b)
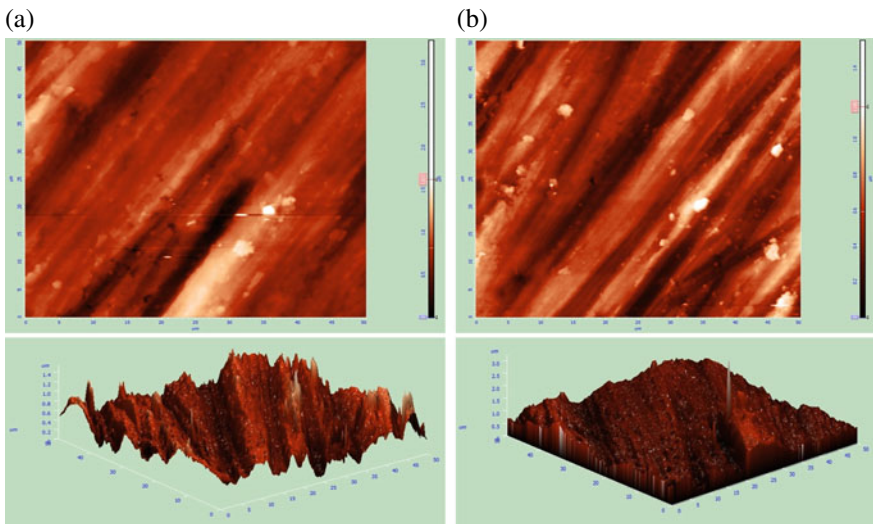
Fig. 4 **a** AFM results for Al-Cu-TiC, **b** AFM results for Al–Si-TiB$_2$

performed mainly in two divisions for analysing the characteristics of the disc brake rotor, structural and thermal [5].

6.1 Structural Analysis

Structural analysis is performed on the disc brake rotor model in a way to find out the structural characteristics and strength of the model. The analysis is performed for both the materials Al-Cu-TiC and Al–Si-Tib2. Various characteristics such as

equivalent strain, equivalent stress, max. shear and principal stress, strain energy and total deformation are analysed in the structural analysis of the disc.

6.2 Thermal Analysis

Thermal analysis is performed to observe the heat generation and check the conductivity of the desired model. Hence, thermal analysis helps in better understanding of the material characterization.

Temperature Range: In the accompanying Fig. 5a and b, red shading shows most extreme temperature and greatest temperature esteem is 65.042 °C for Al-Cu-TiC

(a)
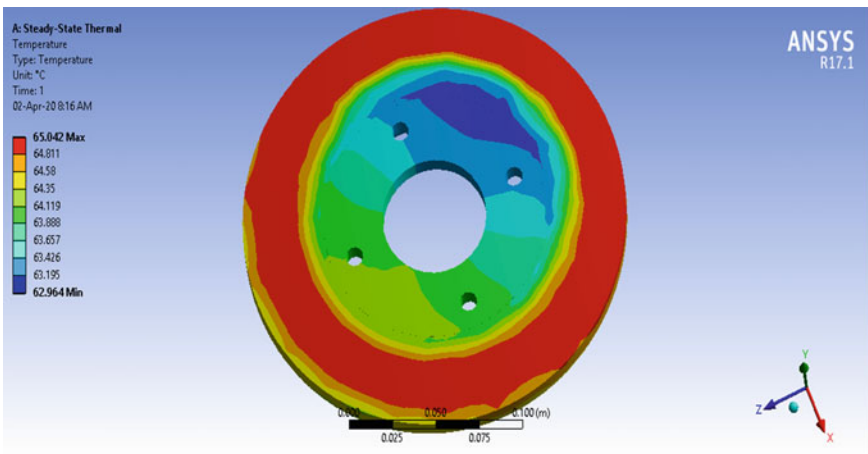
(b)
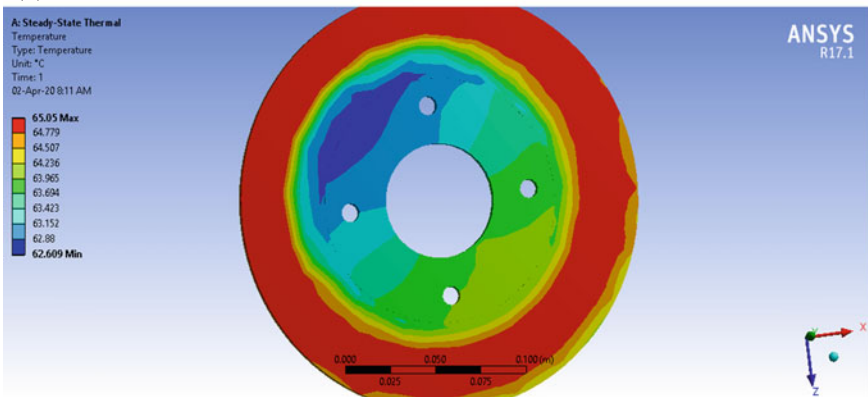
Fig. 5 **a** Temperature range on disc for Al-Cu-TiC. **b** Temperature range on disc for Al–Si-TiB$_2$

though for Al–Si-TiB$_2$ it was 65.05 °C max. Most extreme temperature extend is seen on the brake cushion zone (on account of contact between cushion surface and circle surface). Convection and radiation are considered for heat dissemination. Convection is seemed by and large surface of the plate and film coefficient is considered for constrained convection and material warm conductivity.

7 Conclusions

In the present investigation, mathematical modelling of disc brake rotor has been performed. The two composites were developed and their properties were studied:-

(1) In structural analysis of the disc brake rotor model, it is found that Al–Si-TiB2 has much more strength than Al-Cu-TiC which is observed in the results of equivalent stress, strain and total deformation. This is due to the presence of TiB2 which are readily responsible for higher strength of the entire composite.
(2) Al–Si-TiB2 had greater hardness, tensile strength, yield strength, then the Al-Cu-TiC as seen in the structural analysis of the model.
(3) In the thermal analysis of two composites on observing and analysing the results of temperature range and directional heat flow, it can be concluded that Al–Si-TiB2 has better heat dissipation and better conductivity than Al-Cu-TiC.
(4) In pin on disc test, from the results, it is observed that Al–Si-TiB2 is significantly more wear resistant than Al-Cu-TiC.
(5) In Vickers hardness test, Al–Si-TiB2 possessed greater hardness as compared to the results of Al-Cu-TiC.
(6) By performing the physical testing and numerical modelling, it is concluded that Al–Si-TiB2 can be considered as a better material for the disc brake rotor application.

References

1. Sahoo, S. K., Majhi, J., Sahoo, J. K., Bairagi, A. K., Sahoo, S., & Sahoo, B. P. (2018). Dry sliding wear behaviour of Al-Si-TiB2 in-situ composites. *International Journal of Advanced Mechanical Engineering, 8*(1), 27–36.
2. Mohapatra, J., Nayak, S., & Mahapatra, M. M. (2020) Mechanical and tribology properties of Al-4.5%Cu-5%TiC metal matrix composites for light-weight structures. *International Journal of Lightweight Materials and Manufacture, 3*(2), 120–126.
3. Maleque, M. A., Dyuti, S., & Rahman, M. M. (2010) Material selection method in design of automotive brake disc. In *Proceedings of the World Congress on Engineering* (Vol. 3). London, U.K. (30 June-2 July, 2010).
4. Sahoo, S. K., Majhi, J., Patnaik, S. C., Behera, A., Sahoo, J. K., & Sahoo, B. P. (2017). Characterisation of Al-Si-Tib2 in-situ composite synthesised by casting method. *Material Science, 113,* 49066–49069.

5. Jaiswal, R., Jha, A. R., Karki, A., Das, D., Jaiswal, P., Rajgadia, S., et al. (2016). Structural and thermal analysis of disc brake using solidworks and ansys. *International Journal of Mechanical Engineering and Technology, 7*(1), 67–77.

Advancement in Different Materials Used for Aircraft Structure Processed Through Equal Channel Angular Pressing

Krishna Mohan Agarwal, R. K. Tyagi, and Arshit Kapoor

Abstract Equal channel angular pressing (ECAP) is a forming technique where a metal is exposed to a severe plastic strain with no considerable change in the cross-sectional area of the workpiece. The main principle of the process is to produce the refinements in grains which leads to improvement in mechanical properties of the material used in various aircraft and automotive applications. There has been an tremendous development in materials used in aircraft applications since beginning. In the present study, the advancement in different materials such as aluminum alloys of 7000 series (Al–Zn–Mg–Cu) and 2000 series (Al–Cu–Mg) used for aircraft structure has been studied. The study also includes and suggests the latest technique of ECAP for improving the mechanical properties of materials used for aircraft structures.

Keywords ECAP · Aluminum alloy · Mechanical properties · Aircraft applications

1 Introduction

Al alloys are predominant in materials used in the aircraft industry for more than 80 years because of its well-known mechanical properties, flexibility and easiness in design, inspection techniques and many more benefits. But in recent years, this situation has been changed, Al alloys usage in aircraft industry has been decreased in general decline, and composites have encountered a fast increment in the materials used in the most recent Boeing aircraft F35, Airbus A330, Typhoon, B7B7 [1]. The expanding utilization of composites in the aircraft applications is because of their high explicit quality, preferable fatigue resistance and better corrosion over

K. M. Agarwal (✉) · R. K. Tyagi · A. Kapoor
Mechanical Engineering Department, Amity University, Noida, Uttar Pradesh 201303, India
e-mail: profkmagarwal@gmail.com

R. K. Tyagi
e-mail: rktyagi@amity.edu

A. Kapoor
e-mail: arshitgemini@gmail.com

most metals, yet at the same time, composite materials have numerous drawbacks which are making designers and manufacturers to examine and explore new materials and techniques which could make flight a more economic and effective. A current challenge is therefore to produce materials that can be used in wing and fuselage construction with changes in the cost of the life cycle and structural efficiency [2].

The lightweight alloys were the leading material used in the assembling of superior aeroplane parts because of their following properties—high explicit properties, corrosion resistance, damage resistance and resistance to high temperature. Weight decrease can reduce fuel consumption, increment payload and increment speed. Also, enhanced mechanical properties of the components can bring less maintenance and reduces additional costs. Since the material greatly effects the reduction in cost, airframe makers and material makers center around the improvement of new materials to meet profits and demands [2, 3]. In addition, nibbling wear cause commencement of cracks on the material surface, thereby increasing the fatigue failure of segments. The general hypothesis that distinguishes nibbling conduct and the counteractive action of nibbling is as yet indistinct however in addition, problems such as corrosion hinders the use of aircraft components and have caused a loss of $276 billion annually in the USA, which is more notable than the natural disasters [4].

2 Materials and Methods

2.1 Advances in Materials for Aircraft

The aircraft makers are additionally making efforts to reduce the parts used in aircraft. The requirement can be achieved by applying the latest methodologies. The principal technique is manufacturing thick and large plates having weariness and crack attribute. The subsequent strategy is the execution of joining advancements, for example, erosion mix welding which allows assembling of essential large panels that could be used in fuselage and wings skins. One such example where manufacturers have made all their efforts in advancement of aircraft to improve efficiency [4–6], aluminum suppliers were asked to modify the fuselage and upper wing structure during the Boeing 777 development. The upper wing structure needed greater compressive yield efficiency. Highly attractive was the increased corrosive resistance.

For the instance of fuselage, higher resilience to damage and strength than the occupant 2024-T3 was required for the upper wing construction, aluminum manufacturers also need the 7055-T77511 plate and 7055-T77511 expulsions Alclade 2524-T3 plate and 2524-T351 plate for the skin of the fuselage. Figure 1 shows the general distribution of materials and composites in an aircraft [5]. The utilization of these materials spared a large number of pounds of weight for the Boeing 777. Figure 2 describes the variation and advancement in composition of alloys and composites used in different Boeing aircraft. During the flight, the upper surface of the
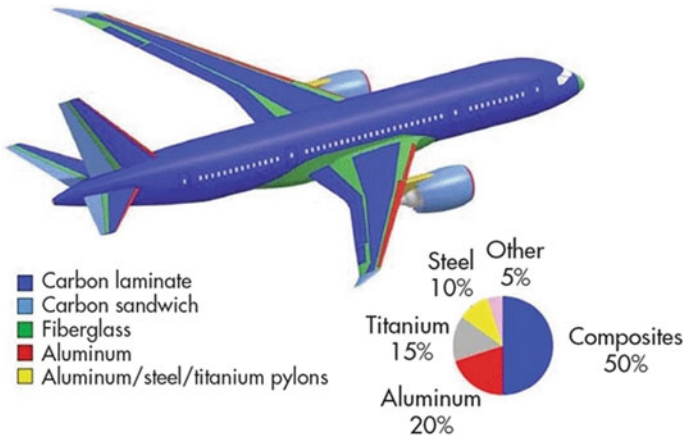
Fig. 1 General distribution of material on an aircraft [5]
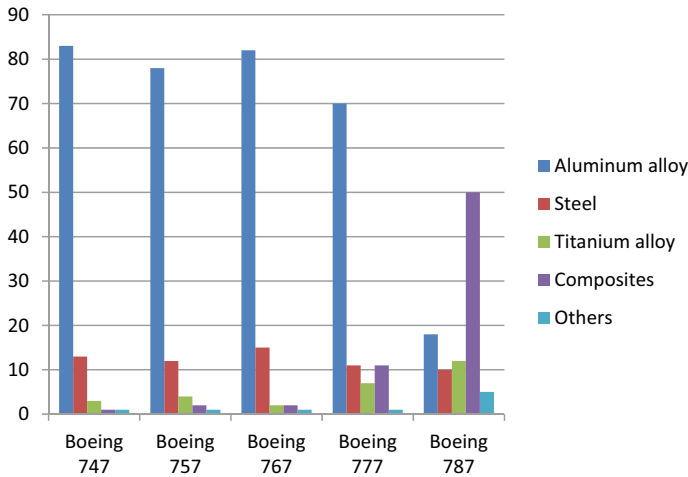
Fig. 2 Composition of different materials used in different Boeing aircraft [5]

wing is under pressure, while the lower surface is under variable loads. This requires the wing materials to provide high elasticity as well as high compressive quality. Al-based combination is one of broadly utilized aircraft materials. For example, due to its moderate yield quality (324 MPa), UTS (37 MPam1/2), and high lengthening rate (21%), 2024 Al-based compound was generally used in fuselages [6].

2.1.1 Advancement in 2000 Series Al–Cu Aluminum Alloys

The 2000 series of Al–Cu alloy is the essential combinations utilized in airframe basic applications where the fundamental structure measure great damage resilience. The 2000 arrangement composites containing magnesium of good quality is the result of precipitation of Al_2Cu and Al_2CuMg stages and predominant damage resilience and great protection from crack development than other arrangements of aluminum alloys. 2024 and 2014 are outstanding the examples for the Al–Cu–Mg alloy. The solubility of Cu in Al is 5.65 wt%. Cu broke up Al_2Cu stage in the Al lattice systems, and magnesium is frequently used to form Al_2CuMg stage in mixing with copper. These two stages of precipitation results in higher quality of aluminium alloys. This improvement prompts in 30% longer life and saving of weight. In the Boeing 777, the 2524 aluminum alloy replaced 2024 as a fuselage layer. Weariness analyses on the 2524 combination showed weariness quality of the whole combination is 70% of yield quality, while weariness quality is about 45% of yield quality for 2024-T351 weakness. The 2224-T351 and 2324-T39 materials offer superior qualities for the lower wing skin applications contrasted with occupant 2024-T351 with comparable durability and erosion resistance. The relatively low yield quality restricts the utilization of 2024 composite in high-pressure locale. To address these shortcomings, a few components have been optimized, such as Ag, Cd(cadmium), In(indium) and Sn(tin), to enhance the mechanical properties of Al–Cu dependent amalgams by improving grain size and microstructure. For example, yield quality (YS), UTS and toughness estimation for Al–Cu–Mg base amalgam increases with Sn material up to 0.06 wt percent, but then decreases with a further rise in Sn content. More improvement of the mechanical properties of Al–Cu-related amalgams could be achieved by regulating the debasements, such as iron and silicon [3–5].

2.1.2 Advancement in 7000 Series Al–Zn Based Alloy

7000 series of alloys, primarily alloyed with zinc, are heat treatable to the highest quality than some other alloy compounds. Zinc has the solubility of 31.6 wt% in aluminum than any other component, and the expansion of Zn substance can improve the quality. The 7000 arrangement of aluminum composites show higher quality when contrasted with different classes of aluminum combinations and are chosen in manufacture of stringers, upper wing skins and even vertical stabilizers. Fatigue failure and compressive force are the basic parameters in the upper wing geometry section plane. The tail of the aircraft, also known as the empennage, consists of a level stabilizer, a vertical stabilizer or equilibrium, and control surface such as rudder and elevators. Basic plan of both the vertical and horizontal stabilizers is basically equivalent to for the wing [4–6].

High-quality aluminum composites, for example, the 7075-T6 are generally utilized in aircraft structures because of their high solidarity to weight proportion, machinability and moderately ease. It is known that consumption diminishes the aircraft structure life significantly. During ordinary activity, aircraft are exposed to

Table 1 Aluminum alloy of 2000 and 7000 series used in various parts of aircraft

	AA 2000 series	AA 7000 series
Fuselages skins	AA2024-T851, AA2024-T8, AA2199-T8E74	AA7075-T6, AA7050-T76, AA7475-T7951
Fuselages stringers	AA2099-T83, 2055-T8E83	AA7349-T76511
Upper wings	AA2055-T8X, AA2195-T82	AA7050-T7651, AA7150-T651
Lower wings	AA2199-T86, AA2060-T8E86	AA7475-T7351, AA7050-T7451
Wing ribs, spars	AA2025-T84	AA7050-T74, AA7010-T76, AA7040-T76

characteristic destructive conditions because of oil, temperature, rain and humidity pressure-driven liquids and saltwater. The most extreme rigidity of the mixture based on Al–Zn is reached at a value of 2.9 wt percent Mg content. Several formulations based on Al–Zn often included 2 wt percent copper to increase stiffness [5]. For example, 7075 combinations (YS ¼510 MPa) show the highest quality of any Al-based composites (Table 1).

2.2 Equal Channel Angular Pressing

In present study research on aluminum-based alloys mainly 2024, 7075 has been done which are used in aircraft in fuselage skin, wing skins, panels, covers, bulkheads and stingers. In the study, it is proved that mechanical properties of these aluminum alloys can be improved if they are passed through ECAP forming process before being used in manufacturing of aircraft. As it has been observed that optimal conditions for most severe strain homogeneity can be achieved with channel angle $\Phi = 90^0$, corner angle $\Psi = 15^0$ and coefficient of friction $\mu = 0.25$. So all the practical and experimental results and researches were compared for channel angle equal to 90°. Figure 3 shows the schematic view of the die used in ECAP process [7, 8].

The most widely recognized SPD procedure is "equal channel angular pressing (ECAP)," first discovered by Segal et al.; which offers ascend to generation of ultra-fine grained mass with no remaining porosity. Die used in ECAP comprises of two channels of a similar cross-area converging at an angle, known as channel angle, for the most parts angle goes from 90° to 150°. The billet was fit into the upper channel with about zero resilience and compelled to leave channel with the help of ram. The misshaping was delivered by basic shear at the crossing plane. ECAP can force extreme plastic strain through rehashed forms without decreasing the workpiece sectional area. The significant distinction of ECAP with torsion or other forms, which is one of a kind in ECAP, is that distortion happens in the quick region of the plane, for example, the shear plane, lying at the crossing point of the two channels. The disfigurement in the ECAP prepared workpiece is extremely weak and homogeneous in confined conditions misshaping zone. Preparing by ECAP is currently a built-up
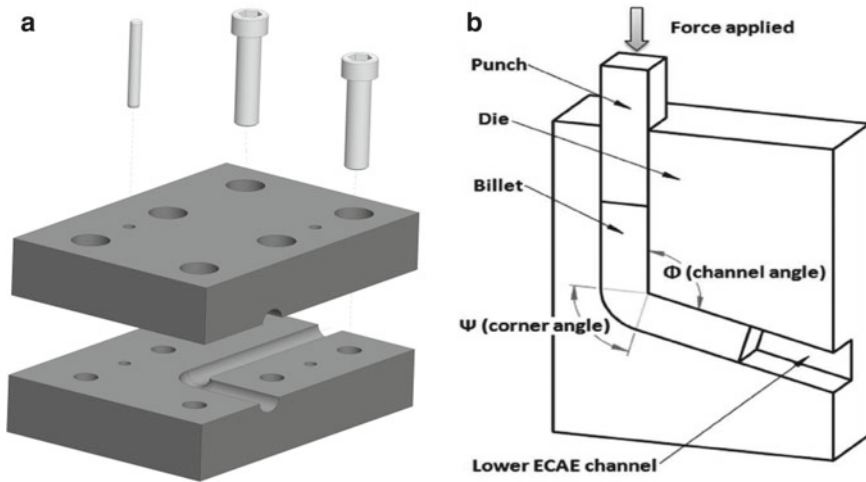
Fig. 3 a Exploded view [15]. **b** Schematic diagram [17]

technique for practice with metals and is the best method for few reasons. To start with, it is generally simple to establish and utilize an ECAP die. Second, extraordinarily high strains might be forced by the repetitive pressing of a similar billet or by creating uncommon multi-pass die. Third, the ECAP tests can be effectively increased to deliver moderately huge mass materials [9–11] where these workpieces have potential for use in range of utilizations from biomedical to the aviation enterprises [12–14]. Fourth, despite the fact that ECAP is commonly utilized with tests in the type of rods or bars, the procedure might be applied likewise to plate tests: For instance, an on-going report depicted the application of ECAP to an aluminum plate. Fifth, ECAP can be consolidated into ordinary mills to use inconsistent preparing [15–17] or into the ECAP-adjust process for the generation of wires. In perspective on these numerous points of interest, it is proper to inspect the standards of preparing through the utilization of ECAP.

3 Result and Discussion

ECAP process is used in different metal and alloys to improve or strengthen their mechanical as well as physical properties so that it can be used in different applications for better efficiency. Different experiments and investigations have been performed by different researchers to get the desired output. Various experimental results for the aluminum alloys (mainly 2024, 7050) used in aircraft processed through ECAP shows the improvement in the desired mechanical, thermal as well as physical properties. It was shown that generous grain refining has been accomplished in a few Al alloys through the ECAP process and that ultrafine grains could be held

at a submicron level in alloys at a subsequent reinforcement temperature of up to 200–300 °C. True to form, these alloys with ultrafine grain microstructure showed high quality and great pressure versatility. In any case, the majority of such works centered on homogenized microstructures and less attention was paid to the effect of different heat treatment conditions preceding ECAP on grain processing during ECAP.

Mao et al. [18] conducted an experimental investigation for the 2024 aluminum alloy after ECAP process. The point of this investigation is to comprehend the impact of starting conditions of heat treatment on microstructure and properties of 2024 aluminum compound after ECAP process. The ECAP alloys are tempered to analyze the heat treatment of a ultrafine grain microstructure at different temperatures. 2024 alloy billets used in investigation have been cut and machined from as-expelled bars to bars of 13 mm diameter across and 80 mm wide. The last specimens were collected by maturing these billets in two different ways: (a) peak matured specimens were matured for 16 h in an oil shower at 190 °C; (b) overly matured specimens were matured for 1 h in a salt shower at 290 °C. Specimens were then exposed to ECAP at 150 or 190 °C, a die with a 90° point channel and a 45^0 point angle. The outcomes got in this examination demonstrate decisively that equal channel angular pressing gives a straightforward and moderately simple method for accomplishing a ultrafine microstructure in 2024 aluminum alloy. During eight passes the standard grain size was reduced to submicron stage of 0.25 μm in both peak matured and over-matured workpiece. Ultrafine grains are sensitively stable at the consequent static toughening temperatures below 200 °C while showing only limited grain development at temperatures up to 300 °C. ECAP prompt extraordinary increment of worry to contrast and average strain solidifying conduct in examples previously ECA pressing [18]. In view of the above outcomes, it uncovers that the ideal properties—most noteworthy pressure and no amazing decrease in malleability—is delivered for a peak matured workpieces twisted at 150 °C utilizing eight passes of ECA pressing. Ordinarily, a couple of dimples are produced in workpiece with no ECA pressing, as saw in the peak matured workpiece. After four passes, huge also, little dimples are seen in the workpiece, wherein the well-grown huge dimples, framed by intersection of these little profound dimples, bolster an enormous familiar strain of the workpiece before fracture. The 0.2% verification tension and UTS of both peak matured and over-matured examples after ECAP rise essentially after that first and also second pass but stay steady from there on, with increasing number of passes, then extending to frustration decreases after one pass and then remains steady or even increases a little in certain examples afterward. A minimum maturing treatment before ECAP effectively improves the quality of the alloy and results in sensitively high quality after ECAP, in comparison with that of the over mature alloy [19–21] (Fig. 4).

Zheng et al. [22], Kai et al. [23] conducted an experimental investigation for the 7050 aluminum alloy after ECAP process. The reason for the present investigation is to explore the elements that were successful in improving the mechanical properties of 7050 aluminum alloy dependent on technique for consolidating ECAP and heat treatment. Transmission electron microscopy (TEM) was conducted at 160 kV on a JEOL 2000. Examples for TEM measurement were 3 mm and decreased to
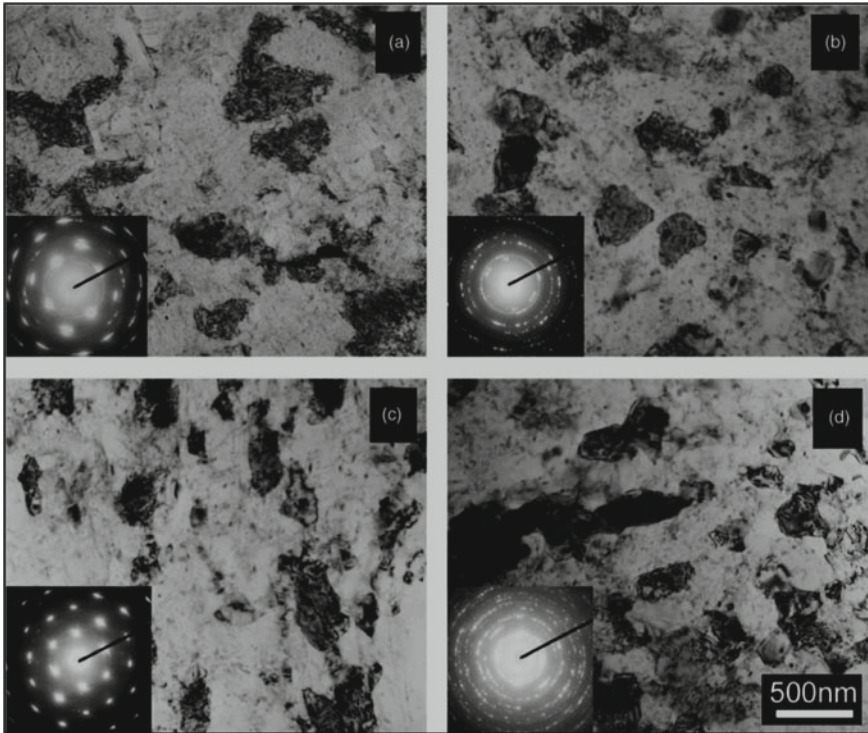
Fig. 4 Transmission electron microscopy results after ECA pressing: **a** Peak matured workpiece after two passes; **b** peak matured workpiece after eight passes, **c** over-matured workpiece after two passes and **d** over-matured workpiece after eight passes [18]

0.1 mm thickness. Estimations of the grain size were made legitimately from the TEM photomicrographs utilizing the straight block strategy. Four conditions were used in the investigation. In condition 1, examples of pre-ECAP enhancement and post-ECAP maturation were shown; in condition 2, examples of pre-ECAP enhancement, post-ECAP short tempering and maturation; in condition 3, examples of pre-ECAP tempering, post-ECAP maturation, ECAP refurbishment and maturation; in condition 4, the specimen was exposed to pre-ECAP and post-ECAP maturation. In condition 1, the tempered specimen was exposed to the ECAP and the shearing groups formed in the specimens. The distance of shearing groups reduced with the quantity of ECAP increasing [24] (Fig. 5).

The efficiency of the four conditions in improving quality was in descending request from conditions 4 to 1. Test strengths in conditions 2 and 3 were affected only by ECAP's first pass, while the qualities of conditions 1 and 4 were influenced by numerous passes of ECAP. In condition 1, the increase in strength only reflected a part strengthening the dislocation. In condition 2, the additional intensity was due to enhancement of grain processing and precipitation strengthening. In condition 3,
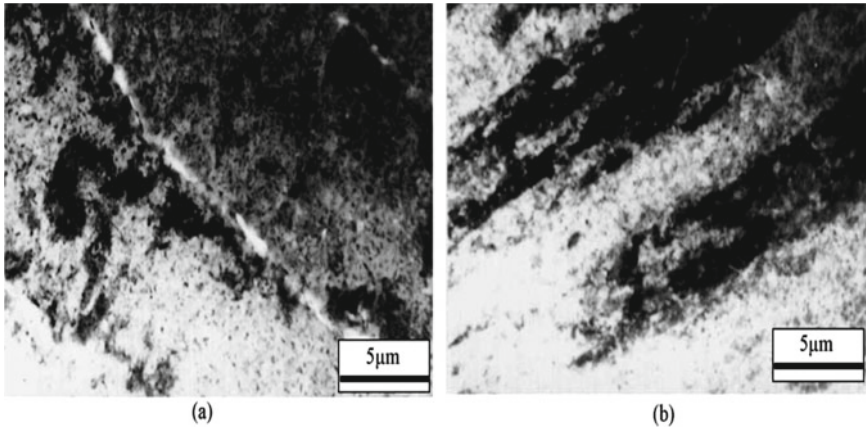
Fig. 5 Microstructures of condition 1 by route A 7050 samples: **a** after one ECAP pass, **b** after four ECAP passes [22]

when compared with condition 2 an extra reinforcing portion of disengagement reinforcing was also figured out. All three mechanisms as of condition 3 had been involved in condition 4. In any case, there were a lot better grains and progressively powerful strains, in this manner, and the quality of condition 4 was most noteworthy in the four conditions. A final elasticity of 677 MPa, which was 30% higher than some material in T6 condition and was achieved in condition 4 after 3 go of ECAP. Due to the fact that the dislocation enhancing mechanism in condition 1 controlled by the enhanced mechanism, the increase in force was mainly due to the accumulation stress quantity, condition 1, ECAP routes effectively improved their strength throughout decreased orders. The pressing routes also had little impact on the mechanical characteristics of the sample [24].

4   Conclusion

Over recent years, the use of the crystalline lattice composite materials has increased over comparison with Al-based alloys based on sheer mechanical properties like higher individual strength and rigidity but still there are many drawbacks of using composites. So ECAP is one of the most important techniques for plastic deformation which can be used on the aluminum alloys (AA2000 series and AA7000 series) that are majorly used in aircraft. Ultrafine grain samples should be produced in fully dense form without modifying the cross-sectional samples. The ECAP is markedly refined and dislocation enhances, thereby significantly improving the strength of the alloys. These aluminum alloys are used in various parts of aircraft such as fuselages skins, fuselages stringers, upper wings, lower wings, wing ribs and spars. The design requirements for aircraft building materials include that the materials possess suitable

mechanical properties under different conditions with proper damage resistance. The most important subject of the ECAP studies was the results of pressing numbers, extrusion mechanisms and die type. In the current study, we found that by using ECAP process for AA2024 and AA7050 its mechanical properties got improved.

References

1. Holt, R. T., Koul, A. K., Zhao, L., Wallace, W., & Beddoes, J. C. (1995). Lightweight materials for aircraft applications. *Materials Characterization, 67,* 41–67.
2. Marsh, G. (2012). Aero engines lose weight thanks to composites. *Reinforced Plastics, 56*(6), 32–35.
3. Huda, Z., & Edi, P. (2013). Materials selection in design of structures and engines of supersonic aircrafts : A review. Mater. Des., vol. 46, pp. 552–560.
4. Dursun, T., & Soutis, C. (2014). Recent developments in advanced aircraft aluminium alloys. *Journal of Materials Science, 56,* 862–871.
5. Holmes, M. (2017). Aerospace looks to composites for solutions. *Reinforced Plastics, 61*(4), 237–241.
6. Zhang, X., Chen, Y., & Hu, J. (2017). Progress in Aerospace Sciences Recent advances in the development of aerospace materials. Prog. Aerosp. Sci., vol. 97, pp. 22–34.
7. Kim, H. S., Seo, M. H., & Hong, S. I. (2001). Plastic deformation analysis of metals during equal channel angular pressing. *Journal of Materials Processing Technology, 113*(1–3), 622–626.
8. Furukawa, M., Horita, Z., Nemoto, M., & Langdon, T. G. (2001). Processing of metals by equal-channel. *Journal Materials Science, 6,* 2835–2836.
9. Olejnik, L., & Rosochowski, A. (2005). Methods of fabricating metals for nano-technology. *Technical Sciences, 53*(4), 413–423.
10. Langdon, T. G. (2007). The principles of grain refinement in equal-channel angular pressing. *Materials Science and Engineering A, 462,* 3–11.
11. Azushima, A., et al. (2008). Severe plastic deformation (SPD) processes for metals. *CIRP Annals Manufacturing Technology, 57,* 716–735.
12. Djavanroodi, F., & Ebrahimi, M. (2010). Effect of die channel angle, friction and back pressure in the equal channel angular pressing using 3D finite element simulation. *Materials Science and Engineering A, 527*(4–5), 1230–1235.
13. Krishna Mohan Agarwal, R. T. (2017). Investigation of mechanical properties of metals and alloys processed after equal channel angular pressing. *AGU International Journal of Engineering and Technology, 5*(5), 53–65.
14. Bruni, C., Cabibbo, M., Ciccarelli, D., & Paoletti, C. (2018). Characterization of double aluminium alloy specimens after ECAP. *Procedia Manufacturing, 15,* 1517–1524.
15. Agarwal, K. M., Tyagi, R. K., & Kapoor, A. (2019). Deformation and strain analysis for grain refinement of materials processed through equal channel angular pressing. *Materials Today Proceedings, 21*(3), 1513–1519.
16. Mohan Agarwal, K., Tyagi, R. K., & Dixit, A. (2019). Theoretical analysis of equal channel angular pressing method for grain refinement of metals and alloys. *Materials Today Proceedings, 25*(4), 668–673.
17. Krishna Mohan Agarwal, A. D., Tyagi, R. K., & Chaubey, V. K. (2019). Comparison of different methods of Severe Plastic Deformation for grain refinement. Series I O P Conference Science Materials. 691, 012074.
18. Mao, J., Kang, S. B., & Park, J. O. (2004). Grain refinement, thermal stability and tensile properties of 2024. *Journal of Materials Processing Technology, 159*(7), 314–320.
19. Xia, K., Wei, W., Wang, F., Bo, Q., Alexandrov, I. V., & Hu, J. (2011). Microstructure, mechanical properties and electrical conductivity of industrial Cu–0. 5% Cr alloy processed by severe plastic deformation. *Materials Science and Engineering A, 528*(3), 1478–1484.

20. Luri, R., Fuertes, J. P., Luis, C. J., Salcedo, D., Puertas, I., & León, J. (2016). Experimental modelling of critical damage obtained in Al-Mg and Al-Mn alloys for both annealed state and previously deformed by ECAP. *Materials and Design, 90,* 881–890.
21. Shaeri, M. H., Shaeri, M., Ebrahimi, M., Salehi, M. T., & Seyyedein, S. H. (2016). Progress in natural science : Materials international effect of ECAP temperature on microstructure and mechanical properties of Al–Zn–Mg–Cu alloy. *Progress in Natural Science Materials International, 26*(2), 182–191.
22. Zheng, L. J., Li, H. X., Hashmi, M. F., Chen, C. Q., Zhang, Y., & Zeng, M. G. (2006). Evolution of microstructure and strengthening of 7050 Al alloy by ECAP combined with heat-treatment. *Journal of Materials Processing Technology, 171,* 100–107.
23. Kai, S., Jin-ling, C., & Zhi-min, Y. I. N. (2009). TEM study on microstructures and properties of 7050 aluminum alloy during thermal exposure. *Transactions of the Nonferrous Metals Society of China, 19*(6), 1405–1409.
24. Horikiri, G., Kitazumi, T., Natori, K., & Tanaka, T. (2017). Improvement in mechanical properties of semi-solid AA7075 aluminum alloys by Equal-Channel Angular Pressing. *Procedia Engineering, 207,* 1451–1456.

Modelling and Simulation of Wind Turbine Blade Hub for Its Life Enhancement Using Epoxy Fibre Glass as Material

Aseem Acharya, Prem Narayan Vishwakarma, and Ajay Sharma

Abstract The hub will experience a number of loadings and other effects; a variety of designs have been conceived to best handle these conditions. The ultimate goal is to conduct finite element analysis on typical hub designs with the purpose of predicting the fatigue life of the hub, for various numbers of cycles and able to increase the fatigue life of the hub while reducing the cost of manufacture by using the composite material. Lift and drag forces along with the angle of attack are the important parameters in a wind turbine system. These parameters decide the efficiency of the wind turbine. The hub encounters various types of effects and various loading conditions. A variety of designs have been recommended to face these conditions. Finite element analysis has been conducted in this paper with aim of forecasting the fatigue life for number of cycles so that the fatigue life is improved along with reduction in manufacturing cost.

Keywords Fatigue life · Lift and drag · Finite element analysis · Turbine hub · Forecasting

1 Introduction
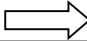
Wind turbine's demand is increasing day by day so turbine industry is increasing day by day. Function of a turbine is extraction of energy from flowing fluids. If electricity is harnessed from mechanical energy, then such machines are called wind generators. Horizontal and vertical both types of wind turbines are prevalent [1, 2]. Since turbulence is produced behind the tower, so the position of the turbine is above the tower which is supporting it. Blades are given a considerable frontal

A. Acharya (✉) · P. N. Vishwakarma · A. Sharma
Department of Mechanical Engineering, Amity University, Noida, Uttar Pradesh, India
e-mail: aseemacharya150399@gmail.com

P. N. Vishwakarma
e-mail: pnvishwakarma@amity.edu

A. Sharma
e-mail: asharma3@amity.edu

Table 1 Components

Blades	There can be 2–3 blades
	Length can extend up to 50 m
Controllers	It regulates the mobility of the turbine
Gearbox	Gearbox is fed with low speed shaft and generator is fed with high speed shaft from the gearbox
Generators	Mechanical energy ⟶ electrical energy
Nacelles	It encases all the components
Rotors	It is the part attaching hub and the blades
Towers	Height is 60–80 m
	It is tri-sectional

offset from the tower. Cyclical loading is experienced by the hub. As a result of gravity, throughout each revolution various different torques are experienced. So, for optimization of hub, different material is tried. Its consequence was increase in the stiffness of the hub and decrease in the weight. It should possess more reliability and should extract out more energy.

2 List of Components

See (Table 1).

3 Simulation Setup

A three-dimensional model is designed and simulated with epoxy fibre glass as material. Analysis of existing material is also conducted [3]. Comparison of both the results is carried out and after that fatigue analysis is done.

3.1 Composition and Properties

See (Table 2).

Table 2 Composition and properties of material

Property	Value
Compressive strength—longitudinal	300 MPa
Compressive strength—transverse	415 MPa
Density	1.90 g/cm^3
Tensile strength—longitudinal	490 MPa
Thermal expansion co-efficient	11*10^-6/K
Upper working temperature	130–150 °C
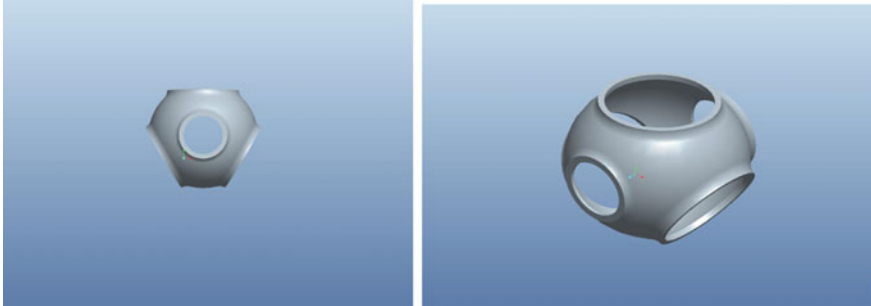
Fig. 1 Three-dimensional model of wind turbine hub in different views

3.2 Model of Hub

The hub is modelled using SolidWorks and then the three-dimensional model is imported to ANSYS after converting into.stp format. After importing, meshing is done (Fig. 1).

3.3 Meshing

Mesh is a group of minute particles or nodes. As more and more elements are seated in a given region, density of the mesh increases. Virtual results become more precise with increase in mesh density (Fig. 2).

Characteristics of meshing

Nodes	62763
Elements	29762
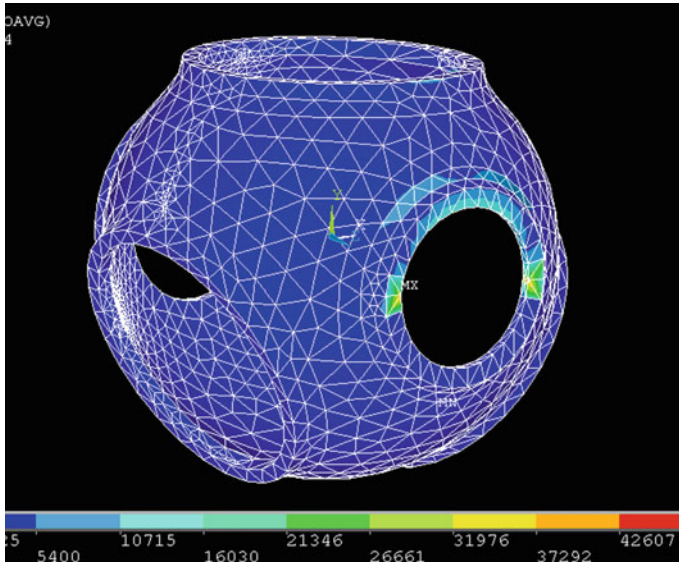
Fig. 2 Meshing of the hub
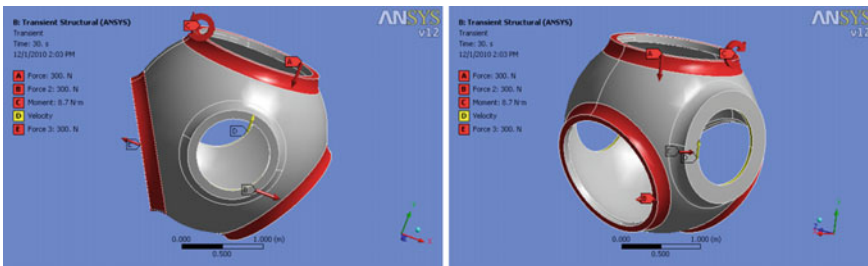
Fig. 3 Transient analysis of the hub

3.4   Simulation Results

See (Figs. 3, 4, 5, 6 and 7).

4   Discussion

Three deciding factors for fatigue analysis are stress life, strain life, and fracture mechanics. Total life of the component can be predicted using stress life. Strain life can only predict the crack initiation. Crack life can be calculated using fracture mechanics. Total life is the summation of crack initiation and crack life. Fatigue
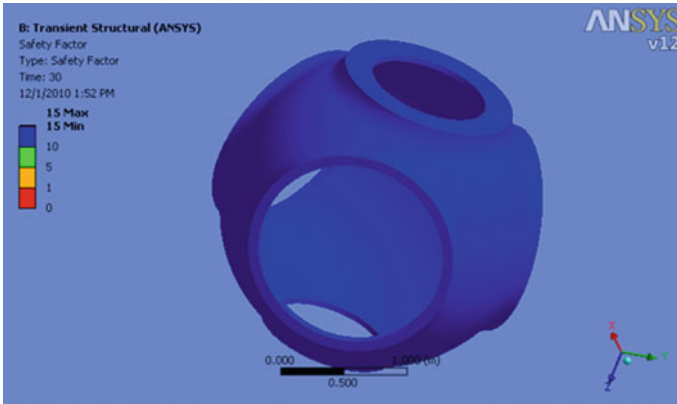
Fig. 4 Total safety factor analysis of hub
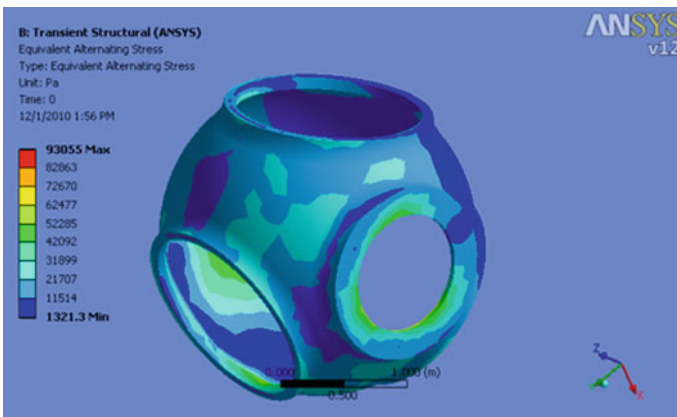
Fig. 5 Alternating stress analysis

analysis can also be classified as low cycle fatigue and high cycle fatigue. If a member experiences more than one lakh cycles, then it is a high cycle fatigue. From Fig. 5, it is evident that the hub will experience a maximum alternating force of 93055 Pa. Maximum and minimum hub life would be e^10. From Fig. 4, maximum safety factor is 15 and minimum safety factor is 1 (Fig. 8).

As the induced alternating stress decreases, the capacity of the component to bear more cycles increases, i.e., life of the hub increases. S-N curve shown above depicts the graphical representation of alternating stress vs no. of cycles for epoxy fibre glass material used in the hub of wind turbine.
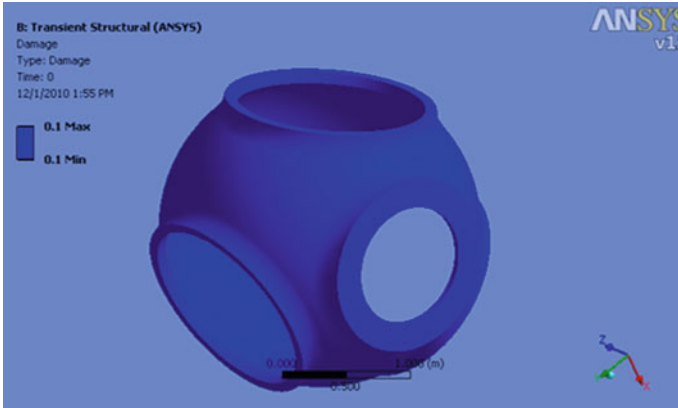
Fig. 6 Damage analysis of hub
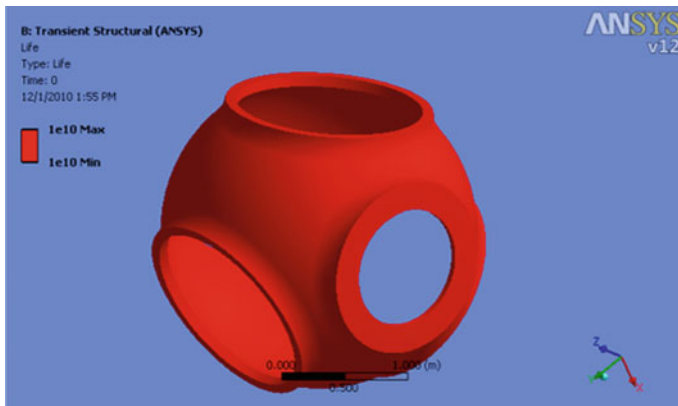
Fig. 7 Life analysis of hub
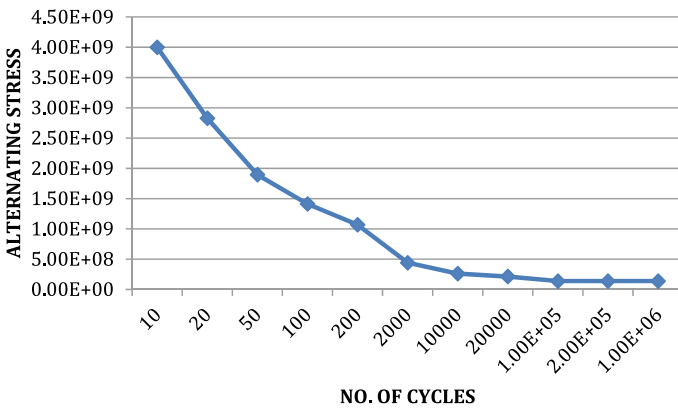
Fig. 8 S-N curve for the fatigue analysis of the hub

5 Conclusion

A new material called epoxy fibre glass was introduced for the hub design and the model was simulated. Then, the fatigue analysis was done and S-N curve was obtained which showed an improvement in the fatigue life of the turbine blade hub. Manufacturing cost was also reduced and stiffness was spiked up. Other parts such as main shaft shall also experience reduction in stresses due to reduced weight. Thus, epoxy fibre glass is a better material to be used in wind turbine blade hub. Thus, by using this new material of epoxy fibre glass in turbine blade hub, we can enhance the total life of the hub, and it will lead to more reliability of the hub.

References

1. Kuppast1, V. V., Chalwa, V. K. N., Kurbet, S. N., & Yadawad, A. M. (2014). Finite element analysis of aluminium alloys for their vibration characteristics. *IJRET: International Journal of Research in Engineering and Technology, 03*(3) NCRIET-2014.
2. Arshad, M., & O'Kelly, B. C. (2020). Offshore wind-turbine structures: A review. In: *Offshore wind-turbine structures: A review*.
3. Rathore, A. S., & Ahmed, S. (2011). Design and analysis of horizontal axis wind turbine rotor. *International Journal of Engineering Science and Technology (IJEST), 3*(11), 7975–7980. ISSN: 0975-5462.

Review on Thermal Spray Coating Methods and Property of Different Types of Metal-Based Coatings

Gaurav Gupta, R. K. Tyagi, S. K. Rajput, Rahul Maan, Siddhant Jacob, and Shiva Verma

Abstract To enhance performance of industrial tools and components, deposition of thin film or coating presents a good option. Coating is done on the surface of the objects such as machine parts, tools, and on other similar components. For protecting components from erosion, wear, and corrosion, this method presents a cost-effective method. Thermal spray is one of the coating methods. Thermal spraying is a well-known technique in industries for improving the surface properties of the components. Thermal spraying can be used to apply coating of different materials such as metals, ceramic blends, alloys, and carbides many more on variety of components. Thermal spray provides benefits like repairing engineering component, improves performance, and extended life of the components. Many materials can be deposited through thermal spray coating such as Zn, Al, Ni, WC, Fe, Cr, and even the combination of materials. These coatings have considerable effect on performance without affecting environment.

Keywords Thermal spray thin film · Steel · Coating · Thin film · Corrosion protection

G. Gupta (✉) · R. K. Tyagi · R. Maan · S. Jacob · S. Verma
Department of Mechanical Engineering, Amity University Uttar Pradesh, Noida 201303, India
e-mail: 15.gaurav@gmail.com

R. K. Tyagi
e-mail: tyagirk1@gmail.com

R. Maan
e-mail: rahulmaan97@gmail.com

S. Jacob
e-mail: jacobsiddhant@gmail.com

S. Verma
e-mail: verma.shiva14@gmail.com

S. K. Rajput
Mechanical Engineering Department, Bundelkhand Institute of Engineering and Technology, Jhansi 284128, India
e-mail: rajput_skumar@rediffmail.com
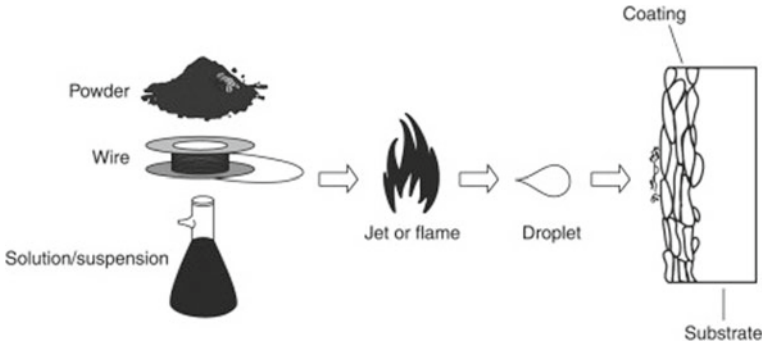
Fig. 1 Basic working of thermal spraying [1]

1 Introduction

Thermal spraying is a well-known technique in industries for improving the surface properties of components. Thermal spraying can be used to apply coating of different material like metals, ceramic blends, wires, alloys, carbides, and many more on variety of components (Fig. 1). A considerable number of industries in the world use this process for censorious application. This process provides resistance to cavitation, wear, oxidation, corrosion, and erosion and also provides insulators in electrical conductors. Thermal spray provides benefits like repairing engineering component, improves performance, and extends the life of the components at very little cost.

Basically in all method of thermal spraying, an energy/heat source and consumable materials (wires or powders) is required. It also requires gases in some cases, and this is needed to move the powder in the gun and then to obtain the necessary melting temperature. Thermal spraying includes the projection of little soft particles onto a cleaned surface where they stick to make a steady coating (Fig. 2). The bonding of the material is commonly mechanical; in some, it may be metallurgical.

Areas of interest/industries include automotive, aerospace, ceramics, and glass manufacturing, corrosion of marine- and land-based infrastructures, printing industry components, processing industries, electrical utilities, textile, plastic industry and industrial applications coated steels, and also in orthopedic and dental applications [2, 3].

2 Different Types of Thermal Spraying Methods

2.1 High-Velocity Oxy-Fuel Method (HVOF)

HVOF coating technique, which comes under thermal spraying, helps in improving the surface properties of the components, hence expanding its life by fundamentally by expanding wear and erosion resistance, and protection from corrosion.
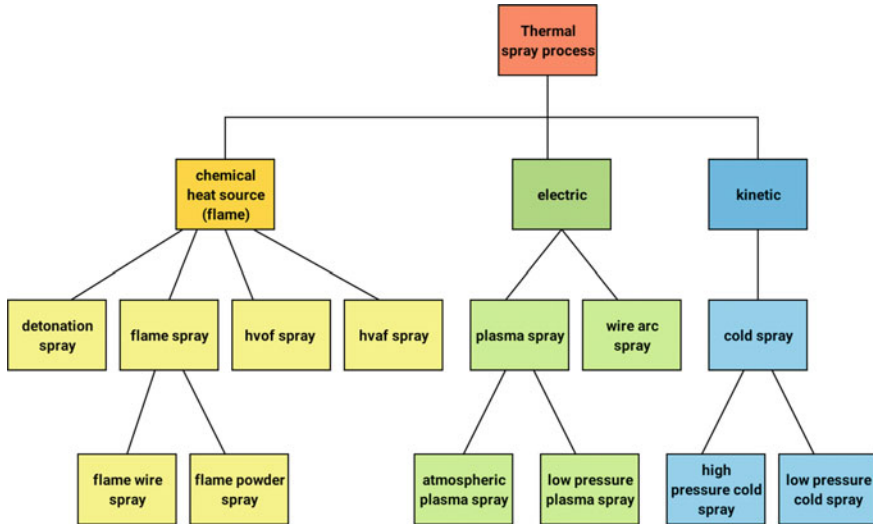
Fig. 2 Classification of thermal spray processes

This method produces coating with different thickness and good adhesion. In this method, burning fuel like propane and kerosene is used for melting powders. Molten powder sprays with high velocity on the required surface and forms layer of coating (Fig. 3). This is a high kinetic process due to its high velocity; it improves smooth finish and provides low porosity and oxide. HVOF coating materials are accessible for thermal spraying incorporate metals, ceramics, metal alloys, plastics, and composites [4–8].
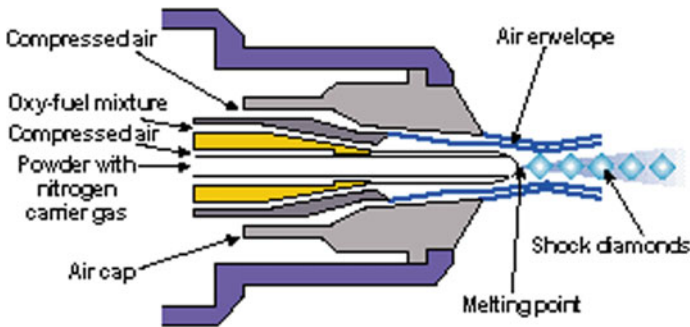
Fig. 3 HVOF gun [9]
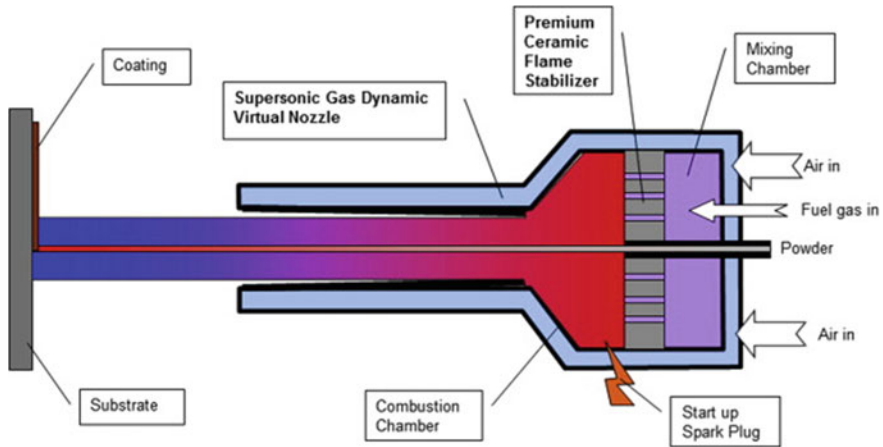
Fig. 4 HVAF gun [12]

2.2 High-Velocity Air–Fuel (HVAF)

HVAF is one of the thermal spray technique and is similar to HVOF. The only difference in this process is that air is used instead of oxygen [10, 11]. HVAF coatings are utilized in applications where high strength, density, and good quality which are required (Fig. 4). New forms of applications which are not reasonable in already existing thermally sprayed coatings are now getting practical. High-velocity air–fuel coatings have high amount of oxides due to the high temperatures of this process [11]. These coatings are basically harder than that obtained using HVOF.

2.3 PLASMA Spraying

To form plasma, an arc is created using electrode and anode in this technique. For getting plasma fire, primary and secondary gases (nitrogen, helium) are heated and ionized. Flame temperature is ranging from 8000 to 14000 K [13–16], and this temperature also depends on mixture of gas used for making flame. High temperature helps in melting materials which have high melting point (Fig. 5). Ni–Cr based and titanium-based coating is done using plasma spray, which gives us good result for improving surface properties due to increase in its cohesion strength [17, 18].

It has the advantage of spraying material like zirconia, tungsten, and many others, those having high melting. Plasma-sprayed coatings are commonly denser, more grounded, and cleaner than the other thermal spray forms. Plasma spray coatings likely record for the vastest scope in thermally sprayed coatings and applications, that makes it most flexible.
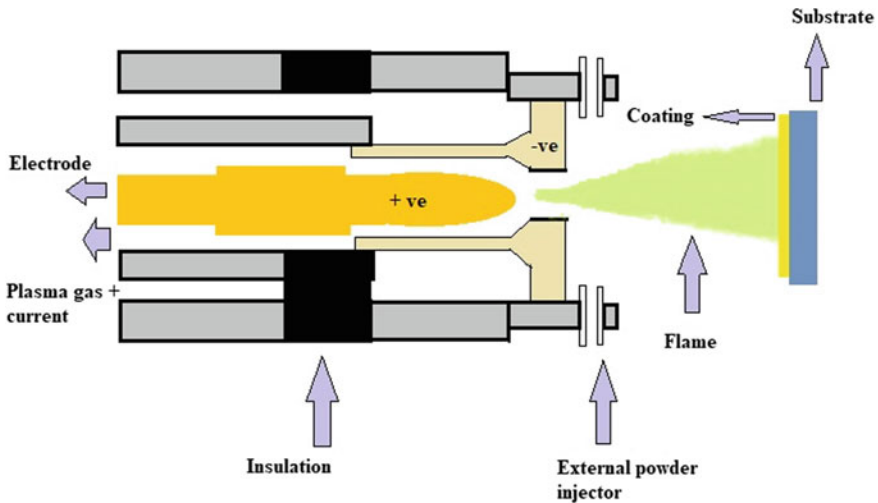
Fig. 5 Plasma spray [19]

2.4 ARC Spray Process

In this technique, an electric arc is generated between two conductive wires. Arc melts the two wires, and high velocity gas (nitrogen gas) atomized the molten metal and sprayed on metal surface. Atomized molten metal particles on the metal surface quickly form a layer of coating. Electric arc spray coatings are regularly denser and more grounded as contrast to other thermal spray technique (Fig. 6). Due to high spray rate and low cost proficiency even for spraying on big surfaces, twin arc spray can be performed using noble gases in controlled atmosphere [20]. The principle uses of arc spray procedure coatings are to protect zinc and aluminum against corrosion. Hence, it offers versatility and high reliability [21].

2.5 Flame Spray Process

Flame spray technique is the oldest technique developed in the field of thermal spray. It requires very low cost investment although it provides good amount of deposition rate, efficiencies, and relatively simplicity in operation. This process utilizes flammable gas as a heat source for melting the material of the coating (Fig. 7). Wide range of available material can be deposited. They can be in form of powder, wire, or rod by utilizing flame spray technique [18, 20].

- **Powder flame spray**: To generate a high temperature combustion zone at the front of the powder mixture, oxygen and acetylene are ignited externally, whereas some designs suggests a concentric set of holes at nozzle exit that provides a constricting
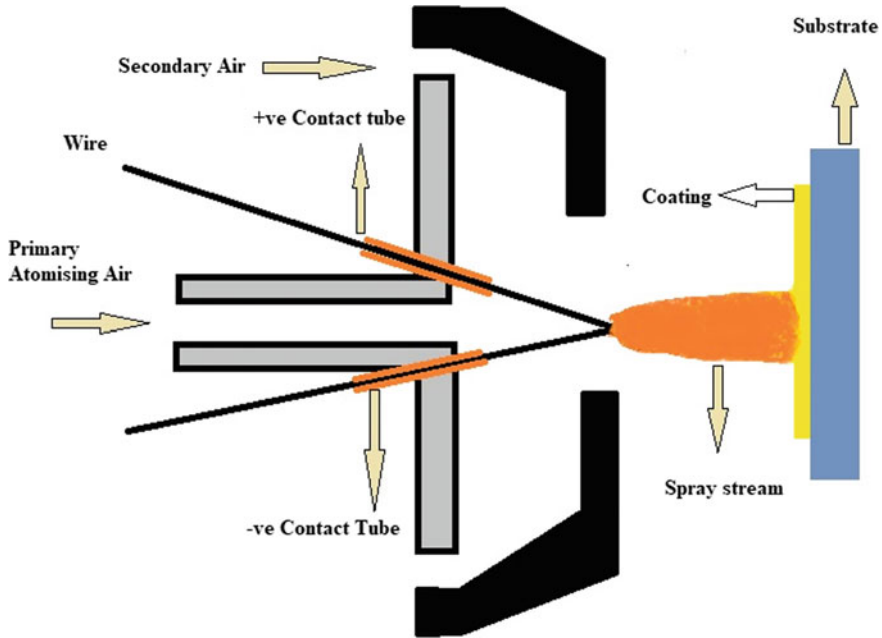
Fig. 6 Arc spray process [19]
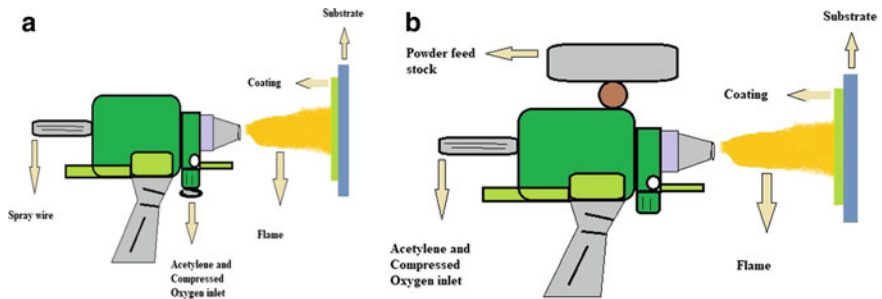
Fig. 7 Flame spray gun **a** wire and **b** powder [24]

air flow to pinch expanding gases generating higher temperature combustion zone helping nozzles to decide spray pattern. This process has the low equipment and processing cost, thus presenting a popular usage.

- **Wire flame spray**: This technique employs basic working principle of powder flame spray but capable of producing denser coatings. It introduces special air caps over the torches through which wires and rods are mechanically fed into the heating zone, which produces a concentrated air jet capable of atomizing tip of molten wire or rod. Significant advantage of these over powders is that the degree of melting is significantly increased results denser coatings [12, 22, 23].

3 Property of Different Types of Metal Based Coating

3.1 Aluminum-Based Coating

Aluminum-based thermal sprayed coating is mostly done by the wire arc spraying method in industry and most endorsed technique for aluminum-based coatings. It makes a passive layer of Al-hydroxide and Al-oxide, which helps in filling defects and helps in the delay of penetration into the coating layer [10]. Addition of some amount of Mg with epoxy sealing coating can help in improving the corrosion resistance and mechanical property. In this coating, Al95%–Mg5% is used. It was reported that corrosion and polarization rate without sealing coating was 79.52 µm/y, 28.08 K $\Omega \cdot cm^2$, whereas with coating, it was reduced to 0.28 µm/y and 5255.65 K$\Omega \cdot cm^2$ [25].

The amount of voids, porosity and density of the coating can negatively or positively affect the corrosion behavior of Al based coatings. The mixing of Re, Si, and Zn in aluminum can prove the self-sealing property of the coating. Corrosion potentials (E_{cor}), polarization rate (R_p), and corrosion rate (I_{cor}) for Al–Zn–Si–Re coating were −0.965 V, 1218.5 $\Omega \cdot cm^2$, and 36.54 µAcm^{-2}, and for Zn-15Al coating, result was −1.112 V, 464.4 $\Omega \cdot cm^2$, and 40.41 µAcm^{-2} [26].

3.2 Zinc-Based Coating

Zn based alloys are having lower in EMF series than steel; therefore, it behave like sacrificial anode when they are coated to steel. This helps the steel against the corrosion in several conditions. Cold spray method increases the life time of Zn coating. Corrosion rate for cold spray is 28.24 µAcm^{-2} and for wire arc spray method is 90 µAcm^{-2} [27]. Mixture of Zn-Al-Mn performed better than Zn coating on steel, when salt spray testing for 600 h [28]. Al, Mn, Re, and Si improved the anticorrosion property of Zn based coating. If Si is added in the Zn-Al-Mg-Re coating mixture, it shows better corrosion resistance. Corrosion resistance will vary according to the amount of Si added in the Zn-Al-Mg-Re coating mixture [29].

3.3 Nickel-Based Coating

Ni based coating also provide as passive layers of Cr_2O_3, oxides of Si/Cr/Ni, and TiO_2. HVOF is most approved technique for nickel-based coatings with low porosity and low oxides, contributes fairly toward anticorrosion. [30].

3.4   Chrome-Based Coating

Thermal sprayed chrome-based coatings are same as that of Ni coating which makes passive layer of Cr_2O_3, responsible for the anti-corrosion property. HVOF is most desirable thermal spray coating technique because of its low oxidation, porosity, high deposition rate, and bonding strength. Analysis shows that chrome-based coatings have very low level of porosity. HVOF parameters viz energy input, torch offset distance, gas composition, flow rate, and cooling of specimen play an important role in the porosity content [30, 31].

3.5   Tungsten Carbide (WC)-Based Coating

WC based coatings shows micro-galvanic corrosion, which is due to the gap between the WC coating that results less corrosion resistance. To overcome this problem, Ni, Cr, B, Si, and Fe are used as binding materials [32]. Adding Cr to WC base resulted formation of Cr2O3 layer as protective layer, and deliver an anticorrosion performance. In this coating, HVOF is most desirable thermal spray technique because of low oxidation, porosity, and high deposition rate [30].

3.6   Iron-Based Coating

Fe based alloys have recently turn on researcher's interest as materials, for making of corrosion and wear-resistant coating. Fe based alloys are not harmful for human as compared to the Ni and Co based alloys [33]. Both Co and Ni are toxic in nature; they are having the allergenic element and are harmful for humans. Because of this, Fe has provided an alternative to the Ni and Co based alloy. Nowadays, Fe based coating is used in the field of beverage and food industry [34]. These types of coating are done using HVOF spray technique. Addition of Ni, Si and Cr can increase the resistance of both corrosion and wear [34, 35].

Fe based high entropy alloys (HEA) coating provides good erosion resistance which prevent the erodent to penetrate coating. HEAs are alloys that are formed by mixing equal amount of five or more alloys (Al-Co-Cr-Fe-Ni-Ti), and its microhardness is about 610 ± 30 VHN [36]. The amorphous coating of Fe based is showing good homogeneous, high hardness, cavitation, erosion resistance, and relatively low cost [37, 38].

Table 1 Brief overview of various thermal spray coatings

S. no	Authors	Coating	Remarks
1	Gu et al. [24]	Al_2O_3	It shows more superior corrosion resistant as compared to Al because it makes dense coating
2	Choe et al. [25]	Al-Mg	Shows more anticorrosion property
3	Jianga et al. [26]	Al-Zn-Si-Re Zn-15Al	Mixing of Re, Si, and Zn in Al can prove the self-sealing property of the coating
4	Chavan et al. [27]	Zn	Zinc coating on steel forms a sacrificial anode on the surface
5	Schuerz et al. [28]	Zn Zn+2 wt.% Al+2 wt.% Mg	Using this formation of dense coating and block the pores, which help in reducing carrion rate
6	Kuiren et al. [29]	Zn-Al-Mg-Re-Si	Formation of $Al_{3.21}Si_{0.47}$ is seen, which provides self-sealing behavior
7	Galedari et al. [30]	Chrome-based coating Nickel-based coating WC based coating	Ni-based coating also provides as passive layers of Cr_2O_3, oxides of Si/Cr/Ni and TiO_2. Microstructural property also play important task in anticorrosion in Ni based coatings
8	Neville et al. [32]	WC based coating	In WC based coatings, we can see micro-galvanic corrosion, which is due to gap in between the WC coating. So to overcome this problem, we use binding material like Ni, Co-Cr, and Co
9	Suh et al. [33]	Co compound	Fe based alloys are not harmful for human as compared to the Ni and Co based alloys
10	Souza et al. [34]	Fe-Cr based amorphous alloys	These types of coating are done by HVOF spray. Addition of Ni, Si, and Cr can increase the resistance of both corrosion and wear

(continued)

Table 1 (continued)

S. no	Authors	Coating	Remarks
11	Srivastava et al. [36]	Fe-Co-Cr-Ni-2Al alloy coating	In Fe based high entropy alloys, coating provides good erosion resistance which prevent the erodent to penetrate coating
12	Guo et al. [37]	Fe based amorphous coatings	The amorphous coating of Fe based is showing good homogeneous, high hardness, cavitation, erosion resistance, and relatively low cost
13	Zhao et al. [39]	YSZ powder	To protect the pipeline, exhaust system, boiler, and fan in power plant from salt corrosive attack, yttria-stabilized zirconia-based coating was used
14	Gulyaev et al. [40, 41]	YSZ	Efficiency reduces with reduction of flow rate. Reduction in temperature increases porosity of coatings—Adjustment of plasma machine settings

3.7 Yttria-Stabilized Zirconia-Based Coating

To protect salt corrosion attack in pipeline, exhaust system, boiler, and fan which are used in the power plant, yttria-stabilized zirconia-based coating is used. It is recommended for protection against salt and for long lasting of equipment. For applying this coating, plasma spray techniques is the best thermal spray technique [39]. Coating properties get effected by adjusting machine parameters. Reduction in temperature affects flow rate thereby reducing efficiency and increase in porosity [40]. Some of the coating, their type, and effect have been summarized in Table 1.

4 Conclusions

1. Thermal spray coating improves the life of the component. Thermal spray coating offers a wide range of methods (electric arc wire spray, HVOF, HVAF, flame spray, plasma spray) and coating materials that can be coated using this technique were studied. Impact of these types of coating on the environment is very less as compared to the typical plating technique. HVOF coating method is widely used

and acceptable coating method. It provides steady coating thickness, excessive hardness, and unbroken layer of coating. This method shows better result in areas like corrosion, erosion, and oxidation.

2. Yttria-stabilized zirconia-based coating and iron-based coating will improve the property of coating by mixing different metal components into them like Ni, Cr, B, Si, and Al.

References

1. Kim, G. E., Champagne, V. K., Trexler, M., & Sohn, Y. (2011). *Processing nanostructured metal and metal-matrix coatings by thermal and cold spraying* (pp. 615–662). Woodhead Publishing Limited.

2. Davis, J. R. (Ed.). (2004). *Handbook of thermal spray technology*. ASM International, USA: TTS ASM Thermal Spray Society.

3. Gupta, G., & Tyagi, R. (2019). An experimental evaluation of mechanical properties and microstructure change on thin-film–coated AISI-1020 steel. *Materials Performance and Characterization, 8*(3), 532–540.

4. Rajasekaran, B., Mauer, G., Vaßen, R., Röttger, A., Weber, S., & Theisen, W. (2010). Development of cold work tool steel based-MMC coating using HVOF spraying and its HIP densification behavior. *Surface and Coatings Technology, 204*(23), 3858–3863.

5. Bolelli, G., Bonferroni, B., Laurila, J., Lusvarghi, L., Milanti, A., Niemi, K., et al. (2012). Micromechanical properties and sliding wear behavior of HVOF-sprayed Fe-based alloy coatings. *Wear, 276–277*, 29–47.

6. Zheng, Z. B., Zheng, Y. G., Sun, W. H., & Wang, J. Q. (2013). Erosion-corrosion of HVOF-sprayed Fe-based amorphous metallic coating under impingement by a sand-containing NaCl solution. *Corrosion Science, 76,* 337–347.

7. Sadeghimeresht, E., Markocsan, N., & Nylén, P. (2017). Microstructural characteristics and corrosion behavior of HVAF- and HVOF-sprayed Fe-based coatings. *Surface and Coatings Technology, 318,* 365–373.

8. Manish, R. (2015). *Thermal sprayed coatings and their tribological performances*. IGI Global.

9. Caltaru, M., Badicioiu, M., & Ripeanu, R. G. (2013). Establishing the tribological behavior of the HVOF hard facing applied at petroleum gate valves. *Journal of the Balkan Tribological Association, 19*(3), 448–460.

10. Guo, R. Q., Zhang, C., Chen, Q., Yang, Y., Li, N., & Liu, L. (2011). Study of structure and corrosion resistance of Fe-based amorphous coatings prepared by HVAF and HVOF. *Corrosion Science, 53*(7), 2351–2356.

11. Hidalgo, V. H., Varela, J. B., Menendez, A. C., & Martinez, S. V. (2001). High temperature erosion wear of flame and plasma sprayed nickel chromium coatings under simulated coal fired boiler atmosphere. *Wear, 247,* 214–222.

12. Vardelle, A., Moreau, C., Akedo, J., Ashrafizadeh, H., Berndt, C. C., Berghaus, J. O., et al. (2016). The 2016 thermal spray roadmap. *Journal of Thermal Spray Technology, 25*(8), 1376–1440. https://doi.org/10.1007/s11666-016-0473-x.

13. Tejero-Martin, D., Rezvani Rad, M., McDonald, A., et al. (2019). Beyond traditional coatings: A review on thermal-sprayed functional and smart coatings. *Journal of Thermal Spray Technology, 28,* 598–644. https://doi.org/10.1007/s11666-019-00857-1

14. Crawmer, D. E. (2013). *Thermal spray processes* (pp. 54–76). Handbook of Thermal Spray Technology: ASM International.

15. Fauchais, P., Vardelle, A., & Dussoubs, B. (2001). Quo vadis thermal spraying? *Journal of Thermal Spray Technology, 10*(1), 44–66.

16. Fauchais, P. (2004). Understanding plasma spraying. *Journal of Physics. D. Applied Physics, 37*(9), R86–R108.

17. Gupta, G., & Tyagi, R. K. (2019). Investigation of titanium as thin film deposited material thereon effect on mechanical properties. In K. Shanker, R. Shankar, & R. Sindhwani (Eds.), *Advances in Industrial and Production Engineering* (pp 315–323). Lecture notes in mechanical engineering. Singapore: Springer. (24 April 2019). https://doi.org/10.1007/978-981-13-6412-9_30, Print ISBN978-981-6411-2, Online ISBN978-981-13-6412-9.

18. Gupta, G., Tyagi, R. K., Rajput, S. K., Saxena, P., Vashisth, A., & Mehndiratta, S. (2020). PVD based thin film deposition methods and characterization/property of different compositional coatings - A critical analysis. *Materials Today: Proceedings.* https://doi.org/10.1016/j.matpr.2020.07.132, ISSN 2214-7853.

19. Tucker, Jr. R. C. (1994). Thermal Spray Coatings, Surface Engineering (Vol. 5, pp. 497–509). ASM Handbook, ASM International.

20. Amin, S., & Panchal, H. (2016). A review on thermal spray coating processes. *International Journal of Current Trends in Engineering & Research., 2*(4), 554–563.

21. Li, R., He, D. Y., Zhou, Z., Zhao, L. D., & Song, X. Y. (2014). High Temperature Corrosion behavior of wire arc sprayed Fe based coating. *Journal of Surface Engineering, 30,* 573–578.

22. Vuoristo, P. (2014). Thermal spray coating processes. In D. Cameron, (Ed.), *Comprehensive materials processing* (Vol. 4, pp. 229–276). Elsevier Ltd.

23. Li, C.-J., Yang, G.-J., & Li, C.-X. (2013). Development of the particle interface bonding in thermal spray coatings: A review. *Journal of Thermal Spray Technology, 22,* p192–p206.

24. Gu, W., Shen, D., Wang, Y., Chen, G., Feng, W., Zhang, G., et al. (2006). Deposition of duplex Al2O3/aluminum coatings on steel using a combined technique of arc spraying and plasma electrolytic oxidation. *Applied Surface Science, 252*(8), 2927–2932.

25. Choe, H. B., Lee, H.-S., & Shin, J.-H. (2014). Experimental study on the electrochemical anti-corrosion properties of steel structures applying the arc thermal metal spraying method. *Mater., 7*(12), 7722–7736.

26. Jiang, Q., Qiang, M., Fei, T., Yi, X., Ren, B.-L., Liu, Z.-M., et al. (2014). Electrochemical corrosion behavior of arc sprayed Al-Zn-Si-RE coatings on mild steel in 35% NaCl solution. *Transactions of Nonferrous Metals Society, 24*(8), 2713–2722.

27. Chavan, N. M., Kiran, B., Jyothirmayi, A., Phani, P. S., & Sundararajan, G. (2013). The corrosion behavior of cold sprayed zinc coatings on mild steel substrate. *Journal of Thermal Spray Technology, 22*(4), 463–470.

28. Schuerz, S., Fleischanderl, M., Luckeneder, G., Preis, K., Haunschmied, T., Mori, G., et al. (2009). Corrosion behaviour of Zn–Al–Mg coated steel sheet in sodium chloride-containing environment. *Corrosion Science, 51*(10), 2355–2363.

29. Kuiren, L., Pengcheng, M., Nianwen, P., Jianshe, C., & Qing, H. (2010). Influence of silicon coating on the corrosion resistance of Zn-Al-Mg-RE-Si alloy. *Journal of Rare Earths, 28,* 378–381.

30. Galedari, S. A., Mahdavi, A., Azarmi, F., Huang, Y., & McDonald, A. (2019). A comprehensive review of corrosion resistance of thermally-sprayed and thermally-diffused protective coatings on steel structures. *Journal of Thermal Spray Technology, 28*(4), 645–677.

31. Sharma, A., Rajput, S. K., & Soni, S. K. (2018). Cyclic high temperature oxidation behavior of bare and NiCr coated mild steel and low alloyed steel. *Materials Today: Proceedings, 5*(9), 18433–18441.

32. Neville, A., Reza, F., Chiovelli, S., & Revega, T. (2006). Assessing metal matrix composites for corrosion and erosion-corrosion applications in the oils sands industry. *Corrosion, 62*(8), 657–675.

33. Suh, M., Thompson, C. M., Brorby, G. P., Mittal, L., & Proctor, D. M. (2016). Inhalation cancer risk assessment of cobalt metal. *Regulatory Toxicology and Pharmacology, 79,* 74–82.

34. Souza, C. A. C., Ribeiro, D. V., & Kiminami, C. S. (2016). Corrosion resistance of Fe-Cr-based amorphous alloys: An overview. *Journal of Non-Crystalline Solids, 442,* 56–66.

35. Sedriks, A. J. (2003). Resistance of stainless steels and nickel alloys. In *Corrosion: Fundamentals, testing, and protection* (Vol. 13(A), pp. 697–702). ASM Handbook, ASM International.

36. Srivastava, M., Jadhav, M., Chethan, Chakradhar, R. P. S., Muni prakash, M., Singh, S. (2019). Synthesis and properties of high velocity oxy-fuel sprayed FeCoCrNi2Al high entropy alloy coating. *Surface and Coatings Technology, 378*, 124950.
37. Guo, W. M., Zhang, J. F., Wu, Y. P., Hong, S., & Qin, Y. J. (2015). Fabrication and characterization of Fe-based amorphous coatings prepared by high-velocity arc spraying. *Materials & Design, 78,* 118–124.
38. Zhang, H., Xie, Y. T., Huang, L. P., Huang, S. S., Zheng, X. B., & Chen, G. (2014). Effect of feedstock particle sizes on wear resistance of plasma sprayed Fe-based amorphous coatings. *Surface & Coatings Technology, 258,* 495–502.
39. Zhao, M., Zhang, L. X., & Pan, W. (2012). Properties of yttria-stabilized-zirconia based ceramic composite abradable coatings. *Key Engineering Materials, 512*, 1551–1554.
40. Gulyaev, I., Kuzmin, V., Kornienko, E., Vyalova, A., Tyryshkin, P., Sergachev, D., et al. (2019). Plasma spraying of thermal barrier coatings using YSZ powders. *Materials Today, 19*(5), 2134–2138.
41. Gupta, G., & Tyagi, R. K. (2021). A newer universal model for attaining thin film of varied composition during sputtering. In V. C. Pandey, P. M. Pandey, & S. K. Garg (Eds.), *Advances in Electromechanical Technologies.* Lecture Notes in Mechanical Engineering. Singapore: Springer. https://doi.org/10.1007/978-981-15-5463-6_56.

Influence of Process Parameters on Weld Width of Tungsten Inert Gas Welded Joints for Low Carbon Steel AISI 1010 Plates

Ashish Pal and R. P. Singh

Abstract The present work deals with the investigation of effect of input welding process parameters on weld width in tungsten inert gas welding process. The important input welding process parameters considered are as welding voltage, welding current, speed of welding, and the feed rate. The plates having dimensions of 75 mm × 50 mm × 5 mm from the material of low carbon steel AISI 1010 are used to obtain the weld. A total of 16 pairs of these plates are required to be welded to have 16 different welds using tungsten inert gas welding process. Welding voltage, welding current, rate of feed, and speed of welding are considered as input welding process parameters, and the weld width is selected as output parameter. Three input welding parameters are kept at constant at a time by varying the fourth parameter to investigate the effect of fourth parameter. In this way, the effect of all input welding parameters on weld width are obtained. And recorded in table number 1 and shown in Figs. 1, 2, 3 and 4. Generally, the weld width increases with increase of current, feed rate, and welding voltage but decreases with welding speed in the present work.

Keywords Tungsten inert gas welding · Depth of penetration · Weld bead · Input process parameters · Travel speed · Welding torch

1 Introduction

Welding is a method of making permanent joint in two or more pieces of materials. It is one of the most popular processes used to join different materials permanently. At the interface of work pieces, an intense amount of heat is supplied with the help of welding electrodes. This heat melts the work piece and sometimes electrodes also to mix up to certain depth of penetration. There are several methods of welding, in which some processes utilize consumable electrodes and other processes weld

A. Pal (✉) · R. P. Singh
Department of Mechanical Engineering, GLA University, Mathura, Uttar Pradesh, India
e-mail: ashish.pal_me17@gla.ac.in

R. P. Singh
e-mail: rudra.singh@gla.ac.in

without addition of the consumable materials [1]. Tungsten inert gas welding process is generally applied to join very hard materials using sometimes filler materials and sometimes without any filler materials [2]. The main purpose of a joint is to make the parts of the structure of required dimensions and as strong as to be capable to bear the loads applied on it. In all popular joining processes, the welding is the cheapest of all any other joining processes [3]. Any material can be welded easily is determined by its weldability; hence, some materials cannot be joined by welding processes as the weldability of these materials is very less. Also it is possible that any welding process may be suitable for some materials but other materials may not be welded properly by that method, this is the reason of applying different welding processes in the joining of different parts of the welding [4].

Very high temperature is developed during a welding a process; hence, if a non-consumable electrode is applied in such processes the electrode material must have very high melting point [5]. Tungsten is used as the non-consumable electrode material which will not melt during welding process. A process in which tungsten material is used as an electrode is commonly known as tungsten inert gas welding process. To obtain the shielding atmosphere in this process, some external source is essential as no filler material for this purpose is used. In this process, a mixture of argon and helium gasses is supplied externally to form a shielding atmosphere which protects the hot molten weld from possible harmful gasses. At welding temperature which is about 20000 °C, the atmospheric gasses react with the weld metal and form weak contaminations if any external shielding gasses are not supplied [6]. Tungsten inert gas welding process is normally applied to weld very sensitive materials effectively which cannot be welded with any other processes. This process was developed during Second World War to weld some sensitive materials like magnesium and stainless steel, etc., efficiently [7]. The constant current characteristics are suitable for tungsten inert gas welding process, so that it can be controlled easily, as this process is a manual one in which the control over voltage is not easy; hence, the constant voltage process becomes difficult. A power source using DC power supply produces one third heat at negative terminals, and the remaining two third heats is produced at positive terminal, so the unconsumable tungsten electrode is connected to negative terminal. In this case, the electrode will not get high heat and will have longer life. The commonly used important input welding process parameters are welding current, speed of welding, welding voltage, and net feed rate. These parameters are optimized to control the mechanical properties of the weld. In case welding voltage is increased, the arc length increases which increases the distance between work piece and the electrode resulting spreading of the molten electrode material at larger surfaces. In case welding current is increased, the heat supplied to faying surfaces also increases, which increases the molten volume. The weld volume is proportional to the product of weld width, depth of penetration and re-enforcement height which indicates that some of these dimensions will increase with increase of the current. The three important parameters of weld bead are depth of penetration, weld width and reinforcement height. If welding speed is decreased the heat input is increased. If the feed rate is increased the volume of weld also increases. The mechanical properties of the weld bead also depend on the structure of the weld. The macroscopic weld parameters of

the process are reinforcement height, depth of penetration, and weld width. The weld width should be maximum for greater strength, and it should be designed to obtain the optimum value of the weld width for given input parameters [8]. The use of TIG today has spread to a variety of metals like stainless steel and mild steel. The activated TIG welding (ATIG) process mainly focuses on increasing the depth of penetration, but the reduction in the width of weld bead attention has not been paid attention to [9]. Direct polarity is the most commonly employed in GTAW. This effect produces a high heat in the work piece and therefore gives a good penetration and a relatively narrow weld shape. When alternating current is used, it is possible to obtain a good combination of oxides elimination (cleanliness) and penetration [10]. Welding input process parameters play very important role in determining the quality or in other words, the mechanical properties which includes hardness, tensile strength, fatigue strength, etc., of the welded joint. Therefore, the proper choice of welding process parameters and its levels are very crucial for obtaining optimal mechanical properties high tensile steels, Al alloy, and titanium alloy. Like other welding system, TIG welding power sources have also improved from basic transformer types to the highly electronic controlled power source today [11]. Compared with high power density (HPD) welding processes, say laser beam welding (LBW), electron beam welding (EBW), and plasma arc welding (PAW), the TIG welding process is cheaper, easier to operate, and has much better gap bridging capability [12].

2　Experimental Procedure

The experiments were performed in the welding science and technology laboratory of the GLA University, Mathura. The welding of specimens is done with the help of a tungsten inert gas welding process. The specimen pieces are cut from a large thin low carbon steel AISI 1010 plate having 50 mm width and 5 mm thickness, with the help of a power hack saw. The dimensions of the specimens were taken as 75 mm × 50 mm × 5 mm. The specimens are cleaned with the help of rough and hard papers to remove rust, dust, and contaminated surface layers. The sensitivity analysis of the input parameters on the reinforcement height with four input welding parameters requires 16 welded pieces in this work. To obtain 16 welds, thirty two pieces, each of dimensions 75 mm × 50 mm × 5 mm were cut. Two pieces are welded in butt position to obtain the required bead. The used power source is a rectifier from which the power was supplied to the work pieces with the help of a system having torch and tungsten electrode. An electric arc is developed in between the work piece and the tungsten electrode. The energy is supplied through the arc and a column of highly ionized gas and metal vapors. The temperature of more than 20000 °C is developed in TIG welding process. The high amount of heat, so developed was used to melt the material and to form the joint. The schematic diagram of a TIG welding system is shown in Fig. 1, and measurement of bead dimensions by metallurgical microscope is shown in Fig. 2.

Fig. 1 Schematic diagram of TIG welding system [11]
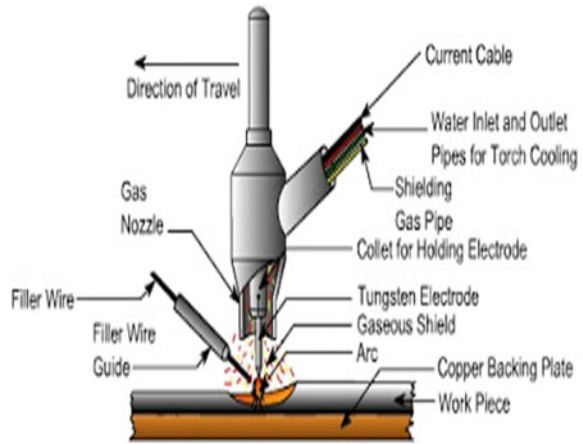
Fig. 2 Measurement of bead dimensions

In this work, four input welding variables selected were current, voltage, speed of welding, and feed rate. The sensitivity analysis can be done if all the input parameters are fixed, and only one parameter is altered, and the effect of this alteration is analyzed. At first, four sets of welds are obtained by having welding current at 150 A, welding voltage at 9.6 V, and welding speed at 1.91 mm/s. Only feed rate is altered as 2.12, 4.23, 6.35, and 8.47 mm/s, respectively, for the welding process. Four sets of welds are obtained by having welding current at 100 A, welding voltage at 9 V, and feed rate at 2.12 mm/s. Only welding speed is altered as 1.19, 1.44, 1.82, and 1.91 mm/s, respectively, for the welding process. Four sets of welds are obtained by having welding current at 100 A, welding speed at 1.19 mm/s, and feed rate at 8.47 mm/s. Only welding voltage is altered as 9, 9.6, 10, and 10.5 V, respectively,

for the welding process. Other four sets of welds are obtained by having welding voltage at 9.6 V, welding speed at 1.44 mm/s, and feed rate at 6.35 mm/s. Only welding current is altered as 100, 125, 150, and 200 A, respectively, for the welding process.

These data are arranged in a Table 1. After welding, all the weld beads obtained are sectioned transversely at two surfaces in such a way that middle portion, 1 mm thick containing weld, heat-affected zone, and base metal are selected for investigation. The welds are generally not proper at start and at end of the work pieces due to several reasons, so these portions are removed. The sectioned parts were ground with the help of emery belt grinders of grades 0, 2, and 3, so that weld bead dimensions become clear and visible. The ground portions were polished with double disk polishing machine. Etching process is done to the polished pieces with the help of a mixture of 2% nitric acid and 98% ethyl alcohol solution. The weld width is measured for every weld with the help of metallurgical microscope and digital sliding caliper and arranged in Table 1. The effect of individual parameters on reinforcement height can be easily analyzed with this table.

Table 1 Variation of weld width with current, voltage, speed of welding, and feed rate

S. no	Current (A)	Voltage (V)	Welding speed (mm/s)	Feed rate (mm/s)	Weld width (mm)
1	150	9.6	1.91	2.12	7.96
2	150	9.6	1.91	4.23	8.01
3	150	9.6	1.91	6.35	8.09
4	150	9.6	1.91	8.47	8.15
5	100	9	1.19	2.12	8.50
6	100	9	1.44	2.12	8.43
7	100	9	1.82	2.12	8.31
8	100	9	1.91	2.12	8.28
9	100	9	1.19	8.47	8.36
10	100	9.6	1.19	8.47	8.41
11	100	10	1.19	8.47	8.49
12	100	10.5	1.19	8.47	8.61
13	100	9.6	1.44	6.35	8.41
14	125	9.6	1.44	6.35	8.45
15	150	9.6	1.44	6.35	8.56
16	200	9.6	1.44	6.35	8.60

3   Result and Discussion

3.1   Effect of Feed Rate on Weld Width

The measurements of weld width for all the weld beads are done using a sliding digital caliper. The results are written in Table 1. From the table, the sensitivity analysis is done.

If the input current, input voltage, and welding speed are fixed at 150 A, 9.6 V, and 1.91 mm/s, respectively, and only feed rate is increased, then the general trend for all the experiments under our study the weld width increases with increase of feed rate. If the feed rate is increased from 2.12 to 4.23 mm/s, the weld width increases from 7.96 to 8.01 mm; if the feed rate is increased from 4.23 to 6.35 mm/s, the weld width increased from 8.01 to 8.09 mm; if the feed rate again increased from 6.35 to 8.47 mm/s, the weld width again increased from 8.09 mm to 8.15 mm. These variations are shown in Fig. 3.

Actually when feed rate increases, more electrode melts per unit time; hence, volume of weldment increases. The input power is proportional to the product of current and voltage and reciprocal to speed of welding. In this case, these three variables are fixed at some values, so the net heat per unit time is fixed. If feed rate increases, then the same heat amounts are used to melt more volume; hence, the temperature of the molten volume becomes lower. Due to this reason, the heat is unable to penetrate to more depth. The volume of weld is proportional to weld width, reinforcement height, and depth of penetration. If the depth of penetration decreases, this implies that the product of weld width and reinforcement height will increase; hence, increase in weld width is according to the convention.

(a) Effect of Feed Rate on Weld Width

(b) Effect of Welding Speed on Weld Width
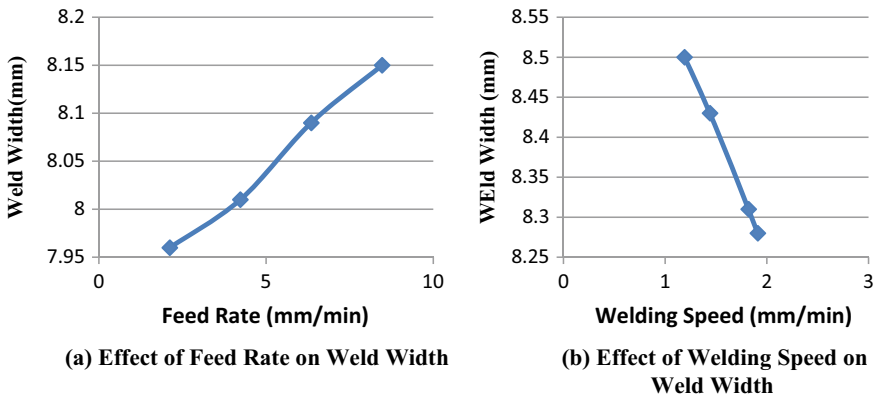
Fig. 3 Effect on weld width

(a) Effect of Welding Speed on Weld Width

(b) Effect of Welding Current on Weld Width
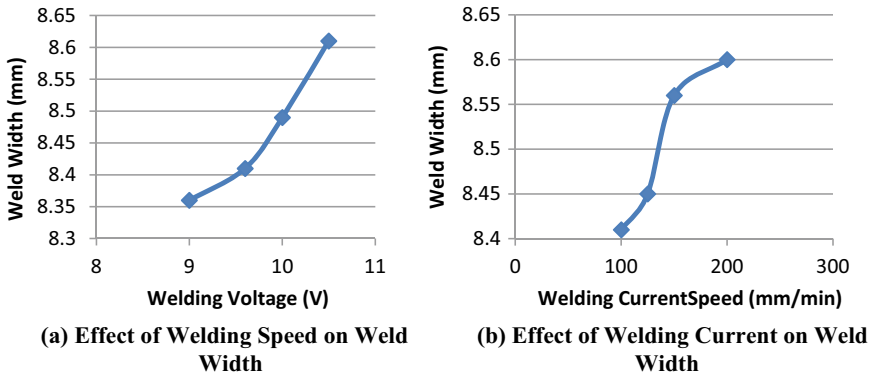
Fig. 4 Effect of welding voltage on weld width

3.2 Effect of Welding Speed on Weld Width

If the input current, input voltage, and feed rate are fixed at 100 A, 9.0 V, and 2.12 mm/s, respectively, and only welding speed is increased, then the general trend for all the experiments under our study the weld width decreased with increase of welding speed. If the welding speed is increased from 1.19 to 1.44 mm/s, the weld width decreased from 8.50 to 8.43 mm, if the welding speed is increased from 1.44 to 1.82 mm/s, the weld width decreased from 8.43 to 8.31 mm, and if the welding speed again decreased from 1.82 to 1.91 mm/s, the weld width again decreased from 8.31 to 8.28 mm. These variations are shown in Fig. 3.

Actually when welding speed is increased the heat rate decreases resulting in less molten volume; hence, volume of weldment decreases. This indicates reduction of weld width, depth of penetration, and reinforcement height with increase of welding speed as the weld volume is proportional to all these three dimensions of the weld.

3.3 Effect of Welding Voltage on Weld Width

If the welding current, welding speed, and feed rate are fixed at 100 A, 1.19, and 6.35 mm/s, respectively, and only the value of welding voltage was increased, then the weld width increased with increase of voltage for our study range of voltage. When voltage changed from 9.0 to 9.6 V, the weld width increased from 8.36 to 8.41 mm, if voltage is increased from 9.6 to 10 V, the weld width increased from 8.41 to 8.49 mm, and if the welding voltage is again increased from 10 to 10.5 V, the weld width again increased from 8.49 to 8.61 mm as shown in Fig. 4a. This can be explained as the voltage increases, the input heat increases and the volume of melted material increases which results in increase of one or more dimensions of the bead. As due to the increase of voltage, the distance between electrode tip and

work piece increases; hence, same heat is distributed at larger area. Actually, the arc is in the form of a cone whose vertex lies at the tip of the electrode; hence, with increase of distance between work piece and the tip of electrode, the surface area covered by molten metal increases; hence, depth of penetration does not increase if welding voltage is increased, so reinforcement height increases. This implies that the variation is according to the convention.

3.4   Effect of Welding Current on Weld Width

If the value of welding voltage, speed of welding, and feed rate are kept as fixed at 9.6 V, 1.44, and 6.35 mm/s and only the value of welding current changes the weld width every time. If the current is increases from 100 to 125 A, the weld width increases from 8.41 to 8.45 mm, if current increases from 125 to 150 A, the weld width increases from 8.45 to 8.56 mm, and if the current further increases from 150 to 200 A, the weld width again increases from 8.56 to 8.60 mm. This indicates that the weld width increases with increase of current for the range of our study as shown in Fig. 4b. It can be explained as the current is increased, the input heat increases and melted volume increases, so one or two or all the three bead dimensions will increase as the product of the three bead dimensions is proportional to the volume of the bead. This implies that the variation of weld width with current is according to the convention.

4   Conclusions

From investigations and sensitivity analysis, it is clear that the welding process is a complicated process, and there is no exact relationship between input and output variables. Only general trend can be observed and predicted with the help of a series of experimental results. The volume of the weld bead is the function of the product of weld width, reinforcement height, and depth of penetration. If this volume increases, all the dimensions may not increase, but some dimensions may increase, and some other dimensions may decrease. If volume is increased, it is possible that weld width, reinforcement height, and depth of penetration all increase, it is also possible that any one dimension increases, and the other two dimensions decrease, and again it is also possible that any two dimensions increase, and the remaining one dimension decreases. The volume of weld is also proportional to heat rate and the heat rate is defined as the product of welding current and welding voltage divided by speed rate. Considering these descriptions, the general trend can be concluded as:

1. Weld width increases if current of welding is increased.
2. Weld width increases if voltage of welding increased.
3. Weld width decreases if speed of welding is increased.

4. Weld width increases if feed rate increased.
5. This research can be very much helpful as the strength of any weld is dependent on its weld width. If optimum value of weld width is obtained, the maximum strength of the weld can be achieved.

5 Recommendations for Future Work

Following are recommendations for future study:

(1) The experiment was performed for low carbon steel, which can be extended to other materials also.
(2) In this experiment, the process of welding utilized was the tungsten inert gas welding process, and other processes like submerged arc welding and shielded metal arc welding process, etc., can also be used.
(3) The ranges of current, voltage, speed, and feed were limited; these can be increased for better exposure of the trend of weld width, with the change of these values.
(4) Artificial neural networks, Taguchi methods, etc., can be used to make clearer the study.

References

1. Juang, S. C., & Tarng, Y. S. (2002). Process parameter selection for optimizing the weld pool geometry in the tungsten inert gas welding of stainless steel. *Journal of Materials Processing Technology, 122*, 33–37.
2. Xi-he, W., Ji-tai, N., Shao-kang, G., Le-jun, W., & Dong-feng, C. (2009). Investigation on TIG welding of SiC-reinforced aluminum–matrix composite using mixed shielding gas and Al–Si filler. *Materials Science and Engineering A, 499*(1), 106–110.
3. Qinglei, J., Yajiang, L., Puchkov, U. A., Juan, W., & Chunzhi, X. (2010). Microstructure characteristics in TIG welded joint of Mo–Cu composite and 18-8 stainless steel. *International Journal of Refractory Metals & Hard Materials, 28*(3), 429–433.
4. Hussain, A. K., Lateef, A., Javed, M., & Pramesh, T. (2010). Influence of welding speed on tensile strength of welded joint in TIG welding process. *International Journal of Applied Engineering Research, 1*(3), 518–527. Dindigul.
5. Sakthivel, T., Vasudevan, M., Laha, K., Parameswaran, P., Chandravathi, K. S., Mathew, M. D., et al. (2011). Comparison of creep rupture behavior of type 316L (N) austenitic stainless steel joints welded by TIG and activated TIG welding processes. *Materials Science and Engineering A, 528*(22), 6971–6980.
6. Tseng, K. H., & Hsu, C. Y. (2011). Performance of activated TIG process in austenitic stainless steel welds. *Journal of Materials Processing Technology, 211*(3), 503–512.
7. Narang, H. K., Singh, U. P., Mahapatra, M. M., & Jha, P. K. (2011). Prediction of the weld pool geometry of TIG arc welding by using fuzzy logic controller. *International Journal of Engineering, Science and Technology, 3*(9), 77–85.
8. Chandra, M. S., Pal, P. K., Bandyopadhyay, A., & Ramesh, R. P. (2018). Determination of tungsten inert gas welding input parameters to attain maximum tensile strength of 316 l austenitic stainless steel. *Journal of Mechanical Engineering, 68*(3), 231–248.

9. Magudeeswaran, G., Nair, S. R., Sundar, L., & Harikannan, N. (2014). Optimization of process parameters of the activated tungsten inert gas welding for aspect ratio of UNS S32205 duplex stainless steel welds. *Defense Technology, 81,* 1–10. Elsevier, DT.
10. Khotiyam, S. K. (2017). Comparison of Hardness and Tensile Strength of TIG and MIG Welding Using Stainless Steel-202. *International Journal of Advance Engineering and Research Development, 4*(12), 264–267.
11. Pradhan, R., Krishna, P. K. M., Asif, S. D., & Murthy, D. S. S. K. (2019). Experimental investigation and comparative study of MIG & TIG welding on SS 202 and SS 304 materials. *International Journal of Recent Scientific Research, 10*(04A), 31678–31683.
12. Zhenyu, F., Huijun, L., Pan, Z., & Dominic, C. (2020). In-depth welding procedure qualification of Keyhole Tungsten Inert Gas welded high hardness grade quenched and tempered steel and dissimilar stainless steel joint. University of Wollongong Thesis Collections, University of Wollongong, Library: research-pubs@uow.edu.au.

Effect of Welding Speed on the Dimensions of Bead in Tungsten Inert Gas Welding Process

Ajit Singh and Rudra Pratap Singh

Abstract Generally, the joining of parts in our industrial life is very important. The industries use joints to increase the length or surfaced area for their requirements and these requirements can be fulfilled generally by joints. Welding is one of the best methods of making joints in which the tungsten inert gas welding is an important method in the welding process. In welding, the beads are formed which are consisted of depth of penetration, weld width and reinforcement height. These dimensions of the beads are the deciding factors of mechanical properties of the weld. In this work, the several experiments were performed with tungsten inert gas welding machine to critically study the effect of welding speed on the dimensions of the bead. All the other input variables except the welding speed were fixed, as the feed rate at 2.12 mm/s, voltage at 9.0 V, welding current at 100 A for whole the experimentation period. Only the values of welding speed were varied and the effect of this variation on depth of penetration, weld width and reinforcement height was investigated. Total six pairs of mild steel plates of dimensions 75 mm × 50 mm × 5 mm were welded for six variations of welding speed. The results were tabulated and were expressed in three different diagrams in which one was for depth of penetration, one was for reinforcement height and one was for weld width. This study explains the sensitivity analysis of the effect of the welding speed on the three dimensions of the weld bead.

Keywords Tungsten inert gas welding · Feed rate · Weld bead · Input process parameters · Reinforcement height

A. Singh (✉) · R. P. Singh
Mechanical Engineering Department, GLA University, Uttar Pradesh, Mathura, India
e-mail: ajit.singh_me17@gla.ac.in

R. P. Singh
e-mail: rudra.singh@gla.ac.in

1 Introduction

In industries, it is essential to join different parts of any machine or structure for working efficiently. The parts of structure which are to be joint may be of same material or dissimilar material [1]. A large number of problems are to be faced in dissimilar welding which may result in cracking of weld and heat affected zone and reduction in strength and other mechanical properties of the whole welded structure. To overcome this problem proper research, investigation and detailed study are needed for welding parameters with their effect on the properties of the weld bead. The mechanical properties of the weld have close relation with the dimensions of the weld bead [2]. Due to the variation of input process parameters, the mechanical properties of the weld vary in the welding process. The welding input process parameters which are generally applied in the work are welding voltage, welding speed, welding current and feed rate. If the weld width is not optimum, the mechanical properties may be lacking. The reinforcement height of the weld must also be proper and optimum. The height of top of the weld surface over bottom surface of base metal, up to which the weld is extended, is known as reinforcement height. From mechanical engineering point of view if reinforcement height is more, it will produce high stress concentration so it should be kept as small as possible. If metallurgical point of view is considered, it shows that reinforcement height should be more for compensating bearing capacity of load by increasing area [3]. The depth of penetration is the depth in the workpiece up to which, the mixing of base metal material with electrode material takes place. The depth of penetration should be as high as in the weld but the volume of the weld material in any particular set of inputs is fixed. The product of depth of penetration, reinforcement height and weld width is generally constant in any particular set of welding input process parameters, so if depth of penetration is decreased, the product of weld bead width and reinforcement height will be increased, and this can be used to explain for other dimensions also. For better strength of the weld, the optimum values of all the dimensions of depth of penetration, reinforcement height and weld width are highly desired [4]. There are a large number of input welding process parameters which have a large effect on the dimension of the weld bead. The input parameters like welding speed, welding voltage, welding current, feed rate, electrode diameter, electrode angle, etc., are very important. The welding process for this study was taken as tungsten inert gas (TIG) welding. TIG welding process generally may utilize non-consumable tungsten electrode in the welding torch using a constant current welding power supply source. Current values in TIG welding process are generally used in the range of 3 A to 300 A, and the voltage values are taken in general is in the range between 10 and 35 V. The TIG welding process may be manual in some cases and semi-automatic in some other cases [5]. In some cases, the filler metal may not be used and only workpieces are fused and mixed in the weld. Argon alone or a mixture of argon and helium mixture may be used as shielding gases to protect the weld from atmospheric contamination. Several materials which may be sensitive, ferrous and non-ferrous can be welded by TIG welding process [6]. A very good weld can be obtained for

all the sensitive materials which may be aluminum, magnesium or copper alloys. The sensitive metals have affinity to react readily with atmospheric gasses to form contaminations in any other processes of welding. If less depth of penetration is needed, direct current electrode positive should be used. If very high current of about 600 A is supplied for welding, then water cooling is required otherwise in low current cases air cooling should be used. The inside diameter of nozzle is generally taken as about three times the diameter of electrode for the better performance of the tungsten inert gas welding process. The speed of welding is inversely proportional to heat rate, it should be optimum for the best weld. Filler metal may or may not be used. Argon helium mixture is generally used as shielding gases to protect the weld from atmospheric contamination [7]. Several materials ferrous and non-ferrous can be welded by TIG process [8]. A stronger weld can be achieved for sensitive materials like aluminum, magnesium and copper alloys also. The sensitive metals react rapidly with air to form contaminations in other processes of welding [9]. If shallow weld is desired, direct current electrode positive is used. If high current of about 600 A is used for welding then water cooling is required otherwise air cooling is preferred [10].

2 Experimental Procedure

TIG welding process is an important arc welding process in which non-consumable tungsten electrodes are used with or without consumable filler metals. Mild steel plates of dimensions 75 mm × 50 mm × 6 mm were cut from a long plate for making the weld. The plates were cut with the help of a power hack saw. A rectifier was utilized for power transmission to the workpieces with the help of a torch and a tungsten electrode. An electric arc was created in between the workpieces and the tungsten electrode. The energy so generated is conducted through the arc and a column of highly ionized gasses and metal vapors. The temperature of about twenty thousand degree centigrade or more is produced in this process. This high heat is used to melt the material and to form the joint. The process of tungsten inert gas welding process is shown in Fig. 1. A weld bead of experiment is shown in Fig. 2. The grinding of specimen is shown in Fig. 3.

The measurement of bead dimensions with the help of metrological microscope is shown in Fig. 4. To investigate the effect of welding speed on the dimensions of weld bead, total 12 mild steel plates all having dimensions of 75 mm × 50 mm × 6 mm were cut from a long plate with the help of a power hack saw. These pieces were rubbed properly with emery papers to remove rust dust, etc., so that after welding the weld is contamination free. The feed rate was fixed at 2.12 mm/s, the voltage was fixed at 9.0 V and the welding current was fixed as 100 A. There were total six welded joints developed to study the effect of welding current. The value of welding speeds were taken as 1.19, 1.28, 1.44, 1.64, 1.82 and 1.91 mm/s, respectively. The weld beads were sectioned transversely at two surfaces in such a way that middle portion containing 1 mm thick complete portion containing weld, heat affected zone
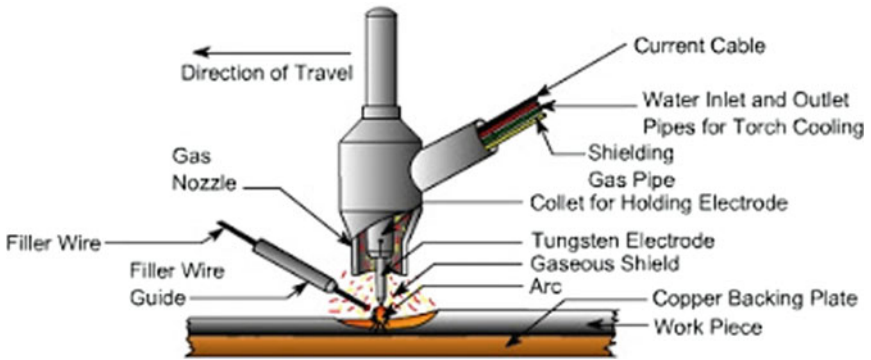
Fig. 1 Tungsten inert gas welding [3]

Fig. 2 Weld obtained in laboratory by TIG welding
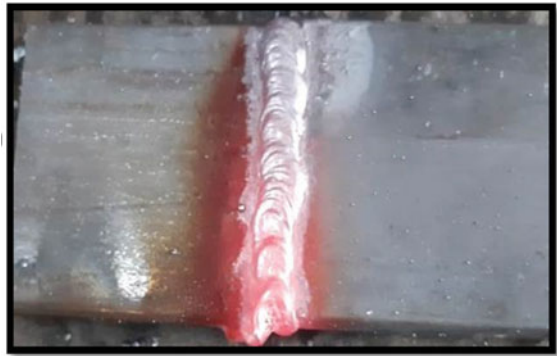
Fig. 3 Grinding of specimen by emery belt

Fig. 4 Measuring bead
dimensions with microscope

Table 1 Variation of weld bead, depth of penetration and reinforcement height with welding speed

S.No	Welding current (A)	Welding voltage (V)	Feed rate (F) (mm/s)	Welding speed (s) (mm/s)	Weld width (mm)	Depth of penetration (mm)	Reinforcement height (mm)
1	100	9	2.12	1.19	8.50	1.79	0.60
2	100	9	2.12	1.28	8.21	1.76	0.58
3	100	9	2.12	1.44	7.89	1.73	0.55
4	100	9	2.12	1.64	7.77	1.71	0.53
5	100	9	2.12	1.82	7.61	1.69	0.49
6	100	9	2.12	1.91	7.38	1.65	0.45

and base metal were selected for investigation. The welds are generally not proper at start and at the end of the workpieces due to several reasons so these portions are not proper for the study hence these portions are removed. The sectioned parts were ground with the help of emery belt grinders of grades 0, 2 and 3 so that weld width, depth of penetration and reinforcement height become clear and visible. The ground portions were polished with double disk polishing machine. Etching process was done to the polished pieces with the help of a mixture of 2% nitric acid and 98% ethyl alcohol solution. The weld width, depth of penetration and reinforcement height were measured for every weld with the help of digital sliding calipers and metrological microscope and tabulated in Table 1. The effect of welding speed on the dimensions of weld beads was studied with the help of the data of the table showing the relation between welding speed with weld width, reinforcement height and depth of penetration.

3   Result and Discussion

The effect of welding speed on weld width and depth of penetration an reinforcement height are shown in Figs. 5, 6 and 7, respectively, and are summarized in articles 3.1, 3.2 and 3.3. The heat rate is the product of welding voltage and welding current when divided by welding speed. Melted volume is proportional to heat rate. The melted volume is proportional to weld width, depth of penetration and reinforcement height. If heat rate is constant and one bead dimension increases due to certain reason then this indicates that the product of the remaining two bead dimension will decrease, which says that in the two dimensions one may increase at the cost of third dimension.
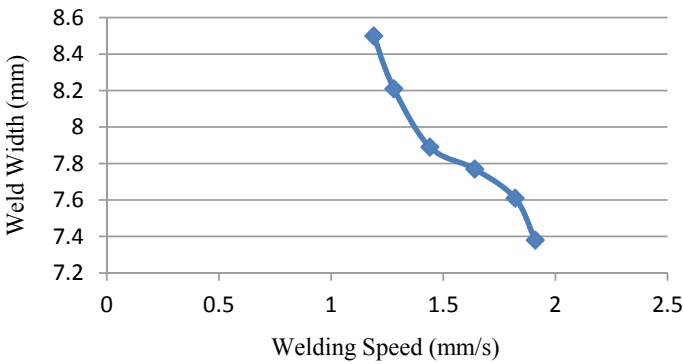
Fig. 5   Effect of welding speed on weld width
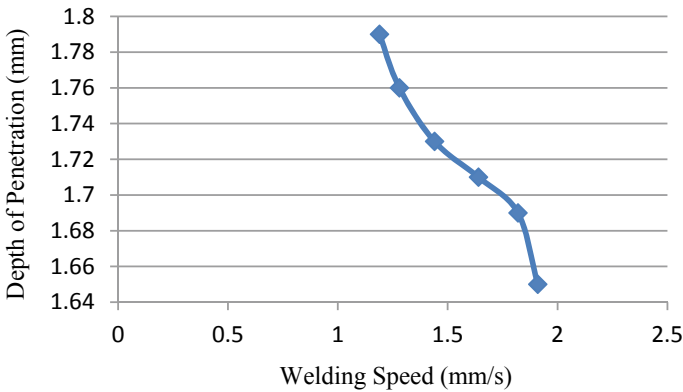
Fig. 6   Effect of welding speed on depth of penetration
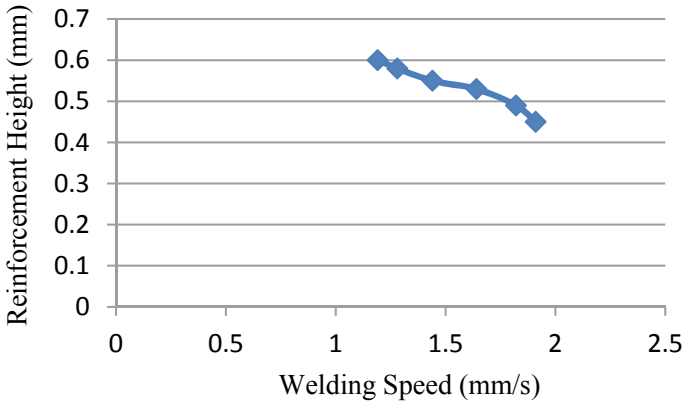
Fig. 7 Effect of welding speed on reinforcement height

3.1 Effect of Welding Speed on Weld Width

The weld width decreased throughout our experimental range with increase of welding speed as shown in Fig. 5. When the welding speed was at 1.19 mm/s, the weld width was found as 8.50 mm. If the speed was increased to 1.28 mm/s, the weld width decreased to 8.21 mm and when the speed was raised to 1.44 mm/s, the weld width decreased to 7.89 mm. When the speed was increased to 1.64 mm/s, the weld width decreased to 7.77 mm and when the speed was increased to 182 mm/s, the weld width decreased to 7.61 mm and finally when the welding speed was increased to 1.91 mm/s, the weld width decreased to 7.38 mm. When the welding speed is increased the input heat decreases as input heat is inversely proportional to the welding speed. The input heat is proportional to melt volume or volume of weld. The weld has three major dimensions as weld width, depth of penetration and reinforcement height. If welding speed is increased, these dimensions can be supposed to be decreased. Sometimes one or more dimensions show opposite behavior, i.e., increases with increase of welding speed in that case the remaining dimensions must compensate for the opposite behavior presented.

3.2 Effect of Welding Speed on Depth of Penetration

The depth of penetration decreased throughout our experimental range with increase of welding speed as shown in Fig. 6. When the welding speed was at 1.19 mm/s, the depth of penetration was found as 1.79 mm. If the speed was increased to 1.28 mm/s, the depth of penetration decreased to 1.76 mm and when the speed was raised to 1.44 mm/s, the depth of penetration decreased to 1.73 mm. When the speed was increased to 1.64 mm/s, the depth of penetration decreased to 1.71 mm and when the

speed was increased to 1.82 mm/s, the depth of penetration decreased to 1.69 mm and finally when the welding speed was increased to 1.91 mm/s, the depth of penetration decreased to 1.65 mm. When the welding speed is increased the input heat decreases as input heat is inversely proportional to the welding speed. The input heat is proportional to melt volume or volume of weld. The weld has three major dimensions as weld width, depth of penetration and reinforcement height. If welding speed is increased, these dimensions can be supposed to be decreased. Sometimes, one or more dimensions show opposite behavior, i.e., increases with increase of welding speed in that case the remaining dimensions must compensate for the opposite behavior presented.

3.3   Effect of Welding Speed on Reinforcement Height

The reinforcement height decreased throughout our experimental range with increase of welding speed as shown in Fig. 7. When the welding speed was at 1.19 mm/s, the reinforcement height was found as 0.60 mm. If the speed was increased to 1.28 mm/s, the reinforcement height decreased to 0.58 mm and when the speed was raised to 1.44 mm/s, the reinforcement height decreased to 0.55 mm. When the speed was increased to 1.64 mm/s, the reinforcement height decreased to 0.53 mm and when the speed was increased to 1.82 mm/s, the reinforcement height decreased to 0.49 mm and finally when the welding speed was increased to 1.91 mm/s, the reinforcement height decreased to 0.45 mm. When the welding speed is increased the input heat decreases as input heat is inversely proportional to the welding speed. The input heat is proportional to melt volume or volume of weld. The weld has three major dimensions as weld width, depth of penetration and reinforcement height. If welding speed is increased, these dimensions can be supposed to be decreased. Sometimes, one or more dimensions show opposite behavior, i.e., increases with increase of welding speed in that case the remaining dimensions must compensate for the opposite behavior presented.

4   Conclusions

The shape of weld bead in case of a welded joint ascertains the mechanical properties of the joint. Weld joint can be designed having optimum mechanical properties with some bead dimensions, which can be recognized with the help of some experiments. This work was aimed to recognize the effect of welding speed on the bead dimensions, which can be used to determine the mechanical properties of the weld. In this work, the relationships of welding speed with weld width, reinforcement height and depth of penetration were represented with the help of some diagrams. The experimental results obtained indicate that:

1. With increasing in welding speed from 1.19 to 1.91 mm/s, the general trend of the weld width was found to decrease from 8.50 to 7.38 mm.
2. With increasing in welding speed from 1.19 to 1.91 mm/s, the general trend of the depth of penetration was found to decrease from 1.79 to 1.65 mm.
3. With increasing in welding speed from 1.19 to 1.91 mm/s, the general trend of the reinforcement height was found to decrease from 0.60 to 0.45 mm. The trend was followed throughout the range of experimentation without any exception.
4. The optimum value of welding speed can be selected as per requirement of weld width, depth of penetration and the reinforcement height with the help of this work.
5. The maximum values of weld width were 8.50 at 1.19 mm/s welding speed, maximum depth of penetration was found to be 1.79 mm at 1.19 welding speed, whereas the maximum value of the reinforcement height was 0.60 at 1.19 mm/s welding speed.
6. The minimum values of weld width were 7.38 mm, the minimum value of depth of penetration was 1.65 mm and the minimum value of reinforcement height was found to be 0.45 mm all at 1.19 mm/s welding speed.

5 Recommendations for Future Work

Following are recommendations for future study:

1. The experiment was performed for low carbon steel, which can be extended to other materials also.
2. In this experiment, the process of welding utilized was the tungsten inert gas welding process, other processes like submerged arc welding and shielded metal arc welding process, etc., can also be used.
3. The range of welding speed was limited from 1.19 to 1.91 mm/s; it can be increased for better exposure of the trend of depth of penetration, weld width and reinforcement height with the change of welding current.
4. 4. Artificial neural networks, Taguchi methods, etc., can be used to make clearer the study.

References

1. Xi-he, W., Ji-tai, N., Shao-kang, G., Le-jun, W., & Dong-feng, C. (2009). Investigation on TIG welding of SiCp-reinforced aluminum–matrix composite using mixed shielding gas and Al–Si filler. *Materials Science and Engineering: A, 499*(1), 106–110.
2. Hussain, A. K., Lateef, A., Javed, M., & Pramesh, T. (2010). Influence of welding speed on tensile strength of welded joint in TIG welding process. *International Journal of Applied Engineering Research, 1*(3), 518–527. Dindigul.

3. Sakthivel, T., Vasudevan, M., Laha, K., Parameswaran, P., Chandravathi, K. S., Mathew, M. D., & Bhaduri, A. K. (2011). Comparison of creep rupture behaviour of type 316L (N) austenitic stainless steel joints welded by TIG and activated TIG welding processes. *Materials Science and Engineering: A, 528*(22), 6971–6980.
4. Narang, H. K., Singh, U. P., Mahapatra, M. M., & Jha, P. K. (2011). Prediction of the weld pool geometry of TIG arc welding by using fuzzy logic controller. *International Journal of Engineering, Science and Technology, 3*(9), 77–85.
5. Karunakaran, N. (2012). Effect of pulsed current on temperature distribution, weld bead profiles and characteristics of GTA welded stainless steel joints. *International Journal of Engineering and Technology, 2*(12).
6. Raveendra, A., & Kumar, B. R (2013). Experimental study on pulsed and non- pulsed current TIG welding of stainless steel sheet (SS304). *International Journal of Innovative Research in Science, Engineering and Technology, 2*(6).
7. Ghetiya, N., & Pandya, D. (2014). Mathematical modeling for the bead width and penetration in activated TIG welding process. *International Conference on Multidisciplinary Research & Practice, 1,* 247–252.
8. Kumar, G. R., Ram, G. D. J., & Sajja Koteswara, R. R. (2016). Effect of activated flux and nitrogen addition on the bead geometry of borated stainless-steel GTA welds. MTAEC9, vol 50 (3), pp. 357.
9. Kurtulmuş, M. (2017). Activated flux TIG welding of austenitic stainless steels. *Journal of Scientific and Engineering Research., 4*(7), 169–177.
10. Balram, Y., Kumar, S., & Babu, S. S. (2019). Effect of Filler wire on weld strength of dissimilar pulsed GTA Monal 400 and ASI 304 weldments. *Materials Today*, 759. (29–06–2019).

Fabrication of Hybrid Material (Al-SiC-Fly Ash) for Industrial Application

Rohan Raj, Kartik Bhardwaj, Sanchit Sharma, Naveen Kumar, and Priyank Srivastava

Abstract With the development, reinforced Metal matrix composites (MMC) is becoming a significant area of research, and it is rapidly growing in various engineering fields because it exhibits exceptional mechanical properties. Keeping this in view, the present study is aimed to focus on formation of hybrid material and discover the numerous possibilities of reinforcing aluminium 7075 with low priced and readily available silicon carbide (SiC) and fly ash (FA) for the development of hybrid material. The reinforcements were added into the aluminium matrix alloy with different weight proportions with the help of stir casting apparatus. The planning of experiments was done through Taguchi's technique, and experiments were conducted on this plan. This technique is employed to analyse the contribution of most influential parameters on aluminium matrix composites (AMC) during stir casting process. L9 orthogonal array is selected for this analysis. The influential parameters associated for achieving the uniform distribution, wettability and porosity in AMC are presented and discussed.

Keywords Hybrid material · Aluminium alloy · Silicon carbide · Fly ash · Stir casting · Taguchi method

R. Raj · K. Bhardwaj · S. Sharma (✉) · N. Kumar · P. Srivastava
Department of Mechanical Engineering, Amity University, Noida, India
e-mail: sanchit2609s@gmail.com

R. Raj
e-mail: rohanraj7920@gmail.com

K. Bhardwaj
e-mail: kartikbhardwaj798@gmail.com

N. Kumar
e-mail: nkumar12@amity.edu

P. Srivastava
e-mail: psrivastava5@amity.edu

1 Introduction

In modern scenario, well-designed materials which have improved and enhanced characteristics are in great demand, and more importance is given for various engineering and technological applications. In many situations, conventional materials do not have the properties for a specific function. Therefore, this type of problem can be solved by hybrid materials. A hybrid material is composed of an intimate mixture of inorganic components, organic components, or both type of components. In recent industrial applications, aluminium MMCs are being widely used. Automotive, aerospace, military, electronic, etc., are the various areas in which its application is done because of its tremendous mechanical properties. The main applications of aluminium in automobile industries are in the production of valve train, piston rod, piston pin, covers, cylinder heads, suspension, driveline, housings of gear box, pumps, brakes, etc. In aerospace industries, the production of missile fins, aircraft electrical ac doors, wing panel, jet engine blades etc. The rest of the paper is structured as Sect. 2: explores the structured Literature Review, Sect. 3: presents the Materials and Methods, Sect. 4: presents the Experimental Procedure, Sect. 5: represents the Results and discussions and Sect. 6: represents the Conclusion.

2 Literature Review

The findings of various research papers regarding the fabrication of MMC's reinforced with

SiC and FA particles by stir casting techniques are summarized below:

Improve mechanical properties of MMC's make them suitable for automobile components like disc brakes, brake drum and other engineering components [1, 2]. When aluminium alloy was mixed with SiC particles using stir casting technique, uniform distribution was observed [3]. When aluminium matrix is mixed with FA, various components like brake drums, differential bearings, covers, cylinder heads, etc., can be made [4]. The density and the thermal expansion coefficient decrease with the addition of FA, whereas, on the positive side, the tensile strength, compressive strength, hardness, damping capacity, dry sliding wear and slurry erosive wear increase [5, 6]. There were technical problems linked with stir casting techniques which are used for the production of aluminium alloy MMC's/SiC to have low porosity, better wettability and uniform distribution of reinforcement. The composite materials that were produced by liquid metallurgy methods show brilliant bonding between the materials when reactive agents such as Mg are added to increase the wettability [7]. A two-step mixing technique improves the wettability of SiC particles, and a better particle distribution is ensured [8]. With the increase in fraction of reinforcement in matrix, an improvement is seen in tensile strength, hardness and yield strength. There is a decrease in % rate of elongation with the addition of FA and SiC in aluminium alloy [9]. The density of Al-SiC, Al-FA and Al-SiC-FA decreases

linearly because both SiC and FA are low density materials [9]. The liquid metallurgy methods are one of the most economical techniques for MMC's production [10]. It is so cost efficient that for the production of composites materials using casting approach, the cost is one third to half that of other techniques [7, 11]. The stirrer plays an important role in stir casting technique. During the stir casting technique, the role of stirrer is to (i) transfer particles into liquid metals and (ii) maintain the particles in the state of suspension [7, 12]. It has been recommended that the stirrer should be placed (0.65–0.7) h below the melt [7, 13]. One of the most important defects that can be faced during production of hybrid material is porosity, oxide inclusions [7, 14]. The process of degassing liquid aluminium is one of the main steps to prevent porosity. Degassing is carried out in a vacuum chamber [15]. It has been seen that with the increase in mould temperature, the soundness of casting will improve, and therefore, it decreases the porosity level. Hence, it is recommended to preheat the die before pouring the melting metal [16]. By mixing aluminium alloy with FA using stir casting technique, high separated density of such composites can be created and improve the mechanical properties. [17]. There is a major role of SiC addition in aluminium alloy-FA composite as it increases micro and macro hardness [18]. The mixing of SiC particles in Al7XXX (7th grade) increases the modulus of elasticity and yield strength, but there is decrease in ultimate compressive strength and ductility [19, 20]. There is a uniform dispersion of reinforcement particles at higher reinforcement contents which improves its microstructure [21]. Results of MMC's showed that there is no reaction between Al matrix and SiC reinforcements through X-ray diffraction [22]. The addition of SiC particles in Al matrix enhances the corrosion resistance [23].

2.1 Parameters Affecting Preparation of Hybrid Materials

So as to get the ideal properties of hybrid, the distribution of the reinforced material in the matrix metal should be even. The porosity level also must be limited. Some of the parameters affecting the preparation of hybrid are discussed below:

(a) The distribution of reinforced materials

If distribution of the reinforced material is not even, then the accumulation of the reinforced material will occur which can result in decreasing the strength values of the base metal. This problem occurs during the casting process and dissolving process. To get rid of this problem continuous stirring of the melting metal at a certain rpm is necessary. This stirring is done with the help of stir casting apparatus [7].

(b) Wettability

Wettability is defined as the ability of fluid to spread on a surface. It is the contact between a fluid and solid surface. It becomes more important to understand how wettability affects the preparation of hybrid. If wettability of the melting metal is poor or say less, then the surface tension of the melting metal will be more which causes

shrinkage of melting metal and increased density which will lead to poor mixing or distribution of reinforced material. Also if the wettability is more, then the surface tension will be less which will decrease the density of melting metal, and hence, all reinforced material will accumulate at one place, and proper mixing will not occur and lead to decreasing the strength values of base metal that is aluminium. It is suggested that the wettability of melting metal should be increased for even distribution of reinforced materials. In order to increase wettability, addition of magnesium (1.5% by weight) is suggested [7].

(c) Porosity

Porosity is defined as the present of voids in the casting. The porosity in hybrid results primarily from air bubbles entering the melting metal either independently or in form of air envelope during addition of reinforcement particles. Presence of porosity in the hybrid leads to decreasing strength of the hybrid [7].

In this study, an attempt is made to fabricate a hybrid material using Aluminium 7075 as base metal with reinforcement SiC and FA. The method available for the production is stir casting technique as it is suitable for study purpose. After reviewing several research papers, three sets of composition are decided for preparation of hybrid material by weight percentage, which are as follows: 95% Aluminium 7075+2.5% Fly ash+2.5% Silicon Carbide 90% and Aluminium 7075+5% Fly ash+5% Silicon Carbide, 85% Aluminium 7075+7.5% Fly ash+7.5% Silicon Carbide.

3 Materials and Methods

3.1 Raw Materials

The matrix metal used in the experimental study was a commercially available Al7075, and FA and SiC were purchased from Indian Abrasives, Faridabad, India. The size of fly ash and silicon carbide particle lies in the range of 16-30 microns.

3.1.1 Selection of Alloy—Aluminium 7075

The main reason for choosing Al7075 is because it is the strongest alloy available and also comparable to many types of steel. Because of its high strength, it is often used where it is subjected to high stress. Major alloying element in Al7075 is zinc as it is responsible for its high strength. Al7075 being lightweight and also its resistance to stress and strain makes it extremely useful in automobile, aerospace, defence equipment and marine industries. When compared to other grades of aluminium alloy, it shows exceptional mechanical properties like tensile strength, yield strength and modulus of elasticity (Table 1).

Table 1 Comparison of mechanical properties of Al-6061 and Al-7075-T6

Property	Al-6061	Al-7075-T6
Tensile strength	290 MPa	572 MPa
Yield strength	276 MPa	503 MPa
Modulus of elasticity	68.9 GPa	71.7 GPa

3.1.2 Silicon Carbide

The second material chosen is silicon carbide. Silicon carbide is used as reinforcement in the form of powder of 400 grit size (16–22 μm approximately and 99% purity) to improve and enhance the properties of conventional materials. Silicon carbide has various applications in cutting tools, ornaments, automobile parts, electronic circuits, structural materials, nuclear fuel particles, etc., because of its high hardness. The silicon carbide reinforced in aluminium materials has many applications like in disc brakes, frames used in bicycles, aerospace and automobile industries. When silicon carbide is poured in the metal matrix composites, it improves the overall strength, corrosion and wear resistance of the material. With the reinforcement of silicon carbide particles in aluminium, many mechanical properties get enhanced. Yield strength improves up to 20%, it lowers the thermal expansion coefficient, modulus of elasticity increases, and wear resistance is more compared to the unreinforced metal matrix (Figs. 1 and 2).

Fig. 1 Silicon Carbide of 400 Grit size

Fig. 2 Powered fly ash

3.1.3 Fly Ash

The third material chosen is fly ash. Fly ash is nothing but a very fine powder of burnt pulverized coal which is a by-product of thermal power plant. This by-product is generated in combustion, and it has very fine particles. Ashes that are settled at bottom are called as bottom ash, and the one rises in the vent or duct is known as fly ash. They are trapped using electrostatic precipitators or other particle filtration equipment can be used. One of the main reasons to use FA as reinforcement or filler in MMCs is that FA is the by-product of combustion of coal. It is present in huge quantity at low costs. Hence, the cost of composites or hybrids can be reduced by incorporating in the metal matrices. It is having high resistivity to the electricity, very low thermal conductivity and density which makes it helpful for making light composites or hybrids. FA as a reinforcement in Al metal matrix decreases cost, density and increases stiffness, hardness, wear. It also improves maintainability, coefficient, damping, etc., which are the basic requirements of industries such as automotive industry.

3.1.4 Magnesium

During melting, the molten aluminium comes in contact with the atmosphere and moisture and forms a layer of aluminium oxide (Al_2O_3). This layer protects the molten metal to react further with atmosphere and moisture. But in stir casting method, the continuous stirring of molten metal occurs which prevents the formation of aluminium oxide layer, and hence, the molten aluminium during stirring remains in contact with the atmosphere and moisture. This contact results in continuous oxidation of molten aluminium. This continuous oxidation reduces the wettability of the aluminium, and the reinforcement particles left unmixed.

$$2Al + 3H_2O \Leftrightarrow Al_2O_3 + 6H$$
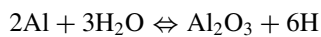
To stop oxidation completely, creation of inert environment becomes an important condition. This method involves numerous complications. Therefore, wetting agent such as magnesium is used an another solution to this problem.

3.2 Techniques for Manufacturing of MMC's

The processes for fabrication of MMC's can be classified into two main groups, i.e. (i) Solid State Processes and (ii) Liquid State Processes. The selection of process depends on many factors like cost, availability, distribution of reinforcement, etc. Therefore, we have selected the stir casting technique.

3.2.1 Stir Casting (Liquid State Casting)

Stir casting is the process in which fabrication of composite materials occurs. In this, a dispersed phase is mixed with melting metal matrix at a certain temperature with the help of mechanical stirring action. It is the easiest and most economical method of preparation of metal matrix composite in liquid state. In stir casting method, first step involves melting of the base metal in the furnace. During melting, the melting metal is stirred continuously with the help of stirrer. During stirring, the silicon carbide and fly ash are reinforced in the melting aluminium. When reinforcement of silicon carbide and fly ash is completed, the melting hybrid is directly poured into the die, and the required shape of the hybrid is obtained after solidification of melting hybrid.

Stir Casting Apparatus

Stir casting apparatus is the apparatus which is basically consisting of two main components, i.e. the furnace and the stirring mechanism. The furnace temperature is controlled with the help of regulating mechanism (Fig. 3).

4 Experimental Procedure

4.1 Specimen Preparation

  i.   Aluminium alloy will be melted; the melt temperature will be raised between 700–800 °C in the furnace.
 ii.   Then, the melt will be stirred for 6–10 min at a speed of 250–350 rpm (uniform).
iii.   Slag will be removed in order to get better melt quality.
 iv.   The required proportion of fly ash will be preheated to 700 °C in a separate oven for 1 h.
  v.   Fly ash particles should lie in range of 16–30 μm.
 vi.   The required proportion of silicon carbide particles will be preheated at 600–800 °C for about 1.5 h [20].
vii.   The particle size of silicon carbide should lie b/w 16–20 μm.
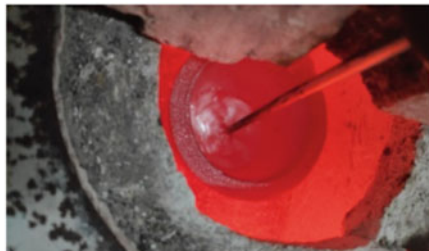
Fig. 3 Stir casting apparatus

Table 2 Influencing parameters at various levels

Factors	Parameters	Level		
		1	2	3
A	Composition of AMC	Al+SiC2.5wt%+FA2.5wt%	Al+SiC5wt%+FA5wt%	Al+SiC7.5wt%+FA7.5wt%
B	Stirring speed (rpm)	250	300	350
C	Stirring time (min)	6	8	10
D	Melting temp. of AMC	700	750	800

viii. The degasser (Degasser-190 tablets) will be introduced to remove the hydrogen from the melt.

ix. To increase the wettability, pure Mg (powdered form) weighing 1.5% by weight of the melt will be used.

x. Now, add the preheated fly ash and silicon carbide along with Mg to melt (maintained 720–730 °C). After the addition of the mentioned components, the mixture will be stirred using an impeller rotating in a speed range of 250–350 rpm for a duration of ten minutes.

xi. The stirring may be continued for another 5 min till uniform mixture is made.

xii. On the other hand, mould is preheated simultaneously to neglect the shrinkage of cast material.

xiii. Finally, it will be poured in the preheated metal moulds at the temperature mentioned below in Table 2.

4.2   Taguchi Technique

Parameters influencing stir casting process are mould design, mould material, mould temperature, pouring temperature, particle feed rate, pouring method, composition of matrix alloy, properties of matrix alloy, stirrer material, stirring time and number of blades.

Composition of AMC, stirring speed, stirring time and melting temperature of AMC are selected according to Taguchi technique as depicted in table given below. This method combines the experimental and logical analysis that helps to find out the most influential parameter on the result response. In addition, to notice the most influencing factors at various levels, different parameters like stirring time, stirring speed, wt% of SiC and wt% of fly ash are taken.

Table 3 Experimental design of L9 orthogonal array

Experiment no.	Experimental values			
	Composition of AMC (A)	Stirring speed (rpm) (B)	Stirring time (min) (C)	Melting Temp. of AMC ($^\circ$C) (D)
1	Al+SiC2.5wt%+ FA 2.5wt%	250	6	700
2	Al+SiC2.5wt%+ FA 2.5wt%	300	8	750
3	Al+SiC2.5wt%+ FA 2.5wt%	350	10	800
4	Al+SiC5wt%+FA 5wt%	250	8	800
5	Al+SiC5wt%+FA 5wt%	300	10	700
6	Al+SiC5wt%+FA 5wt%	350	6	750
7	Al+SiC7.5wt%+ FA 7.5wt%	250	10	750
8	Al+SiC7.5wt%+ FA 7.5wt%	300	6	800
9	Al+SiC7.5wt%+ FA 7.5wt%	350	8	700

4.2.1 Experimental Design of L9 Orthogonal Array

Based on the experimental design of L9 orthogonal array as shown above, nine specimens are prepared (Table 3).

5 Results and Discussions

Based on the experimental design of L9 orthogonal array, required number of specimens are prepared. But due to Coronavirus outbreak, we are unable to conduct the following tests: hardness test, compression test and tensile test. Once the situation gets normal, the following tests would be conducted.

6 Conclusion

The in-depth literature review presented above shows that

- The processing variables like stirring speed, stirring time, composition of aluminium matrix composite and its temperature are some of the significant factors to be considered for the production of hybrid materials in stir casting process. These parameters are considered because they have influential impact on mechanical properties of Al7075.
- Planning of experiments through Taguchi's technique was carried out, and experiments were conducted based on this plan.
- While performing the experiments, mixing of the reinforcements in matrix was observed to be uniform up to 7.5% of fly ash and 7.5% of silicon carbide.
- There was agglomeration of reinforcements at the bottom of crucible when weight percentage was increased beyond 7.5%.
- By combining the conclusion of several research papers along with the literature review presented above, it can be said that 7.5% weight of silicon carbide and 7.5% weight of fly ash demonstrate better hardness and wear resistance when compared to unreinforced Al-SiC-FA.

References

1. Rohatgi, P. K. (1993). Metal Matrix Composites. United States of America Patent 323349.
2. Deuis, R. (1997). Dry Sliding wear of Aluminum Composites. Patent 415435.
3. Vieira, A. A. R. (2009). Dry Sliding wear of Al alloy/SiCp Functionality Graped Composites. Patent 585592,
4. Rohatgi, P. (2006). Applications of fly ash in synthesizing low cost metal matrix composites for automotive and other engineering applications. *Journal of the Minerals Metals & Materials Society, 11,* 71–76.
5. Wu, G. L. C. (2006). Damping Properties of Aluminum Matrix-Fly Ash Composites.
6. Mahendra, K. A., & Radhakrishna, K. (2007). Fabrication of Al-4.5% cu alloy with fly ash metal matrix composites and its chatacterizaton (pp. 58–68).
7. Hashim, J., Looney, L., & Hashmi M. S. J. (1999). Metal matrix composites: Production by stir casting method. *Journal of Materials Processing Technology,* 1–7.
8. Xu, Z. M., & Zhou, W. (1997). Casting of SiC Reinforced Metal Matrix Composites. Patent 358363.
9. Arulshri, K. P., N Iyandurai, N., & Boopathi, M. M. (2013). Evaluation of mechanical properties of Aluminium alloy 2024 reinforced with silicon carbide and fly ash hybrid metal matrix composites. Patent 219229.
10. Surappa, J. M. P. T. M. K. (1997). Development of aluminium based silicon carbide particulates metal matrix composites. *Journal of Minerals and Materials Characterization, VIII.*
11. Schuster, D. M., & Skibo, M. D. (1988). Process for preparation of composite materials containing nonmetallic particles in a metal matrix. United States of America Patent 4786467.
12. Edwards, M. F., Nienow, A. W., & Harnby, N. (1985). *Mixing in process industries.* London.
13. Al-Jarrah, J. A., Ray, S., & Ghosh, P. K. (1998). Solidification processing of Al-Al2O3 composite using turbine stirrer. *Metallurgical and Materials Transactions.*
14. Lloyd, D. (1988). *The Solidification microstructure of particulate reinforced aluminium/SiC composites.* Canada: Kingston.
15. Mer, K. K. S., Kumar, S., & Kala, H. (2014). A review on mechanical and tribological behaviors of stir cast aluminum matrix composites. Ghurdauri.
16. Samuel, A. (1995). Foundry aspects of particulate reinforced aluminum MMCs: Factors controlling composite quality (pp. 65–98).

17. Anilkumar. (2011). Mechanical properties of fly ash reinforced aluminium alloy (Al6061) composites. *International Journal of Mechanical and Materials Engineering,* 41–45.
18. Selvam, J. D. R., Smart, D. S. R., & Dinaharan, I. (2013). Synthesis and characterization of Al6061-Fly Ashp-SiCp composites by stir casting and compocasting methods. Patent 637646.
19. Ramalho, A., Gaspar, M. C., Carvalho, S. F., & Gomes, J. R. (2005). Reciprocating wear tests of Al–Si/SiCp composites: A study of the effect of stroke length, Wear. Patent 545552.
20. Shankar, M. G., Kini, A., Sharma, S. S., Shetty, R., & Jayashree, P. K. (2013). Review on effect of silicon carbide (SiC) on stir cast aluminium metal matrix composites. *International Journal of Current Engineering and Technology.*
21. Alip Kumar, P. G. (2020). Microstructural and mechano-tribological behavior of Al reinforced SiC-TiC hybrid metal matrix composites. *Materials Today.*
22. Gupta, P. (2020). Effect of ceramic reinforcement on the microstructural, mechanical and tribological behavior of Al-Cu alloy metal matrix composite.
23. Kapil Bandil, P. G. (2019). Microstructural, mechanical and corrosion behavior of Al-Si alloy reinforced with SiC metal matrix composite.

Current Scenario in Optimization of Machining Parameters While Electric Discharge Machining for Biocompatible Ti-Alloy: A Review

Subodh Kumar and Vikas Sharma

Abstract   This paper represents the current trends for optimization of process parameters while EDM of biocompatible titanium alloy parameters in terms of peak ampere, pulse on time and pulse off time, etc., on the mechanical properties of titanium alloy (Ti-6Al-4V). Titanium alloy is a hard material which possesses poor ability to get machined by working on traditional machining methods, while using electrical discharge machining (EDM) is very easy to machining titanium alloy. The machining efficiency as well as accuracy is to be improved by using integrated EDM machining mechanism. During the experiments, parameters like discharge peak current and pulse duration had to be varied to find out the effect on the material removal rate (MRR), electrode wear rate (EWR) and relative electrode wear ratio (REWR). In this work, several current research papers on titanium alloy were studied for analysis and investigation. The researchers have given their own views on the performance of the electrical discharge machining process, the materials selected for their study, the effect of machining parameters, etc., in their researches. In this audit paper, it was additionally attempted to consider distinctive research papers containing the exploration and examination made on input yield parameters while working with electrical discharge machining.

Keywords Ti-6Al-4V · EDM · Peak current · Machinability · Material removal rate

1 Introduction

Electrical discharge machining is often used for special form workpiece machining, whatever the strength or hardness of the material. It was first observed by Joseph Priestley in 1770. Since of its excellent properties, titanium components and its alloy

S. Kumar · V. Sharma (✉)
Department of Mechanical Engineering, GLA University, Mathura 281406, India
e-mail: Vikas.sharma@gla.ac.in

S. Kumar
e-mail: subodh.kumar_me17@gla.ac.in

are highly demanded in industries. Titanium is spread extensively across the world. Ninth most common material on earth is titanium. EDM processes are common in the production of complex cavities in difficult to machine materials for use in the automotive, aerospace and bio-industries. EDM is an unusual method of machining process using an erosion mechanism of electric spark between the electrode and the workpiece. Material processing happens in the EDM process by melting and vaporizing the compounds. Both the workpiece and the tool electrode are electrically conductive in nature, and the tool and workpiece have a small gap. A dielectric medium (kerosene or de-ionized water) immerses the instrument and workpiece. Once the potential difference is applied, the electrons start heading towards the workpiece from the tool side. Workpiece is considered as positive and tool is negative. Electrons begin to move from tool to workpiece and collide with dielectric medium molecules. The electrons collide with the molecules, in which they are transformed into ions. This will increase electrons and ion numbers in the gap between tool and workpiece. Despite this ions start, the electrode moves towards the workpiece and moves towards the device. It is important to set electrical current between the tool and the workpiece called plasma. Electrons and ions strike the workpiece and the tool, change its kinetic energy and convert it into heat. Heat temperature reaches up to 10,000 °C. This heat melts out the workpiece material. Therefore, due to the voltage brake down, the current ceases flowing between the device and the workpiece, and the fused material in the workpiece is flushed by moving dielectric fluid. Below figure shows the main parameters that affect performance of EDM process.
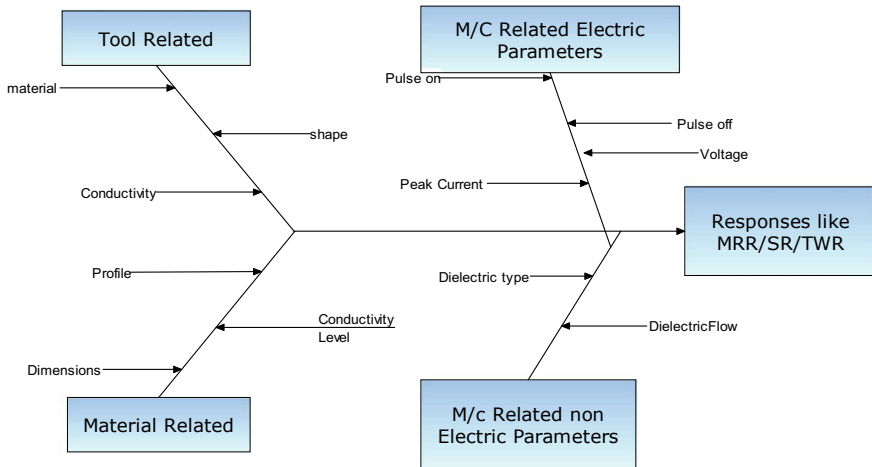
Fig. 1 Fishbone diagram for EDM
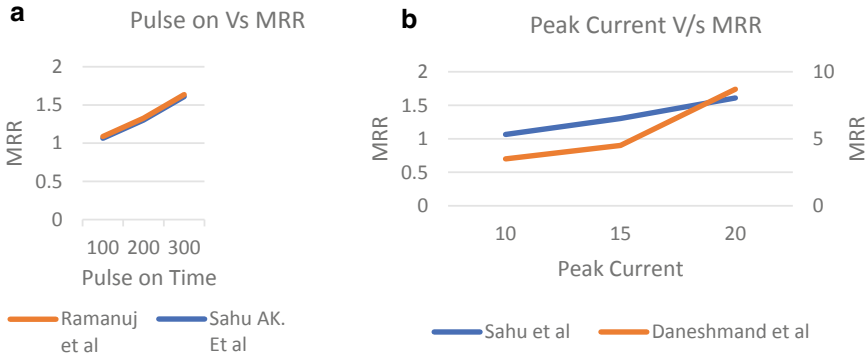
Fig. 2 **a**, **b** Effect of pulse on and current on MRR
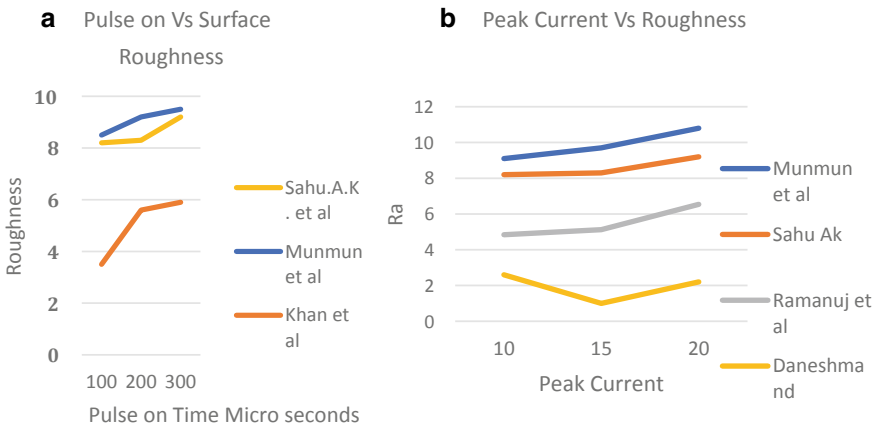
Fig. 3 **a**, **b** Effect of pulse on and current on roughness

2   Literature Review

Kao et al. (2010) investigate using Taguchi method and grey relational analysis to modify the multiple performance characteristics of the EWR, MRR and surface roughness in EDM. The performance off machining of the EWR and surface roughness decreases but MRR increases. Corresponding to ANOVA result found that discharge current mostly effect on surface roughness and increasing in pulse duration MRR increases [1].

Azad et al. (2012) found that during multi-response optimization for micro-EDM drilling voltage and current is the most affecting input parameters. It can be seen that frequency and width are also significant parameters affecting the multiple performance characteristics. They found that MRR increases with increases of discharge energies. Current and voltage are proportional to the MRR [2].

Daneshmand et al. (2013) investigate that the impact of input parameters, i.e., voltage, pulse current, pulse on time and pulse off time on output parameters, i.e., MRR, TWR, EWR and surface roughness using NiTi shape memory alloy and deionized water as the dielectric. Most important factor studied in this work was MRR of NiTi alloy with effect of pulse current and pulse on time which increases the spark energy and increases the MRR. On increases the pulse on time, tool wear rate increases and increase of voltage leads to increase the MRR and TWR [3].

Sainiet et al. (2014) studied on WEDM efficiency and analysed on a material removal rate (MRR) basis. The measurements of the material used were held at 80 mm x 50 mm x 10 mm. Taguchi's approach is used to design the experiments and MINITAB-15 software was used to test the experiments in order to achieve the best optimal set of parameters. They have studied regarding significant parameters and gave optimal set of input factors so as to machine Wire-EDM of Ti-6Al-4V [4].

Prakash et al. (2015) studied that the surface characteristics of PMEDM process. They correlate the input variables with their response. RSM was used to fabricate biocompatible surface. Surface roughness increases with increase in peak current, pulse duration and duty cycle. Higher powder concentration increases surface roughness [5].

Meena et al. (2016) studied that the effect of input parameters, i.e., current, frequency and pulse width on output parameters, i.e., MRR, TWR, EWR and overcut. They found that most important factor is current among the all input parameters. Grey relational analysis can be used for optimization of parameters to get better result [6].

Rao et al. (2016) found that the surface roughness and cutting speed values were found to be increased with increase in Ton and Ip and also decreased with increase of spark gap. The most important factor was that increase in energy per spark increases the cutting speed and surface roughness values which result in increased temperature gradient [7].

Shih-Fu et al. (2017) studied the effect of powder concentration duration of pulse and current value on rate of material removal rate of tool wear and on surface morphology like recast layer. They found that MRR, EWR and surface roughness are decreasing after they have increased with dielectric concentration of HA. Discharge current is specifically indicative for the thickness of recast layer, MRR, EWR and surface roughness. Pure titanium had higher MRR, EWR, surface roughness and recast layer thickness compared to other alloy of titanium [8].

Kumar et al. (2017) studied that the specific process parameters were tested using three specific electrode materials on the surface properties. The quantity of material transferred from the added dielectric liquid to the machined surface improves the consistency of the machined surface and increases the machined surface hardness. They also found that better surface characteristics are obtained at lower current and pulse on time as compared with higher current and pulse on time. This happen because of low energy discharge for less pulse time [9].

Khanna et al. (2017) suggested that the optimization of various machining process on EDM. There are different types of electrodes are used to get better surface finish with high MRR, i.e., copper, aluminium, etc. In most of the cases, Taguchi technique, grey relational analysis and surface respond methodology are used. Nowadays, the

investigation is occurred using powder mixed dielectric fluid to find out the output parameters on the surface of various alloys [10].

Gohil et al. (2017) worked on hybrid method of turning using EDM and found that pulse on time as well as peak current is directly proportional to MRR and inversely proportional to voltage. They also found that higher value of current results in greater discharge energy and creates large crater on surface that reduce surface finish. Polarity is an important parameter, they found material removal rate is higher at straight polarity but in reverse polarity surface found to be smoother. Hence, it can be concluded that the polarity and the peak current are the important factors among all input parameters in EDM process [11].

Khan et al. (2017) investigate the effect on surface roughness and surface structure by input parameters, i.e., peak current, time pulse and servo voltage. On rising peak current, pulse on time and servo voltage, surface roughness is developed. Roughness of the surface at lower ampere was reduced. When they measured the material of the electrode, Cu tool resulted in the best surface finish and the graphite electrode resulted in worst value of surface finish [12].

Verma et al. (2017) found that in die-sinking EDM MRR increases with increase in peak current, gap voltage and pulse on time. In case of surface roughness, it is increased with increase in peak current, gap voltage and duty cycle. The most significant factor correlates with MRR and surface roughness is peak current and gap voltage [13].

Kumar et al. (2018) investigate the titanium alloy machining using EDM. They found the three stages of currents and pulse on time voltage gap. The effect on rate of material removal and surface properties was analysed by using grey relational analysis. High discharge energy is responsible for reduced surface finish. MRR placed at the maximum point on higher discharge current, moderate pulse on time and lowest voltage gap. Surface roughness is found to be higher at higher Ip, Ton and Vg values [14].

Hadad et al. (2018) investigate the effect of factors on MRR, TWR as well as the tool and workpiece surface roughness values were analysed. They noticed that both MRR and TWR developed as the roughness of the tool surface increased. Roughness of tool surface continues to change, while the roughness of the original tool surface is different. They concluded that the roughness of surface area depends on the machining parameters after EDM machining process method [15].

Qudeiri et al. (2018) found that MRR is inversely proportional to the viscosity as well as EWR and surface roughness gets decreased as the viscosity rises. When we use copper electrode, MRR increases and EWR decreased as compared to working with brass electrode. MRR is increased on mixing of certain powder (aluminium powder) into the dielectric fluid [16].

Sahuet et al. (2018) investigate the machining performance of AlSi10Mg (composite tool) electrode along with copper and graphite tool electrodes, prepared through selective laser sintering process. To perform the experiment, they were using Taguchi's L27 orthogonal array. The effect on the output parameters, i.e., MRR, TWR and surface roughness was tested by varying input parameters, i.e., open circuit voltage, discharge current, duty cycle and pulse on time. They obtained better MRR

on increase in open circuit voltage, discharge current and duty cycle. Download current, duty cycle, pulse on time and lower TWR are obtained upon decrease in open circuit voltage [17].

Agarwal et al. (2020) studied the RWR optimization using surface response modelling, Jaya algorithm and TLBO. With the rise in peak current, RWR decreases but rises in Ton and duty factor RWR. They were also found to increase MRR with peak current increase but also increase of TWR on Ip rise. Optimization was achieved to improve MRR with better machined surface efficiency [18].

3   Discussion

While going through the investigation done by the selected researchers, some discussion can be done by seeing process parameters for machining method obtained through electric discharge machining. The experiment of EDM is conducted by changing different controllable process parameters including voltage, current, duty cycle, pulse on time, pulse off time and corresponding output parameters like MRR, TWR and average surface roughness.

3.1   Effect of Parameters on MRR

As the pulse on time increase, energy applied increases; hence, the MRR got increased. We can also check these trends in confirmation with cited authors as shown in figure below. Higher current also enhances the spark intensity resulting increased rate of material removal. Increasing the pulse length provided the requisite time to pass the discharge energy to the workpiece and consequently a high MRR was observed The rate of material removal observed is higher at straight polarity but smoother in reverse polarity.

3.2   Effect of Parameters on Surface Finish

Surface roughness/finish is the second most focused area by researchers, as soon as the pulse on time increase spark intensity increases, hence, the crater formed because of spark increases, this crater decides the roughness of machined surface.

Hence, in both case, as peak current increase or pulse on time increases, crater formed by spark increases and finish get deteriorate above shown figure also confirms the science behind the roughness produced. The average surface roughness of the machined surface improves with an improvement in process parameters like OCV, current, duty cycle and spark time using copper tool electrode followed by graphite.

4   Conclusion and Scope for Future work

After going through above cited current trends by researcher, some conclusions can be drawn for machining of titanium alloy Ti-6Al-4V via EDM.

- Most of researcher used pulse on, pulse off, current and voltage as most influential factors among various other factors.
- MRR and roughness are effected oppositely by most parameters that make machining process more complex even with large number of cascading effect of factors on each other.
- Mostly, the optimization problem tackled with traditional way of design of experiments like Taguchi and GRE, etc.
- Optimization can be done using some newer GUI techniques like support vector machine, backpropagation neural network, TLBO, Jaya can be applied as process is complex in nature. We can use AI-based techniques too in order to optimize the response.
- Authors can focus their study on surface morphology of machined surface as change in surface properties during machining by EDM is seen as an adverse effect of process on workpiece specially in the field of biology for purpose of implants.

References

1. Kao, J. Y., Tsao, C. C., Wang, S. S., & Hsu, C. Y. (2010). Optimization of the EDM parameters on machining Ti-6Al-4V with multiple quality characteristics. *The International Journal of Advance Manufacturing Technology, 47*(1-4), 395-402.
2. Azad, M. S., & Puri, A. B. (2012). Simultaneous optimization of multiple performance characteristics in micro-edm drilling of titanium alloy. *The International Journal of Advance Manufacturing Technology, 61*(9–12), 1231–1239.
3. Daneshmand, S., Kahrizi, E. F., Abedi, E., & Abdolhosseini, M. M. (2013). Influence of machining parameters on electro discharge machining of NiTi shape memory alloy. *International Journal of Electrochemical Science, 8,* 3095–3104.
4. Saini, P. K., & Verma, M. (2014). Experimental investigation of wire-EDM process parameters on MRR of Ti-6al-4v Alloy. *International Journal of Innovative Technology and Exploring Engineering (IJITEE), 4*(5) ISSN: 2278-3075.
5. Prakash, C., Kansal, H. K., Pabla, B. S., & Puri, S. (2015). To optimize the surface roughness and microhardness of beta-Ti alloy in PMEDM process using non-dominated sorting genetic algorithm-II. *International Conference on Recent Advances in Engineering & Computational Sciences (RAECS)* 1-6.
6. Meena, V. K., Singh Azad, M., Singh, S., & Singh, N. (2016). Micro-EDM multiple parameter optimization for cp titanium. *The International Journal of Advanced Manufacturing Technology, 89*(1–4), 897–904.
7. Rao, P. S., Ramji, K., & Satyanarayana, B. (2016). Effect of wire EDM conditions on generation of residual stresses in machining of aluminium 2014 T6 alloy. *Alexandria Engineering Journal, 55*(2), 1077–1084.

8. Shih-Fu, Cong-Yu, & Wang. (2017). Effects of bioceramic particles in dielectric of powder-mixed electrical discharge machining on machining and surface characteristics of titanium alloys. *Journal of materials processing technology, 245,* 70–79.

9. Kumar, S., Singh, R., Batish, A., Singh, T. P., & Singh, R. (2017). Investigating surface properties of cryogenically treated titanium alloys in powder mixed electric discharge machining. *Journal of the Brazilian Society of mechanical Sciences and Engineering, 39*(7), 2635-2648.

10. Khanna, R., Maheswari, R., Modi, A., Tyagi, S., & Rana, T. R. (2017). A review on recent research development on electric discharge machining(EDM). *International Journal, 5*(4), 444-445.

11. Gohil, V., Puri, Y. M. (2017, December). Multi-objective optimization of material removal rate and surface roughness in electrical discharge turning of titanium alloy(Ti-6Al-4V). *Indian journal of Engineering and Material sciences, 24,* 429–436.

12. Khan, Md A. R., & Rahman, M. M. (2017). Surface characteristics of Ti-5-Al-2.5-Sn in EDM using negative polarity of electrode. *The International Journal of Advanced Manufacturing Technology, 92*(1-4), 1-13.

13. Verma, V. & Sahu, R. (2017). Process parameters optimization of die-sinking EDM on titanium grade-V alloy using full factorial design approach. *Materials Today: Proceedings, 4*(2), 1893–1899.

14. Kumar, R., Roy, S., Gunjan, P., & Sahoo, A., Sarkar, D. D., & Das, R. K. (2018). Analysis of MRR and surface roughness in machining Ti-6Al-4V ELI titanium alloy using EDM process. *Procedia Manufacturing, 20,* 358–364.

15. Hadad, M., Bui, L. Q., & Nguyen, C. T. (2018). Experimental investigation of the effect of tool initial surface roughness on the electrical discharge machining performance. *The International journal of Advanced Manufacturing Technology, 95,* 2093-2104.

16. Abu Qudeiri, J. E., Moured, A.-H. I., Ziout, A., Abidi, M. H., Elkaseer, A. (2018). Electric discharge machining of titanium and its alloy. *The International Journal of Advanced Manufacturing Technology, 96*(1-4), 1319-1339.

17. Sahu, A. K., & Mahapatra, S. S. (2018). Optimization of electrical discharge machining of titanium alloy (Ti-6Al-4V) by grey relational analysis based firefly algorithm. *Additive Manufacturing of Emerging Materials* 29-53.

18. Agarwal, N., Shrivastava, N., & Pradhan, M. K. (2020). Optimization of relative wear ratio during EDM of titanium alloy using advanced techniques. *SN Applied Sciences, 2*(1), 99.

Enhancement of Adhesive Wear Resistance of AISI 409 M Steel by Deposition of WC-10Co-4Cr Powder Using GTAW Process

Amit Kumar, Guru Prakash, and N. K. Batra

Abstract AISI 409 M stainless steel is widely used for manufacturing automobile exhaust systems, automotive mufflers, fuel filters, farm equipment, and shipping containers. The shipping containers and farm equipment during transportation and handling experience wear which reduces their life cycle. To improve the life of AISI 409 M stainless steel, WC-10Co-4Cr powder is cladded on the surface of AISI 409 M steel by gas tungsten arc welding (GTAW) process. Extensive characterization by X-ray diffraction (XRD) and SEM imaging of the cladded AISI 409 M was carried out. The hardness of the cladded AISI 409 M steel specimen and AISI 409 M steel was found to be 42 HRC and 6 HRC, respectively. The wear study of cladded AISI 409 M and AISI 409 M steel specimen was done on pin-on-disk equipment. It was found that the cumulative weight loss of the cladded AISI 409 M steel is 69.73% less than by AISI 409 M steel. The structure property relation shows that wear is proportional to hardness of the cladded AISI 409 M steel.

Keywords GTAW · SEM · Hardness · Pin-on-disk

1 Introduction

Martensite stainless steel (MSS) has high strength, toughness, and excellent corrosion resistance [1]. AISI 409 M steel is a type of ferritic stainless steel, which is easy to fabricate, cut, and deform [2]. AISI 409 M steel is widely used in automobile industry for the manufacturing of the automotive exhaust system and mufflers [3]. It is also a standard material for shipping containers due to high ultimate tensile strength of

A. Kumar (✉) · G. Prakash · N. K. Batra
Department of Mechanical Engineering, Maharishi Markandeshwar (Deemed To Be University), Mullana, Ambala, India
e-mail: ak.dto360@gmail.com

G. Prakash
e-mail: gprakash@mt.iitr.ac.in

N. K. Batra
e-mail: nkbatraeng@gmail.com

450 MPa, yield strength 240 MPa, and the hardness of 6 HRC [4]. During shipping, the container is susceptible to wear due to low hardness of AISI 409 M steel. Hence, it is a challenge for engineers and researchers to mitigate the wear.

In recent years, researchers have improved the wear and abrasion resistant of steel by surface modification techniques. Some researchers have deposited WC-10Co-4Cr powder on stainless steel by HVOF process [5–8]. In all these studies, the wear resistance of the stainless steel has been enhanced due to deposition of hard cermet particles on the substrate.

Surface modification of steels can also be done by gas tungsten arc welding (GTAW process). Gas tungsten arc welding (GTAW) is a versatile process of joining of metals and alloys and is used widely in industry. The greatest advantage of the GTAW process is that it can weld many types of metals and alloys in comparison to other arc welding process. GTAW can also weld dissimilar metals to one another such as copper to brass and stainless steel to mild steel [9].

To enhance the hardness of AISI 409 M steel, some researchers have studied the GTAW technique. In recent year, GTAW is widely used to enhance tribological properties of duplex stainless steel [10]. Researcher has used GTAW for surface cladding to enhance the wear resistance and hardness of the AISI 1045 [11]. The tribological wear resistance of AISI 4462 duplex stainless steel has been improved by GTAW process using melting and diffusion [12]. Researchers have deposited TiC-Ni powder on AISI 304 stainless steel by GTAW process and reported that there is improvement in the hardness after cladding [13].

It was found from literature that the cladding and pin-on-disk test of WC-10Co-4Cr coating on AISI 409 M steel by the GTAW welding process has not been studied. In this work, an attempt has been done to study the adhesive wear behavior of AISI 409 M steel and WC-10Co-4Cr cladded AISI 409 M steel. The detailed characterization of worn of AISI 409 M steel and microstructure property correlations is presented in this paper.

2   Experimental Details

2.1   Materials

AISI 409 M steel was used as a substrate having 0.08% C, 11.05% Cr, 0.5% Ni, 0.75% Ti, 0.02% S, 1% Mn, 1% Si and 0.045% P (in wt. %).

WC-10Co-4Cr powder was used for cladding is a hard refractory ceramic material. Powder was manufactured by SUZLER METCO and name of the powder is WOKA-FC.

2.2 Microstructure

To observe the microstructure of AISI 409 M steel, it was polished by standard metallography technique. The microstructure was obtained under the optical microscope (Model- DM750P, Make-Leica). The microstructure observed under scanning electron microscope (SEM) (Model-Evo 18, Make-Zeiss) by using black scattered mode [14]. The SEM specimen was polished by standard polishing technique. The cross section of cladded AISI 409 M steel was also observed under the SEM. The X-ray diffraction pattern of WC-10Co-4Cr powder, AISI 409 M and cladded AISI 409 M steel was observed by using Rigaku X-ray diffractometer with wavelength (λ) of 1.54 A˚. The phase present in WC-10Co-4Cr powder, AISI 409 M and cladded AISI 409 M steel was analyzed by using PDF-2 database of X-Pert High Score software [15].

2.3 Welding Process

AISI 409 M steel specimen with a dimension of 100 mm × 50 mm × 10 mm was used as the substrate material. The surface of the base material was thoroughly cleaned with acetone to remove all the dirt/dust from the layer. 20 gm of WC-10Co-4Cr powder was mixed with 5 gm of organic binder (corn starch) and mixed well. 40 ml of acetone and 20 ml of styrene were blended with the mixture of WC-10Co-4Cr and corn starch, then stirred until it formed a paste. The paste was subsequently placed on the substrate. The paste was left for 24 h in the air to dry. Cladding of AISI 409 M steel with WC-10Co-4Cr powder was done by GTAW welding machine (Model-RS 400, Make-Esab Pvt. Ltd) with DC current straight polarity. Tungsten electrode was used to produce a weld bead with argon shielding gas on the substrate material. The heat input of GTAW depends on the applied current, welding speed and it is calculated by using the Eq. 1. The parameter used during the GTAW operation is shown in Table 1 [16].

$$\text{Heat input} = \frac{0.06 \times \text{current} \times \text{voltage}}{\text{Electrode transverse speed}} \qquad (1)$$

Table 1 GTAW operation parameters

Parameter	Values
Current	200 A
Welding speed	9.68 mm/s
Voltage	90 V
Gas flow rate	24 Psi
Electrode diameter	3.5 mm
Heat input	111.57 J/mm

Subsequent to GTAW cladding process, the cladded AISI 409 M steel was cut by WEDM process (Model-Electronica ELPULS 15, Make-Ecocut)

2.4   Hardness

The hardness of cladded AISI 409 M steel and AISI 409 M steel specimen was measured by Rockwell hardness tester (Model-7005 BHT-UP,Make-Vaiseshika). A diamond indenter was used to indent on the specimen with the load of 150 kg (1471 N) and dwell time of 15 s. 5 readings were taken at different locations on the surface to measure the average hardness of the specimen [17].

2.5   Tribological Test

The wear studies of cladded AISI 409 M and AISI 409 M steel were done on pin-on-disk machine [Model-TR-20, Make-Ducom]. The size of the specimen was 50 mm × 10 mm × 10 mm which is fixed in the sample holder of pin-on-disk wear testing machine. The speed of rotation of the rotating disk was 500 rpm. Three tests were carried out by applying a load of 1, 3, and 5. The test was carried out for 15 min. Weight loss was measured after every 5 min interval by withdrawing the sample. The pin-on-disk experiment was done at 25° C. The weight loss of the specimen due to wear was calculated by using Eq. 2 [18].

$$\text{Weight loss (WL)} = \text{Initial weight} - \text{Final weight} \tag{2}$$

The surface roughness of AISI 409 M and cladded AISI 409 M steel specimen was measured by surface profilometer (Model-SJ-301, Make-Mitutoyo). The measurements were taken before and after wear test. The measuring range is 25 μm.

3   Results and Discussions

3.1   Microstructures

Microstructure investigation of AISI 409 M steel is shown in Fig. 1a. The bright grains are of α-ferrite are observed and are shown by arrows. The dark needle-like structures represents martensite which are shown by arrows. Figure 1b shows the SEM image of the top surface of the AISI 409 M steel specimen after cladding WC-10Co-4Cr grains and are shown by arrows. Figure 1c shows the SEM image of a
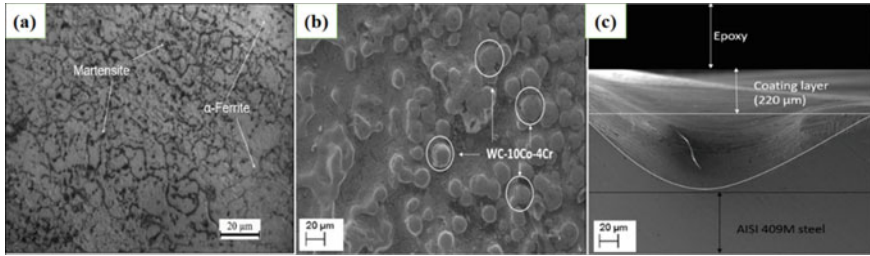
Fig. 1 **a** Optical micrograph of substrate, **b** SEM image of **top surface of** GTAW cladded AISI 409 M, and **c** SEM image of steel cross section of GTAW cladded AISI 409 M

cross section of the cladded AISI 409 M steel specimen. The crater depth of 220 µm is visible as shown in figure. A similar crater has also been reported in [19, 20] after GTAW cladding process.

3.2 XRD Analysis

The X-ray diffraction spectrum of WC-10Co-4Cr powder is shown in Fig. 2a. The main phases present are WC, Cr, and Co4W2C and are clearly illustrated. Figure 2b shows the X-ray diffraction spectrum of AISI 409 M and cladded AISI 409 M steel. The main phase present in AISI 409 M steel is α-ferrite/martensite which are clearly stated. The X-ray diffraction of cladded AISI 409 M steel shows the peaks of α-ferrite/martensite and additionally it shows the peaks of WC. The peaks of WC in cladded AISI 409 M steel confirms that the WC-10Co-4Cr powder is deposited on AISI 409 M steel by GTAW process.
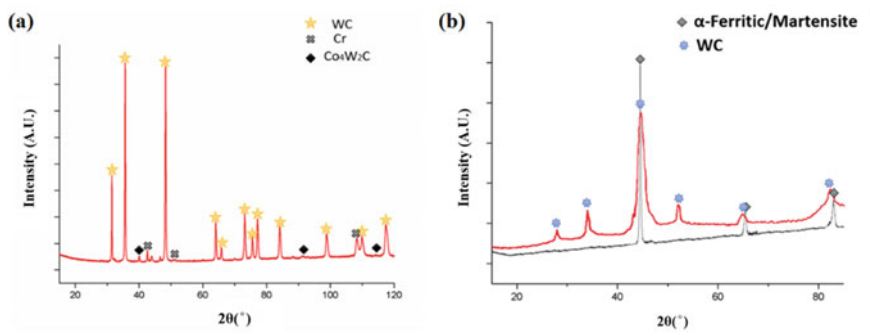
Fig. 2 **a** X-ray diffraction pattern of WC-10Co-4Cr powder and **b** Ray diffraction pattern of AISI 409 M steel and cladded AISI 409 M steel
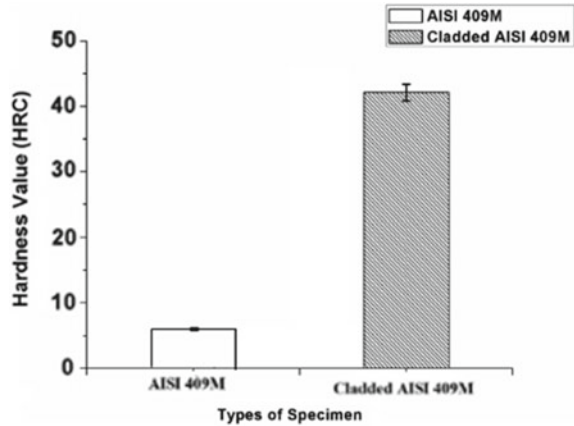
3.3 Hardness

The hardness of AISI 409 M steel and cladded AISI 409 M steel was 6 HRC and 42 HRC, respectively, as shown in Fig. 3. The average hardness of cladded AISI 409 M is seven times higher than that of AISI 409 M steel.

3.4 Pin-On-Disk Wear Test

Figure 4a–c illustrates the variation of cumulative weight loss (WL) with sliding distance for load of 1 kg, 3 kg, and 5 kg for AISI 409 M steel and cladded AISI 409 M steel, respectively. In case of AISI 409 M steel, the WL increases with sliding distance for three loads. Similarly, the WL of the cladded AISI 409 M steel increases with sliding distance for the three loads. It is also observed that the WL of cladded AISI 409 M steel is less than the WL of AISI 409 M steel. The WL of cladded AISI 409 M steel is 62.11%, 73.05%, and 74.05% less than that of AISI 409 M steel for the applied load of 1 kg, 3 kg, and 5 kg, respectively.

Figure 5 a–c illustrates the variation of cumulative wear rate (WR) with respect to time when the applied load is 1 kg, 3 kg, and 5 kg, respectively.

It is observed that wear rate of AISI 409 M steel is higher than that of AISI 409 M steel for all three loads applied during pin-on-disk wear test. The WR of AISI 409 M steel is 62.03%, 73.02%, and 74.08% higher than that of cladded AISI 409 M steel for 1 kg, 3 kg, and 5 kg of loads, respectively.

Figure 6a, b, and c illustrates the coefficient of friction (μ) with sliding distance with different loads for both specimens, where μ is coefficient of friction, F_s is a force of sliding friction, and F_n is a normal force. The low coefficient of friction in cladded AISI 409 M steel specimen is due to fact that the microwelding due to adhesion in case of composite material is less than that of metallic materials. In this
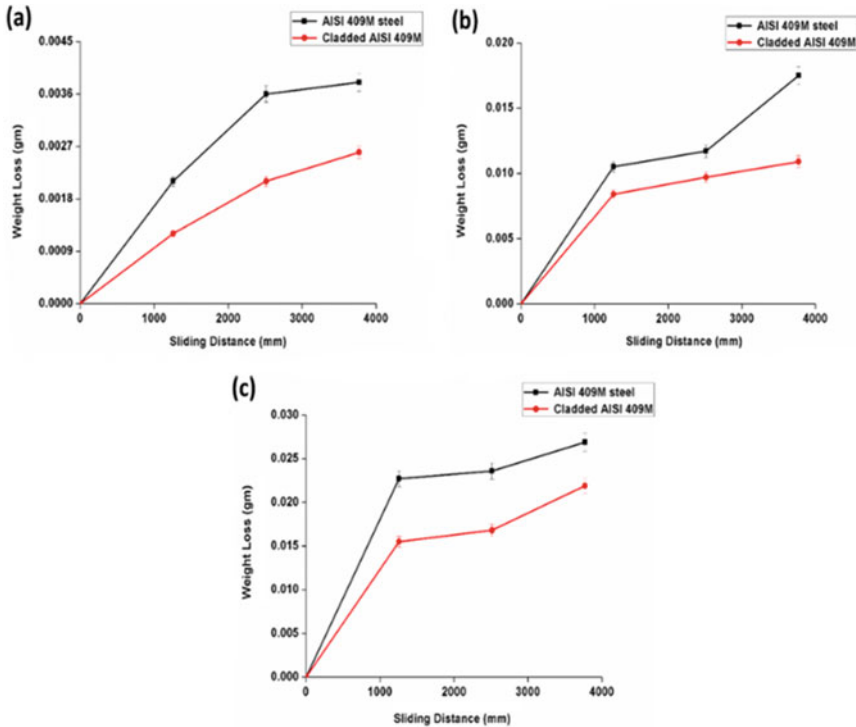
Fig. 4 Plot of weight loss with sliding distance at load of **a** 1 kg, **b** 3 kg, and **c** 5 kg

case, the microwelding of the pin made from AISI 409 M steel with the counter body which is metallic is stronger and hence the μ is higher. This is in agreement with the concept mentioned by Hutchings [21].

3.5 SEM Morphology of Worn Surface

Figure 7a shows the SEM image of AISI 409 M steel before wear. Fine scratches are visible and are shown by arrow. Figure 7b shows the SEM image of the worn surface of AISI 409 M stainless steel specimen. Wear direction is visible in image shown by arrow. Grooves are also observed and shown by arrow. Plastic deformation and plowing of AISI 409 M steel are observed. The presence of groove and plowing material indicates that AISI 409 M steel is ductile in nature.

Figure 7c shows the SEM image of cladded AISI 409 M steel before wear. Figure 7d shows the SEM image of worn surface of cladded AISI 409 M specimens. Some indentations shown by arrow are observed on the worn surface. It is also observed that large portion of the cladded AISI 409 M steel has not worn. The presence of indentations shows that cladded AISI 409 M is brittle in nature.
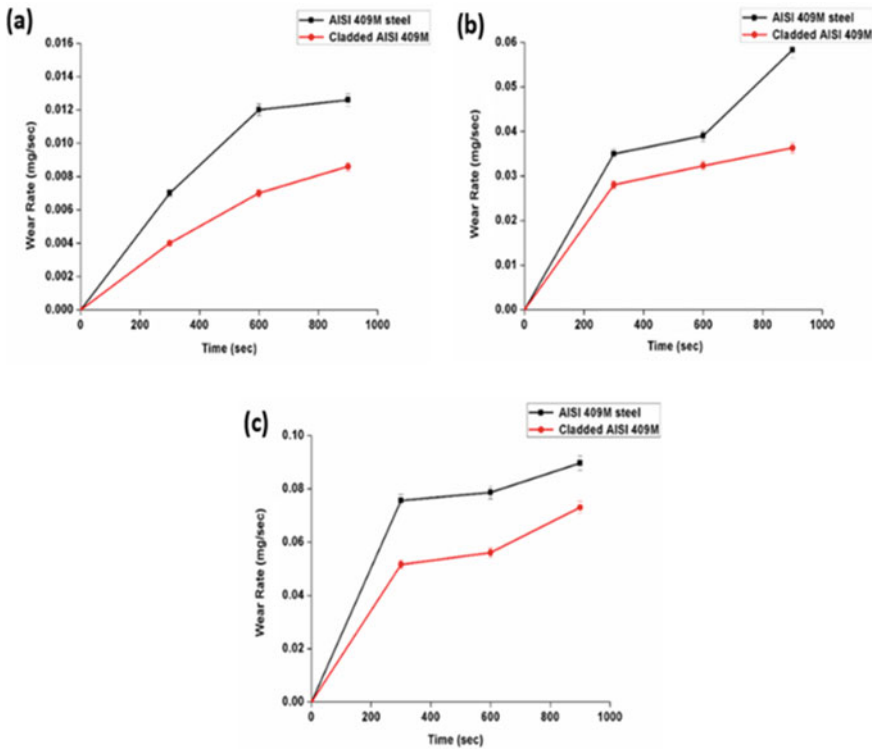
Fig. 5 Plot of wear rate with time at load of **a** 1 kg, **b** 3 kg, and **c** 5 kg

3.6 Surface Roughness

Figure 8a shows the value of average surface roughness Ra of cladded AISI 409 M steel specimens and AISI 409 M steel specimens. For the 3 kg applied load, the increase in Ra before and after wear test of both AISI 409 M steel and cladded AISI 409 M steel is 69.56% and 29.42%, respectively, and has increased after wear test. It implies that there is more wear of AISI 409 M steel in comparison to cladded AISI 409 M steel.

Rz is a surface roughness parameter which is used to measure the difference between the tallest 'peak' and the deepest 'valley' on the surface. Figure 8b illustrates the plot of Rz before and after the wear test for AISI 409 M and cladded AISI 409 M steel. Rz for these two specimens has increased after wear test. The increase in the Rz value of AISI 409 M steel and cladded AISI 409 M steel is 77.87% and 38.40%, respectively, before and after wear test. This is in agreement with SEM micrograph (Fig. 7).
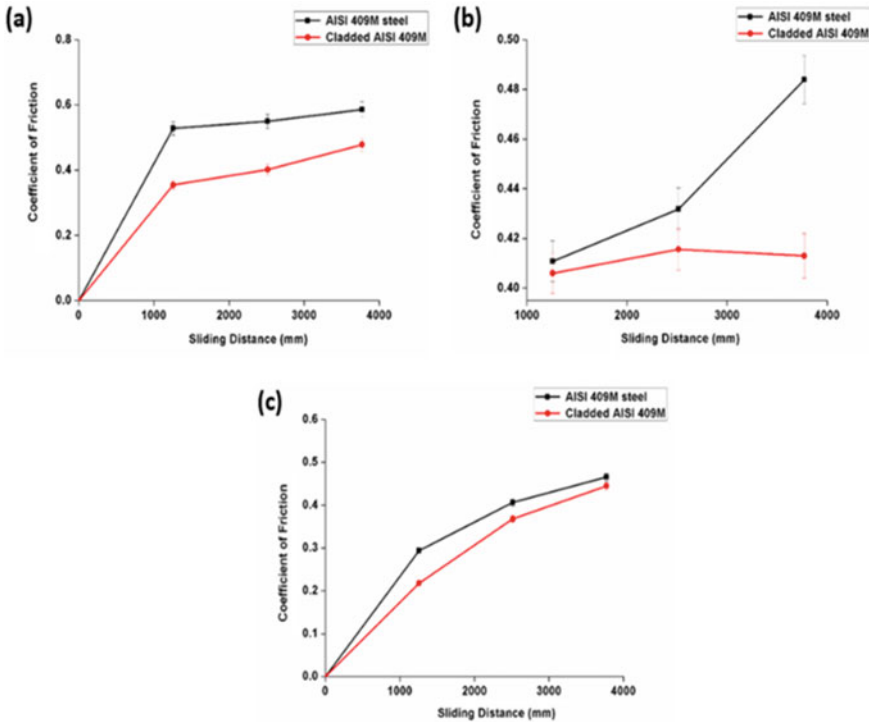
Fig. 6 Plot of average coefficient of friction with sliding distance. **a** 1 kg, **b** 3 kg, and **c** 5 kg

3.7 Analysis

A large portion of no wear zone indicates that high wear resistance of cladded AISI 409 M steel. The high wear resistance of AISI 409 M steel is attributed to high hardness of AISI 409 M steel. Similar enhanced wear resistance and increased microhardness has also been reported in [22] after deposition of hard cermet particle on UNS S31603 and UNS S32760 stainless steels. It is found that that cladded AISI 409 M steel has higher wear resistance in comparison to AISI 409 M steel.

4 Conclusion

- The hardness of top surface of cladded surface was found to be 42 HRC, whereas the hardness of the AISI 409 M steel was 6 HRC. There is a seven times increase in the hardness of the top surface of the cladded layer.
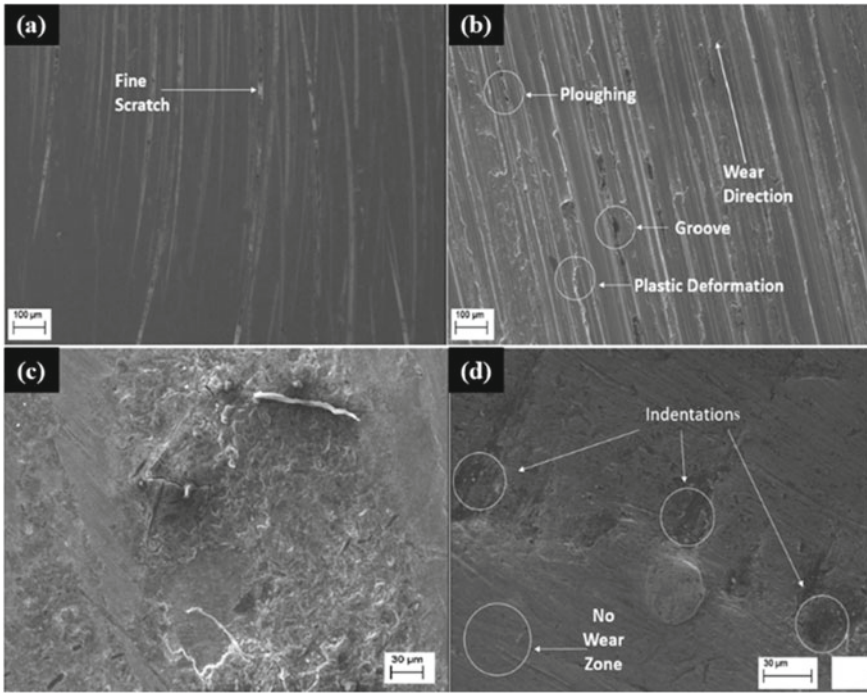
Fig. 7 SEM images of **a** AISI 409 M steel before wear test, **b** AISI 409 M steel after wear test, **c** cladded AISI 409 M steel before wear test, and **d** cladded AISI 409 M steel after wear test

- The weight loss of cladded AISI 409 M steel is 62.11% less than AISI 409 M steel at the load of 1 kg (9.8 N), the weight loss of cladded AISI 409 M steel is 73.05% less than AISI 409 M steel at the load of 3 kg (29.4 N), and the weight loss of cladded AISI 409 M steel is 74.05% less than AISI 409 M steel at the load of 5 kg (49.05 N).
- The wear rate of cladded AISI 409 M steel is 62.03% less than that of AISI 409 M steel at the load of 1 kg (9.8 N), the wear rate of cladded AISI 409 M steel is 73.02% less than AISI 409 M steel at the load of 3 kg (29.4 N), and the wear rate of the cladded AISI 409 M steel is 74.08% less than that of AISI 409 M at the load of 5 kg (49.05 N).
- The enhanced wear resistance of cladded AISI 409 M steel is due to increased hardness in comparison to AISI 409 M steel.
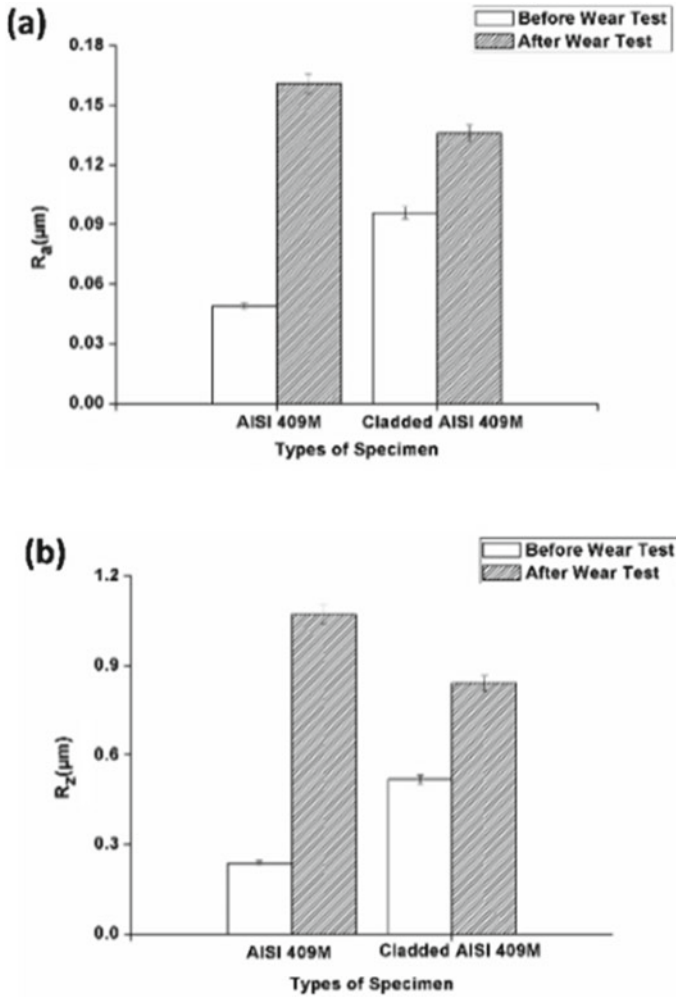
Fig. 8 Plot of **a** average Ra and **b** Rz before and after wear test of AISI 409 M and cladded AISI 409 M steel

References

1. Sreeraj, P., Kannan, T., & Maji, S. (2013). Prediction and optimization of weld bead geometry in gas metal arc welding process using RSM and fimicon. *Journal of Mechanical Engineering, 5*(8), 154–165.
2. Lakshminarayanan, A. K., & Balasubramanian, V. (2012). Sensitization resistance of friction stir welded AISI 409 M grade ferritic stainless steel joints. *The International Journal of Advanced Manufacturing Technology, 59,* 961–967.
3. Campos, T., & Lopes de Oliveira, M. C. (2014) Sensitization behavior of type 409 ferritic stainless steel confronting DL-EPR test and practice W of ASTM A763. *Journal of Materials Engineering and Performance, 23,* 2164–2173.
4. Buytoz, S., & Ulutan, M. (2002). In situ synthesis of SiC reinforced MMC surface AISI 304 stainless steel by GTAW surface alloying. *Surface and Coating Technology, 200*(12), 3698–3704.
5. López, C. E., & Mellor, B. G. (1998). Fracture toughness and crack morphologies in eroded WC–Co–Cr thermally sprayed coatings. *Materials Letters, 37,* 201–210(1998).
6. Prakash, G., & Nath, S. K. (2018). Slurry erosion behaviour of micron sized TiC modified WC-10Co-4Cr coating on 13/4 martensitic stainless steel by high velocity oxy fuel process. *Journal of Materials Today Proceeding, 5,* 17333–17341.
7. Murthy, J. K. N., Rao, D. S., & Venkataraman, B. (2001) Effect of grinding on the erosion behaviour of a WC–Co–Cr coating deposited by HVOF and detonation gun spray processes. *Wear, 249,* 592–600.
8. Yuping, W., & Sheng, H. (2012). Microstructure and cavitation erosion behavior of WC–Co–Cr coating on 1Cr18Ni9Ti stainless steel by HVOF thermal spraying. *International Journal of Refractory Metals and Hard Materials, 32,* 21–26.
9. Ravinder, & Jarial, S K. (2015). Parametric Optimization of TIG welding on stainless steel (202) and Mild steel by using Taguchi method. *International Journal of Enhanced Research in Science Technology & Engineering.* ISSN 2319–7463.
10. Lailatul, P. H., & Maleque, M. A. (2017). Surface modification of Duplex stainless steel with SiC preplacement using GTAW torch cladding. *Advances in Materials and Processing Technologies Conference, 184,* 737–742.
11. Wang, S., Lin, W., & Tsai, Y.Y. (2003). The effects of various ceramic–metal on wear performance of clad layer. *Journal of Materials Processing Technology, 140*(1–3) 682–687.
12. Lailatul, H., & Maleque, M. A. (2017). Hardfacing of duplex stainless steel using melting and diffusion processes. *Materials Science and Engineering, 184,* 012030.
13. Gochhayat, S. R., & Masanta, M. (2015). Tungsten inert gas (TIG) assisted TiC-Ni coating on AISI 304 stainless steel. ethesis.nitrkl.ac.in.
14. Ulutan, M., Mustafa yildirim, M., Soner, B., & Celik, O. N. (2010). Microstructure and wear behaviour of GTAW surfaced alloyed AISI 4140 steel. Society of Tribologists and Lubrication Engineers. 10.1050 10402604.519859.
15. Toro, A., Wojciech, Z., & Misiolek (2003). Correlations between microstructure and surface properties in a high nitrogen martensitic stainless steel. *Acta Materialia, 51,* 3363–3374.
16. Dyuthi, S., Mridha, S., & Shaha, S. K. (2010). Surface modification of mild steel using Tungsten inert gas torch surface cladding. *American Journal of Applied Sciences, 7,* 815–822.
17. Kumar, V., Gupta, R. D., & Batra, N. K. (2014) Comparison of mechanical properties and effect of sliding velocity on wear properties of Al 6061, Mg 4%, Fly ash and Al 6061, Mg 4%, Graphite 4%, Fly ash Hybrid Metal matrix composite. *Procedia Materials Science, 6,* 1365–1375.
18. Pandya, S. N., Nath, S. K., & Chaudhari, G. P. (2009). Friction and wear characteristic of GTAW processed surface modified grey cast iron. *Journal of Scientific Research* (3), 516–527.
19. Soni, L., & Masanta, M. (2015). TiC coating on AISI 304 stainless steel by GTAW cladding using pre-placed powder. ethesis.nitrkl.ac.in

20. Vidarthy, R. S., Dwivedi, D. K., & Vasudevan, M. (2017). Influence of M-GTAW and T-GTAW welding process on microstructure and Mechanical behaviour of 409 ferritic stainless steel. (ASM international) *Journal of Material Engineering and Performance, 26,* 1391–1403.
21. Hutchings, I. (1993). Wear by hard particles: Tribology: Friction and wear of materials (pp. 172–182). London: Arnold.
22. Desouza, V. A., & Nevillle, A. (2003). Corrosion and erosion damage mechanisms during eosion-corosion of WC-Co-Cr cermet coating. *Wear, 255,* 146–156.

Fabrication of Jackfruit Stems Fiber Composites

**G. Srinivasa Rao, Saurav Saha, Ashiq Mohammed,
Rakesh Kumar Phanden, Eswara Krishna Mussada, Gadudasu Babu Rao,
Praveen Kumar Bannaravuri, Umesh Kumar Vates,
Bhupendra Prakash Sharma, Vijay Chaudhary, and Gaurav Gupta**

Abstract The following work has been done to fabricate new composites created by reinforcing newly identified jackfruit stem fibers into an unsaturated polymer resin matrix. The fibers have been extracted by mechanical and chemical processes, and hand layup technique has been used to fabricate the composites. First, the identification of the specimen is done and jackfruit stem fibers are decided to be checked for feasibility of extraction for this study. When it is found that the fibers can be extracted

G. S. Rao (✉) · S. Saha · A. Mohammed · R. K. Phanden · U. K. Vates · B. P. Sharma ·
V. Chaudhary · G. Gupta
Department of Mechanical Engineering, Amity School of Engineering and Technology, Amity University, Noida, India
e-mail: srgorrepati@amity.edu

S. Saha
e-mail: saurav.saha6@gmail.com

A. Mohammed
e-mail: ashiqmohd2011@gmail.com

R. K. Phanden
e-mail: rkphanden@amity.edu

U. K. Vates
e-mail: ukvates@amity.edu

B. P. Sharma
e-mail: bpsharma@amity.edu

V. Chaudhary
e-mail: vchaudhary2@amity.edu

G. Gupta
e-mail: ggupta1@amity.edu

E. K. Mussada
Amity Institute of Technology, Amity University, Noida, India
e-mail: ekmussada@amity.edu

G. B. Rao · P. K. Bannaravuri
Department of Mechanical Engineering, Karunya Institute of Technology and Sciences, Coimbatore, India
e-mail: baburao@karunya.edu

successfully from the jackfruit stem, then both retting process and chemical treatment is used to successfully extract the fibers. After extraction of the fibers, the density of the extracted fibers is to be calculated. After that, the fibers of proper length are used to create composite matrix of polymer resin using a calculated amount of volume fraction of fibers. The composites are then post cured after fabrication and prepared for further studies.

Keywords Natural fibers · Retting · Volume fraction · Composites · Polymer

1 Introduction

Nature has always provided human kind with every basic need since the dawn of mankind. Humans have always sought after the gifts of nature for survival, build civilization, and make advancements. Whether it is food, or wood, or fuel, or metals, every basic necessity we use is a gift of nature. And not a single part of it should be wasted. Every part of what we consume and use should be utilized to the maximum extent. But the modern world has seen wastage of these gifts to a very large extent. Whether it is food from agriculture, or fruits, or wood of trees, or fibers from plants, a major portion of these natural products gets wasted because we do not know how or in what way to maximize its utilization. In this modern world where mankind is searching for artificial advancements for survival, we should take notice of the incredible hidden gifts that the nature has already provided us and research into how to convert natural products into more useful products for the benefit of humans in every possible sphere of life.

Humans tend to throw away stuff they do not deem useful according to their basic needs. This is where science and engineering comes in. Various parts of plants and fruits of many crops and trees are thrown away or left for waste after consumption of the fruit or the necessary parts. These various parts which are left for waste or thrown away can be utilized very efficiently. Recent studies have found that, natural fibers extracted from the waste products, when added to polymer resins act as reinforcement and upgrade the mechanical and thermal properties of the polyester resin matrix. It has been observed that using natural fibers in resin polymer matrices upgrades the properties of the resulting composites. Moreover, the synthetic fibers such as nylon, glass, and carbon can easily be replaced and chosen over low density, high strength of natural fibers. Also, natural fibers are cheap, easily available, and biodegradable as that of synthetic fibers. This is to say that something useful can be made of things that are thrown away as waste and deemed unnecessary. By converting these waste products into natural fiber composites, we can maximize the use of natural products and make sure that no part of it goes waste.

A considerable amount of literature is available about the various studies and reports of natural fibers being used as reinforcement in polymer resin composites.

P. K. Bannaravuri
e-mail: banna.mech@gmail.com

Researches have been carried out on wood flour, wood chips, and pulp to be used as additives in polymer matrix, mainly for cost efficiency and high volume uses [1–3]. Different studies of the world have reported the study of natural fibers like sisal [4], coir [5], jute [6], bamboo [7–11] as additives in thermosetting and thermoplastic polymers. A study regarding the extraction and tensile properties of different natural fibers such as date and vakka [12] has been done. Crop fibers such as sugarcane [13], wheat straw [14, 15], and rice straw [16] have also been used as additives in composites. The effectiveness of the fibers depends on their cellulosic content. In view of the 148 million tons (India) and 567 million tons (world) of rice produced every year, research of rice straw fibers for making composite matrix has been done to a great extent [17]. A study was made to find out the tensile attributes of polymer composites reinforced with elephant grass fiber, extracted by different methods. It was seen that the tensile properties and tensile modulus of the chemically extracted elephant grass fiber composites were 1.45 greater than those of fibers extracted by retting process [18]. Symington and coworkers studied about the effect of moisture on tensile properties of natural fibers such as jute, kenaf, flax, hemp, and coir. They confirmed in their study that jute fiber showed better mechanical properties than the other fibers [19]. Composites reinforced with natural fibers like hemp, coir, sisal, and jute were studied for tensile properties, and it was seen that among them, hemp fiber-reinforced composite showed far better mechanical properties [20]. Thakur et al. did research about the efficient use of raw natural fibers as indispensable components in polymers for developing low-cost eco-friendly composites. Mechanical and thermal properties of composite matrix of jute fibers on alkali treatment were studied [25, 26]. A change in properties was observed by using NaOH solution treatment. There was a study carried out in which composites of polypropylene filled with 30% wheat straw fibers were extracted by both mechanical and chemical treated processes [27]. There were some studies carried out on the potential use of lignocellulose of elephant grass for biogas production [28].

Even though there are large amounts of work available and published on different types of natural fibers and its composites, an effort has been made in this project to introduce a new natural fiber, i.e., jackfruit stem fibers, as reinforcement in the development of new composite material. Jackfruit is a common fruit found all over India. But the problem is that most part of the fruit (outer skin and stem) is thrown away as waste. Now we decided to efficiently use the waste part and convert it into useful additives for polymer resin composites and study the results thereafter. Unsaturated polyester resin will be used for fabricating the matrix as it is relatively cheaper, has minimal shrinkage, and can be molded easily at room temperature. Subsequently, various percentage volumes of jack fruit stem fibers is added to an unsaturated polyester resin to fabricate the newly found reinforced polyester composites, and the extraction processes of jackfruit stem fibers are to be reported.

2 Experimental Procedure

2.1 Materials

The first step was to find a natural fiber which has not been identified yet and previous research work has not been done. After much discussion and reading previous research works regarding natural fibers, it was decided to use jackfruit stem fibers, as no previous work or study had been carried out related to it. The reason jackfruit stem was chosen as the specimen because jackfruits' weights vary from 10–15 kgs, sometimes even reaching about 45 kgs. Therefore, the natural fiber which is to be extracted from the jackfruit stem might have greater tensile properties than other natural fibers. Jackfruit is a seasonal fruit in India, and it is not easily available. The jackfruit stems (shown in Fig. 1) were procured from Alleppey, Kerala.

Polyester resin (unsaturated) of grade ECMALON 4411 was purchased from ECMAS Construction Chemicals Pvt. Ltd., Hyderabad, India. The density of resin is 1258 kg/m^3, Young's modulus is 630 MPa, and tensile strength is 31.5 MPa. Rubber sheets of dimension 24 × 25 cm were purchased from Zenith Industrial Rubber Products Pvt. Ltd., Mumbai, India. The catalyst (methyl ethyl ketone peroxide MEKP) and accelerator (cobalt octoate) were obtained from local sources. Other materials required were also obtained from local sources.

For making the molds for the composite matrices, uniform slots of 160 × 12.5 × 3 mm were cut in the rubber sheets according to ASTM standards. A transparent sheet is then used to cover one side of the rubber sheets such that there are no air gaps or bubbles in between.

Fig. 1 Jackfruit and its dried stems

2.2 Preparation of Fiber

Before the process of extraction, the stems are first delignified. For extraction of the fibers, the first method that we used is the process of retting. After about 30 days, the specimens become soft. They are then taken out of water and beat gently with a plastic mallet. The process is such that the stems are taken out of water, gently tapped on the surface, and then put in water for about 1 min. Then it is again tapped gently on the surface. This process is repeated for about 5 days until the stem flattens and the fibers separate (shown in Fig. 2). The specimens are then dried in the sun and then the fibers are able to be easily separated and extracted. The entire process takes about 50–55 days. Another process we have used for extraction is chemical extraction. In a container, distilled water and NaOH pellets are mixed in a ratio of 1:2 thoroughly. The fiber strips are then soaked in the solution (0.1 N NaOH) for 72 h. After 72 h, they are then taken out of the solution and washed thoroughly with distilled water. Then the fibers strips are taken and dried thoroughly. After that manual extraction follows. Both the mechanically and chemically fibers are then cut to required length according to ASTM standard.

While manual extraction, it was seen that there was inter-branching present in between the fibers. This might be a reason as to how jackfruits stems are able to hold such large masses of the jackfruits. Therefore, to maintain this inter-branching characteristic of jackfruit stem fibers, long strips of fibers are preferred. The fibers strips are then washed and then dried properly in a furnace at 50 °C for about 30 min to remove moisture from the fibers. Therefore, three sets of fibers, each of chemically and mechanically extracted fibers were then separated according to volume fractions of about 0.38, 0.77, 1.16, 1.55, and 1.94, and kept aside (as shown in Fig. 3).

Fig. 2 Fibers being separated after retting process

2.3 Calculation of Density of Fibers

After the fibers have been extracted successfully, the density is then to be calculated. Individual fibers of proper length and size are taken in a small bundle. The mass of this bundle is then measured on an electronic balance and noted. A thin wire is taken to tie and hold the bundle of fibers together. The mass of it is noted too. Then, a 100 ml measuring cylinder is then taken and filled with water up to a mark (70 ml). The initial level of water is noted. Then the wire is then submerged in water inside the measuring cylinder. Using Archimedes' principle, the displacement of water from the initial level is then noted down. The wire is then taken out and dried. Then the wire is used to tie the bundle of fibers. The initial level of water inside the measuring cylinder is noted. Then the bundle is taken and submerged in water inside the measuring cylinder. The displacement of water is then noted.

Therefore, the following calculations are made to determine the density of the fibers:

Mass of fibers taken $(M1) = 2.459$ gms
Mass of rubber band $(M2) = 0.371$ gms
Total mass $(M1 + M2) = 2.824$ gms
Initial level of water $(L1) = 70$ ml
Final level of water for wire $(L2) = 70.4$ ml
Volume of water displaced by the wire $(V1) = 0.4$ ml
Final level of water for the bundle $(L3) = 73.2$ ml
Volume of water displaced by the bundle $(V2) = 3.2$ ml
Volume of water displaced by only fibers $(VT) = V2 - V1 = (3.2 - 0.4)$ ml $= 2.8$ ml

Therefore,

$$\text{Density} = \frac{\text{Mass of fibers}}{\text{Volume of water displaced by the fibers}} = \frac{2.459 \text{gms}}{2.8 \text{ml}}$$
$$= 0.87821 \text{ gms/cm}^3 \text{ or } 878.21 \text{ kg/m}^3$$

Table 1 Density of jackfruit stem fiber composites along with other natural composites [12–16]

S. no.	Name of the composite material	Density (Kg/m^3)	Volume fraction of fiber
1	Plain polyester	1074.5	0.00
2	Rice straw	1258	0.41
3	Sisal	1450	0.37
4	Banana	1350	0.374
5	Vakka	810	0.372
6	Bamboo	910	0.371
7	Gold cane	750	0.43
8	Jowar	922	0.40
9	Coir	1150	–
10	Hemp	1480	–
11	Waste boom grass	864	–
12	Jackfruit stem fiber	878.21	0.38

Therefore, the density of fibers of jackfruit stem is found out to be 878.21 kg/m^3. The density of existing fibers along with jackfruit stem fiber-reinforced composites has been presented in Table 1 for better comparison in the literature [11–16].

It is found that the density of jackfruit stem fiber is less compared to the many existed fibers like rice straw, sisal, banana, coir, hemp, bamboo, jowar and slightly higher than vakka, gold cane, and waste broom grass which may prove to be a good property for fabricating lightweight components.

2.4 Composite Preparation

In the current research work, the composites have been prepared using hand layup method. The rubber sheets are placed over a flat surface and then the fibers are placed unidirectionally inside the molds according to the different volumes. After that, accelerator and catalyst are added to the resin in a quantity of 1.5% by volume of resin each at room temperature. The resin used is Ecmalon 4411. The mixture is then stirred thoroughly to blend uniformly. Then the resin mixture is taken and slowly poured over the mold in an appropriate quantity (as shown in Fig. 4) and then covered properly. It is to be seen that no amount of air or air bubbles is present inside the mold. Deformation and movement of the fibers is to be minimalized for the fabrication of good quality and unidirectional fiber composites. Therefore, a compressive pressure of 0.05 MPa was applied over the mold on a layer of fiber glass and composite specimens were cured for 24 h and avoiding any kind of disturbance to the setup.

Fig. 4 Resin mix is being
poured over the fiber molds

Therefore, fabrication of composites is completed according to volume fractions of
0.38, 0.77, 1.16, 1.55, and 1.94.

3 Results and Discussions

A new natural fiber has been identified and checks for feasibility of extraction and
can be concluded to be used as reinforcement in polymer composites. Thus, this
newly identified natural fiber is then successfully used to fabricate reinforced resin
composites with volume fractions of 0.38, 0.77, 1.16, 1.55, and 1.94 according to
ASTM standards.

4 Conclusion

- The aim of the work has been achieved by identification of a newly found natural
  fiber of jackfruit stem fibers.
- The extraction of the fibers from jackfruit stem has been done using mechanical
  and chemical processes.
- Fabrication of resin composites reinforced with jackfruit stem fibers has been
  done.

- Therefore, in this way, we can see that waste natural products can be used to make useful products or can be rather used as additive in composites and thus create better and reinforced products with better properties.
- That is why one should never waste our natural resources and should always try to maximize their utilization efficiently.

References

1. Hon, D. N. S., & Chao, W. Y. (1993). *Journal of Applied Polymer Science, 50,* 7–11.
2. Raj, R. G., Kokta, B. V., & Daneault, C. (1990). *Journal of Applied Polymer Science, 40,* 645–655.
3. Raj, R. G., Kokta, B. V., Grouleau, G., & Daneailt, C. (1990). *Polymer-Plastics Technology and Engineering, 29,* 339–353.
4. Singh, B., Gupta, M., & Verma, A. (1996). *Polymer Composites, 17,* 910–918.
5. Rout, J., Mishra, M., Tripathy, S. S., Nayak, S. K., & Mohanthy, A. K. (2001). *Composites Science and Technology, 61,* 1303–1310.
6. Albuquerquc dc, A. C., Joseph, K., Carvalho dc, L. H., & Almeida, J. R. M. (2000). *Composites Science and Technology, 60,* 833–844.
7. Amada, S., & Untao, S. (2001). *Composites: Part B, 32,* 451–459.
8. Amada, S., Munekata, T., Nagase, Y., Ichikawa, Y., & Shimizu, H. (1997). *Composites: Part B, 28* B 13–20.
9. Ismail, H., Edyham, M. R., & Wirjosentono, B. (2002). *Journal of Polymer Test, 21,* 139–144.
10. Yao, W., & Li, Z. (2003). *Cement and Concrete Research, 33,* 15–19. Thwe, M. M., & Liao, K. (2003). *Composites Science and Technolog, 63,* 375-387
11. Okubo, K., Fujii, T., & Yamamoto, Y. (2004). *Composites: Part A, 35,* 377–383.
12. Murali Mohan Rao, K., & Mohan Rao, K. (2007). *Journal Composite Structures, 42,* 3266–3272.
13. Zarate, C. N., Aranguren, M. I., & Reboredo, M. M. (2000). *Journal of Applied Polymer Science, 77,* 1832–1840.
14. White, N. M., & Ansell, M. P. (1983). *Journal Materials Science, 18,* 1549–1556.
15. Hornsby, P. R., Hinrichsen, E., & Tarverdi, K. (1997). *Journal Materials Science, 32,* 443–451.
16. Ratna Prasad, A. V., Rao, K. M. M., Rao, K. M., & Anil Kumar, M. (2006). *Indian Journal of Fibre & Textile Research, 31,* 335–338.
17. Calpe, C. (2004). *Proceedings, FAO Rice Conference.* Rome: FAO of United Nations.
18. Murali Mohan Rao, K., Ratna Prasad, A. V., Ranga Babu, M. N. V., Mohan Rao, K., & Gupta, A. V. S. S. K. S. (2007). Tensile properties of elephant grass fiber reinforced polyester composites. *Materials Science, 42,* 3266–3272.
19. Symington, M. C., Banks, W. M., West, O. D., & Pethrick, R. A. (2009). Tensile testing of cellulose based natural fibers for structural composite applications. *Journal of Composite Materials, 43,* 1083–1096.
20. Wambua, P., Ivens, J., & Verpoes, I. (2003). Natural fibers: Can they replace glass fibre reinforced plastics? *Composites Science and Technology, 63,* 1259–1264.
21. Liu, K., Takagi, H., Osugi, R., & Yang, Z. (2012). Effect of lumen size on the effective transverse thermal conductivity of unidirectional natural fiber reinforced composites. *Composites Science and Technology, 72,* 633–639.
22. Han., G., Lei, Y., Wu, Q., Kojima, Y., & Suzuki, S. (2008). Bamboo–fiber filled high density polyethylene composites: Effect of coupling treatment and nanoclay. *Journal of Polymers and Environmant Science, 16,* 123–130.

23. Sharma, B. P., Pugalia, R., Ashish Rao, G. S., & Vates, U. K. (2019a). Tensile behavior of silver date palm leaf reinforced polyester composites advances in engineering design. *Lecture notes in mechanical engineering* (pp. 797–804). Springer, Singapore. Print ISBN: 978-981-13-6468-6, Online ISBN: 978-981-13-6469-3. https://doi.org/10.1007/978-981-13-6469-3_74.

24. Sharma, B. P., Gangawani, R., Akhtar, S., Rao, G. S., & Vates, U. K. (2019b). Flexural properties of silver date palm leaf reinforced polyester composites. Advances in engineering design. *Lecture notes in mechanical engineering* (pp. 789–796). Springer, Singapore. Print ISBN: 978-981-13-6468-6, Online ISBN: 978-981-13-6469-3. https://doi.org/10.1007/978-981-13-6469-3_73.

25. Sharma, B. P., Sareen, S., Tokas, D., Rao, G. S., & Vates, U. K. (2019c). Impact strength of silver date palm leaf reinforced polyester composites. Advances in interdisciplinary engineering. *Lecture notes in mechanical engineering* (pp. 79–84). Springer, Singapore. Print ISBN: 978-981-13-6576-8, Online ISBN: 978-981-13-6577-5. https://doi.org/10.1007/978-981-13-6577-5_9.

26. Sharma, B. P., Akhil, D., Junaid, M., Vates, U. K., & Rao, G. S. (2019d). Mechanical behavior of powder metallurgy processed Al + ZrB2 + Al2O3 metal matrix composites. Advances in industrial and production engineering. *Lecture notes in mechanical engineering* (pp. 597–604). Springer, Singapore. Print ISBN: 978-981-13-6411-2, Online ISBN: 978-981-13-6412-9. https://doi.org/10.1007/978-981-13-6412-9_58.

27. Sharma, B. P., Junaid, M., Akhil, D., Rao, G. S., & Vates, U. K. (2019e). Mechanical behavior of stir-casted Al + ZrB2 + Al2O3 metal matrix composites. Advances in interdisciplinary engineering. *Lecture notes in mechanical engineering* (pp. 71–77). Springer, Singapore. Print ISBN: 978-981-13-6576-8, Online ISBN: 978-981-13-6577-5. https://doi.org/10.1007/978-981-13-6577-5_8.

28. Sharma, B. P., Rao, G. S., & Vates, U. K. (2019f). Powder metallurgy processing and mechanical characterization of iron-based composite reinforced with alumina and zirconium diboride. Advances in industrial and production engineering. *Lecture notes in mechanical engineering* (pp. 303–308). Springer, Singapore. Print ISBN: 978-981-13-6411-2, Online ISBN: 978-981-13-6412-9. https://doi.org/10.1007/978-981-13-6412-9_28.

Analysis of the Composite Sample Under Low Velocity Multi-impact Test: FEA Investigation

Punita Kumari, Ashraf Alam, and Saahil

Abstract The effect of the stacking sequence under multi-impact was investigated in this paper. Finite element (FE) model was prepared for the multi-impact composite sample while taking Hashin failure criteria into account. Force, impact time and absorbed energy of the sample were computed for each impact. The stacking sequence comparison was carried out that depends upon peak force, maximum impact time, absorbed energy and damage region. From the results, it is evident that each impact degrades the material properties and brings it close toward the fatal condition. From FE analysis, it was observed that the backside of the samples gained more damage in comparison with the front side, which could be attributed solely to compression and tension. Analysis of the result discerns that there exists the correlation between absorbed energy and the damage region. The FE model showcased here demonstrates the potential to investigate the damage that occurred to the composite material that was under multiple impacts.

Keywords Composite · Finite element model · Impact parameter · Hashin failure · Multi-impact · Stacking sequence

P. Kumari (✉)
School of Material Science and Engineering, Wuhan University of Technology, 122 Luoshi Road, Wuhan 430070, China
e-mail: punita@whut.edu.cn

A. Alam
Department of Education, University of Delhi, New Delhi, India
e-mail: ashraf_alam@live.com

Saahil
School of Automotive Engineering, Wuhan University of Technology, 122 Luoshi Road, Wuhan 430070, China
e-mail: saahil@whut.edu.cn

505

1 Introduction

The application of the composite material has increased because of its lightweight, anti-corrosion properties, high stiffness, and high strength. Metals are replaced by composite materials in numerous applications, some of which includes the fields such as marine, aerospace, sports, civil and automobile industries. Besides its several advantages, composite structures are vulnerable to impact load. Normally, the impact damage induced to composite structures because of tool drop during maintenance, bird strike, heavy landing, lightning strike and hailstone strike leads to matrix crack, fiber breakage and de-lamination. These are the main modes of failure that composites bear under the impact loading that eventually reduces the performance and service life of the composites [1]. Consequent to it, the impact damage study via numerical study thus becomes a requirement to identify the impact behavior on the composites under impact load [2, 3]. Damage progression and detection of the failure of composites under impact load are difficult to decipher through experimental method [4]. Finite element analysis (FEA) is one of the least expensive methods that is capable to track down various mode of failures [5].

Most recent FEA studies have been carried out in field of the low velocity impact on the composite laminates adapting VUMAT [6, 7]. While carrying out the literature review, the researchers could find limited number of FEA work that has been carried out for composite laminates under repeated or multi-impact. Novelty of this research lies in the fact that this is one of the very few studies that has made an attempt to estimate the damage caused to GFRP due to multi-impact while making use of the continuum shell meshing element. In this research work, a FEA of two different stacking sequences of the composite was developed. In the process, a damage model of composite laminate was developed on the criteria of inter-laminar and intra-laminar damage. Laminates were exposed to multiple low velocity impact and results drawn from the research were compared based on the contact force, the absorbed energy and the damage region. FEA model was developed with continuum shell element for both the different stacking sequences of laminates under multi-impact and a comparison was drawn among them. The computational time was reduced by taking continuum shell; it consequently subjected less burden on the computer during the computation of the simulation work.

2 Prepared FE Model

Intra-laminar model: Inter-laminar contains fiber and matrix damage of the composite material. Hashin failure criteria were taken into account in this work [5], and FE models of the composite samples developed to have the properties of elastic behavior, damage initiation and damage evolution. Proceeding further, the damage starts to the composite lamina layers were modeled as an orthotropic elastic material. It was expected that the in-plane longitudinal and transverse modulus of elasticity will come

out to be equal because the composite sample depends on a plain weave. Damage initiation criteria were modeled using Hashin's failure criteria [2] that recommend four damage initiation mechanism equations, specified as fiber tensile, fiber compressive, matrix tensile and matrix compressive.

Tensile fiber mode

$$\widehat{\sigma_{11}} \geq 0$$
$$\left(\frac{\widehat{\sigma_{11}}}{X_t}\right)^2 + \left(\frac{\widehat{\sigma_{12}}}{S_L}\right)^2 = 1 \tag{1}$$

Compressive fiber mode

$$\widehat{\sigma_{11}} \leq 0$$
$$\left(\frac{\widehat{\sigma_{11}}}{X_c}\right)^2 = 1 \tag{2}$$

Tensile matrix mode

$$\widehat{\sigma_{22}} \geq 0$$
$$\left(\frac{\widehat{\sigma_{22}}}{Y_t}\right)^2 + \left(\frac{\widehat{\sigma_{12}}}{S_L}\right)^2 = 1 \tag{3}$$

Compressive matrix mode

$$\widehat{\sigma_{22}} \leq 0$$
$$\left(\frac{\widehat{\sigma_{22}}}{2S_t}\right)^2 + \left[\left(\frac{Y_c}{2S_T}\right)^2 - 1\right]\frac{\widehat{\sigma_{22}}}{Y_c} + \left(\frac{\widehat{\sigma_{12}}}{S_L}\right)^2 = 1 \tag{4}$$

where Xt and Xc denote the strength in longitudinal tension and compression, Yt and Yc refer to the strength in transverse tensile and compressive, respectively, whereas S_L and S_T refer to shear strength in the longitudinal and transverse. $\widehat{\sigma}_{ij}$ denotes the effective stress in the corresponding direction. In this work, bilinear traction separation law was taken into account.

Inter-laminar model: It contains de-lamination between piles. $K = \frac{\alpha E_3}{h}$ $K_1 = \frac{2G_{13}}{e}$; $K_2 = \frac{2G_{23}}{e}$; $K_3 = \frac{E_3}{e}$.

where, h is the thickness of the sample plies and its $\alpha \gg 1$.

$$G_C = G_{IC} + (G_{IIC} - G_{IC})\left(\frac{G_{Shear}}{G_T}\right)^{\eta} \tag{5}$$

where, Gshear = GII + GIII, and GT = GI + GII + GIII. The BK parameter, η, is computed by curve fitting from experimental values. The critical fracture energy is evaluated through BK equation and the mixed-mode failure separation. The quadratic traction initiation was applied in this model since it works well for mode mixing in failure criteria.

Table 1 Sample identification

Stacking sequence	Group	Impact times	Sample code
[90/0/90/0]2 s	Group A	First	A1
		Second	A2
		Third	A3
		Fourth	A4
[0/90/90/0]2 s	Group B	First	B1
		Second	B2
		Third	B3
		Fourth	B4

Matrix dominating properties were assigned to the interface material and the normal strength was measured using the equality Tn = Yt and shear strength using ts = tt = S_{12}.

Adapted FE model: FE model was generated in ABAQUS/CAE 2018 and in that nonlinear explicit solver was selected to simulate. Composite plate with 16 ply stacking ([90/0/90/0]2 s, [0/90/90/0]2 s different stacking sequences) was modeled with dimensions of 100 mm × 150 mm × 4.8 mm. Impact ball subjected to the coupon with 12 J impact energy for both case (Fig. 1). Continuum shell element (SC8R) was used to mesh the composite part, whereas rigid element (R3D4) was taken for the impact tub (Fig. 2). To minimize the computational time, the impact region was meshed with fine element while the rest of the region was coarse meshed. Additionally, in order to attain the certainty analysis result, hourglass control was selected in this work. To control the deformation, random element distortion occurrence at integration point that is assigned zero in order to continue the simulation (Tables 1 and 2).

The impact tub made fix rotation but it is free to move forward only in Z direction, while a point mass was allocated over it. Amplitude value applied at the impact tub is

Table 2 Physical material properties of composite (E-Glass/sw905-2 lamina)

E_1(GPa)	$E_2 = E_3$(GPa)	$U_{12} = \upsilon_{13}$	υ_{23}	$G_{12} = G_{13}$ (GPa)	G_{23} (GPa)
45.6	8.20	0.278	0.365	5.83	3
S12 = S13 (MPa)	S23 (MPa)	G_{1t} (mJ/mm^2)	G_{1C} (mJ/mm^2)	G_{2T} (mJ/mm^2)	G_{2C} (mJ/mm^2)
65.26	46.00	2691.68	5431.05	69.83	1244.4
X_T (MPa)	X_C(MPa)	$Y_T = Z_T$(MPa)	Yc = Zc(MPa)		
566.67	241.38	20.69	82.96		
K_{11}	Ks	Kt	Density (kg/m^3)		
41e13	29.15e13	29.15e13	2089.34		

Table 3 Impact tub parameter

Impact tub details	
Impact tub weight	7 kg
Impact tub radius	8 mm
Total number of piles	16

Table 4 Cohesive parameter used for composite

t_n (MPa)	T_s (MPa)	t_t (MPa)	GIC (mJ/mm^2)	GIIC (mJ/mm^2)	GIIIC (mJ/mm^2)	β	Density (kg/m^3)
126	252	252	162.66	325.32	325.32	1.45	1366.05

computed through experimental velocity and time curve [2, 5]. The composite plate made it fixed by restricting the movement [1, 8] (Tables 3, 4).
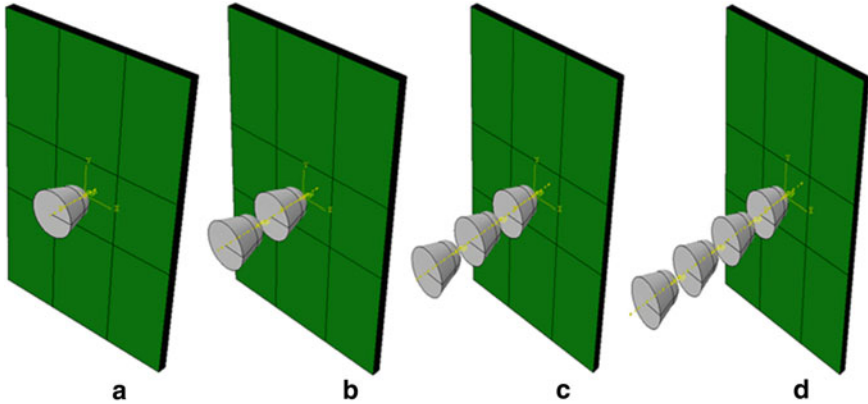
Fig. 1 FE model for impact test. **a** first, **b** second, **c** third, **d** fourth time impact
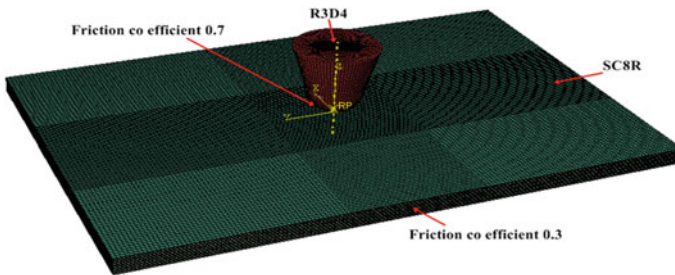
Fig. 2 Meshing of the sample

3 Result and Discussion

Multi-impact test model was developed and impact tests were carried out on both groups of samples. Figures 3a, 4a and Figs. 3b, 4b represent the force-time and absorbed energy-time curve response of impacted sample after impact test. Results showcase that both the group of samples follow similar pattern. It was further observed that the force value achieved through FEA gradually increased with time and after reaching its peak, it slowly fell down [8], and similar phenomenon was observed for other stacking sequences as well. The energy gradually increases with the time and after achieving maximum (less than impact) it starts dwindling and only at one point it remains constant. The comparison was done based upon peak contact force, impact time interval, impact damage region and has been mentioned in Table 5. From Figs. 3a and 4a, it can easily be deciphered that the contact force
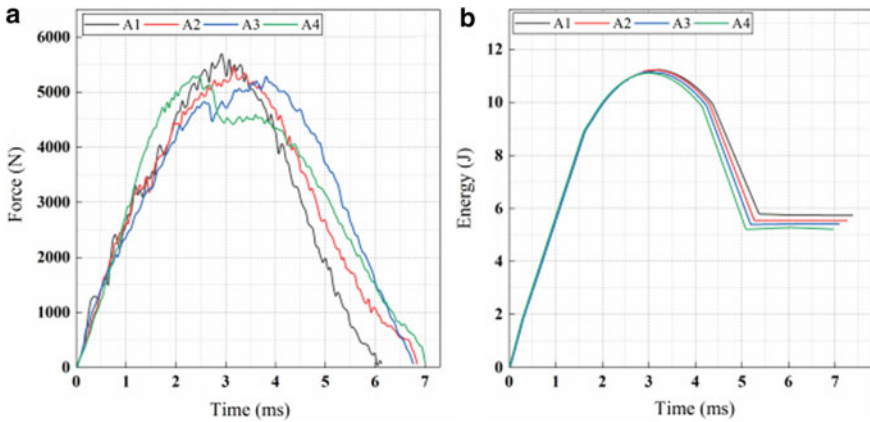
Fig. 3 **a** force-time, **b** absorbed energy-time of samples **a** group under multi-impacts
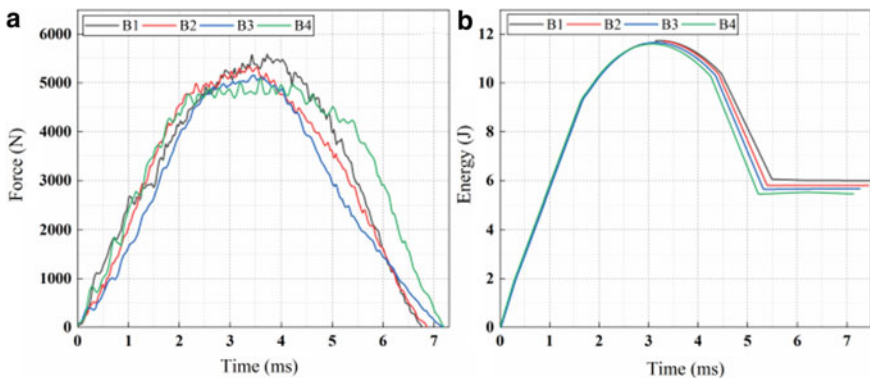
Fig. 4 **a** force-time, **b** absorbed energy-time of samples **b** group under multi-impacts

Table 5 FEA response under low-velocity impact test

Impact times	Maximum force (N)		Time duration (ms)		Absorb energy (J)	
	[A]	[B]	[A]	[B]	[A]	[B]
First	5674.51	5530.39	6.12	6.75	5.73	5.99
Second	5444.92	5329.35	6.84	6.85	5.54	5.79
Third	5186.65	5162.81	6.76	7.12	5.41	5.66
Fourth	5122.01	5020.19	7.00	7.18	5.21	5.45

and the impact time curve follow the order A1 > A2 > A3 > A4 and B1 > B2 > B3 > B4 of the impacted samples, respectively. Impact time duration of the samples can be observed in Figs. 3a and 4a, both of which follows A1 < A2 < A3 < A4 and B1 < B2 < B3 < B4. The energy absorption during multi-impact test is evident from the curves as illustrated in Figs. 3b and 4b. The absorb energy order obtained by both the stacking sequence follows the ranking A1 < A2 < A3 < A4 and B1 < B2 < B3 < B4 (Fig. 5).

Multi-impact is subjected at the center of the samples. First, in the first step, the impact load is subjected to the composites samples; then, the second step was created and assigned the second impact and the same procedure is repeated for third and fourth impact. FE analysis of each impact for group A and group B samples is shown in Fig. 6. Front face of figures demonstrated more damage dent than back face during multi-impact.

An elastic action of the composite samples was observed during FE simulation, the impact tub first strikes the sample surface, and after transmitting the impact energy, the sample rebounds the impact tub back. Moreover, the force-time curve confirms this behavior as has been shown in the curve. The comparison of force, impact time, absorbed energy and damage region of impacted samples for both stacking are obtained by making use of the FE result and has been shown in Fig. 5, and the values are given in Table 5. The damage propagation and evaluation were done through numerical simulation. The top layer of composite patches displayed matrix cracks and failure is first observed during the numerical analysis. A peanut shape damage is witnessed at the front face when the impact tub strikes the samples. Later on, it spreads gradually with increase in the number of impacts as has been showcase in the failure photos of the samples, which were carried out during the simulation. The images of stress, generated on both front and backsides of the sample, are shown in FE analysis figures. During the first impact, when the impact tub collides, the shape of the impact damage is initiated and an increase is visible with the increase in impact time.

Furthermore, each impact increases the dent of the composite samples and is depicted in the FEM photos. Samples [A, B] exhibit more damages than the original composites, and each impact further weakens the composites. This claim is made keeping the simulation results into consideration and is further strengthened by the after impact photos. Samples [A, B] absorbed more damage and showed up
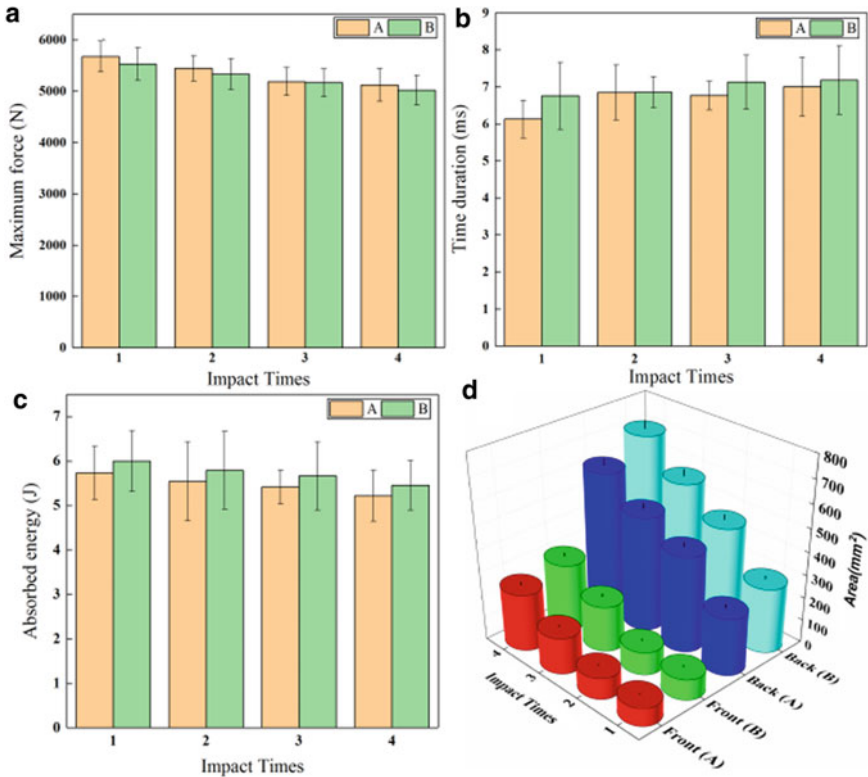
Fig. 5 Compassion graph of **a** peak force, **b** impact time, **c** energy absorption increment, **d** damaged region obtained by FE analysis method

more dent. The front side of the samples exacted dent while the rear side demonstrated del-lamination because of the generation of tensile stress on bending. Experimental studies require more time and material that can be saved by implementing computational method.

4   Conclusion

The sole purpose of the conduction of this research was to explore the stacking sequence influence of composite sample under the multi-impact response. Current investigation leads to the following outstanding outcomes:

- With each impact, the force value get reduces and absorbed energy and impact time get increased. This was revealed in the analysis of both the groups.
- After the first impact, samples displayed high peak force, least impact time and high absorb energy for both the composite groups.
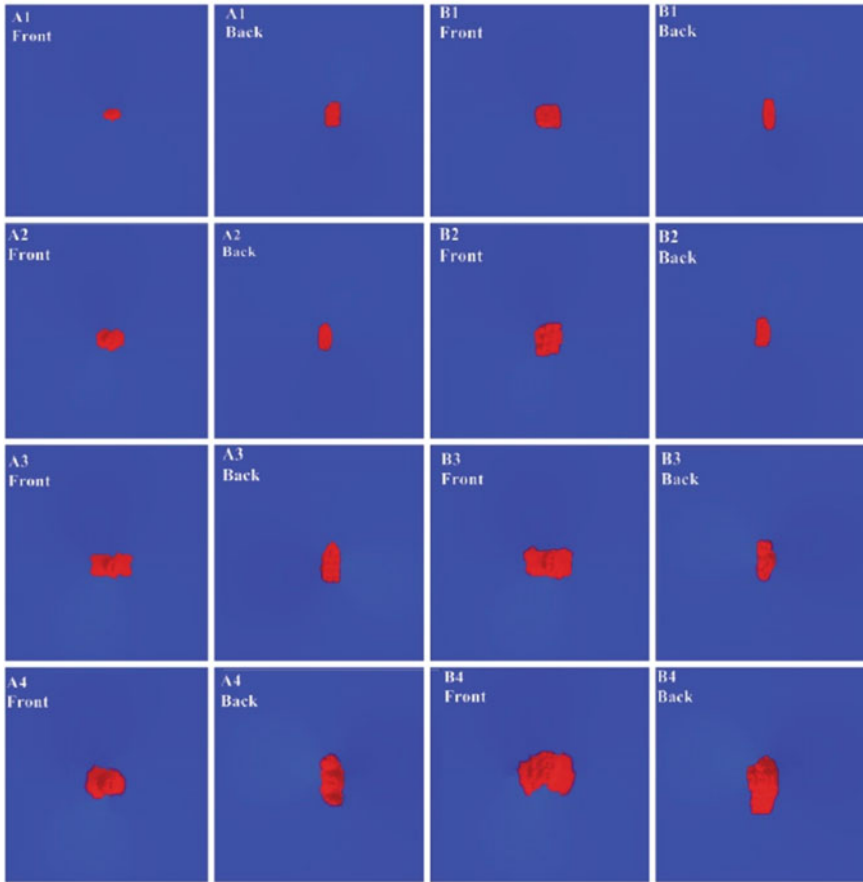
Fig. 6 Failure at the front and back face of samples

- During the fourth impact, both the group samples exhibited a slight contact force, large impact time interval, maximum absorbed energy and came up with highest damage region.
- Group A of composite samples responded good in comparison with group B. It carried high contact force, absorbed less energy, took least impact time and displayed less damage as compared to group B.
- There is a direct connection that was discerned between absorbed energy and damage that developed in the samples after the impact. The sample absorbed more energy and demonstrated more damage during impact.
- FE model for multiple impacts of samples was developed and compared with two different stacking sequences. It displayed reasonable agreement for each impact. The FE images demonstrate that the damage increased after the first impact.

However, 3D solid element could have demonstrated better result than continuum shell element.

Conflict of Interest   Authors declares there is no conflict of interest.

References

1. Kumari, P., Wang, J., Saahil (2019). Tensile after impact test of scarf-repaired composite laminates. *Arabian Journal for Science and Engineering, 44,* 7677–97.
2. Thorsson, S. I., Waas, A. M., & Rassaianc, M. (2018). Low-velocity impact predictions of composite laminates using a continuum shell based modeling approach Part b: BVID impact and compression after impact. *International Journal of Solids and Structures, 155,* 201–12.
3. Gliszczynskia, A., Kubiaka, T., Rozylob, P., Jakubczakc, P., & Bieniaśc, J. (2019). The response of laminated composite plates and profiles under low-velocity impact load. *Composite Structures, 207,* 1–12.
4. Bogenfeld, R., Kreikemeier, J., & Wille, T. (2018). Review and benchmark study on the analysis of low-velocity impact on composite laminates. *Engineering Failure Analysis, 86,* 72–99.
5. Khan, S. H., Sharma, A. P., & Parameswaran, V. (2017). An impact induced damage in composite laminates with intra-layer and inter-laminate damage. *Procedia Engineering, 173,* 409–16.
6. Liao, B. B., & Liu, P. F. (2017). Finite element analysis of dynamic progressive failure of plastic composite laminates under low velocity impact. *Composite Structures, 159,* 567–78.
7. Zhang, C., Duodu, E. A., & Gu, J. (2017). Finite element modeling of damage development in cross-ply composite laminates subjected to low velocity impact. *Composite Structures, 173,* 219–27.
8. Kumari, P., Wang, J., & Khan, S. (2018). Residual tensile strength of the multi-impacted scarf-repaired glass fiber-reinforced polymer (GFRP). *Composites. Materials* (Basel), 11.

Microstructure and Porosity Behavior of Spray Formed Al Alloy Processed by Cold Rolling

Rashmi Mittal, Prabh Simranjit Singh, Rajeev Sehrawat, Deepak Kr Tyagi, Milan Kr Bera, and Anil Sharma

Abstract An efficient spray forming technique was utilized to cast Pb-added Al-Si alloys. It was then rolled to a different percentages (0–80%) using rolling machine and microstructural characteristics as well as porosity behavior of casting alloy were systematically studied. It is noteworthy that the distribution of Pb was nearly uniform all through the aluminum phase and it was mainly at the grain boundary. Also, the grains of aluminum were found to be elongated along the rolling direction after 80% rolling. Porosity was minimum at peripheral region of the deposit and it decreased as rolling percentage is increased.

Keywords Al alloy · Spray deposition · Rolling · Microstructure · Porosity

1 Introduction

The excellent features of aluminum–silicon (Al-Si) alloys, for instance, low density, lightweight, high strength, low corrosion rate, better tribological properties and above all cost-effectiveness of Al-Si alloys have driven its wide utilization in various engineering applications. The conventional method of casting leads to coarse silicon

R. Mittal (✉) · P. S. Singh · R. Sehrawat · D. K. Tyagi · M. K. Bera · A. Sharma
Department of Physics, Maharishi Markandeshwar (Deemed to be University), Mullana 133207, India
e-mail: rashmimittal3@gmail.com

P. S. Singh
e-mail: ashmansidhu@gmail.com

R. Sehrawat
e-mail: rajeev.sehrawat@gmail.com

D. K. Tyagi
e-mail: deepak.tyagi76@gmail.com

M. K. Bera
e-mail: m.k.bera.iitkgp@gmail.com

A. Sharma
e-mail: anil67042@gmail.com

phase which affects the quality of Al-Si alloy. But, the Al-Si alloy quality can be improved drastically if the formation of brittle and coarse primary Si phase is suppressed by employing high cooling rate. On the other hand, spray deposition technique has an added advantage of high cooling rates along with its capability to make perform in a few numbers of steps [1]. The spray formed microstructures have been reported to demonstrate uniform dispersion of fine and equiaxed grains and free of macro-segregation. Indeed, this method exhibits the valuable characteristics of powder metallurgy dispensation with no involvement of many processing steps. Even after taking care of all processing steps, a few amount of porosity always exists in spray deposited preform. This leads to premature fracture due to stress concentration [2]. In this regard, the spray deposited preform must undergo another processing step to prepare fully dense metal sheets. Thus, in order to achieve high mechanical strength as well as to get rid of porosity, many competent methods like annealing, extrusion, forging, rolling, etc., are often employed [3]. Compare to others, rolling is an efficient process to get a dense product because of the presence of generalized stress field along with hydrostatic and deviatoric components [4].

Raju et al. have investigated earlier about the effects of spray casting on the microstructure and wear properties of Al-Si alloys [1]. It has been reported that spray forming is an effective casting method in refining the microstructure of Al-Si alloys. Besides, Dong et al. have reported microstructure, mechanical properties and corrosion behavior of spray formed 7075 alloy with various heat treatments [5]. Again it has been observed that spray cast 7075 alloy is composed of equiaxed grains and some fine secondary phases around the grain boundary. On the other hand, the usefulness of cold densification rolling of a sintered porous metal strip has been studied by Deshmukh et al. [6]. It was evidenced that density became decreases with increasing thickness reduction (25% and above). Moreover, the effect of cold forging process on the microstructures, porosity and wear rate of spray formed Al-Si alloys has also been investigated by Sandeep et al. [3]. It has been observed that porosity is decreased drastically after 50% thickness reduction.

In this present work, Pb-added Al-6Si alloys were spray deposited and then cold rolled to various percentages. Pb is used as a solid lubricant in many alloys, and therefore, Al-Si-Pb alloy can be used in the bearing materials. The change in porosity behavior and microstructural studies for different percentage of rolling are reported [7].

2 Experimental Procedure

The particulars of the spray formed setup engaged in this study have been mentioned somewhere else [5]. In concise, at the temperature of 1073 K, a weight of 700 gm of Al-Si-Pb alloy was melted in a crucible of graphite. At the pressure of 1 MPa, the melt was atomized by convergent-divergent nozzle. Fine droplets deposit on the substrate of copper which was kept at 40 cm from the nozzle and 20 cm in diameter. After some time, from the substrate, the preform was taken off and overspray particles
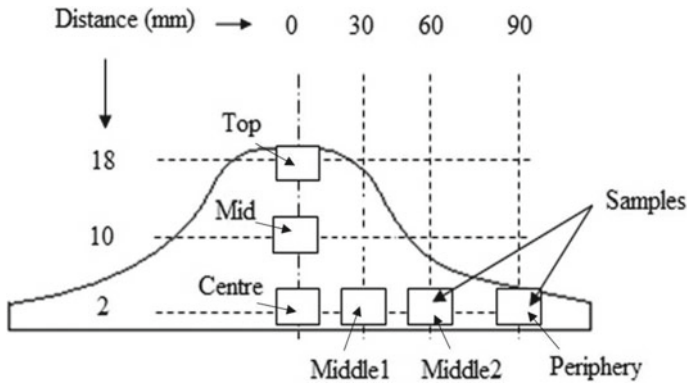
Fig. 1 Sample's locations cut from spray deposit for porosity measurements

were also collected from the tray. From the preform samples were cut as shown in Fig. 1. Subsequent to that, these cut samples were rolled using a rolling machine. In this, the 8 rpm was the speed of the rolls and the rolls diameter were 110 mm.

Samples from the center regions of the preform were cut down for the microstructural study and then cold rolled to different rolling percentage (0–80%). The foresaid samples were grind and polished by means of standard metallographic method of grinding and polishing. These polished samples were etched with Keller's reagent. After that, the samples were examined with Letiz optical microscope and the over spray particles were examined by using scanning electron microscope.

ASTM B 328–96 practice is used to resolve the measured density of the sample from which porosity can be calculated. Four measurements were taken and their mean value reported in the present work.

3 Result and Discussion

3.1 Microstructure

Figure 2 shows the micrograph of spray formed Al-6Si-15Pb alloy for different percentages of rolling, viz., (a) 0; (b) 20; (c) 40; (d) 60 and (e) 80% rolling. These micrographs were taken at center region for different percentages of rolling. The outcome point out that the Si phase (gray in color) is dispersed uniformly with particulate morphology (sub-micron to 5 μm particle size) in the matrix. Whereas fine equiaxed grains of Al (the bright region) has the grain size near about 15 to 25 μm. In this figure, the dark black color shows the Pb phase (as depicted by EDS in Fig. 3). It is observed that the distribution of lead is nearly uniform all through the aluminum phase and it is mainly at the grain boundary. In Fig. 2a, which is for
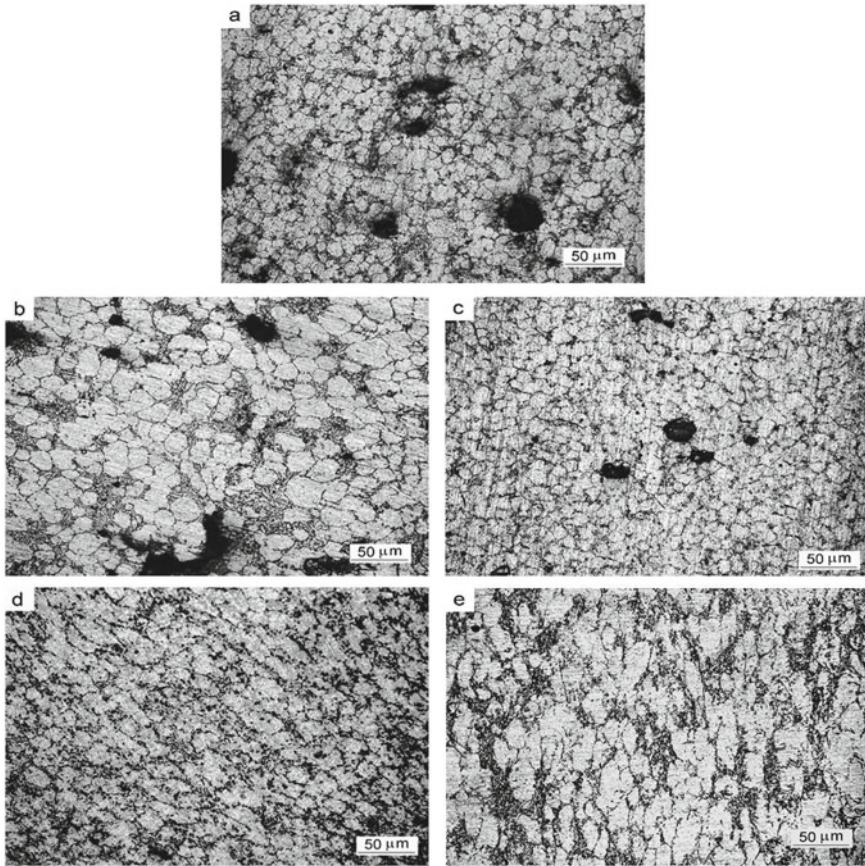
Fig.2 Microstructure at center region of spray cast Al-6Si-15Pb alloy for different percentages of rolling: **a** 0; **b** 20; **c** 40; **d** 60; **e** 80% rolling

without rolling, the size of Pb particles is sub-micron to 5 μm. The aspect ratio of Al-grains is 1.6–2.2 for 20, 40, 60 and 80% rolling.

During rolling, spreading of lead occurs therefore width of the grain boundary increases. As usual grains are lengthened in the direction of rolling as the percentage of rolling increases and with 80% rolling, the aspect ratio of the Al-grains also increases. Cracks were not observed after rolling of the samples in the reported microstructure.

Rapid solidification is the main cause of the microstructural features of the spray deposit material during atomization of the melt in to the very fine droplets. Fragmentation of dendrite arms occurs due to high velocity of the droplets and the turbulent fluid flow surroundings on the rising deposit [7] and thus equiaxed grains. Solidification of the Si phase occurs due to its high freezing temperature at an early stage.
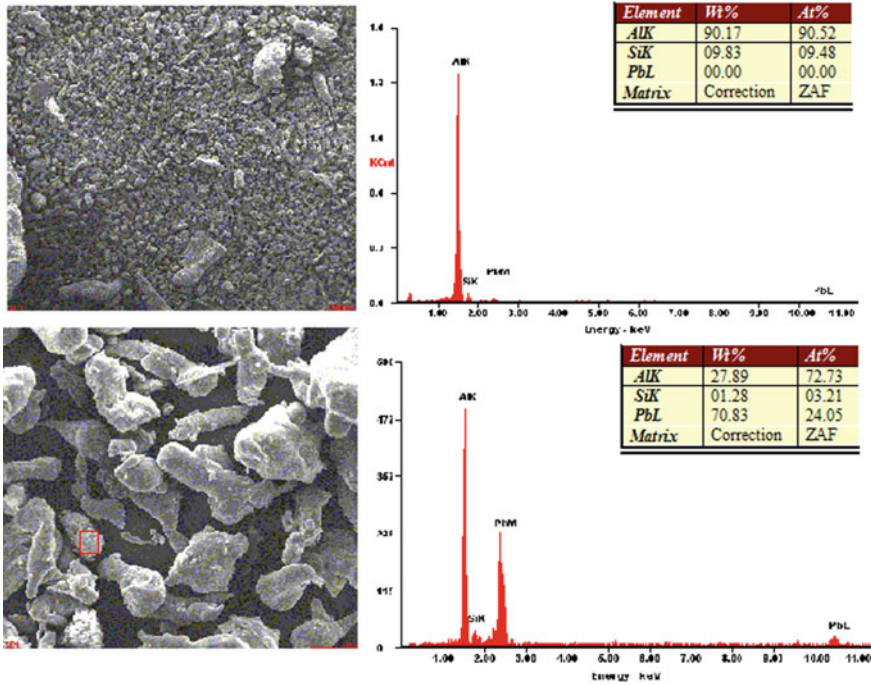
Fig. 3 SEM micrographs with EDS showing the size, shape and some other characteristics of Al-6Si-15Pb alloy spray particles

3.2 Porosity

It is known that the spray deposit perform is not fully dense but there exists a sure amount of porosity in the preform. Figure 4 shows the porosity variation of spray deposited Al-6Si-15Pb alloy versus rolling reduction at different locations of the preform, viz., center, middle 1, middle 2 and periphery. It is observed that the porosity decreases up to the rolling reduction of 60% and then a slight increment is there up to rolling reduction of 80%. In addition, porosity decreases at a faster rate from rolling reduction 40% to that of 60%. Also, the porosity is minimum at peripheral region of the deposit.

The gas entrapments due to turbulent flow during deposition of the droplets causing porosity in the obtained perform. The change in porosity level occurs due to variation of melt percentage in the spray [6]. In the early period of rolling (i.e., about 60% rolling), porosity gets removed by restacking and reshuffling of the spray deposited particles. However, some cracks are formed in the sample at 80% rolling reduction; therefore, a slight increase in porosity is observed.

Fig. 4 Porosity variation of spray deposited Al-6Si-15Pb alloy with rolling reduction at given locations of the preform, viz., center, middle 1, middle 2 and periphery
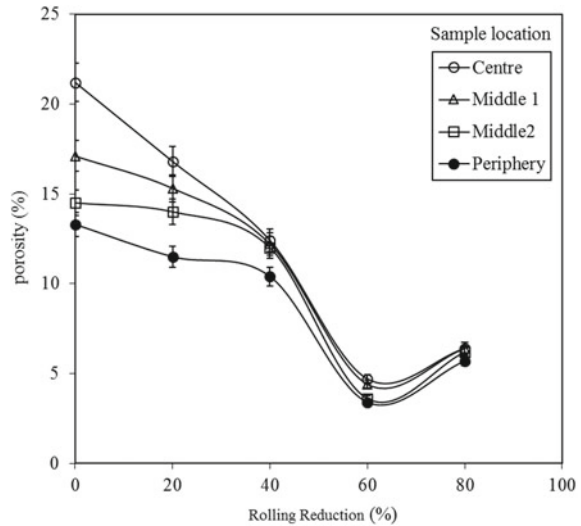
4 Conclusions

1. The distribution of lead is nearly uniform throughout the matrix and most of the lead particles are at the grain boundaries.
2. After eighty percent rolling reduction, aluminum grains are lengthened in the direction of rolling.
3. Porosity is minimum at peripheral region of the deposit.
4. Porosity decreases with the percentage of rolling and it is minimum for 60% rolling. Although, at 80% rolling, there is a slight increase in porosity which may be due to crack formation.

References

1. Raju, K., & Ojha, S. N. (2014). Effect of spray forming on the microstructure and wear properties of Al-Si alloys. *Procedia Mat. Sci., 5,* 345–354.
2. Liu, M., Cui, Z., & Sui, D. (2018). Microstructure and porosity formation of spray formed GCr15 steel billets. *Procedia Manufacturing, 15,* 1671–1677.
3. Kumar, S., Singh, R., & Singh, D. (2018). The Influence of Cold Forging Process on the Microstructure. *Porosity and Wear Behavior of Spray Formed Al-Si Alloys, Materials Today: Proceedings, 5,* 3486–3496.
4. Zhan, M. Y., Chen, Z. H., Yan, H. G., & Xia, W. J. (2007). Deformation behavior of porous 4032 Al alloy perform prepared by spray deposition during hot rolling. *J. Mat. Process. Tech., 182,* 174–180.
5. Dong, Y., Su, R., You, J., & Li, R. (2015). Study on microstructure, mechanical properties and corrosion behavior of spray formed 7075 alloy. *Materials Today Communications, 4,* 109–115.

6. Deshmukh, A. R., Sundararajan, T., Dube, R. K., & Bhargava, S. (1998). Analysis of cold densification rolling of a sintered porous metal strip. *Journal of Materials Science, 84,* 56–72.
7. Singh, D., & Dangwwal, S. (2006). Effects of process parameter on surface morphology of metal powder produces by free fall gas atomization. *Journal of Materials Science, 41,* 3853–3860.

Two-Body Abrasive Wear Behavior of Woven Carbon/Glass/Aramid Polytherimide Reinforced Hybrid Composites

N. K. Batra, Iti Dikshit, and Dilpreet Singh Sidana

Abstract The increased use of composites in industrial applications, recommended knowing their behavior of the developed composites under various working conditions. Wear is an important parameter and its experimental behavior must be known. Polyetherimide (PEI) is a thermoplastic polymer with very good mechanical properties, and its reinforced composite shows a significant tribo-potential. In the present study, wear behavior of woven carbon/glass/aramid fabrics reinforced composite and their hybrid materials are experimentally investigated. Two-body abrasive wear behavior of reinforced composites has been studied out by pin-on-disk apparatus. Abrasive wear rate was calculated at room temperature with grit size 35 µm of silicon carbide paper as a counter face. The abrasive wear studies were carried out at different loads (10, 20, 30 N) at a constant sliding velocity (v = 2 m/s) of steel disk. The wear in the experiment determined by wear loss and specific wear rate as a function of load. The wear loss increases with increasing load. Eventually, with increase in the load, specific wear rate decreases. However, carbon/PEI composite and its hybrid show less wear as compared to glass/PEI and aramid/PEI composite. In addition, photographs of the unworn and worn surface of the specimen have been examined under scanning electron microscope (SEM) to give an insight into the wear mechanisms.

Keywords Composite · Polyetherimide · Wear · Aramid fiber · Carbon fiber · Glass fiber

N. K. Batra · I. Dikshit (✉)
Mechanical Engineering Department, M.M. Deemed to be University Mullana, Ambala 133207, Haryana, India
e-mail: er.itidixit@gmail.com

N. K. Batra
e-mail: nkbatraeng@gmail.com

D. S. Sidana
Credible Future India Pvt. Ltd., Panchukla, Haryana, India
e-mail: dilpreetsidana@gmail.com

1 Introduction

The fiber reinforced composites have the capability to alter the properties such as high specific strength and high specific stiffness as per the need of the material [1]. Due to relatively low density and their tailored made property to have stacking sequence according to the required strength and stiffness in directions of loading [2]. The polymer composite material replacing traditional metal components in automobile application like such as gears, wheels, brake lining, bearings and also in various applications [3, 4]. Composite materials consist of a resin and reinforcement picked according to desired application [5] Polyetherimide (PEI) is an amorphous thermoplastic acquires exceptional mechanical property like high strength and high rigidity at inflated temperature [6]. Its distinguished and exceptional characteristic providing a material capable of meeting the difficult design requirements in food industrial machinery and for tribological application at elevated temperature is a major concern [7]. Among different types of wear, fretting, adhesive, abrasive, erosion and fatigue wear, these are common wear observed in workable situations. In the midst of all types of wear, abrasive wear contributes 63% of the total expense of wear. Abrasive wear is caused due to hard substance or asperities that are forced against; it gets penetrated and move over a solid surface under load, which results material removal, usually from softer material. Abrasive wear exists in the form of two-body and three-body abrasive wear [7]. Fiber mainly carbon, glass and aramid fibers is the main candidates and has been widely employed in the fabrication of reinforced composites [7]. Aramid epoxy reinforced composite due to low friction coefficient shows less wear loss to that of a glass fabric [8].Carbon epoxy composite shows less abrasive wear [9]. Wear behavior due to sliding and abrasive wear on carbon/glass/and aramid fiber hybrid composite and it is concluded that wear rate deduced as the fiber content increases in the hybrid composite [10]. Fabricated elastomer reinforced composite with short glass fiber and adding different fillers (SiC, alumina and carbon fiber) indicated that specific wear rate decline as the grit size of silicon carbide (SiC) increased [11]. Inclusion of fillers (PTFE and graphite) in carbon fiber polyaryletherketone composites shows adverse effect in abrasive wear [12]. The specific wear rate for three-body abrasion wear which shows minimum wear for glass carbon hybrid composites et al. load of 33 N as compared to glass fiber composite [13]. Various composite samples using glass and banana fiber reinforced with epoxy. The wear test was carried out at 30 N at varying speed on glass banana epoxy hybrid composites which shows minimum wear at 400 rpm with a value of 13 microns [14]. After reviewing the literature, it is concluded that very little study reported on wear study of polyetherimide reinforced composite. The experimental study focuses on two-body abrasive wear of the hybrid composite (5% PEI and 10% PEI) is carried out in various loads, i.e., 10 N, 20 N and 30 N on different facing sides, i.e., carbon facing, aramid facing, glass facing of the materials under dry sliding against silicon carbide sandpaper of grit size 35 μm and steel ring.

2   Materials and Methods

2.1   Sample Preparation

Polytherimide (ULTEM 1000) was purchased from PEE CEE Textile store, Kanpur used as a matrix with a density of 1.6 g/cm^3. The PEI is in form of granules dipped into the dichloromethane (DCM or methylene chloride) in the ratio of 1:10 which provides desire viscosity of the mixture. In the present study, woven carbon, glass and aramid fabric supplied from PEE CEE Textile store, Kanpur used for the manufacturing of the composites. Each fabric type has a density of 200 g/m^2.

2.2   Fabrication of the Composite

Fabrics were cut with the help of scissor of dimension of 30 cm × 30 cm. The wrap and weft are two orientations of the weave of fabric. Care must be taken about the direction of cutting of fabric. The direction of cutting plays a major role in the wear performance of the composites. To avoid the misalignment of the weave of the fabric, it was sealed from the strands. After sealing of the fabric, it was dipped in the solution (PEI + DCM) in sealed container for 12 h, so that the solution gets mixed with the fabric and gets entrapped in the weave uniformly. The individual laminate dried in the oven at 1000 °C for 2 h. The samples with different fabric layers of desired thickness were prepared using compression molding machine (Manufacture: Friends Hydraulics, Model: CMP-60/5, Courtsey: MMDU-Mullana). To improve the surface finish of the prepared specimen, the fabric was sandwiched between two thin poly-imide films (0.025 mm). Once the mold reached the desired processing temperature (400 °C) within 20 min, an impregnation pressure of 80 MPa was applied. The no. of breathing in between is two; with duration of 20 s. Breathings are provided so that the excess polymer solution flew away from the fabric. The fabricated composites were cooled at a room temperature under the corresponding pressure. Table 1 shows the configuration and abbreviation of the composites prepared for the study. The hybrid

Table 1 Configuration and description of composites specimen

S. no	Abbreviation	Composition
1	S_{100}	Carbon fabric + polytherimide
2	S_{010}	Aramid fabric + polytherimide
3	S_{001}	Glass fabric + polytherimide
4	S_{011}	Aramid + glass fabric + polytherimide
5	S_{101}	Carbon + glass fabric + polytherimide
6	S_{110}	Carbon + aramid fabric + polytherimide
7	S_{111}	Carbon + glass + aramid fabric + polytherimide

composites are made up of combination of at least two fabrics reinforced with the polymer. The hybrid composite sample has two facing with different fabrics. For instance, S_{111} samples have a two facing one is carbon fabric facing and other facing is aramid fabric facing.

3 Experimental Procedure

Wear test was performed using pin-on-disk wear apparatus (DUCOM India, TR-20LE-PHM 400) at ambient temperature. The apparatus consist of rotating disk made of hardened steel (hardness 68 HRC) with track diameter of 100 mm. The silicon carbide (P400) abrasive paper with grit size 35 μm (as per ASTM standards) was adhered to the rotating disk which rotates at 300 rpm while a normal load was applied through a lever [2]. The specimen pin held stationary of size 10 mm × 10 mm × 3–4 mm in adjustable arm of the apparatus.

A series of experiment were run with a sliding velocity of 2 m/s under various loadings of 10, 20 and 30 N, sliding distance of 1.5 m and contacting time of 5 min. Acetone solution was used to clean the samples earlier and afterward the wear tests. Wear can be calculated by weight loss of the specimen by digital balance. Each specimen experimented for three times and average of wear was reported. The abrasive wear study of the hybrid PEI composite reinforced with carbon, glass and aramid fiber is carried out at various loads. The experiments were carried out on all the specimens and in hybrid composites (S_{011}, $S_{101,}$ S_{110}, S_{111}) wear test for both the facing has been investigated. A scanning electron microscope (Model: Zeiss EVO 50 and EVO 18 special-CRF: IIT Delhi) was used to examine the worn and unworn surfaces of sample S_{001}, S_{010}, S_{100}.

4 Results and Discussion

4.1 Wear Study

Figure 1a–e represents the influence of different load 10, 20 and 30 N on the abrasive wear loss of developed composite at a sliding velocity of 2 m/s. From Fig. 1a, it is obvious that in all the tested samples weight loss is very low at a load of 10 N as the load increase up to 30 N due to plowing mechanism by abrasive particles, material removed will be high as more grooves produced into the specimen [15]. When the load increase on the pin specimen, the interface temperature rises, results in thermal softening which weaken the interfacial bond between matrix and fiber, results in more fragmented and forms debris [16]. It is quite apparent from the graph (1b, 1c), when the hybrid composite wear loss was evaluated for carbon facing; it shows less wear due to its high interfacial adhesion with the matrix as compared to the glass and aramid
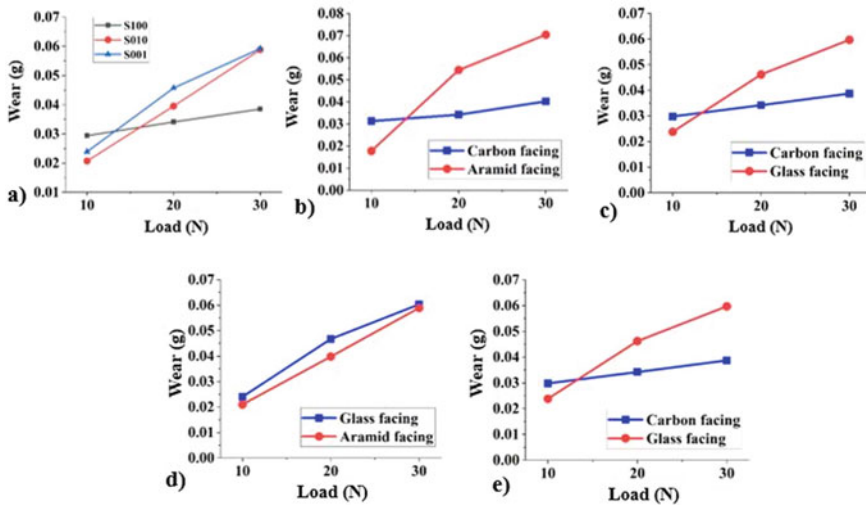
Fig. 1 Variation of weight loss with applied load for **a** S_{100}, S_{010} and S_{001}, **b** S_{110}, **c** S_{101}, **d** S_{011} and **e** S_{111} specimen at 300 rpm speed

facing. It can be easily observed in Fig. 1a–c, initially, during low load conditions, the glass and aramid fiber show better wear resistance than the carbon fiber. But, as the load is increased, due to its high specific modulus and self-lubricating property carbon fiber shows enhanced wear resistance as compared to other specimen [9]. It is important to emphasize that the different facing of the specimen has considerable effect on the weight loss. The carbon facing in the hybrid composite (S_{100}, S_{101}. S_{110}, and S_{111}) shows better wear resistance. The glass facing and aramid facing in the hybrid composite results high wear loss. In case of glass/aramid hybrid composite, aramid facing shows less wear loss due to low coefficient of friction of the fiber.

At high load, larger weight loss is associated due to fiber pullout, matrix fracture and fiber-matrix de-bonding. In case of hybrid reinforced composites, wear rate relies upon various mechanism like micro-cracking, micro-cutting and plowing the fibers get critically flawed results in propagation of debris and secondly how effectively the debris is detached from the surface [17]. Severe conditions like high surface temperature and higher applied load lead to damage and weaken the fiber-matrix bonding leading to more pullout of fibers from the composite in the form of debris as a vicious cycle [18].

4.2 Specific Wear Rate

Specific wear graph shows the interdependency of two parameters, i.e., how the one parameter increase/decrease the value on the other, remaining parameter will be

constant. In this study, our focus is to evaluate the specific wear rate from Fig. 2a–e against the applied load changes from 10 to 30 N on fiber and its hybrid reinforced composites. From Fig. 2, it is recognized that specific wear has its maximum value in the range of $(2–5) \times 10^{-12}$ m^3 /N-m at 10 N and $(1–4) \times 10^{-12}$ m^3 /N-m at load of 30 N. It shows that as the load increases the specific wear decrease which is in agreement with the specific wear equation. Figure 2a shows the specific wear of S_{100}, S_{001} and S_{010} samples, and it could be seen that the highest and lowest specific wear of 3.566 and 1.556×10^{-12} m^3 /N-m at 10 N and 30 N by S_{100} specimen. At the initial stage of the experiment, the samples and disk with SiC paper are in direct contact which results in asperities physically interlocking into the crack. As the disk rotates at low load, the asperity come into contact, and due to shearing, it gets plastically deformed. It is quite predictable from the graphs (2b, c), the carbon facing shows less specific wear at 30 N load, reason already stated in the previous section of wear rate. In S_{111} specimen (Fig. 2e), the carbon facing and glass facing specific wear were evaluated. The carbon facing shows lowest specific wear was 1.711×10^{-12} m^3 /N-m at 30 N load. In glass/aramid (S_{011}) composite, the lowest value is at 3.157 $\times 10^{-12}$ m^3 /N-m at 30 N load for aramid facing. Maximum specific wear is due to unworn of the abrasive particles, with mutlipass run, weight loss in the form of debris, smoothen the rubbed surface which further reduce the abrasiveness of grit, which result in more wear. The wear debris filled in between the grit spacing, which weaken the depth of penetration [19].
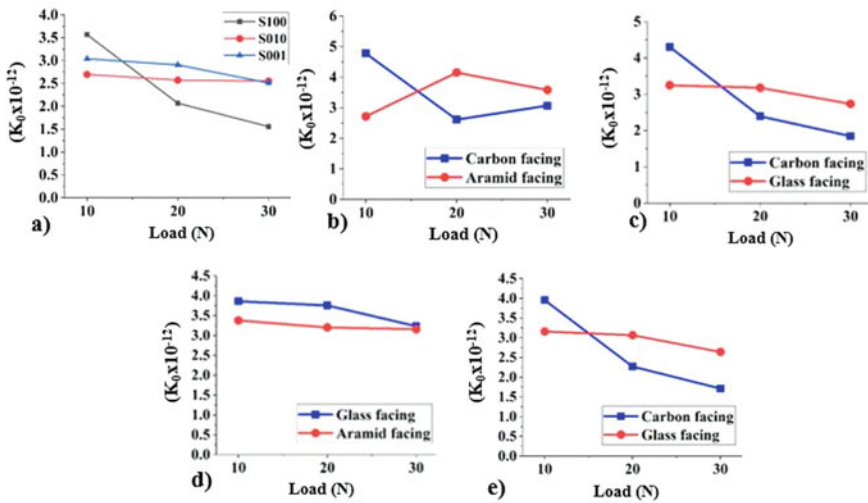
Fig. 2 Specific wear rate as a function of applied load of for **a** S_{100}, S_{010} and S_{001}, **b** S_{110}, **c** S_{101}, **d** S_{011} and **e** S_{111} at 300 rpm speed

4.3 Scanning Microscopy of Developed Composites

The hypothesis of the wear mechanism is justified by SEM images of worn surfaces of the composites at a load of 30 N. Figure 3a–f shows the worn and unworn surfaces of samples S_{100}, S_{001} and S_{010}, respectively. Figure 3a depicts an unworn surface of S_{100} composite clearly conclude that carbon fabrics are closely packed with each other and matrix and after packaging with matrix no fiber pullout is observed. From Fig. 3c, glass fiber adhesion with the polytherimide matrix is not robust as compared to carbon fiber reinforced PEI composites. Propagation of crack and fiber out of matrix in the unworn surface, due to lack of strong bond between the matrix and glass fiber. Figure 3e shows unworn surfaces of S_{010} composites. It can be seen that it shows good adhesive interface between matrix and fiber. Due to adhesion, there is evolution of cloud. Abrasive wear specimen images reported that wear mechanism is due to
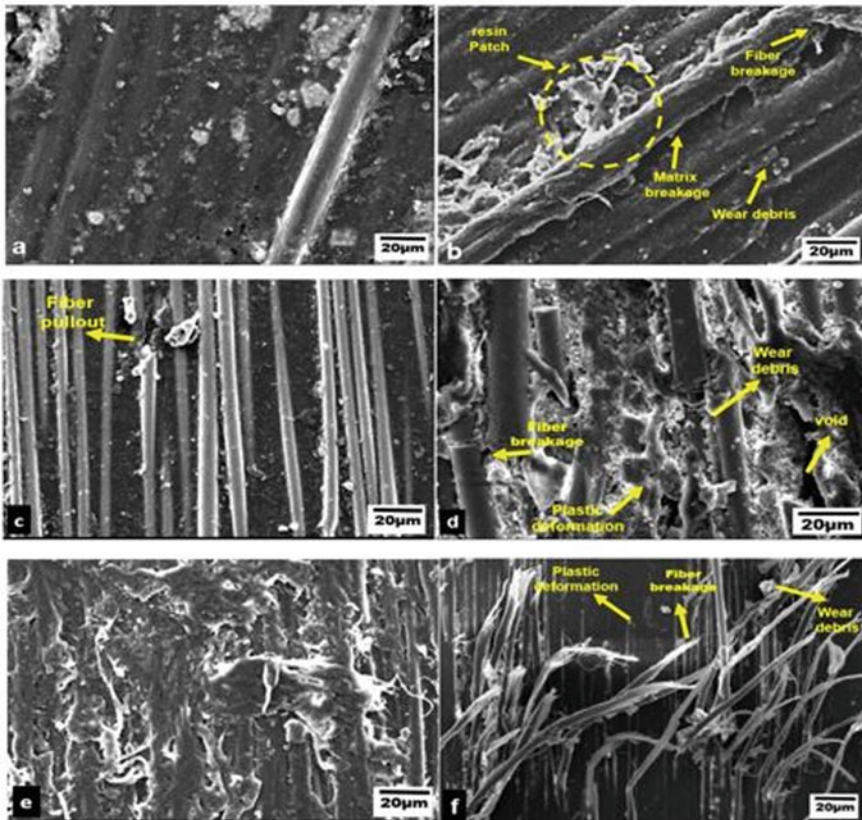
Fig. 3 SEM with magnification (1.00 KX) of **a** unworn surface of S_{100} and **b** worn surface of S_{100} samples, **c** unworn surface of S_{001} and **d** worn surface of S_{001} samples, **e** unworn surface of S_{010} and **f** worn surface of S_{010} samples at 30 N load abraded against SiC paper

micro-plowing, fiber pullout, matrix breakage, creation of debris, micro-cracking and fiber-matrix de-bonding. As the load increased, results in de-bonding of fiber which weaken the interface bonding between fiber and matrix and intensify the material removal from the reinforced composite [20]. Figure 3b shows that how matrix and fiber worn out as the load applied on the carbon reinforced composite. It is quite apparent from SEM image that very minimal amount of matrix was removed from the worn surface of the carbon composite compared to glass and aramid composites (Fig. 3d and 3f). The good adhesive bonding carbon fibers with polytherimide matrix result on low wear and less fiber damage of the composite. Figure 3c depicts the fiber pullout for glass reinforced composites have increased at high load. The reason of fiber breakage is due to low fiber-matrix adhesion and brittle nature of glass which also favor the micro-cutting, cracking of the fiber and degradation of fiber-matrix de-bonding [19]. At high load, the removal of the matrix material contributes the exposure of the fiber region to sliding contact leads to fiber breakage [5]. In all the worn surfaces, due to abrasive particles (SiC) indicate the removal of matrix and deep grooves in the direction of abrasion due to plowing mechanism. From Fig. 3f, it is observed that plowing mechanism also observed in S_{010} composites, a small portion of material detached after displacement from matrix.

5   Conclusion

Following outcome was concluded from the present study:

- The wear loss at 10, 20 and 30 N load was highest for sample S_{111} (with glass fiber facing), i.e., 0.0313 g, S_{110} (with aramid fiber facing), i.e., 0.0544 g S_{101} (with glass fiber facing), i.e., 0.0591 g, respectively, and was minimum for sample S_{100}, i.e., 0.0178 g, 0.0341 g and 0.0385 g, respectively.
- The specific wear at 10, 20 and 30 N load was highest for sample S_{110} (with carbon fiber facing), i.e., 4.78 $\times 10^{-12}$ m^3 /N-m, S_{110} (with aramid fiber facing), i.e., 4.154 $\times$ 10^{-12} m^3 /N-m and S_{110} (with aramid fiber facing), i.e., 3.584 $\times$ 10^{-12} m^3 /N-m, respectively, and was minimum for sample S_{010}, i.e., 2.696 $\times$ 10^{-12} m^3 /N-m, S_{100}, i.e., 2.068 $\times 10^{-12}$ m^3 /N-m, for sample S_{100}, i.e., 1.556 $\times$ 10^{-12} m^3 /N-m, respectively.
- Specific wear rate increased at lower load (10 N) and decreased with increasing load (30 N). Hybrid composites(S_{100} S_{101} S_{110} S_{111}) with carbon fiber showed better abrasion resistance as compared to glass and aramid reinforced composite(S_{001}, S_{010}, S_{011}).
- SEM images show that the glass and aramid fiber reinforced composites show more wear as compared to carbon polytherimide reinforced composites.

References

1. Patil, N., & Prasad, K. (2018). Study of wear mechanism of chopped fiber reinforced epoxy composite filled with graphite and bronze. AIP Conference Proceedings 1943 (2018).
2. Zhao, G., Hussainova, I., Antonov, M., Wang, Q., & Wang, T. (2013). Friction and wear of fiber reinforced polyimide composites. *Wear, 301*(1–2), 122–129.
3. Handbook ASM. (1992). Friction, lubrication and wear technology (p. 48). Materials Park, Ohio: ASM International.
4. Batra, N. K., & Dikshit, I. (2020). Evaluation of mechanical properties of polytherimide reinforced carbon/glass/aramid hybrid composites. *Materials Today: Proceedings.*
5. Hasim, P., & Nihat, T. (2002). Investigation of the wear behaviour of a glass-fiber-reinforced composite and plain polyester resin. *Composites Science and Technology, 62,* 367–370.
6. Mimaroglu, A., Unal, H., & Arda, T. (2007). Friction and wear performance of pure and glass fibre reinforced poly-ether-imide on polymer and steel counterface materials. *Wear, 262*(11–12), 1407–1413.
7. Xian, G., & Zhang, Z. (2005). Sliding wear of polyetherimide matrix composites I. Influence of short carbon fibre reinforcement. *Wear, 258*(5–6), 776–82.
8. Pihtili, H., & Tosun, N. (2002). Effect of load and speed on the wear behaviour of woven glass fabrics and aramid fibre-reinforced composites. *Wear, 252*(11–12), 979–984.
9. Suresha, B., Chandramohan, G., Siddaramaiah, S. P., & Seetharamu, S. Three-body abrasive wear behaviour of carbon and glass fiber reinforced epoxy composites. *Materials Science and Engineering: A, 443*(1–2), 285–91.
10. Cirino, M., Pipes, R. B., & Friedrich, K. (1987). The abrasive wear behaviour of continuous fibre polymer composites. *Journal of Materials Science, 22*(7), 2481–2492.
11. Rajashekaraiah, H., Bheemappa, S., Yang, S. H., & Mohan, S. (2016). Abrasive wear behaviour of thermoplastic copolyester elastomer composites: A statistical approach. *Int J Precis Eng Manuf., 17*(6), 755–763.
12. Harsha, A. P., & Tewari, U. S. (2003). Two-body and three-body abrasive wear behaviour of polyaryletherketone composites. *Polym Test., 22*(4), 403–18.
13. Jesthi, D. K., & Nayak, R. (2020). Influence of glass/carbon fiber stacking sequence on mechanical and three-body abrasive wear resistance of hybrid composites. *Materials Research Express.*
14. Kumar, N. V., Krishna, B. S., & Chandrika, N. S. (2019). Evaluation of properties of glass-banana-fiber reinforced hybrid fiber polymer composite. *Materials Today: Proceedings, 18,* 2137–2141.
15. Basumatary, K. K., Mohanta, N., & Acharya, S. K. (2014). Effect of fiber loading on abrasive wear behaviour of Ipomoea carnea reinforced epoxy composite. *International Journal of Plastics Technolgy, 18*(1), 64–74.
16. Gahr, Z., & Heinz, K. (1987). *Microstructure and wear of materials.* Elsevier.
17. Selmy, A. I., Abd El-baky, M. A., & Hegazy, D. A. (2020). Wear behavior of glass–polyamide reinforced epoxy hybrid composites. *Journal Thermoplastic Composite Materials, 33*(2), 214–35.
18. Bijwe, J., & Rattan, R. Influence of weave of carbon fabric in polyetherimide composites in various wear situations. *Wear, 263*(7–12 SPEC. ISS.), 984–91.
19. Chairman, C. A., Kumaresh Babu, S. P. (2013). Mechanical and abrasive wear behavior of glass and basalt fabric-reinforced epoxy composites. *Journal of Applied Polymer Science, 130*(1), 120–30.
20. Chin, C. W., & Yousif, B. F. (2009). Potential of kenaf fibres as reinforcement for tribological applications. *Wear, 267*(9–10), 1550–1557.

Enhancement of Grain Structure and Mechanical Properties of Scrap Material AA6063 Through ECAP

Krishna Mohan Agarwal, Arshit Kapoor, Bhuwan Gupta, and Priyanka Singh

Abstract The objective of current study is to improve the hardness and tensile strength of Aluminium Alloy 6063 which is used in construction and infrastructure. Practical implementation of our research will be to increase the life span of the material. A cast-iron die is fabricated with a channel carved in it using CNC cutting machine. A hub is put on the die and aluminium alloy material in the form of 20 mm (diameter) rod is passed in the die using a hydraulic press. There will be grain refinement in the structure of the aluminium rod, due to severe plastic deformation, this technique of passing the rod is equal channel angular pressing (ECAP). The few parameters which will be focused are thermodynamics while plastic deformation, homogenizing of aluminium, severe plastic deformation (SPD), melting properties and grain structure The experimental results show that there is the maximum smooth flow when the material is passed in the channel with angle 90°.

Keywords Ultrafine grain structure · Severe plastic deformation · Equal channel angular pressing (ECAP) · Grain refinement · Scrap aluminium alloys

1 Introduction

Aluminium came up in the eighteenth century by a Danish chemist Hans-Christian. The aluminium production technique is also economically feasible and easy conduct.

K. M. Agarwal (✉) · A. Kapoor · B. Gupta
Mechanical Engineering Department, Amity University Uttar Pradesh, Noida, India
e-mail: profkmagarwal@gmail.com

A. Kapoor
e-mail: arshitgemini@gmail.com

B. Gupta
e-mail: kbhuwan30@gmail.com

P. Singh
Civil Engineering Department, Amity University Uttar Pradesh, Noida, India
e-mail: priyanka24978@gmail.com

Uses of aluminium and alloys for various applications for urbanization and globalization have made it as a fully flourished industry. Consistency of innovations for better product and cost-cutting is required because the aluminium profile is used in architecture, medical equipment, automobile industries, small machine components, and major parts used in aeronautical industries being corrosion resistant and it is widely used in motor-water bodies like ships and submarines [1]. The elastic-plastic analysis of the problem is based on the isotropic stress-curve hardening of strains. A section decreases to 75% of the initial segment will be taken into consideration and the order system logs will be created. Therefore, a stress-strain curve introduces the nonlinearity of the material and the finite deformation introduces geometrical nonlinear behaviour. These functions enhance the uncertainty of the elastic-plastic analysis and demonstrate the obligatory numerical assessment of solution [1–3]. The aluminium which is extracted from the scrap material has a disadvantage that the properties are not achieved same as of initial raw aluminium. The reduction in mechanical properties is due to re-processing from scrap. To overcome this problem, this current study suggests that if equal channel angular pressing is performed, this process can enhance microstructure and mechanical properties with large percentage which ultimately increases the application of processed aluminium [4].

1.1 Equal Channel Angular Pressing and Severe Plastic Deformation

Equal channel angular process (ECAP) provides shear deformation and grain refinement in the material because there is one focused passage for the flow. ECAP was one of the most effective methods of severe plastic deformation, first introduced by Segal in the former Soviet Union in 1981. It is a technique used for improving ultrafine grain without changing the cross-section of the sample or workpiece. In ECAP, specimen proportions are not modified as in conventional methods of deformation. Grain refinement on hard material like iron is not economical and practically not possible because it requires a lot of strength and energy utilization. ECAP is a metal forming technique which gives us various advantages with minimal heat generation. The advantages are nano-crystalline structure, ultrafine grain metal and amalgams are formed, no dimensional changes and gives high-level strain superplasticity by grain refinement to nano or submicron level [5–7] (Fig. 1).

1.2 Literature Review

Research paper on grain refinement and in enhancement to its properties is published since 1977. All the research studies have been analysed till the present year and the research gap and problems have been identified.
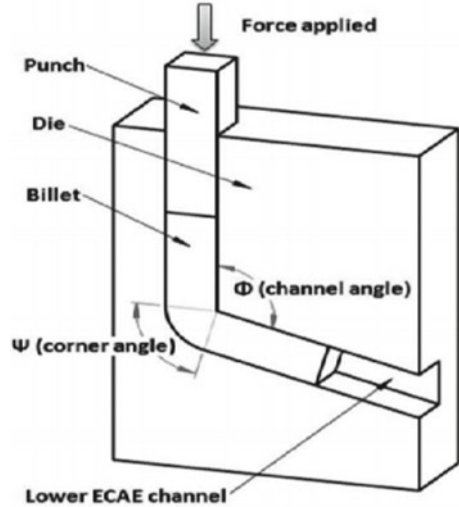
Butler et al. [11] give research method of making fine grain structure to form an alloy having a composition of different elements is heated to form a solid solution of the alloy heating at a melting point temperature. John et al. [12] performed thermo-chemical process on the aluminium alloy like over-ageing, severe plastic deformation and recrystallization. Electron microscopy was used to study microstructure and result shows that the ageing process also termed as heat treatment revealed that there is precipitates' formed during the ageing create preferential nucleation sites for grains. Segal et al. (1985) suggested mechanical and toughness variations by thermal treatment on extruded Aluminium Alloy 6061. There were observable changes noticed in the properties as compared to wrought Aluminium 6061 and the T-6 heat treated one. Fracture toughness was increased by 50% than wrought iron. Zhilyaev et al. [13] suggested there was appreciable progress in modifying the fundamental ECAP process for better efficiency. These amendments were more conventional and well-established processing routes. MSamee et al. [14] had published a research paper based on our studies and using the same material, i.e., Aluminium Alloy 6063. Jia et al. [15], throughout this research, electron backscatter diffraction (EBSD) systematically studied the texture evolution of an Al-8 wt% Zn alloy through equivalent channel angular pressing (ECAP) and isothermal annealing post-ECAP.

1.3 Materials and Methods

The objective of the current study is to improve the hardness and tensile strength of Aluminium Alloy 6063 which is used in construction and infrastructure. Table 1 shows the percentage composition of AA6063 [9]. Practical implementation of the research will increase the life span of the material and will smooth the surface finish of

Table 1 % composition of AA6063

Si	Fe	Cu	Mn	Mg	Zn	Ti	Cr	Al
0.2-0.6	0-0.35	0-0.1	0-0.1	0.45-0.9	0-0.1	0-0.1	0.1	97.65

the material. A cast-iron die is fabricated with a channel carved in it using CNC cutting machine. A hub is put on the die to pass the material in the hub and Aluminium Alloy 6063 is passed through the die using a hydraulic press. Aluminium Alloy 6063 is used in construction, heat exchangers, auto parts, etc. Aluminium and metal scrap are collected from waste or leftover material obtained from industries after processing. It is melted in the furnace at 600o C and with hot top casting aluminium billets will be made after passing the composition test. The current study aims to find the best strain homogeneity without changing the cross-sectional area. The more the number of pass more will be the grain refinement. The die specification for the desired results and the refinement of the material to the maximum are channel angle –90°, corner angle –15°, coefficient of friction –0.2 [5–7].

1.4 Die Design Parameters

Die plays a major role in the distribution of extrusion, price and efficiency are three main considerations in a competitive industry. The efficiency of the extrusion die is crucial to fulfilling consistency requirements. Die efficiency influences the consistency, profitability, recovery and functionality of the goods. Uses of extruded aluminium profiles are growing in the construction, aerospace and high-tech industries. It consists of magnesium and silicon as the alloying elements and it is used in the extrusion process. Various other chemical processes can be done on it like anodizing and welding powder coating. It has higher strength so used in architecture, structures [5–7]. The various parts designed for the experiment conduction are Die 220*160*100 mm H13 Tool Steel, Billet (20 mm cross-sectional area and 50 mm height), plunger and ram. Die is made in two halves upper half and lower half which connect to make a proper channel for which our sample can be passed. Six Allen screws for joining the two halves and two cylindrical pins for alignment are joined (Fig. 2).

2 Conversion of Scrap Material

Aluminium is available is large abundance in earth's crust. It is obtained from bauxite ore by the process called smelting. It is a non-biodegradable though eco-friendly and recyclable. As aluminium is recyclable, it is collected from all over the world. It is collected in the forms of scrap which is the waste or used beverage cans, aluminium
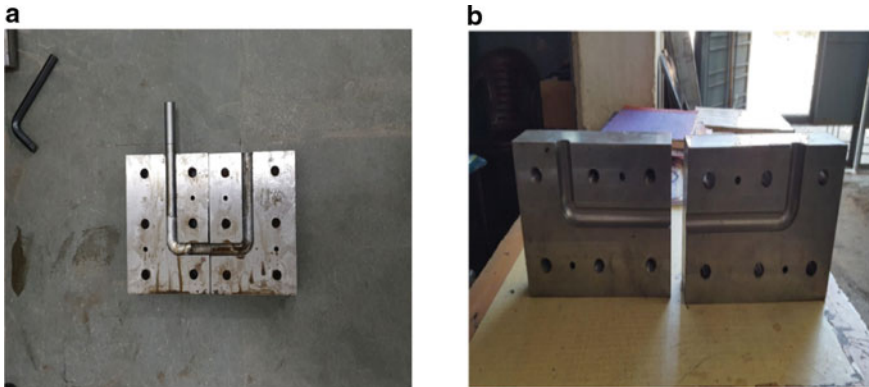
Fig. 2 **a** Top view of both the parts of a die, **b** front view of both the parts of the die

foil, dismantled electronic waste, wires, aluminium from old buildings, etc. The conversion of scrap aluminium available can be converted to the desirable useful workpiece and the processing of the scrap through the processes as shown in Fig. 3. The processes are extraction, sorting, bailing, melting, casting, homogenization, pre-heating, pressing and heat treatment [3, 8].

2.1 ***Extraction***—Aluminium extrusion is the process from which aluminium is recycled into raw products which can be easily moulded or hammered into any shape and size for use (aluminium is highly malleable and ductile). Process for converting aluminium from scrap (collection of waste material) into aluminium profiles is called aluminium extrusion. The industries are running on the extrusion process from more than 100 years.

Fig. 3 Flow diagram of conversion of scrap material into billet [8]
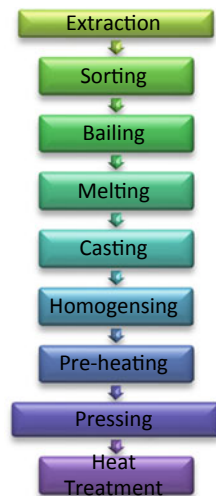
Fig. 4 Dross in aluminium waste [8]

2.2 *Sorting*—There are various physical and chemical methods for sorting out the impurities and physical operations will be economical. Ferrous material can be sorted out with the help of a conveyor belt system having neodymium (NdFeB) magnets. Eddy current separation is similar to magnetic separation, in addition to neodymium magnet, a rotor is added. It has a wide range of conductivity for automotive scrap. Visual inspection test or colour sorting by hand (manual labour) is some other ways of sorting used.

2.3 **Bailing**—The sorted scrap is in bit and pieces. If we pour the bit and pieces in the furnace, it will be very time consuming and difficult to gather at the time of pouring. So it will be convenient that by pressing the scrap into the shape of a cubical block which can be poured into the furnace. Material weight input and output is also easy to calculate. It will save time to transfer the material into a furnace. It will save space.

2.4 **Melting**—Dross is a waste which is gathered from the furnace, it is the remains of the aluminium which is left in the melting process. This dross is collected and can be re-melt to form 99.7% pure aluminium in any shape as per the mould called as ingots.

2.5 **Heat treatment**—It is a process where the temperature is made to rise up to its melting point and the alloy is quenched to make it meta-stable. For AA6063, the Mg_2Si is made to mix it back with solution and quenching helps to precipitate out the Mg_2Si. There can be various methods of quenching like oil, water or air quenching. After the precipitation (ageing process), the strength of alloy is gained back [9] (Fig. 4).

3   Components of Aluminium Extrusion Plant

1. Furnace—The efficiency of a furnace is 9.5%, i.e., the ratio of heat given to the amount of useful metal produced. In this type of industry, there are two types of furnace mainly used, i.e., gas type and electric furnace type [8–12].

2. Hot Top Casting for Logs—In 1933, W.T. Ennor developed DC, i.e., direct chill continuous casting process which is used in aluminium billet casting. The principle of DC casting is that the molten metal is poured from tilting type furnace into a shallow mould of a round cross-sectional shape to give the billet a cylindrical shape [8].

3. Single/Double Puller—Puller is an automated device design to produce the right amount of force on the profile as soon it emerges from die after extrusion. It makes the profiles dimensional, even and twists free [8].

4. Rough Cutting Saw—It is a rough cutting device consisting of blade, chain, scale, measuring electronic control unit (ECU) which measures the length of the profile according to product/customer requirement and then sharply cuts the profile.

5. Hot Log Shear—It is a machine performing scissor operation for the log which is casted. It cuts down the log of aluminium casted into the billets of the required length.

6. Complete Extrusion Section Handling Line—They are the long bed which requires the aluminium profiles to rest and cooling under room temperature and adapt to controlled atmospheric conditions (Fig. 5).

7. Belt Conveyor Systems—The belt conveyor system consists of a minimum of two drums of pulleys depending upon the length of the system, a rubber belt which has high heat resistance from the hot extruded aluminium belt. It is assembled and merged with the extrusion handling line.

8. Stretcher—After the freshly extruded profile is travelled along with the cooling table through the handling line, it is then transferred to the stretcher. Stretching straightens the profiles which get deform in extrusion process and then at molecular level re-arrangement or realignment of aluminium particles take place.
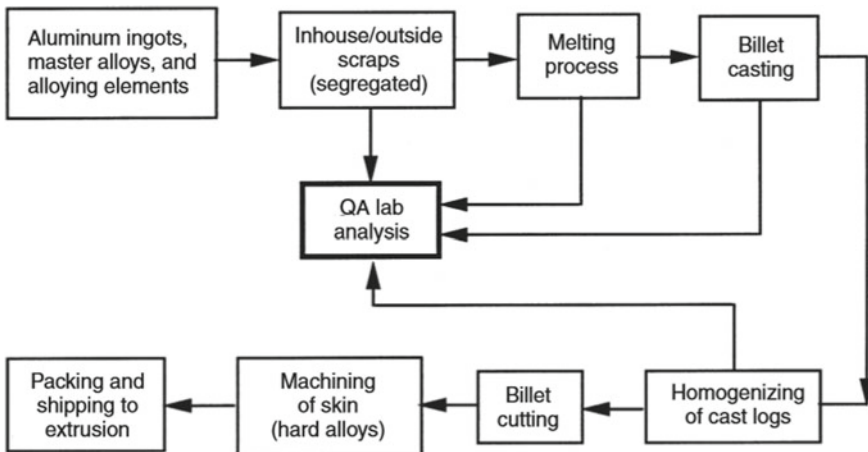
Fig. 5 Functional block diagram of the billet making process [7]

9. Container—It is a room where aluminium profiles are placed on wooden racks and sent to the heat treatment process. Various thermodynamic changes take place creating durability [11].

4 Results and Discussion

This analysis can be done by generally two and three-dimensional problems encompassing the steady-state process. These test results are important for the key knowledge of process limits which will guarantee the metal forming procedure. History of the force analysis in an element can tell us or helps in the prediction of growth and initiation. The area where the plastic flow is contained in which increment of plastic strain is of the series of internment inelastic strain. The elastic material is constrained by strain deformation and it is rigid referring to rigid plastic theory. There is not much availability of equilibrium equations and are not much compatible. In order to determine the process of metal forming under such conditions that will end the defectives of the metal forming, the elastic-plastic principle can be used to forecast the shape of a durable component [7, 13–16]. Nicolae Serban studies the microstructure of AA6063 after and before ECAP. Figure 7 shows the SEM results of AA6063 with 0, 1, 3 and 9 pass. Refinement in grains is clearly visible and after one pass the structure looks more aligned. After 3 passes, the structure looks aligned, dense and homogenous. After 9 passes, the structure is highly homogenous [17] (Figs. 6 and 7).

Davoud Mashhadi [18] studies about the enhancement in mechanical properties before and after ECAP with heat treatment and reports that microhardness has increment of 208% from 34 to 105 HV. Abioye [19] studies about mechanical property enhancement and reports that from 181.46 MPa as initial tensile strength has subsequently increased to 293.54 at 4 pass. Figure 8 shows that the increment has been
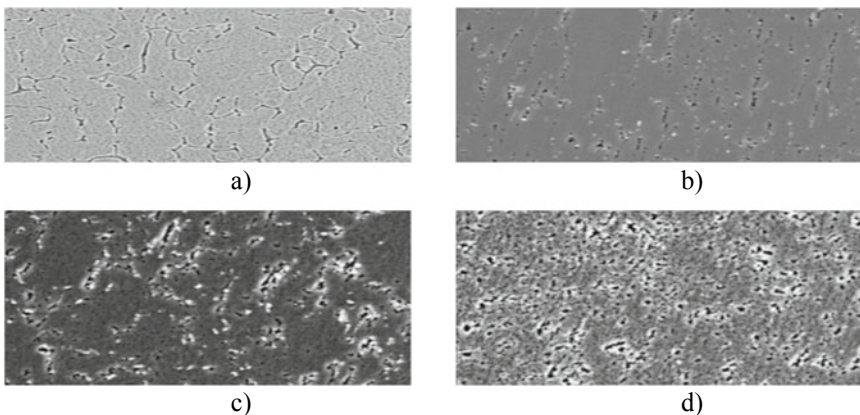
Fig. 6 SEM results of microstructure **a** 0 pass, **b** 1 pass, **c** 3 pass, **d** 9 pass [17]
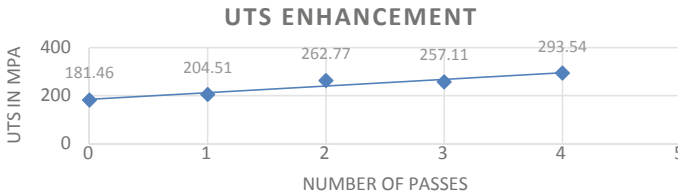
Fig. 7 Enhancement in tensile strength

gradual giving almost 45% increment after 2 passes and 61% after 4 passes. The ultimate grain refinement and enhancement of mechanical properties both are evidently high which ultimately fulfils the requirement.

5   Conclusion

The experimental results show that there is the smoothest flow when the material is passed in the channel with angle equal to 90°, grain boundaries act as obstacles to dislocation motion. High strain imposed through ECAP helps to get the ultrafine grain structure which ultimately enhances the mechanical properties. The approach we proposed to study forming processes is at the beginning of a project. This is a fundamental first attempt at these problems, and more general boundary requirements and constitutive relationships, as well as schemes to minimize computing time and thus costs, are expected to be implemented. For example, if examining the stable state solution is of primary importance, choosing an initial stress field can result in significant computational savings that are far closer to the final field than the unloaded state. A direct attack on the inpatient case can also be possible without examining the temporary alternative as accepted in the present case.

References

1. Grandfield, J. F., & Mcglade, P. T. DC casting of aluminium: Process behaviour and technology.
2. Patel, J. B., et al. (2014). Melt conditioned direct chill casting (MC-DC) process for production of high quality aluminium alloy billets *796,* 149–154. https://doi.org/10.4028/www.scientific.net/MSF.794-796.149.
3. Hoover, S. M., & Crowe, C. R. (1958). Effect of thermal treatment on the mechanical and toughness properties of extruded SiCw/aluminium 6061 metal matrix composite*, 20*.
4. Lucheva, A. P. B., Petkov, A. P. R., Prof., A., & Tzonev, T. (2003). Method for aluminum dross utilization. *3rd BMC-2003-Ohrid,* 259–264.
5. Mohan Agarwal, K., Tyagi, R. K., & Dixit, A. (2020). Theoretical analysis of equal channel angular pressing method for grain refinement of metals and alloys. *Materials Today: Proceedings, 25*(4), 668–673.

6. Mohan Agarwal, K., Tyagi, R. K., Chaubey, V. K., & Dixit, A. (2019). Comparison of different methods of Severe Plastic Deformation for grain refinement. In *IOP Conference Series: Materials Science and Engineering, 691*(1), 012074.

7. Agarwal Krishna Mohan, S. A., Tyagi, R. K., & Bhuwan, G. (2020). Evolution of microstructure through various techniques of severe plastic deformation, Springer Smart Innovation, Systems and Technologies, 251–260.

8. Mechanics, A. (1977). Stress and deformation analysis of the metal extrusion process (pp. 339–353).

9. Khadyko, M., Marioara, C. D., Dumoulin, S., Børvik, T., & Hopperstad, O. S. (2017). Effects of heat-treatment on the plastic anisotropy of extruded aluminium alloy AA6063. *Materials Science and Engineering A, 708*(October), 208–221. https://doi.org/10.1016/j.msea.2017.09.133.

10. Baeck, S., Seok, H., Lee, J., Kim, D., Lee, H., & Oh, K. H. (2002). Texture analysis of aluminum plate produced by Ecap *412,* 685–690.

11. Butler, G., & Mercer, A. D. (1977). Corrosion of some aluminium casting alloys and cast iron in uninhibited alcohol/water coolants. *British Corrosion Journal, 12*(3), 163–170. https://doi.org/10.1179/bcj.1977.12.3.163.

12. Wert, J. A., Paton, N. E., Hamilton, C. H., & Mahoney, M. W. (1981). Grain refinement in 7075 aluminum by thermomechanical processing. *Metallurgical and Materials Transactions A: Physical Metallurgy and Materials Science, 12* A(7), 1267–1276. https://doi.org/10.1007/bf02642340.

13. Zhilyaev, A. P., Oh-ishi, K., Raab, G. I., & McNelley, T. R. (2006). Influence of ECAP processing parameters on texture and microstructure of commercially pure aluminum. *Materials Science and Engineering A, 441*(1–2), 245–252. https://doi.org/10.1016/j.msea.2006.08.029.

14. Frint, S., Hockauf, M., Frint, P., & Wagner, M. F. X. (2016). Scaling up Segal's principle of equal-channel angular pressing. *Materials and Design, 97,* 502–511. https://doi.org/10.1016/j.matdes.2016.02.067.

15. Jia, H., & Li, Y. (2019) Texture evolution of an Al-8Zn alloy during ECAP and post-ECAP isothermal annealing. *Material Characterization, 155*(June), 109794. https://doi.org/10.1016/j.matchar.2019.109794.

16. Agarwal, K. M., Tyagi, R. K., & Kapoor, A. (2019). Deformation and strain analysis for grain refinement of materials processed through equal channel angular pressing. *Materials Today Proceedings, 21*(3), 1513–1519.

17. Serban, N., Cojocaru, V. D., & Butu, M. (2012). Mechanical behavior and microstructural development of 6063-T1 aluminum alloy processed by Equal-Channel Angular Pressing (ECAP): pass number influence. *JOM Journal of the Minerals Metals and Materials Society, 64*(5), 607–614. https://doi.org/10.1007/s11837-012-0311-7.

18. Jafarlou, D. M., Zalnezhad, E., Hamouda, A. S., Faraji, G., Bin Mardi, N. A., & Hassan Mohamed, M. A. (2015) Evaluation of the mechanical properties of AA 6063 processed by severe plastic deformation. *Metallurgical and Materials Transactions A: Physical Metallurgy and Materials Science, 46*(5), 2172–2184. https://doi.org/10.1007/s11661-015-2806-7.

19. Abioye, O. P., et al. (2019). Influence of equal channel angular extrusion on the tensile behavior of Aluminum 6063 alloy. *Procedia Manufacture, 35,* 1337–1343. https://doi.org/10.1016/j.promfg.2019.05.020.

Machine Learning Approach to Predict Compressive Strength of Green Sustainable Concrete

Priyanka Singh, Aman Namdeo, Chakshu Garg, and Krishna Mohan Agarwal

Abstract Sustainable construction contributed to the usage of recycled and waste materials to substitute conventional concrete. This research focuses on prediction of compressive strength of cement concrete substituted by large amounts of waste materials and products with strong mechanical properties and sustainability. It also emphasizes on using analytical model for the prediction of compression strength of the green concrete, so that there is a reduction in the cost of construction, conserve energy, and it will lead to a reduction of CO_2 production from cement industries within reliable limits. In this paper, machine learning approach has been used to predict the compressive strength of green and sustainable concrete. Machine learning empowers machines to learn from their experiences and data provided. The system analyses the datasets and finds different patterns formed in the given data. Then, based on its learnings the machine can make certain predictions. In civil engineering application, a special computing technique called the artificial neural network (ANN) is in huge demand. ANN is a soft computing technique that learns from previous situations and adapts without constraints to a new environment. In this work, a neural network model for prediction of compressive strength of concrete has been illustrated. Different sets of data based upon several concrete design mixes were taken and were fed to the model. The model is then trained for prediction, which are being influenced by several input attributes and were jotted down a linear regression analysis.

Keywords Machine Learning (ML) · Artificial Neural Network (ANN) · Green concrete · Sustainable concrete · Compressive strength · Regression model

P. Singh (✉) · A. Namdeo · C. Garg · K. M. Agarwal
Amity School of Engineering & Technology, Amity University Uttar Pradesh, Noida, India
e-mail: priyanka24978@gmail.com

A. Namdeo
e-mail: aman.rock6755@gmail.com

C. Garg
e-mail: chakshugarg99@gmail.com

K. M. Agarwal
e-mail: profkmagarwal@gmail.com

543

1 Introduction

In construction, early determination of mechanical properties such as compressive strength of concretes is very important as they are required by many design codes as input parameters. In this study, the machine learning and artificial neural network were applied for the prediction of compressive strength of green concrete. Concrete is manufactured by mixing cement, water, fine aggregates, and coarse aggregates in certain proportions to obtain a desired strength. In addition, fly ash, superplasticizers, retarders are added to enhance any desired property depending upon the function of use of concrete in structures. Compressive strength of concrete is dependent upon several parameters most likely to be water–cement ratio, cement strength, quality of concrete material, and quality control during production of concrete. Nominal concrete with admixtures has admirable segregation resistance and deformation property. This concrete has hindrance to segregation and bleeding, fit for filling voids in densely reinforced structure minimizing impediment or blockage. The concrete design mix should be such that composition does not to separate and exorbitantly bleed [1, 2]. The strength developed in concrete is not solely dependent upon water-to-cement ratio, rather there is influence of content of several ingredients of concrete [3, 4]. The typical problems that are being resolved by neural network are supported by computing elements related to each other. Fundamentally, components to analyze problems are like the neurons in the brain that comprises of numerous straightforward computational components set out in layers [5, 6]. Recent development shows application of neural network as widely utilized in the field of civil engineering such as drying shrinkage [7], durability of concrete [8], transporting ready mixed concrete [9, 10]. Concrete workability with metakaolin and fly ash, slump model mechanical behavior of concrete at high temperatures within structures [11], construction smoothness specification pay factor limits [12], and impact of fly ash and silica fume on compressive strength in the long run [13]. The concrete mix proportion in this way acquired is relied upon to result with the lesser number of trials, cost, and time. Concrete design mix proportion generated from artificial neural network is expected to have optimum cement and water contents, accordingly prompting higher toughness and relatively better economic and ecological effects [14].

2 Experimental Setup

The dataset used in this study is a benchmark publicly available online dataset (UCI 2017). This comprehensive dataset allows us to develop a model that is able to predict the compressive strength of green concrete for a wide variety of combinations. Input variables include the amount/ratio of different constituents of concrete as well as the age of testing. Error measures were used to evaluate the performance of the developed model. This dataset contains 1030 instances with a total number of nine quantitative. There are no missing values reported by the dataset providers. Among those random

30% of data were taken for training, testing and to predict the compressive strength of concrete. In the model, nine inputs and one output were estimated for case study. The inputs constitute of cement content per unit concrete volume, slag and fly ash mix proportion blended, water content, superplasticizer content and coarse and fine aggregate proportions, the slump and flow value are also taken into consideration. The model output prediction is for compressive strength 28 days of concrete.

3 Artificial Neural Network Model Design

A robust experimental model is designed to predict upon the deviation in compressive strength depending upon variation of design mixes. The model is such designed into pair of training and testing stages. While training input data values (X1–X9) are introduced into ANN input layers, whereas their corresponding output (Y Dataset) is given as desired target prediction. The input parameters defined as X dataset are considered as independent variables, and the output parameter defined as y dataset is considered as dependent variable (Table 1).

With linear regression analysis in Minitab, an equation of fitted regression model was derived for prediction of compressive strength for the set of input parameters.

Compressive Strength = 140.3 + 0.0593 Cement − 0.0323 Slag + 0.0468 Fly ash − 0.2336 Water + 0.034 Superplasticizer − 0.0548 Coarse Aggregates − 0.0379 Fine Aggregates − 0.2361 Slump + 0.0848 Flow.

Prediction of response value (compressive strength) based on the fitted regression model is shown below in the corresponding figures after analysis with several input criterions (Figs. 1, 2, 3, 4, 5, 6 and 7).

Regression analysis of variance between compressive strength vs input parameters (cement, slag, fly ash, water, superplasticizer, coarse aggregate, fine aggregate) was also performed to determine the P-value.

Table 1 Details of input and output parameters

Input	Parameter
X1	Cement
X2	Slag
X3	Fly ash
X4	Water
X5	Superplasticizer
X6	Coarse aggregate
X7	Fine aggregate
X8	Slump (cm)
X9	Flow (cm)
Output	Parameter
Y	Compressive strength (28-day) (Mpa)
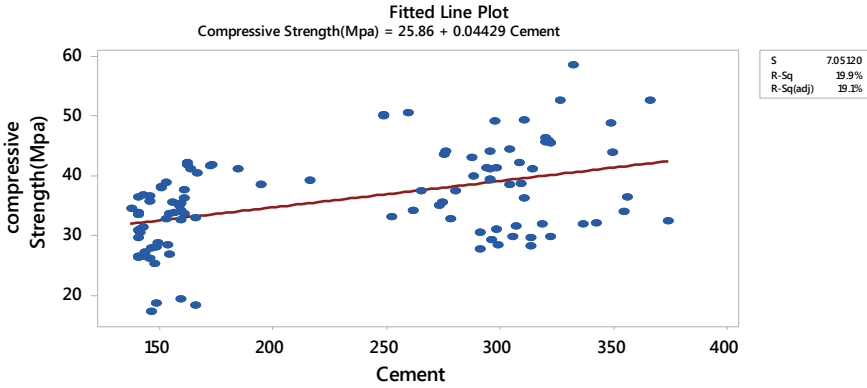
Fig. 1 Fitted line plot between compressive strength (MPa vs cement content)
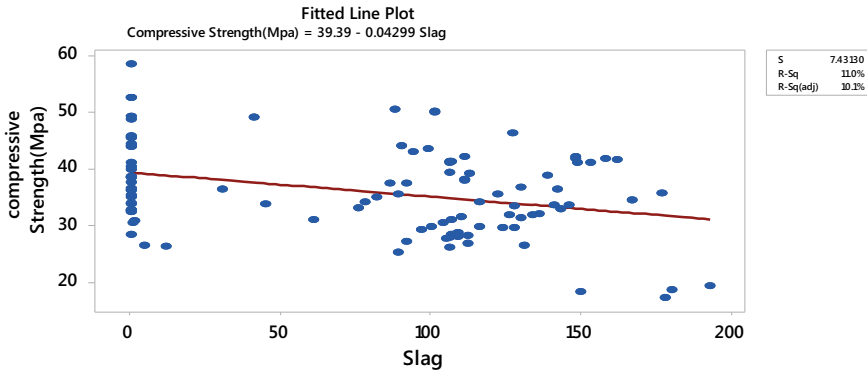
Fig. 2 Fitted line plot between compressive strength (Mpa) versus slag mix content
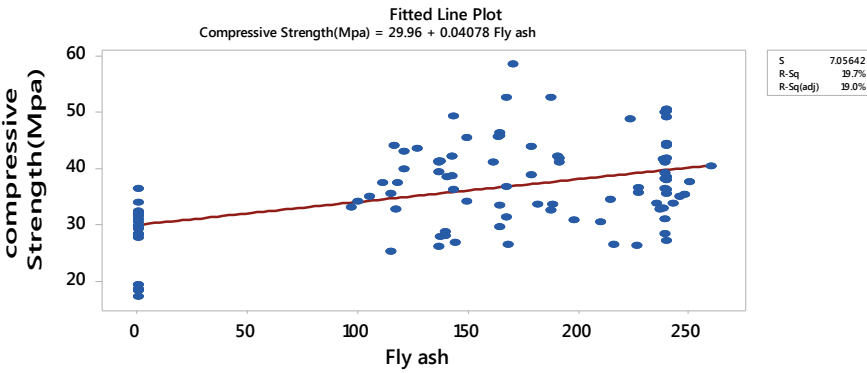
Fig. 3 Fitted line plot between compressive strength (Mpa) versus fly ash mix content
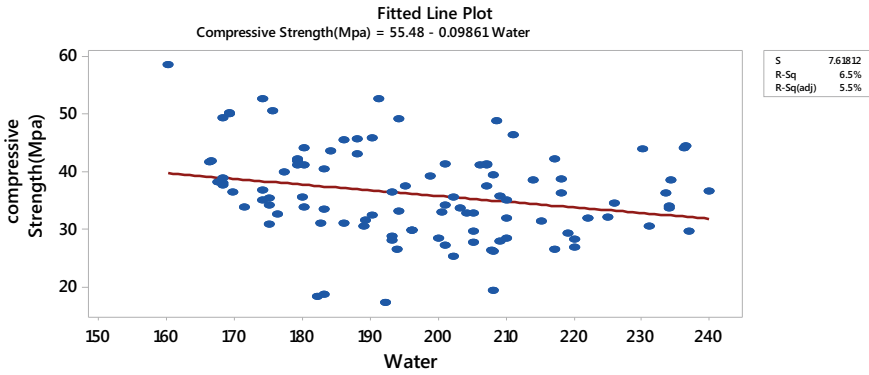
Fig. 4 Fitted line plot between compressive strength (Mpa) versus water content
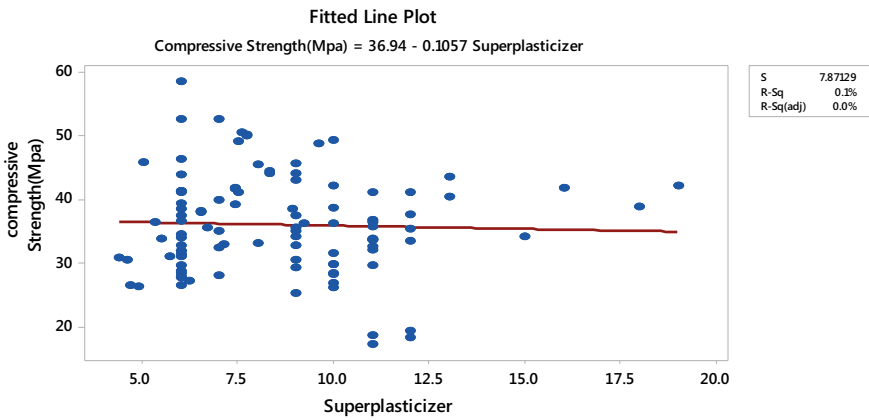
Fig. 5 Fitted line plot between compressive strength (Mpa) versus superplasticizer content
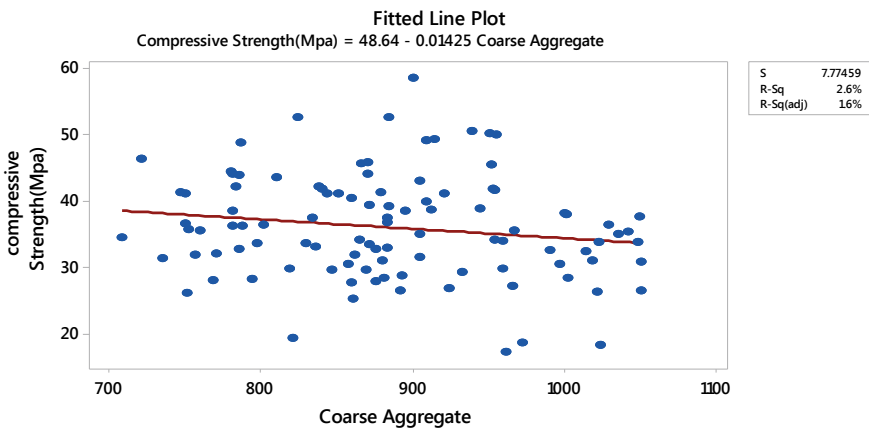
Fig. 6 Fitted line plot between compressive strength (Mpa) versus coarse aggregate content

Fitted Line Plot

Compressive Strength(Mpa) = 50.18 − 0.01912 Fine Aggregate

S	7.78238
R-Sq	2.4%
R-Sq(adj)	1.4%
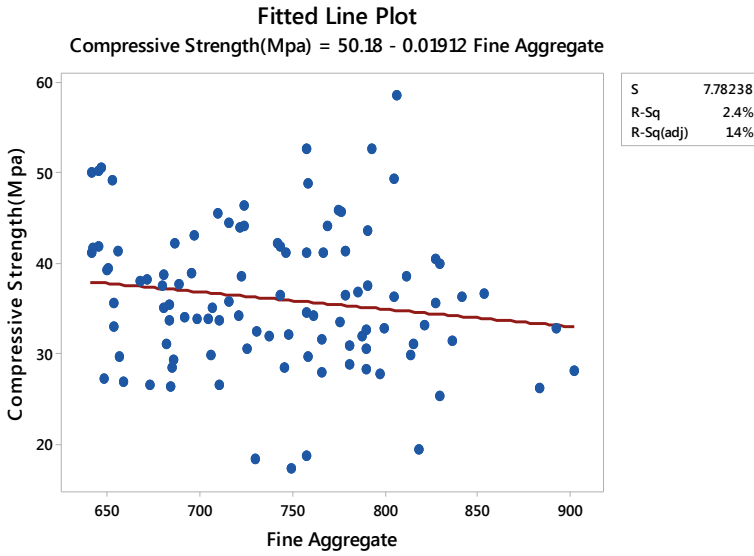
Fig. 7 Fitted line plot between compressive strength (Mpa) versus fine aggregate content

4 Analysis of Variance

The dataset taken into consideration for analysis is normally distributed, and hence, analysis of variance is done to analyze the differences in prediction from the proposed input parameters fitted in the model (Table 2).

Table 2 Analysis of variance

Source	DF	Adj. SS	Adj. MS	F-Value	P-Value
Regression	9	5701.42	633.49	104.23	0
Cement	1	45.62	45.624	7.51	0.007
Slag	1	7.03	7.027	1.16	0.285
Fly ash	1	27.49	27.492	4.52	0.036
Water	1	67.98	67.978	11.18	0.001
Superplasticizer	1	0.43	0.427	0.07	0.792
Coarse aggregate	1	27.09	27.087	4.46	0.037
Fine aggregate	1	11.73	11.73	1.93	0.168
SLUMP (cm)	1	58.75	58.747	9.67	0.002
FLOW (cm)	1	22.46	22.463	3.7	0.058
Error	93	565.24	6.078		
Total	102	6266.66			

Table 3 Model summary

S	R-Squared	R-Squared(adj.)	R-Squared (Pred.)
2.46533	90.98%	90.11%	88.45%

Adjusted sum of squares measures the variation in the output and is clarified by individual unit of model. Adjusted mean squares quantifies how much variety a term clarifies, expecting that every single other term are in the model irrespective of their order of entry, it is the variance around fitted values (Table 3).

5 Interpretation

Normal probability plot of residuals is plotted to verify the assumptions which are normally distributed. Residuals versus fits plot verifies assumption that the residuals have a constant variance as shown in Fig. 10. The histogram of residual is used to determine the skewness of data and outlier's existence in the data. Residual versus order of data verifies assumption that the residuals are uncorrelated with each other.
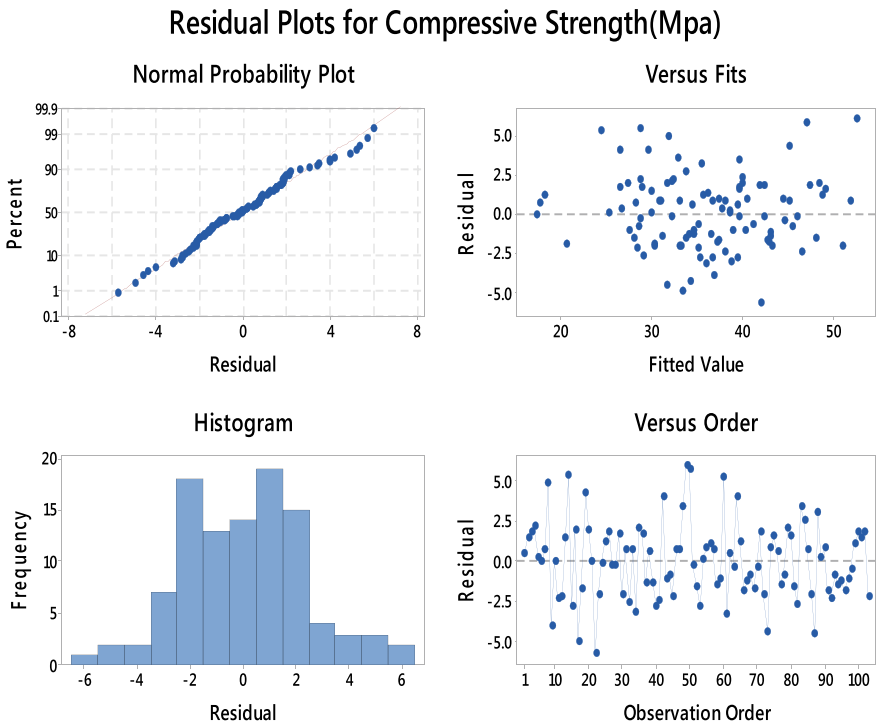
Fig. 8 Residual plots for compressive strength (Mpa)

The compressive strength values that are predicted after being analyzed from the model are being tested for accuracy for determination of errors. Error in data is found out from the difference in Y tested value and Y predicted value (Fig. 8).
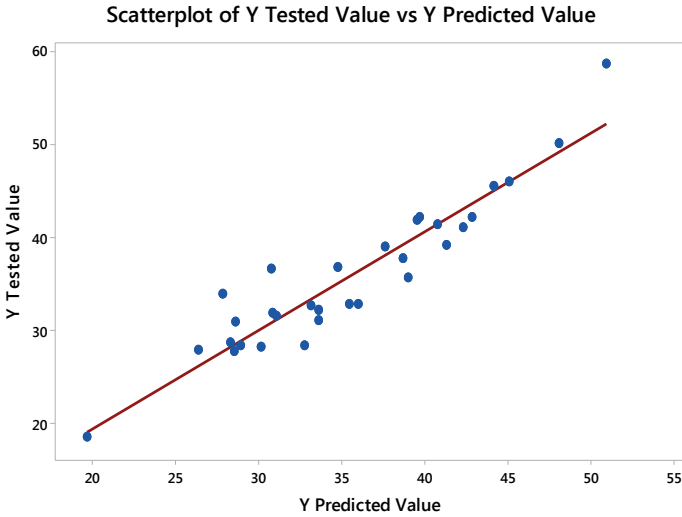
Fig. 9 Scatterplot of Y tested value versus Y predicted value
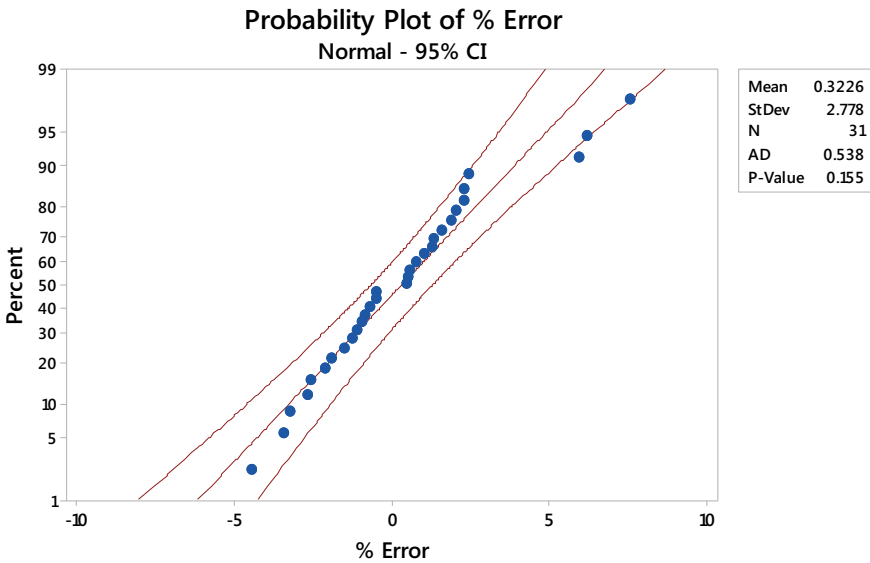
Fig. 10 Probability plot of % error of predicted compressive strength values

Figure 9 shows the scatter plot between Y tested value and Y predicted value. The graph shows clustering of points near about the straight line and shows a positive relationship between Y tested value and Y predicted value; hence, the scatter plot gives the relation as moderately strong between two sets of data.

Figure 10 shows the probability plot for % error in prediction of data at 95% confidence interval. After plotting the graph, it is found out that the p-value is >0.05; hence, the hypothesis is accepted that the prediction from the model is accurate.

Regression Equation for Cement, Water, CA and FA against prediction of Compressive strength.

Compressive Strength = 168.4 + 0.04182 Cement – 0.2680 Water – 0.05764 Coarse Aggregates – 0.0516 Fine Aggregates (Figs. 11 and 12).

Regression Equation for Cement, Water, Fly ash, CA and FA against prediction of Compressive strength.

Compressive Strength = 83.4 + 0.08005 Cement – 0.1803 Water + 0.06938 Fly ash – 0.03365 Coarse Aggregate – 0.01468 Fine Aggregate (Figs. 13 and 14).
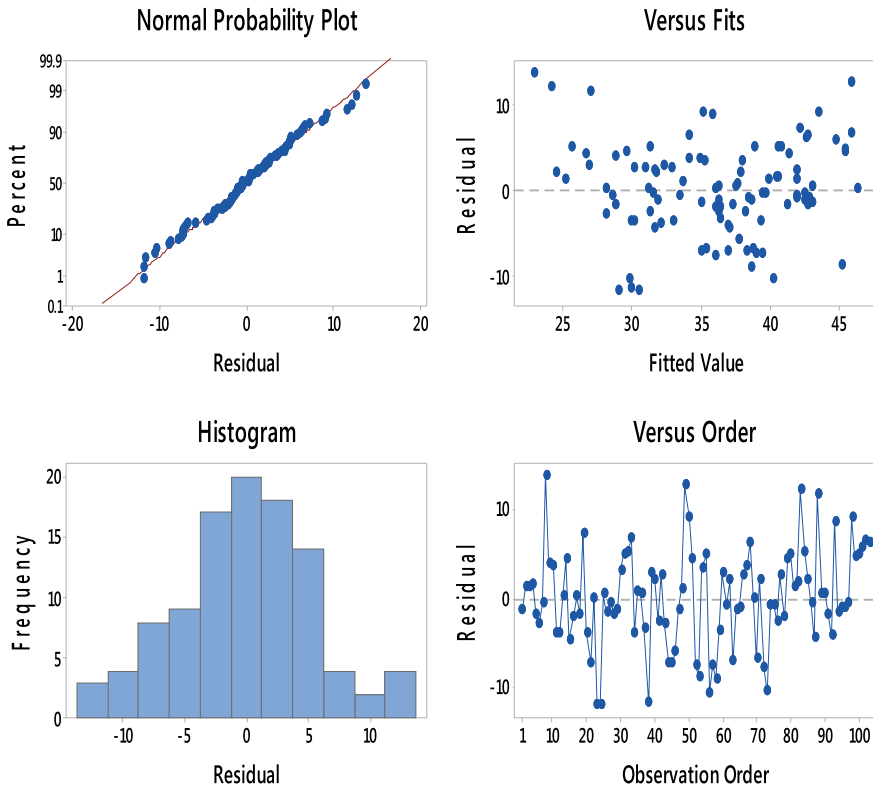
Fig. 11 Residual plots for compressive strength (Mpa)

Probability Plot of Compressive Strength(Mpa)
Normal - 95% CI

Mean	36.04
StDev	7.838
N	103
AD	0.376
P-Value	0.406

Fig. 12 Probability plot of predicted compressive strength values
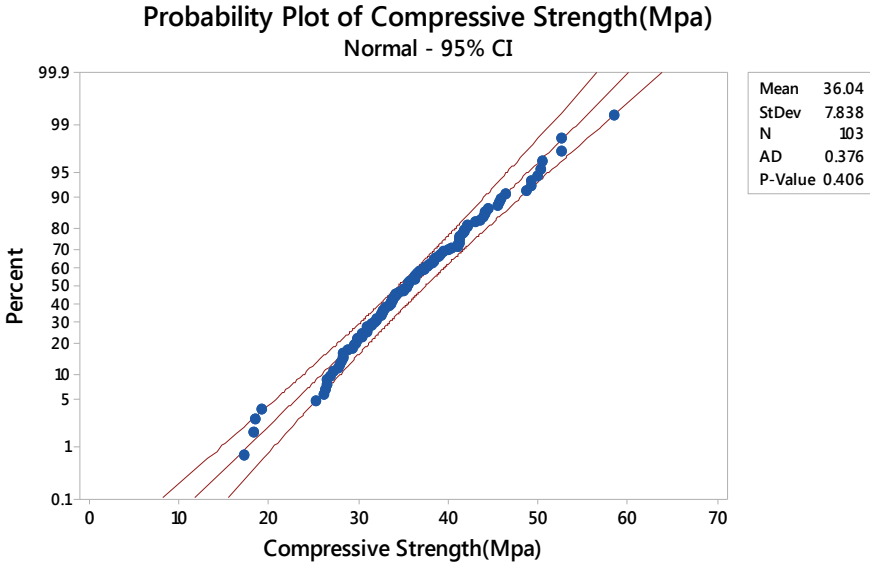
Residual Plots for Compressive Strength(Mpa)
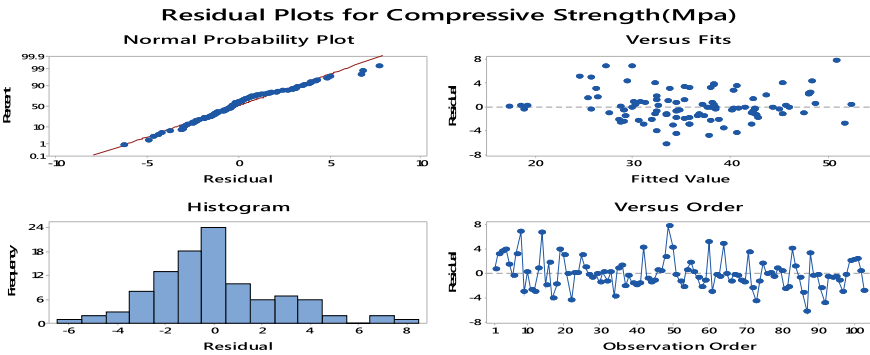
Fig. 13 Residual plots for compressive strength (Mpa)

6   Machine Learning

Machine learning is a technology that enables machines to learn from their experiences and data provided. The system analyses the datasets and finds different patterns formed in the given data. Then, based on its learnings the machine can make certain predictions.

There are many different approaches that can be used for machine learning like supervised learning, unsupervised learning, and reinforcement learning. In order to train a machine, a process has to be followed. Initially, the data has to be collected and
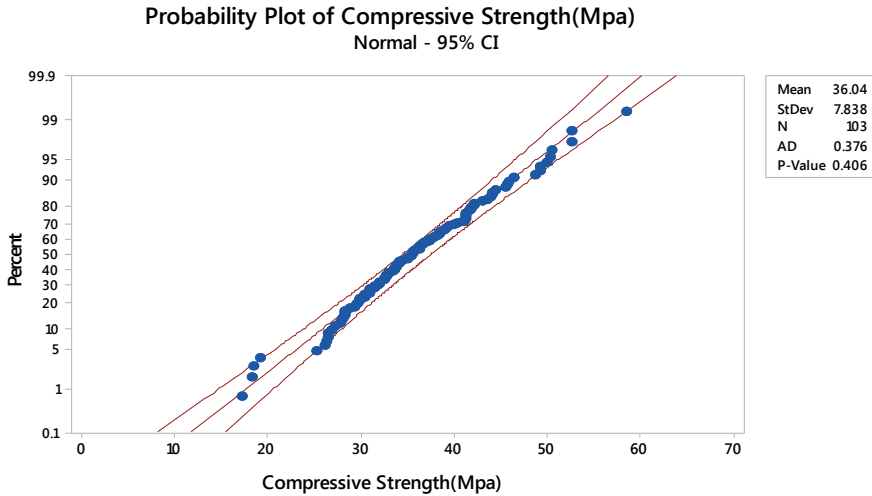
Fig. 14 Probability plot of predicted compressive strength values

prepared. In this work, data has been collected experimentally and has been analyzed in order to apply the machine learning techniques [15–17]. The data comprises of both the input features and the output features. Therefore, supervised learning became handy. Henceforth, dataset preprocessing has been done and importance of different features has been measured to get a better understanding of the data. Also, the data is split into training data and testing data, approximately 30 percent being the testing data. Next the models are to applied and tested for accuracies. Since the data was continuous, various regression models have been applied. Support vector regressor, random forest regressor, decision tree regressor, elastic net regressor, lasso regressor, ridge regressor, and linear regression were some of the models that were tested for precision using root mean square error and R squared method. The ideal value of RMSE is 0 and that of R squared method is 1 (Figs. 15 and 16).

7 Conclusions

In this empirical study, three models were developed from benchmark dataset using ANN and linear regression model. The developed model with their respective inputs for different criterion was tested for their performance by means of regression equation to predict the 28 days compressive strength. Residual plots for compressive strength for different sets of input criterion were being plotted to analyze goodness-of-fit after regression, as it supports to determine whether the ordinary least squares assumptions are being met. With the fulfillment of presumptions, ordinary least

```
Regression type 1

rmse value:
2.338726509238049
r squared value:
0.9060762611451041

rmse value:
2.5264544727915688
0.9014217666592119

Regression type 2

rmse value:
2.352299932039442
r squared value:
0.9049828745283577

rmse value:
2.6012450376861183
r squared value:
0.8954989613350095

Regression type 3

rmse value:
2.3797526587495823
r squared value:
0.9027521212240052

rmse value:
2.7006396663897525
r squared value:
0.8873603319425059
```


Fig. 15 Predicted accuracy of different set of algorithm

squares regression will produce unbiased coefficient estimates with the minimum variance. In machine learning, the ideal value of RMSE is 0 and that of R squared method is 1. Using this knowledge, the best-fit model was chosen to be linear regression. This machine learning model which is about 90% accurate can thereafter be used to predict the compressive strength of concrete.

```
Regression 1
Feature: 0, Score: 0.05739
Feature: 1, Score: -0.03325
Feature: 2, Score: 0.04947
Feature: 3, Score: -0.21656
Feature: 4, Score: 0.07202
Feature: 5, Score: -0.05845
Feature: 6, Score: -0.03857
Feature: 7, Score: -0.15043
Feature: 8, Score: 0.03813
```
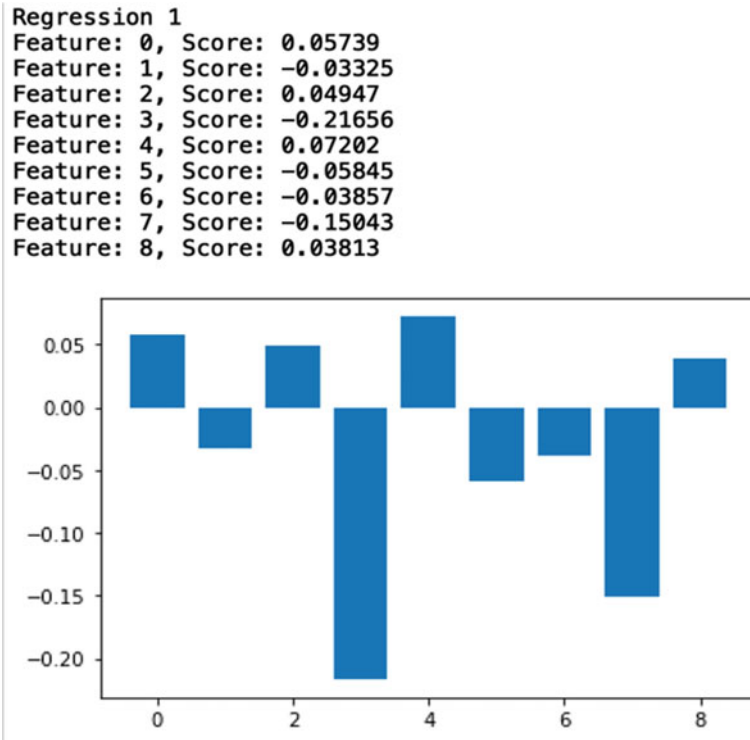

Fig. 16 Predicted effect of variables on the compressive strength of concrete

References

1. Alilou, V. K., & Teshnehlab, M. (2010). Prediction of 28-day compressive strength of concrete on the third day using artificial neural networks. *International Journal of Engineering, 3*(6), 565–576.
2. Singh, P., & Shah, N. D. (2018). An experimental investigation on sustainable concrete with flyash and steel fibers. *International Journal of Civil Engineering and Technology, 9*(6), 1131–1140.
3. Prasad, B.R., Eskandari, H., & Reddy, B.V. (2009). Prediction of compressive strength of SCC and HPC with high volume fly ash using ANN. *Construction and Building Materials, 23*(1), 117–128.
4. Topcu, I. B., & Sarıdemir, M. (2008). Prediction of compressive strength of concrete containing fly ash using artificial neural networks and fuzzy logic. *Computational Materials Science, 41*(3), 305–311.
5. Cook, R., Lapeyre, J., Ma, H., & Kumar, A. (2019). Prediction of compressive strength of concrete: Critical comparison of performance of a hybrid machine learning model with standalone models. *Journal of Materials in Civil Engineering, 31*(11), 04019255.
6. Dao, D. V., Ly, H. B., Trinh, S. H., Le, T. T., & Pham, B. T. (2019). Artificial intelligence approaches for prediction of compressive strength of geopolymer concrete. *Materials, 12*(6), 983.
7. Ni, H.-G., & Wang, J.-Z. (2000). Prediction of compressive strength of concrete by neural networks. *Cement and Concrete Research, 30*(8), 1245–1250.

8. Dantas, A. T. A., Leite, M. B., & de Jesus Nagahama, K. (2013). Prediction of compressive strength of concrete containing construction and demolition waste using artificial neural networks. *Construction and Building Materials, 38*, 717–722.
9. Khademi, F., Akbari, M., & Jamal, S. M. M. (2015). Prediction of compressive strength of concrete by data-driven models." *I-Manager's Journal on Civil Engineering, 5*, 16.
10. Duan, Z.-H., Kou, S.-C., & Poon, C.-S. (2013). Prediction of compressive strength of recycled aggregate concrete using artificial neural networks. *Construction and Building Materials, 40,* 1200–1206.
11. Sarıdemir, M. (2009). Prediction of compressive strength of concretes containing metakaolin and silica fume by artificial neural networks. *Advances in Engineering Software, 40*(5), 350–355.
12. Seyhan, A. T., Tayfur, G., Karakurt, M., & Tanoǧlu, M. (2005). Artificial neural network (ANN) prediction of compressive strength of VARTM processed polymer composites. *Computational Materials Science, 34*(1), 99–105.
13. Başyigit, C., Akkurt, I., Kilincarslan, S., & Beycioglu, A. (2010). Prediction of compressive strength of heavyweight concrete by ANN and FL models. *Neural Computing and Applications, 19*(4), 507–513.
14. Noorzaei, J., Hakim, S. J. S., Jaafar, M. S., & Thanoon, W. A. M. (2007). Development of artificial neural networks for predicting concrete compressive strength. *International Journal of engineering and Technology, 4*(2), 141–153.
15. Nikoo, M., Torabian Moghadam, F., & Sadowski, Ł. (2015). Prediction of concrete compressive strength by evolutionary artificial neural networks. *Advances in Materials Science and Engineering.*
16. Khan, S. U., Ayub, T., & Rafeeqi, S. (2013). Prediction of compressive strength of plain concrete confined with ferrocement using artificial neural network (ANN) and comparison with existing mathematical models. *American Journal of Civil Engineering and Architecture, 1*(1), 7–14.
17. Chopra, P., Sharma, R. K., Kumar, M., & Chopra, T. (2018). Comparison of machine learning techniques for the prediction of compressive strength of concrete. *Advances in Civil Engineering.*

Biodegradable Metal Matrix Composites for Orthopedic Implant Applications: A Review

Kundan Kumar, Ashish Das, and Shashi Bhushan Prasad

Abstract Biodegradable implant metals such as iron (Fe), magnesium (Mg), and Zinc (Zn) and its alloys have attracted extensive interest in biomedical application. Low mechanical strength of Zn, significant slower degradation of Fe, and rapid degradation Mg impede their orthopedic implant application. Further research is going on the development of biodegradable metal matrix composite owing to best suited for biomedical applications. This paper delivers a review of biodegradable metal matrix composites based on corrosion resistance, biocompatibility, and mechanical properties as favorable implant materials for orthopedic applications.

Keywords Orthopedic implant materials · Biodegradable · Biocompatibility

1 Introduction

Numerous orthopedic implant applications, for example, knee, hip, shoulder joint substitutes, bone plates, screws, etc., have been used in different biomaterials which are the area of interest of researchers to improve performance for orthopedic implant applications. These purposes require good corrosion resistance, admirable mechanical property with equitable biocompatibility, and biodegradable implant materials. Different traditionally implant metallic materials such as stainless [1–3], titanium (Ti) and its alloys [4–7], and cobalt-chromium alloys [5, 8, 9] have been suited for the purposes but these are non-biodegradable and need second surgery for removal. However, the other disadvantages of these materials are allergenicity, poor wear resistance, released ions toxicity nature, and deprived bending ductility in the biological environment [10–12]. Also, the stress shielding effect is caused owing to their greater elastic modulus as associated with that of natural bone [6, 7, 13]. Metals, alloys, and

K. Kumar · A. Das (✉) · S. B. Prasad
Department of Production and Industrial Engineering, National Institute of Technology, Jamshedpur 831014, Jharkhand, India
e-mail: ashishdas.1110@gmail.com

K. Kumar
e-mail: kundankumar2k16@gmail.com

composites of the metal matrix are different types of biodegradable implant materials. Biodegradable implant metals and its alloys, for example, zinc (Zn), iron (Fe), and magnesium (Mg), have favorable properties that have received increasing attention from researchers. In spite of admirable processability and higher corrosion resistance, pure Zn exhibits low mechanical strength compared to Mg. It impedes Zn as an orthopedic implant material [14], whereas compared to Mg, Fe, and its alloy exhibit greater mechanical properties; however, they show a considerably gentler degradation and affect their compatibility owing to the ferromagnetic characteristics in vivo [15, 16]. Mg and some of its alloys exhibit low elastic modulus (40–45 GPa) nearer to that of natural bone (10–30 GPa). However, damage to their mechanical strength is earlier than enough bone healing owing to the quick biodegradation of Mg alloys in the biological environment. Some of Mg alloys are suited for present purposes but their all elements are not biocompatible. It impedes their orthopedic implant application. To further improve the properties of biodegradable materials for orthopedic implant applications, research is going on the development of biodegradable metal matrix composites. This paper reviews biodegradable metal matrix composites as implant materials for orthopedic applications.

2   Biodegradable Metal Matrix Composite Development

Metal matrix composites (MMCs) have been developed from the last two decay in order to improve the properties of biodegradable materials for biomedical applications. MMC has at least two constituents. Major constituent is known as metal matrix such as Mg and Zn, and major constituent is known as reinforcement such as hydroxyapatite and tricalcium phosphate. Most commonly metal matrix uses for orthopedic implant applications are Fe, Zn, and Mg. The performance metal matrix can be improved by a feasible approach such as metal matrix composites (MMCs) with choosing the appropriate reinforcements. Further proper selecting of the constituents, size, and concentration of the reinforcements, and method of fabrication can be used to optimize the properties of MMCs with interaction surrounding tissues. Among all metal matrix, composite of Mg matrix has most promising as an implant; after controlling biodegradation rate, hydroxyapatite is most effective and commonly use reinforcement in MMCs for orthopedic application. MMCs with micron size reinforcement have low fracture toughness, poor ductility, and excessive tool wear rate while machining as compared to metal matrix. These limitations have been overcome with use of nanosized (<100 nm) reinforcement and simultaneously improve strength and ductility [17, 18].

2.1 Zn Matrix Composite

Yang et al. [19] were prepared pure Zn matrix composites with reinforcement of hydroxyapatite (HAp) by spark plasma sintering (SPS) for orthopedic implant applications. Bioceramic hydroxyapatite (HAp) is bioactive that supports bone ingrowth, cell osseointegration, and proliferation [20, 21]. It was observed that crystallographic and chemical structures of HAp like to the natural bone [22]. It was found that Zn-HAp composites showed enhanced biocompatibility and adaptable degradation rates together in vivo and in vitro. Zn matrix composite has desirable biodegradability but major limitation is low mechanical strength need of more researches to improve mechanical strength.

2.2 Iron Matrix Composite

Iron-based metal matrix composites (MMCs) are used as biomaterials owing to superior degradation rate as compared to iron and stainless steel. Ulum et al. [23] fabricated a sequence of biomaterials as composites using reinforcements such as b-tricalcium phosphate (TCP), hydroxyapatite (HAp) or TCP-HAp mixes into iron matrix. The presence of these bioceramics enhanced degradation rate. In another article, Ulum et al. [24] also reported that bioactivity of MMCs was improved as compared with pure iron and iron alloys in vivo. Wang et al. [25] prepared composites of iron matrix with bioceramic reinforcement such as calcium silicate. It suggested that iron matrix composites biodegradable bone implants could be an effective approach to improved biomedical performance. The reinforcement such as calcium silicate bioceramic has already established its greater bioactivity and biodegradability as associated with bioceramics such as calcium phosphate, TCP, and HAp in the number of studies [26–28]. Although fewer researches in the field of iron matrix composites biodegradable bone implants have been reported, there is the possibility of enhancing the bioactivity and degradation rate of iron base composites through bioceramic reinforcements. Needed more research efforts to optimize further operational enhancements in bioactivity and degradation rate of iron base composites.

2.3 Mg Matrix Composite

In vivo Mg degrades and liquefies entirely upon satisfying the tissue recuperation with no insert remainders. However, Mg degrades hastily in a bodily atmosphere within the body earlier than sufficient recovery of tissues. These materials also influence the load-bearing performance of orthopedic implants owing to rapid degradation. Mg matrix composites strengthened with diverse nanoscale particles might also improve

Table 1 Mechanical properties of various reinforcements [29]

Reinforcements	Mechanical properties
Al_2O_3	Excellent hardness and wear resistance
ZrO_2	High mechanical strength and toughness
Y_2O_3	Better compressive strength
GNPs	Higher strengthening ability
CPC	Outstanding elastic modulus
Si_3N_4	Improves capability of load bearing
SiC	Increases ductility and compressive strength
HAp	Improves hardness, toughness, and yield strength
FAp	Increases the compressive strength
TCP	Increases hardness

the corrosion resistance. It leads to their precise degradation. The mechanical properties of biodegradable composites of Mg matrix can improve when the addition of numerous types of nanoparticles in Mg matrices via synergistic strengthening mechanisms as shown Table 1.

The capacity of MMCs as new substances for biomedical programs intensive efforts has been made. In spite of the promising features of MMCs, protection and toxicity concerns obstruct their implant applications. Therefore, the biological residences of these composites including cytotoxicity, biocompatibility, and biocorrosion are essential to further explore. The corrosion rate was reduced when using FAp reinforcement particles used in MMCs [30]. Uniform degradation of Mg matrices was caused in the case of the homogeneous dispersion of nanoparticles [31, 32]. Razavi et al. [33, 34] explored composite of AZ91 Mg matrix with several weight fractions (10, 20, and 30 wt%) of FAp. FAp nanoparticles with 20 wt% concentration revealed an excellent promise with the properties of natural bone based on their load-bearing capabilities such as hardness, yield strength, and degradability of implant. The adding of reinforcements such as FAp and HAp in Mg matrix, the corrosion resistance enhanced in physiological environments [30, 31, 35]. Enhancement of corrosion resistance of Mg matrices reported owing to the low solubility of HAp in a physiological environment [36]. Ho et al. [37] prepared magnesium alloy (AZ31B)-hydroxyapatite (5, 10, and 20 wt%) composites using friction stir process and verified Mg alloy-5 wt% HA composite as the highest corrosion resistance within incremental addition of HA owing to localized micro/nano-galvanic couples. Jaiswal et al. [38] fabricated composites of Mg-3Zn matrix and HA (0, 2, 5, and 10 wt%) using powder metallurgy and found that corrosion resistance of Mg-3Zn-5HA to be the optimum among all compositions. However, the formation of large clusters or agglomeration was found in case of the higher concentrations of HAp in the metal matrices ensuring in the choppy degradation system, and therefore, less than 10 wt% of HAp is proposed to use [39–41]. 20 wt% HAp nanoparticles

used in AZ91 Mg matrix led to the porous surface structure of the composite, which unfavorably distressed the ductility and strength of Mg alloys [42]. 5, 10, and 15 wt% concentration of HAp in Mg matrices have been used to manufacture composites and found that 15 wt% HAp in the composite revealed uneven distribution of HAp, foremost to irregular erosion in the composite [43]. Razavi et al. [44] found that Mg/HA composite with spherical HA nanoparticles showed a considerably smaller biodegradation rate compared to the nanocomposite with needle HA nanoparticles. b-TCP nanoparticles used in MMCs revealed higher corrosion resistance [45–48]. As compared to HAp, TCP has a high dissolution rate that could assist to accomplish the whole degradation of insert composite after remedial of cracked bone [41]. CPC helps the creation of fresh bone tissues as it reacts with body fluid, foremost to the quick development of bone and the degradation can be molded to a certain speed both in vivo and in vitro [41]. Feng et al. [49] found that ZK60A matrix composites having lower concentrations of CPC reinforcements (2.5–5 wt%) showed minimum defects, caused in enhanced corrosion resistance, whereas the composites having CPC with 7.5 and 10 wt% exhibited cracks and holes on stacking. Normally, artificial body fluids are not simply degraded to GNPs; nevertheless, their whole degradation can be achieved through humanoid enzymes [50].

Electrochemical and immersion tests in simulated body fluid (SBF) or Hank's solution are used to evaluate corrosion rate of MMCs in vitro. Biomedical applications of MMCs greatly depend on their biocompatibility in bodily surroundings. Commonly, the biocompatibility of MMCs is influenced by their contacts through several biological structures consisting of proteins, cells, and other intricate biomolecules. Biocompatibility and applications of reinforcements are used in MMCs as shown in Table 2.

Table 2 Reinforcements with its biocompatibility and biomedical applications [29]

Biocompatibility Reinforcement	Biocompatibility Reinforcement	Application
Al_2O_3	Cell adhesion, proliferation, and Improves protein adsorption	Knee prosthesis, Bone plate, Bone screws
ZrO_2	Greater bone stability, improves cell viability, and nontoxic and bioinert to blood cells and fibroblast	Bone screw, Femoral head, Artificial knee
Y_2O_3	Cell viability Improves	Implant in dental
GNPs	Nontoxic to cells, no tissue reaction, and biocompatible even in blood contact	Endovascular materials, Bone plates, Bone screw
CPC	Nontoxic to tissues and higher protein adsorption, bioinert and do not cause inflammation, Induce osteoblastic differentiation in progenitor cells	Dental implant, Joint replacements and bone tissue
Si_3N_4	Bone–cell adhesion and Promotes bone fusion in spinal surgery	Spinal fusion devices, Prosthetic hip, Knee joints
SiC	Durable coating for bone prosthetics, slightly toxic	Bone plate, Bone screw, Hip replacement
HAp	The release of Mg ion reduces, Nontoxic and bioactive, osteoblastic differentiation, and excellent cell proliferation	Bone screw and pins, Bone joint
FAp	Osteoconductivity and Enhance cell viability	Bone plate, Bone pins, Bone screw

3 The Different Method Used for Manufacturing MMCs

Numerous processing methods are used for manufacturing MMCs such as powder metallurgy [17], semi-solid casting [17], stir casting [17], disintegrated melt deposition [17], friction stir processing [17], ultrasound-assisted particle dispersion method [51], vacuum cold spraying [52], sol-gel method [53], accumulative roll bonding [17]. Powder metallurgy is the most common method of fabrication of MMCs which is a solid state process. A common, cheap, and fairly simple method of producing MMCs is stir casting where the reinforcement particles are added into the molten matrix metal. A mechanical stirrer like impeller is placed in the molten metal and rotated to get a uniform distribution of the reinforcement with the molten metal. Friction stir processing (FSP), as a derivative from friction stir welding, is newly used in the field of research to integrate nanoparticles within a metallic matrix by solid-state process. It produces bulk or surface nanocomposites. Disintegrated melt deposition is used to produce Mg base nanocomposite, and this process is derived from the stir casting process.

4 Conclusion

Compared to existing titanium (Ti), Zn, Fe, Mg and its alloys, and cobalt-chromium alloys, MMCs possess the fabulous perspective for orthopedic implant applications. The adding of particular nanoparticles as reinforcements to metal matrices improves the possessions of composites. Adjustable corrosion resistance, suitable mechanical properties, and better biocompatibility of MMCs have been reported as compared to metals and alloys. Mg matrix composites are most promising temporary implant biomaterials owing to their excellent properties. Although current development in the area of metal matrix composites for orthopedic implant materials is promising, further broad and efficient researches are stagnant essential with the purpose of recognizing their long-standing orthopedic implant application.

References

1. Muley, S. V., Vidvans, A. N., & Chaudhari, G. P. (2016). Udainiya S Acta Biomaterialia An assessment of ultra fine grained 316L stainless steel for implant applications. *Acta Biomaterialia, 30,* 408–419. https://doi.org/10.1016/j.actbio.2015.10.043.
2. Talha, M., & Behera, C. K. (2013). Sinha OP A review on nickel-free nitrogen containing austenitic stainless steels for biomedical applications. *Materials Science and Engineering C, 33,* 3563–3575. https://doi.org/10.1016/j.msec.2013.06.002.
3. Tang, Y.-C., Katsuma, S., Fujimoto, S., & Hiromoto, S. (2006). Electrochemical study of Type 304 and 316L stainless steels in simulated body fluids and cell cultures. *Acta Biomaterialia, 2,* 709–715. https://doi.org/10.1016/j.actbio.2006.06.003.

4. Ehtemam-Haghighi, S., Prashanth, K. G., & Attar, H. Evaluation of mechanical and wear properties of Ti xNb 7Fe alloys designed for biomedical applications. *Materials & Design, 111,* 592–599. https://doi.org/10.1016/j.matdes.2016.09.029

5. Hinüber, C., Kleemann, C., Friederichs, R. J., et al. (2010). Biocompatibility and mechanical properties of diamond-like coatings on cobalt-chromium-molybdenum steel and titanium-aluminum-vanadium biomedical alloys. *Journal of Biomedical Materials Research, Part A, 95A,* 388–400. https://doi.org/10.1002/jbm.a.32851.

6. Niinomi, M., & Nakai, M. (2011). Titanium-based biomaterials for preventing stress shielding between implant devices and bone. *International Journal of Biomaterials, 2011,* 1–10. https://doi.org/10.1155/2011/836587.

7. Ozan, S., Lin, J., Li, Y., et al. (2018). Deformation mechanism and mechanical properties of a thermomechanically processed β Ti–28Nb–35.4Zr alloy. *Journal of the Mechanical Behavior of Biomedical Materials, 78,* 224–234. https://doi.org/10.1016/j.jmbbm.2017.11.025.

8. Yoda, K., Suyalatu, Takaichi A., et al. (2012). Effects of chromium and nitrogen content on the microstructures and mechanical properties of as-cast Co–Cr–Mo alloys for dental applications. *Acta Biomaterialia, 8,* 2856–2862. https://doi.org/10.1016/j.actbio.2012.03.024.

9. Patel, B., Inam, F., Reece, M., et al. (2010). A novel route for processing cobalt–chromium–molybdenum orthopaedic alloys. *Journal of the Royal Society, Interface, 7,* 1641–1645. https://doi.org/10.1098/rsif.2010.0036.

10. Radha, R., & Sreekanth, D. (2017). Insight of magnesium alloys and composites for orthopedic implant applications—A review. *Journal of Magnesium and Alloys, 5,* 286–312. https://doi.org/10.1016/j.jma.2017.08.003.

11. Ribeiro, A. M., Flores-Sahagun, T. H. S., & Paredes, R. C. (2016). A perspective on molybdenum biocompatibility and antimicrobial activity for applications in implants. *Journal Materials Science, 51,* 2806–2816. https://doi.org/10.1007/s10853-015-9664-y.

12. Biesiekierski, A., Wang, J., Abdel-Hady Gepreel, M., & Wen, C. (2012). A new look at biomedical Ti-based shape memory alloys. *Acta Biomaterialia, 8,* 1661–1669. https://doi.org/10.1016/j.actbio.2012.01.018.

13. Gu, X.-N., & Zheng, Y.-F. (2010). A review on magnesium alloys as biodegradable materials. *Front Mater Sci China, 4,* 111–115. https://doi.org/10.1007/s11706-010-0024-1.

14. Tong, X., Zhang, D., Zhang, X., et al. (2018). Microstructure, mechanical properties, biocompatibility, and in vitro corrosion and degradation behavior of a new Zn–5Ge alloy for biodegradable implant materials. *Acta Biomaterialia, 82,* 197–204. https://doi.org/10.1016/j.actbio.2018.10.015.

15. Saini, M. (2015). Implant biomaterials: A comprehensive review. *World Journal of Clinical Cases, 3,* 52. https://doi.org/10.12998/wjcc.v3.i1.52

16. Dargusch, M. S., Dehghan-Manshadi, A., Shahbazi, M., et al. (2019). Exploring the role of manganese on the mcrostructure, mechanical properties, biodegradability, and biocompatibility of porous iron-based scaffolds. *ACS Biomaterials Science & Engineering, 5,* 1686–1702. https://doi.org/10.1021/acsbiomaterials.8b01497.

17. Malaki, M., Xu, W., Kasar, A. K., et al. (2019). Advanced metal matrix nanocomposites

18. Malaki, M. (2021). *An insight into metal matrix composites with nano size reinforcement*. Elsevier Ltd.

19. Yang, H., Qu, X., Lin, W., et al. (2018). In vitro and in vivo studies on zinc-hydroxyapatite composites as novel biodegradable metal matrix composite for orthopedic applications. *Acta Biomaterialia, 71,* 200–214. https://doi.org/10.1016/j.actbio.2018.03.007.

20. Ohtsuki, C., Kamitakahara, M., & Miyazaki, T. (2009). Bioactive ceramic-based materials with designed reactivity for bone tissue regeneration. *Journal of the Royal Society, Interface, 6,* S349–S360. https://doi.org/10.1098/rsif.2008.0419.focus.

21. Kawahara, H. (1987). Bioceramics for hard tissue replacements. *Clinical Materials, 2,* 181–206. https://doi.org/10.1016/0267-6605(87)90044-8.

22. Edwards, J. T., Brunski, J. B., & Higuchi, H. W. (1997). Mechanical and morphologic investigation of the tensile strength of a bone-hydroxyapatite interface. *Journal of Biomedical Materials Research, 36,* 454–468. https://doi.org/10.1002/(SICI)1097-4636(19970915)36:4%3c454:AID-JBM3%3e3.0.CO;2-D.

23. Ulum, M. F., Arafat, A., Noviana, D., et al. (2014). In vitro and in vivo degradation evaluation of novel iron-bioceramic composites for bone implant applications. *Materials Science and Engineering C, 36,* 336–344. https://doi.org/10.1016/j.msec.2013.12.022.

24. Ulum, M. F., Nasution, A. K., Yusop, A. H., et al. (2015). Evidences of in vivo bioactivity of Fe-bioceramic composites for temporary bone implants. *Journal of Biomedical Materials Research Part B: Applied Biomaterials, 103,* 1354–1365. https://doi.org/10.1002/jbm.b.33315.

25. Wang, S., Xu, Y., Zhou, J., et al. (2017). In vitro degradation and surface bioactivity of iron-matrix composites containing silicate-based bioceramic. *Bioactive Materials, 2,* 10–18. https://doi.org/10.1016/j.bioactmat.2016.12.001.

26. Xu, S., Lin, K., Wang, Z., et al. (2008). Reconstruction of calvarial defect of rabbits using porous calcium silicate bioactive ceramics. *Biomaterials, 29,* 2588–2596. https://doi.org/10.1016/j.biomaterials.2008.03.013.

27. Ni, S., & Chang, J. (2009). In vitro degradation, bioactivity, and cytocompatibility of calcium silicate, dimagnesium silicate, and tricalcium phosphate bioceramics. *Journal of Biomaterials Applications, 24,* 139–158. https://doi.org/10.1177/0885328208094745.

28. Liu, X., Morra, M., Carpi, A., & Li, B. (2008). Bioactive calcium silicate ceramics and coatings. *Biomedicine & Pharmacotherapy, 62,* 526–529. https://doi.org/10.1016/j.biopha.2008.07.051.

29. Shahin, M., Munir, K., Wen, C., & Li, Y. (2019). Magnesium matrix nanocomposites for orthopedic applications: A review from mechanical, corrosion, and biological perspectives. *Acta Biomaterialia, 96,* 1–19. https://doi.org/10.1016/j.actbio.2019.06.007.

30. Fathi, M. H., Meratian, M., & Razavi, M. (2011). Novel magnesium-nanofluorapatite metal matrix nanocomposite with improved biodegradation behavior. *Journal of Biomedical Nanotechnology, 7,* 441–445. https://doi.org/10.1166/jbn.2011.1310.

31. Witte, F., Feyerabend, F., Maier, P., et al. (2007). Biodegradable magnesium – hydroxyapatite metal matrix composites. *28*, 2163–2174. https://doi.org/10.1016/j.biomaterials.2006.12.027

32. Kuśnierczyk, K., & Basista, M. (2017). Recent advances in research on magnesium alloys and magnesium-calcium phosphate composites as biodegradable implant materials. *Journal of Biomaterials Applications, 31,* 878–900. https://doi.org/10.1177/0885328216657271.

33. Razavi, M., Fathi, M. H., & Meratian, M. (2010). Microstructure, mechanical properties and bio-corrosion evaluation of biodegradable AZ91-FA nanocomposites for biomedical applications. *Materials Science and Engineering A, 527,* 6938–6944. https://doi.org/10.1016/j.msea.2010.07.063.

34. Razavi, M., Fathi, M. H., & Meratian, M. (2010). Fabrication and characterization of magnesium–fluorapatite nanocomposite for biomedical applications. *Materials Characterization, 61,* 1363–1370. https://doi.org/10.1016/j.matchar.2010.09.008.

35. Razavi, M., Fathi, M. H., & Meratian, M. (2010). Bio-corrosion behavior of magnesium-fluorapatite nanocomposite for biomedical applications. *Materials Letters, 64,* 2487–2490. https://doi.org/10.1016/j.matlet.2010.07.079.

36. Liu, C., Ren, Z., Xu, Y., et al. (2018). Biodegradable magnesium alloys developed as bone repair materials: A review. Scanning. https://doi.org/10.1155/2018/9216314

37. Ho, Y. H., Joshi, S. S., Wu, T. C., et al. (2020). In-vitro bio-corrosion behavior of friction stir additively manufactured AZ31B magnesium alloy-hydroxyapatite composites. *Materials Science and Engineering C, 109,* 110632. https://doi.org/10.1016/j.msec.2020.110632.

38. Jaiswal, S., Kumar, R. M., Gupta, P., et al. (2018). Mechanical, corrosion and biocompatibility behaviour of Mg-3Zn-HA biodegradable composites for orthopaedic fixture accessories. *Journal of the Mechanical Behavior of Biomedical Materials, 78,* 442–454. https://doi.org/10.1016/j.jmbbm.2017.11.030.

39. Gu, X., Zhou, W., Zheng, Y., et al. (2010). Microstructure, mechanical property, bio-corrosion and cytotoxicity evaluations of Mg/HA composites. *Materials Science and Engineering C, 30,* 827–832. https://doi.org/10.1016/j.msec.2010.03.016.

40. Phil, M. (2010). Mg/Hydroxyapatite composites for potential bio-medical applications Zibiao Li Thesis submitted for the degree of

41. Bommala, V. K., Krishna, M. G., & Rao, C. T. (2019). Magnesium matrix composites for biomedical applications: A review. *Journal of Magnesium and Alloys, 7,* 72–79. https://doi.org/10.1016/j.jma.2018.11.001.

42. Chen, B., Yin, K. Y., & Lu, T. F. (2016). AZ91 Magnesium Alloy/Porous Hydroxyapatite Composite for Potential Application in Bone Repair. *J Mater Sci Technol., 32*, 858–864. https://doi.org/10.1016/j.jmst.2016.06.010.

43. Khanra, A. K., Jung, H. W. A. C., Yu, S. H., & Hong, K. (2010). Microstructure and mechanical properties of Mg—HAP composites. *33*, 43–47

44. Razavi, M., & Huang, Y. (2020). Effect of hydroxyapatite (HA) nanoparticles shape on biodegradation of Mg/HA nanocomposites processed by high shear solidification/equal channel angular extrusion route. *Materials Letters, 267,* 127541. https://doi.org/10.1016/j.matlet.2020.127541.

45. Liu, D. B., Huang, Y., & Prangnell, P. B. (2012). Microstructure and performance of a biodegradable Mg-1Ca-2Zn-1TCP composite fabricated by combined solidification and deformation processing. *Materials Letters, 82,* 7–9. https://doi.org/10.1016/j.matlet.2012.05.035.

46. Ma, X. L., Dong, L. H., & Wang, X. (2014). Microstructure, mechanical property and corrosion behavior of co-continuous β-TCP/MgCa composite manufactured by suction casting. *Materials and Design, 56,* 305–312. https://doi.org/10.1016/j.matdes.2013.11.041.

47. Qu, S., Gong, Y., Yang, Y., et al. (2018). Grinding characteristics and removal mechanisms of unidirectional carbon fibre reinforced silicon carbide ceramic matrix composites. *Ceramics International, 45,* 3059–3071. https://doi.org/10.1016/j.ceramint.2018.10.178.

48. He, S. Y., Sun, Y., Chen, M. F., et al. (2011). Microstructure and properties of biodegradable β-TCP reinforced Mg-Zn-Zr composites. *The Transactions of Nonferrous Metals Society of China (English Ed), 21*, 814–819. https://doi.org/10.1016/S1003-6326(11)60786-3.

49. Feng, A., & Han, Y. (2010). The microstructure, mechanical and corrosion properties of calcium polyphosphate reinforced ZK60A magnesium alloy composites. *The Journal of Alloys and Compounds, 504,* 585–593. https://doi.org/10.1016/j.jallcom.2010.06.013.

50. Kurapati, R., Russier, J., Squillaci, M. A., et al. (2015). Dispersibility-dependent biodegradation of graphene oxide by myeloperoxidase. *Small (Weinheim an der Bergstrasse, Germany), 11,* 3985–3994. https://doi.org/10.1002/smll.201500038.

51. Dieringa, H. (2018). Processing of magnesium-based metal matrix nanocomposites by ultrasound-assisted particle dispersion: A review. *Metals (Basel), 8*(6), 431. https://doi.org/10.3390/met8060431.

52. Liu, Y., Dang, Z., Wang, Y., et al. (2014). Hydroxyapatite/graphene-nanosheet composite coatings deposited by vacuum cold spraying for biomedical applications: Inherited nanostructures and enhanced properties. *Carbon N Y, 67,* 250–259. https://doi.org/10.1016/j.carbon.2013.09.088.

53. Ashuri, M., Moztarzadeh, F., Nezafati, N., et al. (2012). Development of a composite based on hydroxyapatite and magnesium and zinc-containing sol-gel-derived bioactive glass for bone substitute applications. *Materials Science and Engineering C, 32,* 2330–2339. https://doi.org/10.1016/j.msec.2012.07.004.

A Taguchi Approach to Optimize Electrochemical Discharge Machining of E-glass Fibre Reinforced Polymer Composite

Gaurav Saini

Abstract E-glass fibre reinforced polymer composite becomes very popular in advance manufacturing industries due to their attractive mechanical properties. E-glass fibre is an electrically non-conductive material which is very intricate to machine by conventional machining processes and facing many problems. In this research work, the experiments were done according to Taguchi L27 orthogonal array with S/N ratio analysis. DC supply voltage, electrolyte concentration, pulse-on-time, pulse-off-time and inter-electrode gap were used as machining parameters, and their effect were observed as a response characteristic such as tool wear rate (TWR). The experimental results were concluded with the help of analysis of variance (ANOVA) which indicated that voltage was the most dominant factor for tool wear rate followed by pulse-off-time. Further establish the optimal machining parameter combination while machine micro-hole in e-glass fibre reinforced polymer composite using electrochemical discharge machining (ECDM) process and the surface texture of the used tool electrode was analysed by scanning electron microscope (SEM).

Keywords Electrochemical discharge machining · Tool wear rate · E-glass fibre reinforced polymer composite · Taguchi's method

1 Introduction

Advance manufacturing industries need materials which have superior properties such as high strength to stiffness, lightweight, high corrosion resistance, strength-to-weight ratio, and these all properties are present in e-glass fibre reinforced polymer composite. Because of these superior properties, e-glass fibre reinforced polymer composite has got wide application in the production of sports equipment, aircraft components, naval vessels and construction equipments. The potential applications of e-glass fibre reinforced polymer composites there is a need to understand and address the issues related to its machining as these are non-conductive materials and cannot

G. Saini (✉)

Department of Mechanical Engineering, Panjab University SSG Regional Centre, Hoshiarpur 146001, Punjab, India
e-mail: gaurav_saini@pu.ac.in

be machined by any well-known nonconventional machining methods. However, the production of through holes and micro-channel on e-glass fibre has been difficult by conventional machining and facing many problems like poor dimensional accuracy and surface finish. In the view of these facts, it is important to develop and introduce a new machining method for effective machining of electrically non-conducting e-glass fibre reinforced polymer composite. Electrochemical discharge machining process is one of the best hybrid non-conventional methods to machine non-conducting materials. Electrochemical discharge machining (ECDM) concept was firstly developed by Kurafuji in 1968 [1]. It is a non-conventional process used to machine electrically non-conducting materials such as quartz, glass, composite material and ceramics. Cook et al. [2] reported that the process developed by Kurafuji is unlike ECM and EDM and gives a new name to it called discharge machining of non-conductors. They applied the process on non-conducting materials. Ceramics and glass can be cut with new variant, i.e. wire electrochemical discharge machining reported in by Tsuchiya et al. [3]. Jain et al. [4] developed the same process with new name electrochemical spark machining. Allesu et al. [5] reported that material removal from the workpiece is due to the melting of the workpiece. Material removal is the result of a high-temperature etching process suggested by Yang et al. [6]. Fascio et al. [7–9] proposed to use the technique called spark-assisted chemical engraving (SACE) to avoid the confusion with ECM and EDM. The process shown in Fig. 1, tool electrode and auxiliary electrode both submerged in an electrolyte solution. The power supply connected to both the electrodes, i.e. tool electrode and auxiliary electrode. The formation of the hydrogen bubble generated at the tool electrode and around the auxiliary electrode oxygen bubbles is formed when supply voltage reaches to certain value. When applied voltage reaches to the critical voltage electric discharges taking place around the tool electrode results in melting and thermally eroding of the workpiece due to discharge energy [10]. Many researchers have shown their interest to explore the output quality characteristics of ECDM process. Jain et al. [4] experimented on kevlar and glass-epoxy composites by using sodium hydroxide (NaOH) using travelling wire electrochemical spark machining (TW-ECSM). The workpiece and wire were kept in contact with gravity feed mechanism. Effect of voltage and electrolyte concentration on material removal rate, tool wear rate, wire
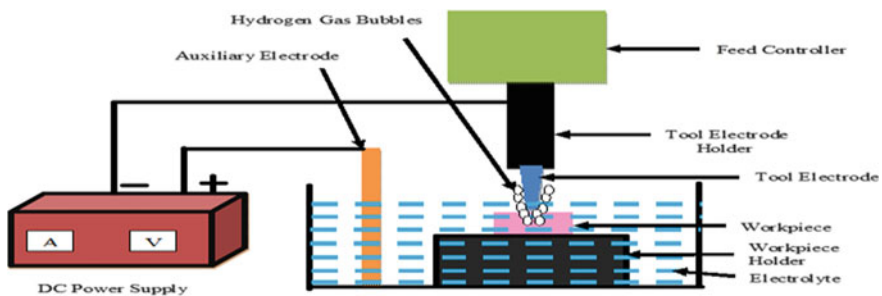
Fig. 1 Schematic sketch of electrochemical discharge machining (ECDM) process

erosion tension and average diameter overcut is analysed by authors also claimed that thermomechanical phenomenon is the main cause of material removal in electrochemical spark machine. Manna and Khas [11] investigated on the micro machining of electrically non-conductive Al_2O_3 ceramic. Authors [12] utilized the developed an electrochemical spark machining set-up for experimental. Mousa et al. [13] reported that tool electrode thermal conductivity controls the heat transfer from the machining zone. Authors find that higher the thermal conductivity great amount of heat transferred from the tool electrode. Han et al. [14] claimed that pulse voltage reduces the thermal damage on the workpiece. ECDM process is used to machine microfluid channels and three-dimensional features in the glass substrate [15, 16]. Many researchers [17–19] optimize the process parameters of ECDM process by Taguchi's methodology. The multi-response optimization of ECDM process can be effectively done with the help of genetic algorithm and PSO (RBFNN) by Shanmukhi et al. [20]

2   Developed Set-Up and Experiment Planning

Figure 2 shows schematic diagram of the developed electrochemical discharge machining (ECDM) set-up. Five machining parameters such as voltage, electrolyte concentration, pulse-on-time, pulse-off-time and inter-electrode gap were used as input parameters, and tool wear rate was observed as output quality characteristics. The selected machining parameters and their levels used for conducting the experiments are listed in Table 1. E-glass fibre reinforced polymer composite used as workpiece. Taguchi method-based design of experiments [21], L27 orthogonal array with process parameters coded and actual values shown in Table 2 was employed for carrying out the experiments. The weight of tool, i.e. electrode before and after each hole machining, was used and determine the tool wear rate. For weighing electrode, the sartorius master series electronic balance of least count 0.01 mg was used. The
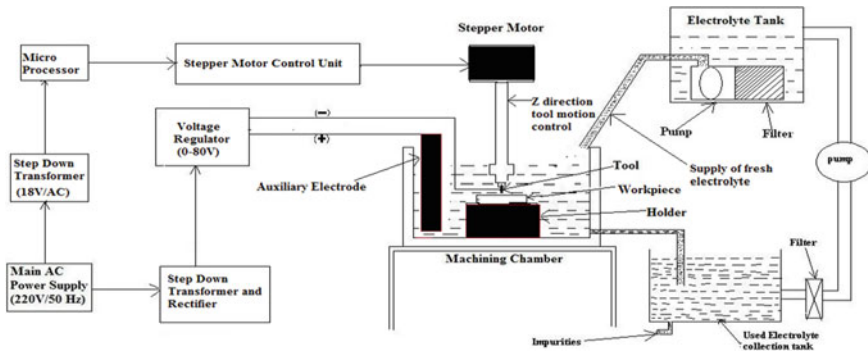
Fig. 2 Schematic diagram of the developed electrochemical discharge machining set-up

Table 1 Machining parameters and their levels selected for experiments

Sr. no	Labels	Machining parameters	Units	Level 1	Level 2	Level 3
1	A	DC supply voltage	Volts	65	70	75
2	B	Electrolyte concentration	g/l	75	80	85
3	C	Pulse-on-time	μ_s	2	4	6
4	D	Pulse-off-time	μ_s	0.10	0.30	0.50
5	E	Inter-electrode gap	mm	100	140	180

analysis of machined surface texture of the holes was done with the help of scanning electron micrographs (SEM).

3 Result and Discussion

Taguchi method is widely used for experimental design and can be used in developing a robust manufacturing system [22]. Taguchi method-based L27 orthogonal array was found suitable which can accumulate all the selected level of the developed ECDM set-up parameters for the study. In Taguchi method, recommend multiple run and the signal-to-noise ratio for optimization of parameters. The S/N ratio is the quality measuring linked to loss function; by maximizing the value of the S/N ratio, the loss associated can be minimized. The S/N ratio is usually treated as response in the experiments and depending upon the responses the three types of S/N ratio are employed [23]. The following equations, i.e. higher the better, lower the better and normal the better, are used for calculations of S/N as follows:

$$\left(S/N\right)_{HB} = -10 \log \left[\frac{1}{T} \sum_{i=1}^{T} \frac{1}{y_i^2} \right] \tag{1}$$

$$\left(S/N\right)_{LB} = -10 \log \left[\frac{1}{T} \sum_{i=1}^{T} y_i^2 \right] \tag{2}$$

$$\left(S/N\right)_{NB} = -10 \log \left[\frac{1}{T} \sum_{i=1}^{T} (y_i - y_o)^2 \right] \tag{3}$$

where T is the number of all data points and y_i is the value of the ith data point. In the present research work, lower the better S/N ratio criterion has been followed for TWR. Table 3 represents L27 orthogonal array with test result and S/N ratio for tool wear rate. The each experiment was carried out with three replications.

The present research investigation was to obtain best optimal parametric combination which can provide less tool wear rate during machining of e-glass fibre reinforced

Table 2 L27 orthogonal array with process parameters coded and actual values

Exp. no	Parameters symbols and their coded values					Parameters name and their actual setting values				
	A (1)	B (2)	C (3)	D (4)	E (5)	Voltage (v)	Electrolyte concentration (g/l)	Pulse-on-time (μs)	Pulse-off-time (μs)	Inter-electrode gap (mm)
1	1	1	1	1	1	65	75	2	0.1	100
2	1	1	2	2	2	65	75	2	0.1	140
3	1	1	3	3	3	65	75	2	0.1	180
4	1	2	1	2	2	65	80	4	0.3	100
5	1	2	2	3	3	65	80	4	0.3	140
6	1	2	3	1	1	65	80	4	0.3	180
7	1	3	1	3	3	65	85	6	0.5	100
8	1	3	2	1	1	65	85	6	0.5	140
9	1	3	3	2	2	65	85	6	0.5	180
10	2	1	1	2	3	70	75	4	0.5	100
11	2	1	2	3	1	70	75	4	0.5	140
12	2	1	3	1	2	70	75	4	0.5	180
13	2	2	1	3	1	70	80	6	0.1	100
14	2	2	2	1	2	70	80	6	0.;1	140
15	2	2	3	2	3	70	80	6	0.1	180
16	2	3	1	1	2	70	85	2	0.3	100
17	2	3	2	2	3	70	85	2	0.3	140
18	2	3	3	3	1	70	85	2	0.3	180

(continued)

Table 2 (continued)

Exp. no	Parameters symbols and their coded values					Parameters name and their actual setting values				
	A (1)	B (2)	C (3)	D (4)	E (5)	Voltage (v)	Electrolyte concentration (g/l)	Pulse-on-time (μs)	Pulse-off-time (μs)	Inter-electrode gap (mm)
19	3	1	1	3	2	75	75	6	0.3	100
20	3	1	2	1	3	75	75	6	0.3	140
21	3	1	3	2	1	75	75	6	0.3	180
22	3	2	1	1	3	75	80	2	0.5	100
23	3	2	2	2	1	75	80	2	0.5	140
24	3	2	3	3	2	75	80	2	0.5	180
25	3	3	1	2	1	75	85	4	0.1	100
26	3	3	2	3	2	75	85	4	0.1	140
27	3	3	3	1	3	75	85	4	0.1	180

Table 3 L27 orthogonal array with test results and S/N ratio for TWR

Trail no	Input parameters					Tool wear rate (mm³/min)			Average TWR	S/N ratio (dB)
	Voltage (V)	Electrolyte concentration (g/l)	Pulse-on-time (μs)	Pulse-off-time (μs)	Inter-electrode gap (mm)	Y_1	Y_2	Y_3	Y (mm³/min)	
1	65	75	2	0.1	100	0.31	0.34	0.33	0.33	9.525
2	65	75	2	0.1	140	0.35	0.34	0.32	0.34	9.345
3	65	75	2	0.1	180	0.29	0.32	0.31	0.31	10.173
4	65	80	4	0.3	100	0.31	0.32	0.31	0.31	10.117
5	65	80	4	0.3	140	0.33	0.35	0.34	0.34	9.396
6	65	80	4	0.3	180	0.31	0.33	0.33	0.32	9.870
7	65	85	6	0.5	100	0.32	0.33	0.33	0.33	9.656
8	65	85	6	0.5	140	0.4	0.45	0.43	0.43	7.290
9	65	85	6	0.5	180	0.29	0.33	0.34	0.32	9.924
10	70	75	4	0.5	100	0.49	0.44	0.47	0.47	6.614
11	70	75	4	0.5	140	0.52	0.48	0.5	0.50	6.055
12	70	75	4	0.5	180	0.43	0.44	0.44	0.44	7.111
13	70	80	6	0.1	100	0.66	0.68	0.67	0.67	3.466
14	70	80	6	0.1	140	0.7	0.69	0.69	0.69	3.286
15	70	80	6	0.1	180	0.65	0.68	0.66	0.66	3.662
16	70	85	2	0.3	100	0.57	0.6	0.58	0.58	4.761
17	70	85	2	0.3	140	0.6	0.6	0.58	0.59	4.598
18	70	85	2	0.3	180	0.52	0.5	0.53	0.52	5.730
19	75	75	6	0.3	100	0.62	0.64	0.62	0.63	3.986

(continued)

Table 3 (continued)

Trail no	Input parameters					Tool wear rate (mm³/min)				Average TWR	S/N ratio (dB)
	Voltage (V)	Electrolyte concentration (g/l)	Pulse-on-time (µs)	Pulse-off-time (µs)	Inter-electrode gap (mm)	Y_1	Y_2	Y_3		Y (mm³/min)	
20	75	75	6	0.3	140	0.68	0.65	0.68		0.67	3.544
21	75	75	6	0.3	180	0.62	0.62	0.61		0.62	4.138
22	75	80	2	0.5	100	0.53	0.51	0.54		0.53	5.597
23	75	80	2	0.5	140	0.63	0.63	0.62		0.63	3.986
24	75	80	2	0.5	180	0.51	0.47	0.49		0.49	6.178
25	75	85	4	0.1	100	0.69	0.7	0.7		0.70	3.123
26	75	85	4	0.1	140	0.76	0.74	0.75		0.75	2.557
27	75	85	4	0.1	180	0.62	0.63	0.63		0.63	3.958

Table 4 ANOVA for TWR (mg/min)

Source	Sum of squares	DOF	Variance	F-ratio	% contribution
D.C. supply voltage (A)	147.95	2	73.97	338.97	82.05
Electrolyte concentration (B)	4.41	2	2.2	10.11	2.45
Pulse-on-time (C)	8.07	2	4.03	18.49	4.48
Pulse-off-time (D)	9.86	2	4.93	22.6	5.47
Inter-electrode gap (E)	6.5	2	3.25	14.89	3.61
Residual error	3.49	16	0.21	–	1.94
Total	180.28	26		–	100.00

polymer composite with electrochemical discharge machining. Analysis of variance (ANOVA) table was constructed by utilizing the detail experiments result during machining of e-glass fibre reinforced polymer composite on the developed ECDM set-up. Table 4 represents the ANOVA for TWR (mg/min). From ANOVA Table 4, it is established that the DC supply voltage is the most dominant process parameters for tool wear rate with 82.05% contribution. However, all other parameters are the significant parameters for TWR. The percentage contribution of parameters in controlling the response, i.e. TWR (mg/min), is quantified and explained in this table. It is also clear from Table 4 that the parameters electrolyte concentration, pulse-on-time, pulse-off-time, and gap between anode and cathode has 2.45, 4.48, 5.47 and 3.61% 'F-test' values, respectively, thereby these are significant for TWR(mg/min). Figure 3 shows the S/N ratio (dB) curves for different process parameters by their factor levels for TWR (mg/min). Lower the better principle was adopted for TWR. Figure 3 depicts that at lower voltage the tool wear rate was minimum due to less spark generated between tool and the workpiece. The observed trend for electrolyte concentration shows that with decrease in electrolyte concentration the tool wear rate decreases as low mobility of the ions at lower level of the electrolyte concentration.
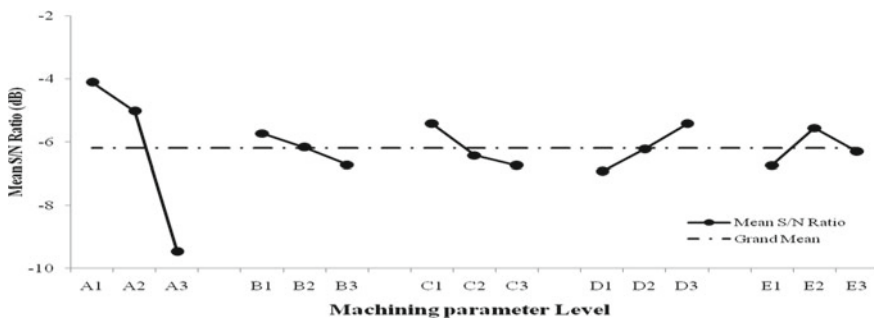
Fig. 3 S/N ratio (dB) by factor level for TWR
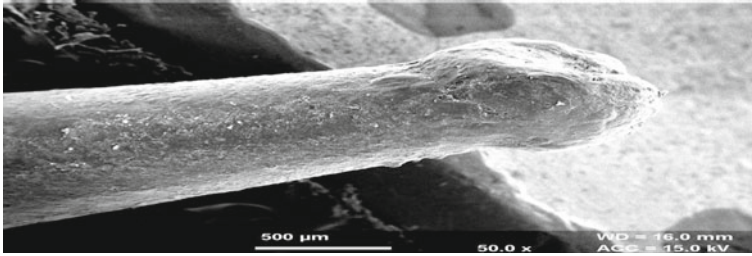
Fig. 4 SEM image of used tool

The decrease in pulse-on-time shows less tool wear rate because low current intensity generated on tool tip at low pulse-on-time. Lower TWR is obtained at higher pulse-off-time, because cooling time period of tool electrode tip increases. It is clear that the TWR decreases up to second level of inter-electrode gap then TWR increases because inter-electrode resistance increases result more heat generation at the tool tip. From the observed results, the optimal parametric combination for less TWR is $A_1B_1C_1D_3E_2$. Figure 4 shows the SEM image of used tool electrode. From Fig. 4, it is clear that the electrode tip is changed due to the formation of the recast layer and deposition of particles and very tiny fibres around the tip of the electrode, thereby changes the tool tip dimension. It is due to high intensity discharges generated at the tool tip, thereby dissolution of more material take place from workpiece simultaneously some of dissolution metal deposited on the tool surface so-called known as recast layer.

4 Conclusion

From the experimental investigation using L27 orthogonal array generated by Taguchi design of experiments, following conclusions were drawn from the study:

1. The developed electrochemical discharge machining set-up can be effectively used for the machining of e-glass fibre reinforced polymer composite.
2. DC supply voltage is the most dominated factor affecting the tool wear rate with 82.05% contribution which is supported by electrolyte concentration, pulse-on-time, pulse-off-time and gap between anode and cathode with 2.45%, 4.48%, 5.47% and 3.61% contribution respectively.
3. Using Taguchi method, the optimal parametric combination for tool wear rate are found to be $A_1B_1C_1D_3E_2$. These combination can be used for effective as well as economical machining of e-glass fibre reinforced polymer composite on developed ECDM set-up.
4. At the higher level of machining parameters, the electrode tool tip dimension changed due to the diffusion of tool electrode particles.

References

1. Kurafuji, H. (1968). Electrical Discharge Drilling of Glass-I. *Annals of the CIRP, 16,* 415.
2. Cook, N. H., Foote, G. B., Jordan, P., & Kalyani, B. N. (1973). Experimental studies in electromachining. *Journal of Engineering for Industry, 95*(4), 945–950.
3. Tsuchiya, H., Inoue, T., & Miyazaki, M. (1985). Wire electro-chemical discharge machining of glasses and ceramics. *Bulletin of the Japan Society of Precision Engineering, 19*(1), 73–74.
4. Jain, V. K., Rao, P. S., Choudhary, S. K., & Rajurkar, K. P. (1991). Experimental investigations into traveling wire electrochemical spark machining (TW-ECSM) of composites. *Journal of Engineering for Industry, 113*(1), 75–84.
5. Allesu, K. (1991). A preliminary qualitative approach of a proposed mechanism of material removal in electrical machining of glass. *European Journal* of *Mechanical Engineering, 36*(3), 201.
6. Yang, C. T., Ho, S. S., & Yan, B. H. (2001). Micro hole machining of borosilicate glass through electrochemical discharge machining (ECDM). In *Key Engineering Materials* (vol. 196, pp. 149-166). Trans Tech Publications Ltd.
7. Fascio, V. (2002). *Etude de la microstructuration du verre par étincelage assisté par attaque chimique: une approche electrochimique", Dissertation Thesis (2691) Swiss Federal Institute of Technology.* Lausanne: EPF.
8. Fascio, V., Langen, H.H., Bleuler, H., & Comninellis, C. (2003). Investigations of the spark assisted chemical engraving. *Electrochemistry Communications, 5*(3), 203–207.
9. Fascio, V., Wüthrich, R., & Bleuler, H. (2004). Spark assisted chemical engraving in the light of electrochemistry. *Electrochimica Acta, 49*(22–23), 3997-4003
10. Antil, P., Singh, S., & Manna, A. (2014). A study on input parameters affecting material removal rate and surface roughness in electrochemical discharge machining process. *International Journal of Advance Research in Science and Technology, 3,* 400405.
11. Manna, A., & Khas, K. (2009). Micro machining of electrically non-conductive Al_2O_3 ceramic. *Journal of Machining and Forming Technologies, 1*(1/2), 101–112.
12. Saini, G., Manna, A., & Sethi, A. S. (2020). Investigations on performance of ECDM process using different tool electrode while machining e-glass fibre reinforced polymer composite. In *Materials Today: Proceedings.*
13. Mousa, M., Allagui, A., Ng, H. D., & Wüthrich, R. (2008). The effect of thermal conductivity of the tool electrode in spark-assisted chemical engraving gravity-feed micro-drilling. *Journal of Micromechanics and Microengineering, 19*(1), 015010.
14. Han, M. S., Min, B. K., & Lee, S. J. (2009). Geometric improvement of electrochemical discharge micro-drilling using an ultrasonic-vibrated electrolyte. *Journal of Micromechanics and Microengineering, 19*(6), 065004.
15. Schopf, M., Beltrami, I., Boccadoro, M., Kramer, D., & Schumacher, B. (2001). ECDM (electro chemical discharge machining), a new method for trueing and dressing of metal bonded diamond grinding tools. *CIRP Annals, 50*(1), 125–128.
16. Kulkarni, A. V. (2007). Electrochemical discharge machining process. *Defence Science Journal, 57*(5), 765–770.
17. Doloi, B., Bhattacharyya, B., & Sorkhel, S. K. (1999). Electrochemical discharge machining of non-conducting ceramics. *Defence Science Journal, 49*(4), 331–338.
18. Jawalkar, C. S., Sharma, A. K., Kumar, P., & Variable, D. (2012). Micromachining with ECDM: Research potentials and experimental investigations. *Channels, 40*(46), 15.
19. Antil, P., Singh, S., & Singh, P. J. (2018). Taguchi's methodology based electrochemical discharge machining of polymer matrix composites. *Procedia Manufacturing, 26,* 469–473.
20. Shanmukhi, K., Vundavilli, P. R., & Surekha, B. (2015). Modeling of ECDM micro-drilling process using GA and PSO trained radial basis function neural network. *Soft Computing, 19*(8), 2193–2202.
21. Montgomery, D. C. (2012). *Design and analysis of experiments.* New York: Wiley.

22. Guillaume, B. G., Nathalie, M., & Christian, G. (2007). Sintering of ceramic powders: Determination of the densification and grain growth mechanisms from the 'grain size/relative density' trajectory. *Scripta Materialia, 75,* 137–140.
23. Byrne, D. M., & Taguchi S. The taguchi approach to parameter design. *Quality Progress, 20*(12), 19–26.

A Brief Study on Machinability of Aluminium Alloys

Jasjeevan Singh, Simranpreet Singh Gill, Manu Dogra, and Rupinder Singh

Abstract The use of aluminium alloys in manufacturing industry has increased substantially in current years. This is basically due to their ability to combine weightlessness and strength in a single material. The current paper focuses on a review of tool wear, power consumption, chip morphology, surface roughness, cutting temperature, cutting coolant, cutting forces and stresses during machining of aluminium alloy. Less work has been reported for use of non-edible/ionic fluids in machining of aluminium alloys we have covered. Thus, a lot of scope exists in the use of non-edible oil and ionic fluids for machining of aluminium alloys. This relevant information will give suitable choice for cutting conditions to the machine operators and engineers during machining of different aluminium alloys.

Keywords Aluminium alloys · Surface integrity · Cutting coolant · Tool material · Surface roughness

1 Introduction

Aluminium a combination of oxygen and other materials in its natural form is the third most ample metal in the earth's crust [1, 2]. A fine reference of aluminium

J. Singh (✉)
Research Scholar, IKGPTU, Kapurthala, Punjab, India
e-mail: jasjeevansingh@yahoo.com

S. S. Gill
Department of Mechanical Engineering, Beant College of Engineering and Technology, Gurdaspur, Punjab, India
e-mail: ritchie_223@yahoo.com

M. Dogra
Department of Mechanical Engineering, Punjab University SSG Regional Centre, Hoshiarpur, Punjab, India
e-mail: mdogra7@gmail.com

R. Singh
Department of Mechanical Engineering, Chandigarh University, Gharuan, Mohali, Punjab, India
e-mail: rupinder_singh302@yahoo.com

Fig. 1 Aluminium
consumption in million
metric tons
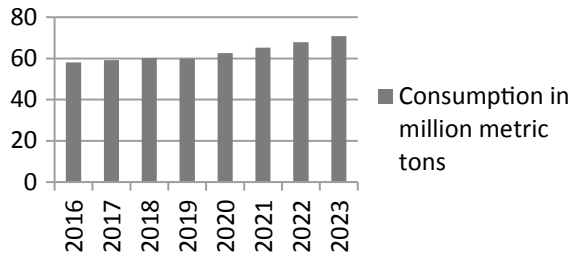
global consumption from 2016 to 2018 including forecast 2023 according to Statista
Research Department is shown in Fig. 1 [3]. Aluminium is widely used due to
malleability, high strength-to-weight ratio and resistance to corrosion. As use of
aluminium has increased in various applications, thus machining requirement of this
alloy has also increased proportionally.

The main applications of aluminium alloy 7075-T7451 are airplane structures [4];
automotive ancillary parts made of A356 aluminium alloy; key structural components
made of 7010 aluminium alloy [5]; wheels, vehicle structure, automotive parts made
of aluminium 6061 alloy [6–9]; parts of infantry combat vehicles, aircrafts made of
aluminium 7039 alloy [10]. Other applications find in electronic, in civil construction
and packaging industries [11].

Aluminium alloys possess low melting point, high thermal and electrical conduc-
tivity and high corrosion resistance. Advanced mechanical properties can be added
to primary aluminium to form alloys with chemical reactions with magnesium, zinc,
copper and iron [12]. High-speed machining is generally used in aeronautics in
view of some advantages over conventional manufacturing processes. On account
of aluminium combinations with high machining speed increases the removal of
metal and diminishes the built up edge (BUE) and burrs [13, 14]. Using high-speed
machining increases in productivity and reduction in cost of product was observed
while machining aluminium alloys [15].

1.1 Machinability Characteristics

Machinability of a material is the ease; it can be machined at low cost with satisfactory
finish. The numerous parameters impact ability of machine tool; anyway they are
not accepted for quantification process. Generally, machinability aspects include
tool life, tool cost, surface quality, power consumption and cutting temperature. An
outline of the review paper is shown in Fig. 2.
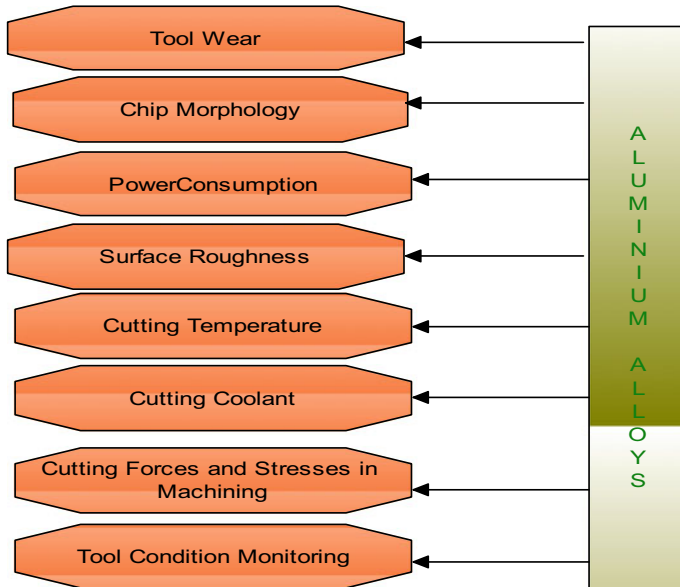
Fig. 2 Outline of paper

1.2 Tool Wear

In machining processes, tool wear affects the life of tool, dimensional accuracy and surface quality. While machining aluminium alloy flank wear is observed due to adhesive and abrasive wear mechanisms [16–18], adhesion the main wear mechanism in dry, turning on Al–Cu alloy is reported by Batista et al. (2019). They deduced that surface quality can be achieved for finishing and roughening operations with 1 mm depth of cut [19]. Crater wear and notch wear in machining Al alloy were reported by Kumar et al. [20].

Polycrystalline diamond (PCD) tools enhanced surface quality and reduced flank wear as compared to other cutting tools reported by Pattnaik et al. [21]. Due to kind diamond like properties, the PCD tools as compared to other multilayered coated tools can be better alternative [22, 23]. The chemical vapour deposition (CVD)-coated carbide drill provides stability in cutting force, less wear and provides machined quality better than PCD tools in machining of SiCp/Al composites [24].

1.3 Chip Morphology

The chips created from the workpiece material indicate material deformation behaviour during machining. Discontinuous and serrated chips as shown in Fig. 3a, b, d were obtained from the microcrystalline diamond (MCD), PCD and nanocrystalline
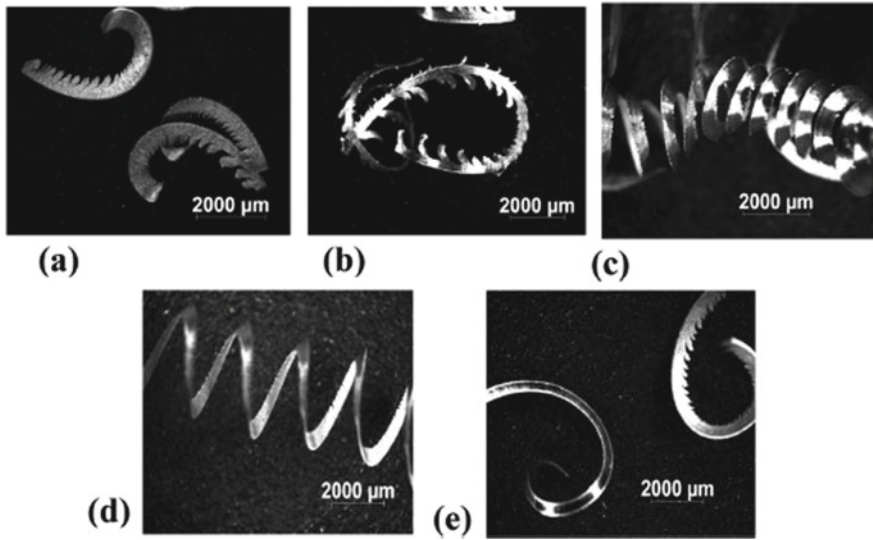
Fig. 3 **a** MCD-coated tool **b** NCD-coated tool **c** BDD-coated tool **d** BMTN-coated tool **e** PCD tool [25]

diamond (NCD) cutting tools while machining aluminium alloy AA2124/25%SiCp MMC. In contrast, Fig. 3c, d continuous chips were obtained from boron-doped diamond (BDD) and boron-doped graded layer (BTMN)-coated tools. BMTN-coated tool shows less wear as compared to MCD, NCD, BDD and PCD tools as reported by Ramasubramanian et al. [25].

Jomma et al. (2017) developed FEM to analyse and simulate serrated chip formation during HSM of AA7075–T651 alloy. He reported that with an increase in the cutting speed chip segmentation intensity increased [26]. Wang et al. 27 too reported onchip formation while HSM Al alloy and Inconel superalloy. They reported the relationship between acoustic emission (AE) signal and chip morphology [27]. The serrated chips are produced due to ductile fracture with cutting speed range from 1000 to 5000 m/min, and fragmented chips are produced due to brittle fracture with cutting speed range from 5000 to 7000 m/min, respectively, reported by Wang et al. [28]. Prakash et al. [25] too reported on chip morphology in micro-end milling of Al alloy employing AE signals [29]. In spite of rake angle, the continuous chips were obtained with small feed (0.1 mm) and segmented chips were obtained with large feed (0.3 mm) for rake angles as shown in Fig. 4 for AA2024-T351 reported by Haddag et al. [30]. In a similar study of material, AA2024-T351 continuous chips were obtained with small feed (0.1 mm) and segmented chips were obtained with large feed (0.3 mm) [31].
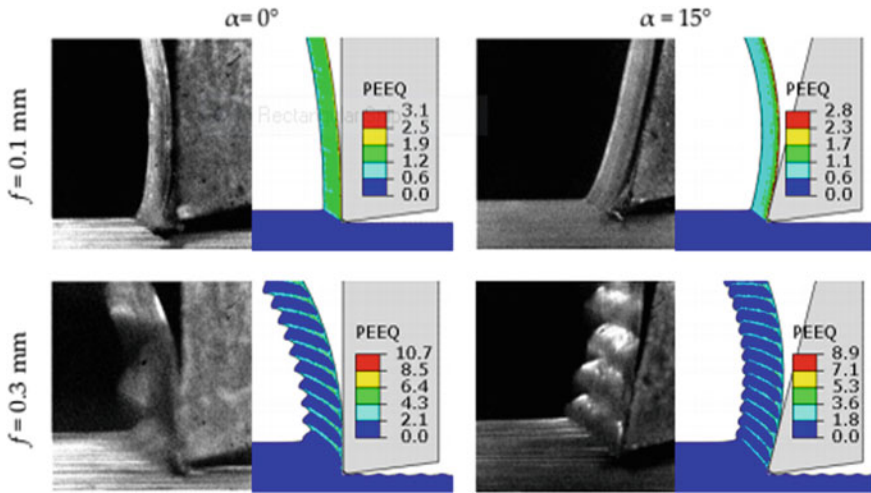
Fig. 4 Experimental versus numerical chips morphology for feeds and rake angles [30]

2 Power Consumption

During cutting energy consumption contributes noteworthy to production costs. The consumption of energy can be forecasted by machinability factors like machine tool components, energy consumption and cutting force which has great impact on the environment. The utilization of energy in actual machines describes about just 15% of the total quantity [32]. Sustainable manufacturing can be achieved by improving energy efficiency. Energy efficiency has gained significance in both industries and academia for many years [33]. Bezzera et al. (2001) reported that at low cutting speed of 25 m/min lowest power consumption can be achieved while reaming aluminium-silicon alloy [34]. Garg et al. [35] reported for turning process, the cutting speed is the most significant input parameter for power consumption [35]. At low speed and higher depth of cut and feed, several researchers found that minimum consumption of energy can be attained [36]. Depth of cut and feed rate are the most influential parameter for minimizing consumption of energy reported by Camposeco-Negrete [37]. Camposeco-Negrete [37] reported that feed rate is the most influential factor (87.79%) followed by depth of cut (6.59%) and cutting velocity (5.18%) while machining AISI 6061 T6 alloy. Energy consumption can be reduced by elevated feed rate, minimum depth of cut and cutting velocity [38].

2.1 Surface Roughness

Surface roughness is considered a vital parameter in manufacturing as decreased in surface roughness usually results in increasing production costs. Apart from

geometric and dimensional aspects, the most essential need is surface quality factor. Bhushan et al. [39] reported that PCD and carbides provide lesser surface roughness of Al alloy as compared to Al composite while turning 7075 Al alloy SiC composite [39]. PCD tool showed good performance than polycrystalline cubic boron nitride (PCBN) tools due to low adherence to work material and higher resistance [40]. Pathak et al. [41] reported that surface finishing can be improved by low feed rate and elevated cutting speed. Machining of Al–(1-2) Fe–1 V–1Si alloys the optimum cutting speed lies in the range of 125–175 m/min [41]. Titanium nitride (TiN) (K10) tool enhanced surface finish than the TP30-coated carbide tool [42]. Surface finish was achieved higher by K10 tool than PCD tool in the work carried out by Chambers and Stephens [43]. The feed rate is the most significant factor affecting surface roughness [44, 45]. Feed rate and spindle speed have great impact on surface roughness followed by radial depth of cut and axial depth of cut [46]. Surface roughness was observed increased with elevated feed rate and increases with increase in particle size. Higher surface roughness was observed while machining B4Cp—6061 composite with 88 μm particle size [47].

2.2 Cutting Temperature

Most broadly used one of the techniques to gauge the temperature in machining is the use of thermocouples. Notwithstanding thermocouples, infrared radiation systems are presumably the second most utilized technique for temperature quantification in machining. Tool wear increases, machining precision, surface integrity, can damage work piece due to high cutting temperature. Kelly et al. [48] used thermocouples to measure cutting temperature of aluminium alloy [48]. Life of tool is controlled by cutting temperature [49]. Due to higher hardness, cutting temperature was observed higher in machining of LM28 alloy than the LM13 alloy [50]. The tool–chip interface temperature was observed linearly with elevated cutting speed. [51]. The spindle speed, feed rate and point angle have a major effect on temperature generation while drilling AA (6351)-B4C composite. Decreasing of above parameters, temperature can be reduced [52]. Low speed, feed rate and depth of cut were chosen to minimize temperature rise in milling of AA6351-B4C composite [53]. Maximum temperature can be reduced in the workpiece by increasing feed per tooth in milling of aluminium alloys [54]. The infrared thermal image system was used to predict temperature in milling of aluminium alloys [55, 56].

2.3 Cutting Coolant

Cutting fluids are mainly responsible to provide lubrication at low cutting speeds and cooling at high cutting speeds. Cutting fluids can be classified as air, neat oils

(fatty oils, extreme pressure oils (EP), mineral oils), water-based cutting fluids (emulsions, synthetic fluids, water) [57]. Cutting fluids protect the surfaces from corrosion, prevent flank wear, evacuation of chips and improve surface quality [18, 48]. Mendes et al. (2006) applied cutting fluid as mist and flood with additives (chlorine, sulphur, phosphorous) in drilling of AA 1050-O Al and, turning of 6262- T6 Al alloy, respectively [58]. Though dry machining is not recommended, lubricant/cooling can be applied economically by minimum quantity lubrication (MQL) method [59, 60], MQL technique using water-based employing titanium dioxide (TiO$_2$) nanofluid was found effectual for edge integrity [61]. MQL method using united lubricants (UNIST) Coolube oil was found to produce acceptable surface integrity [62]. Sunflower oil was used in small quantity lubrication (SQL) method in milling of aluminium alloy. An uncoated carbide tool outperformed over the diamond-coated tools under SQL and dry conditions [63]. Palm oil suits better and minimized cutting force and vibrations in the milling of aluminium MMC than other vegetable oils (coconut, sunflower and soya bean) [64]. Vegetable-based cutting fluids (VBCFs) manifest promising results in terms of tool wear as compared to commercial mineral cutting fluid (CMCF) as reported by Kuram et al. [65]. Neem seed oil was found more effective than soluble oil for the cutting of Al–Mn alloy [66]. Modified (Jatropha and Pongamia) oil as cutting fluids can be used economically as biodegradable and environmental-friendly cutting fluids. The better surface finish was observed for modified Pongamia (MPO) and (MJO) modified Jatropha at low and high speeds, respectively [67]. Jatropha vegetable oil shows better results than canola oil and semi-synthetic oil in machining of 7050-T7451 aluminium alloy. In the same processing conditions with employing Jatropha vegetable oil lifespan of cutting tool exceeded 6 times using flood method as compared to MQL method [68]. Pham et al. (2014) used ionic liquids lubricant in milling of Al 5052 and observed better surface quality achieved with the high viscosity ionic liquid as compared to conventional liquids [69]. Inclusion of Ionic fluid in cutting fluids increased the oil friction coefficient by 4.89% and reduced wear volume by 28.75% reported by Ferri et al. [70].

2.4 Cutting Forces and Stresses in Machining

The knowledge of cutting forces is necessary to the machinist because excellent machine performance, cutting–edge geometry, accuracy, tool selection and tool life and so on closely associated with the resulting cutting forces. FE models were developed to simulate machining processes of aluminium alloys to predict cutting forces [71–73]. Increases in rake angle either due to existence of BUE or fabrication process reduces mechanical forces [74, 75]. Textured tools reduce cutting forces [76, 77].

Cutting forces were reduced by employing and applying 10% fluid concentration at tool–work interface in turning of aluminium alloy AA 6162-T6 [78]. Cutting forces behaviour was analysed by using parametric model for high-speed aluminium alloys as a function of cutting speed and feed rate [79].

3   Tool Condition Monitoring (TCM)

Today condition monitoring systems has been widely accepted by manufacturing concerns for better quality product, prevent tool wear, eliminate inspection and enhance productivity. Condition monitoring is the procedure that evaluates soundness of equipment at regular intervals and uncovers early faults. The applications of tool condition monitoring (TCM) systems contribute to detect tool wear, avert tool breakage and progress in the stability of the machining process. A worn tool in machining operations can result in increase in friction between a piece of work and tool and power consumption elevated too [80, 81]. Gopikrishnan et al. (2014) observed tool condition status using acoustic emission (AE), accelerometer, while turning aluminium alloy. A worn out tool shows elevated dominant frequencies than good tool [82]. AE was used to monitor tool condition while turning Al alloy and observed AE increased with increase in spindle and feed rate. AE was observed higher due to higher tool wear [83]. In a similar study, tool condition monitored while turning aluminium alloy reported by researchers [84–86].

4   Summary

Machining of aluminium is a very easy task by minimizing adherence of material on tool–work interface, good chip evacuation and core strength of tool to endure cutting forces without breaking. In tool design, materials, coatings and geometry are three key elements minimizing these concerns. Diamond coatings in cutting of materials have significantly improved tool life. Maximum efficiency can be achieved in turning of aluminium alloys with high content of silicon with PCD tools or with diamond coatings. Usual wear as flank wear observed in machining of Al alloys and crater or even notch wear observed in alloys containing hard particles. Successful HSM is not possible if elements of coating, material and geometry do not work together. Accurate choice of cutting tools, cutting conditions, lubrication/cooling system is required for successful operation. The utilization of cutting fluid in MQL and flood method will favour all the machining parameters of the material. TCM is significant in any machining operation. AE is one of the most generally utilized signals for TCM owing signal is created by fundamental systems of machining tasks like tool wear, plastic deformation and fracture.

References

1. Budd, G. (1999). *Resources and production of aluminium.* Birmingham: European Aluminium Association.
2. Santos, M. C., Machado, A. R., Sales, W. F., Barrozo, M. A., & Ezugwu, E. O. (2016). Machining of aluminum alloys: A review. *The International Journal of Advanced Manufacturing Technology, 86*(9–12), 3067–3080.
3. https://www.statista.com/statistics/863681/global-aluminum-consumption/. Accessed 16 April 2020.
4. Tang, Z. T., Liu, Z. Q., Pan, Y. Z., Wan, Y., & Ai, X. (2009). The influence of tool flank wear on residual stresses induced by milling aluminum alloy. *Journal of Materials Processing Technology, 209*(9), 4502–4508.
5. Flynn, R. J., & Robinson, J. S. (2004). The application of advances in quench factor analysis property prediction to the heat treatment of 7010 aluminium alloy. *Journal of Materials Processing Technology, 153,* 674–680.
6. Burger, G. B., Gupta, A. K., Jeffrey, P. W., & Lloyd, D. J. (1995). Microstructural control of aluminum sheet used in automotive applications. *Materials Characterization, 35*(1), 23–39.
7. Cole, G. S., & Sherman, A. M. (1995). Light weight materials for automotive applications. *Materials Characterization, 35*(1), 3–9.
8. Lucas, G. (1996). Aluminum structural applications.*Advanced Materials & Processes, 149,* 29–30.
9. Irving, B. (1998). Interest in welded aluminum automobiles gathers momentum worldwide: Aluminium welding. *Welding Journal, 77*(6), 31–35.
10. Anoop, C. A., & Kumar, P. (2013). Application of Taguchi methods and ANOVA in GTAW process parameters optimization for aluminium alloy 7039. *International Journal of Engineering and Innovative Technology (IJEIT), 2.*
11. Shankar, M. R., Chandrasekar, S., Compton, W. D., King, A. H. Characteristics of aluminum 6061-T6 deformed to large plastic strains by machining. *Materials Science and Engineering: A* 410–411:364–368
12. Hatch, J. E. (1984). Aluminum: Properties and physical metallurgy. *American Society for Metals, Ohi,* p 424, Chap. 6.
13. Balkrishna, R., Yung, C. S. Analysis on high-speed face-milling of 7075-T6 aluminum using carbide and diamond cutters. *International Journal of Machine Tools & Manufacture, 41*(12), 1763–1781.4 (1984). https://doi.org/10.1016/s0890-6955(01)00033-5
14. Soren, T. R., Kumar, R., Panigrahi, I., Sahoo, A. K., Panda, A., & Das, R. K. (2019). Machinability behavior of aluminium alloys: A brief study. *Materials Today: Proceedings, 18,* 5069–5075.
15. Subbaiah, A. R., Sivaram, N. M., & Senthil, P. (2017). Parametric optimization of high speed CNC turning operation for improving the surface quality of (AA6063-T6) aluminium alloy components. *International Journal of ChemTech Research, 10*(2), 923–932.
16. Kannan, S., & Kishawy, H. A. (2008). Tribological aspects of machining aluminium metal matrix composites. *Journal of Materials Processing Technology, 198*(1–3), 399–406.
17. Sreejith, P. S. (2008). Machining of 6061 aluminium alloy with MQL, dry and flooded lubricant conditions. *Materials Letters, 62*(2), 276–278. https://doi.org/10.1016/j.matlet.2007.05.019.
18. Roy, P., Sarangi, S. K., Ghosh, A., & Chattopadhyay, A. K. (2009). Machinability study of pure aluminium and Al–12% Si alloys against uncoated and coated carbide inserts. *International Journal of Refractory Metals & Hard Materials, 27*(3), 535–544.
19. Batista, M., Del Sol, I., Gomez-Parra, A., Ramirez-Peña, M., & Salguero, J. (2019). Study of the tool wear process in the dry turning of Al–Cu alloy. *Metals, 9*(10), 1094.
20. Ramasubramanian, K., Arunachalam, N., & Rao, M. R. (2019). Wear performance of nano-engineered boron doped graded layer CVD diamond coated cutting tool for machining of Al-SiC MMC. *Wear, 30*(426), 1536–47.

21. Pattnaik, S. K., Bhoi, N. K., Padhi, S., & Sarangi, S. K. (2018). Dry machining of aluminum for proper selection of cutting tool: tool performance and tool wear. *The International Journal of Advanced Manufacturing Technology, 98*(1–4), 55–65.

22. Ding, X., Liew, W. Y. H., & Liu, X. D. (2005). Evaluation of machining performance of MMC with PCBN and PCD tools. *Wear, 259*(7–12), 1225–1234.7.

23. da Silva, R. B., Machado, Á. R., Ezugwu, E. O., Bonney, J., & Sales, W. F. (2013). Tool life and wear mechanisms in high speed machining of Ti–6Al–4 V alloy with PCD tools under various coolant pressures. *Journal of Materials Processing Technology, 213*(8), 1459–1464.

24. Xiang, J., Xie, L., Gao, F., Yi, J., Pang, S., & Wang, X. (2018) Diamond tools wear in drilling of SiCp/Al matrix composites containing copper. *Ceramics International, 44*(5), 5341–5351.

25. Ramasubramanian, K., Arunachalam, N., & Rao, M. R. (2019). Wear performance of nano-engineered boron doped graded layer CVD diamond coated cutting tool for machining of Al-SiC MMC. *Wear, 426*, 1536–1547.

26. Jomaa, W., Mechri, O., Lévesque, J., Songmene, V., Bocher, P., & Gakwaya, A. (2017). Finite element simulation and analysis of serrated chip formation during high–speed machining of AA7075–T651 alloy. *Journal of Manufacturing Processes, 26,* 445–446.

27. Wang, B., & Liu, Z. (2017). Acoustic emission signal analysis during chip formation process in high speed machining of 7050-T7451 aluminum alloy and Inconel 718 superalloy. *Journal of Manufacturing Processes, 27*, 114–125. https://doi.org/10.1016/j.jmapro.2017.04.003

28. Wang, B., & Liu, Z. (2016). Investigations on deformation and fracture behavior of workpiece material during high speed machining of 7050-T7451 aluminum alloy. *CIRP Journal of Manufacturing Science and Technology, 14,* 43–54. https://doi.org/10.1016/j.cirpj.2016.05.007.

29. Prakash, M., Kanthababu, M., & Rajurkar, K. P. (2015). Investigations on the effects of tool wear on chip formation mechanism and chip morphology using acoustic emission signal in the microendmilling of aluminum alloy. *The International Journal of Advanced Manufacturing Technology, 77*(5–8), 1499–1511.

30. Haddag, B., Atlati, S., Nouari, M., & Moufki, A. (2016). Dry machining aeronautical aluminum alloy AA2024-T351: Analysis of cutting forces, chip segmentation and built-up edge formation. *Metals, 6*(9), 197. https://doi.org/10.3390/met6090197.

31. Kouadri, S., Necib, K., Atlati, S., Haddag, B., & Nouari, M. (2013). Quantification of the chip segmentation in metal machining: Application to machining the aeronautical aluminium alloy AA2024-T351 with cemented carbide tools WC-Co. *International Journal of Machine Tools and Manufacture, 1*(64), 102–113.

32. Pusavec, F., Krajnik, P., & Kopac, J. (2010). Transitioning to sustainable production—Part I: Application on machining technologies. *Journal of Cleaner Production, 18*(2), 174–184.

33. Kaneko, J., Horio, K. (2012). Planning method for fixture conditions of workpiece in continuous multi-axis controlled machining process with consideration of energy consumption about translational axes of machine tool. In *5th CIRP Conference on High Performance Cutting* (pp. 126–131).

34. Bezerra, A. A., Machado, A. R., Souza Jr, A. M., & Ezugwu, E. O. (2001). Effects of machining parameters when reaming aluminium–silicon (SAE 322) alloy. *Journal of Materials Processing Technology, 112*(2–3), 185–198. https://doi.org/10.1016/s0924-0136(01)00561-1

35. Garg, A., Lam, J. S. L., & Gao, L. (2016). Power consumption and tool life models for the production process. *Journal of Cleaner Production, 131,* 754–764.

36. Lv, J., Tang, R., Tang, W., Jia, S., Liu, Y., & Cao, Y. (2018). An investigation into methods for predicting material removal energy consumption in turning. *Journal of Cleaner Production, 193*, 128–139.

37. Camposeco-Negrete, C. (2015). Optimization of cutting parameters using Response Surface Method for minimizing energy consumption and maximizing cutting quality in turning of AISI 6061 T6 aluminum. *Journal of Cleaner Production, 91*, 109–117.

38. Camposeco-Negrete, C. (2013). Optimization of cutting parameters for minimizing energy consumption in turning of AISI 6061 T6 using Taguchi methodology and ANOVA. *Journal of Cleaner Production*, *53*, 195–203.

39. Bhushan, R. K., Kumar, S., & Das, S. (2010). Effect of machining parameters on surface roughness and tool wear for 7075 Al alloy SiC composite. *The International Journal of Advanced Manufacturing Technology, 50*(5–8), 459–469. https://doi.org/10.1007/s00170-010-2529-2.

40. Ding, X., Liew, W. Y. H., & Liu, X. D. (2005). Evaluation of machining performance of MMC with PCBN and PCD tools. *Wear, 259*(7–12), 1225–1234.

41. Pathak, B. N., Sahoo, K. L., & Mishra, M. (2013). Effect of machining parameters on cutting forces and surface roughness in Al-(1-2) Fe-1 V-1Si alloys. *Materials and Manufacturing Processes, 28*(4), 463–469.

42. Sahin, Y., Kok, M., & Celik, H. (2002). Tool wear and surface roughness of Al_2O_3 particle-reinforced aluminium alloy composites. *Journal of Materials Processing Technology, 128*(1–3), pp. 280–291.

43. Chambers, A. R., & Stephens, S. E. (1991). Machining of Al- 5 Mg reinforced with 5 vol.% Saffil and 15 vol.% SiC. *Materials Science and Engineering: A, 135*, 287–290.

44. Bb, R. (2016). Optimization of machining parameters for turning of Al6061 using robust design principle to minimize the surface roughness. *Procedia Technology, 24,* 372–378.

45. Rao, C. J., Rao, D. N, & Srihari, P. (2013). Influence of cutting parameters on cutting force and surface finish in turning operation. *Procedia Engineering, 64*, 1405–1415.

46. Okokpujie, I. P., Ajayi, O. O., Afolalu, S. A., Abioye, A. A., Salawu, E. Y., & Udo, M. (2018). Modeling and optimization of surface roughness in end milling of aluminium using least square approximation method and response surface methodology. *International Journal of Mechanical Engineering and Technology (IJMET), 9*(1), 587–600.

47. Hiremath, V., Badiger, P., Auradi, V., Dundur, S. T., & Kori, S. A. (2016). Influence of particle size on cutting forces and surface roughness in machining of B4Cp-6061 aluminium matrix composites. In *IOP Conference Series: Materials Science and Engineering* (Vol. 114, No. 1, p. 012041). IOP Publishing.

48. Kelly, J. F., & Cotterell, M. G. (2002). Minimal lubrication machining of aluminium alloys. *Journal of Materials Processing Technology, 120*(1–3), 327–334.

49. Nouari, M., List, G., Girot, F, & Coupard, D. (2003). Experimental analysis and optimisation of tool wear in dry machining of aluminium alloys. *Wear, 255*(7–12), 1359–1368.

50. Dwivedi, D. K., Sharma, A., & Rajan, T. V. (2008). Machining of LM13 and LM28 cast aluminium alloys: Part I. *Journal of Materials Processing Technology, 196*(1–3), 197–204.

51. Reis, D. D., & Abrao, A. M. (2005). The machining of aluminium alloy 6351. *Proceedings of the Institution of Mechanical Engineers, Part B: Journal of Engineering Manufacture, 219*(1), 27–33.

52. Samy, G. S., & Kumaran, S. T. (2017). Measurement and analysis of temperature, thrust force and surface roughness in drilling of AA (6351)-B4C composite. *Measurement, 103,* 1–9.

53. Samy, G. S., Kumaran, S. T., & Uthayakumar, M. (2017). An analysis of end milling performance on B 4 C particle reinforced aluminum composite. *Journal of the Australian Ceramic Society, 53*(2), 373–383.

54. Denkena, B., Brüning, J., Niederwestberg, D., & Grabowski, R. (2016). Influence of machining parameters on heat generation during milling of aluminum alloys. *Procedia CIRP, 46,* 39–42.

55. Patru, E.N., Craciunoiu, N., Panduru, D., & Bica, M., June. Study on cutting temperature and surface roughness during the milling process of aluminium alloys. In *IOP Conference Series: Earth and Environmental Science* (Vol. 172, No. 1, p. 012018). IOP Publishing.

56. Tang, Z. T., Liu, Z. Q., Pan, Y. Z., Wanb, Y., & Ai, X. (2009). The influence of tool flank wear on residual stresses induced by milling aluminum alloy. *Journal of Materials Processing Technology, 209,* 4502–4508.

57. Sales, W. F., Diniz, A. E., & Machado, Á. R. (2001). Application of cutting fluids in machining processes. *Journal of the Brazilian Society of Mechanical Sciences, 23*(2), 227–240.

58. Mendes, O. C., Avila, R. F., Abrao, A. M., Reis, P., & Davim, J. P. (2006). The performance of cutting fluids when machining aluminium alloys. *Industrial Lubrication and Tribology., 58*(5), 260–268.

59. Braga, D. U., Diniz, A. E., Miranda, G. W., & Coppini, N. L. (2002). Using a minimum quantity of lubricant (MQL) and a diamond coated tool in the drilling of aluminum–silicon alloys. *Journal of Materials Processing Technology, 122*(1), 127–138.

60. Itoigawa, F., Childs, T. H. C., Nakamura, T., & Belluco, W. (2006). Effects and mechanisms in minimal quantity lubrication machining of an aluminum alloy. *Wear, 260*(3), 339–344.
61. Najiha, M. S., Rahman, M. M., & Kadirgama, K. (2016). Performance of water-based TiO_2 nanofluid during the minimum quantity lubrication machining of aluminium alloy, AA6061-T6. *Journal of Cleaner Production, 135,* 1623–1636.
62. Najiha, M. S., Rahman, M. M., & Kadirgama, K. (2015). Machining performance of aluminum alloy 6061-T6 on surface finish using minimum quantity lubrication. *International Journal of Automotive & Mechanical Engineering, 11.*
63. Iyappan, S. K., & Ghosh, A. (2019). Small quantity lubrication assisted end milling of aluminium using sunflower oil. *International Journal of Precision Engineering and Manufacturing-Green Technology*, 1–9.
64. Shankar et al. (2017). Influence of vegetable based cutting fluids on cutting force and vibration signature during milling of aluminium metal matrix composites. *Jurnal Tribologi, 12,* 1–17.
65. Kuram, E., Ozcelik, B., Huseyin Cetin, M., Demirbas, E., & Askin, S. (2013). Effects of blended vegetable-based cutting fluids with extreme pressure on tool wear and force components in turning of Al 7075-T6. *Lubrication Science, 25*(1), 39–52.
66. Yakubu, S. O., & Bello, M. Y. (2015). Evaluation of neem seed oil as a cutting fluid in orthogonal machining of aluminum manganese alloy (AL-MN) in turning operation. *European Journal of Engineering and Technology, 3*(3).
67. Jeevan, T. P., & Jayaram, S. R. (2018). Performance evaluation of jatropha and pongamia oil based environmentally friendly cutting fluids for turning AA 6061. *Advances in Tribology.*
68. Bork, C. A. S., Gonçalves, J. F. S., & Gomes, J. O. (2015). The Jatropha curcas vegetable base soluble cutting oil as a renewable source in the machining of aluminum alloy 7050–T7451. *Industrial Lubrication and Tribology., 67*(2), 181–195.
69. Pham, M. Q., Yoon, H. S., Khare, V., & Ahn, S. H. (2014). Evaluation of ionic liquids as lubricants in micro milling–process capability and sustainability. *Journal of Cleaner Production, 76*, pp. 167–173.
70. Ferri, C., Lizarazo, S., Troise, M., Iglesias, P. Ionic liquids as additives to cutting fluids to reduce machine tool friction and wear. In *ASME 2018 International Mechanical Engineering Congress and Exposition*,9 Nov 2018. American Society of Mechanical Engineers Digital Collection.
71. Giasin, K., Hodzic, A., Phadnis, V., & Ayvar-Soberanis, S. (2016). Assessment of cutting forces and hole quality in drilling Al2024 aluminium alloy: experimental and finite element study. *The International Journal of Advanced Manufacturing Technology, 87*(5–8), 2041–2061.
72. Haddag, B., Atlati, S., Nouari, M., Barlier, C., & Zenasni, M. (2012). Analysis of the cutting parameters influence during machining aluminium alloy A2024-T351 with uncoated carbide inserts. *Engineering Transactions, 60*(1), 31–39.
73. Davoudinejad, A., Parenti, P., & Annoni, M. (2017). 3D finite element prediction of chip flow, burr formation, and cutting forces in micro end-milling of aluminum 6061-T6. *Frontiers of Mechanical Engineering, 12*(2), 203–214. https://doi.org/10.1007/s11465-017-0421-6.
74. Saglam, H., Unsacar, F., & Yaldiz, S. (2006). Investigation of the effect of rake angle and approaching angle on main cutting force and tool tip temperature. *International Journal of Machine Tools and Manufacture, 46*(2), 132–141.
75. Gómez-Parra, A., Álvarez-Alcón, M., Salguero, J., Batista, M., & Marcos, M. (2013). Analysis of the evolution of the Built-Up Edge and Built-Up Layer formation mechanisms in the dry turning of aeronautical aluminium alloys. *Wear, 302(*1–2), 1209–1218.
76. Sasi, R., Subbu, S. K., & Palani, I. A. (2017). Performance of laser surface textured high speed steel cutting tool in machining of Al7075-T6 aerospace alloy. *Surface and Coatings Technology, 313*, 337–346.
77. Rathod, P., Aravindan, S., & Venkateswara, R. P. (2016). Performance evaluation of novel micro-textured tools in improving the machinability of aluminum alloy (Al 6063). *Procedia Technology, 23*, 296–303.
78. Mendes, O. C., Avila, R. F., Abrao, A. M., Reis, P., & Davim, J. P. (2006). The performance of cutting fluids when machining aluminium alloys. *Industrial Lubrication and Tribology, 58*(5), 260–268.

79. Salguero, J., Batista, M., Calamaz, M., Girot, F., & Marcos, M. (2013). Cutting forces parametric model for the dry high speed contour milling of aerospace aluminium alloys. *Procedia Engineering, 63,* 735–742.
80. Ahuja, I. P. S. & Khamba, J. S. (2008). Total productive maintenance: literature review and directions. *International Journal of Quality & Reliability Management*.
81. Addad, T. H., & Jaaron, A. A. (2012). The applicability of total productive maintenance for healthcare facilities: an implementation methodology. *International Journal of Business, Humanities and Technology, 2*(2), 148–155.
82. Gopikrishnan, A., Kanthababu, M., Balasubramaniam, R. and Ranjan, P. (2014). Tool condition monitoring in microturning of aluminium alloy using multiple sensors. In *Applied Mechanics and Materials* (Vol. 592, pp. 796–800). Trans Tech Publications Ltd.
83. Chockalingam, P., Ervina, E. M. N., & Prabhu, C. M. R. (2018). Tool condition monitoring in turning using acoustic emission. In *AIP Conference Proceedings* (Vol. 2030, no. 1, p. 020310). AIP Publishing LLC.
84. Fang, N., Pai, P. S., & Mosquea, S. (2010). The effect of built-up edge on the cutting vibrations in machining 2024-T351 aluminum alloy. *The International Journal of Advanced Manufacturing Technology, 49*(1–4), 63–71.
85. Inayatullah, O., & Sinnasamy, V. (2017). Condition monitoring of the uncoated carbide cutting tool in turning process of the aluminum alloy 6061 via vibration. *Periodicals of Engineering and Natural Sciences, 5*(3).
86. GARCÍA-SANZ-CALCEDO, J., SALGADO, D. R., & GONZÁLEZ, A. G. (2016). Drilling projects by tool condition monitoring system (TCMS). *Engineering Transactions, 64*(4), 555–561.

Taguchi Multi-machining Characteristics Optimization of W–Al–SiC Alloy

Manoj Kumar and Naveen Anand Daniel

Abstract In this experiment and study, Taguchi techniques and methods are employed to seek out the optimal process parameters for high speed steel cutting tool for machining W–Al–SiC bar. This paper clarifies the findings of the experimental impacts that are gotten to choose appropriate reducing parameters that check that less vitality utilization in high tare CNC machines. Using Taguchi strategy, the test was conducted with an expelled W–Al–SiC aluminum bar on CNC machines with three parameters as a process. Force expended (energy); output characteristic was estimated with the help of a data procurement framework. The info was analyzed and appropriate process parameters were chosen for least utilization. The experimental and study of the results have provided to verify the effectiveness of this approach. The CNC turning machine is used to conduct experiments based on the Taguchi design of experiments (DOE) with an orthogonal L9 array.

Keywords CNC lathe · Aluminum alloy · Taguchi techniques

1 Introduction

Cutting parameters are reflected on metal removal rate and dimensional deviations of the merchandise. Metal removal rate (MRR) which is employed to see and to gauge the standard of a product is one among the foremost quality attributes of a turning product. The Taguchi technique might be utilized a statistical tool's, embraced experimentally to break down the impact of three cutting parameters like feed, cutting velocity and profundity of cut of the aluminum bar [1]. Taguchi method has employed by to determine a correlation between feed rate and cutting speed Taguchi design

M. Kumar (✉)
ABES Engineering College, Ghaziabad, India
e-mail: manojkumar@abes.ac.in

N. A. Daniel
Amity University Uttar Pradesh, Noida, India
e-mail: nadaniel@amity.edu

optimizing technique has been employed in CNC milling so as to enhance the parameters for metal removal rate. Taguchi technique employed in order to see the optimal cutting parameters for MRR in turning of W–Al–SiC alloy [2]. Taguchi method was applied for locating out the optimal value of metal removal rate and surface finishing under optimum cutting condition in turning W–Al–SiC alloy, and the results thereof were analyzed with the assistance of research of variance method. Orthogonal array of Taguchi method plus gray relation analysis for the optimizing two responses like metal removal rate and tool wear rate.

2 Objective

In turning process, surface completion relies on a few info parameters and the association between those parameters. So for finding the optimal cutting parameters for MRR and microstructure of surface completion in turning, Taguchi strategy is applied in this study. This study incorporates the following focuses.

- To study the exhibition characteristics operations of W–Al–SiC bars utilizing HSS cutting apparatus.
- To show a methodical strategy of utilizing Taguchi method design in process control of turning machines.
- To exhibit a utilization of the Taguchi parameter design configuration so as to distinguish the ideal surface roughness execution with a specific mix of cutting boundaries in turning operation.

3 Taguchi's Approach

Taguchi approach could be a very notable procedure that has a logical and proficient strategy for the procedure enhancement and this can be a strong instrument for the arranging of top quality frameworks [3, 4]. The sign to commotion proportion qualities might be isolated into three classifications when the trademark is persistent: ostensible is that the best; smaller the higher and greater are more beneficial attributes. For the negligible cutting temperature, the appropriate response is "smaller is better" and sign to commotion proportion is set per the resulting condition. Quality is regularly drawn nearer to as conformance to determinations [5]. In any case, Taguchi proposes distinctive perspective on quality joined that relates it to cost and misfortune in cash, not simply to the maker at the hour of creation, however, to the purchaser and to the general public as a full. In the event of machining, the vitality expended or the force request shifts on account of commotion factors which are named internal, external and between item clamors [6, 7]. To constrict the outcomes brought about

by these clamor factors, a few countermeasures could likewise be thought of. The first significant is by decision which has includes:

(i) tolerance, (ii) system, (iii) parameter

Following Taguchi method steps:

(i) Select a reasonable output quality characteristic to be optimized.
(ii) Select commotion factors and their levels.
(iii) Select adequate inner and outer arrays. Control factors appointed to inner array and commotion factors to the outer array.
(iv) Execute factual examination dependent on S/N proportion.
(v) Foresee ideal yield execution level dependent on ideal control factor level blend and direct an affirmation investigation to check the outcome.

4 Introduction to Turning Process

Turning is that the procedure acclimated produce barrel-shaped segments on a machine. It will be done physically or utilizing CNC machine. In turning, a tube-shaped bit of texture is pivoted and a cutting execute is crossed along two toma-hawks of movement to give exact measurement and profundities. Turning will be either on the skin of the chamber or on the inside to give rounded segments to various geometries. Turning will be performed physically on traditional machine with focus machines which are not electronic. Then again, turning is likewise done utilizing programmed machines worked by talented mechanical engineers. Present day practice is moving toward the usage of CNC controls like a CNC machine.

5 Optimization of Experiment

The Taguchi strategy is a notable procedure that has a logical and effective technique for process advancement and this can be a solid device for the arranging of prime quality frameworks [8, 9]. Taguchi way to deal with style of trials in simple to receive and apply for clients with restricted information on insights, consequently, increased wide prevalence inside the designing and academic network. This can be a designing procedure for acquiring item and procedure condition, which are negligibly delicate to the shifted reasons for variety, and which produce top-notch items with low turn of events and assembling costs. His commitments have additionally made the professional work just by pushing the use of less exploratory plans, and giving a more clear comprehension of the variety nature, and furthermore the monetary outcomes of value building inside the universe of delivering.

6 Turning Process

Turning may be a broadly utilized machining process within which one point cutter expels material from a pivoting workpiece and creates a cylindrical-shaped surface. The cutter is fed linearly in an exceedingly direction parallel to the axis of rotation. Turning is completed on a CNC lathe machine that offers the facility to show the workpiece at a given rotational speed and to require care of the cutting device at a feed rate and depth of cut. During this way, three cutting boundaries, i.e., cutting rate, feed rate and depth of cut must be decided during a turning operation. A typical technique for evaluation machining execution in an exceedingly turning activity depends on the surface roughness. Essentially, surface unpleasantness is emphatically related to cutting boundaries, as an example, cutting speed, feed rate and depth of cut. Consequently, the optimization of the cutting boundaries smitten by the parameters structure of the Taguchi method is received during this investigation to enhance roughness in an exceedingly tuning.

7 Selection of Cutting Parameters

In a turning activity, it is an imperative undertaking to select cutting parameters for accomplishing high cutting execution. For the most part, the necessary cutting parameters are resolved upheld experience or utilization of a handbook. In any case, this does not ensure that the picked cutting parameters have ideal or close to ideal cutting execution for a particular machine and condition. To choose the cutting parameters appropriately, a few numerical models bolstered relapse method or neural figuring are built to learn the association between the cutting execution and furthermore the cutting parameters. At that point, a target work with imperatives is defined to disentangle the ideal cutting parameters utilizing advancement methods. Thusly, extensive information and ability are required for utilizing this contemporary methodology. In this way, the predetermined model structure is staggeringly exorbitant as far as your time and materials. Taguchi strategy is utilized here to work out the necessary cutting parameters in turning activity. There are number of cutting parameters for turning activities which has profundity of cut, feed rate, cutting pace, embed sweep, assortment of coolant, successive cut and so on. Other than the impacts of cutting parameters, the impacts of their collaborations on surface unpleasantness may touchy for the standard trademark in turning process. The suggested possible scope of cutting parameters for the workpiece material, apparatus and machine utilized is taken from machining handbook as, cutting rate inside the scope of 212–525 rpm, feed rate inside the range 0.35–0.42 mm/rev up and depth of cut inside the scope of 0.5–2 mm, in this way four degrees of the cutting parameters.

8　Results and Discussion

In the present work, the optimization of cutting parameters in turning is finished by use of Taguchi techniques. Three parameters therefore the depth of cut at the four levels are selected make use of Taguchi approach. The L9 orthogonal array has been selected for 9 set of experiments as given within the observation as shown in Table 5. To review the performance characteristic in turning of W–Al–Si–C bar using high speed steel cutter. The results of the metal removal rate as shown in Table 5 are demonstrated that which parameters critical to the method. Usually, the method parameter having the max-min value greater than the half the utmost of max-min value is that the significant process parameters. So from Table 5, cutting speed has less effect or negligible effect on the method. So as to assess the accuracy and efficiency of present work, an example involving the three parameters at three levels was taken from a book and compared with these results for optimization of cutting parameters for turning. Finally, the validation of this work is finished with number of problems available in literature associated with Taguchi method. The main points of validation of this work are discussed within the following section. In this experiment, I have used three factors for three values and conducted 9 experiments. When contrasted with above technique, the Taguchi orthogonal array makes rundown of 9 examinations in an incredibly specific request which spread all variables which is given inside Table 5. Those nine examinations will give 99.96% exact outcome. By utilizing this strategy, the number of analyses diminished to 9 rather than 27 with practically same exactness. Taguchi fought that traditional inspecting is lacking here as there is not any method of getting an arbitrary example of future conditions. Taguchi proposed broadening each trial with an "external exhibit" or symmetrical cluster ought to mimic the irregular condition inside which the examination would work. There is decrement of fabric removal rate with the increasing feed rate; it means there should be some optimized feed rate at which the machining of fabric is benefited. For this developed material/alloy of aluminum, the feed rate is often kept around 0.5 mm/rev and below 0.50 mm/rev for better machining.

In case of normal aluminum alloy, the material removal rate increases as we increase the depth of cut, but for this developed and optimized invented material,

Table 1 Compositions of W–Al–SiC

S.no.	Metal	Range (%)
1.	SiC	14.5
2.	Si	12.5
3.	Mg	0.55
4.	Fe	0.10
5.	W	2.5
6.	Mn	0.10
7.	Ti	3.5
8.	Al	66.25

Table 2 Mechanical properties of W–Al–SiC

Alloy	Tensile strength (MPa)	Modulus of elasticity (GPa)	Hardness (BHN)	Density (gm/cm^3)
W–Al–SiC	295	95	112	3.225

Table 3 Single point cutting tool features

S.no.	Angle	Limiting value	True value
1.	Side rack angle	$6–10^0$	8^0
2.	Back rack angle	$7–9^0$	8^0
3.	Side cutting angle	$10–15^0$	13^0
4.	End cutting angle	$8–12^0$	11^0
5.	Side relief angle	$4–8^0$	8^0
6.	End relief angle	$6–8^0$	7^0

Table 4 Taguchi orthogonal array

S.no.	Spindle speed (rpm)	Feed rate (mm/rev)	Depth of cut (mm)
1.	2	1	1
2.	2	2	1
3.	2	2	2
4.	3	3	2
5.	3	3	3
6.	3	3	2
7.	2	2	3
8.	2	2	3
9.	2	3	2

Table 5 Observation table

S.no	Spindle speed (rpm)	Feed rate (mm/rev)	Depth of cut (mm)	Time (second)	Initial weight (gr.)	Final weight (gr.)	Difference of weight (gr.)	MRR (gr./sec)
1.	213	0.37	1.5	11.5	208	196	12	1.043
2.	213	0.39	1	11.5	196	187	9	0.819
3.	213	0.42	0.5	9.3	187	182	5	0.544
4.	342	0.36	1	8.6	182	171	11	1.295
5.	342	0.39	0.5	7.9	170	166	5	0.642
6.	342	0.42	1.5	7.2	166	165	4	0.564
7.	527	0.36	0.5	5.2	165	162	3	0.589
8.	527	0.39	1.5	5.4	162	156	6	1.133
9.	527	0.42	1	5.3	156	151	5	0.962

at initially, the MRR increases with increment of depth of cut and if we further increase the depth of cut the MRR decreases drastically so with higher depth of cut the machining will be difficult hence again we have to optimized the depth of cut. In my study, we concluded that the depth of cut is below 1 mm and above 0.50 mm with the mentioned speed. With increasing spindle speed, the variation of different parameters is obtained from the Taguchi optimization technique is listed in the observation Table 5. The results obtained from the experiments which show the variation of depth of cut and feed rate on the working parameters on the basis of logarithmic scale are given in Figs. 1 and 2 (Fig. 3).
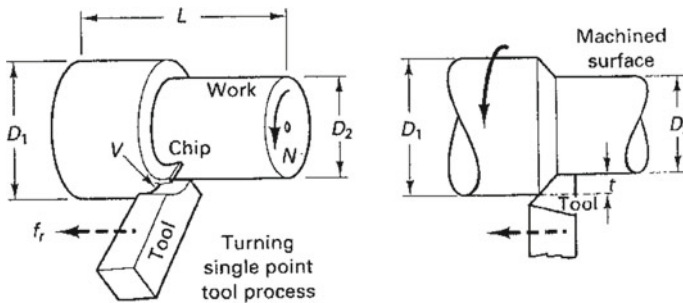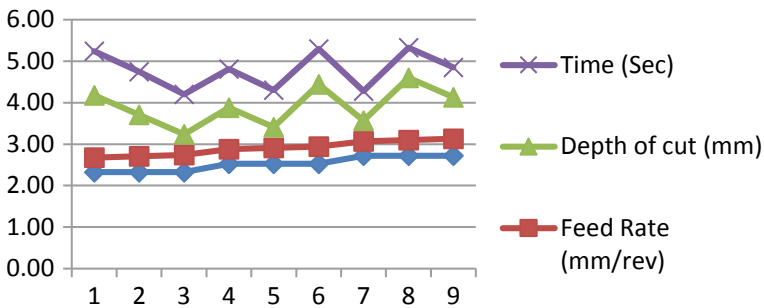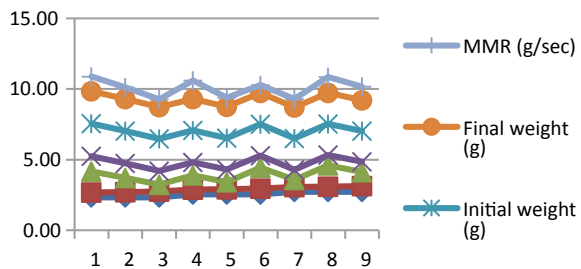

Fig. 1 Basic turning operations

Fig. 2 Comparisons of results obtained from the experiments

Fig. 3 Variation of all the parameters that are obtained experimentally

9   Conclusions

The utilization of symmetrical exhibit with attractive quality capacity examination to advance the W–Al–SiC machining process with various execution attributes has been accounted for during this paper and there results and correlations are appeared previously. The attractive quality capacity examination of the test consequences of surface unpleasantness and force utilization can change over enhancement of the numerous exhibition attributes in streamlining of the sole execution trademark called the composite allure esteem. Subsequently, the enhancement of the convoluted various presentation attributes is frequently significantly streamlined through this methodology. It is indicated that the presentation qualities of the turning procedure W–Al–SiC metal lattice composites like force utilization are improved together by utilizing the strategy proposed during this examination. The MRR is obligated for the surface completing; microstructures moreover a component which ought to be considered to shows signs of improvement surface completion, thus, to improve surface completion, we have to decide the various perspectives like smooth activity, legitimate force utilization, and in this way, the powers created inside the apparatus still as inside the activity.

10   Applications

This material can be used in various applications. The volume to weight ratio is comparatively low with comparison to other types of ferrous and non-ferrous alloys. It can be machined and shaped with easier manner. As we obtained the results and properties obtained of this developed material, it can be also used in some structural applications too. With having tungsten and silicon carbide (SiC), it can resists higher temperature. With having low volume to weight ratio, this material can be used in aerospace applications. Aluminum has less corrosive property and also has greater corrosion resistance it can be used in marine's components creations too because of higher aluminum contents.

11   Future Scope

There is a large requirement of the advanced testing of this developed alloy in case of the properties optimizations in machining and applications. We can use the different two tools for the machining to obtain better values of the machining parameters. We can check the cutting forces and temperature developed during cutting/machining; hence, we can save the tool also. So with these testing, we can increase the tool life with the better machining characteristics.

References

1. Ramanujam, R., Raju, R. (2010). Taguchi multi-machining characteristics optimization in turning of Al-15%SiCp composites using desirability function analysis. *Journal of Studies on Manufacturing*, *1*(2-3), 120-125.
2. Gopalaswami, B. M., et al. (2009). Taguchi method and ANOVA: An approach for process parameter optimization of hard machining while machining hardened steel. *Journal of Scientific & Industrial Research, 68,* 686–695.
3. Singh, Hartaj. (2012). taguchi optimization of process parameters: A review and case study. *International Journal of Advanced Engineering Research and Studies, IJAERS/Vol., I,* 39–41.
4. Krishankant, J. T., Bector, M., & Kumar, R. (2012). Application of Taguchi method for optimizing turning process by the effects of machining parameters. *2*(1). ISSN: 2249 – 8958.
5. Kohli, A., & Dixit, U. S., (2005). A neural-network-based methodology for the prediction of surface roughness in a turning process. *International Journal of Advanced Manufacturing Technology*, *25*, 118–129.
6. Ankit Kumar Saxena1, Angad Yadav2, Ashish Kumar3, Krishna Yadav4. (2018). Optimization of machining parameters for turning of aluminium alloy LM4 using Taguchi method. *International Research Journal of Engineering and Technology (IRJET), 05*(04).
7. Singh, O. P., Kumar, G., & Kumar, M. (2019). Multi performance optimization of shoulder milling process parameters of AA6063 T6 Aluminium Alloy by Taguchi based GRA. *International Journal of Innovative Technology and Exploring Engineering (IJITEE), 8*(10S). ISSN: 2278-3075.
8. Vates, U. K., Sharma, B. P., Kanu, N. J., Daniel, N. A., Subramanian, S., Sharma, P. (2020). Optimization of process parameters of galvanizing steel in resistance seam welding using RSM. In *Proceedings of International Conference in Mechanical and Energy Technology. Smart Innovation, Systems and Technologies*, (vol. 174, pp. 695–706). Singapore: Springer. Print ISBN: 978-981-15-2646-6, Online ISBN: 978-981-15-2647-3. https://doi.org/10.1007/978-981-15-2647-3_65
9. Daniel, N. A., Singh, N. K., Vates, U. K., Sharma, B. P., Subramanian, S. (2019). Optimization of critical parameters of EDD steel in die cavity manufacturing. In *Advances in industrial and production engineering* (pp. 357–363). Lecture Notes in Mechanical Engineering. Singapore: Springer. Print ISBN: 978-981-13-6411-2, Online ISBN: 978-981-13-6412-9. https://doi.org/10.1007/978-981-13-6412-9_34.

Development of Flexible Solar PV Panel Cleaning System

Uren Mistry, Nidhi Panchal, Ujas Modi, Chetan O. Yadav, and P. V. Ramana

Abstract Solar energy is a major renewable source of energy and is now contributing to about 60–70% in the power generation sector for countries like India. Mostly, large solar farms are located in defoliated areas. These areas are more prone to dusty environment and bird droppings. This interference of pollutants reduces the power generating capacity of the PV module up to 50% if the modules are not cleaned over a period of month or two. The goal behind the development of flexible solar panel cleaning system is to minimize the adverse impact of pollutants on the panel surface thereby increasing the output of the PV modules. We have designed a mechanical system comprising of fine spray nozzle, helical brush, wiper, and driving mechanism which are actuated by Arduino UNO and motor driver. Solar PV modules are also incorporated on the roof to sustain power generation for the functioning of the system. This system is flexible to do dry and wet cleaning according to the requirement.

Keywords Dry and wet cleaning · Solar panel · Automatic cleaning · Flexible system · Panel efficiency · Nozzle · Wiper

U. Mistry · N. Panchal (✉) · U. Modi
Mechanical Engineering Department, Sardar Vallabhbhai Patel Institute of Technology (SVIT), Vasad, India
e-mail: nidhipanchal207@gmail.com

U. Mistry
e-mail: urenmistry12@gmail.com

U. Modi
e-mail: Ujasmodi26@gmail.com

C. O. Yadav · P. V. Ramana
Gujarat Technological University, Ahmedabad, Gujarat, India
e-mail: coyadav@gmail.com

P. V. Ramana
e-mail: pvr261@gmail.com

1 Introduction

Energy is indisputably a resource on which humanity has become dependent. Without energy, our society will not function. Historically, fossil fuel has enabled our energy consumption and continues to dominate the energy production. Due to their rapid consumption, a need has arisen to find out other sources of energy generation. The renewable energy resources include solar, wind, tidal, and biogas. Among this, solar energy is available to us in abundance and hence trials are been made to fulfill the world's power requirement with the solar energy. This grave demand of power led to the development of silicon photovoltaic panels. India is blessed with a large amount of sunlight. We receive solar radiation in the range of 4 to 7 kwh/m^2/day [1]. Such a huge amount of radiation is good enough to generate electricity to fulfill our entire electricity requirement using solar PV technology. Electric energy can be produced with photovoltaic (PV) panels from solar energy which is an infinite heat and light source. During this transformation, all of the radiation coming to the surface of the PV panels cannot be converted to electricity. Many losses occur during the related photovoltaic event. These losses are reflection, shadowing, contamination, differences in module specifications, low radiation, temperature, conductor, and inverter losses [6, 7].

A number of environmental factors such as wind speed, humidity, ambient temperature, solar radiation, atmospheric dust, and direction influence the power generation process using installed solar photovoltaic modules [2]. The glass cover transmittance decreases because of accumulation of dust on the surface of PV module, which ultimately decreases the amount of solar irradiation reaching the cells. The dust density of the surface, orientation, the tilt angle, exposure period, dominant wind direction, and site climatic conditions determines the reduction in glass transmittance [3, 4]. Factors such as choosing the appropriate geographical location and beam angle, selecting the right equipment and kept the surfaces of the panels clean should be considered to minimize these losses [7–9].

Shadowing effect occurs when the PV panels does not receive the same amount of incident irradiance level throughout the system due to obstacles. Under this effect, the panels absorb the power instead of producing it. The short circuit current of the shaded cell reduces to around 90%. Shadowing effect also results into generation of hotspots. The cells adjacent to the shaded cells push the current through the shaded regions in order to complete the circuit which will result in heating of shaded regions causing hotspots to generate. Even a single shaded cell in a module affects the overall module performance. Thus, the overall power loss of the module corresponds to the shaded area. Bypass diodes are used to reduce the impact of shadow effect and protect the solar panel. It allows current to pass shaded cells and thereby reduce the voltage losses through the module. Bypass diodes also serves another purpose, namely prevention of hotspots.

In order to prove the severity of the defined issue, we captured thermal images of the panel's surfaces depicting the variation in temperature observed over the panel surfaces due to deposition of birds excrete.

(1.a)   (1.b)   (1.c)
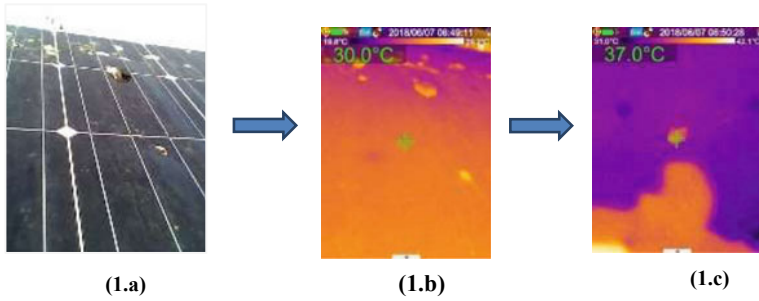
Fig. 1 Thermal image taken from the handheld thermal imaging camera

The pictorial demonstration in Fig. 1. (1.a) shows a picture of the birds excrete sticked on the panel surface. Figure 1 (1.b) shows the thermal image of the surface without birds dropping with temperature of about 30 degrees Celsius. (1.c) shows a huge difference of 7 °C in temperature as compared to that indicated in Fig. 1 (1.b) as it shows the temperature of the spot with excrete sticked on it. Hence this temperature variation proves that the issue of birds excretes is a severe issue which leads to the heating of the panels thereby contributing in their performance decrement. Soiling losses refer to loss in power resulting from snow, dirt, dust, and other particles that cover the surface of the PV module.

Dust is a thin layer that covers the surface of the solar array, and the typical dust particles are less than 10 mm in diameter but this depends on the location and its environment. Dust is generated from many sources such as pollution by wind, pedestrian volcanic eruptions, and vehicular movements among many others [8]. The layers of dust accumulated on the panel affects the panel output of daily, weekly, and monthly basis.

The graph shown in Fig. 2 is the output data obtained from a 20 kW solar farm. The graph depicts that within the duration of one week starting from May 27 Saturday to June 2 Friday, there is continuous decrement in the power output generated. Power generated is reduced to about 50%.

Once the panels are installed on their rigid fabricated support, they are expected to generate power for next 20–25 years. In order to retain the panels to its maximum power generation capacity, they should be cleaned in regular interval of time. A dirty

Fig. 2 Graph showing the decreasing rate of power generated
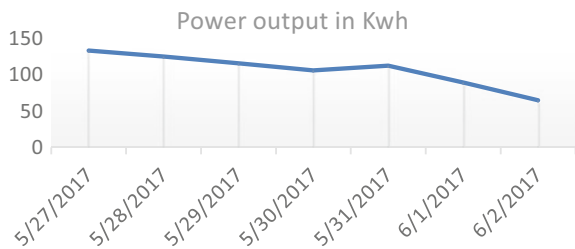
panel when cleaned manually consumes approximately minimum 2–2.5 L of water per minute per panel. Hence, water requirement for a huge number of solar panels installed in an array increases to tons of water. So, in arid region, where the power losses are more prone to occur, cleaning of panels is difficult due to scarcity of water. Also, cleaning of solar farms stretched in large acres of land is labor intensive and time consuming. Also due to frequent scrubbing of panels, scratches are developed on the top of the toughen glass resulting in reducing the absorption capacity of the panels.

There are many cleaning methods apart from manual cleaning which are electrostatic cleaning and robotic cleaning.

1.1 Manual Cleaning

It is only feasible for residential solar installation. It is more labor intensive, time consuming, and there are high chances that scratches may be formed due to frequent brushing as well as huge wastage of water [5].

1.2 Electrostatic Cleaning Method

An electrodynamics screen placed on the solar panel can automatically remove dust from the dusty solar panel without any use of water or any other moving parts; more than 98% of the dust on a glass placed can be removed using electrostatic travelling waves generated by a four-phase rectangular voltage applied to a transparent conveyer consisting of transparent indium tine oxide electrodes. This technology is not suitable for use in mega solar system because the electrodes are very expensive [5].

1.3 Robotic System

This system is used for brushing away the dust on the solar panel with or without using water. This mode of cleaning reduces the labor cost and time required for cleaning but the power consumption and initial cost tend to be very high for robotic system. Some of the robotic system consumes power from the solar panel installed on the device. It has a greater number of moving parts whose reliability is of concern [5].

2 Objective

In this paper, our main objective is to solve the adversities caused by shadowing, soiling, and bird dropping and to minimize the water, time, and manpower consumed during regular cleaning of the panels by developing a flexible semi-automatic system. Hence, our proposed system is developed to conduct cleaning process with or without using water as per the requirement.

3 Methodology and Design

The goal behind this project is to develop a flexible solar panel cleaning system that can help us to solve the problems of power loss due to soiling, bird dropping, shadow, etc., to achieve this goal; we have designed a system by considering the efficient driving mechanism, materials, and components. This system is modified in way to make it flexible enough to undertake dry, wet, or both simultaneously depending on the weather conditions and geographical location of the solar farms. Also, a single person can easily handle the system and can install it on the row of the solar panel.

3.1 Material Selection

In order to make it light weighted, we choose aluminum alloy-6082. This material has excellent corrosion resistance properties and has tensile strength of 150 max MPa, 40 HB hardness with good machinability. Side plates and core of the helical brush are made up of this aluminum alloy. The fabrication of the rotating helical brush comprises of nylon bristles of thickness of 0.15–0.2 mm diameter to make the helical brush. Nylon material does not generate the scratches on the panel and harm the panel in both dry and wet cleaning. Also, it can easily blow off the suspended dust particles in dry cleaning, sticky bird dropping in wet cleaning. Note that the thickness of the bristles changes as the location of the solar farm's changes and also with the type of the dust particles the panels is going to be in contact sticky particulate require the bristles quite thicker than the ones used in dry and arid regions.

3.2 Nylon Helical Brush

Initially, we choose the single start nylon helical brush which has single time point of contact with panel in complete one rotation. We can also provide double start to helical brush to increase the number of contacts per rotation which will improve the

cleaning rate. "Pitch of helical brush" also influences the type of cleaning obtained as an output. Pitch of the brush is decided 'with lesser tilt angles require brush with less pitch, i.e., a denser brush to sweep out the dust toward the edge of the panels.

3.3 Driving Mechanism

Now talking about the driving mechanism, so there are many driving mechanisms like gear train, belt drive, chain drive. In this system, we had chosen the chain and sprocket as a driving mechanism because of its flexibility and advantages. The center distance and alignment are not so critical for chain drive compared with gear drive. It gives flexible drive and can easily isolate vibrations over gear drive. In addition, chain drive can transmit high torque with low speed than belt drive. The strength flexibility of chain drive is higher than other driving mechanisms. Also, it is available with all the possible standard sizes in market due to which maintenance of the system is much easier if there is any interruption caused in functioning of the mechanism.

3.4 Motor

Apart from these, we have selected high torque DC motor which gives adequate torque of 70 N-Cm and stall torque of 200 N-Cm with required rpm of 30 for driving the mechanism and 300 for the helical brush. So, system can easily cross obstacles and the small bridges which will arise between two panels during the cleaning. For this calculation, we have used below-mentioned Eqs. (1) and (2).

$$v = r * \frac{2 * \pi N}{60} \tag{1}$$

$$T = F * r \tag{2}$$

where, v = liner speed of the wheel m/s.

r = radius of wheel in m.

N = rpm of the wheel.

T = minimum torque required to rotate the wheel in N-m.

F = force on each wheel in N.

3.5 Power Transmission

Power is transmitted from the top plate to the bottom plates by connecting the motions of all the four wheels altogether. These connectors are type of hollow pipe which eliminate the vibration and buckling during the motion of the robot. This function of four-wheel drive eliminates the twisting of the robot due to speed variation between the wheels.

3.6 Self-charging

The system has its solar panel mounted over the top to charge the battery so that no additional power is required to charge the battery. At the front end, series connection of flat fan nozzle to spray fine water droplets and at the rear end wiper is assembled. Electrical system and driving mechanism are isolated from rain, dust, and environmental pollutants by placing them into an isolated box. An additional plugin socket is also available in order to charge the battery if there is any urgent requirement or the self-charging panel is not able to store enough power to recharge the battery fully (Fig. 3).

4 Working

A solar panel mounted over the system charges the 12 V DC battery which is in turn transmits the power to the motors. The Arduino UNO board is used to give command to the motor driver and the proximity sensors. When the motor receives the actuating signal, the system starts to move along the rows of the panels covering six panels per minute while the helical brush moves in the opposite direction. Along with the movement of the robot along the panels, the water is supplied through the flat fan nozzles. The wiper is installed at the rear end of the robot to enable it to wipe out even the smallest drop of water leaving the panel surface dry. The simultaneous working of the nylon helical brush, nozzle, and the wiper cleans the panels in the smooth manner (Fig. 4).

The chain and sprocket driving mechanism allows the robot to move without vibration due to which the panel's life is not risked. The proximity sensors will allow us to control the movement of the system by restricting its movement by sensing the presence of obstacle if any.

The flowchart shown in Fig. 5 represents the programmable circuit of motor driver and proximity sensor with the Arduino UNO board. The first step is to interface the sensor and driver with Arduino UNO circuit. Using the "IF AND THEN" condition, we put up a condition in which as soon as the IR sensor senses the presence of any metal object which turn on the LED light and stops the operation of the motor at that
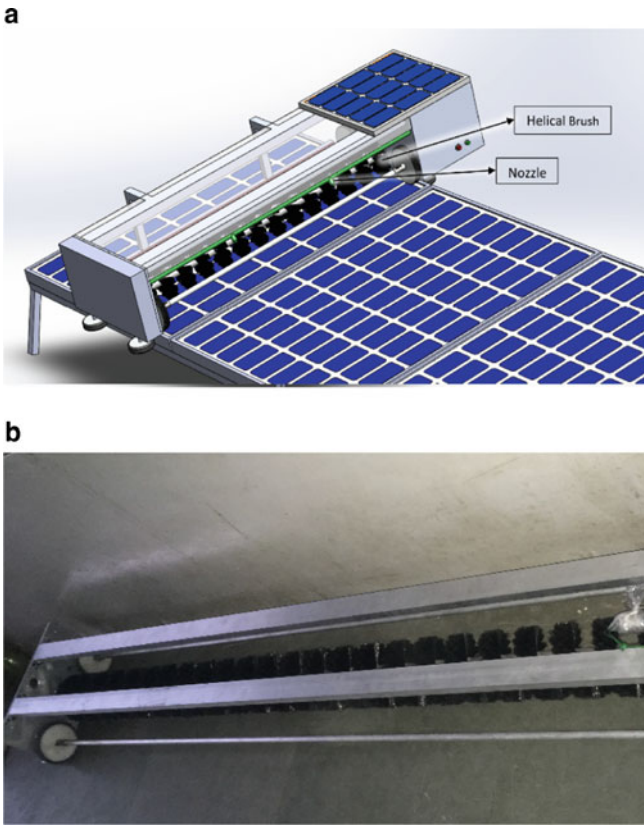
Fig. 3 **a** Rear side of model showing the nozzle assembly. **b** Front side of nozzle with wiper
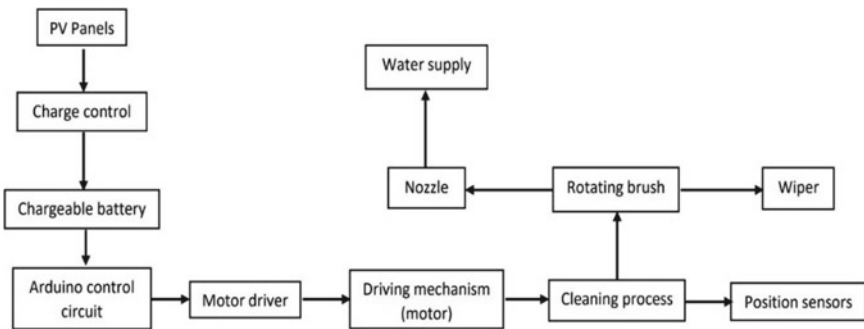
Fig. 4 Process flow chart

Fig. 5 Flowchart showing connection made between Arduino UNO, motor driver and proximity sensors
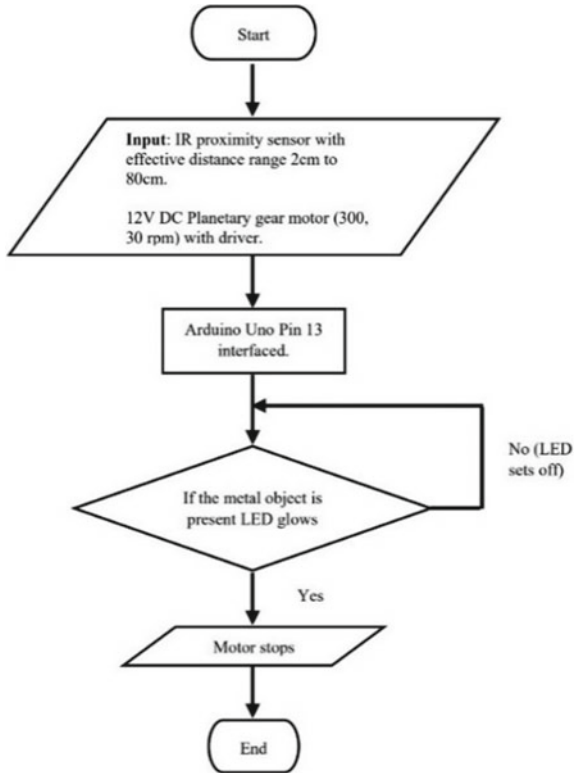
very instant. We have used IR proximity sensors with effective detection distance of 2–30 cm and detection angle of 35°. IR proximity is suitable for precise object positioning because of its high repeatability. Due to its non-contact output, it has a long life and requires practically no maintenance. The sensor operates at the 3.3 kHz of response frequency. The system continues to move along its pre-defined path if there is no presence of metal obstacle. By providing the automation to our system, we have tried to reduce the human interference as much as possible. For further advancement, it is also possible to add Bluetooth connections to the Arduino Uno board and also sensors which can sense the presence of predefined layer of dust accumulated on the surface and can undergo cleaning automatically.

5   Limitations

- The solar panel mounted over the system may not be able to generate enough power to drive the system during cloudy days. Hence provision of external charging should be there to charge the battery in such environmental condition.

- There is no automatic cleaning arrangement being made for the panels mounted over the top of the robot.

6 Conclusion

The crucial impact of dust accumulation, bird excrete, and shadowing effect on the generated output and the potential solutions introduced so far studied. To minimize the water consumption and other obstacles faced in achieving maximum output, we have developed a system which requires less human interference. The mounting of different components makes the system flexible enough to undertake cleaning with or without usage of water depending on different geographical locations and environmental conditions. We have used Arduino programming to interface the sensor and motor drivers on the system. This will give automatic motion to the system. In the future work, trials will be conducted in order to quantify the benefit by comparing the power generation of the cleaned and uncleaned solar PV panels.

7 Future Scope

- A docking yard can be fabricated attached to the end of solar panel rows. This can help to keep the robot isolated from the environmental impurities. Provision of external charging can also be provided at this docking yard.
- Temperature sensors, LDR sensors, photo electric sensors, Wi-Fi connections can also be loaded in the programs to help the robot to sense the presence of dust and bird droppings and to undertake the cleaning function automatically when given any command by Wi-Fi connections.

References

1. Jiang, Y., & Abu Qahouq, J. A. (2011). Multiple solar panels maximum power point tracking using the output current. In: *2011 IEEE 33rd International Telecommunications Energy Conference (INTELEC)*, Amsterdam (pp. 1–5).
2. Devaraj, S., Selvan, P., David Blessley, S., Sankaranarayana Murthy, A., & Wesley Moses Samdoss, S. (1993). *An Innovative Method of Solar Panel Cleaning System MS El- Shobokshy, FM Hussein, Sol Energy, 51*, 505.

3. Elminir, H. K., Ghitas, A. E., Hamid, R. H., ElHussainy, F., Beheary, M. M., & Abdel-Moneim, K. M. (2006). *Energy Conversion and Management, 47,* 3192.
4. Elminir, H. K., Ghitas, A. E., Hamid, R. H., ElHussainy, F., Beheary, M.M. & Abdel Moneim, K. M. (2006). *Energy Conversion and Management, 47*, 3192.
5. Ramesh Kumar, T., Najeeb, N. S., & Soori, P. K. (2018). A low-cost and energy-efficient smart dust cleaning technique for solar panel system. In: *International Conference on Smart Grid and Clean Energy Technologies.*
6. Mutluer, M., & Erat, A. (2019). A new intelligent system design for cleaning the photovoltaic solar panel surface. *Editorial Board Members of IJEAT, 6*(1), 8–16.
7. Chouder, S. S. (2009). Analysis model of mismatch power losses in PV systems. *Journal of Solar Energy Engineering, 131*(2).
8. Maghami, M. R., Hizam, H., Gomes, C., Radzi, M. A., Rezadad, M. I., & Hajighorbani, S. (2016). Power loss due to soiling on solar panel—A review. *Renewable and Sustainable Energy Reviews, 59,* 1307–1316.
9. Touati, F. A., Al-Hitmi, M. A., & Bouchech, H. J. Study of the effects of dust, reltive humidity, and temperature on solar PV performance in Doha, comparison between monocrystalline and amorphous PVS. *International Journal of Green Energy, 10*, 680–689.

Effect of Metallic Fillers on Mechanical Properties of FRP Composite

Aditya Pratap Singh, Avinash Yadav, Srashti Mishra, K. L. A. Khan, and Anurag Gupta

Abstract Using of fibre reinforced polymer (FRP) composites, due to their high specific modulus and corrosion resistance properties, becomes a common practice as an alternative to heavyweight metallic materials. Using metallic fillers in FRP composites provides electromagnetic shielding but can affect their mechanical and thermal properties. In this study, glass fibre reinforced polyester composite sheets are fabricated with mild steel as filler. Mild steel filler is extracted from gear grinding waste of CNC machine. An experiment is conducted to check the effect of metallic filler on tensile and flexural strength of FRP composite. Both flexural and tensile strength first decrease on the addition of filler content up to 15% while an increment has been observed when filler content is increased from 15 to 25% which is explained on the basis of dispersion of filler and bonding of filler particles with resin molecules.

Keywords FRP · Electromagnetic shielding · Specific modulus · Filler · Flexural strength · Tensile strength

1 Introduction

Due to their low weight along with structural stability, FRP composites have attracted the interest of research scholars. Heavyweight, low specific modulus traditional materials are being replaced by low weight, high specific modulus FRP composites, mainly in automobile and aircraft. Originally, FRP composites are electrical insulator and thus fail to avoid turbulence in aircraft, if used, as unable to provide

A. P. Singh · A. Yadav · S. Mishra (✉)
Department of Mechanical Engineering, KIET Group of Institutions, Ghaziabad, India
e-mail: srashti.1640166@kiet.edu

A. P. Singh
e-mail: aditya.1640011@kiet.edu

A. Yadav
e-mail: avinash.1640038@kiet.edu

K. L. A. Khan · A. Gupta
Mechanical Engineering, KIET Group of Institutions, Ghaziabad, India

electromagnetic shielding. Klemperer et al. [1] reported that though material need not be electrically conductive in order to provide shielding, it enhances the effect. In scrubber, where limited electrical conductivity is required, continuous wrapping of aluminium fibre on FRP pipes is being used [2]. Currently, use of FRP composites is common in applications requiring electrical insulation but there are applications which require it to be an electrical conductor. Filling metallic material in resin of FRP composites prove to be a successful approach in order to do so. Ha et al. [3] reported that the electrical conductivity of carbon fibre-based FRP can be improved as high as four times using silver nano-particles. Kupke et al. [4] discussed various methods to improve electrical conductivity including using conductive resin or filling resin with conductive fillers. In their study, carbon black particles were used and showed that their electrical conductivity follows the percolation theory. The mechanical properties were not compromised for the sake of the addition of carbon black filler content up to the value of 1.5% by weight. Tsangaris et al. [5], in their studies assisted by percolation theory, show a rapid increment in electrical conductivity of FRP composite at critical phase when a chaotic mixture of copper, aluminium, or zinc randomly distributed in electrically insulated matrix. So sufficient study has been done to prove the fact that electrical conductivity can be improved using metallic or conductive fillers. It is equally important to maintain the balance between electrical, mechanical, and thermal properties of the composite in order to use them in practical applications. Pujan et al. [6] conducted a study on glass fibre-based epoxy composite using aluminium powder as filler which shows decrement in tensile strength on adding filler. Glass fibre reinforced polymer (GFRP) composites have advantages such as high specific modulus, good stiffness, and corrosion resistance when compared to traditional materials [7]. Glass fibre shows high tensile and laminate strength along with fatigue, heat, and chemical resistance. Isophthalic polyester resin shows good adhesion to glass fibre and have good strength, heat, and chemical stability. So isophthalic polyester and fibre glass, together, can form chemically and mechanically stable structure. Anurag et al. [7] in their study show that tensile strength of pultruded GFRP (PGFRP) composite, when the mixture of carbon black (CB), bagasse fibre (BF), and calcium carbonate ($CaCO_3$) used as filler, increases with the increase of bagasse fibre while decreases with the increase of carbon black and calcium carbonate. Anurag et al. [8] conducted an experiment to study the effect of fibre as well as filler percentage on various properties in an unsaturated polyester-based GFRP with calcium carbonate ($CaCO_3$) as filler. With constant matrix %, the composition of reinforcement and filler was varied to check their impact on toughness variation, impact, and tensile strength. Glass fibre content increased the properties whereas there was a decrement with filler %. The reason for this was given to be the cluster formation of filler particles. However, the finishing was better with increased filler material. In an attempt for multi-response optimization of mechanical properties of PGFRP, Anurag et al. [9] found optimized combination of

hybrid filler of BG, CF, and $CaCO_3$ and on compression of PGFRP, improvement in cross-sectional shrinkage, bending strength, and hardness was observed with decrement in tensile strength. Hiremath et al. [10] added aluminium hydroxide powder as filler in different % with 50% glass fibre as reinforcement and rest of the matrix material (epoxy resin). Their concern was to study the effect of the filler on mechanical as well as fire retardant properties of GFRP. The results revealed that with the increase in % of filler added, the tensile as well as flexural strength decreases. However, the fire retardation increased with the increase in filler content. It can be inferred that the addition of filler in the resin can affect the mechanical properties of composite and thus there is a requirement of studying mechanical properties also.

2 Experimental Details

2.1 Material Used

Gear grinding waste. Gear grinding waste released by CNC machine was obtained from Nav Bharat Engineering Works, Ghaziabad, in the form of mixture of mild steel and coolant (see Fig. 1).

Resin and reinforcement. Below-mentioned material was procured from Maliwara, Nehru Nagar, Ghaziabad.

Unsaturated Isophthalic Polyester Resin; Methyl–Ethyl Ketone Oxide; Cobalt 6%; Glass fibre–Woven: 450 gsm (bidirectional, at 90º) Chopped-strand mat: 350 gsm; Polyester Film: Thickness 75 μ.

Fig.1 Grinding waste

3 Experimentation

3.1 Extraction of Filler

Filler was extracted from gear grinding waste. It was in the form of the mixture of mild steel and coolant, so there was a need to separate mild steel particles from the waste coolant. This process was done through a set of operations as mentioned below:

- Coolant was removed by burning in the open hearth.
- Unburnt carbon particles in ash were removed by decantation technique.
- Wet filler obtained after decantation was dried out by heating in bottom loading furnace.
- Then again to make material purer, it was separated using magnetic separation.
- At last, to gain fine and uniform particle size, sieve separation had done to using 53-μ sieve.

3.2 Filler Size Estimation

After extraction of filler material from grinding waste in fine powdered form (see Fig. 2), it had become necessary to estimate filler size so as to predict its effect more accurately on inherited characteristics of resin when mixed in it. Filler size is estimated using microscope in the laboratory of KIET School OF Pharmacy, Ghaziabad (see Fig. 3). Size of 50 particles was observed manually through microscopic view on micrometer. Average size of filler particles is 27.71 μm.

Fig. 2 Separated mild steel filler

Fig. 3 Microscope for size estimation

3.3 Preparation of GFRP Sheets

In total, six GFRP sheets were prepared containing 0, 5, 10, 15, 20, and 25% mild steel filler in the resin.

Matrix Preparation. Matrix was prepared using unsaturated isophthalic polyester resin which is a thermosetting polymer with long chain cross-link covalent bonding. It is taken 3 times of the weight of reinforcement. Methyl-ethyl ketone (MEK) peroxide, a colourless, flammable organic peroxide, non-reactive to water with flash point at 20º F [11], used as hardener which causes cross linkage of monomers of the resin by creating free radicals. In actual, it starts the reaction and responsible for hardening of resin. It is taken 1–2% of the volume of resin. Cobalt 6% solution is used as promoter. It is also known as accelerator as it makes reaction fast and allows the curing of matrix at room temperature. It was added 0.2% of resin content. Metallic filler was added from 0 to 25% of resin by mass to the matrix with increment of 5% each time. These four contents were measured accurately and mixed with a paint brush thoroughly. Matrix was prepared and used instantly to fabricate the composite; otherwise, it would have solidified in very less time.

Moulding-hand layup method. Moulding of FRP composite was done by hand lay-up method. Moulding was performed on flat wooden table with smooth surface. On a polyester film layering of resin was done first followed by woven glass fibre reinforcement. Again layer of resin was painted followed by chopped strand fibre and finally layer of woven glass fibre with resin at interface and top surface. It was finally covered with a polyester film and trapped air bubbles were removed using a roller. Polyester films were removed after drying of the composite.

The whole procedure was repeated for fabrication of GFRP composite sheets with different percentage of filler content (see Fig. 4). Bidirectional woven glass fibre is used to get uniform strength in both directions (perpendicular) as strength is supported by fibre orientation.
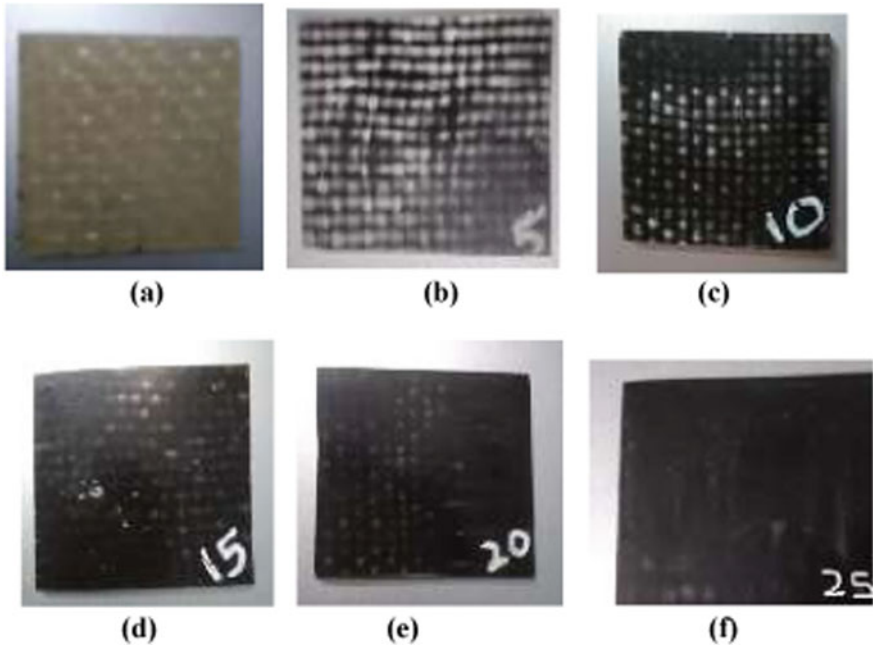
Fig. 4 Fabricated GFRP sheets with different filler content **a** 0%, **b** 5%, **c** 10%, **d** 15%, **e** 20%, **f** 25%

3.4 Preparation of Specimen

Specimens for flexural strength test were cut out from FRP sheets. The cutting procedure was done using a hand grinder. Three rectangular pieces were cut from sheets with different filler content so that testing results would be more accurate. So total 18 specimens were prepared as per ASTM D790 standards.

Similarly, 18 specimens were prepared for tensile strength test according to ASTM D638 (see Fig. 5). In addition, these specimens were given dumb-bell shape using bench grinder. Dimensions of specimens were varied and calculation of strength done accordingly.
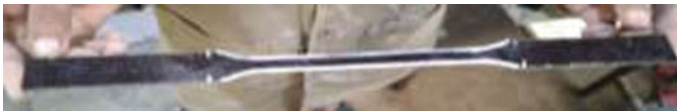
Fig. 5 Dumb-bell shaped tensile test specimen with 50 mm gauge length

3.5 Testing

Flexural Strength Test. After preparation, each of the specimen was tested for flexural strength on universal testing machine (UTM), using three-point bend fixture as per ASTM D790 (see Fig. 6). The whole testing procedure was done in Material Science Laboratory, Department of Mechanical Engineering, KIET Group Of Institutions, Ghaziabad. Specimen placed over the platform and load was applied on it by a probe attached to a movable cross-head till fracturing of the specimen. Load at the time of fracture was noted down.

Flexural strength can be calculated using maximum load during fracture of specimen. The whole system during the loading condition acted as simply supported beam over the stage in which single load was acted in middle by the probe.

Tensile Test. Tensile strength was tested on computerized UTM, Material Science Laboratory, Department of Mechanical Engineering, KIET Group Of Institutions, Ghaziabad, as per ASTM D638 test method. Dumb-bell-shaped specimen was assembled in between flat serrated jaws. Measurements such as width, thickness, and gauge length were fed in the UTM software and it was set to tensile test with rectangular specimen. Test was started from computer program. Strain was increased at a uniform rate till fracture. All the calculations were done by UTM software and digitalized graphs were obtained.

Fig. 6 3-Point bend fixture for flexural strength test

Fig. 7 Flexural strength versus filler % chart
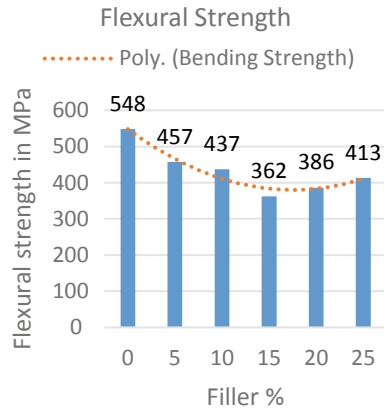
4 Results and Discussions

4.1 Flexural Strength Test

Result. When filler content varies from 0 to 15%, average value of flexural strength decreases from 548 to 362 MPa and with further increase of filler content up to 25%, average value of flexural strength increases to 413 MPa. A two-degree polynomial curve is best fitted in this trend of variation as (see Fig. 7).

Discussion. Flexural strength observed in the specimen without filler content was 548 MPa. As composite was filled with metallic filler material (MS), it was decreased to 457, 437, and 362 MPa for 5, 10, and 15% filler content specimen, respectively. Due to low filler content, its dispersion may have caused the formation of stress concentration zone and thus there is a decrement in flexural strength. Flexural strength of specimens was increased for the specimens with 20 and 25% filler content, i.e., 386 and 413 MPa, respectively. The flexural strength of GFRP composite with mild steel micro particle filler decreases up to 15% of filler amount and then start improving afterwards. This is because up to 15%, metal filler not sufficient to maintain continuity of filler in the composite so that these particles develop stress concentration zone. As the filler increases above 15%, the continuity can be seen from Fig. 4.

4.2 Tensile Strength Test

Result. Tensile strength observed, 134 MPa, for specimen with no filler content was maximum. The decrement in tensile strength with filler content was observed as 71, 57, and 57 MPa for 5, 10, and 15% filler content specimens, respectively. As

Fig. 8 Tensile strength
versus filler % chart
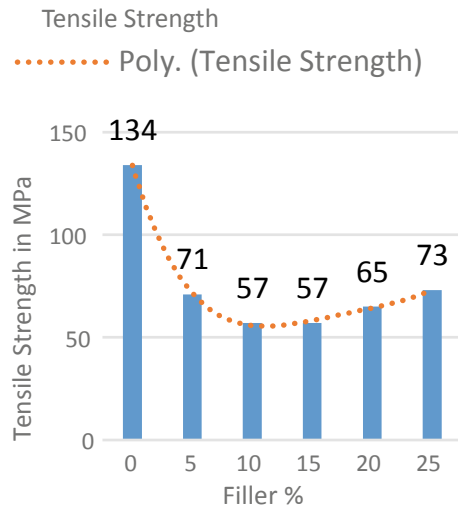
filler content increased further, tensile strength also improved and observed as 65 and 73 MPa for 20 and 25% filler content specimens, respectively. Figure 8 shows tensile strength of specimen with different filler content and trend line of four-degree polynomial best suits the values.

Discussion. The reason behind the behaviour of mild steel micro-filler particle on tensile strength of GFRP composite is quiet similar as discussed for flexural strength but the reduction of tensile strength is higher than the flexural strength because of the stress concentration zones developed in the composite are much dominant in longitudinal direction as compared to the lateral directions and the stress transfer between fibre is not as good as in lateral directions by filler particles.

5 Conclusion

The results show that the average tensile strength and flexural strength decrease up to 15% filler content. This may have caused by formation of stress concentration zones at some places due to non-uniform dispersion of metal filler particles mixed in resin. On further increase of filler content, tensile strength as well as flexural strength of GFRP composite shows improvement due to better dispersion of metal caused by increased % of filler in composite. It was also observed that the decrease in the tensile strength is more as comparative to the flexural strength. It was found that due to inclusion of mild steel micro-particle as filler in GFRP composite, composites start showing susceptibility to magnetization although measurement of magnetization is not carried out.

References

1. Klemperer, C., & Maharaj, D. (2009). Composite electromagnetic interference shielding materials for aerospace applications. *Composite Structures, 91*(4), 467–472.
2. (2002). *Conductivity And FRP Composites* (p. 1). [ebook] Dayton, OH: Industrial Fiberglass Specialties, Inc. Retrieved July 5, 2020, from https://www.ifs-frp.com/wp/pdf/technical-bulletins/conductivity.pdf.
3. Ha, M. S., Kwon, O. Y., & Choi, H. S. (2010). Improved electrical conductivity of CFRP by conductive nano-particles coating for lightning strike protection. *Composites Research, 23*(1), 31–36.
4. Kupke, M., Wentzel, H., & Schulte, K. (1998). Electrically conductive glass fibre reinforced epoxy resin. *Materials Research Innovations, 2*(3), 164–169.
5. Tsangaris, G. M., & Kazilas, M. C. (2002). Conductivity and percolation in epoxy resin/conductive filler composites. *Materials Science and Technology, 18*(2), 226–230.
6. Sarkar, P., Modak, N., & Sahoo, P. (2017). Mechanical characteristics of aluminium powder filled glass epoxy composites. *International Journal of Engineering and Technologies, 12,* 1–14.
7. Gupta, A., Walia, R., & Singh, H. (2019). Effect of fillers on tensile strength of pultruded glass fiber reinforced polymer composite. *Indian Journal of Engineering and Material Sciences, 22,* 62–70.
8. Gupta, A., Walia, R., & Singh, H. (2014). Effect of glass fiber and filler volume fraction variation on mechanical properties of GFRP composite. In *Proceedings of the International Conference on Research and Innovations in Mechanical Engineering.* Lecture Notes in Mechanical Engineering (pp. 407–414)
9. Gupta, A., Vaishya, R., Khan, K., Walia, R., & Singh, H. (2019). Multi-response optimization of hybrid filler composition for pultruded jute fiber reinforced polymer composite. *Materials Research Express, 6*(11), 115324.
10. Hiremath, P., Arunkumar, H., & Shettar, M. (2017). Investigation on effect of aluminium hydroxide on mechanical and fire retardant properties of GFRP-Hybrid composites. *Materials Today: Proceedings, 4*(10), 10952–10956.
11. Pubchem.ncbi.nlm.nih.gov. (2020). *Methyl Ethyl Ketone.* Retrieved July 6, 2020, from https://pubchem.ncbi.nlm.nih.gov/compound/Methyl-ethyl-ketone.

Effect of Packing Factor on the Electrical Performance of Semitransparent Photovoltaic Thermal (SPVT) System: An Experimental Approach

V. K. Chopra, R. K. Mishra, V. K. Dwivedi, and B. Mohapatra

Abstract Hybrid photovoltaic thermal (PVT) systems are used for generating electricity as well as to regulate the heating effect of PV module. In different applications of hybrid PVT systems, the main emphasis is given on the electrical energy. In present paper, mathematical modeling is done for semitransparent photovoltaic thermal (SPVT) collector with air as the working fluid. The working fluid (air) sweeps away the excessive heat associate with the PV module and the temperature of module gets lowered which increases the electrical efficiency of PVT system. SPVT air collectors with three cases having different packing factors are considered. Case-I: SPVT air collector with 80Wp PV module (0.81 packing factor); Case-II: SPVT air collector with 50Wp (0.52 packing factor); Case-III: SPVT air collector with 25Wp (0.31 packing factor). The expression for electrical efficiency has been developed for all the three cases. For the circulation of air, a wooden duct of cross section of 0.86 m 0.63 m $\times$ 0.05 m is incorporated below the PVT module. Also a 10 W (D.C) fan is also used for force mode of operation. The result depicts that in case-III, PV module has 0.7% more efficiency than the efficiency of module in case-II and 1.7% more than the efficiency of module in case-I.

V. K. Chopra · B. Mohapatra
Galgotias University, Yamuna Expressway, Greater Noida, UP 201310, India
e-mail: vivek_chopra17@yahoo.co.in

B. Mohapatra
e-mail: bmohapatra9@gmail.com

R. K. Mishra (✉)
Galgotias College of Engineering and Technology, 1, Knowledge Park, Phase II, Greater Noida 201306, India
e-mail: bhu.rajeev@gmail.com

V. K. Dwivedi
Madan Mohan Malaviya University of Technology, Deoria Road, Singhariya, Kunraghat, Gorakhpur 273016, India
e-mail: vkdwivedi94@gmail.com

1 Introduction

Kern and Russel [1] proposed the innovative idea of coupling between PV and thermal system. Raghuraman [2] developed various techniques for PVT system to evaluate its performance. Evans [3] has developed a simplified procedure for predicting PV array output with a less number of input information. Lalovic et al. [4] proposed an economical PVT system by using amorphous silicon cells (a-Si). Loferski et al. [5] explained different results of air-based PVT system. Nann and Emery [6] extensively studied the effect of change in spectral solar radiation on efficiency with the help of spectral model named SEDES2. Garg and Adhikari [7] studied the effect of various parameters (design and operation) to evaluate the performance of PVT hybrid systems. To study the reliability of PVT system, Hamdy et al. [8] proposed the different techniques for analytical treatment. Muntasser et al. [9] proposed the future growth of PV module in under developed countries globally. Hegazy [10] extensively studied in four different models of the dual performance (electric as well as thermal) based on blowing air in the flat plate PVT air collector. Sopian et al. [11] developed and investigated hybrid solar collector for drying applications based on particular space heating with the help of air blown above and below the module. To reduce the heating effect below the solar panel, Kalogirou [12] has proposed uncoated PVT module by using heat exchanger attached below the panel particularly for the territorial environments of Cyprus country. Lee et al. [13] proposed the modeling and thermal analysis of PVT system incorporated with the building and the outcomes of hybrid PVT are magnificent. Chow [14] studied all the constrains while developing the PVT collector as a specific vital model. Jones and Underwood [15] analyzed the effect of module temperature of PV cells that is well under the limits with the calculated data of variable changes under flux of radiant energy per unit area. Zondag et al. [16] and Chow [14] investigated the reduction of efficiency in electrical form of energy of PVT cells system. Mohamad [17] discussed solar-tracking design using programmable logic controller (PLC) so to escalate the PV cells system efficiency. Tiwari et al. [18] have discussed that the thermal efficiency of PVT system can be escalated if it is properly utilized by the system. He et al. [19] presented a new design of solar collector incorporated with natural circulation of water. Zhou et al. [20] investigated that performance of PV cells system mainly depends upon solar radiations (W/m^2) and temperature (°C) of it. Tripanagnostopoulos [21] presented an economical dual heat extraction enhanced modified incorporated with hybrid PVT solar energy systems. Jie et al. [22] analyzed the performance of SPVT system by using an innovative heat pump. Zondag [23] rigorously reviewed on different innovative works on collectors and PVT system by various scientists till 2006. Dubey and Tiwari [24] has claimed a significant increase from 33.0 to 64.0% efficiency due to rise in coated area of photovoltaic thermal. (PVT) solar heating system incorporated with water flow system. Dubey et al. [25] have investigated the efficiency in electrical form of energy systems of different PVT hybrid collectors. Skoplaki and Palyvos [26] have presented various correlations in a simplified equations to be applicable in PV cells systems or bunches ascended on L-shaped frames which allow

systems to stand both horizontally and vertically. Tiwari et al. [27] have proposed the detail result and modelling of PV thermal integrated with air and water as heat exchanger or heat carrier similarly in photovoltaic thermal hybrid systems.

In this paper, we have considered glass-to-glass PV modules of 80Wp, 50Wp, and 25Wp having packing factors of 0.81, 0.52, and 0.31, respectively in three cases viz. case-I, case-II, and case-III. It is the sun intensity and ambient temperature-based numerically solved logical expression for the electrical efficiency of PVT air duct systems. The mathematical model developed is experimentally validated for Delhi/NCR climate. In Hi-tech institute of engineering and technology, Ghaziabad, U.P, India, experimental setups have been installed.

2 System Description

The cross-sectional view of glass-to-glass PVT module with air duct is shown in Fig. 1. In this figure, solar energy strikes on the modules of different packing factors, where area (Am) 0.5332 m^2 of PV module for different three cases are same. Figure 2 shows the duct which is incorporated with the PVT module having dimensions of 0.86 m × 0.63 m × 0.05 m. The arrangements are also done for the force circulation of air in system below the PV module with the help of a 10w DC fan which is
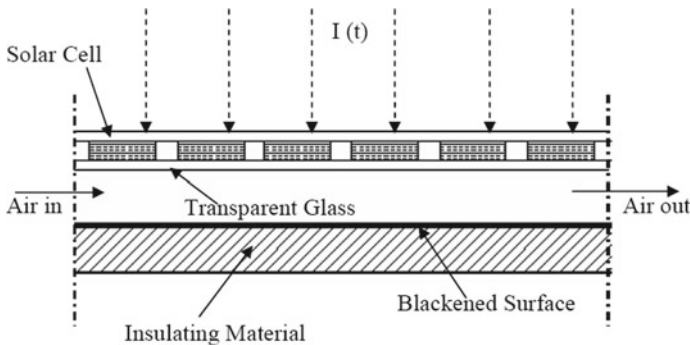
Fig. 1 Cut sectional view of glass to glass PV module with duct

Fig. 2 Duct incorporated with DC fan in PVT system
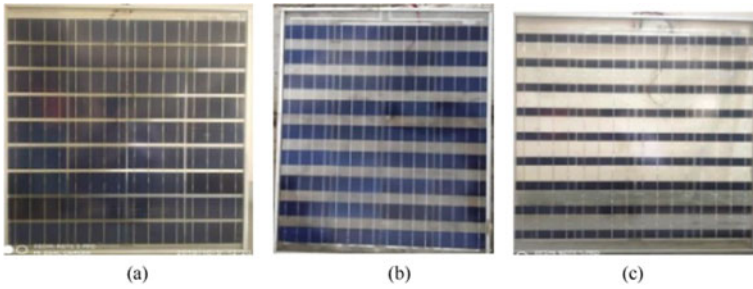
Fig. 3 Photovoltaic modules used in different PVT configurations **a** 80 Wp **b** 50 Wp and **c** 25 Wp

Table 1 Design parameters of SPVT module with air duct

Parameters	Values	Parameters	Values
Am (m^2)	0.5332	$\dot{m} f$ (kg/m^2)	0.6513
α c	0.9	C f (J/kg/K)	1012
βc (80Wp)	0.81	β0	0.0045
βc (50Wp)	0.523	hif (W/m^{2}K)	2.8 + 3v; v = 1 m/s 5.7 + 3. 8v; v = 1 m/s
βc(25Wp)	0.313	h0 (W/m^2 K)	0.003
α b	0.85	l g (m) Kg(W/mK) V(m/s)	0.816
τ g	0.95		1.0
ηm	12%		
η0	14%		

energized by the same PVT module. Modules used in three cases I, II, and III have been shown in Fig. 3a–c, respectively. The designed parameters are shown in Table 1.

3 Mathematical Modeling

The equation of energy balance of PVT modules can be written as Mishra and Tiwari [27]:

(a)   For solar cells PVT systems:

The energy balance equation for solar cell of PV module can be written:

$$\alpha_c \beta_c \tau_g I(t)bdx = U_{tca}(T_c - T_a)bdx + U_{bcf}(T_c - T_f)bdx + (\eta_m.)\beta_c \cdot I(t)bdx \tag{1}$$

Now U_{tca} and U_{bcf} are explained as

$$U_{tca} = \left[\frac{L_g}{K_g} + \frac{1}{h_o}\right]^{-1} \quad U_{bcf} = \left[\frac{L_g}{K_g} + \frac{1}{h_{if}}\right]^{-1}$$

From the Eq. (1), temperature of cell is:

$$T_c = \frac{T_f U_{bcf} + T_a U_{tca} + I(t)\alpha_c \beta_c \tau_g - I(t)_m \beta_c}{U_{bcf} + U_{tca}} \tag{2}$$

PV cells electrical efficiency which is temperature dependant can be given as

$$\eta_c = \eta_0 (1 - \beta_0 (\bar{T}_c - T_a)) \tag{3}$$

For blackened absorber plate

$$(1 - \beta_c)\tau_g \tau_g I(t)bdx = U_{bpa}(T_p - T_a)bdx + h_{pf}(T_p - T_a)bdx \tag{4}$$

From Eq. (4), temperature of the plate is given by

$$T_p = \frac{I(t)\alpha_b(1 - \beta_c)\tau_g^2 + T_a U_{bpa} + T_f h_{pf}}{h_{pf} + U_{bpa}} \tag{5}$$

(b)   Duct having flow of air

Air flowing through duct, the energy balance expression given by,

$$\dot{m}fcf\frac{dTf}{dx} = h_{pf}(T_p - T_f)b + U_{bcf}(T_c - T_f) \tag{6}$$

Initial conditions in analysis of Eq. (6) given by: Tf at x = L, Tf = Tfo and when Tf at x = 0, Tf = Tfi On solving Eq. (6) by Eqs. (5) and (2) given by:

$$T_{fo} = \left(\frac{f(t)}{a}\right)(1 - e^{-ax}) + T_{fi}\,e^{-ax} \tag{7}$$

where, $f(t) = \left(\frac{b}{\dot{m}fcf}\right)[\{((hpf)/(h_{pf} + U_{bpa}))I(t)\alpha_b(1 - \beta_c)\tau_g^2)\}$
$$+ \{(U_{bpa})/(h_{pf} + U_{bpa})\}T_a + \{((U_{bcf})/((U_{tca} + (U_{bcf})\}U_{tca}T_a$$
$$+ \{((U_{bcf})/((U_{tca} + (U_{bcf})\}\{(I(t)\alpha_c\beta_c\tau_g - I(t)_m\beta_c)\}]$$

where, $a = \left(\frac{b}{\dot{m}fcf}\right)\{((-hpf)/(h_{pf} + U_{bpa})) + h_{pf} + \{((U_{bcf})/((U_{tca} + (U_{bcf}))\}U_{tca}\}$ (8)

Below the PV module, air duct is incorporated in which for the whole length, the mean temperature of air given as

$$\bar{T}_f = \frac{1}{L} \int_0^L T_{f(x)} dx$$

$$= \left(\frac{f(t)}{a}\right)\left[1 - \left((\dot{m}fcf)/(A_m\left\{\left(\frac{-hpf}{(h_{pf}+U_{bpa})}\right)+h_{pf}+\left\{\frac{(U_{bcf})}{(U_{tca}+U_{bcf})}\right\}U_{tca}\right\}\right]\right]$$

$$\left(1 - e^{-A_m\left\{\left(\frac{-hpf}{(h_{pf}+U_{bpa})}\right)+h_{pf}+\left\{\frac{(U_{bcf})}{(U_{tca}+U_{bcf})}\right\}U_{tca}\right\}/\dot{m}fcf}\right)$$

$$+ T_{fi}\,\dot{m}fcf/\left[A_m\left\{\left(\frac{-hpf}{(h_{pf}+U_{bpa})}\right)+h_{pf}+\left\{\frac{(U_{bcf})}{(U_{tca}+U_{bcf})}\right\}U_{tca}\right\}\right]$$

$$\left(1 - e^{-A_m\left\{\left(\frac{-hpf}{(h_{pf}+U_{bpa})}\right)+h_{pf}+\left\{\frac{(U_{bcf})}{(U_{tca}+U_{bcf})}\right\}U_{tca}\right\}/\dot{m}fcf}\right)$$

If $T_{fi} = T_a$ and $T_f = \bar{T}_f$, in Eqs. (8), (7) and (3),
The efficiency of electrical energy for temperature dependent obtained as

$$\eta_c = \eta_0(1 - \beta_0 Um) \tag{9}$$

where $Um = \dfrac{\left(\frac{f(t)}{a}\right)\left[1 - (Ux)\right]\left(1 - e^{-U_t}\right) + T_a\left[Ux\right]\left(1 - e^{-1/Ux}\right)\right]U_{bcf} - U_{bcf}]\ \ +I(t)\alpha_c\beta_c\tau_g - I(t)_m\beta_c}{U_{bcf} + U_{tca}}$

where $U_t = A_m\left\{\left(\frac{-hpf}{(h_{pf}+U_{bpa})}\right)+h_{pf}+\left\{\frac{(U_{bcf})}{(U_{tca}+U_{bcf})}\right\}U_{tca}\right\}$

where $U_x = (\dot{m}fcf)/(U_t)$
The various nomenclatures used in modeling are given in Table 2.

4 Methodology

The solar intensity I(t), ambient temperature (T_a), and module temperature module (Tm) are obtained for climatic condition of Delhi, India. The following methodologies are used to determine the electrical efficiency of PV module with different packing factors and the effect of cell temperature on efficiency of PVT systems.

Step 1: Mathematical modeling of the system has been done using MATLAB R2017a.
Step 2: The calculations are done on the basis of designed parameters shown in Table 1.

Table 2 Nomenclatures used in modeling

A_m module area (m^2)
L module length (m)
b module breadth (m)
lg length of glass(m)
dx elemental length (m)
$\dot{m}f$ fluid mass flow rate (kg/m^2)
c_f fluid specific heat (J/kg K)
I(t) sun radiation (W/m^2)
h heat loss coefficient (W/m^2)
K thermal conductivity (W/mK)
h_o heat loss coefficient from top (W/m^2)
T temperature (°C)

Step 3: Efficiency of electrical form of energy and cell temperature is calculated using Eqs. (2) and (9), respectively, on the basis of above-mentioned climatic data and designed parameters.

Step 4: The experimental process which is shown in Fig. 9 and the different models validations have been performed in Hi-Tech institute of engineering and technology, Ghaziabad, U.P., India.

5 Results and Discussions

The variation of solar intensity and ambient temperature on hourly basis on which different parameters evaluated has been shown in Fig. 4. In this figure, at 8:00 AM, the intensity is as low as 374 W/m^2 so as the ambient temperature is on 31.6 °C. Afterwards, as the day progresses and around 12:00 noon, ambient temperature shoots up to 37.3 °C and the intensity also rises to 1032 W/m^2. In Fig. 5, the graph
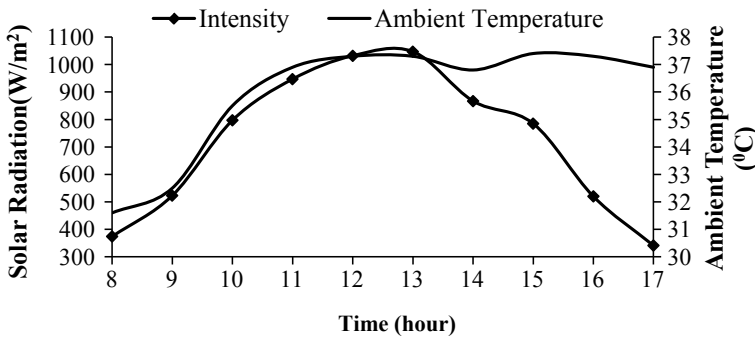
Fig. 4 Hourly variation of intensity and ambient temperature for a clear day in the month of June 2019
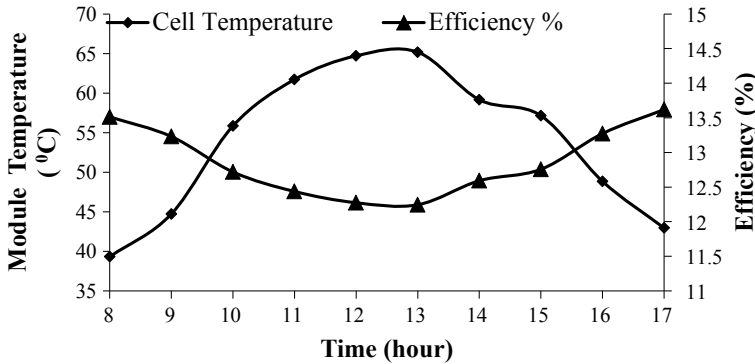
Fig. 5 Hourly variation of cell temperature (Tc) and electrical efficiency (%) of Case-I for June 2019

shown of case-I depicts the variation of electrical efficiency and cell temperature on hourly basis. The plot shown in Fig. 5 gives clear information that initially at 8:00AM when module temperature is 39.3 °C, the electrical efficiency of module is 13.51%. As the day progresses at 12:00 noon, the module temperature increases to 64.7 °C, efficiency decreases to 12.27%. Further at 4:00 PM, temperature of the module decreases to 48.84 °C, whereas efficiency increases from 12.27 to 13.27%, so the decrease in electrical efficiency as the cell temperature increases. The experimental observation for case-I is shown in Table 3. The similar type of variation of in case-II shown in Fig. 6 that in morning, at 8:00 AM, the cell temperature and electrical efficiency are 33.65 °C and 13.87%, respectively. At this point, cell temperature is at minimum value, whereas efficiency is at maximum value. As the day progresses, cell temperature increased from 33.65 °C to 48.09 °C, whereas the efficiency of module decreases from 13.87 to 13.257%. So the effect in this case is same as in case-I, only difference is the individual values of cell temperature and efficiencies during 8:00
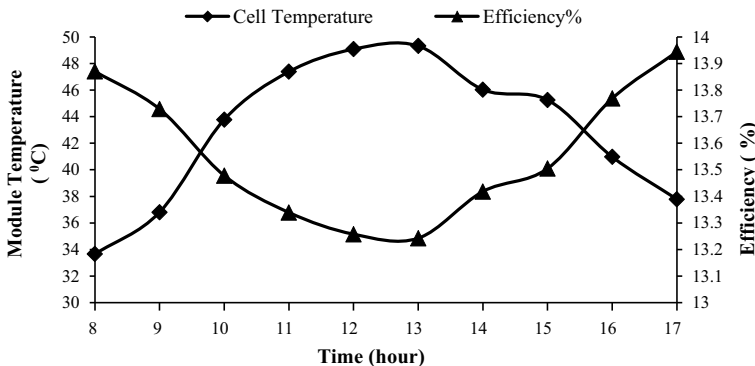
Fig. 6 Hourly variation of cell temperature (Tc) and electrical efficiency (%) of case-II for June 2019

Am to 5:00 PM. In case-III as shown in Fig. 7. The readings of cell temperature and electrical efficiency vary in same fashion as in case-I and in case-II. Here, also from 8:00 AM to 12:00 noon, cell temperature increases from 29.53 °C to 37.69 °C and during this duration, electrical efficiency decreases from 14.13 to 13.97%. When cell temperature decreased to 34.02 °C at 5:00PM, efficiency of module is increased to 14.18%.

The hourly variation of cell temperature Tc and electrical efficiency of different three cases has been shown in Fig. 8. From Fig. 8, it is clearly seen that the efficiency of the PV module in case-III varies from 14.13 to 14.18% on hourly basis. Whereas in case-II, it varies from 13.87 to 13.944% also in case-I, efficiency variation is from 13.51 to 13.618%. Therefore, electrical efficiency of module in case-III has always
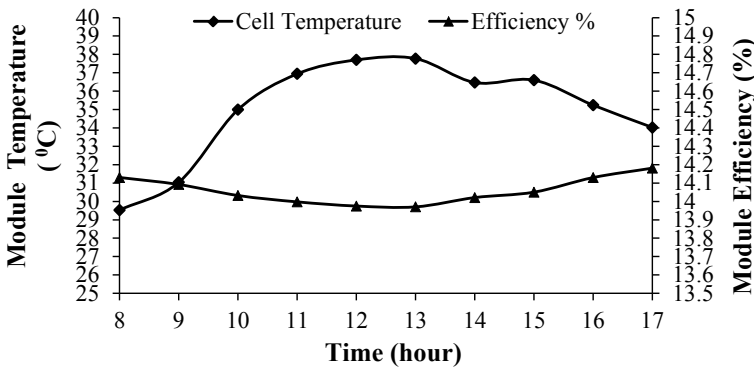
Fig. 7 Hourly variation of cell temperature (Tc) and electrical efficiency (%) of case-III for June 2019
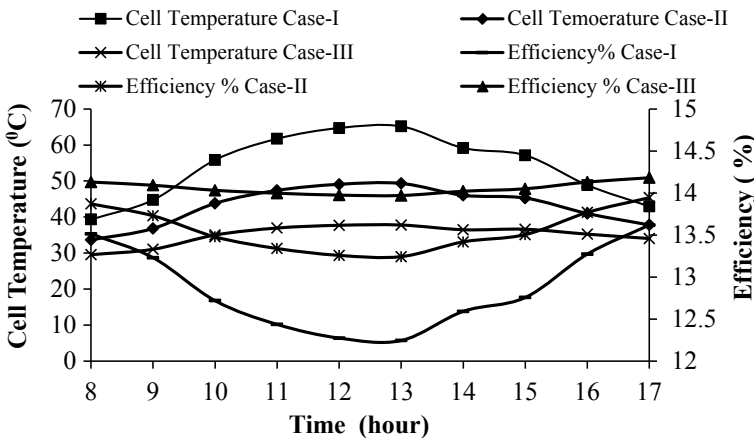
Fig. 8 Hourly variation of cell temperature Tc, and electrical efficiency of different cases for June 2019
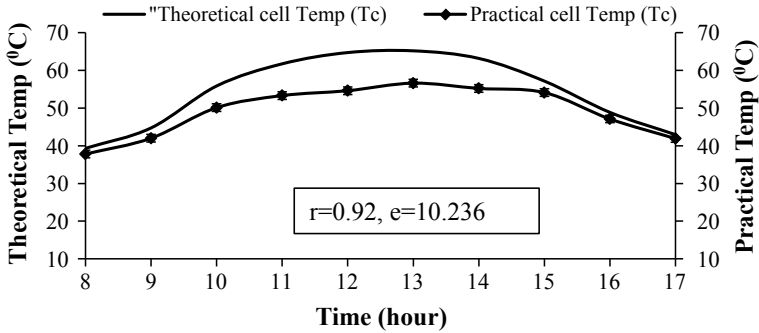
Fig. 9 Comparison of theoretical and experimental values of cell temperature (Tc) for case-I for June 2019

greater value (from 8:00 AM to 5:00 PM) as compared to case-II and case-I as the PV module in the case-III has lowest cell temperature (29.53–34.02 °C) among the three cases.

The PVT collector for case-I with air duct is experimented which is tilted at 30°, equal to the latitude of Delhi and NCR. An hourly-based validated graph is shown in Fig. 9. In this, at 8:00 AM, theoretical temperature is 39.32 °C and practical temperature of module is 37.8 °C which is lesser than theoretical one. Similarly, for other values like at 4:00PM, theoretical temperature of module is 48.8 °C and practical cell temperature is 47.1 °C which shows the theoretical values are greater than the practical values.

In the present work on comparing theoretical and practical cell temperature of PV module in case-I, the correlation coefficient (r) [27] is found to be 0.92 and root mean square percent deviation (e) [27] is 10.236. Thus, a good agreement has been obtained between theoretical and experimental values as shown in Fig. 1.

6 Conclusions

In this work, following observations to sum up as:

(1) Mathematical modeling is done for semitransparent photovoltaic thermal (SPVT) collector with air as the working fluid.
(2) The result depicts that in case-III (SPVT air collector with 25Wp PV module (0.31 packing factor), PV module has 0.7% more efficiency than the efficiency of module in case-II (SPVT air collector with 50Wp PV module (0.52 packing factor) and 1.7% more than the efficiency of module in case-I (SPVT air collector with 80Wp (0.81 packing factor)).

(3) Developed model was experimentally validated for case-I.
(4) A good agreement has been obtained between theoretical and experimental values.

References

1. Kern, E. C., & Russell, M. C.: Analysis on an hybrid collectors tends to minimize the backup energy requirement of typical residential systems, especially those using heat pumps.
2. IEEE Photovoltaic specialists Conf, 13, pp. 780619-24.
3. Raghuraman, P. (1981). Analytical predictions of liquid and air photovoltaic/thermal flat plate collector performance. *Solar Energy Engineering, 103,* 291–298.
4. Evans, D. L. (1981). Simplified method for predicting photovoltaic array output. *Solar Energy, 27,* 555–560.
5. Lalovic, B. A. (1986). Hybrid amorphous silicon photovoltaic and thermal solar collector. *Solar Cells, 19,* 131–138.
6. Loferski, J., Ahmad, J. M., & Pandey, A. (1998). Performance of photovoltaic cells incorporated into unique hybrid photovoltaic/thermal panels of a 2.8 KW resident solar energy system. In *Proceedings of the 1988 annual meeting American solar energy society*, (pp. 427–432). Cambridge, Massachusetts.
7. Nann, S., & Emery, K. (1992). Spectral effect on PV-device rating. *Solar Energy Materials and Solar Cell, 27,* 189–216.
8. Garg, H. P., & Adhikari, R. S. (1997). Conventional hybrid photovoltaic/thermal (PV/T) air heating collectors: steady state simulation. *Renewable Energy, 11*(3), 363–385.
9. Hamdy, M. A., Beshir, M. E., & Elmarsy, S. E. (1989). Reliability analysis of photovoltaic systems. *Applied Energy, 33,* 253–263.
10. Muntasser, A., Bara, M. F., Quadri, H. A., El-Tarabelsi, R., & La-Azebi, I. F. (2000). Photovoltaic marketing in developing countries. *Applied Energy, 65*(1–4), 67–72.
11. Hegazy, A. A. (2000). Comparative study of the performance of four photovoltaic/thermal solar air collectors. *Energy Conversion and Management, 41*(8), 861–881.
12. Sopian, K., Liu, H. T., Kakac, S., & Veziroglu, T. N. (2000). Performance of a double pass photovoltaic thermal solar collector suitable for solar drying systems. *Energy Conversion and Management, 91,* 17–28.
13. Kalogirou, S. A. (2001). Effect of fuel cost on the price of desalination water: a case for renewable. *Desalination, 138,* 137–144.
14. Lee, W. M., Infield, D. G., Gottschalg, R. (2001). Thermal modeling of building integrated PV systems. In *Proceedings of 17th PV Solar Energy Conference.* Munich (pp. 2754–2757).
15. Chow, T. T. (2003). Performance analysis of photovoltaic collector by explicit dynamic model. *Solar Energy, 75*(2), 143–152.
16. Jones, A. D., & Underwood, C. P. (2001). A thermal model for photovoltaic systems. *Solar Energy, 70*(4), 349–359.
17. Tiwari, A., & Sodha, M. S. (2006). Performance evaluation of hybrid PV/thermal water/air heating system: A parametric study. *Renewable Energy, 31*(15), 2460–2474.
18. Mohamad-Al, A. (2004). Efficiency improvements of photo- voltaic panels using a Sun–tracking system. *Applied Energy 79*, 345–354 (2004).

19. Tiwari, G. N., Meraj, Md., Khan, M. E., Mishra, R. K., Garg, V.: Improved Hottel-Whillier-Bliss equation for N-photovoltaic thermal-compound parabolic concentrator (N-PVT-CPC) collector. *Solar Energy 166*, 203–212 (2018).
20. He, W., Chow, T.-T., Ji, J., Lu, J., Pei, G.,& Chan, L.-S. (2006). Hybrid photovoltaic and thermal solar-collector designed for natural circulation of water. *Applied Energy, 83*, 199–210.
21. Zhou, W., Yang, H., & Fang, Z. (2007). A novel model for photovoltaic array performance prediction. *Applied Energy, 84,* 1187–1198.
22. Tripanagnostopoulos, Y., & Tonui, J. K. (2007). Improved PV/T solar collectors with heat extraction by forced or natural air circulation. *Renewable Energy, 32,* 623–637.
23. Jie, J., He, H. F., Chow, T. T., Gang, P., Wei, H., & Liu, K. L. (2008). Distributed dynamic modeling and experimental study of PV evaporator in a PV/T solar assisted heat pump. *International Journal of Heat and Mass Transfer, 52,* 1365–1373.
24. Zondag, H. A. (2008). Flat Plate PV-Thermal collectors and systems: A review. *Renewable and Sustainable Energy Reviews, 12,* 891–959.
25. Dubey, S., & Tiwari, G. N. (2008). Thermal modeling of combined system of photovoltaic thermal (PV/T) solar water heater. *Solar Energy, 82,* 602–612.
26. Dubey, S., Sandhu, G. S., & Tiwari, G. N. (2009). Analytical expression for electrical efficiency for PVT hybrid air collector. *Applied Energy, 86,* 697–705.
27. Skoplaki, E., & Palyvos, J. A. (2009). On the temperature dependence of photovoltaic module electrical performance, a review of efficiency/power correlations. *Solar Energy, 83,* 614–624.

Challenges and Materials in Artificial Organ Manufacturing

Sumit Budhiraja, Prerna Priya Ashok, and K. Mathiyazhagan

Abstract Additive manufacturing (AM), is also known as rapid prototyping, is considered as a revolution in field of manufacturing and fabrications and boosted the development in biomedical fabrication. The 3D printing technique is mostly utilized in the field of medical for the manufacturing of medical equipment and surgical equipment, especially 3D biomedical printing which means 3D printing of substance which are biologically compatible to human body, blood and cells in the field of tissue fabrications. The main aim of tissue fabrications and engineering is to produce the artificial organ which is functional and viable. To fulfill this objective, investigation of various manufacturing techniques and materials is required. The process is difficult as it includes multiple aspects of human physiology, like types of multiple cell culturing, vasculature, nerve innervation, and interactions with nearby cells. This paper objective is to find the suitable material, is difficult task and, need in-depth focus on why it is difficult & what are the factors influencing the negative role of effective utilization of 3D printing tissue engineering. Also, this paper focuses on comparative study of materials in economic perspective human organ manufacturing. At the end, the conclusion elaborates about the applications and challenges of additive manufacturing in medical field and the alternative materials for organ tissue manufacturing.

Keywords Challenging factors · Additive manufacturing · Hydrogels · Scaffolds manufacturing · Artificial organ · Tissue regeneration

S. Budhiraja (✉) · P. P. Ashok · K. Mathiyazhagan
Department of Mechanical Engineering, Amity University Noida, Noida, India
e-mail: sumitbsb46@gmail.com

P. P. Ashok
e-mail: prernabsb46@gmail.com

K. Mathiyazhagan
e-mail: kmathiyazhagan@amity.edu

1 Introduction

Organ failure [1] is the main reason for death everywhere on earth in spite of developments in interventional, pharmacological, and surgical therapies. Bio-artificial structure fabrication is the biggest dream beyond the memory of man. Since the beginning of this mortality, individuals have attempted a lot of methods to drag out life through substitution or reclamation of flawed/deficient organs.

As of now, orthotropic organ transplantation is the hardly efficient method to accomplish this, whereas it is constrained by problems like shortage of donor, expensive, immune repudiation, and social conflict. With fast improvements in technology, some developed material manufacturing techniques are.

- "Multi-nozzle rapid prototyping (MNRP),"
- "Additive combined molding (or additive combined molds),"
- "Decellularized matrix regeneration,"
- "Electrophoresis."

Allogeneic organ transplantation [2] is the currently used way for curing the deficient organs, and various processes have been established with the help of various sources of donor. But this method highly restricts people who can be treated with this method due to various problems like serious lack of donating person's organs, including immunological rejection complications and donating person's location.

The AM technique provides the technique to accurate development over the well-designed structure, including "pore size, shape, orientation, interconnectivity, and branching." AM approach has a lot of benefits which help to attain biomimetic structures with "specific construct patterns, elements of material, degradation kinetics, mechanical strength, and biological effects" that are manufactured precisely.

1.1 Literature Review

"Vienken [2] investigated that mechanical stability, surface variability, and sterilizability in polymers as material are important for the manufacturing of artificial organs in his paper Polymers in nephrology characteristics and needs. Nahmias et al. [3] presented an effectively material and cheap technique for designing cells on discretionary surfaces incorporating organic gels with little loss of suitability or capacity in their paper cell patterning on biological gels via cell spraying through a mask. Wang et al. [2] stated various merits and demerits about the manufacturing techniques used in the fabricating of the bio-artificial organs in their paper Rapid prototyping as a tool for manufacturing bio-artificial livers. Wang et al. [4] found the solutions to various biological, biomaterial, and engineering challenges for the manufacturing of artificial liver in their paper Rapid prototyping as a tool for manufacturing bio-artificial livers. Li et al. [5] described the administering-dependent tissue framework creation technique by and without the joining of live cells including the stream pace

of the gel apportioned and the pore size and porosity of the platforms manufactured in their paper A brief review of dispensing-based rapid prototyping techniques in tissue scaffold fabrication: role of modelling on scaffold properties prediction. Wang et al. [6] explained the ongoing patterns and the exceptional difficulties looked by the producer in assembling of the fake organs in his paper Recent Trends and Challenges in Complex Organ Manufacturing. Chmielewski [7] explained the modification in chitosan by gamma ray irradiation, electron beam irradiation, and chitosan grafting. A brief review is about application in healthcare products, food safety, radiotherapy, radiation protection, environmental, and nuclear technology in their paper Chitosan and radiation chemistry. Kalita [8] described a few RP advances and the uses in medical building in impersonating the auxiliary complexities of organic structures in their paper Rapid prototyping in biomedical engineering: structural intricacies of biological materials. Rath et al. [9] arranged and examined a moderate corrupting heparin-joined hyaluronan (HA) hydrogel in their paper Hyaluronan-based heparin-incorporated hydrogels for generation of axially vascularized bio-artificial bone tissues: in vitro and in vivo evaluation in poly(lactide-co-lactide)-β-tri-calcium phosphate-poly(ε-caprolactone) composite system. Guvendiren et al. [10] highlighted the scope of injectable shear-diminishing hydrogel frameworks being created, with an emphasis on the different instruments of arrangement and shear-diminishing and their utilization in biomedical applications in their paper Shear-thinning hydrogels for biomedical applications. Wang [11] stated the advantages and disadvantages of the current cell-loaded RP methods for complex organ fabricating in their paper Intelligent Freeform Manufacturing of Complex Organs. Marga et al. [12] described about the scaffold-free approaches, utilizes natural self-get together and bioprinting and the innovation and related uses for building vascular and nerve joins in their paper Toward engineering functional organ modules by additive manufacturing. Ikada [13] explained the various properties, their relationship, and testing methods of hydrogels in their paper Biocompatibility of Hydrogels. Zhu et al. [14] investigated cytocompatibility and mechanical property of modified two-dimensional and three-dimensional platforms with biodegradable poly(butylene terephthalate)-co-poly(butylene succinate)-b-poly(ethylene glycol) (e.g., PTSG), as artificial salivary gland material in their paper The preparation of decorated poly(L-lysine)–Gly-Arg-Gly-Asp-Ser modified poly(butylene terephthalate)- co-poly(butylene succinate-b-poly(ethylene glycol) copolymer scaffolds and their effects on manufacturing artificial salivary gland. Ahmed [15] reviewed the writing concerning features of hydrogels depending upon different aspects, physical and concoction qualities of these items, and specialized possibility of their usage in their paper Hydrogel: Preparation, characterization, and applications: A review. Murphy et al. [16] reviewed the use of three-dimensional bioprinting to tissue and organ sketching, the primary methods for tissue printing builds, the various sorts of bioprinters and the effect on the inscribed cell develop and sequencing process of printing a cell, the impediments of ebb and flow advancements and the difficulties for future research in their paper 3D bioprinting of tissues and organs. Li et al. [17] reported on a half and half hydrogel that consolidates very high firmness, quality, and strength, while keeping up physical respectability in electrolyte arrangements in their paper Stiff, strong,

and tough hydrogels with good chemical stability. Ahn et al. [18] stated the history and kinds of 3D printers, the order of 3D bioprinters, and the innovation used to make counterfeit tissues and organs in their paper Three-Dimensional Bioprinting Equipment Technologies for Tissue Engineering and Regenerative Medicine. Park et al. [19] reviewed about the current technical development, difficulties, and future possibilities of 3D bioprinting for designing hard tissues in their paper Advances in Three-Dimensional Bioprinting for Hard Tissue Engineering. Agarwala [20] outlined the present state in bioprinting innovation, recognizes various sorts of procedures and portrays the bio-inks. Current difficulties and restrictions restraining the development of this field are additionally talked about in their paper A Perspective on 3D Bioprinting Technology: Present and Future. Nakamura et al. [29] applied the strategy of biofabrication can give a capability of leap forward to build exceptionally modern 3D platforms and to produce a few complex 3D tissues and organs. In light of this idea, we have ever built up a few machines for this reason, for example, an inkjet 3D bioprinter to develop complex and multi-composite 3D structures and normally plan and build fake LNs in their paper Engineering of Artificial Lymph Node. Zadpoor et al. [21] reviewed the use of added substance producing procedures in studies tending to biomaterials, (re)generation of tissues and organs, malady models, sedate conveyance frameworks, inserts, restorative instruments, prosthetics, orthotics, and AM articles utilized for therapeutic perception and correspondence in their paper Additive Manufacturing of Biomaterials, Tissues, and Organs. Zhang et al. [22] described late advances of 3D bioprinting innovation and related bio-inks reasonable for the printing procedure, the uses of this innovation in creation of biomimetic builds of a few agent tissues and organs, including vein, heart, liver, and ligament and future challenges in 3D bioprinting just as potential answers for further improvement in their paper 3D Bioprinting for Tissue and Organ Fabrication. Naseer et al. [23] report on a bio-acoustic power designing system, which uses surface acoustic waves (SAWs) for the fast game plan of cells inside an extracellular lattice based hydrogel, for example, gelatin methacryloyl (GelMA) in their paper Surface acoustic waves induced micropatterning of cells in gelatin methacryloyl (GelMA) hydrogels. Ratheesh et al. [24] explained the different framework creation procedures, sorts of polymers and biomaterials utilized for the manufacture forms, different fields of utilizations, and various difficulties looked in their creation of platforms in regenerative treatment in their paper 3D Fabrication of Polymeric Scaffolds for Regenerative Therapy. Wang et al. [1] overviewed the inborn/outward properties of the gelatin-based hydrogels in organ 3D bioprinting territories with trend setting innovations, hypotheses, and standards, the best in class of the physical/concoction crosslinking techniques for the gelatin-based hydrogels being utilized to beat the feeble mechanical properties is featured. A multicellular model produced using fat inferred immature microorganism expansion and separation in the predefined 3D builds is stressed. Multi-spout expulsion based organ 3D bioprinting advances have the recognized potential to inevitably make implantable biofake organs for purposes, for example, modified organ reclamation, high-throughput medication screening and metabolic disorder model foundation in their paper Gelatin-Based Hydrogels for Organ 3D Bioprinting. Wu et al. [25] demonstrated the GG/PEGDA twofold system

hydrogel can possibly print human-scale living tissues and organs in their paper 3D bioprinting of gellan gum and poly(ethylene glycol) diacrylate-based hydrogels to produce human-scale constructs with high fidelity. Saroia et al. [26] examined organic improvement in the structure and cross-connecting associations of characteristic or manufactured hydrogels. The techniques and plan criteria impact the concoction and mechanical properties and association of seeding cells when the implantations are likewise illustrated. The approach of bioprinting methods alongside late improvement has additionally been checked on and a few abilities and weaknesses are called attention to for further advancement of hydrogels-based frameworks and choice of bioprinting innovation relying upon their application in their paper: A review on biocompatibility nature of hydrogels with 3D printing techniques, tissue engineering application and its future prospective. Gupta et al. [27] introduced about the different kinds of ordinary and late 3D printing advances, biomaterials, and added substances which change its physical properties and abridged the utilizations of 3D printing method in restorative applications and depicted the likelihood to build goals and print single cell layer utilizing piezoelectric transducer at the printer head in FDM-based printing strategy in their paper A Review on 3D Printable Techniques for Tissue Engineering. Holzmeister et al. [28] reviewed late discoveries on the epitome of microorganisms and eukaryotic cells in inorganic grids, for example, silica gels or bonds in their paper: Artificial inorganic biohybrids: The functional combination of microorganisms and cells with inorganic materials. Macko et al. [29] demonstrated concepts of designing, editing, and producing organs for educational and training purposes in their paper CAE/FDM Methods for Design and Manufacture Artificial Organs for Exercises Purposes."

1.2 Overview of Hydrogel Bioprinting Technologies

The creation [21] of standard structure and phony cell along with the help of included substance fabricating (AM) is one of the best accomplishments secured by the researchers. 3D printing of biological materials for the most part known as bio-inks that makes 3D composition like skeletons structure and cells. The bio-inks are made out of the unequivocal biological compatible materials with the objective that it could be invigorate cell affiliations, authentic progress, and their ability in the period of and resulting to print. Biological compatibility of these structures is fundamental for the bioprinting since it should take an intrigue really during departure, so the standard reason for blending of the specialists is on the physical practices and interchanged accomplice techniques for these structures to get mindful or unequivocal explanation. The blend of biomaterials [22] along with the live cells additionally gives a prospect mix to this bioprinting of self-supporting plans. Plus, the biocompatible materials in like way fortify cell sensibility as no cytotoxic and provide suitable creating features for present minute.

2   Comparison of Various Manufacturing Techniques

See Table 1.

3   Biological Terms

3.1   Tissue Grafting

It has been known for quite a while [8, 16, 24]. Having the antiquarianism proof that is, the lost tooth was supplanted through hand-cut ivory "inserts" the right on time, as old Egyptian occasions. Cell joining could be isolated onto the four significant classifications as per the hereditary connection between the benefactor and the beneficiary. It is of four types; they are **autogenous tissue graft (autograft), isogenous tissue graft (isograft), allogenous tissue graft (allograft), and xenogenous tissue graft (xenograft).**

3.2   Biomaterials

The term "Biomaterials" [8, 16, 24] successfully characterized as "materials of manufactured just as of characteristic inception within the contact with cell/tissue, blood, and natural liquids, or expected for the use of prosthetic, symptomatic, remedial, or capacity principle that do not unfavorably influence the living creature and its parts."

3.3   Bioactive Materials

The biological active material [8, 16, 24] inspires a particular organic reaction at the coherence of the material, in which the conclusion comes in the arrangement of the connection among the tissues and the material. Models incorporate "hydroxyapatite, polylactides" and biological-active glass pottery.

3.4   Scaffold Architecture

The biological creation process [8, 16, 24] is a difficult errand for mechanical architects. The manufacture of different complicated structures, for example, the kidney, will depend on a few stages and an expansive range of exceptionally planned gear.

Table 1 Merits and demerits of various artificial organ manufacturing techniques

Manufacturing technique	Advantages	Disadvantages	References
Bioplottering	High material range Biomaterials can be merged, mixed, and integrated	Low bond strengths Not highly accurate Processing time is high	[30]
3D printing	Support surface is not required Processing time is high Supportable to biomaterials and cells Support structure not required Non-toxic and non-disturbing components Use water as merger	Powdered form material is required Intermolecular bonding is weak Lined surface finished Machining is required	[24]
3D bio-assembly	High material range Compatible for biomolecules	High processing time Weak accuracy Weak stiffness and elasticity	[32]
Cell printing	Low response time and processing time High precision Compatible for natural polymers	Low stiffness and elasticity Weak printability	[6]
Cell patterning	Low response time and processing time High precision	Low stiffness and elasticity Weak printability 3D structures have low accuracy	[3]
Direct-write assembly	High stiffness and elasticity Compatible for biomolecules	Need preprocessing and solvents for the process Indirect involvement of cells	[31]
Robot dispensing (RPBOD)	Allows axis control Have multiple discharging heads	Low material range High processing time Low mechanical strengths Preprocessing is required	[16]
LD writing	Good precision Compatible for high limits of cells High response rate	High processing time Allows only two-axis control	[27]
Photo-patterning	Incorporates precised spatial distribution of scaffold Allows manufacturing of complex parts inside the specimen Low processing time	Use UV rays Used only with photo reactive biodegradable polymers Require a lot of expensive devices for processing	[14]

Table 1 (continued)

Manufacturing technique	Advantages	Disadvantages	References
Stereolithography (SLA)	Low response time High precision	Use UV rays Used only with photoreactive biodegradable polymers	[31]
3D Photofabrication	Used for manufacturing of macroporous structures High precision	Use UV rays Used only with photoreactive biodegradable polymers	[7]
Selective laser sintering(SLS)	Produce microporous scaffold Low processing time High material range and precision	Powdered form material is required Material trapped into micropores are difficult to remove Requires high temperature Lined surface finish	[24]
3D Micropatterning	Incorporates precised spatial distribution of scaffold Low processing time	Use UV rays Used only with photoreactive biodegradable polymers	[23]
Inkjet bioprinting	Low printability High viability	Difficult to realize Limited to features Poor mechanical property	[18]

3.5 Pore Size

It is a basic parameter [8, 16, 24] which decides the cell development and vascularization. It contrasts within the sort of cell. The ideal diameter scope of pores still stays an inquiry.

3.6 Surface Topography

It mainly [8, 16, 24] of the surface harshness has a powerful job in cell grid connection. Geography upgrades the separation of ancestor tissues into their modified passage. The unpleasant powder surface shaped from a powder-based quick response system may upgrade cell grip. Scaffolds morphology of small-scale and nanoscale structures improves the incitement of tissue arrangement, diffraction, extension, relocation, multiplication, quality articulation, and so forth.

3.7 Biopaper

The biological paper [8, 16, 24] is characterized as procedure capable and biomimetic tissue combination-tolerant hydrogels particularly intended for bioprinting process. A perfect hydrogel utilized for organ printing ought to pursue certain attributes, for example, biocompatible, biodegradable, upgrades touchy, quick cementing, normally inferred hydrogels, minimal effort, and so forth. "The hepatic hydrogel sheet modules installed with HepG2 cells were manufactured either with hexagonal microarchitecture or with no microarchitecture."

3.8 Cell Viability and Vascularization

The appropriation of the origin cells of the platforms which makes huge test in cells building [8, 16, 24]. The utilization of Petridishes for origin cells neglects for convey tissues somewhere internally the frameworks with constant state dissemination. So as to conquer these problems, cell structure of the 3D frameworks had cultivated through the enhancement of biological reactor innovations.

3.9 Autonomous Self-assembly

In the another form the deal with repeating original cells is to use undeveloped organ improvement so that guide [8, 16, 24]. The prior tissues wedge of the making cells produce their own possesses ECM sectors, comfortable tissues indicate and by own governing coalition and creating to surrender the ideal origin small range engineering or capacity. A 'platform free' form of this methodology utilizes self-amassing cell spheroids that experience combination and cell association to copy creating tissues.

3.9.1 Hydrogels

Hydrogels [15] had a place with liquid substances materials having less than 90% of H_2O material by weight. As we know that hydrogels have more prominent overrunning features for O_2 and furthermore having no any reaction to outside structures, all these are put in the sector of biological medical as origin and internal ocular focal point. Specialists consistently took a shot at searching the structures for few substitution of extra cell grid (ECM) for auxiliary assist of the tissue, and hydrogels are probably the better material in which they have incredible similarity with regular ECM.

The common advantages of the colloidal gel [10] are biologically compatible, biologically degradable, and effectively infused in vitro for development then explicit

situation, extraordinary convey facility of the supplements at the time of improvement development and could be without much of a stretch be adjusted for the use in better places. It likewise has a few confinements: It for the most part gives low mechanical quality, is hard to deal with, requires higher sanitized situation, and is costly for therapy.

3.9.2 Types of Hydrogels

See Table 2.

4 Challenges

See Table 3.

5 Test Required

5.1 Printability

A suitable material has a very important property of being accurate and precise deposition along the suitable spatial and temporal control. There are few kinds of bioprinting technologies, namely inkjet which has limitations on substance viscosity, while others, like microextrusion, require material to have specific shear-thinning properties or crosslinking mechanisms. Processing parameters like nozzle gauge, determine the shear stress to which the tissues get revealed also the time, which is appropriate to the substances to be submitted to form a three-dimensional structure.

5.2 Viscosity

The measure of a substance's resistance to motion under an applied force is called as viscosity.

Table 2 Properties of Hydrogels

Hydrogel	Properties	References
Collagen	• Mechanical properties of single molecules of collagen • Manipulation of collagen fibers mechanical characterization • Effects of relative humidity on physical properties of modern vellum and can be made in various kinds of gels, sponges, etc	[10, 12]
Gelatin	• Less stable at high temperature • Mechanical strength is high but it is brittle when dry and gummy when moist • It is a translucent and colorless • Typically, gelatin can be dispersed in a relatively concentrated acid. Such dispersions are stable for 10–15 days with little or no chemical changes and are suitable for coating purposes or for extrusion into a precipitating bath	[15, 33]
Pullulan	• Made from the yeast, for instance, development Aureobasidium pullulans • Its powder is white with no taste and smell and not dissolvable in any normal or inorganic solvents beside the water • Due to the properties of water-dissolvable and unsafe nature, pullulan is used in clinical application, for instance, drugs carrier, the game plan of syrups and packaging material	[13, 19]
Hyaluronic acid	• The largest amounts of it are found in the skin, connective tissues, and eyes • It is to retain water to keep the tissues well lubricated and moist	[17, 28]
Poly (lactic and glycolic) acid-based	• Allow modifications in surface • Easy to transportation	[10, 25]
Polyethylene oxide- and polyethylene glycol-based	• High mechanical strength • Easy to handle for scaffold structures and chemical composition • Thermo-sensitivity is high	[8, 15]
Polycaprolactone-based	• Mechanical properties are low • Low cell adhesion and impact resistance is high	[17, 23]

Table 3 Challenges recorded in papers till now

Serial no	Challenges	References
1	Medication polymer trades as exemplified in tricky impacts related with the utilization of ACE inhibitors and negatively charged biomaterials	[2, 15]
2	The non-appearance of a functional wellspring of utilitarian cells for extended length use	[4, 8]
3	Finding reasonable frameworks for various tissues and responsive complex creation methods for tissue improvement	[20, 33]
4	Building complex extended vascular and bile-channel structures	[20, 27]
5	Cell-source selection	[1, 19]
6	Cell-induced differentiation	[20, 24]
7	Gene regulation	[20, 33]
8	Cell–cell, cell–compose, cell–dissolvable sign exchanges	[20, 30]
9	Pulsatile culture in vitro and transplantation in vivo	[14, 20]
10	Fabricated polymers for vascular and biliary structures: new sharp biomaterials blend; cell-affiliation limit; trademark dissolvable choice; mechanical-quality basic; debasement rate rule	[8, 33]
11	Fundamental polymers for different cell headway and division: cell similarity; cell-stay plan; crosslinking or change authority confirmation; debasement rate rule	[13, 29]
12	Polymer change for consecutive appearance of changed portions: discharge profile rule	[9, 20]
13	Rational structure and delineating: vascular and biliary framework creation and their game plan; diverse leveled multi-tissue plan and appearing; anatomical age	[12, 20]
14	RP advancement improvement: multi-meander aimlessly or syringe revelation making; mishandling programming	[20, 22]
15	Perfused bioreactor structure and use: reenactment of blood dispersal and transport properties of upgrades, oxygen, and nerve	[20, 26]
16	RP of heterotypic cells and structures	[18, 20]
17	Pass on a high thickness of the basic cells, both competently and dependably, all through the make volume	[6, 13]
18	Understanding the highlights and segments of heterotypic cell-correspondence pathways	[2, 20]
19	Segment of lacking cells into various sorts of hepatic cell	[17, 20]
20	Technique selection	[4, 9]
21	Need distinct command over pore size, pore interconnectivity, porosity and spatial development of pores inside the stage	[5, 28]
22	Combining cells and proteins in the creation methodology since they are generally finished under brutal conditions, for example, high temperature or inside observing trademark solvents	[5, 31]
23	Innovative mechanical power, which may cause cell hurt and an inability to accomplish the ideal cell number and cell development in the stage	[5, 16]

(continued)

Table 3 (continued)

Serial no	Challenges	References
24	The mechanical quality was not acceptable to help the cell social requests utilizing gelatin	[6, 29]
25	Less limit and adaptability of the hoarding methodology	[6, 10]
26	Depicting the structure–work relationship of multicellular frameworks with the target that the most outrageous constraint of living cells as steady substances can be comprehends it	[6, 17]
27	Angiogenesis, vasculogenesis, comparably as parenchymal and mesenchymal tissue recovery in one make ought to be balanced in a fitting neighborliness way guaranteeing multifunctional insistence	[6, 21]
28	A productive confirmation of the strategy and things is required	[1, 6]
29	Affiliations or synergistic impacts of various cells and progression factors	[1, 29]
30	Long-term storage and viability maintenance	[6, 15]
31	Reduced molecular weight chitosan	[7, 21]
32	Design and improvement of systems with perfect properties	[8, 11]
	Restore the assistant features and physiological components of trademark tissues without ominously hurting the near to tissues	[1, 19]
33	Define the term biocompatibility or biocompatible, as both these explanations are emotional and a material which is ideal for a particular application may not work acceptably at a substitute zone in the body	[4, 25]
	Ceramics showcase poor mechanical quality and low break improvement resistance, which limit their vocations to non-load-bearing applications	[8, 26]
34	Bulk properties with a biocompatible surface, a material's surface can be modified in such a way so as to improve its bioactivity, without yielding its mass material properties	[11, 24]
37	Problem of biofilms	[8, 32]
38	Adjusting the substance character of the surface frequently includes changing its hydrophobicity	[12, 16]
39	Material preservation	[19, 25]
40	Laser approach requires a strong substrate, and material wastage can be high an aftereffect of powder scattering during arranging	[29, 30]
41	Issue related with powder stream rate, however the two approach permit reusing and reuse of unmelted powder	[8, 19]
42	While coordinating materials in semi-strong structure, gravity makes complex structures breakdown	[8, 27]
43	Making of enormous makes with full feasibility and utilitarian turn of events	[9, 30]
44	Autograft transparency and the related frightfulness in their making sure about	[9, 22]
45	A little bit at a time rules to join specific cell types in their various positions	[11, 28]

Table 3 (continued)

Serial no	Challenges	References
46	Merge biomaterials, including live cells and headway factors, into the predesigned stage materials	[8, 26]
47	Debasement rate encourages the rate at which cells inside them store their own cell and tissue unequivocal extracellular lattice (ECM)	[12, 30]
48	Progress of the normal ECM is dull	[12, 34]
49	Additional items of the debasing framework may encroach with standard tissue improvement and lead to unsettling influence and mechanical disappointment	[18, 24]
50	Obliged accessibility of provider tissue, requital of at any rate one working nerves, conceivable awfulness at the advertiser site	[21, 22]
51	Created vascular affiliations make it conceivable to make vascularized tissues	[7, 20]
52	Alter improvements expected to print liquid plastics and metals to the printing of touchy, living regular materials	[19, 34]
53	Reproduce the complex more diminutive extension plan of extracellular framework (ECM) parts and differing cell types in adequate targets to underline ordinary breaking point	[21, 30]
54	Specific affects identified with the sensitivities of living cells and the headway of tissues	[5, 34]
55	Increasing print resolution and speed	[16, 28]
56	Nature of the trim cell covering, it will by and large be hard to completely target and position cells	[3, 34]
57	Find materials that are not just immaculate with ordinary materials and the printing method in any case can in like way give the ideal mechanical and practical properties for tissue makes	[15, 34]
58	Poor biocompatibility, dangerous pollution things, and loss of mechanical properties during defilement	[21, 22]

5.3   *Shear-Thinning Property*

Gathering of fluids with shear stress as a movement of shear rate: Pseudoplastic, Bingham and Bingham pseudoplastic all show minimization in possible thickness with developing shear rate.

5.4   *Response and Transition Time*

The scale of chronology taken for a system or person, reacting to the provided stimulus or event, is called as response time. The **time** taken by the material changing its state is called as transition time.

5.5 *Mechanical Properties*

By their nature [8, 16, 24], colloidals are vastly inflamed solids which are water-inflamed, cross-linked, and hydrophilic chemical compounds. The inheritances of a especial colloidals are excessively imperative in choosing which substances are applicable for a given utilization. However, these similar inheritances are highly relying on the sensible conditions. With this consolidation of sectors, it is important that colloidals inheritances are resolved and that they are deliberate under conditions which are as close to the sedentary conditions as possible. The testing of mechanical properties is done by testing **stiffness and elasticity.**

6 Conclusions and Future Scopes

Organ making be a tangled, wide methodology that unites accessory degree generally crucial style, biomaterial decision, various cell bargain, and tissue recovery. The RP passing on frameworks, by applying superimposed PC-driven declaration of planned materials into 3D cluttered structures, has the well-being to blend information and methodologies from cell science, material science, mechanics, tissue building, and clinical strategy to make pleasing organ analogs unequivocally by abuse living cells, built controllers, and stage biomaterials. Multi-meander aimlessly RP strategy will be utilized for future capable assessments of overwhelmed organ passing on methodologies to shape potential to make organ analogs with genuinely reproducible muddled models and variable material affiliation.

Future normal framework bearing of this structure embodies the resulting points of view: (1) Biological difficulties, for example, cell-source choice: make cells, young microorganisms; cell-activated parcel: cell headway factors and various affiliations; game-plan rule: time movement; cell–cell, cell–network, cell–dissolvable sign facilitated endeavors; pulsatile culture in vitro and transplantation in vivo; (2) biomaterial challenges, for example, fake polymers for vascular and biliary structures: new staggering biomaterials amalgamation, cell-affiliation limit, basic dissolvable decision, mechanical-quality interest, debasement rate rule; natural polymers for changed cell improvement and division: cell equivalence, cell-get style, crosslinking or alteration manager decision, pollution rate rule; compound modification for successive unharness of different fragments: discharge profile rule; (3) engineering inconveniences for example critical style and appearing, vascular, and biliary structure creation and their methodology, arranged multi-tissue style and delineating, anatomical diversion; RP advancement improvement: multi-meander aimlessly or syringe pledge making, misusing programming; perfused bioreactor style and use: age of circulation system, transport properties of upgrades, gas and nerve; RP of heterotypic cells and frameworks.

References

1. Wang, X., Ao, Q., Tian, X., Fan, J., Tong, H., Hou, W., & Bai, S. (2017). Gelatin-Based hydrogels for organ 3D bioprinting. *Polymers, 9*(12), 401.
2. Vienken, J. (2002). Polymers in nephrology characteristics and needs. *The International Journal of Artificial Organs*, *(5), 470–479. https://doi.org/10.1177/039139880202500518
3. Nahmias, Y., Arneja, A., Tower, T. T., Renn, M. J., & Odde, D. J. (2005). Cell patterning on biological gels via cell spraying through a mask. *Tissue Engineering, 11*(5–6), 701–708. https://doi.org/10.1089/ten.2005.11.701.
4. Wang, X., Yan, Y., & Zhang, R. (2007). Rapid prototyping as a tool for manufacturing bioartificial livers. *Trends in Biotechnology, 25*(11), 505–513. https://doi.org/10.1016/j.tibtech.2007.08.010.
5. Li, M. G., Tian, X. Y., & Chen, X. B. (2009). A brief review of dispensing-based rapid prototyping techniques in tissue scaffold fabrication: The role of modelling on scaffold properties prediction. *Biofabrication, 1*(3), 032001. https://doi.org/10.1088/1758-5082/1/3/032001.
6. Wang, X., Yan, Y., & Zhang, R. (2010). Recent trends and challenges in complex organ manufacturing. *Tissue Engineering Part B: Reviews, 16*(2), 189–197.
7. Chmielewski, A. G. (2010). Chitosan and radiation chemistry. *Radiation Physics and Chemistry, 79*(3), 272–275. https://doi.org/10.1016/j.radphyschem.2009.11.002.
8. Kalita, S. J. (2010). Rapid prototyping in biomedical engineering: structural intricacies of biological materials. *Bio-integration of Medical Implant Materials*, 349–397.
9. Rath, S. N., Pryymachuk, G., Bleiziffer, O. A., Lam, C. X. F., Arkudas, A., & Ho, S. T. B. (2011). Hyaluronan-based heparin-incorporated hydrogels for the generation of axially vascularized bioartificial bone tissues: In vitro and in vivo evaluation in a PLDLLA–TCP–PCL-composite system. *Journal of Materials Science: Materials in Medicine, 22*(5), 1279–1291.
10. Guvendiren, M., Lu, H. D., & Burdick, J. A. (2012). Shear-thinning hydrogels for biomedical applications. *Soft Matter, 8*(2), 260–272.
11. Wang, X. (2012). Intelligent freeform manufacturing of complex organs. *Artificial Organs, 36*(11), 951–959. https://doi.org/10.1111/j.1525-1594.2012.01499.x.
12. Marga, F., Jakab, K., Khatiwala, C., Shepherd, B., Dorfman, S., & Hubbard, B. (2012). Toward engineering functional organ modules by additive manufacturing. *Biofabrication, 4*(2), 022001.
13. IKADA, Y. (2001). Biocompatibility of hydrogels. Gels Handbook, 388–407.
14. Zhu, J., Zhang, Y., Xu, N., Wang, L., Xiang, X., & Zhu, X. (2013). The preparation of PLL–GRGDS modified PTSG copolymer scaffolds and their effects on manufacturing artificial salivary gland. *Journal of Biomaterials Science, Polymer Edition*, *24*(15), 1721–1739.
15. Ahmed, E. M. (2015). Hydrogel: Preparation, characterization, and applications: A review. *Journal of Advanced Research*, *6*(2), 105–121.
16. Murphy, S. V., & Atala, A. (2014). 3D bioprinting of tissues and organs. *Nature Biotechnology*, *32*(8), 773–785. https://doi.org/10.1038/nbt.2958.
17. Li, Jianyu, Suo, Zhigang, & Vlassak, Joost J. (2014). Stiff, strong, and tough hydrogels with good chemical stability. *Journal of Materials Chemistry B*, *2*(39), 6708–6713.
18. Ahn, S. H., Lee, J., Park, S. A., & Kim, W. D. (2016). Three-dimensional bioprinting equipment technologies for tissue engineering and regenerative medicine. *Tissue Engineering and Regenerative Medicine*, *13*(6), 663–676.
19. Park, S.-H., Jung, C. S., & Min, B.-H. (2016). Advances in three-dimensional bioprinting for hard tissue engineering. *Tissue Engineering and Regenerative Medicine*, *13*(6), 622–635.
20. Agarwala, S. (2016). A perspective on 3D bioprinting technology: Present and future. *Journal of Engineering and Applied Science, 9*(4), 931.
21. Zadpoor, A. A., & Malda, J. (2016). Additive manufacturing of biomaterials, tissues, and organs. *Annals of Biomedical Engineering, 45*(1), 1–11.
22. Zhang, Y. S., Yue, K., Aleman, J., Mollazadeh-Moghaddam, K., Bakht, S. M., & Yang, J. (2016). 3D bioprinting for tissue and organ fabrication. *Annals of Biomedical Engineering, 45*(1), 148–163.

23. Naseer, S. M., Manbachi, A., Samandari, M., Walch, P., Gao, Y., & Zhang, Y. S. (2017). Surface acoustic waves induced micropatterning of cells in gelatin methacryloyl (GelMA) hydrogels. *Biofabrication, 9*(1), 015020. https://doi.org/10.1088/1758-5090/aa585e.

24. Ratheesh, G., Venugopal, J. R., Chinappan, A., Ezhilarasu, H., Sadiq, A., & Ramakrishna, S. (2017). 3D fabrication of polymeric scaffolds for regenerative therapy. *ACS Biomaterials Science & Engineering, 3*(7), 1175–1194.

25. Wu, D., Yu, Y., Tan, J., Huang, L., Luo, B., Lu, L. et al. (2018). 3D bioprinting of gellan gum and poly (ethylene glycol) diacrylate based hydrogels to produce human-scale constructs with high-fidelity. *Materials & Design.*

26. Saroia, J., Yanen, W., Wei, Q., Zhang, K., Lu, T., & Zhang, B. (2018). A review on biocompatibility nature of hydrogels with 3D printing techniques, tissue engineering application and its future prospective. *Bio-Design and Manufacturing.* https://doi.org/10.1007/s42242-018-0029-7.

27. Gupta, S., Bissoyi, A., & Bit, A. (2018). A review on 3D printable techniques for tissue engineering. BioNanoScience.

28. Holzmeister, I., Schamel, M., Groll, J., Gbureck, U., & Vorndran, E. (2018). Artificial inorganic biohybrids: The functional combination of microorganisms and cells with inorganic materials. *Acta Biomaterialia, 74,* 17–35.

29. Macko, M., Szczepański, Z., Mikołajewski, D., Nowak, J., Mikołajewska, E., & Furtak, J. (2019). CAE/FDM methods for design and manufacture artificial organs for exercises purposes. *Current Topics in Behavioral Neurosciences*, 462–469.

30. Landers, R., & Mulhaupt, R. (2000). Desktop manufacturing of complex objects, prototypes and biomedical scaffolds utilizing computer-assisted design combined with computer-guided 3D plotting of polymers and reactive oligomers. *Macromolecular Materials and Engineering, 282,* 17–21.

31. Deliormanlı, A. M. (2019). Direct Write Assembly of Graphene/Poly(ε-Caprolactone) Composite Scaffolds and Evaluation of Their Biological Performance Using Mouse Bone Marrow Mesenchymal Stem Cells. Applied Biochemistry and Biotechnology.

32. Wenger R. & Giraud M.(2018). 3D Printing Applied to Tissue-Engineered Vascular Grafts. Applied Sciences. https://doi.org/10.3390/app8122631.

33. Matai, I., Kaur, G., Seyedsalehi, A., McClinton, A., & Laurencin, C. T. (2019). Progress in 3D bioprinting technology for tissue/organ regenerative engineering. Biomaterials, 119536.

34. Kou, G., Ergu, D., Chen, Y., & Lin, C. (2016). Pairwise comparison matrix in multiple criteria decision making. *Technological and Economic Development of Economy, 22*(5), 738–765.

Study on Microstructure, Mechanical, and Thermal Properties of High-Entropy Alloys

Sushil Kumar and Satpal Sharma

Abstract The research focus in almost all applications is currently high-entropy alloys (HEAs). HEAs comprise several main elements which can extend considerably more than conventional alloys by the possible number of HEA compositions. Different alloy structures with improved property combinations have been explored in the last 15 years to identify HEA systems, resulting in an extraordinary development of this area. This paper discusses a few essential topics in the field: core effects, phase development, mechanical features, high temperature, and corrosion behavior. It also outlines existing issues and future recommendations for product technology and research.

Keywords Mechanical strength, high entropy alloys · High-entropic components · Alloy model

1 Introduction

Functional alloys, like steels, aluminum, magnesium, titanium, or nickel-based alloys generally are formed on the alloy design which controls the production of the stage with one or two major elements of the alloy. Although the inoculation, grain grinding, corrosion, scavenging or melting of additional elements are often included in a variety of alloy systems such as these are not designed to interfere with the production phases a researcher in this field revealed an advanced idea of "high Entropy alloys," which consist of five or more equimolar and almost equimolar elements at a specific rate of 5–35 [1, 2]**.**

The unique aspect of HEAs that have instilled an interest in these structures is that they seem to tend to form solid solutions rather than forming orderly intermetallic phases, which the large entropy of the blending considers stabilized [3]**.**

S. Kumar (✉) · S. Sharma
Mechanical Engineering, School of Engineering, Gautam Buddha University, Greater Noida, India
e-mail: sushil_eng@yahoo.com

S. Sharma
e-mail: satpal78sharma@gmail.com

But the advancement of HEAs has shown that solid solutions mixing might not be enough to offer a discreet stable solution but only composites (in the HEA scope) that can be named solid methodologies are recognized [4]. The research suggested that high entropy composites should be made from minor differences in the atomic size and for that absolute mixture, enthalpy should be close to zero, in order to develop a solid solutions. Reports suggest variations of atomic size <6.5%; a mixing enthalpy came to be in between 215 from 5 kJ mol range while the mixing entropy would be in ≈12–17.5 J K-1 mol^{-1} ranges. HEAs have been documented with high mechanical strength and high specific strength at both room temperatures and higher temperatures. Their compressive strength and corrosion with their excellent thermal conductivity also showed an important interest in HEAs as successful applicants for various applications.

The main objective of this work to study the previous researches for identifying the methods, materials, and different parameters used in the formation of high-entropy alloys to provide a further advancement in this field using some different combinations or methods in future.

2 Concepts of High-Entropy Alloys

The topic of discussions in recent years has been microstructures and the outstanding features of high-entropy alloys. The majority of its micro-structural characteristics depend on different effects in preparing HEAs. Four core effects were previously studied for period solidity and strong features in HEAs [5]. The following are the four effects.

2.1 Effect of High Entropy on HEAs

According to high-entropy effect, the free energy of solid solution phases decreases due to the higher mixing entropy in HEAs and at higher temperatures, simplifies their development. The vast amount of components required for the synthesis of HEA entropy (ΔS_{mix}) has increased, leading to the decrease of the total (ΔS_{mix}) and a more stable form of the basic structure of solid solutions [2, 6, 7]. The entropy has high effect on characterization of different alloys formed after mixing different properties to show high entropy for their applications.

2.2 Effect of Lattice Distortion on HEAs

The lattice distortion effects are generally defined as the movement or deviation of a crystal lattice from a perfectly defined structure of any material. The multi-component

structure in the solid HEAs formulation contributes to high button amount of stress, largely due to different nuclear mass associated with standard functionality [8, 9]. This effect can be generally seen in HEAs due to their arrangement style of atoms.

2.3 Sluggish Diffusion Effect

Low-dissemination surface morphology contributes immensely to the exceptional superior properties such as high electron density alloys. The thermodynamic properties of increased-entropy alloy propagation have never been tested explicitly. Numerous researches have suggested the slow absorption in HEAs, which reduces the spill rate in one stage of the multi-element matrix, which directly slows down the process. Fresh transitions from the ancient period, many different kinds of atoms must be distributed cooperatively to carry out the composition partitioning [10–13].

2.4 Cocktail Effect

Usually, the cocktail equation indicates that this can lead to unpredictable characteristics, which cannot be derived from any particular element when several elements in an alloy system have been mixed [3, 14, 15]. The characteristics of HEAs definitely contribute to the characteristics of the components. Added light elements, for example, decreases alloy density. However, in addition to the characteristics of single component elements, the linkage between components should be viewed. For reference, Al is a soft item with a low melting temperature. However, Al can be applied to harden HEAs.

3 Classification HEAs on the Basis of Thermodynamics

The major factor simplifying the component different stages is the electron density mixture for most high-entropy alloys. The argument is based on the second act of quantum mechanics for a framework for isothermic and isobaric purposes that gives stability if Gibbs' fusion power G reaches the permissible importance [16]. Take into account the argument of an alloy forming Fig. 4. Enhanced framework of crystal, (a) BCC, (b) FCC [17]. The free energy transition of the mix from the elementary state to the alloyed one can be expressed in the form of the $\Delta G_{mix} = \Delta H_{mix} - T\Delta S_{mix}$ from its component elements under isobaric conditions. The balanced state is therefore the lowest free energy state. Following Boltzmann's relationship between entropy and the complexity of systems, ΔS_{mix} per mole can be calculated as Rln(n) in which R is the gas constant for the formation of a disordered equivocated solution. The results of this study show an increase in mixing entropy with the number of equimolar alloy
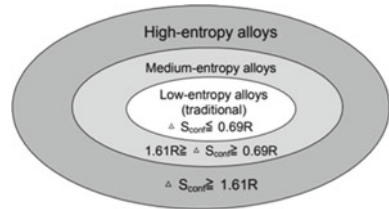
components. This clearly demonstrates that perhaps the rotational velocity of solution mixing significant increase from negative value, along with nonequimolar enzymes, to maximum amounts for normal composite material. Since the thermodynamically stable condition with multiple main components is massive, at the very same significance as the ΔS_{mix}, while the multimodal transport molecule state is limited, at the very same real worth, especially at high temperatures, has a more stable impact on reducing the mixing energy free. In contrast, the enthalpy of multi-element random solid solutions ΔH_{mix} is not significantly lower than that of the ordered intermodal compounds, given that, like the latter, the former has many pairs of atoms which are not similar. It allows a mixing entropy very efficient in reducing the free energy of mixing random solid solutions, with the exception of cases where stronger (covalent, ionic) connections predominate between other elements (e.g., reaction to O), it results in powerful iterations of the material, like oxides, borides, sugars, nitrides, silicates dispersed into the composite material. We strongly recommend that the metal universe be divided into three communities depending on the combining electron density actual impact, as can be seen in decreased-entropy composites are contemporary components. Moderate-entropy materials are the prototypes with at leastfive main components. And standard size-entropic composites are the materials with 2–4 key elements. In variable-entropy alloys the intermetallic compounds occurrence of the problematic solution cycle is found in the most important sectors. The fixation of the simple crystal structure process is very important with regard to the mechanical properties in these items [2].

Figure 1 shows the categories of alloys with respect to entropy. Entropy plays a significant role in selecting an alloy material. As different applications require different entropy rates, maximum the entropy maximum the efficiency will be provided by the alloy material. So, a lot of measures and researches have been going on to increase the entropy of traditional alloy materials with different techniques and materials.

4 Phase and Crystal Structure

Phases in HEAs are normally differently categorized in the literature. These are often defined as solid discrete solutions (i.e., FCC, BCC), solid solution ordered (i.e., B2 and $L1_2$), and intermetallic processes (i.e., laves stages). This categorization may

lead to confusion since intermetal phases can also by definition be classified as well-ordered solid solutions; these have variations of structure and are usually arranged. In this context, it is recommended to categorize phases according to the framework (straightforward/complex) and order (ordered/unordered).

4.1 Simple Solid Solution or Intermetallic

In most scientists' knowledge, the most commonly seen as-cast HEAs are simple organizations (SDPs and SOPs). These easy phases are due to the high-entropy effect stated in the first section of this paper. In addition to the single phases, various types of COPs are also observed in HEAs, such as σ, μ, and laves. Because the HEAs are unique to simple phases with more than five elements, numerous studies have been conducted on the formation synthesis.

As per the classical Hume-Rothery rules, differences in atomic size, electron content, and electro negativity differences affect the forming of solid binary solutions [3]. In addition to these factors, HEA 's main stage formation parameters are enthalpy and entropy mixing. Various tests were conducted regarding the impact of these constraints on HEAs phase development: the development of single or diverse phases depends completely on the mixture potential energy (H_{mix}), the blending gravitational waves (S_{mix}), and variation in atomic sizes (δ). Crystal structure of simple solid solution phases.

When a HEA has a single phase, virtually, every single solid-solution phase observed in HEAs is structured with BCC or FCC [18–21]. The critical factor determining whether the alloy crystallizes into the BCC or FCC structure appears VEC (electron-valence value, alloy-VEC is calculated based on a weighted average VEC for the component). Guo et al. have summarized the relationship between the VEC and the many HEAs structure [22]. They also found that the structure of the FCC is stabilized where the VEC is greater than 8. The BCC structure is stable if the VEC of the alloy is smaller than 6.87. The VEC values between 6.87 and 8 show co-existence of the FCC and BCC phases [22]. However, until now, the mechanism behind the VEC effect on the formation of phases has not been fully understood.

4.2 Tendency to Form Nanostructures and Amorphous Phases

In addition to the high-entropy effect, multiple main elements also cause the trend to form nanophases, which enhance the formation of simple solution phases [18]. Numerous nanoprecipitates are seen in the matrix using TEM bright field and dark field images. Typically, nanophases in the high-entropy cast alloy matrix

are commonly found. This is difficult to see in the conventional alloys as-cast microstructure.

It also explains the effect of kinetics. The diffusive transformation can take place in the matrix in two ways: (1) spinodal decomposition and (2) precipitation. The creation of a new phase involves the collective distribution of a wide variety of atoms for partitioning the composition during the transformation process. In high-entropy alloys, the movement for such a partition of several forms of substitution solution atoms would be sluggish, resulting in nanophases [18] gradually. The "confusion principle" in the multiplied alloys [23]. Is associated with this principle studies have shown the phase formation sequence of a different aluminum content alloy cooling $Al_xCoCrCuFeNi$ [18]. The liquid phase forms dendritic and inter-dendritic stages of solid resolution followed by (nano) precipitation for the low level of aluminum. The molten stage serves to reinforce and shapes stable solution neuronal and inter-dendritic aspects usually accompanied by spinodal decomposition, which generates submicron augmented and then nanoprecipitation structural elements for a greater extent of activation temperature.

5 Different Behaviors of HEAs

5.1 Mechanical Behavior of HEAs

A significant number of experiments were performed to test the mechanical activity of HEAs. Two equi-atomic multi-element alloys, including arc molding and hot rolling, were produced in a study. One was a CrMnFeCoNi, a high-entropy quinary alloy, and the other a CrFeCoNi, a quaternary medium-entropy alloy. Their tensile performance is studied at -196 to $1000\,°C$ temperature and 10–3 and 10–1 s-1 strain rates. The two alloys showed a strong dependence on temperature on strength and low dependency on the strain. The temperature-dependent strength in pure FCC metals is not generally found in FCC solid solution alloys in some binary FCCs [7].

The evaluation of CrCoNi's mechanical properties at cryogenic temperatures, which showed the strength-toughness properties that exceed that of all high-entropy alloys and most multiple phases alloys was conducted as a single, facially centered cubic solid solution. At room temperature, the alloy has a tensile strength of nearly $1\,GPa$, a failure strain of 70%, and K_{JIc} fractures of more than $200\,MPa\,m^{1/2}$; CrCoNi alloy strength, ductility, and hardness increase to performance levels of over $1.3\,GPa$ at cryogenic temperatures, a failure strain of 90%, and K_{JIc} values of $275\,MPa\,m^{1/2}$ at room temperature. These properties appear to be the consequence of continuous constant stress harding, which is the result of strong dislocation activity and nano-twinning deformation-induced, to suppress plastic instability.

More analysis was performed using multiple element $Al_xCoCrCuFeNi$ alloys (x $=$ the molar aluminum content from 0 to 3.0) and their mechanical properties were synthesized using a well-defined method for the molding and casting of the arcing.

These alloys showed promising mechanical characteristics with excellent resistance to wear and high temperatures.

5.2 Thermal Behavior of HEAs

The high-entropy alloys (HEAs) are the most advantageous solution for use in high-temperature applications for forming a simple solid solution. To date, research into HEAs has been based on research into the different characteristics of equimolar or near-equimolar alloys consisting of almost similar elements. This trial is aimed at investigating Ti's effect on $AlCr_{1.5}CuFeNi_2Ti_x$ thermal activity (x = 0, 0.25, 05, 0.75, 1 molar related). At different temperatures, between 300 and 500 K, the thermal conductivity of the alloy was calculated by a thermal disc constant analyzer. This study concluded that the alloy's thermal conductivity decreases when the amount of titanium is decreased, but the thermal conductivity increases when the temperature is increasing [24].

5.3 Effect of Corrosion on HEAs

The corrosion behavior of most of the novel high-entropy alloys is yet to be studied. A study with a purpose to study and investigate the effect of Ti on the corrosion of $AlCr_{1.5}CuFeNi_2Ti_x$ (x = 0, 0.25, 0.5, 0.75, 1 in molar ratio) alloys was conducted. After the complete experiment, the minimum and maximum values of corrosion rate were found to be 0.068 and 0.300 mmpy for Ti_0 and $Ti_{0.75}$, respectively [24]. Similar study investigated the effect of the Al content on the corrosion behavior of $Al_xCrFe_{1.5}MnNi_{0.5}$ HEAs [25]. The addition of aluminum significantly affected the evolution of phase structures. The microstructure changed from the FCC + α-FeCr ($CrFe_{1.5}MnNi_{0.5}$), to FCC + BCC ($Al_{0.3}CrFe_{1.5}MnNi_{0.5}$), and eventually to BCC ($Al_{0.5}CrFe_{1.5}MnNi_{0.5}$) structures as the Al content increased, which was in accordance with other studies [26, 27].

6 Conclusion

In distinction to simply about 30 common conventional alloys, high-entropy alloys are countless. They can be refined and analyzed as normal metals. The formation of solution phases and the multi-purpose components causes slow diffusion with high entropy and the consequential micro-structures repeatedly comprises of nanophases and still amorphous parts. Owing to their unique mechanical and thermal microstructures, a variety of opportunities to manufacture new alloys are waiting for development, in a number of situations more than traditional ones. The analysis offers a

systematic report on the microstructures, mechanical efficiency, and thermal conductivity of HEAs for the introduction of quality and technique of data collection. In the future, some more combinations or techniques can be utilized for preparing a high-entropy alloy for different applications. Further considering these studies discussed in this paper, a new study can be proposed with keeping in mind the problems and their solutions for newer application.

References

1. Yeh, J. W., et al. (2004). Nanostructured high-entropy alloys with multiple principal elements: Novel alloy design concepts and outcomes. *Advanced Engineering Materials, 6*(5), 299–303. https://doi.org/10.1002/adem.200300567.
2. Yeh, J. W., Chen, Y. L., Lin, S. J., & Chen, S. K. (2007). High-entropy alloys—A new era of exploitation. *Materials Science Forum, 560,* 1–9. DOI: https://doi.org/10.4028/.
3. Zhang, Y., Zhou, Y. J., Lin, J. P., Chen, G. L., & Liaw, P. K. (2008). Solid-solution phase formation rules for multi-component alloys. *Advanced Engineering Materials, 10*(6), 534–538. https://doi.org/10.1002/adem.200700240.
4. Yang, X., & Zhang, Y. (2012). Prediction of high-entropy stabilized solid-solution in multi-component alloys. *Materials Chemistry and Physics, 132*(2–3), 233–238. https://doi.org/10.1016/j.matchemphys.2011.11.021.
5. Yeh, J. W. (2013). Alloy design strategies and future trends in high-entropy alloys. *Jom, vol. 65*(12), 1759–1771. https://doi.org/10.1007/s11837-013-0761-6.
6. Gludovatz, B. et al. (2016). Exceptional damage-tolerance of a medium-entropy alloy CrCoNi at cryogenic temperatures. *Natural Communication, 7*, 1–8. https://doi.org/10.1038/ncomms10602.
7. Gali, A., & George, E. P. (2013). Tensile properties of high- and medium-entropy alloys. *Intermetallics, 39*, 74–78. https://doi.org/10.1016/j.intermet.2013.03.018.
8. Yeh, J., Chen, S., Gan, J., Lin, S., & Chin, T. (2010). *Communications: Formation of Simple Crystal Structures in Cu-Co-Ni-Cr-Al-Fe-Ti-V Alloys with Multiprincipal Metallic Elements* (Vol. 35, no. August 2004, pp. 2533–2536).
9. Yeh, J. W., Chang, S. Y., Der Hong, Y., Chen, S. K., & Lin, S. J. (2007). Anomalous decrease in X-ray diffraction intensities of Cu-Ni-Al-Co-Cr-Fe-Si alloy systems with multi-principal elements. *Materials Chemistry and Physics, 103*(1), 41–46. https://doi.org/10.1016/j.matchemphys.2007.01.003.
10. Tsai, K. Y., Tsai, M. H., & Yeh, J. W. (2013). Sluggish diffusion in Co-Cr-Fe-Mn-Ni high-entropy alloys. *Acta Materialia, 61*(13), 4887–4897. https://doi.org/10.1016/j.actamat.2013.04.058.
11. Kulkarni, K., & Chauhan, G. P. S. (2015). Investigations of quaternary interdiffusion in a constituent system of high entropy alloys. *AIP Advances, 5*(9). https://doi.org/10.1063/1.4931806.
12. Vaidya, M., Trubel, S., Murty, B. S., Wilde, G., & Divinski, S. V. (2016). Ni tracer diffusion in CoCrFeNi and CoCrFeMnNi high entropy alloys. *The Journal of Alloys and Compounds, 688,* 994–1001. https://doi.org/10.1016/j.jallcom.2016.07.239.
13. Divinski, S. V., Pokoev, A. V., Esakkiraja, N., & Paul, A. (2018). A Mystery of 'Sluggish Diffusion' in High-Entropy Alloys: The Truth or a Myth? *Diffus Found, 17,* 69–104. DOI: https://doi.org/10.4028/.
14. Tong, C.-J. et al. (2005). Microstructure characterization of Al. *Metallurgical and Materials Transactions A: Physical Metallurgy and Materials Science, 36*(4), 881–893.
15. Ranganathan, S. (2003). Alloyed pleasures: Multimetallic cocktails. *Current Science, 85*(10), 1404–1406.

16. Hsu, C.-Y., Yeh, J.-W., Chen, S.-K., & Shun, T.-T. (2004). Wear resistance and high-temperature compression strength of Fcc CuCoNiCrAl. *Metallurgical and Materials Transactions A: Physical Metallurgy and Materials Science, 35*(5), 1465–1469.

17. Tong, C. J. et al. (2005). Mechanical performance of the AlxCoCrCuFeNi high-entropy alloy system with multiprincipal elements. *Metallurgical and Materials Transactions A: Physical Metallurgy and Materials Science, 36(5)*, 1263–1271. https://doi.org/10.1007/s11661-005-0218-9.

18. Tong, C. J. et al. (2005). Microstructure characterization of AlxCoCrCuFeNi high-entropy alloy system with multiprincipal elements. *Metallurgical and Materials Transactions A: Physical Metallurgy and Materials Science, 36(4)*, 881–893. https://doi.org/10.1007/s11661-005-0283-0.

19. Senkov, O. N., Wilks, G. B., Miracle, D. B., Chuang, C. P., & Liaw, P. K. (2010). Refractory high-entropy alloys. *Intermetallics, 18*(9), 1758–1765. https://doi.org/10.1016/j.intermet.2010.05.014.

20. Tung, C.C., Yeh, J.W., Tsung Shun, T., Chen, S. K., Huang, Y. S. & Chen, H. C. (2007). On the elemental effect of AlCoCrCuFeNi high-entropy alloy system. *Materials Letters, 61*(1), 1–5. https://doi.org/10.1016/j.matlet.2006.03.140.

21. Senkov, O. N., Scott, J. M., Senkova, S. V., Miracle, D. B., & Woodward, C. F. (2011). Microstructure and room temperature properties of a high-entropy TaNbHfZrTi alloy. *The Journal of Alloys and Compounds, 509*(20), 6043–6048. https://doi.org/10.1016/j.jallcom.2011.02.171.

22. Guo, S., Ng, C., Lu, J., & Liu, C. T. (2011). Effect of valence electron concentration on stability of fcc or bcc phase in high entropy alloys. *Journal of Applied Physics, 109*(10). https://doi.org/10.1063/1.3587228.

23. . Lindsay Greer, A. (1993). Confusion by design. *Nature, 366*(366), 303–304.

24. Kukshal, V., Patnaik, A., & Bhat, I. K. (2018). Corrosion and thermal behaviour of AlCr1.5CuFeNi2Tix high-entropy alloys. *Materials Today: Proceedings, 5*(9), 17073–17079. https://doi.org/10.1016/j.matpr.2018.04.114.

25. Lee, C. P., Chang, C. C., Chen, Y. Y., Yeh, J. W., & Shih, H. C. (2008). Effect of the aluminium content of AlxCrFe1.5MnNi0.5 high-entropy alloys on the corrosion behaviour in aqueous environments. *Corrosion Science, 50*(7), 2053–2060. https://doi.org/10.1016/j.corsci.2008.04.011.

26. Zhang, Y., et al. (2014). Microstructures and properties of high-entropy alloys. *Progress in Materials Science, 61*, no. October 2013, 1–93. https://doi.org/10.1016/j.pmatsci.2013.10.001.

27. Senkov, O. N., Senkova, S. V., & Woodward, C. (2014). Effect of aluminum on the microstructure and properties of two refractory high-entropy alloys. *Acta Materialia, 68,* 214–228. https://doi.org/10.1016/j.actamat.2014.01.029.

Optimization of Friction Stir Welding Parameters for Similar Base Material Combinations

Abhishek Chauhan and Sanjeev Kumar

Abstract In this investigation, FSW was carried out for similar base material combinations. Friction stir welding of plates having 6 mm thickness made up of AA2014 aluminium alloy, AZ31 magnesium alloy, and Al-SiC composite was done using alloy steel tool. The welding was carried out at different levels of rotational speed, feed rate, pin shape, and preheating. The effect of these welding parameters was studied on tensile strength and yield strength of the welded joints. The optimization of the selected parameters of friction stir welding was done using the Taguchi technique to suggest the optimal parameter values to the modern engineers. Analysis of results shows that rotational speed is a critical parameter which affects the tensile properties. The other significant parameters which affect strength of the joints are feed rate, material, and preheating.

Keywords Friction stir welding · Pin shape · Rotational speed · Tensile strength · Optimization

1 Introduction

1.1 Process, Principle, and Materials

The development of friction stir welding was started at the Welding Institute in the early 90s [1, 2]. The friction stir welding involves components which are joined by applying pressure and rotating motion of the tool. The friction between plates and tool raises the temperature of the plates due to heating which causes deformation of material [3]. In FSW, tool having cylindrical shoulder with a pin of different shapes is rotated at a fixed speed, and with proper feed rate it moves between the interfaces

A. Chauhan (✉)
UIET, PUSSGRC, Hoshiarpur, India
e-mail: mecherabhishek@yahoo.co.in

S. Kumar
Punjab Engineering College (Deemed to be University), Chandigarh, India
e-mail: skthakkarpec@yahoo.com

Fig. 1 Working of friction
stir welding process [4]
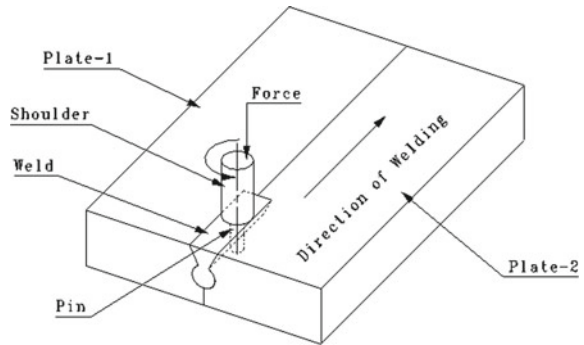
of the plates to be joined. The workpieces are fixed on the back plate using clamps so
that joining plates do not get apart. The length of the pin is less than the thickness of
the plates. The tool shoulder should touch the surface of the workpiece to generate
heat. The pin moves against the workpiece for stirring and plastic deformation takes
place which can be seen in Fig. 1.

Both tool rotation and traversing speed are the important parameters which help
in the formulation of defect-free joints [5]. Due to large number of advantages, FSW
is widely used in industries like ship building and marine, aerospace, railways and
land transportation. FSW is widely used to weld aluminium alloys [6], magnesium
alloys [7], steels [8], dissimilar alloys [9], and composites materials [10]. A lot of
researches are going on to weld metal matrix composites (MMCs), nickel, titanium,
lead, zinc, etc., using this process. Proper understanding is required to apply FSW
on any material and further evaluation of mechanical properties is needed to use it
for production purposes. So here is an attempt to understand FSW process and its
welding parameters with regard to mechanical properties.

1.2   Important Process Parameters

Tool Material: The quality of welding depends directly on tool material. The material
of the tool should have proper shear as well as compressive strength. It should have
good oxidation and wear resistance along with low thermal conductivity [11].

Tool Shape: The tool shape should be in such a way that tool maintains sufficient
downward pressure required for forging of material and it must prevent material from
extruding out of the sides of the shoulder. Mainly FSW tool comprises of cylindrical
pin and shoulder [11].

Tool Rotation and Welding Speed: These two parameters are most important for the
generation of sufficient heat and stirring of material. The tool speed should increase
and welding speed should decrease for proper heating of the materials [11].

Welding Forces: The different forces acting on the tool are downward force, traverse force, and lateral force. The forces acting on the tool should be less to prevent breakage of the tool [11].

Preheat: The preheating the material is important to generate temperature required for plastic deformation of the material. It provides defect-free joints and improves weld quality.

1.3 *Optimization of FSW Parameters*

FSW affects the mechanical properties of the welded joints, so there is lot of research going on to find out the optimized parameters for friction stir welding. The optimization of process parameters of FSW was done using Taguchi-based gray relational analysis to find out maximum tensile strength of the welded joints [12]. The optimization of friction stir processing parameters was done using Taguchi technique and their effect on hardness of brass plates was investigated using L9 orthogonal array [13]. The optimization of welding parameters of FSW process was done using Taguchi method to see their effect on fracture toughness energy and crack initiation energy [14]. The optimization of the control factors was carried out using Taguchi technique, and effect of these control factors on mechanical and microstructure properties was investigated [15]. The optimization of FSW parameters was carried out using L9 orthogonal array. The optimized input and output parameters were found out so that strong FSW joints can be produced for aerospace applications [16]. The properties like tensile strength, yield strength, hardness, etc., are affected by the friction stir welding parameters. The quality joints can be formed using optimized values of parameters. The optimized parameters can be used for the production process. The optimization techniques such as Taguchi, response surface method, gray relational analysis, and adaptive neurofuzzy inference systems (ANFIS) give optimal process parameters. The optimized parameters can be used to weld similar and dissimilar materials and will give improved mechanical properties [17].

2 Experimental Methodology

The selection of base materials and process parameters for the experimentation along with results of mechanical testing at different selected process parameters is presented here.

Fig. 2 Tools used for FSW

2.1 Base Materials and Tool

The base materials that were selected for welding are aluminium alloy having AA2014 grade, magnesium alloy having AZ31 grade, and aluminium composite reinforced with SiC. These materials were selected on the basis of their availability and useful applications. The material used for welding tool was alloy steel having EN31 grade which was further hardened and quenched. Three different shapes of pin used for the experiments were cylindrical, tapered, and threaded which is shown in Fig. 2.

2.2 Equipment and Fixture Used for Welding

The fabrication of joints using friction stir welding (FSW) was done on the vertical knee-type milling machine fitted with specially designed tool. The speed of the machine was from 30 to 2000 rpm. A back plate was used to carry out the experimentation. The mechanical clamps were used to fix the work pieces on the machine. For preheating the base material, dielectric heater was used. The picture of a fixture used for the process is given in Fig. 3.

Fig. 3 Fixture developed for
FSW process

2.3 Working Range of Parameters

The FSW process requires selection of relevant process parameters and their working
range. The pilot experiments were done to find the working range of the selected
parameters which are given in Table 1. Based upon the working range, three levels
of each selected parameters were taken.

Table 1 Process parameters working range

Parameters	Rotational speed, N (rpm)	Feed rate, S (mm/min)	Pin shape	Preheating	Material
Range	600–1200	20–35	Tapered - non-tapered	With or without	Al alloy, Mg alloy, and Al composite

2.4 Design of Experiment

The Taguchi approach was used to evaluate the effects of process parameters on mechanical properties of joints and to find optimal parameters. This method is preferred because it helps to identify the number of experiments that is to be performed according to limits of factors and levels used. The L18 orthogonal array was selected and different levels were replaced with actual values to be varied for similar material workpieces.

2.5 Experimentation and Results

As per orthogonal array, eighteen experiments were performed. Trials were conducted three times to account for any variations. All the welding experiments were performed on the vertical milling machine by following the designed matrix. After the welding of the plates, mechanical tests were performed and results are shown in Table 2.

3 Analysis for Results Obtained

3.1 Signal-to-Noise Ratio Analysis

The S/N ratio selected was larger the better for tensile strength and yield strength and was calculated using the following relation:

$$\eta = -10\,\mathbf{log}(1/\mathbf{n}\,\Sigma Y^2)$$

where n is the number of experiments and Y is the response value. Response tables for S/N ratio for tensile strength and yield strength are given in Tables 3 and 4. Interactive graphs for S/N ratio of tensile strength and yield strength are given in Figs. 4 and 5, respectively. These graphs show the effect of control factors on S/N ratio.

Table 2 Output responses

Experiment no./design factors	A	B	C	D	E	UTS (MPa)	YS (MPa)
1	Room temp	Al alloy	20	600	Cylindrical	102	80
2	Room temp	Al alloy	25	900	Tapered	120	98
3	Room temp	Al alloy	35	1200	Threaded	122	99
4	Room temp	Mg alloy	20	600	Tapered	95	79
5	Room temp	Mg alloy	25	900	Threaded	112	90
6	Room temp	Mg alloy	35	1200	Cylindrical	120	98
7	Room temp	Al composite	20	900	Cylindrical	118	96
8	Room temp	Al composite	25	1200	Tapered	110	89
9	Room temp	Al composite	35	600	Threaded	100	79
10	150	Al alloy	20	1200	Threaded	140	118
11	150	Al alloy	25	600	Cylindrical	112	90
12	150	Al alloy	35	900	Tapered	129	107
13	150	Mg alloy	20	900	Threaded	117	96
14	150	Mg alloy	25	1200	Cylindrical	122	98
15	150	Mg alloy	35	600	Tapered	105	87
16	150	Al composite	20	1200	Tapered	122	99
17	150	Al composite	25	600	Threaded	105	88
18	150	Al composite	35	900	Cylindrical	120	98

Table 3 Main effects of tensile strength

Parameters	Preheating		Material		Feed rate		Tool rotation		Pin shape	
Levels	Means	S/N data	Means	S/N data	Means	S/N data	Means	S/N data	Means	S/N data
L1	111.00	40.875	120.833	41.600	111	40.873	103.166	40.259	115.666	41.248
L2	119.111	41.485	111.833	40.939	113.5	41.088	119.333	41.527	113.5	41.054
L3	-	-	112.5	41.000	116	41.255	122.666	41.752	116	41.236

Table 4 Main effects of yield strength

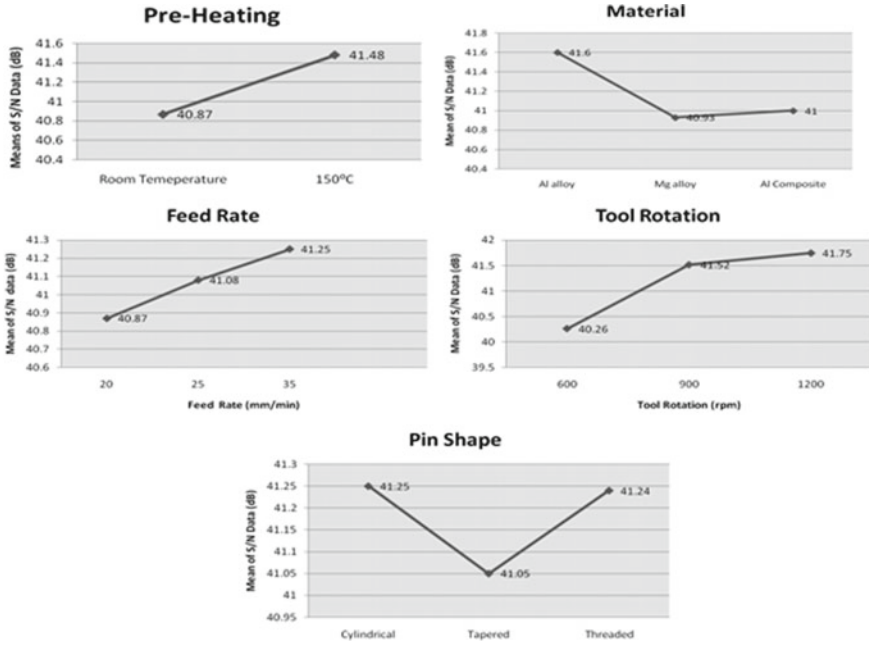| Parameters	Preheating		Material		Feed rate		Tool rotation		Pin shape	
Levels	Means	S/N data	Means	S/N data	Means	S/N data	Means	S/N data	Means	S/N data
L1	89.78	39.027	98.666	39.818	90	39.050	83.833	38.455	93.333	39.377
L2	97.888	39.777	91.333	39.187	92.166	39.282	97.5	39.768	93.166	39.342
L3	–	–	91.5	39.202	94.666	39.482	100.166	39.983	95	39.487

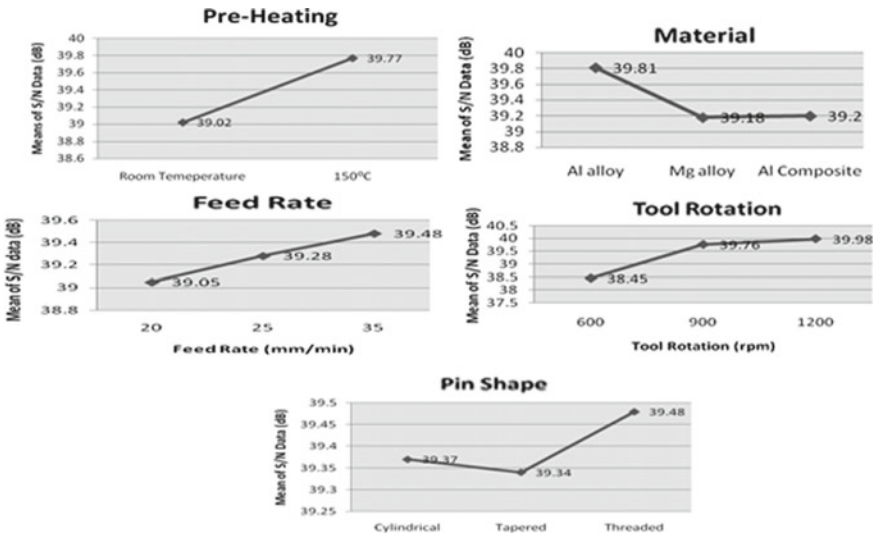**Fig. 4** Interactive graphs for S/N ratio of tensile strength

Fig. 5 Interactive graphs for S/N ratio of yield strength

Table 5 ANOVA table for tensile strength

ANOVA table of S/N ratios	DOF	SS	Variance	F ratio	Percentage of contribution	Significance
Preheating	1	1.679	1.679	95.379	**14.010**	**Significant**
Material	2	1.601	0.801	45.478	**13.360**	**Significant**
Feed rate	2	0.648	0.324	18.417	**5.410**	**Significant**
Tool rotation	2	7.773	3.886	220.798	**64.865**	**Significant**
Pin shape	2	0.141	0.071	4.014	1.179	Insignificant
Error	8	0.141	0.018		1.175	–
Total	17	11.983		–	–	
F ratio tabulated for preheating: (1, 8) = 5.32 and F ratio tabulated for other parameters: (2, 8) = 4.46 at 95% confidence limits						

Table 6 ANOVA table for yield strength

ANOVA table of S/N ratios	DOF	SS	Variance	F ratio	Percentage of contribution	Significance
Preheating	1	2.531	2.531	29.987	**18.199**	**Significant**
Material	2	1.556	0.778	9.216	**11.187**	**Significant**
Feed rate	2	0.867	0.433	5.137	**6.235**	**Significant**
Tool rotation	2	8.212	4.106	48.633	**59.031**	**Significant**
Pin shape	2	0.068	0.034	0.404	0.490	Insignificant
Error	8	0.675	0.084	–	4.855	–
Total	17	13.911		–	–	
F ratio tabulated for preheating: (1, 8) = 5.32 and F ratio tabulated for other parameters: (2, 8) = 4.46 at 95% confidence limits						

3.2 Analysis of Variance

The significant process parameters were found out using analysis of variance (ANOVA) test. It also depicts the effect of different process parameters on properties such as tensile strength and yield strength. Fisher ratio (F) is used to find the significance of the parameter. ANOVA results for all the responses of S/N ratio for tensile strength and yield strength are given are in Tables 5 and 6, respectively.

3.3 Estimation of Optimum Conditions

The highest value of S/N ratio for different parameters gives the estimated optimum conditions or factor levels. The estimated optimum mean of tensile strength and yield strength comes out to be 134.40 and 111.04 MPa, respectively.

Table 7 Confirmation experiment results

Mechanical property	Predicted value (MPa)	Actual value (MPa)
Tensile strength	134.4	138
Yield strength	111.04	114

3.4 Confirmation Experiments

The confirmation experiments were done at optimum parameter combinations to validate the results obtained during the analysis phase. The results of confirmation experiments are presented in Table 7.

4 Conclusions

From this research, an attempt has been made to suggest optimal values of FSW parameters for similar combinations of different alloys. The following important conclusions are derived:

1. FSW of AA2014 aluminium alloy, AZ31 magnesium alloy, and Al-SiC composite can be done using the conventional vertical milling machine.
2. The analysis of tensile strength shows that with the increase in tool rotational speed and feed rate, tensile strength of the joints gets increased. Preheating the base material improves the tensile strength of the welds. The cylindrical pin shape has better contact surface at the interfaces of the joints which results in improved stirring which increases the strength of weld.
3. The ANOVA test for tensile strength of welded joints shows that tool rotation significantly affects the tensile strength of the welded joints with 64.86% of contribution while other significant parameters are preheating, material, and feed rate. However, the effect of pin shape is found to be insignificant.
4. The ANOVA test for yield strength of welded joints shows that tool rotation significantly affects the yield strength of the joints with 59.03% of contribution while other significant parameters are preheating and material. However, the effect of pin shape on yield strength is found to be insignificant.
5. The tool rotation is most critical process parameter for improving tensile properties. The high rotational speed generates more heat input which results in better stirring and deformation of material and improves the mechanical properties.
6. The optimization of the selected parameters of friction stir welding using Taguchi technique gives optimal parameter values to the modern engineers. Therefore, this experimental study has established experimental data which may be useful for the academia and industry.

References

1. Thomas, W. M., Nicholas, E. D., Needham, J. C., Murch, M. G., Templesmith, P., & Dawes, C. J. (1991). *GB Patent Application No., 9125978,* 8.
2. Rhodes, C. G., Mahoney, M. W., Bingel, W. H., Spurling, R. A., & Bampton, C. C. (1997). Effects of friction stir welding on microstructure of 7075 aluminium. *Scriptamaterialia, 36*(1), 69–75.
3. Zahmatkesh, B., Enayati, M. H., & Karimzadeh, F. (2010). Tribological and microstructural evaluation of friction stir processed Al2024 alloy. *Materials and Design, 31*(10), 4891–4896.
4. Mishra, R. S., & Mahoney, M. W. (2007). *Friction stir welding and processing* (2007).
5. Franchim, A. S., Fernando, F. F., & Dilermando, N. T. (2011). Microstructural aspects and mechanical properties of friction stir welded AA2024-T3 aluminium alloy sheet. *Materials and Design, 32*(10), 4684–4688.
6. Rajakumar, S., & Balasubramanian, V. (2012). Correlation between weld nugget grain size, weld nugget hardness and tensile strength of friction stir welded commercial grade aluminium alloy joints. *Journal of Materials and Design 34*, 242–251.
7. Forcellese, A., Gabrielli, F., & Simoncini, M. (2012). Mechanical properties and microstructure of joints in AZ31 thin sheets obtained by friction stir welding using "pin" and "pinless" tool configurations. *Journal of Materials and Design, 34,* 219–229.
8. Cho, H. H., Kang, S. H., Kim, S. H., Oh, K. H., Kim, H.J., Chang, W.S., et al. (2012). Microstructural evolution in friction stir welding of high-strengthlinepipe steel. *Journal of Materials and Design, 34*, 258–267.
9. Arivazhagan, N., Narayanan, S., Singh, S., Prakash, S., & Reddy, G. M.: High temperature corrosion studies on friction welded low alloy steel and stainless steel in air and molten salt environment at 650 $^{\circ}$C. *Journal of Materials and Design 34*, 459–468.
10. Hoover, W. R., Duralcan.: T. M. (1990). Design and manufacturing of advanced composites. In *Proceedings of the Fifth Annual ASM/ESD Advanced Composite Conference, Dearborn, MI* (p. 211).
11. Chauhan, A., & Kumar, S. (2018). Effect of friction stir welding parameters on impact strength of the AZ31 magnesium alloy joints. *International Journal of Mechanical and Production Engineering Research and Development, 8*(2), 615–622.
12. Kundu, J., & Singh, H. (2016). Friction stir welding: multi-response optimisation using Taguchi-based GRA. *Production & Manufacturing Research, 4*(1), 228–241.
13. Meena, K., Kumar, A., & Pandya, S. N. (2017). Optimization of friction stir processing parameters for 60/40 brass using taguchi method. *Materials Today: Proceedings, 4*(2), 1978–1987.
14. Raweni, A., Majstorović, V., Sedmak, A., Tadić, S., & Kirin, S. (2018). Optimization of AA5083 friction stir welding parameters using Taguchi method. *Tehničkivjesnik, 25*(3), 861–866.
15. Ma, Z., Li, Q., Ma, L., Hu, W., & Xu, B. (2019). Process parameters optimization of friction stir welding of 6005A-T6 aluminum alloy using taguchi technique. *Transactions of the Indian Institute of Metals, 72*(7), 1721–1731.
16. Ramesha, K., Sudersanan, P. D., Santhosh, N., Ravichandran, G., Manjunath, N.: Optimization of friction stir welding parameters using taguchi method for aerospace applications. In *Advances in structures, systems and materials* (pp. 293–306). Singapore: Springer.
17. Chauhan, A., & Kumar, S. (2018). An overview of optimization techniques used for friction stir welding process parameters. *Research Journal of Engineering and Technology, 9*(1), 21–26.

Review of Materials and Processes Used in 4D Printing

Ajay K. S. Singholi and Ajay Sharma

Abstract Applications of smart materials are widely popular in various industries like medical, defence, space research, aerospace, etc. These smart materials are used to perform certain dynamic functions and reduce number of components required for dynamic functions. The dynamic functions are related to shape changing ability of the material. Generally, due to flexibility and economic point of view, all applications of smart materials follow conventional methods to make smart materials in use. Researchers have shown interest toward use of smart materials in 3D-printing methods exist in additive manufacturing and named this as 4D printing. The aim of the paper is wide go through on smart materials that are used in various 3D-printing methods. All smart materials (Alloys and polymers) have different set of physical, mechanical, thermal, and chemical properties. These properties are the root of the use of the smart material for a particular type of 3D-printing methods. AS each 3D-printing method differ from other in principle and the use of input smart material. This paper emphasizes on the 3D-printing processes in light of use of smart materials. This study will help in easy characterization of 4D-printing methods based on various materials.

Keywords 4D printing · Smart materials · Shape memory effect · Shape memory polymers (SMP)

1 Introduction

Additive manufacturing since its evolution continuously providing rapid solutions to complex design problem in economic way and in minimum time. Developments of 3D printing in additive manufacturing forcing us to believe printing any design with

A. K. S. Singholi
Professor, G.B. Pant Engineering College, New Delhi, India
e-mail: ajay.igit@gmail.com

A. Sharma (✉)
Research Scholar, USICT, Guru Gobind Singh Indraprastha University, New Delhi, India
e-mail: ajayrcert21@gmail.com

any material and at anywhere. These may be polymers, alloy, hydrogels, or any hybrid composites. These are already used in bio-engineering, space crafts, medical equipment and accessories, tissue engineering, chemical engineering, soft robotics, and making of various types of electronic devices in conventional way. The emphasis on any type of material in 3D printing further provided lead to the use of smart materials in 3D printing. Where 3D-printed object may show properties like shape memory effect or self-healing effects [1]. Tibbitts in his self-assembly laboratory showed transformable 3D-printed objects using self-healing and programmable materials; the complete process named as 4D printing [2, 3]. In 4D printing, a 3D-printed object shows dynamic behavior when exposed to external stimuli. Most commonly found stimulus are water, heat, light, pressure, and magnetic effect. This behavior is similar to that of shape memory materials where programmed material on application of stimuli transforms its permanent shape to temporary desired shape and return to its permanent or original shape when stimuli removed. This change in shape occurs due to certain properties of material. These properties specifically temperature and density are key factor to make the object dynamic when exposed to stimuli. These properties make the material suitable for 3D-printing method. Further to add dynamic behavior in 3D-printed objects design is the key parameter, when material used in the process is not smart. Few researchers made composites using different combinations and arrangements of materials to make them suitable for 4D printing; these composites are called as printed active composites(PAC). Researchers not stopped on only conventional smart materials in 3D printing even many tailored properties of materials with various methods of 3D printing to create landmark in 4D printing. With the change in properties of material and development of new materials corresponding 3D printing processes also get varies. This paper will discuss 4D-printing materials, their classifications, and their use in different 3D-printing processes.

2 Materials for 4D Printing

Materials play major role in 4D printing as a 4D-printed object is mend to behave systematically and in predictive manner when this object is exposed to external stimuli. In other words, one can say the object must sense the stimuli and response dynamically. Here, this is simply related to the major property of the material that is called shape memory property. These types of materials transform into another shape on giving some stimulus and recovered the original shape when stimulus is removed. The materials with such property are called as shape memory materials. These materials exhibit shape memory effect and this varies from materials to materials. For example, shape memory always has higher shape memory than shape memory polymers. Though SMAs having higher shape memory but SMPs are preferred over a wide range of applications. Based on their shape changing and recovery action, these SMPs are divided in three categories as 1-way, 2-way, and 3-way type SMPs. In programmable matter, we are able to change the properties (porosity, conductivity,
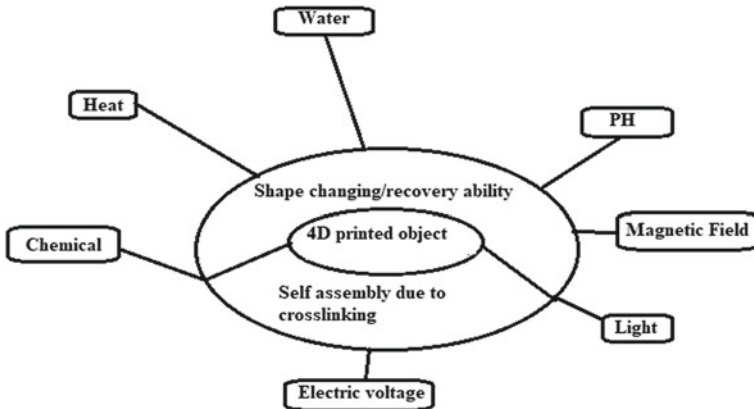
Fig. 1 Characteristics of 4D-printed object

magnetic properties, flexibility, and so on) of material to make the object ready for self-assembly and self-replicating to make the desired shape [2, 4] (Fig. 1).

2.1 Classification of Materials Used in 4D Printing

(a) **Shape memory polymers and their composites** these have existence in industry since more than 35 years in different forms. Jinlian Hu et al. reviewed about different structure, classifications, mechanism, modeling, and applications of SMPs covering all aspects [5]. In first paper of 4D printing, Tibbits et al. showcased various transformation of 3D-printed hydrophilic polymer. Further they also embedded shape memory alloys using material jet process on Connex multi-material printer to make a 4D-printed object [2, 6]. Yu et al. also used inkjet printing to demonstrate the controlled sequence of different sets of epoxy-based polymer [7] using thermal stimulation. Zarek et al. explored various molecular weights of methacrylated polycaprolactone for the preparation of ink and found the sample 10,000 gm per mole has the best shape memory properties [8]. Thus, fabricate different sets of jewelry and show accessories using digital light processing printing method. He also used PCL(methaacrylated polycaprolactone) to make a personalized trachea stent [9]. For another use of polymers as combination were used many researchers for creating different types of foldable and non-foldable stimulus responsive structures [10–12].

(b) **Hydrogels** are inspired from nature. These alter their shape by absorbing and releasing water in the upper and lower limits of critical temperature. Iconic entanglement (ICE) hydrogels are used in 3D printing and provide stiff object. These hydrogels entangle with other polymer and metal network to create

stiffed part on stimulation and vice versa. The cause behind this is coil-globule transition. Bakarich and his team used a widely studied thermal responsive covalent cross-linked network of poly(N-isopropylacrylamide) hydrogel (PNI-PAAm) ink for demonstration of reversible transition [13]. 3D-printed valves of this hydrogel was experimented and tested with various concentration of NIPAAm with fix amounts of covalent cross-linkers and UV initiator in the range of 20°–60°. Another hydrophilic polyurethane hydrogel ink poly(N-isopropylacrylamide) (poly(NIPAM)) with tuned modulus of elasticity and swelling properties used in 3D printing to make robust hinges as active component [14]. Baker et al. manufactured polyurethane hydrogel filament and used it as 3D-printed hinges of different geometries to make different origami fold and unfolds on actuation [15]. Another inspiration of making 4D-printed hydrogel architecture was encoded from plant as hydration trigged behavior controlled by the proper alignment of cellulose fibrils within plant cell walls [16]. The addition of fibrils in hydrogels make introduction of anisotropy. Various reviews on use of hydrogel in different 3D-printing methods with demonstration of various transforming shapes and applications have been done in past and still in process [4, 14–19].

(c) **Self-assembly and self-healing materials** are the materials those attain a final shape with combining several individual components when some stimulus is provided. At the same time, self-healing materials have tendency to recover any loss of materials (like in case of wound) and attain original shape. This was first showed by self-assembly laboratory of MIT and later by many researchers [6, 20–26].

(d) **Piezoelectric crystals** are another newly preferred materials in 3D printing due to their thermomechanical and electromechanical responses. Review of piezoelectric crystals as base material or with thermoplastic materials/binders in different 3D-printing methods (FDM, selective laser sintering(SLS), direct printing, droplet printing, stereo lithography (SLA), etc., have been discussed with probable challenges [27, 28]. Piezoelectric ceramics like lead zirconium titanate (PZT) and barium titanate (BT) used to made sensors of different shapes by inkjet printing, FDM, SLS, and SLA methods [29–33]. Further, poly vinylidene fluoride(PVDF) [34] and BT nanoparticles embedded photo liable polymer based sensors are also made successfully by FDM method [35].

3   Processes for 4D Printing

4D printing depends on use of suitable/smart material for selected process and design of the object. These two points tends to create the 4D-printed parts that show dynamic behavior when exposed to stimuli. Conventional methods of making products from shape memory materials, hydrogels, and piezoelectric crystals were quite popular before ushering of 3D printing. Tibbits showed the way for making objects using smart materials by using multi-materials printing. After that FDM, SLA, SLS, direct

ink jet printing were common trend for using single material or tailored materials [7, 26, 36–38]. Materials like hydrogels required synthesis by proper mixing to use in SLA printing [7, 9]. Preparation of filament for FDM printing is also performed by various researchers to get the desired properties for shape memory effect. 3D-printed piezoelectric crystal sensor also been made using SLA methods utilized in many ways [30–33]. Also various comparisons of 3D-printing processes for piezoelectric crystals were made by Sampada Bodkhe et al. 2019 [28] nicely. Selection of printing method depends on glass transition temperature of shape memory polymers. Seven categories of 3D-printing processes (FDM,SLA,SLS, binder jetting,sheet lamination, poly jet, and SLS) as per ASTM standards 52900,2015 for different type of materials [39–41].Commonly, commercially, 3D printing techniques use liquid photo polymer in material jetting, SLA, extrusion-based printing or FDM using polymeric filaments, binder jetting and metallic or ceramic-based powder using in SLS. G.sossou et al. reviewed 3D printing of smart materials and printed voxel-based hydrogel valve with polyjet printing. Different materials and corresponding processes are summarized in Table 1.

4 Conclusion

We have reviewed various smart materials and the printing methods where they have been used a raw material. At the same time, we found that commonly used materials like PLA and its variant, ABS, Teflon, etc., are also been used in 3D-printing process to demonstrate the fourth dimension. This is because of the design adaptation and in some case, took the benefit of their thermos responsiveness when sandwiched. As expansion of each material is different when exposed to external stimuli. Also variation in glass transition temperature plays crucial role while selecting printing method. Shape memory programming is required to exhibit two-way memory by using different loadings in many cycles. Otherwise, we see one-way memory exhibition with no recovery. As a commonly available and most widely published researcher started from FDM. Later, tailored filaments made the way toward 4D printing even in the case of piezoelectric crystal also. Due to temperature limitation and brittleness caused due to the previous methods, polyjet, binder jet, SLA, and SLS are in popular demand in increasing order. In the later methods, material can easily combined with other adhesive or inert material or can be printed in another's matrix. There are more challenges in 4D-printing materials and processes that researchers are working on. Due to this, capabilities of the printed part will be more increased. In the near future, 4D-printed products will be used in fabrication of sensors, smart fabrics, medical devices and accessories, space applications, robotics, electronic actuators, and many more.

Table 1 Materials and corresponding 3D-printing method

Sr.no.	Material	Process	References
1.	Shape memory alloys (SMAs) and polymers	Material jetting, Connex multi-material printer	[2, 6, 42–47]
2.	Hydrogel with inert polymeric material	Polyjet	[4]
3.	Soybean oil epoxidized acrylate	SLA	[48]
4.	SMP(Tango black plus and vero white)	Polyjet, Object connex 3	[26]
5.	PNI-PAAm hydrogel ink	Extrusion printer	[49]
6.	poly(NIPAM) hydrogel ink	Extrusion printer	[14]
7.	Epoxy-based polymer	Material jetting, Object Connex 260 multi-material printer	[7]
8.	Methacrylated polycaprolactone polymer	SLA, Digital light processing printing, PICO plus 39 (385 nm UV source)	[8, 9]
9.	Printed active composite(Gray 60 with Tango black matrix)	Material jetting, Object Connex 260 multi material, object 3D printer	[10, 12]
10.	Polyurethane hydrogel	FDM(Extrusion method)	[15]
11.	Cellulose hydrogel ink	DLP, ABG 10000, Aerotech	[16]
12.	Piezoelectric crystal(PZT,PVDF,PLLA(Poly L lactic acid) and BT)	FDM	[30, 31]
13.	Piezoelectric polymer composite (BT nanoparticle and photo resin based)	SLA	[32, 33, 35]
14.	PVDF/photopolymer resin-based piezoelectric crystal	SLA	[34]

References

1. Lu, B., Li, D., & Tian, X. (2015). 3D Printing—Perspective development trends in additive manufacturing and 3D printing. *Engineering, 1*(1), 85–89.
2. Campbell, T. A., Tibbits, S., & Garrett, B. (2014). The next wave: 4D printing programming the material world. *Atlanta Council* .
3. Tibbits, S. McKnelly, C., Olguin, C., Dikovsky, D., & Hirsch, S. (2014) 4D printing and universal transformation. ACADIA 14: Design Agency. In *Proceedings of the 34th Annual Conference of the Association for Computer Aided Design in Architecture* (pp. 539–548).
4. Sossou, G., Demoly, F., Montavon, G., & Gomes, S. (2018). Design for 4D printing: rapidly exploring the design space around smart materials. *Procedia CIRP, 70*, 120–125.
5. Hu, J., Zhu, Y., Huang, H., & Lu, J. (2012). Recent advances in shape-memory polymers: Structure, mechanism, functionality, modeling and applications. *Progress in polymer science* (Vol. 37, no. 12, pp. 1720–1763). Elsevier Ltd.
6. Tibbits, S. (2014). 4D printing: Multi-material shape change. *Architectural Design, 84*(1), 116–121.

7. Yu, K., Ritchie, A., Mao, Y., Dunn, M. L., & Qi, H. J. (2015). Controlled sequential shape changing components by 3D printing of shape memory polymer multimaterials. *Procedia IUTAM, 12*, 193–203.

8. Zarek, M., et al. (2016). 4D printing shape memory polymers for dynamic jewellery and fashionwear. *Virtual and Physical Prototyping, 11*(4), 263–270.

9. Zarek, M., Mansour, N., Shapira, S., & Cohn, D. (2017). 4D printing of shape memory-based personalized endoluminal medical devices. *Macromolecular Rapid Communications, 38*(2), 1–6.

10. Ge, Q., Dunn, C. K., Qi, H. J., & Dunn, M. L. (2014). Active origami by 4D printing. *Smart Materials and Structures, 2*3(9).

11. Ge, Q., Qi, H. J., & Dunn, M. L. (2013). Active materials by four-dimension printing. *Applied Physics Letters, 103*(13).

12. Teoh, J. E. M., An, J., Feng, X., Zhao, Y., Chua, C. K., & Liu, Y. (2018). Design and 4D printing of cross-folded origami structures: A preliminary investigation. *Materials (Basel), 11*(3).

13. Bakarich, S. E., Iii, R. G., & Spinks, G. M. 4D *Printing with mechanically robust, thermally actuating hydrogels* (pp. 1211–1217).

14. Naficy, S., Gately, R., Gorkin, R., Xin, H., & Spinks, G. M. (2017). 4D printing of reversible shape morphing hydrogel structures. *Macromolecular Materials and Engineering, 302*(1), 1600212.

15. Baker, A. B., Bates, S. R. G., Llewellyn-Jones, T. M., Valori, L. P. B., Dicker, M. P. M., & Trask, R. S. (2019). 4D printing with robust thermoplastic polyurethane hydrogel-elastomer trilayers. *Materials and Design, 163,* 107544.

16. Gladman, A. S., Matsumoto, E. A., Nuzzo, R. G., Mahadevan, L., & Lewis, J. A. (2016). Biomimetic 4D printing. *Nature Materials, 15*(4), 413–418.

17. Erol, O., Pantula, A., Liu, W., & Gracias, D. H. (2019). Transformer hydrogels: A review. *Advanced Materials Technologies, 4*(4), 1–27.

18. Roy, D., Cambre, J. N., & Sumerlin, B. S. (2010). Future perspectives and recent advances in stimuli-responsive materials. *Progress in Polymer Science, 35*(1–2), 278–301.

19. Mao, Y., et al. (2016). 3D printed reversible shape changing components with stimuli responsive materials. *Scientific Reports, 6*(April), 1–13.

20. Mao, Y., Yu, K., Isakov, M. S., Wu, J., Dunn, M. L., & Jerry Qi, H. (2015). Sequential self-folding structures by 3D printed digital shape memory polymers. *Scientific Reports 5*, 1–12.

21. Pei, E., & Loh, G. H. (2018). Technological considerations for 4D printing: an overview. *Progress in Additive Manufacturing, 3*(1), 95–107.

22. Pei, E. (2014). 4D printing - Revolution or fad? *Assembly Automatio, 34*(2), 123–127.

23. Meng, H., & Li, G. (2013). A review of stimuli-responsive shape memory polymer composites. *Polymer (UK), 54*(9), 2199–2221.

24. Habault, D., Zhang, H., & Zhao, Y. (2013). Light-triggered self-healing and shape-memory polymers. *Chemical Society Reviews, 42*(17), 7244–7256.

25. Kuang, X., Chen, K., Dunn, C. K., Wu, J., Li, V. C. F., & Qi, H. J. (2018). 3D printing of highly stretchable, shape-memory, and self-healing elastomer toward novel 4D printing. *ACS Applied Materials & Interfaces, 10*(8), 7381–7388.

26. Bodaghi, M., Damanpack, A. R., & Liao, W. H. (2016). Self-expanding/shrinking structures by 4D printing. *Smart Materials and Structures, 25*(10), 1–15.

27. Cholleti, E. R. (2018). A Review on 3D printing of piezoelectric materials. *IOP Conference Series: Materials Science and Engineering, 455*(1).

28. Bodkhe, S., & Ermanni, P. (2018). Challenges in 3D printing of piezoelectric materials To. *Journal of Physics D: Applied Physic* https://doi.org/10.1088/1361-6463/aad7de.

29. Kuscer, D., Noshchenko, O., Uršič, H., & Malič, B. (2013). Piezoelectric properties of ink-jet-printed lead zirconate titanate thick films confirmed by piezoresponse force microscopy. *Journal of the American Ceramic Society, 96*(9), 2714–2717.

30. Chen, X., et al. (2019). Helical-Like 3D ultrathin piezoelectric element for complicated ultrasonic field. *Advanced Functional Materials, 29*(32), 1–11.

31. Llewellyn-Jones, T. M., Drinkwater, B. W., & Trask, R. S. (2016). 3D printed components with ultrasonically arranged microscale structure. *Smart Materials and Structures, 25*(2), 0–6.
32. Cheng, J., Chen, Y., Wu, J. W., Ji, X. R., & Wu, S. H. (2019). 3d printing of BaTiO3 piezoelectric ceramics for a focused ultrasonic array. *Sensors (Switzerland), 19*(19).
33. Chen, Z., et al. (2016). 3D printing of piezoelectric element for energy focusing and ultrasonic sensing. *Nano Energy, 27,* 78–86.
34. Kim, H., et al. (2019). 3D printing of polyvinylidene fluoride/photopolymer resin blends for piezoelectric pressure sensing application using the stereolithography technique. *MRS Communication, 9*(3), 1115–1123.
35. Composite, N. À. P., & AI, K. I. M. E. T. (2014). 3D optical printing of piezoelectric materials. *ACS Nano* (10), 9799–9806.
36. Ge, Q., Sakhaei, A. H., Lee, H., Dunn, C. K., Fang, N. X., & Dunn, M. L. (2016). Multimaterial 4D printing with tailorable shape memory polymers. *Scientific Reports, 6*(April), 1–11.
37. Bodaghi, M., Damanpack, A. R., & Liao, W. H. (2017). Adaptive metamaterials by functionally graded 4D printing. *Materials and Design, 135,* 26–36.
38. Khoo, Z. X., et al. (2015). 3D printing of smart materials: A review on recent progresses in 4D printing. *Virtual and Physical Prototyping, 10*(3), 103.
39. All3DP GmbH, All3DP. (2019). https://all3dp.com/1/types-of-3d-printers-3d-printing-technology/.
40. Lee, J. Y., An, J., & Chua, C. K. (2017). Fundamentals and applications of 3D printing for novel materials. *Applied Materials Today, 7*, 120–133.
41. ISO/ASTM 52900, Additive Manufacturing-general principles-terminology. (2015). https://www.iso.org/obp/ui/#iso:std:iso-astm:52900:ed-1:v1:en.
42. Additive Manufacturing Materials. https://www.spilasers.com/application-additive-manufacturing/additive-manufacturing-materials/.
43. Mousanezhad, D., et al. (2015). Hierarchical honeycomb auxetic metamaterials. *Scientific Reports, 5,* 1–8.
44. Che, K., Yuan, C., Wu, J., Jerry Qi, H., & Meaud, J. (2016). Three-Dimensional-Printed multi-stable mechanical metamaterials with a deterministic deformation sequence. *The* Journal of Applied *Mechanics, 84*(1), 011004.
45. Rafsanjani, A., Akbarzadeh, A., & Pasini, D. (2015). Snapping mechanical metamaterials under tension. *Advanced Materials, 27*(39), 5931–5935.
46. Gao, W., et al. (2015). The status, challenges, and future of additive manufacturing in engineering. *CAD Computer-Aided Design, 69,* 65–89.
47. Bodaghi, M., et al. (2017). Adaptive metamaterials by functionally graded 4D printing. *Materials and Design, 11*(4), 1–11.
48. Miao, S., et al. (2016). 4D printing smart biomedical scaffolds with novel soybean oil epoxidized acrylate. *Scientific Reports, 6*(March), 1–10.
49. Bakarich, S. E., Gorkin, R. M., In H. P., & Spinks, G. M. (2015). 4D printing with mechanically robust, thermally actuating hydrogels. *Macromolecular Rapid Communications, 36*(12), 1211–1217.

Tribological Properties and Morphological Analysis of Waste Fishbone-Filled Carbon-/Jute-Reinforced Polymer Composite

N. K. Batra, Iti Dikshit, and Harsimran Singh

Abstract Using fishbone powder as a new biomass in processing nano-filled composites to evaluate the feasibility of using and developing a novel composite material for engineering application. In the present study, tribological behaviour of waste fishbone powder is reinforced with carbon/jute fabric hybrid in polyester matrix. The waste fishbone powder was used as nanofiller reinforced with polyester matrix in weight percentage of 5%. Dry sliding wear and friction tests were conducted on pin-on-disc apparatus with varying parameter, i.e., applied load and sliding distance with a sliding velocity of 2 m/s, evaluated in the form of wear loss and coefficient of friction (COF). It was found that the wear loss and friction of carbon/jute polyester-reinforced hybrid composites increased with fishbone as a filler, it was found that the cumulative weight loss of unfilled hybrid composite is 20% less than nano-filled fishbone hybrid composite. UFP_{300} (70% polyester and 30% carbon fiber) sample shows the minimum wear loss and coefficient of friction among all the samples. The wear behavior of fabricated samples was explained and evaluated through SEM study in terms of the analysis of transfer film and its interfacial adhesion of transfer with the counterface surface of the disc.

Keywords Coefficient of friction (COF) · Fishbone powder (FBP) · Carbon fiber (CF) · Jute fiber

N. K. Batra · I. Dikshit (✉) · H. Singh
Mechanical Engineering Department, M.M. Deemed to be University Mullana, Ambala, Haryana 133207, India
e-mail: er.itidixit@gmail.com

N. K. Batra
e-mail: nkbatraeng@gmail.com

H. Singh
e-mail: harsimran.singh00001@gmail.com

1 Introduction

The increasing demand of materials with high wear resistance resulted in development of fiber-reinforced composites. Due to self-lubrication property of polymer which leads to low friction and high wear resistance make it relevant choice for the tribological application such as bearing, cams, components of engines, and many more [1]. Polymer-reinforced composite considered a feasible solution in replacement of metal-based materials in many application like automobile, marine, and aircraft industries, due to their good strengths and low densities [2]. Composites made with natural fiber compose good strength-to-weight ratio. Natural fibers can be serve as reinforcement not only to improve strength but also maintain optimal weight of composite [3]. Properties of natural composites depend on fiber and the interfacial adhesion of the matrix with fiber [4]. Nanocomposites development is one of recent trend in research in which particle filled, whose at least one dimension of the particle should be in nanometer. Polymer in nanocomposite can be filled with nanosized organic or inorganic particle filler. The incorporation of inorganic filler as compared to organic filler has ease of manufacturing, reducing the manufacturing cost, decrement in surface roughness, fire retardancy, and tremendous enhancement in mechanical properties such as tensile, impact strength [5, 6]. Occasionally, addition of filler produces hindrance in composite like brittleness and opacity [7]. To reduce the environmental waste many waste products is used as filler in the recent study like eggshell, bone powder, shellfish shell etc. Bone is a natural composite consists of 50–60% mineral, 30–40% matrix and 10–20% of water, in the form of hydoxyapatite, type I collagen, non-collagen proteins [8]. Mechanical and tribological behavior of recycled polyethylene-reinforced with cow bone particles varying from 5–25% shows that improvement in wear, tensile strength, and hardness as cow bone particles wt% increase while the impact strength and rigidity decreases [9]. Epoxy composite reinforced with carbonized and uncarbonized as cow bone powder with varying 10–60%. The mechanical properties were evaluated, and it was concluded that increasing the weight percentage of bone powder from 10 to 40 wt% improves the mechanical properties, further increase in the filler percentage shows decrement in the properties [10]. Tensile property of three types of composite, i.e., cuttle bone filled epoxy composites(CB/EP), heat treated cow bone epoxy composite(HB/EP), and commercial $CaCO_3$ epoxy composite (CC/EP) shown better adhesion between filler and epoxy and hence shows higher tensile properties [11]. As the consumption of sea food increases, which in turn increase the disposal concern and contributing to the landfills. The motivation of the research in the development of novel agro-based (fish bone) composite is based on this alarming challenge. The aim of present study is to investigate the capability of using fish bone as filler in polymer-reinforced hybrid composite to fabricate a novel composite which is biodegradable with improve mechanical and tribological properties. To study the tribological behavior of the carbon/jute hybrid composites with nanosized fish bone powder, pin on disc tester was employed to determine the coefficient of friction (COF), and wear loss of the developed composites.
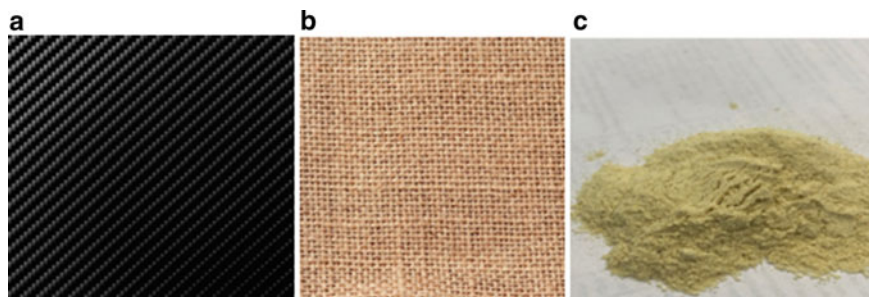
Fig. 1 **a** Carbon fabric **b** Jute fabric **c** Fishbone powder

2 Experimental

2.1 Material and Fabrication Methodology

The thermosetting matrix used in the study was unsaturated polyester resin, which was obtained from Crystic Resin Private Limited, Faridabad (India). Woven carbon fabric (360 g/m²) of commercial grade obtained from PEE CEE Textile store, Kanpur, India. Jute fiber is always known as strong, course, environment friendly, and organic and biodegradable. Jute fibers were collected from local market as shown in Fig. 1. The fish bone (biological name: Separate Seenghala) is comprised of high percentage of calcium and phosphorus. Fishbone powder is most bio-available, biodegradable, produced by without any chemical treatment. The fishbone was cleaned using distilled water mixed with ethanol to remove blood stains, oil, dust, and any other foreign particles from the bone. The bones were then boiled in the water. After cleaning, the bones were dried in electric furnace at a temperature of 200 °C. The bones were crushed using planetary ball milling machine (Insmart: Speed up to 1200 rpm) by putting the bones into a vessel (stainless steel: 500 ml), with hardened stainless steel ball (diameter: 10 mm). The bones were sieved having particle mesh size of 60 μm at 800 rpm rotated for 20 min. Two sets of unsaturated polyester resin were prepared to prepare two types of sample, i.e., unfilled composite (FBP 0%) and filled composites (FBP 5%). The weight percentages of the constituents are shown in Table 1. For dispersing the fishbone powder (FBP) into the unsaturated polyester, sigma mixer was used which comprising of two opposing blades rotating at a speed of 50 rpm for 30 min at room temperature.

2.2 Synthesis of Composite

Carbon and jute woven in compatibility with unsaturated polyester resin were used as reinforcement. The composites were prepared by compression technique using

Table 1 Composition of laminates

S.no.	Abbreviation	Composition
UFP$_{300}$	Carbon–carbon–carbon	70% polyester + 30% CF
FPR$_{305}$	Carbon–carbon–carbon	65% polyester + 30% CF + 5% FBP
UFP$_{210}$	Carbon–jute–carbon	70% polyster + 20% CF + 10% JF
FPR $_{215}$	Carbon–jute–carbon	65% polyester + 20% CF + 10% JF + 5%FBP
UFP$_{120}$	Jute–carbon–jute	70% polyester + 20% JF + 10% CF
FPR $_{125}$	Jute–carbon–jute	65% polyester +20% JF + 10%CF + 5%FBP

a commercially available as compression molding machine (Manufacture–Friends Hydraulics, Model–CMP-60/5 Courtesy: MMDU-Mullana). The stacking sequence in the preparation of sample consisted of the positioning of the fabric, one over the other, spreading the resin in between the reinforcement.

To prevent the damage of assembled stack, the plates on which reinforcement were stacked were covered with releasing agent. The six specimens were made for the study in which three specimens contain FBP filler materials. Subsequently, the laminates cured for 24 h. The laminates are molded at the temp of 160 °C with 200–240 bar pressure and the duration of molding is 5 min. Specimen was cut by diamond tip hand cutter for the pin on disc test of size $50 \times 10 \times 10$ mm.

3 Experiment Detail

3.1 Adhesive Wear

Ungreased sliding wear tests were executed to identify the tribological properties of unfilled and FBP nano-filled composite on pin on disc apparatus designed and manufactured by DUCOM, India, TR-20LE-PHM 400 at room temperature as per ASTM-G99-05 at a constant velocity of 2 m/s and pressure of 3 MPa. The test rig consists of rotating disk made of hardened steel (hardness 68 HRC) with track diameter of 100 mm considered as counter face. The sample pin of size 10 mm $\times$ 10 mm $\times$ 3 mm fixed in the long flexible arm of the apparatus. The contacting time between the disk and pin specimen was for 5 min. Petroleum ether with 50% alcohol is used to clean the samples and the counter face. The wear loss is determined by the weight loss before and after the experiment using digital weighing machine. The test was conducted at 100, 150, and 200 mm sliding distance with a variation of load of 30 and 50 N. For every sample, three experiments were carried out for each condition and the average of wear loss and coefficient of friction was calculated.

4   Results and Discussion

4.1   Wear Loss

To study the effect of sliding distance for unfilled and filled 5% of FBP nanofiller composites against sliding distance in Fig. 2a–d with varying applied load of 30 and 50 N. At different load, wear loss increases with increase in sliding distance for the entire fabricated specimen. In Fig. 2a, b, carbon-reinforced composite (UPR$_{300}$) shows minimum wear loss as compared to other sample of 0.00867 gm and 0.0153 gm for load of 30 and 50 N, respectively, at sliding distance of 200 mm without addition of nanofiller. It is noticeable from Fig. 2a, b, the maximum wear loss for UPR$_{120}$ composite for sliding distance of 200 mm at a load of 30 and 50 N is 0.012 and 0.018gm, respectively. At 30 N load UPR$_{300}$ and FPR$_{305}$ samples at 200 mm sliding distance shows a serve increase in wear loss by 38.35% with the addition of FBP nanofiller (5%). Figure 2c, d shows the wear loss of all the samples with varying percentage of nanofiller (5%) at a load of 30 and 50 N with different sliding distance. Due to low adhesion of jute fabric with polyester and its high coefficient of friction, sample FPR$_{125}$ shows the maximum wear loss of 0.0167 gm and 0.03 gm at 30 and 50 N for 5%FBP filler at 200 mm sliding distance. Due to high specific modulus and self-lubricating property, carbon fiber shows minimum wear loss as compared
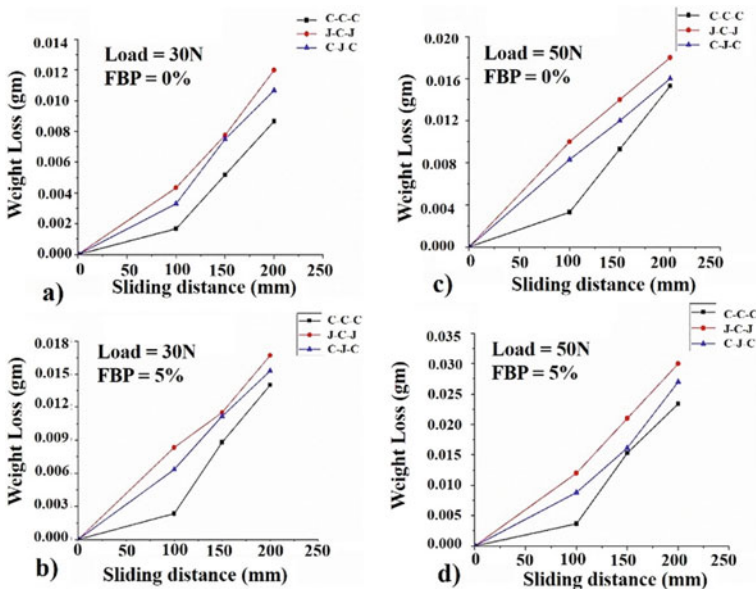

Fig. 2 Wear loss as a function of sliding distance **a** unfilled samples at 30 N load **b** unfilled samples at 50 load. **c** 5% by vol. nano-filled samples at 30 N load **d** 5% by vol. nano-filled samples at 50 N load

to other samples. However, at 200 mm, the wear loss for filled composite (FPR$_{305}$) is 34.15% higher when compared to weight loss of unfilled composite (UPR$_{300}$). The wear rate of polymer-reinforced composite depends on load, sliding velocity, sliding distance, and surface temperature. As the sliding distance increases from 100 to 200 mm, wear loss increases for all the samples with different applied load. One of the important reasons of increase in weight loss is due to thermal softening. A low softening layer leads to high wear resistance. Due to increase in sliding distance, contact time increases and surface contact temperature increases which result in thickening of softening polyester layer and it get detached from the surface of the pin specimen in the form of wear debris [12]. The unfilled composite shows less wear rate as compared to the filled composites. With the addition of filler, a rough surface developed due to which homogenous and compact structure is not developed. The filler does not form a protective layer for wear resistant and due to weaken bonding strength between the filler and the matrix, it themselves gets deformed and dislodged and get separated during sliding which convert the dry sliding wear into three body abrasive wear which results in high wear [13]. During dry sliding wear, polymer matrix slide over the metal surface of the disc and hence transfer film is formed, which strongly influence the wear behavior of the composite. With the addition of nanofiller, the transfer film becomes thick and grumpy and uniform covering of counter face is lacking in lieu of which there is lack of interfacial adhesion between transfer film and disc counter face and wear is in the form of large fragments and bulk flakes of transfer film which results in high wear.

4.2   Coefficient of Friction

The result for coefficient of friction shows same trend as in case of wear loss result, i.e., specimen filled with FBP nanofiller shows high coefficient of friction as compared to specimen with 0% of FBP. To study the effect of applied load and sliding distance, the coefficient of friction (COF) is plotted against the sliding distance for nanofiller FBP filled and unfilled composites at 30 and 50 N load in Fig. 3a–d. With increase in the sliding distance (100,150, and 200 mm) coefficient of friction increases for all the samples. At 100 mm, sliding distance samples show low coefficient of friction because, at the starting of the experiment, both the apparatus disc and the specimen are at ambient temperature. The rotation of metal disc in contact with pin specimen, as the sliding distance increases, it will increase the interfacial temperature due to heat generation which result in increase in frictional force [14]. It is quite visible from Fig. 3a that the COF for unfilled carbon-reinforced composites (UPR$_{300}$) at 200 mm sliding distance, is 0.18 at a load of 3 kg whereas in Fig. 3b for 5 wt% filled carbon composites (FPR$_{305}$), the coefficient of friction at 200 mm normal load. The COF will increase as the filler will be added to the composites as compared to unfilled composites. This is because due to partial rubbing of nanofiller and the metal surface of the disc of the apparatus, which reduce the lubricating property of the polymer matrix which further result in agitating the self-lubricating matrix
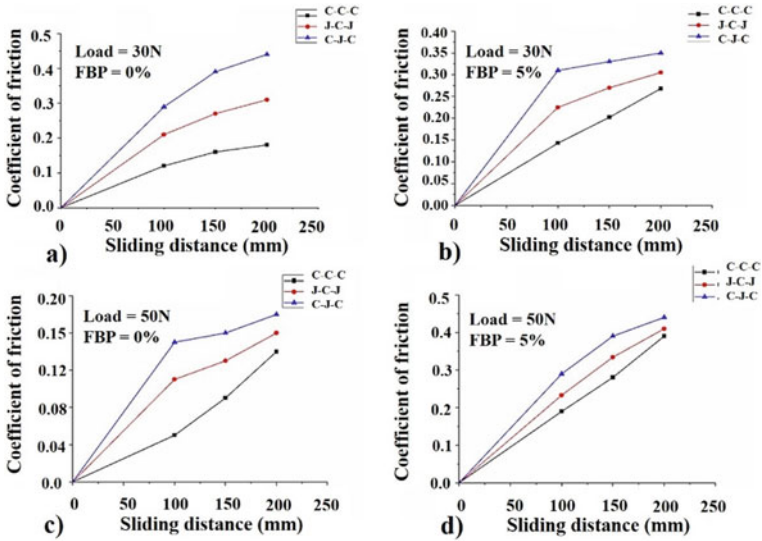
Fig. 3 Coefficient of friction as function of sliding distance **a** unfilled specimen at a load of 30 N **b** 5% by vol. nano-filled samples at 30 N load. **c** unfilled specimen at a load of 50 N load **d** 5% by vol. nano-filled samples at 50 N load

transfer film by the indentation of hard inorganic filler. With the inclusion of FBP filler in hybrid composites, these filler particles contribute to ploughing effect which further increases the friction.

4.3 SEM Analysis of Composites

In order to explore the wear-enhancing mechanism of nano-filler fishbone powder (FBP), the microstructures of hybrid-reinforced polyester composites with 5 wt% nano-filled composite for preferred specimen under a load of 5 kg with a sliding distance at 200 mm were observed by SEM.

Specifically, SEM micrographs in Fig. 4a with 5% nano-filled FPR_{305} (for 1.50 K X magnification photo) exhibit that carbon fibers did not pull out from the polyester matrix readily due to the better adhesion between fiber–matrix. At the time of sliding of the specimen generates heat at the interface which results in thermal softening of the polyester matrix and few wear debris would get entrenched into the matrix cause less wear and form a masking layer for fiber. Figure 4c depicts sample FPR_{215} in which the wear is in the form of micro-cracks, debris voids of the matrix with no fiber breakage. With the addition of filler material, at high load detachment of matrix results in the loss of fibers in the form hefty and prolonged fragments thus contributing in uncovering of fibrous area to sliding contact wear as serve fiber breakage leading to worn debris formation which cause abrasion on the counterface surface results
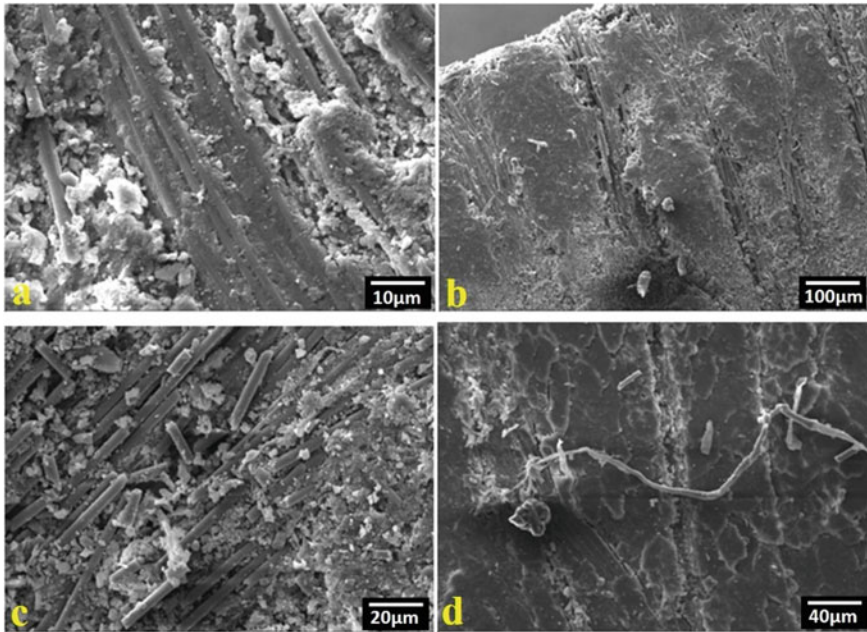
Fig. 4 Scanning electron micrograph worn surface of **a** FPR$_{305}$(1.5KX) **b** FPR$_{305}$(Magnification 200X) samples 200 mm sliding distance at 50 N load. **c** FPR$_{215}$ (Magnification 1.00KX) **d** FPR$_{125}$ (500X) samples 200 mm sliding distance at 50 N load

in exaggerating the roughness on the counterface as shown in Fig. 4b. As depicted in Fig. 4d, the transfer layer is thick and does not cover the whole surface of the counterface. In Fig. 4c, small wear debris is generated in FPR$_{215}$ filled composites. As the sliding distance increases resulted in bulk exfoliation of the transfer film, which cause high wear rate as the nanofiller added to the specimen. The heterogeneous distribution of filler due to lack of compaction is quite visible in the SEM images of composites with nano-filler composites. The particles are not uniformly distributed and hence result in particle agglomeration. The transfer films in case of unfilled composites were steady and well retained to the surfaces. Figure 4d shows the transfer layer is scattered with patchy surface showing agglomeration of the worn particles in diverse position of the counter face and leaving other position uncovered. The flexural strength of the material assesses the adhesion bonding between the filler and the matrix. As seen in preliminary study [15], as the filler material added to the composites, flexural strength reduces so as the wear loss.

5   Conclusion

This study reports the utilization of waste fishbone powder as a nanofiller in polyester hybrid composites.

- The wear loss for unfilled hybrid composite at 100, 150, and 200 mm sliding distance with 30 and 50 N load was highest for sample UFP_{120} is 0.012 and 0.018 gm, respectively. Whereas for filled hybrid composite with 5% FBP was highest for sample UFP_{125} is 0.0167 and 0.03 gm, respectively.
- The coefficient of friction (COF) for unfilled hybrid composite at 100, 150, and 200 mm sliding distance with 30 and 50 N loads was highest for sample UFP_{120} is 0.44 and 0.18, respectively. Whereas for filled hybrid composite with 5% FBP was highest for sample UFP_{125} is 0.305 and 0.41, respectively.
- In filled composites, the wear particles are in the form of long and hefty fragment probably due to exfoliation of transfer film from the counterface.
- SEM micrographs surface details revealed when composites subjected at higher load due to fracture of fiber, the micro-cracks and fiber pull out are prominent effect on the worn surface of the specimens.

References

1. Renukappa, N. M., Suresha, B., Devarajaiah, R. M., & Shivakumar, K. N. (2011). Dry sliding wear behaviour of organo-modified montmorillonite filled epoxy nanocomposites using Taguchi's techniques. *Materials and Design, 32*(8–9), 4528–4536.
2. Sampathkumaran, P., Seetharamu, S., Thomas, P., & Janardhana, M. (2005). A study on the effect of the type and content of filler in epoxy–glass composite system on the friction and slide wear characteristics. *Wear, 259*(1–6), 634–641.
3. Ashok Kumar, M., Ramachandra Reddy, G., Siva Bharathi, Y., Venkata Naidu, S., & Naga Prasad Naidu, V. (2010). Frictional coefficient, hardness, impact strength, and chemical resistance of reinforced sisal-glass fiber epoxy hybrid composites. *Journal of Composite Materials, 44*(26), 3195–3202.
4. Ramnath, B. V., Kokan, S. J., Raja, R. N., Sathyanarayanan, R., Elanchezhian, C., Prasad, A. R., et al. (2013). Evaluation of mechanical properties of abaca–jute–glass fiber reinforced epoxy composite. *Materials and Design, 51,* 357–366.
5. Wang, W. Y., Wang, G. Q., Zeng, X. F., Shao, L., & Chen, J. F. (2008). Preparation and properties of nano-CaCO3/acrylonitrile-butadiene-styrene composites. *Journal of Applied Polymer Science, 107*(6), 3609–3614.
6. Batra, N. K., & Dikshit, I. (2020). Evaluation of mechanical properties of polytherimide reinforced carbon/glass/aramid hybrid composites. In *Materials Today: Proceedings.*
7. Alexandre, M., & Dubois, P. (2000). Polymer-layered silicate nanocomposites: preparation, properties and uses of a new class of materials. *Materials Science and Engineering: R: Reports, 28*(1–2), 1–63.
8. Abd Razak, S. I., Ahmad Sharif, N. F., & Abdul Rahman, W. A. (2012). Biodegradable polymers and their bone applications: A review. *International Journal of Basic and Applied Sciences, 12,* 31–49.

9. Agunsoye, J. O., Talabi, S. I., Awe, O., & Kelechi, H. (2013). Mechanical properties and tribological behaviour of recycled polyethylene/cow bone particulate composite. *Journal of Materials Science Research, 2*(2), 41.

10. Omah, A. D., Aigbodion, V. S., Madu, S. C., Oji, E. O., Uyor, U. U., & Ude, S. (2019). Experimental correlation between the production parameter and mechanical properties of functional epoxy-cow bone particulate composites. *The International Journal of Advanced Manufacturing Technology, 101*(9–12), 2465–2474.

11. Periasamy, K., & Mohankumar, G. C. (2016). Sea coral-derived cuttlebone reinforced epoxy composites: Characterization and tensile properties evaluation with mathematical models. *Journal of Composite Materials, 50*(6), 807–823.

12. Pıhtılı, H., & Tosun, N. (2002). Effect of load and speed on the wear behaviour of woven glass fabrics and aramid fibre-reinforced composites. *Wear, 252*(11–12), 979–984.

13. Schwartz, C. J., & Bahadur, S. (2001). The role of filler deformability, filler–polymer bonding, and counterface material on the tribological behavior of polyphenylene sulfide (PPS). *Wear, 251*(1–12), 1532–1540.

14. Ahmed, K. S., Khalid, S. S., Mallinatha, V., & Kumar, S. A. (2011). Dry sliding wear behavior of SiC/Al$_2$O$_3$ filled jute/epoxy composites. *Materials and Design, 1980–2015*(36), 306–315.

15. Singh, H., Batra, N. K., & Dikshit, I. (2020). Development of new hybrid jute/carbon/fishbone reinforced polymer composite. In *Materials Today: Proceedings*.